EAST EUROPEAN JOURNAL OF PHYSICS. 3. 4-12 (2026)
DOI:10.26565/2312-4334-2026-3-01 ISSN 2312-4334

QUANTUM INFORMATION AND ENERGY SPECTRUM OF THE ULTRA GENERALIZED EXPONENTIAL–HYPERBOLIC POTENTIAL VIA THE NIKIFOROV–UVAROV METHOD

Etido P. Inyang[1]*, Jonathan E. Osang[2], Samuel E. Mopta[3]
[1]*Department of Physics, Faculty of Science, National Open University of Nigeria, Jabi-Abuja, Nigeria*
[2]*Department of Physics, University of Cross River State, Calabar, Nigeria*
[3]*Department of Physics, University of Calabar, Calabar, Nigeria*
**Corresponding Author e-mail: einyang@noun.edu.ng*
Received April 17, 2026; revised June 26, 2026; accepted June 30, 2026

This study presents a comprehensive investigation of quantum information measures for the one-dimensional Ultra Generalized Exponential–Hyperbolic Potential (UGEHP) within the framework of the Schrödinger equation. Analytical solutions for the energy eigenvalues and corresponding wave functions are obtained using the Nikiforov–Uvarov method. These solutions serve as the basis for evaluating Shannon entropy and Fisher information in both position and momentum spaces. The numerical results show that the total Shannon entropy satisfies the Beckner–Białynicki-Birula–Mycielski (BBM) inequality, while the Fisher information adheres to the Stam–Cramér–Rao bounds, thereby confirming consistency with fundamental quantum uncertainty principles. In addition, the energy spectrum exhibits a pronounced dependence on the screening parameter and quantum numbers, indicating the tunable confinement properties of the potential. The combined analysis establishes a clear connection between energy quantization, wavefunction localization, and information-theoretic measures, offering deeper insight into the effectiveness of the UGEHP model in describing complex quantum systems.
Keywords: *Probability density; Information-theoretic measures; Ultra Generalized Exponential–Hyperbolic Potential; Energy spectrum; Bound-state solutions*

INTRODUCTION

In recent years, quantum information theory has attracted considerable interest due to its deep impact on quantum computing, quantum communication, and fundamental physics. Among the different methods used to investigate quantum information measures, potential models have emerged as effective tools for gaining insights into the behavior of quantum systems [1,2]. Quantum information measures (QIM), including Shannon entropy, Fisher information, Rényi entropy, and Tsallis entropy, are essential for examining the localization and delocalization characteristics of wavefunctions (WF) in confined quantum systems [3,4]. These measures provide valuable insights into quantum uncertainty, correlations, and entanglement, which are essential for applications in quantum computing and information processing. While these techniques have been extensively applied to different potential models [5-7], studies specifically focusing on the Ultra Generalized Exponential–Hyperbolic Potential (UGEHP) remain limited. Due to its flexibility and tunability, the UGEHP serves as an ideal model for exploring complex quantum systems under external constraints. This potential encompasses a broad class of models, generalizing well-known potentials such as the Morse, Pöschl-Teller, and Eckart potentials [8]. It has been particularly useful in describing diatomic molecular interactions [9,10] and quarkonium systems [11,12] in both relativistic and non-relativistic frameworks. The functional form of the UGEHP includes multiple adjustable parameters, allowing for a detailed investigation of quantum information measures in relation to system confinement and external influences. Notably, this potential has emerged as an effective model for examining the interplay between quantum information measures and potential-driven quantum dynamics. This study aims to systematically analyze the information-theoretic properties and bound state energy associated with the UGEHP, providing new insights into its role in Quantum information measures.

The potential is expressed in the form [9].

$$V(r_o)=\frac{A_o e^{-4\alpha_o r_o}+B_o e^{-2\alpha_o r_o}}{r_o^{\,2}}+\frac{C_0 e^{-2\alpha_o r_o}-d_o\cosh(\delta_o\alpha_o r_o)e^{-\alpha_o r_o}+G_0\cos ech\ \alpha_o r_o\ e^{-\alpha_o r_o}}{r_o}+J_o, \tag{1}$$

where α_o is the screening parameter. The parameters $A_o, B_o, C_o, d_0, J_0, G_0, \delta_0$ are potential strengths.
when $\delta_o=1$

$$\cosh\alpha_o r_o=\frac{e^{\alpha_o r_o}+e^{-\alpha_o r_o}}{2},\cos ech\alpha_o r_o=\frac{2}{e^{\alpha_o r_o}-e^{-\alpha_o r_o}}. \tag{2}$$

The dependence of the potential on distance is illustrated in Figure 1.

Recent advancements in quantum information theory have highlighted the crucial role of entropic measures in understanding the uncertainty and information content of quantum states [13]. Shannon entropy serves as a global

Cite as: E.P. Inyang, J.E. Osang, S.E. Mopta, East Eur. J. Phys. 3, 4 (2026), https://doi.org/10.26565/2312-4334-2026-3-01

indicator of the uncertainty and randomness associated with electron localization and delocalization [14]. In contrast, Fisher information measures the sensitivity of a WF to external perturbations, making it essential in quantum metrology and estimation theory [15].

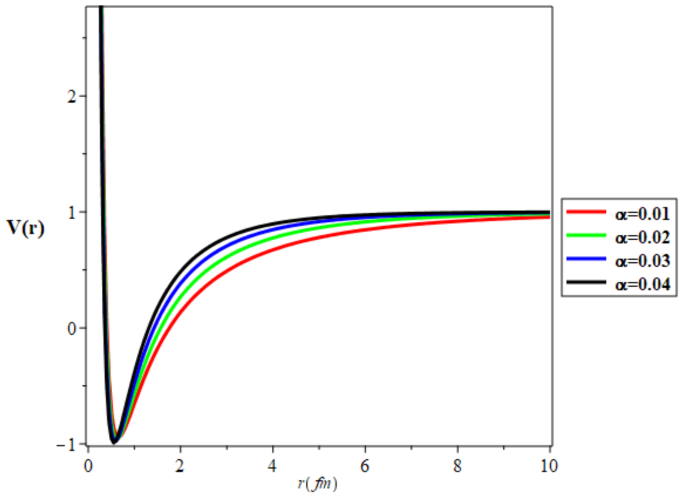

Figure 1. Variation of the Ultra Generalized Exponential–Hyperbolic Potential with position for different screening parameters and the arbitrary parameters $A_0 = 0.1, J_0 = -0.5, B_0 = 2, G_0 = 0.1, d_0 = 4, \delta_0 = 1, C_0 = 4$

In recent years, Shannon entropy has garnered considerable attention among quantum physics researchers due to its broad applications in modern quantum communication systems [16,17]. Its significance lies in its function as a generalized form of Heisenberg's uncertainty principle, providing a quantitative measure of uncertainty in quantum systems while also characterizing various physical properties [17]. Beckner-Białynicki-Birula and Mycielski (BBM) [18] introduced a novel formulation of Heisenberg's uncertainty principle in quantum mechanics, expressed as:

$$S_T = S_{r_o} + S_p \geq D\left(1 + 2\ln\pi\right), \tag{3}$$

In this context, D signifies the spatial dimension, while S_{r_o} *and* S_p represent the Shannon entropies in coordinate and momentum spaces, respectively. The total Shannon entropy, denoted as S_T, is the sum of these two components. The expressions for S_{r_o} *and* S_p are provided in references [19–21].

$$\begin{aligned} S_{r_o} &= -\int \left|\Psi\left(r_o,\theta_o,\varphi_o\right)\right|^2 \ln\left|\Psi\left(r_o,\theta_o,\varphi_o\right)\right|^2 d^3 r_o, \\ S_p &= -\int \left|\varphi_o\left(p\right)\right|^2 \ln\left|\varphi_0\left(p\right)\right|^2 d^3 p, \end{aligned} \tag{4}$$

where $d^3 r_o = r_o^{\,2} dr d\Omega, d^3 p = p^2 dp d\Omega, and\ d\Omega = \sin\theta_o d\theta_o d\varphi$ is the solid angle with $\Psi\left(r_o,\theta_o,\varphi\right)$ being the normalized wave function in the special coordinate. Also, $\rho\left(r_o\right) = \left|\Psi\left(r_o,\theta_0,\varphi\right)\right|^2$ is the probability density in the spatial co-ordinate, $\rho\left(p\right) = \left|\phi\left(p\right)\right|^2$ is the probability density in the momentum space and $\phi\left(p\right)$ is the associated normalized Fourier transform [21]. It should be noted that the entropy measures evaluated in this work correspond solely to the radial component of the wavefunction associated with the Ultra Generalized Exponential–Hyperbolic Potential. In the general three-dimensional framework, the total Shannon entropy comprises both radial and angular contributions. However, since the present study focuses on the radial solutions of the Schrödinger equation and the influence of the potential parameters on the radial probability density, only the radial contribution has been considered. Therefore, the reported entropy values represent radial Shannon entropies rather than the complete three-dimensional Shannon entropy [22]. The global measure is important because it enables researchers to analyze the uncertainty associated with the probability distribution. In contrast, Fisher information quantifies the efficiency of a measurement procedure in estimating quantum limits [23]. This information-theoretic tool primarily captures local variations in probability density [24]. Fisher information plays a crucial role in density functional theory [25], statistical estimation, and molecular chemical reactivity [26]. It is also strongly correlated with physical properties such as magnetic susceptibility and kinetic energy [27], providing valuable insights into electron correlation and atomic structure in both coordinate and momentum spaces [28].

As it is written,

$$\left.\begin{aligned} I_{r_0} &= \int \frac{|\rho'(r_0)|^2}{\rho(r_0)} dr_0 = 4\int |\psi'(r_0)|^2 \, dr_0 = 4\langle p^2\rangle - 2(2l+1)|m|\langle r_0^{-2}\rangle \\ I_p &= \int \frac{|\rho'(p)|^2}{\rho(p)} dp = 4\int |\psi'(p)|^2 \, dp = 4\langle r_0^2\rangle - 2(2l+1)|m|\langle p^{-2}\rangle \end{aligned}\right\}. \tag{5}$$

Unlike, the Shannon entropy that satisfied the BBM inequality, the Fisher information fulfill the Stam inequalities $I_{r_o} \le 4\langle r_o^2\rangle; I_p \le 4\langle p^2\rangle$ [29], and the Cramer–Rao inequalities $I_{r_o} \ge \frac{9}{\langle r_o^2\rangle}; I_p \ge \frac{9}{\langle p^2\rangle}$ [30]. Generally, for an arbitrary angular momentum quantum number of any central potential model, the two products of the Fisher information must satisfy the relation [30]

$$I_{r_o} I_p \ge 4\langle r_o^2\rangle\langle p^2\rangle\left[2 - \frac{2l+1}{l(l+1)}|m|\right]^2, \tag{6}$$

Extensive studies have explored Shannon entropy and Fisher information using well-motivated potential models. Udoh et al. [31] applied the Nikiforov–Uvarov functional analysis (NUFA) approach to solve the radial Schrödinger equation (SE) for the shifted Morse potential, deriving analytical energy eigenvalues and eigenfunctions, and analyzing quantum information measures. Nath and Roy [32] obtained exact solutions to the non-central Makarov potential and studied information-theoretic parameters for low-lying states. Inyang et al. [33] investigated the QIM with the screened modified Kratzer-Yukawa potential using the Nikiforov-Uvarov (NU) method, while Ikot et al. [34] applied NUFA to the Möbius square potential, both analyzing Shannon entropy and Fisher information. Onate et al. [35] employed supersymmetric techniques for the Morse potential to evaluate QIM and thermodynamic properties. Bloch and Cohen [36] linked Fisher information to an enhanced uncertainty principle. Omugbe et al. [37] used supersymmetric WKB for the QIM assessments, Boumali and Labidi [38] studied the Dirac oscillator under energy-dependent potentials, and Onate et al. [39] solved the SE for the Eckart-Manning-Rosen potential. In this work, the SE, an essential tool in quantum mechanics, is solved using the NU method [40] for the UGEHP. The derived energy equation and WF will serve as the foundation for analyzing QIM, including Shannon entropy, Fisher information, and bound-state energy. To the best of our knowledge, this has not been presented in the literature.

2. THE SOLUTION OF THE SCHRÖDINGER EQUATION WITH THE UGEHP

In this study, the NU method is employed to solve the SE, with detailed formulations available in Reference [40]. The radial Schrödinger equation for a spherically symmetric potential is given by [41]

$$\frac{d^2R(r_o)}{dr_o^2} + \left[\frac{2\mu}{\hbar^2}\left(E_{nl} - V(r_o)\right) - \frac{l(l+1)}{r_o^2}\right]R(r_o) = 0, \tag{7}$$

where E_{nl} is the eigenvalue, $R(r_o)$ is the eigenfunction, $\hbar$ is the reduced Planck's constant, r_o is the radial distance and μ is the reduced mass.

To address the centrifugal barrier in Equation (7), we employ the Greene-Aldrich approximation scheme (GAAS) [42]. This method provides an effective approximation for the centrifugal term, ensuring accuracy within a specific validity range $\alpha_o << 1$, . Under these conditions, the centrifugal term transforms into the following expression:

$$\frac{1}{r_o^2} \approx \frac{4\alpha_o^2}{\left(1 - e^{-\alpha_o r_o}\right)^2} \Rightarrow \frac{1}{r_o} \approx \frac{2\alpha_o}{\left(1 - e^{-2\alpha_o r_o}\right)}. \tag{8}$$

Substituting Eqs. (1), (2), and (8) into Eq. (7) and introducing an appropriate coordinate transformation $q_o = e^{-2\alpha_o r_o}$ gives

$$\frac{d^2\psi(q_o)}{dq_o^2} + \frac{1-q_o}{q_o(1-q_o)}\frac{d\psi(q_o)}{dq_o} + \frac{1}{\left[q_o(1-q_o)\right]^2}\begin{bmatrix} -\left(\varepsilon^2 + \alpha_{o1}\right)q_o^2 + \\ \left(2\varepsilon^2 - \alpha_{o2}\right)q_o - \left(\varepsilon^2 - \alpha_{o3}\right)\end{bmatrix}\psi(q_o) = 0, \tag{9}$$

where:

$$\left.\begin{aligned}
-\varepsilon^2 &= \frac{\mu}{2\alpha_o{}^2\hbar^2}\left(E_{nl}-J_o\right),\\
\alpha_{o1} &= \frac{2\mu}{4\alpha_o{}^2\hbar^2}\left(4\alpha_o{}^2A_o-2\alpha_oC_0+\alpha_od_o\right),\\
\alpha_{o2} &= \frac{2\mu}{4\alpha_o{}^2\hbar^2}\left(4\alpha_o{}^2B_o+2\alpha_oC_o\right),\\
\alpha_{o3} &= \frac{2\mu}{4\alpha_o{}^2\hbar^2}\left(4\alpha_oG_o-\alpha_od_o\right)+l\left(l+1\right)
\end{aligned}\right\}. \tag{10}$$

For this research, the NU method is employed, as outlined in Ref. [40]. This approach yields the eigenvalue and eigenfunction equations, which are expressed as follows:

$$E_{nl} = -\frac{2\alpha_o{}^2\hbar^2}{\mu}\left[\frac{\frac{\mu}{2\alpha_o{}^2\hbar^2}\left(4\alpha_oG_o+2\alpha_oC_o-4\alpha_o{}^2A_o-2\alpha_od_o+\frac{2\alpha_o{}^2\hbar^2}{\mu}l\left(l+1\right)\right)}{2\left(n+\chi_0\right)}+\frac{\left(n+\chi_0\right)}{2}\right]^2 \tag{11}$$

$$+4\alpha_oG_o-\alpha_od_o+\frac{2\alpha_o{}^2\hbar^2}{\mu}\left[l\left(l+1\right)\right]+J_o$$

where:

$$\chi_0 = \frac{1}{2}+\sqrt{\frac{2\mu}{\hbar^2}\left(A_o+B_0+\frac{G_0}{\alpha_0}\right)+\frac{1}{4}+l\left(l+1\right)} \tag{12}$$

The WF is expressed in terms of the Jacobi polynomial as follows:

$$\psi_{nl}\left(q_o\right) = \mathrm{N}_{nl}\, q_o^{\sqrt{\varepsilon^2+\alpha_{o3}}}\left(1-q_o\right)^{\left(\frac{1}{2}+\frac{1}{2}\sqrt{\alpha_{o1}+\alpha_{o2}+\alpha_{o3}+\frac{1}{4}}\right)} P_n^{\left(2\sqrt{\varepsilon^2+\alpha_{o3}},\,2\sqrt{\alpha_{o1}+\alpha_{o2}+\alpha_{o3}+\frac{1}{4}}\right)}\left(1-2q_o\right), \tag{13}$$

where N_{nl} represents the normalization constant, which can be determined by applying the normalization condition:

$$\int_0^\infty R_{nl}(r_o)R_{nl}^*(r_o)dr_o = 1 \tag{14}$$

3. RESULTS AND DISCUSSION

The wave functions and energy eigenvalues of the Schrödinger equation with the Ultra Generalized Exponential–Hyperbolic Potential (UGEHP) are obtained analytically using the Nikiforov–Uvarov method. Based on these solutions, Shannon entropy and Fisher information are evaluated in both position and momentum spaces to investigate the information-theoretic properties of the system.

Tables 1 and 2 present the calculated Shannon entropies and Fisher information, respectively, for the ground state at different values of the screening potential parameter (SPP), ranging from 0.01 to 0.10. The results in Table 1 show that the total Shannon entropy satisfies the Beckner–Białynicki-Birula–Mycielski (BBM) inequality, which establishes a fundamental lower bound on the sum of the position- and momentum-space entropies. This confirms that the uncertainty associated with the quantum system is accurately captured. Similarly, the Fisher information values reported in Table 2 satisfy the Stam–Cramér–Rao (SCR) inequality, demonstrating consistency with the fundamental limits of statistical estimation and measurement precision in quantum mechanics. These findings validate the theoretical framework employed and further emphasize the intimate connection between quantum uncertainty and information-theoretic measures.

Table 3 presents the variation of the energy eigenvalues of the UGEHP with the principal quantum number (n), angular momentum quantum number (l), and screening parameter (α_o). The results display the characteristic behavior expected for quantum systems governed by short-range interaction potentials. For a fixed value of α_o, the energy eigenvalues increase with increasing (n), corresponding to transitions from lower to higher excited states. As the particle occupies larger spatial regions in these excited states, it becomes less tightly bound within the potential well, resulting in a reduction in the magnitude of the binding energy.

For a given value of (n), the energy eigenvalues also increase with increasing angular momentum quantum number (l). This behavior arises from the centrifugal contribution to the effective potential, which introduces a repulsive term proportional to ($l(l+1)/r^2$). As l increases, the particle is pushed away from the central region of the potential, leading to reduced localization and higher energy levels. Consequently, the degeneracy commonly associated with ideal central potentials is lifted, reflecting the non-Coulombic nature of the UGEHP.

The influence of the screening parameter (α_o) is equally significant. As α_o increases, the energy eigenvalues shift toward higher values, indicating weaker binding of the system. Physically, stronger screening reduces the effective range of the interaction potential and weakens its confining capability, thereby producing less localized quantum states. Conversely, smaller values of α_o correspond to weaker screening and stronger confinement, resulting in lower energy eigenvalues and enhanced localization. These results demonstrate that the UGEHP provides a highly tunable framework for controlling the spectral properties of quantum systems. Furthermore, the dependence of the energy spectrum on n, l, and α_o directly influences wave-function localization and consequently affects the behavior of Shannon entropy and Fisher information, establishing a clear relationship between spectral characteristics and quantum information measures.

To further illustrate the localization properties of the system, Figure 2 depicts the ground-state wave function in position space for various values of the screening parameter. It is observed that decreasing the screening parameter leads to a more sharply peaked wave function that shifts toward shorter distances, indicating stronger localization and enhanced confinement of the particle. In contrast, increasing the screening parameter broadens the wave function, reflecting weaker confinement and greater spatial delocalization.

A similar trend is observed in Figure 3, which shows the corresponding probability density distributions. As the screening parameter decreases, the probability density becomes more concentrated and exhibits a higher peak, indicating an increased likelihood of finding the particle within a localized spatial region. Conversely, increasing the screening parameter results in a broader probability distribution, consistent with reduced confinement. These graphical results support the trends observed in the energy spectrum and information-theoretic quantities, further confirming the strong influence of the screening parameter on the localization and quantum behavior of the system.

Table 1. Shannon entropies for the ground state for the Ultra Generalized Exponential–Hyperbolic Potential

α_o	S_{r_o}	S_p	$S_T \geq 2.14473$
0.01	2.457340	0.123150	2.58049
0.02	2.218196	0.190375	2.40857
0.03	2.107611	0.244707	2.35232
0.04	2.047531	0.288308	2.33584
0.05	2.014564	0.322102	2.33667
0.06	1.998876	0.338815	2.33769
0.07	1.995648	0.343301	2.33895
0.08	2.002399	0.338093	2.34049
0.09	2.017946	0.324438	2.34238
0.10	2.041994	0.302725	2.34472

Table 2. Fisher Information entropies for the ground state for the Ultra Generalized Exponential–Hyperbolic Potential

α_o	I_{r_o}	I_p	$I_{r_o} I_p \geq 4$
0.01	0.552196	8.333156	4.601897
0.02	0.574371	8.347331	4.794750
0.03	0.591231	8.355159	4.939883
0.04	0.670146	8.391088	5.623137
0.05	0.682951	8.404442	5.739414
0.06	0.699872	8.417453	5.891126
0.07	0.700436	8.426681	5.902263
0.08	0.712074	8.432596	6.004092
0.09	0.735457	8.467918	6.227006
0.10	0.740081	8.601521	6.365387

Table 3 Energy eigenvalues (in eV) of the Ultra Generalized Exponential–Hyperbolic Potential with the parameters $\{A_0 = 0.1, J_0 = -0.5, B_0 = 2, G_0 = 0.1, d_0 = 4, \hbar = \mu = 1, C_0 = 4\}$ for various values of α_o = 0.01, 0.02, 0.03 and 0.04

n	l	α_o = 0.01	α_o = 0.02	α_o = 0.03	α_o = 0.04
0	0	−0.540123	−0.580658	−0.621715	−0.663342
1	0	−0.540528	−0.582224	−0.625141	−0.669298
	1	−0.540524	−0.582195	−0.625054	−0.669112
2	0	−0.541104	−0.584345	−0.629689	−0.677129
	1	−0.541107	−0.584363	−0.629744	−0.677243
	2	−0.541112	−0.584394	−0.629831	−0.677419

n	l	$\alpha_o = 0.01$	$\alpha_o = 0.02$	$\alpha_o = 0.03$	$\alpha_o = 0.04$
3	0	−0.541820	−0.586942	−0.635240	−0.686681
	1	−0.541833	−0.587025	−0.635479	−0.687169
	2	−0.541855	−0.587166	−0.635866	−0.687941
	3	−0.541883	−0.587332	−0.636303	−0.688790
4	0	−0.542659	−0.589981	−0.641744	−0.697894
	1	−0.542684	−0.590140	−0.642191	−0.698798
	2	−0.542729	−0.590413	−0.642928	−0.700253
	3	−0.542787	−0.590739	−0.643778	−0.701894
	4	−0.542850	−0.591076	−0.644630	−0.703506
5	0	−0.543614	−0.593444	−0.649180	−0.710742
	1	−0.543653	−0.593687	−0.649850	−0.712086
	2	−0.543724	−0.594105	−0.650967	−0.714278
	3	−0.543815	−0.594613	−0.652278	−0.716796
	4	−0.543916	−0.595146	−0.653615	−0.719316
	5	−0.544021	−0.595667	−0.654892	−0.721692
6	0	−0.544678	−0.597324	−0.657534	−0.725211
	1	−0.544733	−0.597655	−0.658436	−0.727010
	2	−0.544832	−0.598228	−0.659955	−0.729976
	3	−0.544960	−0.598932	−0.661761	−0.733428
	4	−0.545105	−0.599681	−0.663628	−0.736937
	5	−0.545255	−0.600421	−0.665435	−0.740292
	6	−0.545403	−0.601127	−0.667130	−0.743410

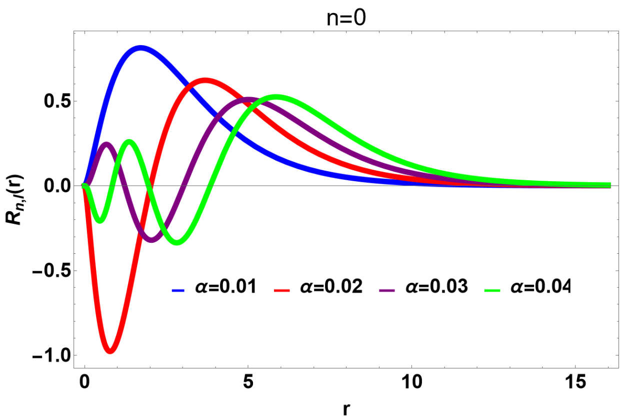

Figure 2. The ground state wave function in position space is analyzed for different values of the screening potential parameter

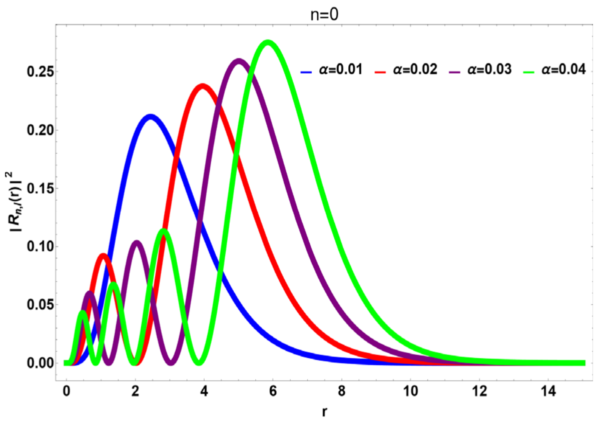

Figure 3. The probability density of the ground state in position space is examined for different values of the screening potential parameter

4. CONCLUSIONS

In this work, the Schrödinger equation for the Ultra Generalized Exponential–Hyperbolic Potential has been solved using the Nikiforov–Uvarov method, yielding an expression for the energy eigenvalues and corresponding wave functions. The resulting energy spectrum demonstrates a clear dependence on the principal and angular momentum quantum numbers, as well as on the screening parameter, confirming the tunable nature of the potential in controlling quantum confinement. The analysis of Shannon entropy and Fisher information in both position and momentum spaces reveals that the system satisfies the BBM and Stam–Cramér–Rao inequalities, thereby reinforcing the consistency of the results with fundamental quantum mechanical uncertainty relations. Moreover, the interplay between energy quantization and information-theoretic measures highlights the connection between spectral properties and wavefunction localization. Overall, the findings establish the UGEHP as a robust and versatile model for investigating quantum information measures in bound systems, with potential applications in molecular physics and quantum information science.

Availability of Data and Materials
All data presented in this study are derived from the analytical equations provided within the article.

Competing Interests
The authors declare that they have no competing interests.

Funding
This research was supported by the Tertiary Education Trust Fund (TETFUND) of Nigeria through the Institutional-Based Research Grant at the National Open University of Nigeria (NOUN) (Grant No. NOUN/TETFIBR25/FACSCIENCES/063).

Acknowledgements
Dr. Etido P. Inyang gratefully acknowledges the TETFUND of Nigeria for financial support via the Institutional-Based Research Grant at NOUN (Grant No. NOUN/TETFIBR25/FACSCIENCES/063).

Authors'Contributions
E. P. Inyang: Conceptualization, resources, investigation, and funding acquisition. **J. E. Osang:** Validation and computation.
S. E. Mopta: Writing—review and editing.
All authors have read and approved the final version of the manuscript.

ORCID
Etido P. Inyang, https://orcid.org/0000-0002-5031-3297; **Samuel E. Mopta,** https://orcid.org/0009-0007-3114-9843

REFERENCES
[1] E.P. Inyang, A.E.L. Aouami, N. Ali, R. Endut, N.R. Ali, & S.A. Aljunid, "Information entropies with Varshni-Hellmann potential in higher dimensions," Physics Open, **20**, 100220 (2024). https://doi.org/10.1016/j.physo.2024.100220
[2] E.P.Inyang, I.M. Nwachukwu, C.C. Ekechukwu, I.B. Ekong, E.S. William, K.M. Lawal, J. Simon, *et al*., "Analytical Solution of The Class of Inversely Quadratic Yukawa Potential with Application to Quantum Mechanical Systems," Eurasian Physical Technical Journal, **21**(4), 118–130 (2024). https://doi.org/10.31489/2024No4/118-130
[3] J.S. Dehesa, A.I. Aptekarev, V.S. Buyarov, & R.J. Yáñez, "Strong asymptotics of Laguerre polynomials and information entropies of two-dimensional harmonic oscillator and one-dimensional Coulomb potentials," Journal of Mathematical Physics, **39**(6), 3050-3060 (1998). https://doi.org/10.1063/1.532238
[4] S.H. Patil, & K.D. Sen, "Scaling properties of net information measures for bound states of spherical model potentials confined with finite barrier," Journal of Chemical Sciences, **124**(1), 241-245 (2012). https://doi.org/10.1007/s12039-012-0222-8
[5] E. Omugbe, O.E. Osafile, I.B. Okon, E.S. Eyube, E.P. Inyang, U.S. Okorie, A. Jahanshir, & C.A. Onate, "Non-relativistic bound state solutions with α-deformed Kratzer-type potential using the super-symmetric WKB method: Application to theoretic-information measures," The European Physical Journal D, **76**(4), 72 (2022). https://doi.org/10.1140/epjd/s10053-022-00395-6
[6] E.P. Inyang, A.E.L. Aouami, N. Ali, R. Endut, N. Rusli, & S.A. Aljunid, "Determination of probability density, position and momentum uncertainties, and information theoretic measures using a class of inversely quadratic Yukawa potential," Scientific Reports, **15**, 10565 (2025). https://doi.org/10.1038/s41598-024-78969-0
[7] I.B. Okon, C.A. Onate, R. Horchani, O.O. Popoola, E. Omugbe, E.S. William, U.S. Okorie, *et al*., "Thermomagnetic properties and its effects on Fisher entropy with Schioberg plus Manning-Rosen potential (SPMRP) using Nikiforov-Uvarov functional analysis (NUFA) and supersymmetric quantum mechanics (SUSYQM) methods," Scientific reports, **13**(1), 8193 (2023). https://doi.org/10.1038/s41598-023-34521-0
[8] F.C.E. Lima, A.R.P. Moreira, C.A.S. Almeida, C.O. Edet, & N. Ali, "Quantum information entropy of a particle trapped by the Aharonov–Bohm-type effect," Physica Scripta, **98**(6), 065111 (2023). https://doi.org/10.1088/1402-4896/acd309
[9] R.H. Parmar, "Solution of the Ultra Generalized Exponential–Hyperbolic Potential in Multi-dimensional Space," Few-Body Systems, **61**(4), 39 (2020). https://doi.org/10.1007/s00601-020-01572-2
[10] E.P. Inyang, N. Ali, R. Endut, & S.A. Aljunid, "Energy Spectra, Expectation Values, and Thermodynamic Properties of HCl and LiH Diatomic Molecules," Eurasian Physical Technical Journal, **21**(1(47)), 124–137 (2024). https://doi.org/10.31489/2024No1/124-137
[11] E.P. Inyang, J.E. Ntibi, E.A. Ibanga, F. Ayedun, E.P. Inyang, E.E. Ibekwe, E.S. William, & I.O. Akpan, "Thermodynamic properties and mass spectra of a quarkonium system with Ultra Generalized Exponential–Hyperbolic Potential," Communication in Physical Sciences, **7**(2), 97–114 (2021).
[12] J.E. Ntibi, E.P. Inyang, E.P. Inyang, E.S. William, & E.E. Ibekwe, "Solutions of the N-dimensional Klein-Gordon Equation with Ultra Generalized Exponential–Hyperbolic Potential to Predict the Mass Spectra of Heavy Mesons," Jordan Journal of Physics, **15**(4), 393–402 (2022). https://doi.org/10.47011/15.4.8
[13] V. Majernik, & E. Majernikova, "Standard and entropic uncertainty relations of the finite well," Journal of Physics A: Mathematical and General, **35**(27), 5751-5761 (2002). https://doi.org/10.1088/0305-4470/35/27/314
[14] C.E. Shannon, & W. Weaver, "A mathematic theory of communication," Bell Syst. Tech. J. **7**(3), 379-423 (1948).
[15] M. Ghafourian, & H. Hassanabadi, "Shannon information entropies for the three-dimensional Klein-Gordon problem with the Poschl-Teller potential," Journal of the Korean Physical Society, **68**(11), 1267-1271 (2016). https://doi.org/10.3938/jkps.68.1267
[16] E.P. Inyang, I.B. Okon, F.O. Faithpraise, E.S. William, P.O. Okoi, & E.A. Ibanga, "Quantum mechanical treatment of Shannon entropy measure and energy spectra of selected diatomic molecules with the modified Kratzer plus generalized inverse quadratic Yukawa potential model," Journal of Theoretical and Applied Physics, **17**(4), (2023). https://doi.org/10.57647/j.jtap.2023.1704.40
[17] C. Onate, I.B. Okon, J.A. Akinpelu, O.O. Ajani, O. Adedewe, & B.B. Deji-Jinadu, "Shannon entropy and thermodynamic properties of an inversely quadratic Yukawa potential model," Journal of the Nigerian Society of Physical Sciences, **6**(4), 2134-2134 (2024). https://doi.org/10.46481/jnsps.2024.2134
[18] I. Bialynicki-Birula, "Formulation of the uncertainty relations in terms of the Rényi entropies," Physical Review A—Atomic, Molecular, and Optical Physics, **74**(5), 052101 (2006). https://doi.org/10.1103/PhysRevA.74.052101
[19] S. Majumdar, N. Mukherjee, & A.K. Roy, "Information entropy and complexity measure in generalized Kratzer potential," Chemical Physics Letters, **716**, 257-264 (2019). https://doi.org/10.1016/j.cplett.2018.12.032
[20] Pooja, A. Sharma, R. Gupta, & A. Kumar, "Quantum information entropy of modified Hylleraas plus exponential Rosen Morse potential and squeezed states," International Journal of Quantum Chemistry, **117**(11), e25368 (2017). https://doi.org/10.1002/qua.25368

[21] A.N. Ikot, G.J. Rampho, P.O. Amadi, U.S. Okorie, M.J. Sithole, & M.L. Lekala, "Quantum information-entropic measures for exponential-type potential," Results in Physics, **18**, 103150 (2020). https://doi.org/10.1016/j.rinp.2020.103150
[22] S. Majumdar, N. Mukherjee, & A.K. Roy, "Information entropy in excited states in confined quantum systems," (No. arXiv: 2401.02645). https://doi.org/10.48550/arXiv.2401.02645
[23] S.B.Sears, R.G. Parr, & U. Dinur, "On the quantum-mechanical kinetic energy as a measure of the information in a distribution," Israel Journal of Chemistry, **19**(1-4), 165-173 (1980). https://doi.org/10.1002/ijch.198000018
[24] E.P. Inyang, F. Ayedun, E.A. Ibanga, & K.M. Lawal, "Analytical Solutions to the Schrödinger equation with collective potential models: application to Quantum Information Theory," East European Journal of Physics, (4), 87-98 (2022). https://doi.org/10.26565/2312-4334-2022-4-07
[25] C.N. Isonguyo, K.J. Oyewumi, & O.S. Oyun, "Quantum information-theoretic measures for the static screened Coulomb potential," International Journal of Quantum Chemistry, **118**(15), e25620 (2018). https://doi.org/10.1002/qua.25620
[26] R.A.Fisher, "Theory of statistical estimation," in: *Mathematical proceedings of the Cambridge philosophical society*, **22**(5), 700-725 (1925). Cambridge University Press.
[27] R.G. Parr, & Y.A. Wang, "Kohn-Sham method as a free-energy minimization at infinite temperature," Physical Review A, **55**(4), 3226 (1997). https://doi.org/10.1103/physreva.55.3226
[28] E. Romera, P. Sánchez-Moreno, & J.S. Dehesa, "The Fisher information of single-particle systems with a central potential," Chemical physics letters, **414**(4-6), 468-472 (2005). https://doi.org/10.1016/j.cplett.2005.08.032
[29] E. Romera, P. Sánchez-Moreno, & J.S. Dehesa, "The Fisher information of single-particle systems with a central potential," Chemical physics letters, **414**(4-6), 468-472 (2005). https://doi.org/10.1016/j.cplett.2005.08.032
[30] A. Dembo, T.M. Cover, & J.A. Thomas, "Information theoretic inequalities," IEEE Transactions on Information theory, **37**(6), 1501-1518 (1991). https://doi.org/10.1109/18.104312
[31] M.E. Udoh, P.O. Amadi, U.S. Okorie, A.D. Antia, L.F. Obagboye, R. Horchani, N. Sulaiman, & A.N. Ikot, "Thermal properties and quantum information theory with the shifted Morse potential," Pramana, **96**(4), 222 (2022). https://doi.org/10.1007/s12043-022-02463-3
[32] D. Nath, & P. Roy, "Time-dependent rationally extended Pöschl–Teller potential and some of its properties," The European Physical Journal Plus, **135**(10), 1-13 (2020). https://doi.org/10.1140/epjp/s13360-020-00815-9
[33] E.P.Inyang, E. Omugbe, M. Abu-Shady, & E.S. William, "Investigation of quantum information theory with the screened modified Kratzer and a class of Yukawa potential model," The European Physical Journal Plus, **138**(11), 969 (2023). https://doi.org/10.1140/epjp/s13360-023-04617-7
[34] A.N.Ikot, G.J. Rampho, P.O. Amadi, M.J. Sithole, U.S. Okorie, & M.I. Lekala, "Shannon entropy and Fisher information-theoretic measures for Mobius square potential," The European Physical Journal Plus, **135**(6), 503 (2020). https://doi.org/10.1140/epjp/s13360-020-00525-2
[35] C.A.Onate, I.B. Okon, U.E. Vincent, E. Omugbe, E.S. Eyube, M.C. Onyeaju, & G.O. Jude, "Theoretic measure and thermal properties of a standard Morse potential model," Journal of Molecular Modeling, **29**(2), 34 (2023). https://doi.org/10.1007/s00894-022-05441-z
[36] Y. Bloch, & E. Cohen, "The identification of mean quantum potential with fisher information leads to a strong uncertainty relation," Foundations of Physics, **52**(6), 117 (2022). https://doi.org/10.1007/s10701-022-00638-x
[37] E. Omugbe, O.E. Osafile, I.B. Okon, A. Jahanshir, I.J. Njoku, & C.A. Onate, "Fisher information entropies and the strength of an oscillator under a mixed hyperbolic Pöschl–Teller potential function," Indian Journal of Physics, **97**(12), 3411-3417 (2023). https://doi.org/10.1007/s12648-023-02676-1
[38] A. Boumali, & M. Labidi, "The solutions on one-dimensional Dirac oscillator with energy-dependent potentials and their effects on the Shannon and Fisher quantities of quantum information theory," Journal of Low Temperature Physics, **204**(1), 24-47 (2021). https://doi.org/10.1007/s10909-021-02596-6
[39] C.A.Onate, M.C. Onyeaju, A.N. Ikot, J.O.A. Idiodi, & J.O. Ojonubah, "Eigen solutions, Shannon entropy and fisher information under the Eckart Manning Rosen potential model," Journal of the korean physical society, **70**(4), 339-347 (2017). https://doi.org/10.3938/jkps.70.339
[40] A.F. Nikiforov, & V.B. Uvarov, *Special functions of mathematical physics*, Vol. 205, (Basel, Birkhäuser, 1988).
[41] R. Shankar, *Principles of Quantum Mechanics*, 2nd ed., (Springer, New York, 1994).
[42] R.L. Greene, & C. Aldrich, "Variational wave functions for a screened Coulomb potential," Physical Review A, **14**(6), 2363 (1976). https://doi.org/10.1103/PhysRevA.14.2363

APPENDIX A: Review of Nikiforov-Uvarov (NU) method

The NU method was proposed by Nikiforov and Uvarov [40] to transform Schrödinger-like equations into a second-order differential equation via a coordinate transformation $x_c = x_c(r)$, of the form

$$\psi''(x_c) + \frac{\tilde{\tau}(x_c)}{\sigma(x_c)}\psi'(s) + \frac{\tilde{\sigma}(x_c)}{\sigma^2(x_c)}\psi(x_c) = 0 \tag{A1}$$

where $\tilde{\sigma}(x_c)$, and $\sigma(x_c)$ are polynomials, at most second degree and $\tilde{\tau}(x_c)$ is a first-degree polynomial. The exact solution of Eq.(A1) can be obtain by using the transformation.

$$\psi(x_c) = \phi(x_c)\, y(x_c) \tag{A2}$$

This transformation reduces Eq.(A1) into a hypergeometric-type equation of the form

$$\sigma(x_c)\, y''(x_c) + \tau(x_c)\, y'(x_c) + \lambda y(x_c) = 0 \tag{A3}$$

The function $\phi(x_c)$ can be defined as the logarithm derivative

$$\frac{\phi'(x_c)}{\phi(x_c)} = \frac{\pi(x_c)}{\sigma(x_c)} \tag{A4}$$

With $\pi(x_c)$ being at most a first-degree polynomial. The second part of $\psi(x_c)$ being $y(x_c)$ in Eq. (A2) is the hypergeometric function with its polynomial solution given by Rodrigues relation as

$$y(x_c) = \frac{B_{nl}}{\rho(x_c)}\frac{d^n}{dx_c{}^n}\left[\sigma^n(x_c)\rho(x_c)\right] \tag{A5}$$

where B_{nl} is the normalization constant and $\rho(x_c)$ the weight function which satisfies the condition below;

$$\left(\sigma(x_c)\rho(x_c)\right)' = \tau(x_c)\rho(x_c) \tag{A6}$$

where also

$$\tau(x_c) = \tilde{\tau}(x_c) + 2\pi(x_c) \tag{A7}$$

For bound solutions, it is required that

$$\tau'(x_c) < 0 \tag{A8}$$

The eigenfunctions and eigenvalues can be obtained using the definition of the following function $\pi(s)$ and parameter λ, respectively:

$$\pi(s) = \frac{\sigma'(s) - \tilde{\tau}(s)}{2} \pm \sqrt{\left(\frac{\sigma'(s) - \tilde{\tau}(s)}{2}\right)^2 - \tilde{\sigma}(s) + k\sigma(s)} \tag{A9}$$

and

$$\lambda = k_- + \pi'_-(x_c) \tag{A10}$$

The value of k can be obtained by setting the discriminant in the square root in Eq. (A9) equal to zero. As such, the new eigenvalues equation can be given as

$$\lambda + n\tau'(x_c) + \frac{n(n-1)}{2}\sigma''(x_c) = 0, (n = 0,1,2,...) \tag{A11}$$

КВАНТОВИЙ ІНФОРМАЦІЙНИЙ ТА ЕНЕРГЕТИЧНИЙ СПЕКТР УЛЬТРАУЗАГАЛЬНЕНОГО ЕКСПОНЕНЦІАЛЬНО-ГІПЕРБОЛІЧНОГО ПОТЕНЦІАЛУ ЗА ДОПОМОГОЮ МЕТОДУ НІКІФОРОВА-УВАРОВА

Етідо П. Іньянг[1], Джонатан Е. Осанг[2], Семюел Е. Мопта[3]
[1]*Кафедра фізики, Факультет природничих наук, Національний відкритий університет Нігерії, Джабі-Абуджа, Нігерія*
[2]*Кафедра фізики, Університет штату Крос-Рівер, Калабар, Нігерія.*
[3]*Кафедра фізики, Університет Калабара, Калабар, Нігерія.*

Це комплексне дослідження квантових інформаційних мір для одновимірного ультраузагальненого експоненціально-гіперболічного потенціалу (УУГГП) в рамках рівняння Шредінгера. Аналітичні розв'язки для власних значень енергії та відповідних хвильових функцій отримані за допомогою методу Нікіфорова-Уварова. Ці розв'язки слугують основою для оцінки ентропії Шеннона та інформації Фішера як у просторі положення, так і в просторі імпульсу. Числові результати показують, що повна ентропія Шеннона задовольняє нерівність Бекнера-Бялиницького-Бірули-Міцельського (BBM), тоді як інформація Фішера дотримується меж Стама-Крамера-Рао, що підтверджує узгодженість з фундаментальними принципами квантової невизначеності. Крім того, енергетичний спектр демонструє виражену залежність від параметра екранування та квантових чисел, що вказує на властивості налаштованого обмеження потенціалу. Комбінований аналіз встановлює чіткий зв'язок між квантуванням енергії, локалізацією хвильової функції та інформаційно-теоретичними заходами, пропонуючи глибше розуміння ефективності моделі UGEHP в описі складних квантових систем.

Ключові слова: *щільність ймовірності; інформаційно-теоретичні заходи; ультраузагальнений експоненціально-гіперболічний потенціал; енергетичний спектр; розв'язки зв'язаних станів*

East European Journal of Physics. **3.** 13-19 (2026)
DOI:10.26565/2312-4334-2026-3-02 ISSN 2312-4334

THEORETICAL STUDY OF THE VIBRATIONAL SPECTRUM OF THE CESIUM DIMER USING A HYBRID INTERACTION MODEL

Samuel E. Mopta[1], Victor C. Onuabuchi[2], Etido P. Inyang[3]*
[1]*Department of Physics, University of Calabar, Calabar, Nigeria*
[2]*Department of Industrial Physics, Enugu State University of Science and Technology, Enugu, Nigeria*
[3]*Department of Physics, Faculty of Science, National Open University of Nigeria, Jabi-Abuja, Nigeria*
**Corresponding Author e-mail: einyang@noun.edu.ng*
Received April 16, 2026; revised June 20, 2026; accepted June 24, 2026

The present study investigates the quantum properties of the cesium dimer (Cs_2) using a hybrid interaction model that combines the Möbius square potential with the screened Kratzer potential (MSSKP). The vibrational energy levels are obtained analytically by solving the Schrödinger equation within the framework of the parametric Nikiforov–Uvarov (pNU) method. The calculated spectra exhibit excellent agreement with available experimental Rydberg–Klein–Rees (RKR) data, demonstrating the validity of the proposed model. Comparative analysis with established potential models, namely the Morse and Manning–Rosen potentials, reveals the superior predictive performance of the MSSKP approach. In particular, the MSSKP model achieves a minimum mean absolute error (MAE) of 0.0234 cm^{-1}, compared with 0.2364 cm^{-1} and 0.0517 cm^{-1} for the Morse and Manning–Rosen potentials, respectively. These results highlight the enhanced accuracy and reliability of the MSSKP model in describing the vibrational spectrum of Cs_2. The findings further provide valuable insights into molecular structure, bonding interactions, and quantum behavior, underscoring the potential of the proposed framework for applications in quantum chemistry, molecular spectroscopy, and the theoretical modeling of diatomic molecular systems.
Keywords: *Hybrid interaction model; Mean absolute error; Rydberg–Klein–Rees (RKR) data; Analytical method, Molecular spectroscopy*

1. INTRODUCTION

Accurate theoretical descriptions of molecular systems remain a central pursuit in quantum mechanics and molecular physics, where the interplay between nuclear motion and interatomic forces governs the vibrational, rotational, spectroscopic, and thermodynamic behavior of molecules [1–3]. Among these systems, diatomic molecules serve as fundamental models for understanding molecular interactions due to their relative simplicity and rich physical characteristics [4]. The cesium dimer (Cs_2) is of particular interest because of its unique electronic configuration, large atomic mass, pronounced relativistic effects, and wide applicability across various fields, including atomic physics, molecular spectroscopy, quantum computation, and precision metrology [5]. Cesium dimer (Cs_2) plays a key role in the advancement of atomic clocks, laser cooling technologies, and the exploration of long-range molecular interactions and potential energy surfaces [6]. Despite its importance, achieving a precise theoretical representation of Cs_2 remains challenging due to its highly anharmonic vibrational structure.

Over the years, numerous molecular potential models such as the Morse, Kratzer, Rosen–Morse, and Tietz–Hua potentials have been developed to approximate interatomic interactions in diatomic molecules [7–9]. While these models are analytically convenient and effective for light molecules, their accuracy decreases significantly for heavy diatomic systems such as Cs_2, particularly in higher vibrational and rotational states. This limitation arises because many traditional potentials lack sufficient flexibility to accurately describe the potential energy surface near the dissociation limit, often leading to deviations from experimental data obtained through spectroscopic methods such as Rydberg–Klein–Rees (RKR) analysis [10–12]. A detailed theoretical description of Cs_2 requires potential functions that represent both short- and long-range interactions and incorporate essential molecular parameters, such as the dissociation energy, the equilibrium bond length, and screening effects. An adaptable framework that satisfies these requirements is the Möbius Square–Screened Kratzer Potential (MSSKP) model [13,14]. The Möbius square potential, a relatively recent development in molecular interaction modeling, introduces distinctive geometric features associated with confinement effects in molecular systems. In contrast, the screened Kratzer potential incorporates a screening parameter that effectively modulates long-range intermolecular interactions. The combination of these two forms yields a hybrid potential that simultaneously accounts for short-range confinement and screened long-range behavior, thereby providing a more comprehensive and flexible theoretical framework for the analysis of molecular structure and dynamics.

Solving the radial Schrödinger equation within this hybrid potential framework provides valuable insight into bound-state energy eigenvalues and the corresponding wavefunctions—quantities that are essential for predicting

Cite as: S.E. Mopta, V.C. Onuabuchi, E.P. Inyang, East Eur. J. Phys. 3, 13 (2026), https://doi.org/10.26565/2312-4334-2026-3-02

vibrational spectra, molecular stability, and related physical properties [15,16]. Analytical techniques such as the Nikiforov–Uvarov (NU) method [17] are particularly advantageous in this context, as they enable exact or approximate solutions of second-order differential equations derived from the Schrödinger equation, even for complex potential forms. Recent studies have continued to investigate Cs_2 using a variety of potential models and solution techniques. Approaches based on the Tietz–Hua, improved Rosen–Morse, generalized Pöschl–Teller, Manning–Rosen, and deformed exponential-type potentials have been employed to determine the rovibrational spectra of Cs_2 with varying degrees of agreement with experimental observations [18–20]. For example, the Tietz–Hua potential has demonstrated improved consistency with spectroscopic data compared to the Morse potential, particularly at higher vibrational levels. Similarly, the improved Rosen–Morse potential has proven effective in modeling the rotational–vibrational spectra of heavy dimers, showing enhanced agreement with experimental measurements.

Building on these developments, the present work investigates the quantum bound states described by the Möbius Square plus Screened Kratzer Potential (MSSKP) [21]. This hybrid potential is particularly well suited for analyzing vibrational and rotational spectra, as well as the discrete energy levels of diatomic molecules such as Cs_2, where an accurate representation of interatomic interactions is essential. Owing to its well-resolved vibrational structure, Cs_2 provides a valuable benchmark for evaluating theoretical models and validating spectroscopic predictions. Although both the Möbius square potential and the screened Kratzer potential have been extensively studied in isolation, their combined formulation has not yet been systematically explored. This study addresses that gap by solving the Schrödinger equation within the MSSKP framework for the Cs_2 molecule. The resulting energy eigenvalues are compared with experimental data obtained from Rydberg–Klein–Rees (RKR) analysis to assess the accuracy and reliability of the proposed potential. The findings align with ongoing efforts to develop more refined potential energy models in quantum chemistry and molecular physics. Ultimately, this work contributes to a deeper understanding of heavy diatomic molecules and strengthens the theoretical foundation for future experimental and computational investigations.

The interaction potential adopted in this study is written in the following form [21].

$$V(r_z) = Y_0\left(\frac{A_0 + B_0 e^{-\alpha_z r_z}}{1-e^{-\alpha_z r_z}}\right)^2 - 2D_e\left(\frac{r_e}{r_z} - \frac{r_e^2}{2r_z^2}\right)e^{-\alpha_z r_z}\ . \tag{1}$$

The dissociation energy is denoted by D_e, whereas r_e represent the equilibrium bond length parameter. Furthermore, A_0, B_0, and Y_0 corresponds to the strength of the Möbius square potential, while α_z are the screening parameter.

2 THE THEORY

The quantum dynamics of a particle confined within a potential field are described by the time-independent Schrödinger equation. For the hybrid potential examined in this study, the corresponding radial equation can be written as [22]:

$$\frac{d^2\psi_{nl}}{dr_z^2} + \left(\frac{2\mu_z}{\hbar^2}E_{nl} - \frac{2\mu_z}{\hbar^2}V(r_z) - \frac{l(l+1)}{r_z^2}\right)\psi_{nl}(r_z) = 0\,. \tag{2}$$

Here, l represents the angular momentum quantum number, μ_z is the reduced mass, r_z denotes the particle distance, and $\hbar$ is the reduced Planck constant.
Inserting Equation (1) into Equation (2) gives

$$\frac{d^2\psi_{nl}(r_z)}{dr_z^2} + \left(\frac{2\mu_z}{\hbar^2}E_{nl} - \frac{2\mu_z}{\hbar^2}\left(Y_0\left(\frac{A_0 + B_0 e^{-\alpha_z r_z}}{1-e^{-\alpha_z r_z}}\right)^2 - 2D_e\left(\frac{r_e}{r_z} - \frac{r_e^2}{2r_z^2}\right)e^{-\alpha_z r_z}\right) - \frac{l(l+1)}{r_z^2}\right)\psi_{nl}(r_z) = 0\,, \tag{3}$$

In Equation (3), the centrifugal contribution is handled through the Greene–Aldrich approximation [23], a procedure that has been effectively employed in several recent studies [24,25]. This approach yields a reliable treatment of the centrifugal term for $\alpha_z << 1$, , leading to the following expression:

$$r_z^{-2} \approx \alpha_z^2\left(1-e^{-\alpha_z r_z}\right)^{-2},\ r_z^{-1} \approx \alpha_z\left(1-e^{-\alpha_z r_z}\right)^{-1}. \tag{4}$$

To facilitate the solution, an appropriate change of variable, $y_z = e^{-\alpha_z r_z}$, is introduced. By applying this transformation in conjunction with Equation (4) to Equation (3), and carrying out the required algebraic simplifications, the radial equation is reduced to the standard Schrödinger form, expressed as follows:

$$\frac{d^2\psi(y_z)}{dy_z^2} + \frac{1-y_z}{y_z(1-y_z)}\frac{d\psi(y_z)}{dy_z} + \frac{1}{y_z^2(1-y_z)^2}\begin{bmatrix} -\left(\varepsilon_z^2 + \delta^2 + \kappa_1\right)y_z^2 + \\ \left(2\varepsilon_z^2 - 2\delta^2 + \kappa_1 - \kappa_2\right)y_z \\ -\left(\varepsilon_z^2 + \delta^2 + \lambda\right) \end{bmatrix}\psi(y_z) = 0, \tag{5}$$

where

$$\left.\begin{array}{l} -\varepsilon_z^2 = \dfrac{2\mu_z E_{nl}}{\alpha_z^2 \hbar^2}, \quad \delta^2 = \dfrac{8\mu_z A_0^2 Y_0}{\alpha_z \hbar^2}, \quad \kappa_1 = \dfrac{4\mu_z A_0 B_0 D_e r_e}{\alpha_z \hbar^2}, \\ \kappa_2 = \dfrac{4\mu_z B_0^2 D_e r_z^2}{\hbar^2}, \quad \lambda = l(l+1) \end{array}\right\}. \tag{6}$$

Tezcan and Sever [26] demonstrated that the parametric Nikiforov–Uvarov (pNU) method provides a more straightforward and efficient procedure for determining both energy eigenvalues and the corresponding wavefunctions. Compared with the conventional Nikiforov–Uvarov approach [17], the pNU technique offers greater implementation simplicity and improved computational efficiency. Its principal advantage lies in its direct applicability and the high accuracy of solutions obtained for wave equations associated with a wide range of potential energy functions. Based on their formulation, the standard form of the equation is written as follows:

$$\psi''(t) + \frac{(b_1 - b_2 t)}{t(1-b_3 t)}\psi'(t) + \frac{1}{t^2(1-b_3 t)^2}\left[-T_0 t^2 + T_1 t - T_2\right]\psi(t) = 0 . \tag{7}$$

Using Equation (7), the expressions for the energy eigenvalues and their corresponding wavefunctions were derived and are presented as follows:

$$b_2 n - (2n+1)b_5 + \left[2b_8 + n(n+1)\right]b_3 + b_7 + (2n+1)\sqrt{b_9} + \sqrt{b_8}\left[2\sqrt{b_9} + b_3(2n+1)\right] = 0 . \tag{8}$$

$$\psi(t) = N_{nl} t^{b_{12}} (1-b_3 t)^{-b_{12} - \frac{b_{13}}{b_3}} p_n^{\left(b_{10}-1, \frac{b_{11}}{b_3} - b_{10} - 1\right)}(1-2b_3 t) . \tag{9}$$

The parametric constants featured in Equations (8) and (9) are calculated using the following expressions:

$$\left.\begin{array}{l} b_1 = b_2 = b_3 = 1, b_4 = 0.5(1-b_1), b_5 = 0.5(b_2 - 2b_3), \\ b_6 = b_5^2 + T_0, b_7 = 2b_4 b_5 - T_{1,} \\ b_8 = b_4^2 + T_2, b_9 = b_3(b_7 + b_3 b_8) + b_6, \\ b_{10} = b_1 + 2b_4 + 2\sqrt{b_8}, \\ b_{11} = b_2 - 2b_5 + 2\left(\sqrt{b_9} + b_3\sqrt{b_8}\right), \\ b_{12} = b_4 + \sqrt{b_8}, \\ b_{13} = b_5 - \left(\sqrt{b_9} + b_3\sqrt{b_8}\right) \end{array}\right\} \tag{10}$$

By comparing Equations (5) and (7), the parametric constants in Equation (10) are obtained as follows:

$$\left.\begin{array}{l} T_0 = \varepsilon_z^2 + \delta^2 + \kappa_1 \\ T_1 = 2\varepsilon_z^2 - 2\delta^2 + \kappa_1 - \kappa_2 \\ T_2 = \varepsilon_z^2 + \delta^2 + \lambda \\ and \\ b_1 = b_2 = b_3 = 1, b_4 = 0, b_5 = -0.5, \\ b_6 = \dfrac{1}{4} + \varepsilon_z^2 + \delta^2 + \kappa_1, b_7 = -2\varepsilon_z^2 + 2\delta^2 - \kappa_1 + \kappa_2 \\ b_8 = \varepsilon_z^2 + \delta^2 + \lambda, b_9 = \dfrac{1}{4} + \delta^2 + \delta^2 + 2\delta^2 + \kappa_2 + \lambda, \\ b_{10} = 1 + 2\sqrt{\varepsilon_z^2 + \delta^2 + \lambda}, \\ b_{11} = 2 + \sqrt{8\delta^2 + 4\kappa_2 + 1 + 4\delta^2 + 4\delta^2 + 4\lambda} + 2\sqrt{\varepsilon_z^2 + \delta^2 + \lambda}, \\ b_{12} = \sqrt{\varepsilon_z^2 + \delta^2 + \lambda}, \\ b_{13} = -\dfrac{1}{2} - \left[\dfrac{1}{2}\sqrt{8\delta^2 + 4\kappa_2 + 1 + 4\delta^2 + 4\delta^2 + 4\lambda} + \sqrt{\varepsilon_z^2 + \delta^2 + \lambda}\right] \end{array}\right\} \tag{11}$$

By substituting Equations (6) and (11) into (8) and (9), the resulting expressions for the energy eigenvalues and their corresponding wavefunctions are obtained as:

$$E_{nl}=Y_0A_0^2+\frac{\alpha_z^2\hbar^2 l(l+1)}{2\mu_z}-\frac{\alpha_z^2\hbar^2}{8\mu_z}\left[\frac{\left(n+\frac{1}{2}+\sqrt{\left(l+\frac{1}{2}\right)^2+\frac{2\mu_z D_e r_e^2}{\hbar^2}+\frac{2\mu_z Y_0}{\alpha_z^2\hbar^2}\left(A_0+B_0\right)^2}\right)^2+\frac{4\mu_z D_e r_e}{\alpha_z\hbar^2}++\frac{2\mu_z Y_0\left(A_0^2-B_0^2\right)}{\alpha_z^2\hbar^2}+l(l+1)}{n+\frac{1}{2}+\sqrt{\left(l+\frac{1}{2}\right)^2+\frac{2\mu_z D_e r_e^2}{\hbar^2}+\frac{2\mu_z Y_0}{\alpha_z^2\hbar^2}\left(A_0+B_0\right)^2}}\right]^2. \tag{12}$$

and

$$\psi(t)=N_{nl}t^{\sqrt{\varepsilon^2+\delta^2A_0^2+l(l+1)}}\left(1-t\right)^{\frac{1}{2}+\left(\sqrt{\delta^2(A_0+B_0)^2+\kappa_2+\left(\frac{1}{2}+l\right)^2}\right)}p_n^{\left(2\sqrt{\varepsilon^2+\delta^2A_0^2+l(l+1)},\left(2\sqrt{\delta^2(A_0+B_0)^2+\kappa_2+\left(\frac{1}{2}+l\right)^2}\right)\right)}(1-2t) \tag{13}$$

where N_{nl} represents the normalization constant, as obtained from Equation (14).

$$\int_0^\infty\left|\psi_{nl}(r_z)\right|^2 dr_z=1. \tag{14}$$

3. RESULTS AND DISCUSSION

This research focuses on the vibrational energy states of Cs_2. Using the spectrum, the energy levels were determined via Equation (12), which was then employed to examine the system's quantum characteristics. All computations utilized the conversion factors $1\text{ amu}=931.494028\,\text{MeV}/c^2$ and $\hbar c=1973.29\,\text{eVÅ}$, as specified in reference [27]. In molecular spectroscopy, the force constant k_e plays a crucial role because it characterizes the curvature of the potential energy curve at the equilibrium bond distance. Mathematically, it is obtained by taking the second derivative of the potential energy with respect to the internuclear separation r, evaluated at the equilibrium position $k_e=\left.\frac{d^2V(r)}{dr^2}\right|_{r=r_e}$.

For a diatomic molecule, this constant is directly connected to the harmonic vibrational frequency ω_e at equilibrium (C). The relationship is expressed as $k_e=\mu_z\omega_e^2$, where μ_z denotes the reduced mass of the molecule.

When applying the Möbius square plus screened Kratzer potential (MSSKP), the value of the force constant is obtained through the Varshni conditions. These conditions ensure that the minimum of the proposed potential corresponds properly to the experimentally observed spectroscopic equilibrium configuration [28,29]. The analysis of the $3^3\sum_g^+$ electronic state of the Cs_2 molecule is based on the experimental molecular constants $D_e=2722.28\ cm^{-1}$, $r_e=5.3474208\dot{A}$, $\mu_z=66.38\,amu$ and $\omega_e=28.8918\ cm^{-1}$ reported in references [18,20]. From these parameters, the quantity $\alpha_z=\left(\frac{\mu_z\omega_e^2}{2D_e}\right)$ is evaluated, forming the basis for calculating the vibrational energy levels of the cesium dimer.

To assess the accuracy of the model, the mean absolute error (MAE) is computed using the expression $MAE=\frac{1}{v}\sum_{n=0}^{10}\left|E_n^{Com.}-E_n^{RKR}\right|$. In this formulation, E_n^{RKR} represents the theoretical energy obtained from the model, E_n^{RKR} corresponds to the reference energy derived from the Rydberg–Klein–Rees (RKR) data, and v denotes the total number of available experimental data points. The vibrational energy levels obtained for Cs_2, expressed in cm^{-1}, are presented in Table 1.

The Rydberg–Klein–Rees (RKR) method is fundamentally grounded in experimental spectroscopic data and is widely regarded as a reliable benchmark because it reconstructs the molecular potential energy curve directly from observed transition frequencies. In contrast, analytical potential models such as the Morse and Manning–Rosen functions are commonly used to describe anharmonic vibrational motion. The Morse potential provides a reasonable representation of bond stretching, whereas the Manning–Rosen potential introduces an additional shape parameter that improves its flexibility.

Despite their usefulness, both models have limitations in accurately describing molecular behavior at very short internuclear distances as well as in the asymptotic long-range region. These shortcomings become more pronounced at higher vibrational quantum numbers, where noticeable deviations from expected trends occur.

To address these limitations, the Möbius square plus screened Kratzer potential (MSSKP) proposed in this study incorporates features that effectively capture both short-range confinement and long-range screening effects. For Cs_2, the model achieves a mean absolute error (MAE) of 0.0234 cm^{-1}, which is significantly lower than the values obtained using the Morse (0.2364 cm^{-1}) and Manning–Rosen (0.0517 cm^{-1}) potentials. Moreover, the vibrational energy levels predicted by the MSSKP are in excellent agreement with experimental RKR results, demonstrating its superior accuracy and reliability in modeling the vibrational behavior of heavy diatomic molecules.

Table 1. Calculated vibrational energies for the $3^3\sum_g^+$ state of Cs_2 compared with Rydberg–Klein–Rees (RKR) data and earlier theoretical results (units in cm^{-1}).

n	RKR [10-12]	Manning–Rosen Potential [20]	Morse Potential [20]	Present Study (MSSKP)
0	14.4248	14.4266	14.4267	14.4255
1	43.1680	43.1756	43.1652	43.1712
2	71.7657	71.7818	71.7504	71.7700
3	100.2211	100.2448	100.1822	100.2305
4	128.5375	128.5645	128.4608	128.5450
5	156.7182	156.7409	156.5860	156.7258
6	184.7663	184.7737	184.5579	184.7692
7	212.6851	212.6628	212.3765	212.6760
8	240.4778	240.4080	240.0418	240.4430
9	268.1477	268.0091	267.5537	268.0805
10	295.6980	295.4661	294.9123	295.5872
		MAE = 0.05170	MAE = 0.23640	MAE = 0.02340

4. CONCLUSIONS

In this work, the Möbius square plus screened Kratzer potential (MSSKP) model has been successfully employed to describe quantum bound states, with analytical solutions obtained through the parametric Nikiforov–Uvarov (pNU) method. Application of the model to the cesium dimer (Cs_2) demonstrates its remarkable ability to accurately reproduce the vibrational energy spectrum. The calculated results exhibit excellent agreement with available experimental Rydberg–Klein–Rees (RKR) data, yielding a minimum mean absolute error of 0.0234 cm^{-1} and outperforming conventional potentials such as the Morse and Manning–Rosen models. These findings confirm the reliability, accuracy, and predictive strength of the MSSKP framework in modeling molecular vibrational dynamics. Furthermore, the proposed potential provides a valuable theoretical basis for understanding molecular structure, bonding characteristics, and quantum behavior. Owing to its effectiveness and versatility, the MSSKP model may serve as a powerful tool in molecular spectroscopy and quantum chemistry, with potential applications to more complex systems, including polyatomic molecules, excited electronic states, nanostructured materials, and related quantum-mechanical problems [30–39].

Data Availability Statement

All results presented in this study were obtained through the numerical evaluation of analytically derived expressions. No external datasets were used or generated in this work.

Disclosure Statement

The authors declare that there are no conflicts of interest regarding the publication of this article.

Acknowledgements

Dr. Etido P. Inyang gratefully acknowledges the National Open University of Nigeria for awarding the 2025 Senate Research Grant.

Funding

This research was supported by the National Open University of Nigeria through the 2025 Senate Research Grant (NOUN/SRG25/FASC/027).

Author Contributions

E. P. Inyang: Conceptualization, resources, investigation, and funding acquisition.
S. E. Mopta: Writing – review and editing.
V. C. Onuabuchi: Validation and computational analysis.
All authors have read and approved the final version of the manuscript.

ORCID

Samuel E. Mopta, https://orcid.org/0009-0007-3114-9843; **Victor C. Onuabuchi,** https://orcid.org/0000-0002-8373-5859; **Etido P. Inyang,** https://orcid.org/0000-0002-5031-3297

REFERENCES

[1] K.M. Merz Jr., "Using quantum mechanical approaches to study biological systems." Accounts of Chemical Research, **47**(9), 2804-2811 (2014). https://doi.org/10.1021/ar5001023
[2] F. O. Faithpraise, & E. P. Inyang, "Bound state and ro-vibrational energies eigenvalues of selected diatomic molecules with a class of inversely quadratic Yukawa plus Hulthén potential model," East European Journal of Physics, (3), 158-166 (2023). https://doi.org/10.26565/2312-4334-2023-3-12
[3] E. S. William, S. O. Inyang, I. B. Okon, O. A. Akinde, E. P. Inyang, M. U. Aka, & O. O. Ekerenam, "Theoretical computation of eigenenergies, expectation values and thermodynamic functions of shifted Deng-Fan-Hellmann potential in external fields," Computational and Theoretical Chemistry, **1244**, 115068. (2025). https://doi.org/10.1016/j.comptc.2025.115068
[4] E. P.Inyang, "Quantum expectation values and Shannon entropy in diatomic molecular systems," Journal of Mathematical Chemistry, **63**(8), 1732-1752 (2025). https://doi.org/10.1007/s10910-025-01738-5
[5] W. E. Ernst, R. Huber, S. Jiang, R. Beuc, M. Movre, & G. Pichler, "Cesium dimer spectroscopy on helium droplets," The Journal of chemical physics, **124**(2), (2006). https://doi.org/10.1063/1.2155431
[6] A. Bauch, "Caesium atomic clocks: function, performance and applications," Measurement Science and Technology, **14**(8), 1159-1173 (2003). https://doi.org/10.1088/0957-0233/14/8/301
[7] M. Abu-Shady, & E. M. Khokha, "A precise estimation for vibrational energies of diatomic molecules using the improved Rosen–Morse potential," Scientific Reports, **13**(1), 11578 (2023). https://doi.org/10.1038/s41598-023-37888-2
[8] C. A. Onate, M. C. Onyeaju, E. Omugbe, I. B. Okon, & O. E. Osafile, "Bound-state solutions and thermal properties of the modified Tietz–Hua potential," Scientific Reports, **11**(1), 2129 (2021). https://doi.org/10.1038/s41598-021-81428-9
[9] A. B. Al-Othman, & A. S. Sandouqa, "Comparison study of bound states for diatomic molecules using Kratzer, Morse, and modified Morse potentials," Physica Scripta, **97**(3), 035401 (2022). https://doi.org/10.1088/1402-4896/ac514c
[10] R. Rydberg, "Über einige potentialkurven des Quecksilberhydrids," Zeitschrift für Physik, **80**(7), 514-524 (1933). https://doi.org/10.1007/BF02057312
[11] O. Klein, "Zur berechnung von potentialkurven für zweiatomige moleküle mit hilfe von spektraltermen," Zeitschrift für Physik, **76**(3), 226-235 (1932).https://doi.org/10.1007/BF01341814
[12] A.L.G. Rees, "The calculation of potential-energy curves from band-spectroscopic data," Proceedings of the Physical Society, **59**(6), 998-1008 (1947). https://doi.org/10.1088/0959-5309/59/6/310
[13] M. Farout, M. Yasin, & S.M. Ikhdair, "Approximate bound state solutions for certain molecular potentials," J. Appl. Math. Phys, **9**(4), 736-750 (2021). https://doi.org/10.4236/JAMP.2021.94052
[14] E.P. Inyang, & E. Obisung, "The study of electronic states of NI and ScI molecules with screened Kratzer Potential," East Eur. J. Phys. (3), 32–38 (2022). https://doi.org/10.26565/2312-4334-2022-3-04
[15] C.P. Onyenegecha, C.J. Okereke, I.J. Njoku, C.A. Madu, R.U. Ndubuisi, & U.K. Nwajeri, "Approximate solutions of Schrodinger equation and expectation values of Inversely Quadratic Hellmann-Kratzer (IQHK) potential," The European Physical Journal Plus, **137**(1), 147 (2022). https://doi.org/10.1140/epjp/s13360-021-02315-w
[16] E.S. William, E.P. Inyang, & E.A. Thompson, "Arbitrary l-solutions of the Schrödinger equation interacting with Hulthén-Hellmann potential model," Revista mexicana de física, **66**(6), 730-741 (2020). https://doi.org/10.31349/revmexfis.66.730
[17] A.F. Nikiforov, & V.B. Uvarov, *Special functions of mathematical physics*, Vol. 205, (Basel: Birkhäuser, 1988).
[18] X.T. Hu, J.Y. Liu, & C.S. Jia, "The 33Σg+ state of Cs_2 molecule," Computational and Theoretical Chemistry, **1019**, 137-140 (2013). https://doi.org/10.1016/j.comptc.2013.06.020
[19] R. Horchani, N. Al-Kindi, & H. Jelassi, "Ro-vibrational energies of caesium molecules with the Tietz-Hua oscillator," Molecular Physics, **119**(4), e1812746 (2021). https://doi.org/10.1080/00268976.2020.1812746
[20] J.Y. Liu, X.T. Hu, & C.S. Jia, "Molecular energies of the improved Rosen− Morse potential energy model," Canadian Journal of Chemistry, **92**(1), 40-44 (2014). https://doi.org/10.1139/cjc-2013-0396
[21] I.B.Okon, O.O. Popoola, E. Omugbe, A.D. Antia, C.N. Isonguyo, & E.E. Ituen, "Thermodynamic properties and bound state solutions of Schrodinger equation with Mobius square plus screened-Kratzer potential using Nikiforov-Uvarov method," Computational and Theoretical Chemistry, **1196**, 113132 (2021). 10.1016/j.comptc.2020.113132
[22] Shankar, R., *Principles of Quantum Mechanics*, 2nd Ed., (Springer, New York, 1994).
[23] R.L. Greene, & C. Aldrich, "Variational wave functions for a screened Coulomb potential," Physical Review A, **14**(6), 2363 (1976). https://doi.org/10.1103/PhysRevA.14.2363
[24] E.S. William, E.P. Inyang, I.O. Akpan, J.A. Obu, A.N. Nwachukwu, & E.P. Inyang, "Ro-vibrational energies and expectation values of selected diatomic molecules via Varshni plus modified Kratzer potential model," Indian Journal of Physics, **96**(12), 3461-3476 (2022). https://doi.org/10.1007/s12648-0222-02308-0
[25] E.P. Inyang, N.R. Ali, & S.A. Aljunid, "Energy spectra, expectation values, and thermodynamic properties of HCl and LiH diatomic molecules," Eurasian Physical Technical Journal, **21**(1), 124–137 (2024). https://doi.org/10.31489/2024No1/124-137
[26] C. Tezcan, & R. Sever, "A general approach for the exact solution of the Schrödinger equation," International Journal of Theoretical Physics, **48**(2), 337-350 (2009). https://doi.org/10.1007/s10773-008-9806-y
[27] E.P. Inyang, E.S. William, J.E. Ntibi, J.A. Obu, P.C. Iwuji, & E.P. Inyang, "Approximate solutions of the Schrödinger equation with Hulthén plus screened Kratzer Potential using the Nikiforov–Uvarov–functional analysis (NUFA) method: an application to diatomic molecules," Canadian Journal of Physics, **100**(10), 463-473 (2022). https://doi.org/10.1139/cjp-2022-0030
[28] Y.P. Varshni, "Comparative study of potential energy functions for diatomic molecules," Reviews of Modern Physics, **29**(4), 664 (1957). https://doi.org/10.1103/RevModPhys.29.664
[29] National Institute of Standards and Technology (NIST), NIST Constants Database. https://physics.nist.gov/cuu/Constants/
[30] P.M. Korusenko, O.V. Petrova, & A.S. Vinogradov, "Atomic and Electronic Structure of Metal–Salen Complexes [M (Salen)], Their Polymers and Composites Based on Them with Carbon Nanostructures: Review of X-ray Spectroscopy Studies," Applied Sciences, **14**(3), 1178 (2024). https://doi.org/10.3390/app14031178
[31] *The exploration of supramolecular systems and nanostructures by photochemical techniques*, Vol. 78, edited by P. Ceroni, (Springer Science & Business Media, 2011).

[32] K. Kharisova, D. Lukyanov, P. Korusenko, E. Beletskii, A. Vereshchagin, O. Levin, *et al*., “Synthesis, properties and applications of carbon nanomaterials functionalized with anionic groups,” Nano-Structures & Nano-Objects, **39**, 101258 (2024). https://doi.org/10.1016/j.nanoso.2024.101258
[33] M. Doser, E. Auffray, F.M. Brunbauer, I. Frank, H. Hillemanns, G. Orlandini, & G. Kornakov, “Quantum systems for enhanced high energy particle physics detectors,” Frontiers in Physics, **10**, 887738 (2022). https://doi.org/10.3389/fphy.2022.887738
[34] V.K. Adamchuk, A.S. Vinogradov, G.G. Vladimirov, S.L. Molodtsov, G.V. Prudnikova, S.I. Fedoseenko, & A.M. Shikin, “Study of nanostructured materials by optical and photoelectron spectroscopy,” Crystallography Reports, **51**(5), 870-880 (2006). https://doi.org/10.1134/S106377450605018X
[35] S.M. Morton, D.W. Silverstein, & L. Jensen, “Theoretical studies of plasmonics using electronic structure methods,” Chemical reviews, **111**(6), 3962-3994 (2011). https://doi.org/10.1021/cr2000325
[36] H. Ma, S.Q. Pan, W.L. Wang, X. Yue, X.H. Xi, S. Yan, & B. Ren, “Surface-enhanced Raman spectroscopy: current understanding, challenges, and opportunities,” Acs Nano, **18**(22), 14000-14019 (2024). https://doi.org/10.1021/acsnano.4c02670
[37] S.D. Bass, & M. Doser, “Quantum sensing for particle physics,” Nature Reviews Physics, **6**(5), 329-339 (2024). https://doi.org/10.1038/s42254-024-00714-3
[38] Y. Afik, F. Fabbri, M. Low, L. Marzola, J.A. Aguilar-Saavedra, M.M. Altakach, *et al*., “Quantum information meets high-energy physics: input to the update of the European strategy for particle physics,” The European Physical Journal Plus, **140**(9), 855 (2025). https://doi.org/10.1140/epjp/s13360-025-06752-9
[39] C. Maraveas, “Quantum and nonlinear metamaterials for the optimization of greenhouse covers,” AgriEngineering, **7**(10), 334 (2025). https://doi.org/10.3390/agriengineering7100334

ТЕОРЕТИЧНЕ ДОСЛІДЖЕННЯ КОЛИВАЛЬНОГО СПЕКТРА ЦЕЗІЄВОГО ДИМЕРУ ЗА ВИКОРИСТАННЯМ ГІБРИДНОЇ МОДЕЛІ ВЗАЄМОДІЇ

Самуель Е. Мопта[1], Віктор К. Онуабучи[2], Етідо П. Іньянг[3]
[1]Кафедра фізики, Університет Калабара, Калабар, Нігерія
[2]Кафедра промислової фізики, Державний університет науки і технологій Енугу, Енугу, Нігерія
[3]Кафедра фізики, Факультет природничих наук, Національний відкритий університет Нігерії, Джабі-Абуджа, Нігерія

У цьому дослідженні вивчаються квантові властивості димеру цезію (Cs_2) за допомогою гібридної моделі взаємодії, яка поєднує потенціал квадратів Мебіуса з екранованим потенціалом Кратцера (MSSKP). Рівні коливальної енергії отримані аналітично шляхом розв'язання рівняння Шредінгера в рамках параметричного методу Нікіфорова-Уварова (pNU). Розраховані спектри демонструють чудову відповідність з доступними експериментальними даними Ридберга-Клейна-Ріса (RKR), що демонструє валідність запропонованої моделі. Порівняльний аналіз з усталеними моделями потенціалів, а саме з потенціалами Морзе та Маннінга-Розена, показує вищу прогностичну ефективність підходу MSSKP. Зокрема, модель MSSKP досягає мінімальної середньої абсолютної похибки (MAE) 0,0234 $см^{-1}$ порівняно з 0,2364 $см^{-1}$ та 0,0517 $см^{-1}$ для потенціалів Морзе та Маннінга-Розена відповідно. Ці результати підкреслюють підвищену точність та надійність моделі MSSKP в описі коливального спектру Cs_2. Отримані дані також надають цінне розуміння молекулярної структури, взаємодій і зв'язків, а також квантової поведінки, підкреслюючи потенціал запропонованої моделі для застосування в квантовій хімії, молекулярній спектроскопії та теоретичному моделюванні двохатомних молекулярних систем.
Ключові слова: *гібридна модель взаємодії; середня абсолютна похибка; дані Ридберга-Кляйна-Ріса (RKR); аналітичний метод, молекулярна спектроскопія*

East European Journal of Physics. 3. 20–43 (2026)
DOI: 10.26565/2312-4334-2026-3-03 ISSN 2312-4334

EXACT TRAVELING WAVES AND BIFURCATION STRUCTURE OF A COUPLED KUDRYASHOV-TYPE NONLINEAR SCHRÖDINGER SYSTEM VIA THE MODIFIED EXTENDED MAPPING METHOD

Wafy M. Hasan[1,2], Hamdy M. Ahmed[3,*], Ahmed M. Ahmed[1], Haytham M. Rezk[1], Wafaa B. Rabie[4,5]
[1]*Department of Mathematics, Faculty of Science, Al-Azhar University, Cairo, Egypt*
[2]*Department of Basic Sciences, Faculty of Engineering Technology, ElSewedy University of Technology, Cairo, Egypt*
[3]*Department of Physics and Engineering Mathematics, Higher Institute of Engineering, El Shorouk Academy, Cairo, Egypt*
[4]*Department of Mathematics, Faculty of Science, Luxor University, Taiba Luxor, Egypt*
[5]*Luxor National University, Faculty of Computing, Information Technology, and Artificial Intelligence, Luxor, Egypt*
[*]*Corresponding Author e-mail: hamdy_17eg@yahoo.com*
Received May 15, 2026; revised June 20, 2026; accepted July 6, 2026

This study obtains exact traveling wave solutions and conducts a bifurcation analysis for the coupled (1+1)-dimensional Kudryashov's equation. This system of nonlinear Schrödinger-type equations models the simultaneous propagation of optical pulses in a birefringent fiber, incorporating critical higher-order effects like cubic-quartic dispersion and nonlinearities for enhanced physical accuracy. By applying the modified extended mapping method (MEMM), the coupled partial differential equations are systematically reduced to a manageable ordinary differential equation. This reduction allows for the construction of a broad spectrum of exact solutions such as bright and dark solitons, periodic waves, periodic singular solutions, along with singular solitons, in addition to hyperbolic, exponential, rational, and Weierstrass elliptic function solutions. A key component of the work is a detailed bifurcation analysis of the resulting planar dynamical system. This analysis identifies critical parameter thresholds and classifies all possible qualitative behaviors of the wave solutions, mapping out regions of existence for different solution types. The physical implications of both the derived solutions and the bifurcation structure are discussed in the context of nonlinear optics, particularly for pulse dynamics and stability in dual-polarization optical communication systems. The results demonstrate the efficacy of MEMM and provide new insights that contribute to the understanding and design of advanced optical waveguides.

Keywords: *Nonlinear Schrödinger equations; Birefringent optical fibers; Higher-order dispersion; Modified extended mapping method (MEMM); Exact traveling wave solutions; Bifurcation analysis*

1. INTRODUCTION

Partial differential equations (PDEs) serve as cornerstone mathematical models in numerous scientific and engineering fields, enabling the description of phenomena that evolve in both space and time. They are especially vital for capturing wave propagation, fluid flow, and other processes in which nonlinearity generates intricate structures such as shocks, turbulent states, and solitary waves. For example, the nonlinear Navier–Stokes model remains the principal instrument for examining intricate fluid dynamics, encompassing turbulence, vortex generation, and wave-breaking phenomena [1, 2]. Similarly, the Korteweg–de Vries model has occupied a pivotal position in clarifying the characteristics of nonlinear wave evolution and the appearance of solitons in shallow-water environments [3, 4]. The utility of PDEs extends far beyond classical physics: in environmental and geophysical contexts, they are routinely employed to model atmospheric and oceanic wave dynamics, while nonlinear advection–diffusion equations are used to track pollutant transport in air and water bodies [5, 6]. Engineering disciplines also rely heavily on PDEs for studying shock-wave phenomena, optical pulse evolution in fibers [7, 8], climate variability, and extreme meteorological events [9, 10]. The extraordinary breadth of these applications highlights the indispensable role of PDEs in tackling real-world problems across diverse domains.

Exact solutions to nonlinear evolution equations (NLEEs) can be constructed through a rich array of analytical techniques. Notable examples include the extended sinh–Gordon equation expansion method, which exploits known solutions of the sinh–Gordon equation to generate new solutions for wider classes of NLEEs [11]; the modified extended tanh-function method, which enhances the classical tanh expansion to yield richer solution families [12]; the modified extended direct algebraic approach, offering a structured framework that converts complex NLEEs into solvable algebraic systems [13, 14]; and the modified extended mapping method, which establishes versatile functional mappings to interconnect different solution types and thereby broaden the scope of treatable equations [15, 16]. Additional powerful tools encompass the modified Sardar sub-equation technique [17], the extended F-expansion method [18, 19], the improved modified extended tanh-function scheme [20, 21], the extended simplest equation method [22], Riccati–Bernoulli and Bäcklund Methods [23], among others. Taken together, these approaches offer vital tools for investigating advanced physical processes—such as wave propagation, fluid instabilities, and heat transfer phenomena—while linking rigorous theoretical advances with practical implementations across mathematical, physical, and engineering disciplines. The study

Cite as: W.M. Hasan, H.M. Ahmed, A.M. Ahmed, H.M. Rezk, W.B. Rabie, East Eur. J. Phys. 3, 20 (2026), https://doi.org/10.26565/2312-4334-2026-3-03

of coupled nonlinear evolution equations (NLEEs) within optical settings continues to be an important research domain owing to their capacity to represent intricate wave interactions in birefringent fibers. Motivated by the need to uncover richer dynamical behaviors and transition mechanisms in such highly nonlinear systems—beyond what traditional solution methods reveal—this study focuses on deriving exact traveling wave solutions and performing a comprehensive bifurcation analysis for the coupled system of nonlinear Schrödinger equations with cubic-quartic dispersions and higher-order nonlinearities [24], given by

$$iu_t + ia_1 u_{xxx} + a_2 u_{xxxx} + \frac{a_3 u}{\alpha_1 |u|^6 + \alpha_2 |u|^4 |v|^2 + \alpha_3 |u|^2 |v|^4 + \alpha_4 |v|^6} + \frac{a_4 u}{\left(\beta_1 |u|^2 + \beta_2 |v|^2\right) \sqrt{|u|^2 + |v|^2}}$$
$$+ \left(\beta_3 |u|^2 + \beta_4 |v|^2\right) u \sqrt{|u|^2 + |v|^2} + \left(\gamma_1 |u|^6 + \gamma_2 |u|^4 |v|^2 + \gamma_3 |u|^2 |v|^4 + \gamma_4 |v|^6\right) u = 0, \tag{1}$$

$$iv_t + ib_1 v_{xxx} + b_2 v_{xxxx} + \frac{b_3 v}{\delta_1 |v|^6 + \delta_2 |v|^4 |u|^2 + \delta_3 |v|^2 |u|^4 + \delta_4 |u|^6} + \frac{b_4 v}{\left(\lambda_1 |v|^2 + \lambda_2 |u|^2\right) \sqrt{|v|^2 + |u|^2}}$$
$$+ \left(\lambda_3 |v|^2 + \lambda_4 |u|^2\right) v \sqrt{|v|^2 + |u|^2} + \left(\mu_1 |v|^6 + \mu_2 |v|^4 |u|^2 + \mu_3 |v|^2 |u|^4 + \mu_4 |u|^6\right) v = 0, \tag{2}$$

where $u = u(x,t)$ and $v = v(x,t)$ represent wave profiles in two components of a birefringent optical fiber. The constants a_i, b_i for $i = 1,2$ govern third-order dispersion (3OD) and fourth-order dispersion (4OD), respectively, while a_j, b_j for $j = 3,4$ and $\alpha_l, \beta_l, \gamma_l, \delta_l, \lambda_l, \mu_l$ for $l = 1,2,3,4$ describe nonlinear interactions, including self-phase modulation (SPM) and cross-phase modulation (XPM). These parameters characterize intricate wave dynamics, which are essential for comprehending soliton evolution and stability within nonlinear optical frameworks. Although the model does not retain the classical group-velocity-dispersion (second-derivative) term, it is conventionally classified within the nonlinear Schrodinger family in the optics literature: near the zero-dispersion wavelength the standard GVD coefficient vanishes, and the leading dispersive contributions become the third- and fourth-order terms retained here, giving rise to the so-called cubic-quartic nonlinear Schrodinger equation [24]. The extended trial function method has been employed in [24] to derive cubic-quartic optical soliton solutions, including bright and singular solitons, periodic solutions, and Jacobi elliptic function solutions, for specific cases of the power-law nonlinearity parameter ($n = 1,2,3$). This approach transformed the coupled system into ordinary differential equations, solved using a polynomial ansatz, and provided valuable insights into soliton dynamics under differential group delay in nonlinear optical systems. In contrast, this study builds upon the framework established by Biswas et al. by applying the modified extended mapping method (MEMM) to the same coupled system defined by Eqs. (1) and (2). Unlike the extended trial function method, which relies on a polynomial ansatz, MEMM utilizes series expansions and mapping functions to derive a broader range of exact solutions, including solitons, periodic waves, and singular structures. This approach enhances the flexibility in handling the complex nonlinearities and higher-order dispersions inherent in the system, potentially yielding novel solutions not captured by the extended trial function method. By leveraging MEMM, this research aims to provide a more comprehensive set of analytical solutions, offering deeper insights into wave stability, interaction dynamics, and their applications in optimizing optical communication systems. The study also includes graphical representations and bifurcation analysis to validate the solutions and explore qualitative transitions in wave behavior, further distinguishing it from the work of Biswas et al. The motivation for this study stems from the need to advance our understanding of complex wave interactions in nonlinear optical systems, particularly through the exploration of coupled nonlinear partial differential equations (NPDEs) like Eqs. (1) and (2). These equations model intricate phenomena in birefringent optical fibers, where cubic-quartic dispersions and higher-order nonlinearities, such as those described by Kudryashov's law, govern soliton dynamics. By applying the modified extended mapping method (MEMM), this research aims to derive novel exact wave solutions, including solitons and periodic waves, that—together with bifurcation analysis—offer deeper insights into wave stability, interaction patterns, and critical parameter-induced transitions under differential group delay. These results are critical for optimizing optical communication systems, enhancing signal transmission robustness, and addressing challenges in nonlinear optics, thereby contributing to both theoretical advancements and practical applications in high-speed data transfer and photonics.

The manuscript is structured into six principal parts. Section 1 furnishes an introduction, describing the background and aims. Section 2 elaborates on the MEMM methodology. Section 3 delineates exact solutions for the coupled model. Section 4 offers graphical illustrations to depict the results. Section 5 delivers the bifurcation analysis, and Section 6 summarizes the work and discusses its implications for nonlinear optics and allied domains.

2. MODIFIED EXTENDED MAPPING METHOD

The MEMM provides a powerful and systematic procedure for deriving exact traveling-wave solutions of NPDEs [25]. The main steps of the method are described as follows:

Phase I: Consider a general NPDE expressed as:

$$F(u, u_t, u_x, u_{xx}, u_{xxx}, u_{xxxxx}, u_{xxxxxx}, \dots) = 0, \tag{3}$$

where $u = u(x,t)$ is the unknown function and F is a polynomial in u and its partial derivatives.

Phase II: Introduce the wave transformation

$$u(x,t) = \Phi(\xi), \quad \xi = x - at, \quad a \in \mathbb{R} - \{0\}, \tag{4}$$

in which a denotes the wave speed. Substituting (4) into (3) reduces the equation to an ordinary differential equation (ODE)

$$G(\Phi, \Phi', \Phi'', \Phi''', \dots) = 0. \tag{5}$$

Phase III: Assume a solution of the form

$$\Phi(\xi) = \sum_{i=0}^{N} p_i\, \mathcal{W}^i(\xi) + \sum_{i=1}^{N} q_i\, \mathcal{W}^{-i}(\xi) + \sum_{i=2}^{N} r_i\, \mathcal{W}^{i-2}(\xi)\, \mathcal{W}'(\xi) + \sum_{i=1}^{N} s_i\, \frac{\mathcal{W}'(\xi)}{\mathcal{W}^i(\xi)}, \tag{6}$$

where p_i, q_i, r_i, and s_i are constants to be determined, and the auxiliary function $\mathcal{W}(\xi)$ satisfies

$$\mathcal{W}'(\xi) = \sqrt{c_0 + c_1\mathcal{W} + c_2\mathcal{W}^2 + c_3\mathcal{W}^3 + c_4\mathcal{W}^4 + c_5\mathcal{W}^6}, \tag{7}$$

with real coefficients c_j $(j = 0, 1, \dots, 5)$.
Phase IV: Determine the positive integer N by balancing the highest-order derivative term with the leading nonlinear term in the ODE (5).
Phase V: Insert the ansatz (6) together with the relation (7) into the ODE (5). This yields a polynomial in powers of $\mathcal{W}$ (and terms involving $\mathcal{W}'$). Setting the coefficients of all independent terms to zero produces a system of algebraic equations for the unknowns p_i, q_i, r_i, s_i, a and the parameters c_j. Solving this system using symbolic software such as Maple, Mathematica, or MATLAB delivers explicit parameter values, from which a broad spectrum of exact solutions—including hyperbolic, trigonometric, elliptic, exponential, and rational functions—are obtained for the original NPDE (3).

3. CONSTRUCTION OF EXACT SOLUTIONS

In this section, the Modified Extended Mapping Method (MEMM) is systematically applied to construct exact traveling wave solutions for the coupled Kudryashov's system, Eqs. (1) and (2). The derivation begins with the standard traveling wave reduction introduced in the previous section. Subsequently, the core algorithm of the MEMM is implemented to obtain a spectrum of closed-form analytical solutions. The solutions are in the form:

$$\begin{aligned} u(x,t) &= U(\xi)\, e^{i(-kx+\omega t+\theta)}, \\ v(x,t) &= V(\xi)\, e^{i(-kx+\omega t+\theta)}, \end{aligned} \tag{8}$$

and

$$\xi = x - c\,t, \tag{9}$$

with θ, k, ω, and c being non-zero constants; here c stands for the wave propagation speed, k signifies the frequency, ω indicates the wave number, and θ denotes the phase constant. We begin by applying the wave ansatz given in Eqs. (8) to Eqs. (1) and (2), and subsequently separate the real and imaginary components, which generate the equations that follow

$$\begin{aligned} \mathrm{Re}_1: \quad & a_2U^{(4)}(\xi) + \left(3ka_1 - 6k^2a_2\right) U''(\xi) + \gamma_1U^7(\xi) + \gamma_2U^5(\xi)V^2(\xi) + \gamma_3U^3(\xi)V^4(\xi) + \gamma_4U(\xi)V^6(\xi) \\ & + \beta_3U^3(\xi)\sqrt{U^2(\xi)+V^2(\xi)} + \beta_4U(\xi)V^2(\xi)\sqrt{U^2(\xi)+V^2(\xi)} + \left(-\omega - k^3a_1 + k^4a_2\right) U(\xi) + \\ & \frac{a_4U(\xi)}{\sqrt{U^2(\xi)+V^2(\xi)}\,\left(\beta_1U^2(\xi)+\beta_2V^2(\xi)\right)} + \frac{a_3U(\xi)}{\alpha_1U^6(\xi) + \alpha_2U^4(\xi)V^2(\xi) + \alpha_3U^2(\xi)V^4(\xi) + \alpha_4V^6(\xi)} = 0, \end{aligned} \tag{10}$$

$$\begin{aligned} \mathrm{Re}_2: \quad & b_2V^{(4)}(\xi) + \left(3kb_1 - 6k^2b_2\right) V''(\xi) + \mu_1V^7(\xi) + \mu_2U^2(\xi)V^5(\xi) + \mu_3U^4(\xi)V^3(\xi) + \mu_4U^6(\xi)V(\xi) \\ & + \lambda_3V^3(\xi)\sqrt{U^2(\xi)+V^2(\xi)} + \lambda_4U^2(\xi)V(\xi)\sqrt{U^2(\xi)+V^2(\xi)} + \left(-\omega - k^3b_1 + k^4b_2\right) V(\xi) + \\ & \frac{b_4V(\xi)}{\sqrt{U^2(\xi)+V^2(\xi)}\,\left(\lambda_2U^2(\xi)+\lambda_1V^2(\xi)\right)} + \frac{b_3V(\xi)}{\delta_4U^6(\xi) + \delta_3U^4(\xi)V^2(\xi) + \delta_2U^2(\xi)V^4(\xi) + \delta_1V^6(\xi)} = 0, \end{aligned} \tag{11}$$

$$\mathrm{Im}_1: \quad (-a_1 + 4ka_2)\, U^{(3)}(\xi) + \left(c + 3k^2a_1 - 4k^3a_2\right) U'(\xi) = 0, \tag{12}$$

$$\mathrm{Im}_2: \quad (-b_1+4kb_2)\,V^{(3)}(\xi)+\left(c+3k^2b_1-4k^3b_2\right)V'(\xi)=0, \tag{13}$$

Differentiating Eqs. (12) and (13) once with respect to ξ yields explicit expressions for $U^{(4)}(\xi)$ and $V^{(4)}(\xi)$, respectively; substituting these into Eqs. (10) and (11), giving

$$\begin{aligned}\mathrm{Re}_1: \quad & \left(\frac{3ka_1^2-15k^2a_1a_2+a_2\left(c+20k^3a_2\right)}{a_1-4ka_2}\right)U''(\xi)+\gamma_1U^7(\xi)+\gamma_2U^5(\xi)V^2(\xi)\\ & +\gamma_3U^3(\xi)V^4(\xi)+\gamma_4U(\xi)V^6(\xi)+\beta_3U^3(\xi)\sqrt{U^2(\xi)+V^2(\xi)}+\beta_4U(\xi)V^2(\xi)\sqrt{U^2(\xi)+V^2(\xi)}\\ & +\frac{a_4U(\xi)}{\sqrt{U^2(\xi)+V^2(\xi)}\left(\beta_1U^2(\xi)+\beta_2V^2(\xi)\right)}+\frac{a_3U(\xi)}{\alpha_1U^6(\xi)+\alpha_2U^4(\xi)V^2(\xi)+\alpha_3U^2(\xi)V^4(\xi)+\alpha_4V^6(\xi)}\\ & +\left(-\omega-k^3a_1+k^4a_2\right)U(\xi)=0,\end{aligned} \tag{14}$$

$$\begin{aligned}\mathrm{Re}_2: \quad & \left(\frac{3kb_1^2-15k^2b_1b_2+b_2\left(c+20k^3b_2\right)}{b_1-4kb_2}\right)V''(\xi)+\mu_1V^7(\xi)+\mu_2U^2(\xi)V^5(\xi)\\ & +\mu_3U^4(\xi)V^3(\xi)+\mu_4U^6(\xi)V(\xi)+\lambda_3V^3(\xi)\sqrt{U^2(\xi)+V^2(\xi)}+\lambda_4U^2(\xi)V(\xi)\sqrt{U^2(\xi)+V^2(\xi)}\\ & +\frac{b_4V(\xi)}{\sqrt{U^2(\xi)+V^2(\xi)}\left(\lambda_2U^2(\xi)+\lambda_1V^2(\xi)\right)}+\frac{b_3V(\xi)}{\delta_4U^6(\xi)+\delta_3U^4(\xi)V^2(\xi)+\delta_2U^2(\xi)V^4(\xi)+\delta_1V^6(\xi)}\\ & +\left(-\omega-k^3b_1+k^4b_2\right)V(\xi)=0.\end{aligned} \tag{15}$$

Let

$$V(\xi)=A\,U(\xi), \tag{16}$$

under the condition $A\neq\{0,1\}$. Then, Eqs. (14) and (15) can be rewritten as

$$\begin{aligned}&\left(\frac{3ka_1^2-15k^2a_1a_2+a_2(c+20k^3a_2)}{a_1-4ka_2}\right)U^5(\xi)U''(\xi)+\left(\gamma_1+A^2\gamma_2+A^4\gamma_3+A^6\gamma_4\right)U(\xi)^{12}\\ &+\sqrt{1+A^2}\left(\beta_3+A^2\beta_4\right)U(\xi)^9+\left(-\omega-k^3a_1+k^4a_2\right)U^6(\xi)+\frac{a_4U^3(\xi)}{\sqrt{1+A^2}\left(\beta_1+A^2\beta_2\right)}\\ &+\frac{a_3}{\alpha_1+A^2\alpha_2+A^4\alpha_3+A^6\alpha_4}=0,\end{aligned} \tag{17}$$

$$\begin{aligned}&A\left(\frac{3kb_1^2-15k^2b_1b_2+b_2(c+20k^3b_2)}{b_1-4kb_2}\right)U^5(\xi)U''(\xi)+A\left(A^6\mu_1+A^4\mu_2+A^2\mu_3+\mu_4\right)U(\xi)^{12}\\ &+A\sqrt{1+A^2}\left(A^2\lambda_3+\lambda_4\right)U(\xi)^9+A\left(-\omega-k^3b_1+k^4b_2\right)U^6(\xi)+\frac{Ab_4U^3(\xi)}{\sqrt{1+A^2}\left(A^2\lambda_1+\lambda_2\right)}\\ &+\frac{Ab_3}{A^6\delta_1+A^4\delta_2+A^2\delta_3+\delta_4}=0.\end{aligned} \tag{18}$$

For recovering closed form solutions, the transformation:

$$U(\xi)=F(\xi)^{\frac{1}{3}}, \tag{19}$$

is applied to Eqs. (17) and (18). Thus they change to

$$\begin{aligned}&\left(\frac{3ka_1^2-15k^2a_1a_2+a_2(c+20k^3a_2)}{9(a_1-4ka_2)}\right)\left(3F(\xi)F''(\xi)-2F'(\xi)^2\right)+\left(\gamma_1+A^2\gamma_2+A^4\gamma_3+A^6\gamma_4\right)F(\xi)^4\\ &+\sqrt{1+A^2}\left(\beta_3+A^2\beta_4\right)F(\xi)^3-\left(\omega+k^3a_1-k^4a_2\right)F(\xi)^2+\frac{a_4F(\xi)}{\sqrt{1+A^2}\left(\beta_1+A^2\beta_2\right)}\\ &+\frac{a_3}{\alpha_1+A^2\alpha_2+A^4\alpha_3+A^6\alpha_4}=0,\end{aligned} \tag{20}$$

$$A\left(\frac{3kb_1^2-15k^2b_1b_2+b_2(c+20k^3b_2)}{9(b_1-4kb_2)}\right)\left(3F(\xi)F''(\xi)-2F'(\xi)^2\right)+A\left(A^6\mu_1+A^4\mu_2+A^2\mu_3+\mu_4\right)F(\xi)^4$$
$$+A\sqrt{1+A^2}\left(A^2\lambda_3+\lambda_4\right)F(\xi)^3-A\left(\omega+k^3b_1-k^4b_2\right)F(\xi)^2+\frac{Ab_4F(\xi)}{\sqrt{1+A^2}\left(A^2\lambda_1+\lambda_2\right)}$$
$$+\frac{Ab_3}{A^6\delta_1+A^4\delta_2+A^2\delta_3+\delta_4}=0. \tag{21}$$

The previous Eqs. (20) and (21) have the same form under the following constraint conditions:

$$\left.\begin{aligned}
&\frac{3ka_1^2-15k^2a_1a_2+a_2(c+20k^3a_2)}{9(a_1-4ka_2)}=\frac{3kb_1^2-15k^2b_1b_2+b_2(c+20k^3b_2)}{9(b_1-4kb_2)},\\
&\gamma_1+A^2\gamma_2+A^4\gamma_3+A^6\gamma_4=A^6\mu_1+A^4\mu_2+A^2\mu_3+\mu_4,\\
&\sqrt{1+A^2}\left(\beta_3+A^2\beta_4\right)=\sqrt{1+A^2}\left(A^2\lambda_3+\lambda_4\right),\\
&\omega+k^3a_1-k^4a_2=\omega+k^3b_1-k^4b_2,\\
&\frac{a_4}{\sqrt{1+A^2}\left(\beta_1+A^2\beta_2\right)}=\frac{b_4}{\sqrt{1+A^2}\left(A^2\lambda_1+\lambda_2\right)},\\
&\frac{a_3}{\alpha_1+A^2\alpha_2+A^4\alpha_3+A^6\alpha_4}=\frac{b_3}{A^6\delta_1+A^4\delta_2+A^2\delta_3+\delta_4}.
\end{aligned}\right\} \tag{22}$$

Hence, Eq. (20) can be reformulated as

$$\sigma_1\left(3F(\xi)F''(\xi)-2F'(\xi)^2\right)+\sigma_2F(\xi)^4+\sigma_3F(\xi)^3-\sigma_4F(\xi)^2+\sigma_5F(\xi)+\sigma_6=0, \tag{23}$$

where

$$\begin{aligned}
&\sigma_1=\frac{3ka_1^2-15k^2a_1a_2+a_2(c+20k^3a_2)}{9(a_1-4ka_2)},\quad \sigma_2=\gamma_1+A^2\gamma_2+A^4\gamma_3+A^6\gamma_4,\\
&\sigma_3=\sqrt{1+A^2}\left(\beta_3+A^2\beta_4\right),\quad \sigma_4=\omega+k^3a_1-k^4a_2,\\
&\sigma_5=\frac{a_4}{\sqrt{1+A^2}\left(\beta_1+A^2\beta_2\right)},\quad \sigma_6=\frac{a_3}{\alpha_1+A^2\alpha_2+A^4\alpha_3+A^6\alpha_4}.
\end{aligned} \tag{24}$$

To ascertain the solution structure, the balancing method is employed on Eq. (23), which yields $N = 1$. Accordingly, following Eq. (6), the function $F(\xi)$ takes the form:

$$F(\xi)=p_0+p_1\mathcal{W}(\xi)+q_1\frac{1}{\mathcal{W}(\xi)}+s_1\frac{\mathcal{W}'(\xi)}{\mathcal{W}(\xi)}, \tag{25}$$

in which p_0, p_1, q_1, and s_1 represent undetermined constants. Substituting $F(\xi)$ from Eq. (25) together with Eq. (7) into Eq. (23), we collect the coefficients corresponding to $\mathcal{W}^i$ for $i \in [-4, 8]$, $\mathcal{W}^j\mathcal{W}'$ for $j \in [-4, 4]$, $\mathcal{W}^k\mathcal{W}'^2$ for $k \in [-4, 0]$, $\mathcal{W}^l\mathcal{W}'^3$ for $l \in [-4, 2]$, and $\mathcal{W}^{-4}\mathcal{W}'^4$. Equating all these coefficients to zero generates an algebraic system; solving this system provides the analytical solutions to Eqs. (1) and (2), presented below:

Case Study 1: $c_0 = c_1 = c_3 = c_5 = 0$.
Solving the resulting algebraic system produces two consistent parameter sets.

[1.1] $p_0=-\dfrac{2\sigma_3}{5\sigma_2}$, $p_1=\dfrac{\sqrt{-8c_4\sigma_3^4-625c_4\sigma_2^3\sigma_6}}{5\sqrt{2c_2}\sigma_2\sigma_3}$, $q_1=0$, $s_1=0$, $\sigma_1=\dfrac{8\sigma_3^4+625\sigma_2^3\sigma_6}{200c_2\sigma_2\sigma_3^2}$, $\sigma_4=\dfrac{-8\sigma_3^4+125\sigma_2^3\sigma_6}{40\sigma_2\sigma_3^2}$, $\sigma_5=\dfrac{-8\sigma_3^4+625\sigma_2^3\sigma_6}{500\sigma_2^2\sigma_3}$.

[1.2] $p_0=-\dfrac{2\sigma_3}{5\sigma_2}$, $p_1=\dfrac{2\sqrt{-c_4\sigma_1}}{\sqrt{\sigma_2}}$, $q_1=0$, $s_1=0$, $\sigma_4=\dfrac{25c_2\sigma_1\sigma_2-6\sigma_3^2}{25\sigma_2}$, $\sigma_5=\dfrac{2(25c_2\sigma_1\sigma_2\sigma_3-2\sigma_3^3)}{125\sigma_2^2}$, $\sigma_6=\dfrac{8(25c_2\sigma_1\sigma_2\sigma_3^2-\sigma_3^4)}{625\sigma_2^3}$.

From subcase [1.1] the following explicit solutions are obtained:
[1.1.1] If $c_2 > 0$, $c_4 < 0$, $\sigma_2\sigma_3 \neq 0$, and $(8\sigma_3^4 + 625\sigma_2^3\sigma_6) > 0$, then

$$u_{1.1.1}(x,t) = \frac{1}{(10\sigma_2\sigma_3)^{1/3}}\left(-4\sigma_3^2 + \sqrt{2\left(8\sigma_3^4 + 625\sigma_2^3\sigma_6\right)}\,\operatorname{sech}\left[\sqrt{c_2}(x-ct)\right]\right)^{1/3} e^{-i(kx-\theta-t\omega)}, \tag{26}$$

$$v_{1.1.1}(x,t) = \frac{A}{(10\sigma_2\sigma_3)^{1/3}}\left(-4\sigma_3^2 + \sqrt{2\left(8\sigma_3^4 + 625\sigma_2^3\sigma_6\right)}\,\operatorname{sech}\left[\sqrt{c_2}(x-ct)\right]\right)^{1/3} e^{-i(kx-\theta-t\omega)}, \tag{27}$$

represent bright soliton waveforms.

[1.1.2] If $c_2 < 0$, $c_4 > 0$, $\sigma_2\sigma_3 \neq 0$, and $(8\sigma_3^4 + 625\sigma_2^3\sigma_6) > 0$, then

$$u_{1.1.2}(x,t) = \frac{1}{(10\sigma_2\sigma_3)^{1/3}}\left(-4\sigma_3^2 - \sqrt{2\left(8\sigma_3^4 + 625\sigma_2^3\sigma_6\right)}\,\sec\left[\sqrt{-c_2}(x-ct)\right]\right)^{1/3} e^{-i(kx-\theta-t\omega)}, \tag{28}$$

$$v_{1.1.2}(x,t) = \frac{A}{(10\sigma_2\sigma_3)^{1/3}}\left(-4\sigma_3^2 - \sqrt{2\left(8\sigma_3^4 + 625\sigma_2^3\sigma_6\right)}\,\sec\left[\sqrt{-c_2}(x-ct)\right]\right)^{1/3} e^{-i(kx-\theta-t\omega)}, \tag{29}$$

correspond to singular periodic waveforms.

[1.1.3] If $c_2 < 0$, $c_4 > 0$, $\sigma_2\sigma_3 \neq 0$, and $(8\sigma_3^4 + 625\sigma_2^3\sigma_6) > 0$, then

$$u_{1.1.3}(x,t) = \frac{1}{(10\sigma_2\sigma_3)^{1/3}}\left(-4\sigma_3^2 - \sqrt{2\left(8\sigma_3^4 + 625\sigma_2^3\sigma_6\right)}\,\csc\left[\sqrt{-c_2}(x-ct)\right]\right)^{1/3} e^{-i(kx-\theta-t\omega)}, \tag{30}$$

$$v_{1.1.3}(x,t) = \frac{A}{(10\sigma_2\sigma_3)^{1/3}}\left(-4\sigma_3^2 - \sqrt{2\left(8\sigma_3^4 + 625\sigma_2^3\sigma_6\right)}\,\csc\left[\sqrt{-c_2}(x-ct)\right]\right)^{1/3} e^{-i(kx-\theta-t\omega)}, \tag{31}$$

correspond to singular periodic waveforms.

From subcase [1.2] the following explicit solutions are obtained:
[1.2.1] If $c_2 > 0$, $c_4 < 0$, $\sigma_1 < 0$, and $\sigma_2 > 0$, then

$$u_{1.2.1}(x,t) = \left(\frac{2}{5\sigma_2}\right)^{1/3}\left(5\sqrt{c_2\sigma_1\sigma_2}\,\operatorname{sech}\left[\sqrt{c_2}(x-ct)\right] - \sigma_3\right)^{1/3} e^{-i(kx-\theta-t\omega)}, \tag{32}$$

$$v_{1.2.1}(x,t) = A\left(\frac{2}{5\sigma_2}\right)^{1/3}\left(5\sqrt{c_2\sigma_1\sigma_2}\,\operatorname{sech}\left[\sqrt{c_2}(x-ct)\right] - \sigma_3\right)^{1/3} e^{-i(kx-\theta-t\omega)}, \tag{33}$$

represent bright soliton waveforms.

[1.2.2] If $c_2 < 0$, $c_4 > 0$, $\sigma_1 < 0$, and $\sigma_2 > 0$, then

$$u_{1.2.2}(x,t) = \left(\frac{2}{5\sigma_2}\right)^{1/3}\left(5\sqrt{c_2\sigma_1\sigma_2}\,\sec\left[\sqrt{-c_2}(x-ct)\right] - \sigma_3\right)^{1/3} e^{-i(kx-\theta-t\omega)}, \tag{34}$$

$$v_{1.2.2}(x,t) = A\left(\frac{2}{5\sigma_2}\right)^{1/3}\left(5\sqrt{c_2\sigma_1\sigma_2}\,\sec\left[\sqrt{-c_2}(x-ct)\right] - \sigma_3\right)^{1/3} e^{-i(kx-\theta-t\omega)}, \tag{35}$$

correspond to singular periodic waveforms.

[1.2.3] If $c_2 < 0$, $c_4 > 0$, $\sigma_1 < 0$, and $\sigma_2 > 0$, then

$$u_{1.2.3}(x,t) = \left(\frac{2}{5\sigma_2}\right)^{1/3}\left(5\sqrt{c_2\sigma_1\sigma_2}\,\csc\left[\sqrt{-c_2}(x-ct)\right] - \sigma_3\right)^{1/3} e^{-i(kx-\theta-t\omega)}, \tag{36}$$

$$v_{1.2.3}(x,t) = A\left(\frac{2}{5\sigma_2}\right)^{1/3}\left(5\sqrt{c_2\sigma_1\sigma_2}\,\csc\left[\sqrt{-c_2}(x-ct)\right] - \sigma_3\right)^{1/3} e^{-i(kx-\theta-t\omega)}, \tag{37}$$

correspond to singular periodic waveforms.

Case Study 2: $c_1 = c_3 = c_5 = 0$.
Solving the resulting algebraic system produces three consistent parameter sets.

[2.1] $p_0 = -\dfrac{2\sigma_3}{5\sigma_2}$, $p_1 = \pm\dfrac{2\sqrt{-c_4\sigma_1}}{\sqrt{\sigma_2}}$, $q_1 = 0$, $s_1 = 0$, $\sigma_4 = \dfrac{25c_2\sigma_1\sigma_2 - 6\sigma_3^2}{25\sigma_2}$, $\sigma_5 = \dfrac{2(25c_2\sigma_1\sigma_2\sigma_3 - 2\sigma_3^3)}{125\sigma_2^2}$, $\sigma_6 = -\dfrac{2(25c_2\sigma_1\sigma_2 - 2\sigma_3^2)^2}{625\sigma_2^3}$.

[2.2] $p_0 = -\dfrac{2\sigma_3}{5\sigma_2}$, $p_1 = 0$, $q_1 = \pm\dfrac{c_2\sqrt{-\sigma_1}}{\sqrt{c_4\sigma_2}}$, $s_1 = 0$, $\sigma_4 = -\dfrac{2(25c_2\sigma_1\sigma_2 + 3\sigma_3^2)}{25\sigma_2}$, $\sigma_5 = -\dfrac{4(25c_2\sigma_1\sigma_2\sigma_3 + \sigma_3^3)}{125\sigma_2^2}$, $\sigma_6 = -\dfrac{8(50c_2\sigma_1\sigma_2\sigma_3^2 + \sigma_3^4)}{625\sigma_2^3}$.

[2.3] $p_0 = -\dfrac{2\sigma_3}{5\sigma_2}$, $p_1 = \pm\dfrac{2\sqrt{-c_4\sigma_1}}{\sqrt{\sigma_2}}$, $q_1 = \pm\dfrac{c_2\sqrt{-\sigma_1}}{\sqrt{c_4\sigma_2}}$, $s_1 = 0$, $\sigma_4 = -\dfrac{2(25c_2\sigma_1\sigma_2 + 3\sigma_3^2)}{25\sigma_2}$, $\sigma_5 = -\dfrac{4(25c_2\sigma_1\sigma_2\sigma_3 + \sigma_3^3)}{125\sigma_2^2}$, $\sigma_6 = -\dfrac{8(50c_2\sigma_1\sigma_2\sigma_3^2 + \sigma_3^4)}{625\sigma_2^3}$.

From subcase [2.1] the following explicit solutions are obtained:

[2.1.1] If $c_2 < 0$, $c_4 > 0$, $\sigma_1 < 0$, $\sigma_2 > 0$, and $c_0 = \dfrac{c_2^2}{4c_4}$, then

$$u_{2.1.1}(x,t) = \frac{1}{(5\sigma_2)^{1/3}}\left(-2\sigma_3 \pm 5\sqrt{2c_2\sigma_1\sigma_2}\tanh\left[\frac{\sqrt{-c_2}(x-ct)}{\sqrt{2}}\right]\right)^{1/3} e^{-i(kx-\theta-t\omega)}, \tag{38}$$

$$v_{2.1.1}(x,t) = \frac{A}{(5\sigma_2)^{1/3}}\left(-2\sigma_3 \pm 5\sqrt{2c_2\sigma_1\sigma_2}\tanh\left[\frac{\sqrt{-c_2}(x-ct)}{\sqrt{2}}\right]\right)^{1/3} e^{-i(kx-\theta-t\omega)}, \tag{39}$$

represent dark soliton waveforms.

[2.1.2] If $c_2 > 0$, $c_4 > 0$, $\sigma_1 < 0$, $\sigma_2 > 0$, and $c_0 = \dfrac{c_2^2}{4c_4}$, then

$$u_{2.1.2}(x,t) = \frac{1}{(5\sigma_2)^{1/3}}\left(-2\sigma_3 \pm 5\sqrt{-2c_2\sigma_1\sigma_2}\tan\left[\frac{\sqrt{c_2}(x-ct)}{\sqrt{2}}\right]\right)^{1/3} e^{-i(kx-\theta-t\omega)}, \tag{40}$$

$$v_{2.1.2}(x,t) = \frac{A}{(5\sigma_2)^{1/3}}\left(-2\sigma_3 \pm 5\sqrt{-2c_2\sigma_1\sigma_2}\tan\left[\frac{\sqrt{c_2}(x-ct)}{\sqrt{2}}\right]\right)^{1/3} e^{-i(kx-\theta-t\omega)}, \tag{41}$$

correspond to singular periodic waveforms.

From subcase [2.2] the following explicit solutions are obtained:

[2.2.1] If $c_2 < 0$, $c_4 > 0$, $\sigma_1 < 0$, $\sigma_2 > 0$, and $c_0 = \dfrac{c_2^2}{4c_4}$, then

$$u_{2.2.1}(x,t) = \frac{1}{(5\sigma_2)^{1/3}}\left(-2\sigma_3 \pm 5\sqrt{2c_2\sigma_1\sigma_2}\coth\left[\frac{\sqrt{-c_2}(x-ct)}{\sqrt{2}}\right]\right)^{1/3} e^{-i(kx-\theta-t\omega)}, \tag{42}$$

$$v_{2.2.1}(x,t) = \frac{A}{(5\sigma_2)^{1/3}}\left(-2\sigma_3 \pm 5\sqrt{2c_2\sigma_1\sigma_2}\coth\left[\frac{\sqrt{-c_2}(x-ct)}{\sqrt{2}}\right]\right)^{1/3} e^{-i(kx-\theta-t\omega)}, \tag{43}$$

correspond to singular soliton waveforms.

[2.2.2] If $c_2 > 0$, $c_4 > 0$, $\sigma_1 < 0$, $\sigma_2 > 0$, and $c_0 = \dfrac{c_2^2}{4c_4}$, then

$$u_{2.2.2}(x,t) = \frac{1}{(5\sigma_2)^{1/3}}\left(-2\sigma_3 \pm 5\sqrt{-2c_2\sigma_1\sigma_2}\cot\left[\frac{\sqrt{c_2}(x-ct)}{\sqrt{2}}\right]\right)^{1/3} e^{-i(kx-\theta-t\omega)}, \tag{44}$$

$$v_{2.2.2}(x,t) = \frac{A}{(5\sigma_2)^{1/3}}\left(-2\sigma_3 \pm 5\sqrt{-2c_2\sigma_1\sigma_2}\cot\left[\frac{\sqrt{c_2}(x-ct)}{\sqrt{2}}\right]\right)^{1/3} e^{-i(kx-\theta-t\omega)}, \tag{45}$$

correspond to singular periodic waveforms.

From subcase [2.3] the following explicit solutions are obtained:

[2.3.1] If $c_2 < 0$, $c_4 > 0$, $\sigma_1 < 0$, $\sigma_2 > 0$, and $c_0 = \dfrac{c_2^2}{4c_4}$, then

$$u_{2.3.1}(x,t) = \frac{1}{(5\sigma_2)^{1/3}}\left(-2\sigma_3 \pm 5\sqrt{2c_2\sigma_1\sigma_2}\left(\coth\left[\frac{\sqrt{-c_2}(x-ct)}{\sqrt{2}}\right] + \tanh\left[\frac{\sqrt{-c_2}(x-ct)}{\sqrt{2}}\right]\right)\right)^{1/3} e^{-i(kx-\theta-t\omega)}, \tag{46}$$

$$v_{2.3.1}(x,t) = \frac{A}{(5\sigma_2)^{1/3}}\left(-2\sigma_3 \pm 5\sqrt{2c_2\sigma_1\sigma_2}\left(\coth\left[\frac{\sqrt{-c_2}(x-ct)}{\sqrt{2}}\right] + \tanh\left[\frac{\sqrt{-c_2}(x-ct)}{\sqrt{2}}\right]\right)\right)^{1/3} e^{-i(kx-\theta-t\omega)}, \tag{47}$$

are combo singular-dark soliton solutions.

[2.3.2] If $c_2 > 0$, $c_4 > 0$, $\sigma_1 < 0$, $\sigma_2 > 0$, and $c_0 = \dfrac{c_2^2}{4c_4}$, then

$$u_{2.3.2}(x,t) = \frac{1}{(5\sigma_2)^{1/3}}\left(-2\sigma_3 \pm 5\sqrt{-2c_2\sigma_1\sigma_2}\left(\cot\left[\frac{\sqrt{c_2}(x-ct)}{\sqrt{2}}\right] + \tan\left[\frac{\sqrt{c_2}(x-ct)}{\sqrt{2}}\right]\right)\right)^{1/3} e^{-i(kx-\theta-t\omega)}, \tag{48}$$

$$v_{2.3.2}(x,t) = \frac{A}{(5\sigma_2)^{1/3}}\left(-2\sigma_3 \pm 5\sqrt{-2c_2\sigma_1\sigma_2}\left(\cot\left[\frac{\sqrt{c_2}(x-ct)}{\sqrt{2}}\right] + \tan\left[\frac{\sqrt{c_2}(x-ct)}{\sqrt{2}}\right]\right)\right)^{1/3} e^{-i(kx-\theta-t\omega)}, \tag{49}$$

correspond to singular periodic waveforms.

Case Study 3: $c_3 = c_4 = c_5 = 0$
Solving the resulting algebraic system produces six consistent parameter sets.

[3.1] $p_0 = -\dfrac{2\sigma_5}{c_2\sigma_1+\sigma_4}$, $p_1 = 0$, $q_1 = -\dfrac{6c_1\sigma_1\sigma_5}{c_2^2\sigma_1^2-\sigma_4^2}$, $s_1 = 0$, $\sigma_2 = 0$, $\sigma_3 = \dfrac{5(c_2^2\sigma_1^2-\sigma_4^2)}{12\sigma_5}$, $\sigma_6 = \dfrac{8(2c_2\sigma_1+\sigma_4)\sigma_5^2}{3(c_2\sigma_1+\sigma_4)^2}$.

[3.2] $p_0 = -\dfrac{5(c_2\sigma_1-\sigma_4)}{6\sigma_3}$, $p_1 = 0$, $q_1 = -\dfrac{5c_1\sigma_1}{2\sigma_3}$, $s_1 = 0$, $\sigma_2 = 0$, $\sigma_5 = \dfrac{5(c_2^2\sigma_1^2-\sigma_4^2)}{12\sigma_3}$,
$\sigma_6 = \dfrac{25(c_2\sigma_1-\sigma_4)^2(2c_2\sigma_1+\sigma_4)}{54\sigma_3^2}$.

[3.3] $p_0 = -\dfrac{2\sigma_3}{5\sigma_2}$, $p_1 = 0$, $q_1 = \dfrac{2\sqrt{-c_0\sigma_1}}{\sqrt{\sigma_2}}$, $s_1 = 0$, $\sigma_4 = \dfrac{25c_2\sigma_1\sigma_2-6\sigma_3^2}{25\sigma_2}$, $\sigma_5 = \dfrac{2(25c_2\sigma_1\sigma_2\sigma_3-2\sigma_3^3)}{125\sigma_2^2}$,
$\sigma_6 = \dfrac{8(25c_2\sigma_1\sigma_2\sigma_3^2-\sigma_3^4)}{625\sigma_2^3}$.

[3.4] $p_0 = \dfrac{\sqrt{2(c_2\sigma_1-\sigma_4)}}{\sqrt{3\sigma_2}}$, $p_1 = 0$, $q_1 = \dfrac{2\sqrt{-c_0\sigma_1}}{\sqrt{\sigma_2}}$, $s_1 = 0$, $\sigma_3 = -\dfrac{5\sqrt{\sigma_2(c_2\sigma_1-\sigma_4)}}{\sqrt{6}}$,
$\sigma_5 = \dfrac{1}{9}\left(-\dfrac{2c_2\sigma_1\sqrt{6(c_2\sigma_1-\sigma_4)}}{\sqrt{\sigma_2}} - \dfrac{\sqrt{6(c_2\sigma_1-\sigma_4)}\sigma_4}{\sqrt{\sigma_2}}\right)$, $\sigma_6 = \dfrac{2(5c_2^2\sigma_1^2-4c_2\sigma_1\sigma_4-\sigma_4^2)}{9\sigma_2}$.

[3.5] $p_0 = \dfrac{-2\sigma_3+\sqrt{4\sigma_3^3+125\sigma_2^2\sigma_5}}{5\sigma_2}$, $p_1 = 0$, $q_1 = \dfrac{c_1\sqrt{4\sigma_3^3+125\sigma_2^2\sigma_5}}{5c_2\sigma_2\sqrt{\sigma_3}}$, $s_1 = 0$, $\sigma_1 = \dfrac{-4\sigma_3^3-125\sigma_2^2\sigma_5}{25c_2\sigma_2\sigma_3}$,
$\sigma_4 = \dfrac{-8\sigma_3^3+125\sigma_2^2\sigma_5}{50\sigma_2\sigma_3}$, $\sigma_6 = -\dfrac{25\sigma_2\sigma_5^2}{2\sigma_3^2}$.

[3.6] $p_0 = \dfrac{5\sigma_5^2+\sqrt{5\sigma_5(5\sigma_5^3+\sigma_3\sigma_6^2)}}{\sigma_3\sigma_6}$, $p_1 = 0$, $q_1 = \dfrac{c_1\sqrt{5\sigma_5(5\sigma_5^3+\sigma_3\sigma_6^2)}}{c_2\sigma_3\sigma_6}$, $s_1 = 0$, $\sigma_1 = \dfrac{2(5\sigma_5^3+\sigma_3\sigma_6^2)}{5c_2\sigma_5\sigma_6}$,
$\sigma_2 = -\dfrac{2\sigma_3^2\sigma_6}{25\sigma_5^2}$, $\sigma_4 = \dfrac{10\sigma_5^3-\sigma_3\sigma_6^2}{5\sigma_5\sigma_6}$.

From subcase [3.1] the following explicit solutions are obtained:
[3.1.1] If $c_2 > 0$, $(c_2^2\sigma_1^2 - \sigma_4^2) \neq 0$, and $c_0 = 0$, then

$$u_{3.1.1}(x,t) = 2^{1/3}\left(-\frac{\left(c_2\sigma_1(5+\sinh\left[\sqrt{c_2}(x-ct)\right]) - \sigma_5(-1+\sinh\left[\sqrt{c_2}(x-ct)\right])\sigma_4\right)}{(c_2^2\sigma_1^2-\sigma_4^2)(-1+\sinh\left[\sqrt{c_2}(x-ct)\right])}\right)^{1/3} e^{-i(kx-\theta-t\omega)}, \tag{50}$$

$$v_{3.1.1}(x,t) = 2^{1/3}A\left(-\frac{\left(c_2\sigma_1(5+\sinh\left[\sqrt{c_2}(x-ct)\right]) - \sigma_5(-1+\sinh\left[\sqrt{c_2}(x-ct)\right])\sigma_4\right)}{(c_2^2\sigma_1^2-\sigma_4^2)(-1+\sinh\left[\sqrt{c_2}(x-ct)\right])}\right)^{1/3} e^{-i(kx-\theta-t\omega)}, \tag{51}$$

are hyperbolic solutions.
[3.1.2] If $c_2 < 0$, $(c_2^2\sigma_1^2 - \sigma_4^2) \neq 0$, and $c_0 = 0$, then

$$u_{3.1.2}(x,t) = 2^{1/3}\left(-\frac{\sigma_5}{c_2\sigma_1+\sigma_4} - \frac{6c_2\sigma_1\sigma_5}{(c_2^2\sigma_1^2-\sigma_4^2)(-1+\sin\left[\sqrt{-c_2}(x-ct)\right])}\right)^{1/3} e^{i(-kx+\theta+t\omega)}, \tag{52}$$

$$v_{3.1.2}(x,t) = 2^{1/3}A\left(-\frac{\sigma_5}{c_2\sigma_1+\sigma_4} - \frac{6c_2\sigma_1\sigma_5}{(c_2^2\sigma_1^2-\sigma_4^2)(-1+\sin\left[\sqrt{-c_2}(x-ct)\right])}\right)^{1/3} e^{i(-kx+\theta+t\omega)}, \tag{53}$$

are periodic solutions.

From subcase [3.2] the following explicit solutions are obtained:
[3.2.1] If $c_2 > 0$, $(c_2^2\sigma_1^2 - \sigma_4^2) \neq 0$, and $c_0 = 0$, then

$$u_{3.2.1}(x,t) = 2^{1/3}\left(-\frac{\sigma_5\left(c_2\sigma_1(5+\sinh\left[\sqrt{c_2}(x-ct)\right]) - (-1+\sinh\left[\sqrt{c_2}(x-ct)\right])\sigma_4\right)}{(-1+\sinh\left[\sqrt{c_2}(x-ct)\right])(c_2^2\sigma_1^2-\sigma_4^2)}\right)^{1/3} e^{-i(kx-\theta-t\omega)}, \tag{54}$$

$$v_{3.2.1}(x,t) = 2^{1/3}A\left(-\frac{\sigma_5\left(c_2\sigma_1(5+\sinh\left[\sqrt{c_2}(x-ct)\right]) - (-1+\sinh\left[\sqrt{c_2}(x-ct)\right])\sigma_4\right)}{(-1+\sinh\left[\sqrt{c_2}(x-ct)\right])(c_2^2\sigma_1^2-\sigma_4^2)}\right)^{1/3} e^{-i(kx-\theta-t\omega)}, \tag{55}$$

are hyperbolic solutions.
[3.2.2] If $c_2 < 0$, , $\sigma_3 \neq 0$, and $c_0 = 0$, then

$$u_{3.2.2}(x,t) = \left(\frac{5}{6}\right)^{1/3}\left(-\frac{c_2\sigma_1(5+\sin\left[\sqrt{-c_2}(x-ct)\right])}{\sigma_3(-1+\sin\left[\sqrt{-c_2}(x-ct)\right])} + \frac{\sigma_4}{\sigma_3}\right)^{1/3} e^{-i(kx-\theta-t\omega)}, \tag{56}$$

$$v_{3.2.2}(x,t) = A\left(\frac{5}{6}\right)^{1/3}\left(-\frac{c_2\sigma_1(5+\sin\left[\sqrt{-c_2}(x-ct)\right])}{\sigma_3(-1+\sin\left[\sqrt{-c_2}(x-ct)\right])} + \frac{\sigma_4}{\sigma_3}\right)^{1/3} e^{-i(kx-\theta-t\omega)}, \tag{57}$$

are periodic solutions.

From subcase [3.3] the following explicit solutions are obtained:
[3.3.3] If $c_2 > 0$, $c_0 > 0$, $\sigma_1 < 0$, $\sigma_2 > 0$, and $c_1 = 0$, then

$$u_{3.3.3}(x,t) = \left(-2\sqrt{-\frac{c_2\sigma_1}{\sigma_2}}\,\mathrm{csch}\left[\sqrt{c_2}(x-ct)\right] + \frac{2\sigma_3}{5\sigma_2}\right)^{1/3} e^{-i(kx-\theta-t\omega)}, \tag{58}$$

$$v_{3.3.3}(x,t) = A\left(-2\sqrt{-\frac{c_2\sigma_1}{\sigma_2}}\,\mathrm{csch}\left[\sqrt{c_2}(x-ct)\right] + \frac{2\sigma_3}{5\sigma_2}\right)^{1/3} e^{-i(kx-\theta-t\omega)}, \tag{59}$$

correspond to singular soliton waveforms.
[3.3.4] If $c_2 < 0$, $c_0 > 0$, $\sigma_1 < 0$, $\sigma_2 > 0$, and $c_1 = 0$, then

$$u_{3.3.4}(x,t) = \left(-2\sqrt{\frac{c_2\sigma_1}{\sigma_2}}\,\csc\left[\sqrt{-c_2}(x-ct)\right] + \frac{2\sigma_3}{5\sigma_2}\right)^{1/3} e^{-i(kx-\theta-t\omega)}, \tag{60}$$

$$v_{3.3.4}(x,t) = A\left(-2\sqrt{\frac{c_2\sigma_1}{\sigma_2}}\,\csc\left[\sqrt{-c_2}(x-ct)\right] + \frac{2\sigma_3}{5\sigma_2}\right)^{1/3} e^{-i(kx-\theta-t\omega)}, \tag{61}$$

correspond to singular periodic waveforms.

From subcase [3.4] the following explicit solutions are obtained:
[3.4.3] If $c_2 > 0$, $c_0 > 0$, $\sigma_1 < 0$, $\sigma_2 > 0$, $(6c_2\sigma_1 - 6\sigma_4) > 0$, and $c_1 = 0$, then

$$u_{3.4.3}(x,t) = \frac{1}{(3\sqrt{\sigma_2})^{1/3}}\left(6\sqrt{-c_2\sigma_1}\,\text{csch}\left[\sqrt{c_2}(x-ct)\right] + \sqrt{6c_2\sigma_1 - 6\sigma_4}\right)^{1/3} e^{-i(kx-\theta-t\omega)}, \tag{62}$$

$$v_{3.4.3}(x,t) = \frac{A}{(3\sqrt{\sigma_2})^{1/3}}\left(6\sqrt{-c_2\sigma_1}\,\text{csch}\left[\sqrt{c_2}(x-ct)\right] + \sqrt{6c_2\sigma_1 - 6\sigma_4}\right)^{1/3} e^{-i(kx-\theta-t\omega)}, \tag{63}$$

correspond to singular soliton waveforms.
[3.4.4] If $c_2 < 0$, $c_0 > 0$, $\sigma_1 < 0$, $\sigma_2 > 0$, $(6c_2\sigma_1 - 6\sigma_4) > 0$, and $c_1 = 0$, then

$$u_{3.4.4}(x,t) = \frac{1}{(3\sqrt{\sigma_2})^{1/3}}\left(-6\sqrt{c_2\sigma_1}\,\csc\left[\sqrt{-c_2}(x-ct)\right] + \sqrt{6c_2\sigma_1 - 6\sigma_4}\right)^{1/3} e^{-i(kx-\theta-t\omega)}, \tag{64}$$

$$v_{3.4.4}(x,t) = \frac{A}{(3\sqrt{\sigma_2})^{1/3}}\left(-6\sqrt{c_2\sigma_1}\,\csc\left[\sqrt{-c_2}(x-ct)\right] + \sqrt{6c_2\sigma_1 - 6\sigma_4}\right)^{1/3} e^{-i(kx-\theta-t\omega)}, \tag{65}$$

correspond to singular periodic waveforms.

From subcase [3.5] the following explicit solutions are obtained:
[3.5.5] If $c_2 > 0$, $(4\sigma_3^3 + 125\sigma_2^2\sigma_5) > 0$, and $c_0 = \dfrac{c_1^2}{4c_2}$, then

$$u_{3.5.5}(x,t) = \frac{-1}{(5\sigma_2)^{1/3}}\left(2\sigma_3 + \frac{(c_1 + 2e^{\sqrt{c_2}(x-ct)}c_2)\sqrt{4\sigma_3^3 + 125\sigma_2^2\sigma_5}}{(c_1 - 2e^{\sqrt{c_2}(x-ct)}c_2)\sqrt{\sigma_3}}\right)e^{i(-kx+\theta+t\omega)}, \tag{66}$$

$$v_{3.5.5}(x,t) = \frac{-A}{(5\sigma_2)^{1/3}}\left(2\sigma_3 + \frac{(c_1 + 2e^{\sqrt{c_2}(x-ct)}c_2)\sqrt{4\sigma_3^3 + 125\sigma_2^2\sigma_5}}{(c_1 - 2e^{\sqrt{c_2}(x-ct)}c_2)\sqrt{\sigma_3}}\right)e^{i(-kx+\theta+t\omega)}, \tag{67}$$

are an exponential solutions.

From subcase [3.6] the following explicit solutions are obtained:
[3.6.5] If $c_2 > 0$, $\sigma_5 > 0$, $(5\sigma_5^4 + \sigma_3\sigma_5\sigma_6^2) > 0$, and $c_0 = \dfrac{c_1^2}{4c_2}$, then

$$u_{3.6.5}(x,t) = \frac{1}{(\sigma_3\sigma_6)^{1/3}}\left(5\sigma_5^2 - \frac{\sqrt{5}(c_1 + 2e^{\sqrt{c_2}(x-ct)}c_2)\sqrt{5\sigma_5^4 + \sigma_3\sigma_5\sigma_6^2}}{c_1 - 2e^{\sqrt{c_2}(x-ct)}c_2}\right)^{1/3} e^{i(-kx+\theta+t\omega)}, \tag{68}$$

$$v_{3.6.5}(x,t) = \frac{A}{(\sigma_3\sigma_6)^{1/3}}\left(5\sigma_5^2 - \frac{\sqrt{5}(c_1 + 2e^{\sqrt{c_2}(x-ct)}c_2)\sqrt{5\sigma_5^4 + \sigma_3\sigma_5\sigma_6^2}}{c_1 - 2e^{\sqrt{c_2}(x-ct)}c_2}\right)^{1/3} e^{i(-kx+\theta+t\omega)}, \tag{69}$$

are an exponential solutions.

Case Study 4: $c_0 = c_1 = c_2 = c_5 = 0$.
Solving the resulting algebraic system produces the consistent parameter set.

[4.1] $p_0 = \dfrac{-5c_3\sqrt{-\sigma_1\sigma_2} - 4\sigma_3\sqrt{c_4}}{10\sigma_2\sqrt{c_4}},\ p_1 = -\dfrac{2\sqrt{-c_4\sigma_1}}{\sqrt{\sigma_2}},\ q_1 = 0,\ s_1 = 0,\ \sigma_4 = -\dfrac{3(25c_3^2\sigma_1\sigma_2 + 16c_4\sigma_3^2)}{200c_4\sigma_2},$
$\sigma_5 = \dfrac{-125c_3^3\sigma_2^{3/2}(-\sigma_1)^{3/2} - 150c_3^2\sigma_1\sigma_2\sigma_3\sqrt{c_4} - 32c_4^{3/2}\sigma_3^3}{1000c_4^{3/2}\sigma_2^2}.$

From subcase [4.1] the following explicit solutions are obtained:
[4.1.1] If $c_4 \neq 0$, $\sigma_1 < 0$, and $\sigma_2 > 0$, then

$$u_{4.1.1}(x,t) = \left(\frac{c_3\sqrt{-\sigma_1}\left((x-ct)^2c_3^2 + 12c_4\right)}{2\left(-(x-ct)^2c_3^2 + 4c_4\right)\sqrt{c_4\sigma_2}} - \frac{2\sigma_3}{5\sigma_2} \right)^{1/3} e^{i(-kx+\theta+t\omega)}, \tag{70}$$

$$v_{4.1.1}(x,t) = A\left(\frac{c_3\sqrt{-\sigma_1}\left((x-ct)^2c_3^2 + 12c_4\right)}{2\left(-(x-ct)^2c_3^2 + 4c_4\right)\sqrt{c_4\sigma_2}} - \frac{2\sigma_3}{5\sigma_2} \right)^{1/3} e^{i(-kx+\theta+t\omega)}, \tag{71}$$

are rational solutions.

Case Study 5: $c_0 = c_1 = c_5 = 0$.
Solving the resulting algebraic system produces two consistent parameter sets.

[5.1] $p_0 = \dfrac{5\sigma_5^2 + \sqrt{5\sigma_5(5\sigma_5^3 + \sigma_3\sigma_6^2)}}{\sigma_3\sigma_6}$, $p_1 = \dfrac{4c_4\sqrt{5\sigma_5(5\sigma_5^3 + \sigma_3\sigma_6^2)}}{c_3\sigma_3\sigma_6}$, $q_1 = 0$, $s_1 = 0$, $\sigma_1 = \dfrac{8(5c_4\sigma_5^3 + c_4\sigma_3\sigma_6^2)}{5c_3^2\sigma_5\sigma_6}$,
$\sigma_2 = -\dfrac{2\sigma_3^2\sigma_6}{25\sigma_5^2}$, $\sigma_4 = \dfrac{10\sigma_5^3 - \sigma_3\sigma_6^2}{5\sigma_5\sigma_6}$.
[5.2] $p_0 = \dfrac{5c_3\sqrt{-\sigma_1\sigma_2} - 4\sigma_3\sqrt{c_4}}{10\sigma_2\sqrt{c_4}}$, $p_1 = \dfrac{2\sqrt{-c_4\sigma_1}}{\sqrt{\sigma_2}}$, $q_1 = 0$, $s_1 = 0$, $\sigma_4 = -\dfrac{25c_3^2\sigma_1\sigma_2 + 48c_4\sigma_3^2}{200c_4\sigma_2}$,
$\sigma_5 = -\dfrac{25c_3^2\sigma_1\sigma_2\sigma_3 + 16c_4\sigma_3^3}{500c_4\sigma_2^2}$, $\sigma_6 = -\dfrac{(25c_3^2\sigma_1\sigma_2 + 16c_4\sigma_3^2)^2}{20000c_4^2\sigma_2^3}$.
From subcase [5.1] the following explicit solutions are obtained:
[5.1.1] If $c_2 > 0$, $\sigma_5 > 0$, $(5\sigma_5^3 + \sigma_3\sigma_6^2) > 0$, and $c_2 = \dfrac{c_3^2}{4c_4}$, then

$$\begin{aligned} u_{5.1.1}(x,t) = \left(\frac{\sqrt{\sigma_5}}{c_3^2\sigma_3\sigma_6}\right)^{1/3} & \Bigg(c_3^2\left(5\sigma_5^{3/2} + \sqrt{5(5\sigma_5^3 + \sigma_3\sigma_6^2)}\right) \\ & -4c_2c_4\sqrt{5(5\sigma_5^3 + \sigma_3\sigma_6^2)}\left(1 + \tanh\left[\frac{\sqrt{c_2}(x-ct)}{2}\right]\right)\Bigg)^{1/3} e^{-i(kx-\theta-t\omega)}, \end{aligned} \tag{72}$$

$$\begin{aligned} v_{5.1.1}(x,t) = A\left(\frac{\sqrt{\sigma_5}}{c_3^2\sigma_3\sigma_6}\right)^{1/3} & \Bigg(c_3^2\left(5\sigma_5^{3/2} + \sqrt{5(5\sigma_5^3 + \sigma_3\sigma_6^2)}\right) \\ & -4c_2c_4\sqrt{5(5\sigma_5^3 + \sigma_3\sigma_6^2)}\left(1 + \tanh\left[\frac{\sqrt{c_2}(x-ct)}{2}\right]\right)\Bigg)^{1/3} e^{-i(kx-\theta-t\omega)}, \end{aligned} \tag{73}$$

represent dark soliton waveforms.

[5.1.2] If $c_2 > 0$, $\sigma_5 > 0$, $(5\sigma_5^3 + \sigma_3\sigma_6^2) > 0$, and $c_2 = \dfrac{c_3^2}{4c_4}$, then

$$\begin{aligned} u_{5.1.2}(x,t) = \left(\frac{\sqrt{\sigma_5}}{c_3^2\sigma_3\sigma_6}\right)^{1/3} & \Bigg(c_3^2\left(5\sigma_5^{3/2} + \sqrt{5(5\sigma_5^3 + \sigma_3\sigma_6^2)}\right) \\ & -4c_2c_4\sqrt{5(5\sigma_5^3 + \sigma_3\sigma_6^2)}\left(1 + \coth\left[\frac{\sqrt{c_2}(x-ct)}{2}\right]\right)\Bigg)^{1/3} e^{-i(kx-\theta-t\omega)}, \end{aligned} \tag{74}$$

$$v_{5.1.2}(x,t) = A\left(\frac{\sqrt{\sigma_5}}{c_3^2\sigma_3\sigma_6}\right)^{1/3} \Bigg(c_3^2\left(5\sigma_5^{3/2} + \sqrt{5(5\sigma_5^3 + \sigma_3\sigma_6^2)}\right)$$

$$-4c_2c_4\sqrt{5(5\sigma_5^3+\sigma_3\sigma_6^2)}\left(1+\coth\left[\frac{\sqrt{c_2}(x-ct)}{2}\right]\right)\Bigg)^{1/3} e^{-i(kx-\theta-t\omega)}, \quad (75)$$

correspond to singular soliton waveforms.

From subcase [5.2] the following explicit solutions are obtained:

[5.2.1] If $c_2>0$, $\sigma_1<0$, $\sigma_2>0$, and $c_2=\dfrac{c_3^2}{4c_4}$, then

$$u_{5.2.1}(x,t)=\frac{1}{(10c_3\sigma_2\sqrt{c_4})^{1/3}}\Bigg(5c_3^2\sqrt{-\sigma_1\sigma_2}-4c_3\sigma_3\sqrt{c_4}$$
$$-20c_2c_4\sqrt{-\sigma_1\sigma_2}\left(1+\tanh\left[\frac{\sqrt{c_2}(x-ct)}{2}\right]\right)\Bigg)^{1/3} e^{-i(kx-\theta-t\omega)}, \quad (76)$$

$$v_{5.2.1}(x,t)=\frac{A}{(10c_3\sigma_2\sqrt{c_4})^{1/3}}\Bigg(5c_3^2\sqrt{-\sigma_1\sigma_2}-4c_3\sigma_3\sqrt{c_4}$$
$$-20c_2c_4\sqrt{-\sigma_1\sigma_2}\left(1+\tanh\left[\frac{\sqrt{c_2}(x-ct)}{2}\right]\right)\Bigg)^{1/3} e^{-i(kx-\theta-t\omega)}, \quad (77)$$

represent dark soliton waveforms.

[5.2.2] If $c_2>0$, $\sigma_1<0$, $\sigma_2>0$, and $c_2=\dfrac{c_3^2}{4c_4}$, then

$$u_{5.2.2}(x,t)=\frac{1}{(10c_3\sigma_2\sqrt{c_4})^{1/3}}\Bigg(5c_3^2\sqrt{-\sigma_1\sigma_2}-4c_3\sigma_3\sqrt{c_4}$$
$$-20c_2c_4\sqrt{-\sigma_1\sigma_2}\left(1+\coth\left[\frac{\sqrt{c_2}(x-ct)}{2}\right]\right)\Bigg)^{1/3} e^{-i(kx-\theta-t\omega)}, \quad (78)$$

$$v_{5.2.2}(x,t)=\frac{A}{(10c_3\sigma_2\sqrt{c_4})^{1/3}}\Bigg(5c_3^2\sqrt{-\sigma_1\sigma_2}-4c_3\sigma_3\sqrt{c_4}$$
$$-20c_2c_4\sqrt{-\sigma_1\sigma_2}\left(1+\coth\left[\frac{\sqrt{c_2}(x-ct)}{2}\right]\right)\Bigg)^{1/3} e^{-i(kx-\theta-t\omega)}, \quad (79)$$

correspond to singular soliton waveforms.

Case Study 6: $c_2=c_4=c_5=0$

Solving the resulting algebraic system produces two consistent parameter sets.

[6.1] $p_0=\dfrac{5\sigma_4}{6\sigma_3}$, $p_1=-\dfrac{5c_3\sigma_1}{2\sigma_3}$, $q_1=0$, $s_1=0$, $\sigma_2=0$, $\sigma_6=\dfrac{25(27c_0c_3^2\sigma_1^3+9c_1c_3\sigma_1^2\sigma_4+\sigma_4^3)}{54\sigma_3^2}$,
$\sigma_5=-\dfrac{5(3c_1c_3\sigma_1^2+\sigma_4^2)}{12\sigma_3}$.

[6.2] $p_0=\dfrac{5c_1\sqrt{-\sigma_1\sigma_2}-4\sigma_3\sqrt{c_0}}{10\sigma_2\sqrt{c_0}}$, $p_1=0$, $q_1=\dfrac{2\sqrt{-c_0\sigma_1}}{\sqrt{\sigma_2}}$, $s_1=0$, $\sigma_4=-\dfrac{3(25c_1^2\sigma_1\sigma_2+16c_0\sigma_3^2)}{200c_0\sigma_2}$,
$\sigma_5=\dfrac{125c_1^3\sigma_2^{3/2}(-\sigma_1)^{3/2}+1000c_0^2c_3\sigma_2^{3/2}(-\sigma_1)^{3/2}-150c_1^2\sigma_1\sigma_2\sigma_3\sqrt{c_0}-32\sigma_3^3c_0^{3/2}}{1000c_0^{3/2}\sigma_2^2}$.

From subcase [6.1] the following explicit solutions are obtained:

[6.1.1] If $c_3>0$, $c_0\neq0$, and $c_1\neq0$, then

$$u_{6.1.1}(x,t)=\left(\frac{5}{6\,\sigma_3}\right)^{1/3}\left(\sigma_4-3c_3\sigma_1\wp\left[\frac{\sqrt{c_3}}{2}(x-ct);g_1,g_2\right]\right)^{1/3} e^{i(-kx+\theta+t\omega)}, \quad (80)$$

$$v_{6.1.1}(x,t) = A\left(\frac{5}{6\,\sigma_3}\right)^{1/3}\left(\sigma_4 - 3c_3\sigma_1\wp\left[\frac{\sqrt{c_3}}{2}(x-ct);g_1,g_2\right]\right)^{1/3} e^{i(-kx+\theta+t\omega)}, \tag{81}$$

are Weierstrass elliptic solution, where $\wp(z;g_1,g_2)$ is the Weierstrass elliptic function with $g_1 = -\frac{4c_1}{c_3}$ and $g_2 = -\frac{4c_0}{c_3}$.

From subcase [6.2] the following explicit solutions are obtained:
[6.2.1] If $c_3 > 0$, $\sigma_1 < 0$, $\sigma_2 > 0$, $c_0 \neq 0$, and $c_1 \neq 0$, then

$$u_{6.2.1}(x,t) = \frac{1}{(10\,\sigma_2)^{1/3}}\left(5c_1\sqrt{-\frac{\sigma_1\sigma_2}{c_0}} - 4\sigma_3 + \frac{20\sqrt{-c_0\sigma_1\sigma_2}}{\wp\left[\frac{\sqrt{c_3}}{2}(x-ct);g_1,g_2\right]}\right)^{1/3} e^{-i(kx-\theta-t\omega)}, \tag{82}$$

$$v_{6.2.1}(x,t) = \frac{A}{(10\,\sigma_2)^{1/3}}\left(5c_1\sqrt{-\frac{\sigma_1\sigma_2}{c_0}} - 4\sigma_3 + \frac{20\sqrt{-c_0\sigma_1\sigma_2}}{\wp\left[\frac{\sqrt{c_3}}{2}(x-ct);g_1,g_2\right]}\right)^{1/3} e^{-i(kx-\theta-t\omega)}, \tag{83}$$

are Weierstrass elliptic solution, where $\wp(z;g_1,g_2)$ is the Weierstrass elliptic function with $g_1 = -\frac{4c_1}{c_3}$ and $g_2 = -\frac{4c_0}{c_3}$.

Case Study 7: $c_1 = c_3 = 0$.
Solving the resulting algebraic system produces three consistent parameter sets.

[7.1] $p_0 = -\frac{\sqrt{2(c_2\sigma_1-\sigma_4)}}{\sqrt{3\sigma_2}}$, $p_1 = 0$, $q_1 = -\frac{2\sqrt{c_0-\sigma_1}}{\sqrt{\sigma_2}}$, $s_1 = 0$, $\sigma_3 = \frac{5\sqrt{\sigma_2(c_2\sigma_1-\sigma_4)}}{\sqrt{6}}$, $c_5 = 0$,
$\sigma_5 = \frac{1}{9}\left(\frac{2c_2\sigma_1\sqrt{6(c_2\sigma_1-\sigma_4)}}{\sqrt{\sigma_2}} + \frac{\sigma_4\sqrt{6(c_2\sigma_1-\sigma_4)}}{\sqrt{\sigma_2}}\right)$, $\sigma_6 = \frac{2(5c_2^2\sigma_1^2 - 36c_0c_4\sigma_1^2 - 4c_2\sigma_1\sigma_4 - \sigma_4^2)}{9\sigma_2}$.
[7.2] $p_0 = -\frac{5(c_2\sigma_1-\sigma_4)}{3\sigma_3}$, $p_1 = 0$, $q_1 = -\frac{5\sqrt{-2c_0\sigma_1(c_2\sigma_1-\sigma_4)}}{\sqrt{2}\sigma_3}$, $s_1 = 0$, $\sigma_2 = \frac{6\sigma_3^2}{25(c_2\sigma_1-\sigma_4)}$,
$\sigma_5 = \frac{5(2c_2^2\sigma_1^2 - c_2\sigma_1\sigma_4 - \sigma_4^2)}{9\sigma_3}$, $\sigma_6 = \frac{25(c_2\sigma_1-\sigma_4)(5c_2^2\sigma_1^2 - 36c_0c_4\sigma_1^2 - 4c_2\sigma_1\sigma_4 - \sigma_4^2)}{27\sigma_3^2}$, $c_5 = 0$.
[7.3] $p_0 = -\frac{2\sigma_3}{5\sigma_2}$, $p_1 = 0$, $q_1 = -\frac{2\sqrt{-c_0\sigma_1}}{\sqrt{\sigma_2}}$, $s_1 = 0$, $\sigma_4 = \frac{25c_2\sigma_1\sigma_2 - 6\sigma_3^2}{25\sigma_2}$, $\sigma_5 = \frac{2(25c_2\sigma_1\sigma_2\sigma_3 - 2\sigma_3^3)}{125\sigma_2^2}$,
$\sigma_6 = -\frac{8(625c_0c_4\sigma_1^2\sigma_2^2 - 25c_2\sigma_1\sigma_2\sigma_3^2 + \sigma_3^4)}{625\sigma_2^3}$, $c_5 = 0$.
From subcase [7.1] the following explicit solutions are obtained:
[7.1.1] If $c_2 > 0$, $c_0 > 0$, $c_4 > 0$, $\sigma_1 < 0$, $\sigma_2 > 0$, and $(c_2\sigma_1 - \sigma_4) > 0$, then

$$u_{7.1.1}(x,t) = \frac{1}{3^{1/3}}\left(\frac{6c_0c_4\sigma_1}{\sqrt{-c_0c_2c_4\sigma_1\sigma_2\operatorname{csch}^2[\sqrt{c_2}(x-ct)]}} - \sqrt{\frac{6(c_2\sigma_1-\sigma_4)}{\sigma_2}}\right)^{1/3} e^{i(-kx+\theta+t\omega)}, \tag{84}$$

$$v_{7.1.1}(x,t) = \frac{A}{3^{1/3}}\left(\frac{6c_0c_4\sigma_1}{\sqrt{-c_0c_2c_4\sigma_1\sigma_2\operatorname{csch}^2[\sqrt{c_2}(x-ct)]}} - \sqrt{\frac{6(c_2\sigma_1-\sigma_4)}{\sigma_2}}\right)^{1/3} e^{i(-kx+\theta+t\omega)}, \tag{85}$$

correspond to singular soliton waveforms.

[7.1.2] If $c_2 < 0$, $c_0 > 0$, $c_4 < 0$, $\sigma_1 < 0$, $\sigma_2 > 0$, and $(c_2\sigma_1 - \sigma_4) > 0$, then

$$u_{7.1.2}(x,t) = \frac{1}{(3\sigma_2)^{1/3}}\left(\frac{6\sigma_1\sqrt{-c_0c_4\sigma_2}}{\sqrt{c_2\sigma_1\csc^2[\sqrt{-c_2}(x-ct)]}} - \sqrt{6\sigma_2(c_2\sigma_1-\sigma_4)}\right)^{1/3} e^{i(-kx+\theta+t\omega)}, \tag{86}$$

$$v_{7.1.2}(x,t) = \frac{A}{(3\sigma_2)^{1/3}}\left(\frac{6\sigma_1\sqrt{-c_0c_4\sigma_2}}{\sqrt{c_2\sigma_1\csc^2[\sqrt{-c_2}(x-ct)]}} - \sqrt{6\sigma_2(c_2\sigma_1-\sigma_4)}\right)^{1/3} e^{i(-kx+\theta+t\omega)}, \tag{87}$$

correspond to singular periodic waveforms.

From subcase [7.2] the following explicit solutions are obtained:
[7.2.1] If $c_2 > 0$, $c_0 > 0$, $c_4 > 0$, $\sigma_1 < 0$, and $(c_2\sigma_1 - \sigma_4) > 0$, then

$$u_{7.2.1}(x,t) = \left(\frac{5}{3\sigma_3}\right)^{1/3}\left(-c_2\sigma_1 + \sigma_4 - \sqrt{\frac{-6c_0c_4\sigma_1(c_2\sigma_1 - \sigma_4)}{c_2\operatorname{csch}^2\left[\sqrt{c_2}(x-ct)\right]}}\right)^{1/3} e^{i(-kx+\theta+t\omega)}, \tag{88}$$

$$v_{7.2.1}(x,t) = A\left(\frac{5}{3\sigma_3}\right)^{1/3}\left(-c_2\sigma_1 + \sigma_4 - \sqrt{\frac{-6c_0c_4\sigma_1(c_2\sigma_1 - \sigma_4)}{c_2\operatorname{csch}^2\left[\sqrt{c_2}(x-ct)\right]}}\right)^{1/3} e^{i(-kx+\theta+t\omega)}, \tag{89}$$

correspond to singular soliton waveforms.

[7.2.2] If $c_2 < 0$, $c_0 > 0$, $c_4 > 0$, $\sigma_1 < 0$, and $(c_2\sigma_1 - \sigma_4) > 0$, then

$$u_{7.2.2}(x,t) = \left(\frac{5}{3\sigma_3}\right)^{1/3}\left(-c_2\sigma_1 + \sigma_4 - \sqrt{\frac{-6c_0c_4\sigma_1(c_2\sigma_1 - \sigma_4)}{c_2\sec^2\left[\sqrt{-c_2}(x-ct)\right]}}\right)^{1/3} e^{i(-kx+\theta+t\omega)}, \tag{90}$$

$$v_{7.2.2}(x,t) = A\left(\frac{5}{3\sigma_3}\right)^{1/3}\left(-c_2\sigma_1 + \sigma_4 - \sqrt{\frac{-6c_0c_4\sigma_1(c_2\sigma_1 - \sigma_4)}{c_2\sec^2\left[\sqrt{-c_2}(x-ct)\right]}}\right)^{1/3} e^{i(-kx+\theta+t\omega)}, \tag{91}$$

correspond to singular periodic waveforms.

From subcase [7.3] the following explicit solutions are obtained:
[7.3.1] If $c_2 > 0$, $c_0 > 0$, $c_4 > 0$, $\sigma_1 < 0$, and $\sigma_2 > 0$, then

$$u_{7.3.1}(x,t) = \left(\frac{2}{5\sigma_2}\right)^{1/3}\left(-\sigma_3 - \sqrt{\frac{-25c_0c_4\sigma_1\sigma_2}{c_2\operatorname{csch}^2\left[\sqrt{c_2}(x-ct)\right]}}\right)^{1/3} e^{i(-kx+\theta+t\omega)}, \tag{92}$$

$$v_{7.3.1}(x,t) = A\left(\frac{2}{5\sigma_2}\right)^{1/3}\left(-\sigma_3 - \sqrt{\frac{-25c_0c_4\sigma_1\sigma_2}{c_2\operatorname{csch}^2\left[\sqrt{c_2}(x-ct)\right]}}\right)^{1/3} e^{i(-kx+\theta+t\omega)}, \tag{93}$$

correspond to singular soliton waveforms.

[7.3.2] If $c_2 < 0$, $c_0 > 0$, $c_4 < 0$, $\sigma_1 < 0$, and $\sigma_2 > 0$, then

$$u_{7.3.2}(x,t) = \left(\frac{2}{5\sigma_2}\right)^{1/3}\left(-\sigma_3 - \sqrt{\frac{-25c_0c_4\sigma_1\sigma_2}{c_2\csc^2\left[\sqrt{-c_2}(x-ct)\right]}}\right)^{1/3} e^{i(-kx+\theta+t\omega)}, \tag{94}$$

$$v_{7.3.2}(x,t) = A\left(\frac{2}{5\sigma_2}\right)^{1/3}\left(-\sigma_3 - \sqrt{\frac{-25c_0c_4\sigma_1\sigma_2}{c_2\csc^2\left[\sqrt{-c_2}(x-ct)\right]}}\right)^{1/3} e^{i(-kx+\theta+t\omega)}, \tag{95}$$

correspond to singular periodic waveforms.

Case Study 8: $c_1 = c_3 = c_5 = 0$.
Solving the resulting algebraic system produces two consistent parameter sets.

[8.1] $p_0 = -\dfrac{2\sigma_3}{5\sigma_2}$, $p_1 = 0$, $q_1 = \dfrac{2\sqrt{c_0 - \sigma_1}}{\sqrt{\sigma_2}}$, $s_1 = 0$, $\sigma_4 = \dfrac{25c_2\sigma_1\sigma_2 - 6\sigma_3^2}{25\sigma_2}$, $\sigma_5 = \dfrac{2(25c_2\sigma_1\sigma_2\sigma_3 - 2\sigma_3^3)}{125\sigma_2^2}$,
$\sigma_6 = -\dfrac{8(625c_0c_4\sigma_1^2\sigma_2^2 - 25c_2\sigma_1\sigma_2\sigma_3^2 + \sigma_3^4)}{625\sigma_2^3}$.
[8.2] $p_0 = -\dfrac{2\sigma_3}{5\sigma_2}$, $p_1 = \dfrac{2\sqrt{-c_4\sigma_1}}{\sqrt{\sigma_2}}$, $q_1 = \dfrac{2\sqrt{-c_0\sigma_1}}{\sqrt{\sigma_2}}$, $s_1 = 0$, $\sigma_4 = \dfrac{25c_2\sigma_1\sigma_2 - 150\sigma_1\sigma_2\sqrt{c_0c_4} - 6\sigma_3^2}{25\sigma_2}$,
$\sigma_5 = \dfrac{2(25c_2\sigma_1\sigma_2\sigma_3 - 150\sigma_1\sigma_2\sigma_3\sqrt{c_0c_4} - 2\sigma_3^3)}{125\sigma_2^2}$.

From subcase [8.1] the following Jacobi elliptic solutions are obtained:
[8.1.1] If $0 \leq m \leq 1$, $c_0 = 1$, $c_2 = -(1+m^2)$, $c_4 = m^2$, $\sigma_1 < 0$, and $\sigma_2 > 0$, then

$$u_{8.1.1}(x,t) = \left(\frac{2\sqrt{-\sigma_1}}{\sqrt{\sigma_2}\,\mathrm{cd}[(x-ct)]} - \frac{2\sigma_3}{5\sigma_2}\right)^{1/3} e^{i(-kx+\theta+t\omega)}, \tag{96}$$

$$v_{8.1.1}(x,t) = A\left(\frac{2\sqrt{-\sigma_1}}{\sqrt{\sigma_2}\,\mathrm{cd}[(x-ct)]} - \frac{2\sigma_3}{5\sigma_2}\right)^{1/3} e^{i(-kx+\theta+t\omega)}, \tag{97}$$

are Jacobi elliptic solutions.
If $m = 0$, then

$$u_{8.1.1a}(x,t) = \left(\frac{2\sqrt{-\sigma_1}\,\sec[(x-ct)]}{\sqrt{\sigma_2}} - \frac{2\sigma_3}{5\sigma_2}\right)^{1/3} e^{i(-kx+\theta+t\omega)}, \tag{98}$$

$$v_{8.1.1a}(x,t) = A\left(\frac{2\sqrt{-\sigma_1}\,\sec[(x-ct)]}{\sqrt{\sigma_2}} - \frac{2\sigma_3}{5\sigma_2}\right)^{1/3} e^{i(-kx+\theta+t\omega)}, \tag{99}$$

correspond to singular periodic waveforms.
[8.1.2] If $0 \leq m \leq 1$, $c_0 = -m^2$, $c_2 = 2m^2 - 1$, $c_4 = -m^2 + 1$, and $\sigma_1, \sigma_2 < 0$, then

$$u_{8.1.2}(x,t) = \left(\frac{2}{5}\right)^{1/3}\left(-\frac{5\,m\sqrt{\sigma_1\sigma_2} + \sigma_3\,\mathrm{nc}\,[(x-ct)]}{\sigma_2\,\mathrm{nc}\,[(x-ct)]}\right)^{1/3} e^{-i(kx-\theta-t\omega)}, \tag{100}$$

$$v_{8.1.2}(x,t) = A\left(\frac{2}{5}\right)^{1/3}\left(-\frac{5\,m\sqrt{\sigma_1\sigma_2} + \sigma_3\,\mathrm{nc}\,[(x-ct)]}{\sigma_2\,\mathrm{nc}\,[(x-ct)]}\right)^{1/3} e^{-i(kx-\theta-t\omega)}, \tag{101}$$

are Jacobi elliptic solutions.
If $m = 1$, then

$$u_{8.1.2a}(x,t) = \left(\frac{2}{5}\right)^{1/3}\left(-\frac{5\,\sqrt{\sigma_1\sigma_2}\,\mathrm{sech}[(x-ct)] + \sigma_3}{\sigma_2}\right)^{1/3} e^{-i(kx-\theta-t\omega)}, \tag{102}$$

$$v_{8.1.2a}(x,t) = A\left(\frac{2}{5}\right)^{1/3}\left(-\frac{5\,\sqrt{\sigma_1\sigma_2}\,\mathrm{sech}[(x-ct)] + \sigma_3}{\sigma_2}\right)^{1/3} e^{-i(kx-\theta-t\omega)}, \tag{103}$$

represent bright soliton waveforms.
[8.1.3] If $0 \leq m \leq 1$, $c_0 = -1$, $c_2 = -m^2 + 2$, $c_4 = m^2 - 1$, and $\sigma_1, \sigma_2 < 0$, then

$$u_{8.1.3}(x,t) = \left(\frac{2}{5}\right)^{1/3}\left(-\frac{5\sqrt{\sigma_1\sigma_2} + \sigma_3\,\mathrm{nd}[(x-ct)]}{\sigma_2\,\mathrm{nd}[(x-ct)]}\right)^{1/3} e^{-i(kx-\theta-t\omega)}, \tag{104}$$

$$v_{8.1.3}(x,t) = A\left(\frac{2}{5}\right)^{1/3}\left(-\frac{5\sqrt{\sigma_1\sigma_2} + \sigma_3\,\mathrm{nd}[(x-ct)]}{\sigma_2\,\mathrm{nd}[(x-ct)]}\right)^{1/3} e^{-i(kx-\theta-t\omega)}, \tag{105}$$

are Jacobi elliptic solutions.
If $m = 1$, then

$$u_{8.1.3a}(x,t) = \left(\frac{2}{5}\right)^{1/3}\left(-\frac{5\,\sqrt{\sigma_1\sigma_2}\,\mathrm{sech}[(x-ct)] + \sigma_3}{\sigma_2}\right)^{1/3} e^{-i(kx-\theta-t\omega)}, \tag{106}$$

$$v_{8.1.3a}(x,t) = A\left(\frac{2}{5}\right)^{1/3}\left(-\frac{5\,\sqrt{\sigma_1\sigma_2}\,\mathrm{sech}[(x-ct)] + \sigma_3}{\sigma_2}\right)^{1/3} e^{-i(kx-\theta-t\omega)}, \tag{107}$$

represent bright soliton waveforms.
[8.1.4] If $0 \leq m \leq 1$, $c_0 = \frac{1}{4}$, $c_2 = \frac{m^2}{2} - 1$, $c_4 = \frac{m^4}{4}$, $\sigma_1 < 0$, and $\sigma_2 > 0$, then

$$u_{8.1.4}(x,t) = \left(\frac{\sqrt{-\sigma_1}(1+\mathrm{dn}[(x-ct)])}{\sqrt{\sigma_2}\,\mathrm{sn}[(x-ct)]} - \frac{2\sigma_3}{5\sigma_2}\right)^{1/3} e^{i(-kx+\theta+t\omega)}, \tag{108}$$

$$v_{8.1.4}(x,t) = A\left(\frac{\sqrt{-\sigma_1}(1+\mathrm{dn}[(x-ct)])}{\sqrt{\sigma_2}\,\mathrm{sn}[(x-ct)]} - \frac{2\sigma_3}{5\sigma_2}\right)^{1/3} e^{i(-kx+\theta+t\omega)}, \tag{109}$$

represent Jacobi elliptic function waveforms.
When $m = 0$ or $m = 1$, we obtain singular periodic or singular soliton forms, respectively.

$$u_{8.1.4a}(x,t) = \left(\frac{2\sqrt{-\sigma_1}\csc[(x-ct)]}{\sqrt{\sigma_2}} - \frac{2\sigma_3}{5\sigma_2}\right)^{1/3} e^{i(-kx+\theta+t\omega)}, \tag{110}$$

$$v_{8.1.4a}(x,t) = A\left(\frac{2\sqrt{-\sigma_1}\csc[(x-ct)]}{\sqrt{\sigma_2}} - \frac{2\sigma_3}{5\sigma_2}\right)^{1/3} e^{i(-kx+\theta+t\omega)}, \tag{111}$$

or

$$u_{8.1.4b}(x,t) = \left(\frac{(\coth[(x-ct)] + \sqrt{-\sigma_1}\operatorname{csch}[(x-ct)])}{\sqrt{\sigma_2}} - \frac{2\sigma_3}{5\sigma_2}\right)^{1/3} e^{i(-kx+\theta+t\omega)}, \tag{112}$$

$$v_{8.1.4b}(x,t) = A\left(\frac{(\coth[(x-ct)] + \sqrt{-\sigma_1}\operatorname{csch}[(x-ct)])}{\sqrt{\sigma_2}} - \frac{2\sigma_3}{5\sigma_2}\right)^{1/3} e^{i(-kx+\theta+t\omega)}. \tag{113}$$

From subcase [8.2] the following Jacobi elliptic solutions are obtained:
[8.2.1] If $0 \le m \le 1$, $c_0 = 1$, $c_2 = -(1+m^2)$, $c_4 = m^2$, $\sigma_1 < 0$, and $\sigma_2 > 0$, then

$$u_{8.2.1}(x,t) = \left(\frac{2}{5}\right)^{1/3}\left(\frac{5\sqrt{-\sigma_1\sigma_2} + 5m\sqrt{-\sigma_1\sigma_2}\operatorname{cd}^2[(x-ct)] - \sigma_3\operatorname{cd}[(x-ct)]}{\sigma_2\operatorname{cd}[(x-ct)]}\right)^{1/3} e^{-i(kx-\theta-t\omega)}, \tag{114}$$

$$v_{8.2.1}(x,t) = A\left(\frac{2}{5}\right)^{1/3}\left(\frac{5\sqrt{-\sigma_1\sigma_2} + 5m\sqrt{-\sigma_1\sigma_2}\operatorname{cd}^2[(x-ct)] - \sigma_3\operatorname{cd}[(x-ct)]}{\sigma_2\operatorname{cd}[(x-ct)]}\right)^{1/3} e^{-i(kx-\theta-t\omega)}, \tag{115}$$

are Jacobi elliptic solutions.
If $m = 0$, then

$$u_{8.2.1a}(x,t) = \left(\frac{2\sqrt{-\sigma_1}\sec[(x-ct)]}{\sqrt{\sigma_2}} - \frac{2\sigma_3}{5\sigma_2}\right)^{1/3} e^{i(-kx+\theta+t\omega)}, \tag{116}$$

$$v_{8.2.1a}(x,t) = A\left(\frac{2\sqrt{-\sigma_1}\sec[(x-ct)]}{\sqrt{\sigma_2}} - \frac{2\sigma_3}{5\sigma_2}\right)^{1/3} e^{i(-kx+\theta+t\omega)}, \tag{117}$$

correspond to singular periodic waveforms.
[8.2.2] If $0 \le m \le 1$, $c_0 = \frac{1}{4}$, $c_2 = \frac{m^2}{2} - 1$, $c_4 = \frac{m^4}{4}$, $\sigma_1 < 0$, and $\sigma_2 > 0$, then

$$u_{8.2.2}(x,t) = \left(\frac{\sqrt{-\sigma_1}(1+\operatorname{dn}[(x-ct)])}{\sqrt{\sigma_2}\operatorname{sn}[(x-ct)]} + \frac{m^2\sqrt{-\sigma_1}\operatorname{sn}[(x-ct)]}{1+\sqrt{\sigma_2}\operatorname{dn}[(x-ct)]} - \frac{2\sigma_3}{5\sigma_2}\right)^{1/3} e^{i(-kx+\theta+t\omega)}, \tag{118}$$

$$v_{8.2.2}(x,t) = A\left(\frac{\sqrt{-\sigma_1}(1+\operatorname{dn}[(x-ct)])}{\sqrt{\sigma_2}\operatorname{sn}[(x-ct)]} + \frac{m^2\sqrt{-\sigma_1}\operatorname{sn}[(x-ct)]}{1+\sqrt{\sigma_2}\operatorname{dn}[(x-ct)]} - \frac{2\sigma_3}{5\sigma_2}\right)^{1/3} e^{i(-kx+\theta+t\omega)}, \tag{119}$$

represent Jacobi elliptic function waveforms.
When $m = 0$ or $m = 1$, we obtain singular periodic or singular soliton forms, respectively.

$$u_{8.2.2a}(x,t) = \left(\frac{2\sqrt{-\sigma_1}\csc[(x-ct)]}{\sqrt{\sigma_2}} - \frac{2\sigma_3}{5\sigma_2}\right)^{1/3} e^{i(-kx+\theta+t\omega)}, \tag{120}$$

$$v_{8.2.2a}(x,t) = A\left(\frac{2\sqrt{-\sigma_1}\csc[(x-ct)]}{\sqrt{\sigma_2}} - \frac{2\sigma_3}{5\sigma_2}\right)^{1/3} e^{i(-kx+\theta+t\omega)}, \tag{121}$$

or

$$u_{8.2.2b}(x,t) = \left(\frac{2}{5\sigma_2}\right)^{1/3}\left(5\sqrt{-\sigma_1\sigma_2}\coth[(x-ct)] - \sigma_3\right)^{1/3} e^{-i(kx-\theta-t\omega)}, \tag{122}$$

$$v_{8.2.2b}(x,t) = A\left(\frac{2}{5\sigma_2}\right)^{1/3}\left(5\sqrt{-\sigma_1\sigma_2}\coth[(x-ct)] - \sigma_3\right)^{1/3} e^{-i(kx-\theta-t\omega)}. \tag{123}$$

4. GRAPHICAL OVERVIEW

This section provides graphical illustrations of chosen exact solutions obtained in Section 3, concentrating on the amplitude distributions $|u(x,t)|$ and $|v(x,t)|$ to emphasize principal wave forms, following conventional practices in nonlinear optics to depict soliton and periodic dynamics. The visualizations include three-dimensional (3D) plots depicting spatiotemporal evolution and two-dimensional (2D) overlays illustrating wave profiles at fixed time, facilitating analysis of propagation dynamics, nonlinear interactions, and dispersion effects in the coupled (1+1)-dimensional Kudryashov's equation. The selected cases encompass a variety of solution types: bright solitons, singular periodic waves, dark solitons, singular solitons, and exponential solutions. Each figure corresponds to a specific solution type, with parameter values detailed in Table 1. These visualizations exhibit the model's capability to represent varied wave behaviors within birefringent optical waveguides, highlighting stability, periodicity, together with localization under different conditions.

Table 1. Numerical parameters employed for the depicted solutions.

Figure	Solution Form	Equations	Parameter Set
1	Bright Soliton	(26), (27)	$c = 0.65$, $k = 0.58$, $\omega = 0.05$, $\theta = 0.54$, $A = 1.95$, $\alpha_1 = 0.50$, $\alpha_2 = 0.55$, $\alpha_3 = 0.70$, $\alpha_4 = 0.90$, $\beta_3 = 0.001$, $\beta_4 = 0.05$, $\gamma_1 = 0.75$, $\gamma_2 = 0.49$, $\gamma_3 = 0.35$, $\gamma_4 = -0.25$, $c_2 = 1.15$, and $c_4 = -0.20$
2	Singular Periodic	(34), (35)	$c = 0.05$, $k = 1.95$, $\omega = 0.75$, $\theta = 0.58$, $A = 1.80$, $a_1 = -1.35$, $a_2 = 1.20$, $\beta_3 = 1.57$, $\beta_4 = 0.75$, $\gamma_1 = 1.15$, $\gamma_2 = 0.45$, $\gamma_3 = 0.75$, $\gamma_4 = 0.80$, $c_2 = -0.22$, and $c_4 = 0.2$
3	Dark Soliton	(38), (39)	$c = 0.60$, $k = 0.64$, $\omega = 0.10$, $\theta = 0.50$, $A = 1.50$, $a_1 = 0.30$, $a_2 = 0.65$, $\beta_3 = 0.03$, $\beta_4 = 0.85$, $\gamma_1 = 1.75$, $\gamma_2 = 1.45$, $\gamma_3 = 1.85$, $\gamma_4 = 2.15$, $c_2 = -0.15$, and $c_4 = 0.2$
4	Singular Soliton	(58), (59)	$c = 0.55$, $k = 0.52$, $\omega = 0.12$, $\theta = 0.65$, $A = 2.35$, $a_1 = 0.15$, $a_2 = 0.85$, $\beta_3 = 0.01$, $\beta_4 = 0.05$, $\gamma_1 = 0.25$, $\gamma_2 = 0.91$, $\gamma_3 = 0.65$, $\gamma_4 = -0.04$, $c_0 = 0.2$, and $c_2 = 0.1$.
5	Exponential	(68), (69)	$c = 0.62$, $k = 0.47$, $\omega = 0.15$, $\theta = 0.45$, $A = 1.95$, $a_3 = 1.55$, $a_4 = 1.64$, $\alpha_1 = 0.10$, $\alpha_2 = 0.48$, $\alpha_3 = 0.20$, $\alpha_4 = 0.001$, $\beta_1 = 0.65$, $\beta_2 = 4.85$, $\beta_3 = 0.15$, $\beta_4 = 0.05$, $c_1 = 0.85$, and $c_2 = 0.40$

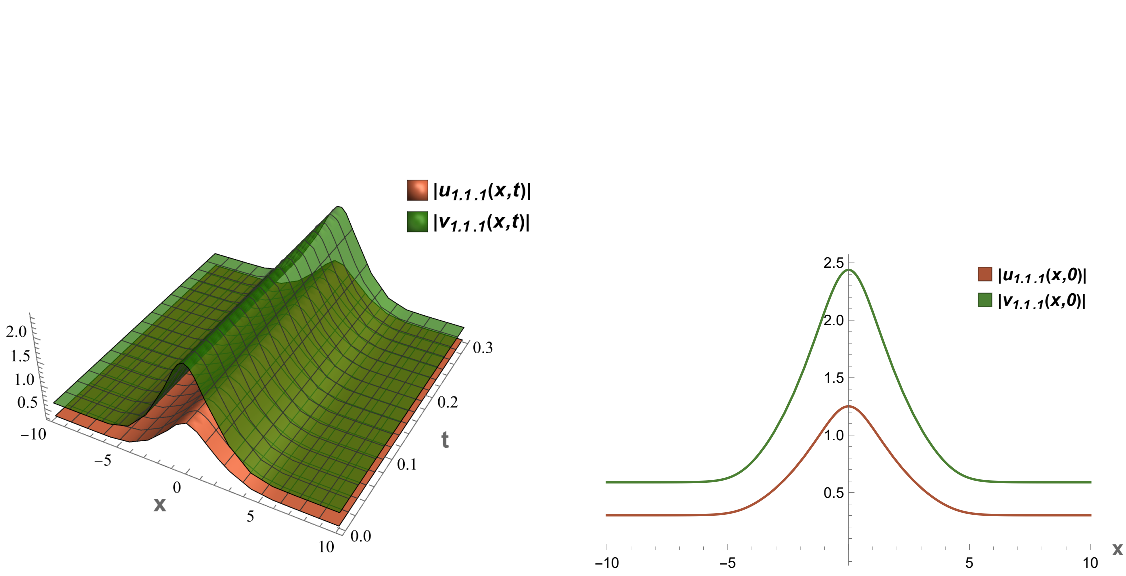

(a) 3-Dimension **(b)** 2-Dimension

Figure 1. Spatiotemporal behavior of the bright soliton wave in Eqs. (26) and (27).

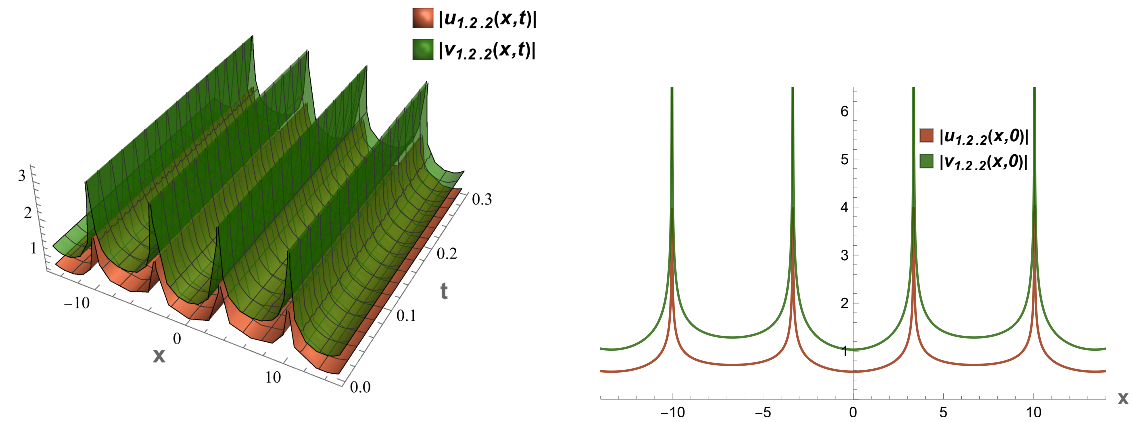

(a) 3-Dimension **(b)** 2-Dimension

Figure 2. Spatiotemporal behavior of the singular periodic wave in Eqs. (34) and (35).

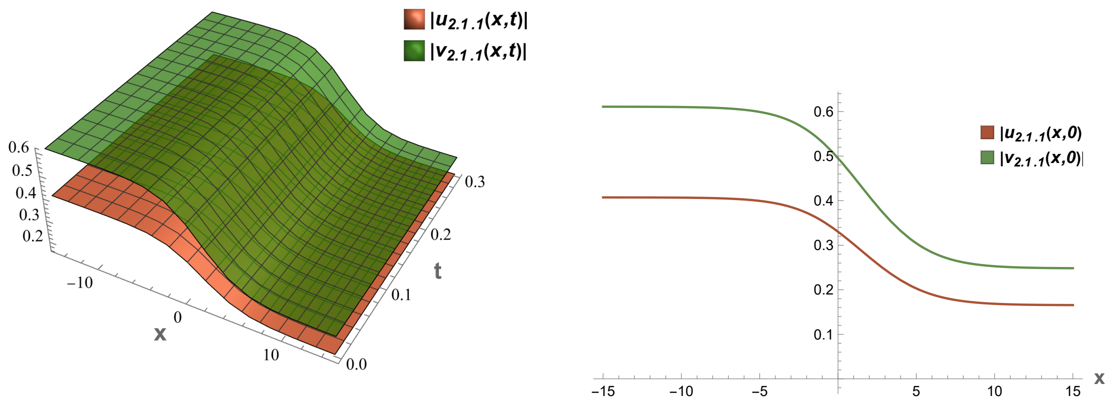

(a) 3-Dimension **(b)** 2-Dimension

Figure 3. Spatiotemporal behavior of the dark soliton wave in Eqs. (38) and (39).

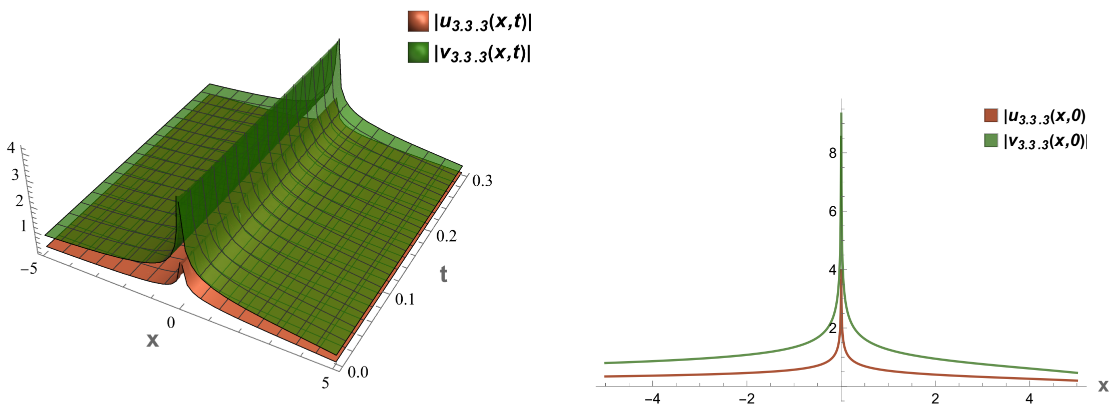

(a) 3-Dimension **(b)** 2-Dimension

Figure 4. Spatiotemporal behavior of the singular soliton wave in Eqs. (58) and (59).

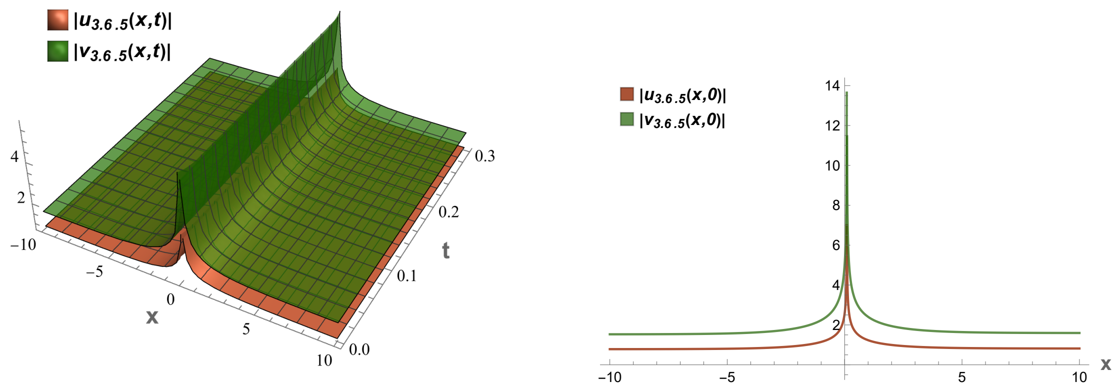

(a) 3-Dimension **(b)** 2-Dimension

Figure 5. Spatiotemporal behavior of the exponential wave in Eqs. (68) and (69).

5. BIFURCATION ANALYSIS

Bifurcation analysis provides a systematic framework for investigating qualitative changes in the dynamical behavior of nonlinear systems as parameters vary. For traveling wave equations, this approach reveals critical thresholds where solution profiles undergo transitions—for instance, between periodic and solitary waves, or between bounded and unbounded behavior [26, 27, 28, 29, 30]. In this section, we perform a detailed bifurcation analysis of the fourth-order nonlinear ordinary differential equation (23) obtained via the MEMM reduction.

5.1. Planar Dynamical System Formulation

To analyze the traveling wave dynamics, we introduce the variable $y = F'(\xi)$ and convert the second-order ODE (23) into a two-dimensional autonomous system:

$$\frac{dF}{d\xi} = y, \qquad \frac{dy}{d\xi} = \frac{2}{3}\frac{y^2}{F} - \frac{1}{3\sigma_1 F}P(F), \tag{124}$$

where $P(F) = \sigma_2 F^4 + \sigma_3 F^3 - \sigma_4 F^2 + \sigma_5 F + \sigma_6$. This system is singular along the line $F = 0$ due to the division by F. To remove this mathematical singularity while preserving the topological structure of the phase portrait, we apply the geometric singular perturbation method via the time-rescaling transformation $d\xi = F\,d\tau$. This yields the *regular* system:

$$\frac{dF}{d\tau} = Fy, \qquad \frac{dy}{d\tau} = \frac{2}{3}y^2 - \frac{1}{3\sigma_1}P(F). \tag{125}$$

Systems (124) and (125) are topologically equivalent except on the singular line $F = 0$.

5.2. Hamiltonian Structure and First Integral

System (125) is conservative and admits a Hamiltonian formulation. A first integral can be obtained via direct integration, yielding the conserved quantity

$$H(F, y) = F^{-4/3}y^2 + \frac{1}{\sigma_1}\left(\frac{\sigma_2}{4}F^{8/3} + \frac{2\sigma_3}{5}F^{5/3} - \sigma_4 F^{2/3} - 2\sigma_5 F^{-1/3} - \frac{\sigma_6}{2}F^{-4/3}\right) = h, \tag{126}$$

where h is a constant. Level curves $H(F, y) = h$ define the trajectories in the phase plane: closed orbits correspond to periodic traveling waves, homoclinic orbits to solitary waves, and heteroclinic orbits to kink or anti-kink waves.

5.3. Equilibrium Points and Linear Stability

Equilibrium points of the regular system (125) satisfy $Fy = 0$ and $\frac{2}{3}y^2 - \frac{1}{3\sigma_1}P(F) = 0$. Excluding the singular line $F = 0$, we obtain $y = 0$ and consequently $P(F) = 0$. Hence, equilibria are of the form $(F_i, 0)$, where F_i are the real roots of the quartic polynomial

$$P(F) = \sigma_2 F^4 + \sigma_3 F^3 - \sigma_4 F^2 + \sigma_5 F + \sigma_6 = 0. \tag{127}$$

The number of real equilibria can be 0, 2, or 4 (counting multiplicities), depending on the parameter values. Linearizing (125) about an equilibrium $(F_i, 0)$ gives the Jacobian matrix

$$J(F_i, 0) = \begin{bmatrix} 0 & F_i \\ -\dfrac{1}{3\sigma_1} P'(F_i) & 0 \end{bmatrix}, \tag{128}$$

where $P'(F) = 4\sigma_2 F^3 + 3\sigma_3 F^2 - 2\sigma_4 F + \sigma_5$. The characteristic equation is $\lambda^2 + \dfrac{F_i P'(F_i)}{3\sigma_1} = 0$, yielding eigenvalues

$$\lambda = \pm\sqrt{-\frac{F_i P'(F_i)}{3\sigma_1}}. \tag{129}$$

Defining $\Delta_i = -\dfrac{F_i P'(F_i)}{3\sigma_1}$, the stability type is determined as follows. When $\Delta_i > 0$, the eigenvalues are real with opposite signs, corresponding to a saddle point (unstable). When $\Delta_i < 0$, the eigenvalues are purely imaginary, corresponding to a center (stable, surrounded by periodic orbits). The degenerate case $\Delta_i = 0$ requires higher-order analysis. Because the system is conservative (Hamiltonian), centers are nonlinearly stable and give rise to families of periodic orbits.

5.4. Phase Portraits and Numerical Illustrations

To illustrate the rich dynamical behavior, we examine three representative parameter sets. For each, we compute the equilibrium points, classify their stability, and plot the phase portrait along with a sample temporal evolution.

Case 1. Parameters: $\sigma_1 = 1,\ \sigma_2 = 1,\ \sigma_3 = 0,\ \sigma_4 = 40,\ \sigma_5 = 0,\ \sigma_6 = 144$. The quartic factors as $P(F) = (F-2)(F+2)(F-6)(F+6)$, giving four equilibria: $(\pm 2, 0)$ and $(\pm 6, 0)$. Linear stability analysis shows that at $F = \pm 6$ we have $\Delta < 0$, indicating centers, while at $F = \pm 2$ we have $\Delta > 0$, indicating saddles. The phase portrait (Fig. 6a) displays two families of periodic orbits encircling the centers, separated by heteroclinic orbits connecting the saddles. The corresponding temporal profiles (Fig. 6b) exhibit periodic oscillations around $F = \pm 6$.

Case 2. Parameters: $\sigma_1 = 1,\ \sigma_2 = 1,\ \sigma_3 = 0,\ \sigma_4 = 18.25,\ \sigma_5 = 0,\ \sigma_6 = 36$. Here $P(F) = (F-4)(F+4)(F-1.5)(F+1.5)$, yielding equilibria at $(\pm 1.5, 0)$ and $(\pm 4, 0)$. Stability analysis confirms centers at $F = \pm 4$ and saddles at $F = \pm 1.5$. The phase portrait (Fig. 7a) again shows two centers surrounded by periodic orbits, with separatrices emanating from the saddles. Temporal evolution (Fig. 7b) confirms the periodic motion around the centers.

Case 3. Parameters: $\sigma_1 = 1,\ \sigma_2 = 1,\ \sigma_3 = -2,\ \sigma_4 = 45,\ \sigma_5 = -34,\ \sigma_6 = 80$. The polynomial factors as $P(F) = (F+5)(F+2)(F-1)(F-8)$, with equilibria at $(-5, 0), (-2, 0), (1, 0), (8, 0)$. Stability analysis reveals centers at $F = -5$ and $F = 8$, and saddles at $F = -2$ and $F = 1$. Despite the lack of symmetry, the phase portrait (Fig. 8a) retains the characteristic structure of two centers separated by saddle points. The temporal dynamics (Fig. 8b) display periodic oscillations around each center.

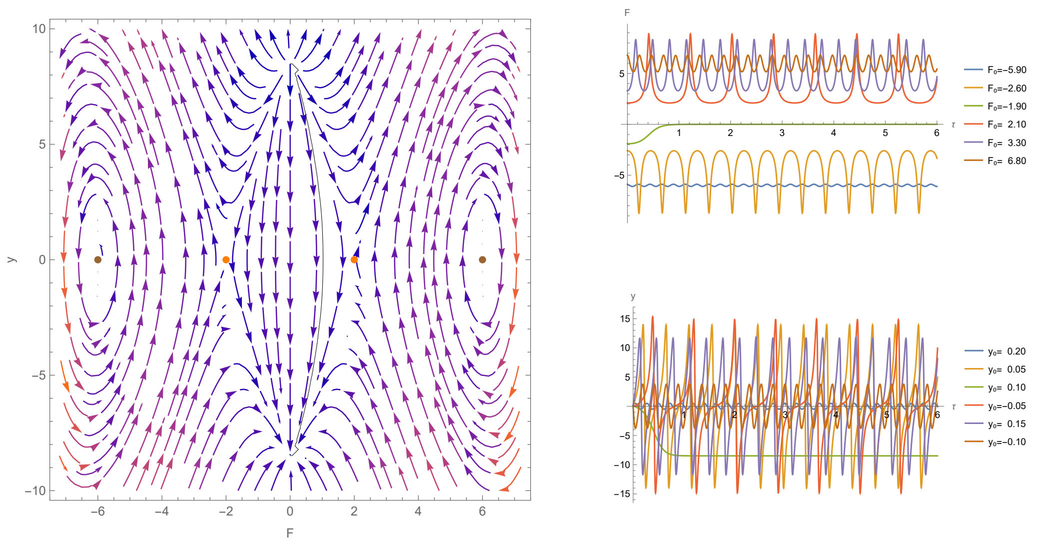

(a) Phase portrait in the (F, y)-plane for the regularized system (125).

(b) Temporal evolution of $F(\tau)$ and $y(\tau)$ for a trajectory near the center at $F = 6$.

Figure 6. Bifurcation structure for Case 1: two centers at $F = \pm 6$ and two saddles at $F = \pm 2$. Closed orbits correspond to periodic traveling waves, while the separatrices demarcate regions of distinct dynamical behavior.

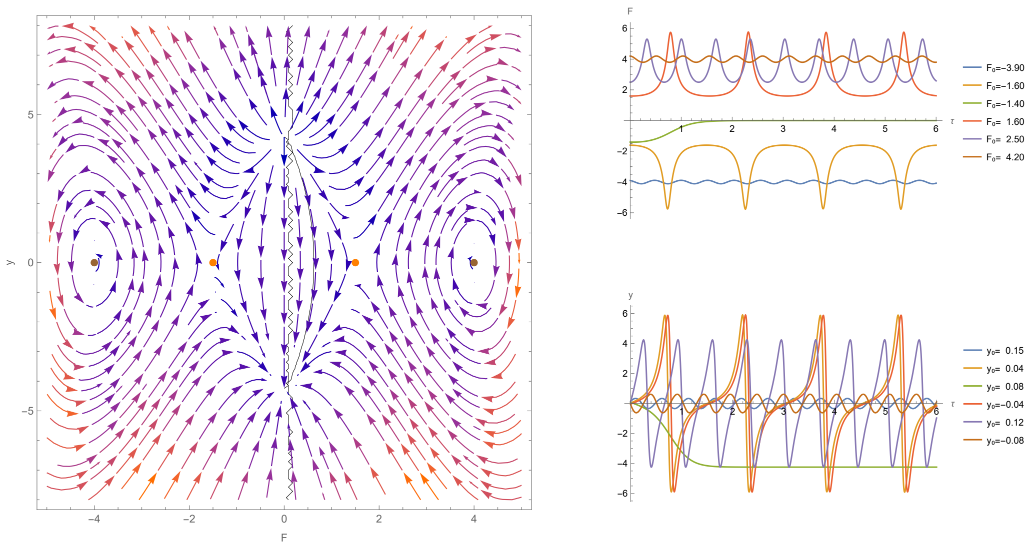

(a) Phase portrait for the regularized system (125).

(b) Temporal evolution of $F(\tau)$ and $y(\tau)$ for a periodic orbit around $F = 4$.

Figure 7. Bifurcation structure for Case 2: centers at $F = \pm 4$ and saddles at $F = \pm 1.5$. The Hamiltonian level curves generate families of periodic solutions and heteroclinic connections.

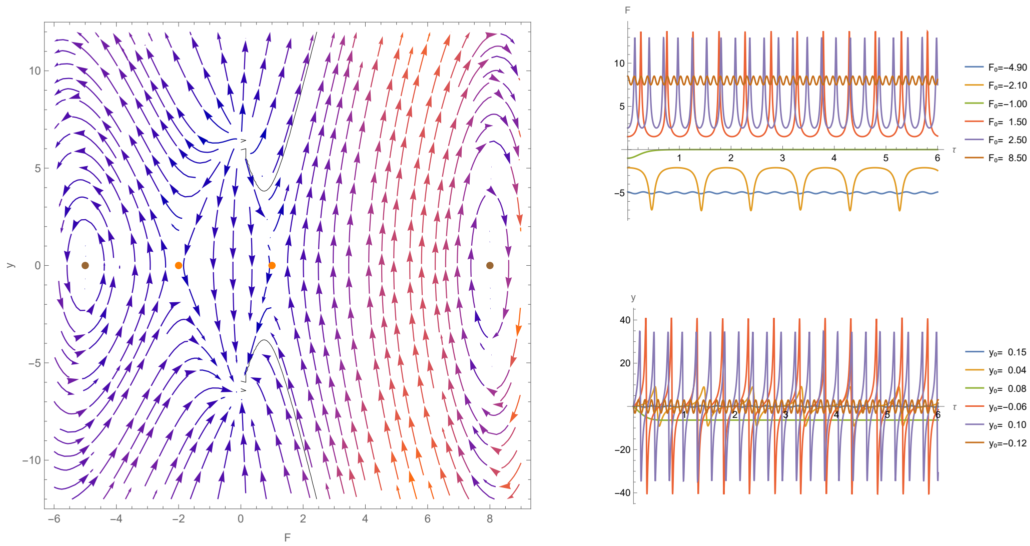

(a) Phase portrait for the regularized system (125).

(b) Temporal evolution of $F(\tau)$ and $y(\tau)$ for a trajectory near the center at $F = 8$.

Figure 8. Bifurcation structure for Case 3: centers at $F = -5$ and $F = 8$, saddles at $F = -2$ and $F = 1$. The asymmetric arrangement still yields two disjoint families of periodic orbits, illustrating the robustness of the Hamiltonian structure.

5.5. Bifurcation Interpretation

The parameter σ_6 (or any of the σ_i) can be treated as a bifurcation parameter. As it varies, the roots of $P(F)$ coalesce or split, leading to saddle-node bifurcations where equilibria appear or disappear. In a conservative system like (125), Hopf bifurcations are absent because eigenvalues are always symmetric about the imaginary axis. However, degenerate bifurcations (e.g., when $\Delta_i = 0$) may occur, leading to cusps or higher-order singularities. The phase portraits presented correspond to generic cases where all equilibria are hyperbolic (non-degenerate). The existence of periodic orbits around each center follows directly from the Hamiltonian nature and the non-degeneracy condition $\Delta_i < 0$. Moreover, the separatrices emanating from the saddles form homoclinic or heteroclinic loops, which in the original wave variable correspond to solitary wave or front solutions. In summary, the bifurcation analysis reveals that the traveling wave dynamics of the Kudryashov model are organized by a Hamiltonian planar system with up to four equilibria. The qualitative behavior—whether the wave profile is periodic, solitary, or unbounded—is determined by the level set of the Hamiltonian and the arrangement of saddles and centers. This geometric perspective complements the explicit solutions obtained via MEMM and provides a global view of the solution space.

6. CONCLUSIONS

In this research, we have successfully employed the Modified Extended Mapping Method (MEMM) to construct a comprehensive set of exact traveling wave solutions for the coupled (1+1)-dimensional Kudryashov's equation, a nonlinear partial differential equation pivotal for modeling complex wave phenomena in birefringent optical fibers. The MEMM proved to be a powerful and systematic tool, transforming the coupled nonlinear PDEs into an ordinary differential equation, thereby enabling the derivation of diverse analytical solutions. These solutions encompass a wide range of forms, including bright and singular solitons, periodic waves, rational, exponential, Weierstrass elliptic, and Jacobi elliptic functions, each capturing distinct wave dynamics relevant to applications in nonlinear optics, optical communication systems, and other nonlinear systems. The modulation instability analysis provided critical insights into the stability of steady-state solutions, highlighting the interplay between dispersion and nonlinearity. The incorporation of 3D and 2D visualizations further elucidated the spatiotemporal evolution of these solutions, offering a clear interpretation of wave propagation and interaction behaviors. This study significantly enhances the analytical framework for investigating higher-order nonlinear wave equations, providing robust tools for theoretical and applied research in nonlinear science. The analytical solutions to the coupled Kudryashov's equation offer a deeper understanding of the intricate nonlinear dynamics governed by this model, particularly in describing solitary wave interactions, periodic wave patterns, and singular structures in birefringent fibers. The diversity of solution types—ranging from hyperbolic and trigonometric to elliptic and rational forms—underscores the equation's versatility in capturing a broad spectrum of physical behaviors under various parametric conditions. The graphical representations, including 3D plots depicting wave evolution and 2D plots illustrating temporal profiles, bridge the gap between mathematical solutions and their physical implications. These visualizations highlight the MEMM's efficacy in uncovering complex wave patterns, such as soliton stability and periodic oscillations, which are critical for applications in nonlinear optics, optical communication systems, and birefringent fiber modeling. Compared to Biswas et al.'s initial study [24], which utilized the extended trial function method, the MEMM expands the solution landscape by providing new analytical solutions, including elliptic and rational solutions, thereby enhancing the theoretical comprehension of the model's integrability and dynamical behavior. However, the dependence on specific parameter constraints (e.g., c_i values) to obtain these solutions suggests potential limitations in their generalizability, particularly for arbitrary initial or boundary conditions. Additionally, the presence of singular solutions indicates regions of instability that require further investigation to assess their physical relevance. These considerations highlight the need for complementary numerical or experimental studies to validate the practical applicability of the derived solutions. This study opens several promising directions for future research. First, numerical simulations could be conducted to verify the stability and long-term behavior of the derived analytical solutions, especially under realistic physical conditions relevant to systems modeled by the Kudryashov's equation, such as birefringent fibers or optical wave propagation. Such simulations could also explore the impact of external perturbations or variable coefficients on wave dynamics. Second, extending the MEMM to other higher-order or multidimensional nonlinear PDEs, such as those in plasma physics or geophysical fluid dynamics, could further demonstrate its robustness and versatility, potentially uncovering new solution classes. Third, a deeper investigation into the integrability properties of the Kudryashov's equation using alternative techniques, such as the inverse scattering transform or Painlevé analysis, could provide additional insights into its soliton interactions and non-integrable regimes. Additionally, integrating machine learning-based approaches to approximate solutions or predict wave behaviors could complement the analytical framework, particularly for complex parameter spaces. Finally, linking the derived solutions to experimental data from relevant physical systems, such as optical fiber experiments or photonic studies, could enhance their practical utility, enabling applications in wave prediction, signal transmission optimization, or advanced material design. These prospective efforts are expected to consolidate the link bridging theoretical progress with practical implementations within nonlinear wave studies.

ORCID

Wafy M. Hasan, https://orcid.org/0000-0002-7942-6033; **Hamdy M. Ahmed**, https://orcid.org/0000-0001-8772-3663; **Ahmed M. Ahmed**, https://orcid.org/0000-0002-5829-5038; **Haytham M. Rezk**, https://orcid.org/0000-0001-6782-7908; **Wafaa B. Rabie**, https://orcid.org/0009-0001-1696-1266

REFERENCES

[1] M. D. Graham, and D. Floryan, "Exact coherent states and the nonlinear dynamics of wall-bounded turbulent flows," Annual Review of Fluid Mechanics, **53**(1), 227-253 (2021). https://doi.org/10.1146/annurev-fluid-051820-020223

[2] E. Åkervik, and M. Vartdal, "The role of wave kinematics in turbulent flow over waves," Journal of Fluid Mechanics, **880**, 890-915 (2019). https://doi.org/10.1017/jfm.2019.70810.1017/jfm.2019.708

[3] M. M. Khater, "Advanced computational techniques for solving the modified KdV-KP equation and modeling nonlinear waves," Optical and Quantum Electronics, **56**(1), 6 (2024). https://doi.org/10.1007/s11082-023-05581-3

[4] B. Kopçasız, ”Qualitative analysis and optical soliton solutions galore: scrutinizing the (2+ 1)-dimensional complex modified Korteweg–de Vries system,” Nonlinear Dynamics, **112**(23), 21321-21341 (2024). https://doi.org/10.1007/s11071-024-10036-9

[5] D. Moreira, P. Xavier, A. Palmeira, and E. Nascimento, ”New approach to solving the atmospheric pollutant dispersion equation using fractional derivatives,” International Journal of Heat and Mass Transfer, **144**, 118667 (2019). https://doi.org/10.1016/j.ijheatmasstransfer.2019.118667

[6] N. M. Jamil, and I. Khan, ”Unravelling the Influence of Advection and Diffusion on the Spatial and Temporal Evolution of Pollutant Concentration,” Journal of Advanced Research in Fluid Mechanics and Thermal Sciences, **119**(2), 1-12 (2024). https://doi.org/10.37934/arfmts.119.2.112

[7] U. Younas, T. A. Sulaiman, and J. Ren, ”On the study of optical soliton solutions to the three-component coupled nonlinear Schrödinger equation: applications in fiber optics,” Optical and Quantum Electronics, **55**(1), 72 (2023). https://doi.org/10.1007/s11082-022-04254-x

[8] M. Arshad, F. Yasin, S. F. Aldosary, H. Rezazadeh, M. Farman, and M. A. Hosseinzadeh, ”Rational function solutions of higher-order dispersive cubic-quintic nonlinear Schrödinger dynamical model and its applications in fiber optics,” Mathematical Methods in the Applied Sciences, **48**(4), 5300-5314 (2025). https://doi.org/10.1002/mma.10604

[9] G. A. Meehl, F. Zwiers, J. Evans, T. Knutson, L. Mearns, and P. Whetton, ”Trends in extreme weather and climate events: issues related to modeling extremes in projections of future climate change,” Bulletin of the American Meteorological Society, **81**(3), 427-436 (2000). https://doi.org/10.1175/1520-0477(2000)081⟨0427:TIEWAC⟩2.3.CO;2

[10] A. Moazami, V. M. Nik, S. Carlucci, and S. Geving, ”Impacts of future weather data typology on building energy performance – Investigating long-term patterns of climate change and extreme weather conditions,” Applied Energy, **238**, 696-720 (2019). https://doi.org/10.1016/j.apenergy.2019.01.085

[11] A. Irshad, N. Ahmed, U. Khan, S. T. Mohyud-Din, I. Khan, and E. S. M. Sherif, ”Optical solutions of Schrödinger equation using extended Sinh–Gordon equation expansion method,” Frontiers in Physics, **8**, 73 (2020). https://doi.org/10.3389/fphy.2020.00073

[12] H. H. Hussein, H. M. Ahmed, and W. Alexan, ”Analytical soliton solutions for cubic-quartic perturbations of the Lakshmanan-Porsezian-Daniel equation using the modified extended tanh function method,” Ain Shams Engineering Journal, **15**(3), 102513 (2024). https://doi.org/10.1016/j.asej.2023.102513

[13] I. A. Ibrahim, W. M. Taha, M. Alobaidi, A. F. Jameel, E. Bashier, and N. H. Alshirawi, ”Oblique Closed Form Solution for Some Type Fractional Evolution Equations in Physical Problem by Using the Homogeneous Balance Method,” Mathematical Modelling of Engineering Problems, **11**(1), (2024). https://doi.org/10.18280/mmep.110120

[14] A. R. Seadawy, H. M. Ahmed, W. B. Rabie, and A. Biswas, ”An alternate pathway to solitons in magneto-optic waveguides with triple-power law nonlinearity,” Optik, **231**, 166480 (2021). https://doi.org/10.1016/j.ijleo.2021.166480

[15] Y. Alhojilan, H. M. Ahmed, and W. B. Rabie, ”Stochastic solitons in birefringent fibers for Biswas–Arshed equation with multiplicative white noise via Itô calculus by modified extended mapping method,” Symmetry, **15**(1), 207 (2023). https://doi.org/10.3390/sym15010207

[16] W. B. Rabie, H. M. Ahmed, I. Samir, and M. Alnahhass, ”Optical solitons and stability analysis for NLSE with nonlocal nonlinearity, nonlinear chromatic dispersion and Kudryashov’s generalized quintuple-power nonlinearity,” Results in Physics, **59**, 107589 (2024). https://doi.org/10.1016/j.rinp.2024.107589

[17] M. I. Khan, A. Farooq, K. S. Nisar, and N. A. Shah, ”Unveiling new exact solutions of the unstable nonlinear Schrödinger equation using the improved modified Sardar sub-equation method,” Results in Physics, **59**, 107593 (2024). https://doi.org/10.1016/j.rinp.2024.107593

[18] K. J. Wang, F. Shi, J. H. Liu, and J. Si, ”Application of the extended F-expansion method for solving the fractional Gardner equation with conformable fractional derivative,” Fractals, **30**(07), 2250139 (2022). https://doi.org/10.1142/S0218348X22501390

[19] S. Zhang, and T. Xia, ”A generalized F-expansion method and new exact solutions of Konopelchenko–Dubrovsky equations,” Applied Mathematics and Computation, **183**(2), 1190-1200 (2006). https://doi.org/10.1016/j.amc.2006.06.043

[20] W. M. Hasan, H. M. Ahmed, A. M. Ahmed, H. M. Rezk, and W. B. Rabie, ”Exploring highly dispersive optical solitons and modulation instability in nonlinear Schrödinger equations with nonlocal self phase modulation and polarization dispersion,” Scientific Reports, **15**(1), 27070 (2025). https://doi.org/10.1038/s41598-025-09710-8

[21] W. B. Rabie, and H. M. Ahmed, ”Dynamical solitons and other solutions for nonlinear Biswas–Milovic equation with Kudryashov’s law by improved modified extended tanh-function method,” Optik, **245**, 167665 (2021). https://doi.org/10.1016/j.ijleo.2021.167665

[22] W. B. Rabie, A. R. Seadawy, and H. M. Ahmed, ”Highly dispersive Optical solitons to the generalized third-order nonlinear Schrödinger dynamical equation with applications,” Optik, **241**, 167109 (2021). https://doi.org/10.1016/j.ijleo.2021.167109

[23] K. A. Rashedi, M. Y. Almusawa, H. Almusawa, T. S. Alshammari, and A. Almarashi, ”Applications of Riccati–Bernoulli and Bäcklund Methods to the Kuralay-II System in Nonlinear Sciences,” Mathematics, **13**(1), 84 (2024). https://doi.org/10.3390/math13010084

[24] A. Biswas, A. Sonmezoglu, M. Ekici, A.Kh. Alzahrani, and M.R. Belic, ”Cubic–quartic optical solitons with differential group delay for Kudryashov’s model by extended trial function,” Journal of Communications Technology and Electronics, **65**, 1384-1398 (2020). https://doi.org/10.1134/S1064226920120037

[25] W. B. Rabie, T. A. Khalil, N. Badra, H. M. Ahmed, M. Mirzazadeh, and M. S. Hashemi, ”Soliton solutions and other solutions to the (4+1)-Dimensional Davey–Stewartson–Kadomtsev–Petviashvili equation using modified extended mapping method,” Qualitative theory of dynamical systems, **36**(2), 87 (2024). https://doi.org/10.1007/s12346-023-00944-3

[26] W. M. Hasan, W. B. Rabie, A. M. Ahmed, H. M. Rezk, and H. M. Ahmed, "Construction of new travelling wave solutions and bifurcation analysis for the (2+1)-dimensional extended KP-BO equation utilizing the improved modified extended tanh-function method," International Journal of Computer Mathematics, **102**(12), 2214-2227 (2025). https://doi.org/10.1080/00207160.2025.2541068

[27] W. M. Hasan, H. M. Ahmed, A. M. Ahmed, H. M. Rezk, and W. B. Rabie, "Novel Soliton and Periodic Wave Solutions of the (3+1)-Dimensional Shallow Water Wave Equation with Bifurcation Analysis," Scientific Reports, **15**(1), 36490 (2025). https://doi.org/10.1038/s41598-025-21052-z

[28] Q. Cai, K. Tan, J. Li. Bifurcations and exact traveling wave solutions for the regularized Schamel equation. Open Mathematics, 19(1) (2021): 1699-1712. https://doi.org/10.1515/math-2021-0136

[29] A. A. Elmandouh, and M. E. Elbrolosy, "New traveling wave solutions for Gilson-Pickering equation in plasma via bifurcation analysis and direct method," Mathematical Methods in the Applied Sciences, 1-19 (2022). https://doi.org/10.1002/mma.8506

[30] W. Zhu, Y. Xia, and Y. Bai, "Traveling wave solutions of the complex Ginzburg-Landau equation with Kerr law nonlinearity," Applied Mathematics and Computation, **382**, 125342 (2020). https://doi.org/10.1016/j.amc.2020.125342

ТОЧНІ БІЖУЧІ ХВИЛІ ТА БІФУРКАЦІЙНА СТРУКТУРА ЗВ'ЯЗАНОЇ НЕЛІНІЙНОЇ СИСТЕМИ ШРЕДІНГЕРА ТИПУ КУДРЯШОВА ЗА ДОПОМОГОЮ МОДИФІКОВАНОГО МЕТОДУ РОЗШИРЕНОГО ВІДОБРАЖЕННЯ

Вафі М. Хасан[1,2], Хамді М. Ахмед[3], Ахмед М. Ахмед[1], Хайтам М. Резк[1], Вафаа Б. Рабі[4,5]

[1]*Кафедра математики, Факультет природничих наук, Університет Аль-Азхар, Каїр, Єгипет*

[2]*Кафедра фундаментальних наук, Факультет інженерних технологій, Технологічний університет Ель-Севеді, Каїр, Єгипет*

[3]*Кафедра фізики та інженерної математики, Вищий інженерний інститут, Академія Ель-Шорук, Каїр, Єгипет*

[4]*Кафедра математики, Факультет наук, Луксорський університет, Тайба, Луксор, Єгипет*

[5]*Луксорський національний університет, Факультет обчислювальної техніки, інформаційних технологій та штучного інтелекту, Луксор, Єгипет*

У цьому дослідженні отримано точні розв'язки біжучої хвилі та проведено біфуркаційний аналіз для зв'язаного (1+1)-вимірного рівняння Кудряшова. Ця система нелінійних рівнянь типу Шредінгера моделює одночасне поширення оптичних імпульсів у двопроменепроменевому волокні, включаючи критичні ефекти вищого порядку, такі як кубічно-квартикова дисперсія та нелінійності, для підвищення фізичної точності. Застосовуючи модифікований метод розширеного відображення (MEMM), зв'язані диференціальні рівняння з частинними похідними систематично зводяться до керованого звичайного диференціального рівняння. Це зведення дозволяє побудувати широкий спектр точних розв'язків, таких як яскраві та темні солітони, періодичні хвилі, періодичні сингулярні розв'язки, а також сингулярні солітони, на додаток до гіперболічних, експоненціальних, раціональних та еліптичних функцій Вейєрштрасса. Ключовим компонентом роботи є детальний біфуркаційний аналіз результуючої плоскої динамічної системи. Цей аналіз визначає порогові значення критичних параметрів та класифікує всі можливі якісні поведінки хвильових рішень, відображаючи області існування для різних типів рішень. Фізичні наслідки як отриманих рішень, так і біфуркаційної структури обговорюються в контексті нелінійної оптики, зокрема для динаміки імпульсів та стабільності в системах оптичного зв'язку з подвійною поляризацією. Результати демонструють ефективність MEMM та надають нові знання, що сприяють розумінню та проектуванню передових оптичних хвилеводів.

Ключові слова: *нелінійні рівняння Шредінгера; двопроменепроменеві оптичні волокна; дисперсія вищого порядку; модифікований метод розширеного відображення (MEMM); точні рішення біжучої хвилі; біфуркаційний аналіз*

East European Journal of Physics. 3. 44–53 (2026)
DOI: 10.26565/2312-4334-2026-3-04 ISSN 2312-4334

ON THE NUCLEAR STRUCTURE AND STELLAR WEAK RATES OF NEUTRON-RICH $^{104-116}$Rh ISOTOPES

Abdul Kabir[1*], **Jameel-Un Nabi**[2], **Rahat Badshah**[1], **Ayesha Anjum**[2]
[1]*Department of Space Science, Institute of Space Technology, Islamabad, 44000, Pakistan*
[2]*Department of Physics, University of Wah, Wah cantt, 47040, Pakistan*
[*]*Corresponding Author e-mail: kabirkhanak1@gmail.com*
Received April 3, 2026; revised June 22, 2026; accepted July 10, 2026

The nuclear ground state and beta decay properties of neutron-rich odd-odd and odd-A $^{104-116}$Rh isotopes are studied by utilizing the relativistic mean-field (RMF) and proton-neutron quasi-particle random phase approximation (pn-QRPA) models. Potential energy surfaces and potential energy curves are examined to investigate the nuclear deformations, nuclear stability, and shape phase transitions. The Gamow-Teller (GT) strength distributions and β-decay properties are obtained based on a deformed pn-QRPA framework. The computed half-lives and log *ft* values are in good agreement with existing experimental data, supporting the utilization of nuclear models. Additionally, stellar weak interaction rates are calculated as a function of density and temperature, emphasizing their influence on nucleosynthesis in astrophysical environments. For neutron-rich Rh isotopes, the results provide useful nuclear structural data and reliable inputs for the *r*-process modeling.

Keywords: *pn-QRPA; Nuclear ground state properties; Stellar weak rates; Potential energy surfaces; Log ft*

1. INTRODUCTION

The GT strength of atomic nuclei is extensively investigated and applied in nuclear and astrophysical research. It makes a substantial contribution to nuclear spectroscopy. Accurate modeling and a more comprehensive understanding of foundational nuclear processes depend on precise measurements and underlying theories related to the low-energy nuclear structure, including the GT strengths, half-lives, and stellar weak rates. The study of the available nuclear ground state properties remains a fundamental pillar in nuclear astrophysics today. It provides the information needed to comprehend the forces that dominate many-body nucleonic systems [1].

The neutron-rich nuclei are mostly unstable and have unique properties such as structural evolution, different shell closures, altered binding energies, and distinct β decay patterns compared to stable isotopes. Neutron-rich nuclei primarily decay via the β^- mechanism, where a neutron transforms into a proton by emitting an electron. Before decay, the nucleus is far from the stability line. The decay changes the element (e.g., Rh decays to Pd) and moves the nucleus closer to the line of stability, balancing the neutron-proton ratio. Particularly, the β^- decay properties, including the half-lives and GT strength, provide essential information about the stellar weak interaction rates that play an important role in nucleosynthesis processes [2]. The beta decay properties are calculated using the pn-QRPA model [3–5]. The neutron-rich nuclei in the mass range $A \sim$ 110-120 have attracted considerable attention from both theoretical and experimental studies as they show rapid variation observed in their ground-state structure and low-lying excited states [6, 7]. The information about the nuclear structure is carried by the GT strength distribution. It largely depends on the ground-state deformation of the parent nuclei [8]. Neutron-rich nuclei in the mass range $A \sim$ 104–113 exhibit rapid structural evolution due to deformation, pairing correlations, and shell effects. A large number of nuclei in this mass region are located far from the valley of β stability and are therefore not accessible to experimental investigations. Consequently, their properties must be studied using theoretical approaches. It is estimated that nearly 6000 nuclei exist between the valley of β stability and the neutron drip line. This specific location makes Rh isotopes ideal for studying the conflict between the effects of the spherical shell and the initial phases of collective deformation [9–13]. Nuclear density functional theory provides the theoretical foundation for the analysis of nuclear ground-state properties, especially nuclear deformation and nuclear shape transitions from oblate to prolate shapes. In the present analysis, we employed the RMF model with the density-dependent meson (DD-ME2) interaction to extract the nuclear deformation of the nuclei under investigation. The pn-QRPA model has been used for spectroscopic investigations including log *ft* values, half-lives and stellar weak rates [14] of Rh nuclei. Both RMF and pn-QRPA models are widely employed for the investigation of nuclear structure and β decay properties. The RMF framework is based on a small number of parameters optimized using nuclear matter properties and experimental data of stable nuclei located near the valley of β stability [15].

The present work is structured as follows. Section 2 provides a brief explanation of the theoretical foundation. Section 3 discusses nuclear ground state parameters including decay half-lives, weak decay rates, predicted GT strength, and log *ft* values. The final portion contains our concluding observations.

Cite as: A. Kabir, J.-Un Nabi, R. Badshah, A. Anjum, East Eur. J. Phys. 3, 44 (2026), https://doi.org/10.26565/2312-4334-2026-3-04

2. THEORETICAL FRAMEWORKS

2.1. The RMF Model

The RMF model describes how nuclei exchange mesons and photons [16]. The incompressibility and surface attributes of nuclei were challenging for the initially proposed version of the RMF framework. In order to accomplish this, a nonlinear framework of RMF was developed [17]. Following the introduction of further model versions, such as DD-ME2 and DD-PC1, the concept was referred to as covariant density functional theory (CDFT) [18,19]. In the present investigation, we used the DD-ME2 version of the model. Conventional quantum hydrodynamics uses Dirac fermions coupled to meson exchange as an effective Lagrangian to describe a nuclide [20,21]. The RMF approach defines the simplest set of meson fields for determining the bulk and single-particle nuclear parameters, employing the isoscalar scalar (σ), isoscalar vector (ω), and isovector vector (ρ) meson fields [7,22]. The Lagrangian density can be expressed as follows:

$$
\begin{aligned}
L = \bar{\psi}[\gamma_\mu(i\partial^\mu - \Gamma_\omega\omega^\mu - \Gamma_\rho\vec{\tau}\cdot\vec{\rho}_\mu) - (M - \Gamma_\sigma\sigma) - e\gamma^\mu A_\mu \frac{1-\tau_3}{2}]\psi + \frac{1}{2}(\partial^\mu\sigma\partial_\mu\sigma - m_\sigma^2\sigma^2) \\
-\frac{1}{4}\Omega^{\mu\nu}\Omega_{\mu\nu} + \frac{1}{2}m_\omega^2\omega^\mu\omega_\mu - \frac{1}{4}\vec{R}^{\mu\nu}\cdot\vec{R}_{\mu\nu} + \frac{1}{2}m_\rho^2\vec{\rho}^\mu\cdot\vec{\rho}_\mu - \frac{1}{4}F^{\mu\nu}F_{\mu\nu},
\end{aligned} \tag{1}
$$

where Γ_σ, Γ_ω, and Γ_ρ are the coupling constants and depend on the (nucleon) density and are described as

$$\Gamma_i(\rho) = \Gamma_i(\rho_{\text{sat}})f_i(x), \tag{2}$$

where $i = \sigma, \omega$ and ρ mesons. $f(x)$ is a function of $x = \rho_b/\rho_{\text{sat}}$, where ρ_b is the baryon density and ρ_{sat} is the baryon density at saturation in symmetric nuclear matter. For σ or ω meson, the respective $f(x)$ is

$$f_j(x) = a_j\frac{1+b_j(x+d_j)^2}{1+c_j(x+d_j)^2}, \quad \text{where } j = \sigma, \omega, \tag{2}$$

where for the ρ meson,

$$f_\rho(x) = e^{(-a_\rho(x-1))}. \tag{3}$$

Modifying the Lagrangian with reference to $\bar{\psi}$ yields the single-nucleon Dirac equation with nucleon self-energies [23,24]. We utilize the Dirac-Hartree-Bogoliubov (DIRHB) code [23] to generate the PEC and PES of $^{104-116}$Rh as a function of β_2 and γ, using DD-ME2 [25] interactions. The β_2 and γ are calculated below:

$$\beta_2 = \sqrt{a_{20}^2 + 2a_{22}^2} \ \text{ and } \ \gamma = \arctan(\sqrt{2}\,\frac{\mathrm{a}_{22}}{\mathrm{a}_{20}}), \tag{4}$$

where a_{20} and a_{22} are the deformation parameters computed via Ref. [23]. Quadrupole moment constraints were used in RMF calculations to achieve these calculations. The pairing correlations, which are assumed to be essential for open-shell nuclei, were investigated using the Bardeen-Cooper-Schrieffer (BCS) method. Furthermore, the ground state variables stated above were determined utilizing the constant G approximation [26].

2.2. The pn-QRPA Model

The stellar weak rates are described within the framework of the pn-QRPA model. The Hamiltonian of the pn-QRPA model is structured as follows:

$$H^{QRPA} = H^{sp} + V^{pair} + V_{GT}^{pp} + V_{GT}^{ph} \tag{5}$$

where H^{sp}, V^{pair}, V_{GT}^{pp} and V_{GT}^{ph} are the single-particle Hamiltonians, the pairing potential, the particle-particle, and the particle-hole strength, respectively. The wave functions and energy of a single particle were assessed using the Nilsson approach [27]. The Nilsson potential variables have been selected based on Ref. [28]. The Q-energies were analyzed utilizing the mass excess from Ref. [29] and β_2 from the RMF Ref. [30]. These assessments were conducted independently for protons (neutrons), employing a constant pairing force of strength G (G_n for neutrons and G_p for protons):

$$V_{pair} = -G\sum_{jkj'k'}(-1)^{l+j-k}s_{jk}^\dagger s_{j-k}^\dagger \times (-1)^{l'+j'-k'}s_{j'-k'}s_{j'k'},$$

Only positive numbers k and k' are to be summed over. The nucleon's spherical basis ($s_{jk}, s_{jk}^\dagger$) is transformed into a deformed basis ($d_{k\alpha}, d_{k\alpha}^\dagger$) using:

$$d_{k\alpha}^\dagger = \Sigma_j D_j^{k\alpha}s_{jk}^\dagger, \tag{6}$$

The Hamiltonian was diagonalized via an additional quantum number α to create $D^{k\alpha}$. The Bogoliubov transformation was applied to obtain the quasi-particle basis ($q_{k\alpha}^\dagger, q_{k\alpha}$).

$$q_{k\alpha}^\dagger = u_{k\alpha}d_{k\alpha}^\dagger - v_{k\alpha}d_{\bar{k}\alpha}, \tag{7}$$

$$q^{\dagger}_{\bar{k}\alpha} = u_{k\alpha} d^{\dagger}_{\bar{k}\alpha} + v_{k\alpha} d_{k\alpha}, \tag{8}$$

$\bar{k}$ denoted k's time-reversed state. The occupancy was determined using the BCS equations, with the basis $v^2_{k\alpha} + u^2_{k\alpha}$ = 1. The random phase approximation (RPA) framework is used to handle the residual interaction introduced in the Hamiltonian that establishes ground-state correlation. The pn-QRPA phonon creation operators are as follows:

$$A^{\dagger}_{\omega}(\mu) = \sum_{pn} [X^{pn}_{\omega}(\mu) q^{\dagger}_{p} q^{\dagger}_{\overline{n}} - Y^{pn}_{\omega}(\mu) q_n q_{\overline{p}}], \tag{9}$$

X_{ω} and Y_{ω} are the phonon amplitudes, while n and p are the quasi-particle states. The sum p-n pairings satisfy $\mu = k_n - k_p$=(1, 0, -1) and $\pi_n \cdot \pi_p$=1. The RPA expresses the eigenvalue as ω, which is the excitation energy. The particle-particle interaction (κ) and particle-hole interaction (χ) are the GT forces that are considered to be residual forces within the framework of pn-QRPA. The basis for the particle-particle forces is expressed as:

$$V^{pp}_{GT} = -2\kappa \sum_{\mu=-1}^{1} (-1)^{\mu} O^{\dagger}_{\mu} O_{-\mu}, \tag{10}$$

with

$$O^{\dagger}_{\mu} = \sum_{j_p k_p j_n k_n} < j_n k_n \mid (t_{\pm}\sigma_{\mu})^{\dagger} \mid j_p k_p > \times (-1)^{l_n + j_n - k_n} s^{\dagger}_{j_p k_p} s^{\dagger}_{j_n - k_n}.$$

Furthermore, in order to examine the χ interaction, we employed:

$$V^{ph}_{GT} = +2\chi \sum_{\mu=-1}^{1} (-1)^{\mu} U_{\mu} U^{\dagger}_{-\mu}, \tag{11}$$

with

$$U_{\mu} = \sum_{j_p k_p j_n k_n} < j_p k_p \mid t_{\pm}\, \sigma_{\mu} \mid j_n k_n > s^{\dagger}_{j_p k_p} s_{j_n k_n}. \tag{12}$$

Incorporating the residual interaction is essential for accurately reproducing reported GT strength and has a significant effect on the computed GT strength. The GT matrix element has been computed using

$$B_{GT}(\omega) = |\langle \omega, \mu || \tau_{-} \sigma_{\mu} || QRPA \rangle|^2. \tag{13}$$

The partial half-lives ($t_{1/2}$) were analyzed using the following formula.

$$t_{1/2} = \frac{\kappa}{(g_A/g_V)^2 f(A,Z,E) B_{GT}(\omega) + f(A,Z,E) B_F(\omega)}, \tag{14}$$

g_A/g_V is the ratio of axial and vector coupling constants, and κ = 6143 s [27]. $f(A,Z,E)$ is the phase space integral. B_F and B_{GT} are the Fermi and GT matrix elements, respectively. The beta-decay half-lives are computed as

$$T_{1/2} = \left(\sum_{0 \le \omega \le Q} (\frac{1}{t_{1/2}}) \right)^{-1}. \tag{15}$$

For additional analysis of Eq. (5), see [28, 29]. Taking into account the above relation, we obtain the relation for the *ft* as follows:

$$ft = \frac{\kappa}{(g_A/g_V)^2 B_{GT} + B_f} \tag{16}$$

The stellar weak rates were calculated from the initial state i to the final state f by utilizing

$$\lambda^{\beta^-/PC}_{if} = \ln 2 \frac{f^{\beta^-/PC}_{if}(\rho, T, E_f)}{(ft)_{if}}. \tag{17}$$

The $(ft)_{if}$ is represented as:

$$ft_{if} = (g_A/g_V)^2 B^{if}_{GT} + B^{if}_F, \tag{18}$$

$$B^{if}_{GT} = \frac{1}{2\mathcal{J}+1} \langle \psi_f \parallel \sum_k \tau^k_{-} \overrightarrow{\sigma}^k \parallel \psi_i \rangle|^2, \tag{19}$$

$$B_F^{if} = \frac{1}{2\mathcal{J}+1}\langle\psi_f \parallel \sum_k \tau_-^k \parallel \psi_i\rangle|^2. \tag{20}$$

where $\mathcal{J}$ is the angular momentum of the initial state. The analysis of nuclear matrix elements and the creation of low-lying excited states in our present investigation may be mentioned in [29]. The phase space integrals $f_{if}^{\beta^-/PC}$ are defined to be dimensionless and depend on certain stellar variables, including the stellar density and stellar temperature. Phase space integrals are expressed as:

$$f_{if}^{\beta^-} = \int_1^{E_\beta} E_k\sqrt{E_k^2-1}(E_\beta - E_k)^2 F(Z,E_k)(1-G_-)dE_k. \tag{21}$$

The f_{if}^{PC} for positron capture was evaluated using:

$$f_{if}^{PC} = \int_{E_l}^{\infty} E_k\sqrt{E_k^2-1}(E_\beta + E_k)^2 F(-Z,E_k)G_+ dE_k, \tag{22}$$

where E_k and E_β are the electron kinetic energy and the threshold energy during capture or emission. Energies are stated in units of the electron rest mass ($m_e c^2$). We further adopted natural units ($\hbar = c = m_e = 1$), where m_e is the electron rest mass. $F(+Z, E_k)$ is calculated using the approach described in Ref. [30]. We determined the β decay kinematics with:

$$E_\beta = m_p - m_d + E_p - E_d, \tag{23}$$

E_p, m_p and m_d, E_d denotes the parent and daughter nuclei's respective excitation energies and masses. The functions $G_\mp$ mentioned in equation (21) are defined as:

$$G_- = \left[\exp\left(\frac{E_k - E_f}{k_b T}\right)+1\right]^{-1}, \tag{24}$$

$$G_+ = \left[\exp\left(\frac{E_k + 2 - E_f}{k_b T}\right)+1\right]^{-1}, \tag{25}$$

where k_b refers to the Boltzmann constant and E_f is the Fermi energy of the electron. The number density of protons and neutrons was calculated by

$$\rho Y_e N_A = \frac{1}{\pi^2}\left(\frac{m_e c}{h}\right)^3 \int_0^\infty (G_- - G_+)p^2 dp, \tag{26}$$

Y_e and N_A represent the electron-proton ratio and Avogadro number, respectively. p represents the momentum of leptons. Stellar rates are determined with:

$$\lambda^{\beta^-/PC} = \sum_{if} P_m \lambda_{if}^{\beta^-/PC}, \tag{27}$$

where P_m represents the parent nucleus occupation probability. We summed the initial and final states until our computed rates reached the desired level of convergence.

3. RESULTS AND DISCUSSION

We conducted a systematic analysis of the nuclear deformation for $^{104-116}$Rh based on the potential energy curves (PEC's) and potential energy surfaces (PES's), utilizing the RMF model. For this purpose, we computed the total binding energy of the nuclei by constraining the β_2 and γ via the RMF model with the DD-ME2 interaction. The PEC and PES allow us to accurately demonstrate the phase shape transition of a particular isotope favors a prolate, oblate or spherical shape. In order to obtain the PEC, we set a zero reference point at the minimum energy. The difference between the binding energy at the particular β_2 and lowest binding energy, is plotted against β_2. In the mean-field model, a reliable convergence can be achieved by considering as many shells of harmonic oscillators of Fermion (N_F) and boson (N_B). However, the computation time increases significantly as the N_F, and N_B increases. We calculate the ground-state observable keeping N_F = 12 and N_B = 12. Increasing the nucleon number causes a transition in the shape of the nuclei, especially around magic numbers or mid shells. It is evident from PEC's analysis as displayed in Fig. 1 that nuclei possessing the neutron numbers N = 59 and 60 have a prolate shape, while N = 62, 63, 64, 65, 67, 68, 69, and 71 exhibit an oblate shape in the ground state. However, the N = 60 and 61 isotopes have substantial shape coexistence. ^{106}Rh has two local minima at β_2 = -0.275 on Ex = 0.0 MeV and at β_2 = 0.2 on Ex = 0.107 MeV via the DD-ME2 interaction. To generate the PES for the listed nuclei, considerations were given to both β_2 and γ deformations. Quadrupole shape deformations can be expressed in terms of polar coordinates β_2 and γ. The prolate and oblate shapes are related to $\gamma = 0°$, and $\gamma = 60°$, respectively. On the other hand, degrees of freedom are associated with the triaxial form ($0 \leq \gamma \leq 60$). In this particular analysis, the restrictions were execute to the PES and deformations in the β_2-γ plane ($0 \leq \gamma \leq 60$). The minima spread in the γ direction indicates a tendency of gamma softness. From the PES's analysis as mentioned in Fig. 2, ^{104}Rh has a prolate shape in its ground state, while ^{105}Rh, ^{106}Rh, ^{107}Rh, and ^{108}Rh have triaxial shapes. These isotopes have both the prolate

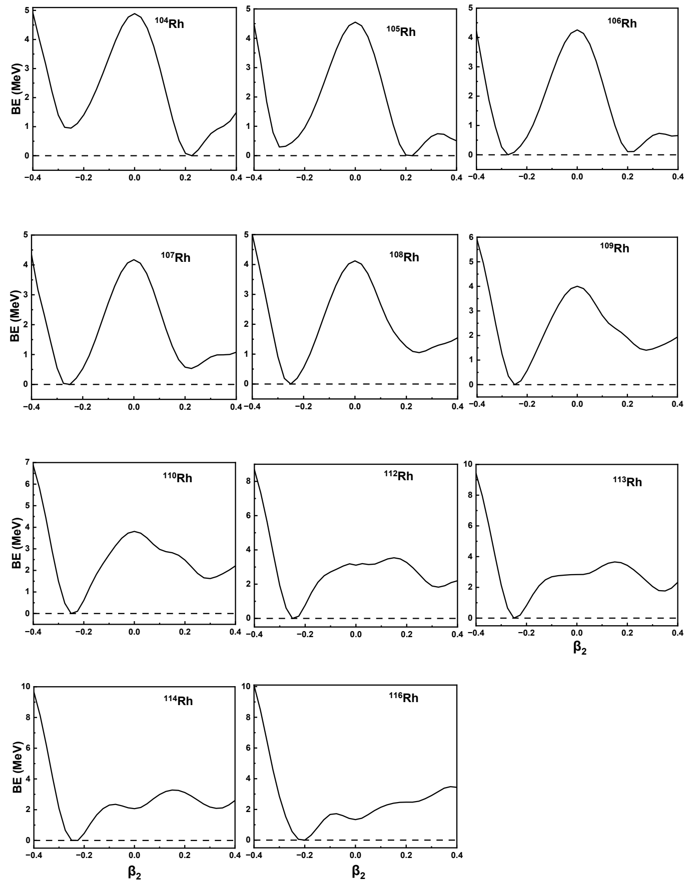

Figure 1. Calculated PECs for Rh isotopes using the RMF with DD-ME2 interaction.

and oblate minima on the PEC plot against β_2. Compared to the prolate energy minima, the oblate energy minima for ^{105}Rh, ^{106}Rh, ^{107}Rh, and ^{108}Rh are shallower. As a result, the ground state of these nuclei is more likely in a prolate shape. Furthermore, the present investigation predicts the coexistence with minimal energy difference in $^{104-116}$Rh isotopes. The present model-based extracted β_2, along with the existing β_2 from Ref. [32], is displayed in Table 1.

Table 1. The computed β_2 for $^{104-116}$Rh along with β_2 from Ref. [32].

Nuclei	[32]	This work
^{104}Rh	0.217	0.225
^{105}Rh	0.217	0.225
^{106}Rh	0.250	-0.275
^{107}Rh	0.250	-0.250
^{108}Rh	0.250	-0.250
^{109}Rh	0.262	-0.250
^{110}Rh	-0.248	-0.250
^{112}Rh	-0.248	-0.250
^{113}Rh	-0.248	-0.250
^{114}Rh	-0.258	-0.225
^{116}Rh	-0.258	0.250

In the subsequent part of our analysis, we employed the deformed pn-QRPA model to investigate the β decay properties, using the deformed pn-QRPA model. We used nuclear deformations from two different models, including the RMF model with DDME2 interaction and the FRDM model. Let us define our recipe: the beta decay properties investigated based on the deformation taken from the FRDM model is represented by pn-QRPA-FRDM, while the deformation taken from the RMF-DDME2-based interaction is represented by pn-QRPA-DDME2. Table 2 displayed the log ft values calculated using the pn-QRPA-FRDM and pn-QRPA-DDME2 along with experimental data [34] for ^{105}Rh, ^{113}Rh, and ^{114}Rh. The ratio between the computed and measured data is almost a factor of ≈ 1.5, which shows that the calculated log

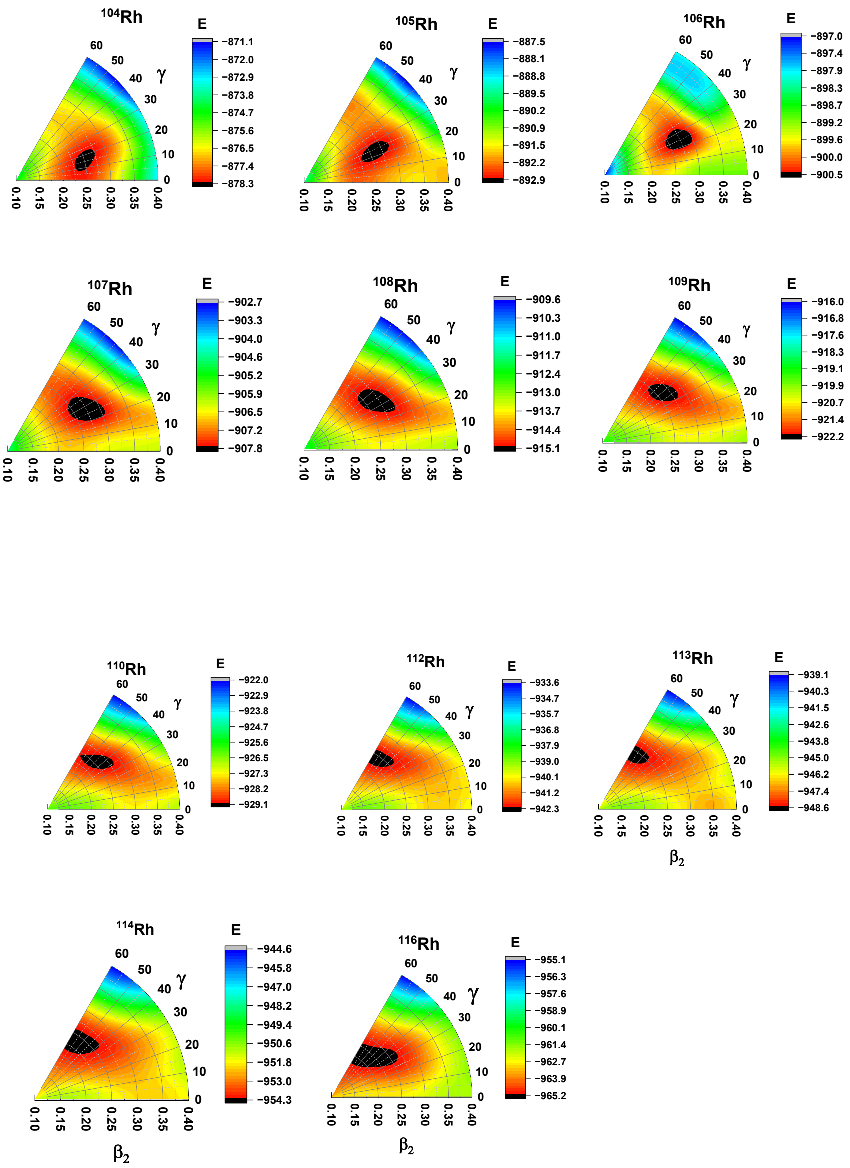

Figure 2. Calculated PES for Rh isotopes using the RMF with DD-ME2 interaction.

ft's are in good agreement with the experimental data. Figure 3 displays the comparison of the GT strength distributions, computed via the pn-QRPA-FRDM and pn-QRPA-DDME2 for ^{113}Rh as a function of excitation energy in the daughter nucleus. The experimental data exhibit a fragmented GT strength distribution, with most of the strength concentrated below 1.2 MeV. However, both pn-QRPA-FRDM and pn-QRPA-DDME2 calculations reproduce the general fragmentation pattern and the presence of low-lying GT transitions, which play a crucial role in determining the β-decay half-life. The calculations using both deformations predict relatively stronger GT strength at lower excitation energies. In contrast, model approximations, such as the omission of deformation effects in the daughter nuclei, may cause slight discrepancies between the computed and experimental results. Moreover, Fig. 3b represents the similar behavior for ^{114}Rh as is observed for ^{113}Rh, where the GT strength is distributed over a wide range of excitation energies with dominant contributions at low energies. The overall agreement between the calculated and experimental GT distributions demonstrates the reliability of the pn-QRPA-FRDM and pn-QRPA-DDME2 deformations as input parameters for the prediction of β-decay properties of neutron-rich Rh nuclei. Figure 4 compares our calculated half-lives for Rh nuclei with measured data [33]. Our predicted half-lives for Rh nuclei are about a factor of two greater or lower than the experimental data.

After examining the terrestrial half-lives, log ft values, and the GT strength distribution, considerations were given to the stellar weak rates, including the electron emission rates (λ^{β^-}) and positron capture rates (λ^{pc}) for the selected Rh nuclei. The stellar β-decay rates are important input parameters for simulating the late phases of massive stars. Other factors, e.g., magnetorotational effects [35], may also destabilize the stellar core. The stellar β-decay rates strongly depend

Table 2. Experimental [34] and calculated log ft values for neutron-rich Rh nuclei. Ratios are given to two decimal places.

Decay	E (keV)	log $ft_{\mathrm{Exp.}}$	log $ft_{\mathrm{pn-QRPA-FRDM}}$	log $ft_{\mathrm{pn-QRPA-DDME2}}$	pn-QRPA-FRDM/Exp.	pn-QRPA-DDME2/Exp.
			^{105}Rh → ^{105}Pd			
$7/2^+ \to 5/2^+$	0	5.729	4.42	4.44	1.29	1.29
$7/2^+ \to 7/2^+$	306.31	5.749	4.42	5.78	1.30	1.01
$7/2^+ \to 5/2^+$	319.23	5.118	4.42	4.92	1.16	1.04
$7/2^+ \to 7/2^+$	442.42	6.860	4.42	4.16	1.55	1.65
			^{113}Rh → ^{113}Pd			
$7/2^+ \to 5/2^+$	0	5.400	4.61	3.61	1.17	1.50
$7/2^+ \to 7/2^+$	189.51	5.900	4.59	5.24	1.28	1.13
$7/2^+ \to 5/2^+,7/2^+$	349.15	5.000	5.66	5.25	1.13	1.05
$7/2^+ \to 5/2^+,7/2^+$	372.99	6.700	5.13	4.59	1.31	1.46
$7/2^+ \to 5/2^+,7/2^+$	409.24	5.190	4.46	5.64	1.16	1.09
			^{114}Rh → ^{114}Pd			
$1^+ \to 0^+$	0	5.900	5.33	3.80	1.11	1.55
$1^+ \to 2^+$	332.61	6.000	5.11	3.79	1.17	1.58
$1^+ \to 2^+$	694.64	5.700	5.11	5.42	1.12	1.05
$1^+ \to 0^+$	1115.50	6.100	5.60	4.15	1.09	1.47
$1^+ \to 2^+$	1391.66	6.100	5.60	4.15	1.09	1.47

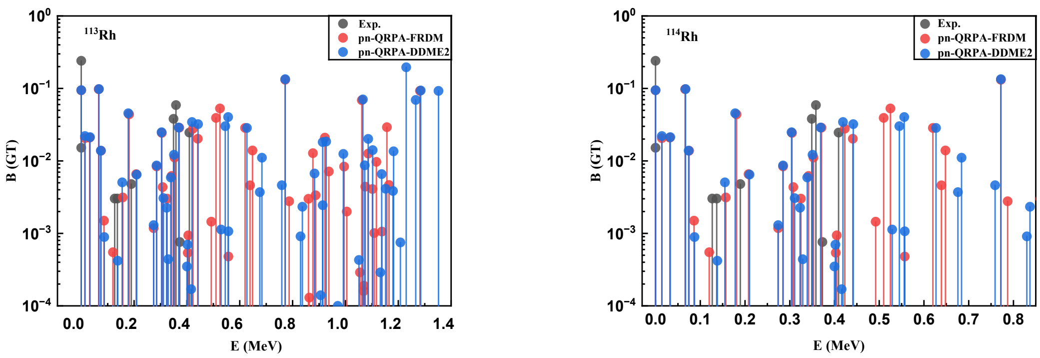

(a) (b)

Figure 3. The GT strength distribution for $^{113-114}$Rh calculated using pn-QRPA-FRDM and pn-QRPA-DDME2-based deformations along with experimental data [34].

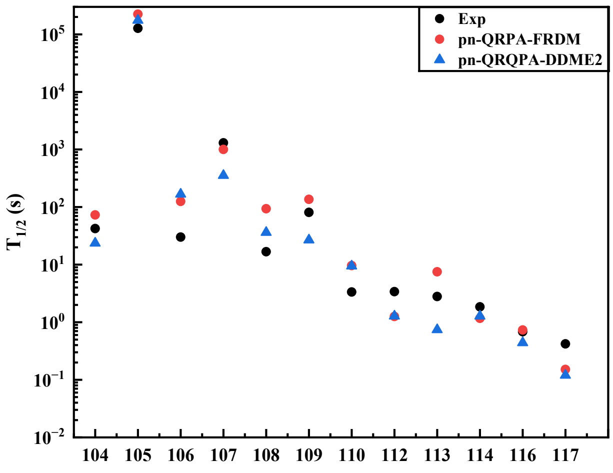

(A)

Figure 4. The present model-based and experimental [33] beta decay half-lives for the Rh nuclei.

on temperature and densities. At finite stellar temperatures, the parent nuclei are thermally populated, and their thermal excitation influences the total weak rates. We analyzed the stellar weak rates at the densities $\rho Y_e = 10^7$, 10^9, and 10^{11} g

Table 3. The sum of $\lambda^{\beta^-}+\lambda^{pc}$ for ^{104,105}Rh isotopes on various densities and temperatures.

ρY_e	T_9	^{104}Rh		^{105}Rh	
		pn-QRPA-FRDM	pn-QRPA-DDME2	pn-QRPA-FRDM	pn-QRPA-DDME2
10^7	3	5.00×10^{-3}	2.68×10^{-8}	4.25×10^{-3}	1.62×10^{-4}
	5	1.14×10^{-2}	1.53×10^{-5}	8.42×10^{-3}	1.79×10^{-3}
	10	1.75×10^{-1}	8.83×10^{-3}	5.33×10^{-2}	1.76×10^{-1}
	25	2.05×10^{2}	1.92×10^{1}	8.98×10^{0}	1.42×10^{2}
	30	8.54×10^{2}	8.88×10^{1}	2.92×10^{2}	5.32×10^{2}
10^9	3	7.33×10^{-8}	7.16×10^{-14}	1.37×10^{-4}	1.65×10^{-9}
	5	2.32×10^{-5}	8.62×10^{-9}	1.15×10^{-1}	6.46×10^{-6}
	10	6.75×10^{-3}	1.59×10^{-4}	5.11×10^{1}	9.56×10^{-3}
	25	6.25×10^{1}	5.83×10^{0}	4.20×10^{2}	4.36×10^{1}
	30	4.04×10^{2}	4.20×10^{1}	1.07×10^{2}	2.53×10^{2}
10^{11}	3	2.62×10^{-39}	6.34×10^{-45}	8.41×10^{23}	3.48×10^{-40}
	5	2.95×10^{-24}	2.43×10^{-27}	1.09×10^{-23}	4.45×10^{-24}
	10	1.94×10^{-12}	7.50×10^{-14}	1.72×10^{-12}	1.03×10^{-11}
	25	4.30×10^{-3}	4.04×10^{-4}	2.20×10^{-4}	3.28×10^{-3}
	30	1.19×10^{-1}	1.23×10^{-2}	4.25×10^{-2}	7.62×10^{-2}

cm^{-3} and at the temperatures T_9 = 3, 5, 10, 25, 30. We have displayed the stellar weak rates for $^{104-116}$Rh in Tables (3-6) using the recipe as mentioned above. Generally, the stellar weak rates decrease with density and increase with temperature. Utilizing both types of interactions, one can see that the stellar rates computed via the deformation taken from the FRDM are many orders of magnitude higher than the rates computed via the deformation taken from the RMF-DDME2-based interactions at low densities and low temperatures. However, at higher temperatures, $T_9\approx30$, the rates are enhanced by a factor of 10 or less.

Table 4. The sum of $\lambda^{\beta^-}+\lambda^{pc}$ for ^{106,107,108}Rh isotopes on various densities and temperatures.

ρY_e	T_9	^{106}Rh		^{107}Rh		^{108}Rh	
		pn-QRPA-FRDM	pn-QRPA-DDME2	pn-QRPA-FRDM	pn-QRPA-DDME2	pn-QRPA-FRDM	pn-QRPA-DDME2
10^7	3	1.51×10^{-5}	2.35×10^{-7}	4.25×10^{-2}	7.42×10^{-2}	2.86×10^{-2}	7.42×10^{-2}
	5	7.86×10^{-5}	8.21×10^{-5}	6.10×10^{-2}	1.08×10^{-1}	6.10×10^{-2}	1.08×10^{-1}
	10	1.65×10^{-2}	2.23×10^{-2}	7.91×10^{-1}	7.34×10^{-1}	7.91×10^{-1}	7.34×10^{-1}
	25	5.85×10^{1}	2.68×10^{1}	6.18×10^{2}	2.13×10^{2}	6.18×10^{2}	2.13×10^{2}
	30	2.87×10^{2}	1.19×10^{2}	2.32×10^{3}	7.23×10^{2}	2.32×10^{3}	7.23×10^{2}
10^9	3	1.88×10^{-11}	3.16×10^{-12}	6.44×10^{-7}	2.62×10^{-6}	6.44×10^{-7}	2.62×10^{-6}
	5	4.12×10^{-8}	8.60×10^{-8}	1.11×10^{-4}	4.01×10^{-4}	1.11×10^{-4}	4.01×10^{-4}
	10	1.62×10^{-4}	5.28×10^{-4}	3.42×10^{-2}	5.86×10^{-2}	3.42×10^{-2}	5.86×10^{-2}
	25	1.77×10^{1}	8.17×10^{0}	1.89×10^{2}	6.67×10^{1}	1.89×10^{2}	6.67×10^{1}
	30	1.36×10^{2}	5.64×10^{1}	1.10×10^{3}	3.44×10^{2}	1.10×10^{3}	3.44×10^{2}
10^{11}	3	1.27×10^{-42}	1.50×10^{-43}	1.92×10^{-38}	2.70×10^{-37}	6.17×10^{-1}	3.36×10^{-1}
	5	1.03×10^{-26}	1.39×10^{-26}	1.31×10^{-23}	1.36×10^{-22}	9.75×10^{-1}	4.03×10^{-1}
	10	5.01×10^{-14}	1.80×10^{-13}	1.09×10^{-11}	3.73×10^{-11}	9.92×10^{-2}	1.23×10^{0}
	25	1.21×10^{-3}	5.66×10^{-4}	1.31×10^{-2}	5.10×10^{-3}	9.75×10^{1}	1.05×10^{2}
	30	3.98×10^{-2}	1.66×10^{-2}	3.25×10^{-1}	1.05×10^{-1}	4.24×10^{2}	3.49×10^{2}

Table 5. The sum of $\lambda^{\beta^-}+\lambda^{pc}$ for ^{109,110,112}Rh isotopes on various densities and temperatures.

ρY_e	T_9	^{109}Rh		^{110}Rh		^{112}Rh	
		pn-QRPA-FRDM	pn-QRPA-DDME2	pn-QRPA-FRDM	pn-QRPA-DDME2	pn-QRPA-FRDM	pn-QRPA-DDME2
10^7	3	6.17×10^{-1}	3.36×10^{-1}	4.25×10^{-1}	1.63×10^{0}	5.97×10^{-2}	1.11×10^{1}
	5	9.75×10^{-1}	4.03×10^{-1}	4.76×10^{-1}	2.00×10^{0}	8.27×10^{-2}	1.24×10^{1}
	10	9.92×10^{-2}	1.23×10^{0}	2.11×10^{0}	4.75×10^{0}	2.40×10^{1}	2.40×10^{1}
	25	9.75×10^{1}	1.05×10^{2}	7.77×10^{2}	2.03×10^{2}	2.04×10^{2}	2.19×10^{2}
	30	4.24×10^{2}	3.49×10^{2}	2.74×10^{3}	6.16×10^{2}	5.44×10^{2}	6.05×10^{2}
10^9	3	2.11×10^{-7}	3.67×10^{-4}	1.06×10^{-1}	2.89×10^{-2}	1.53×10^{-9}	1.99×10^{-1}
	5	2.08×10^{-5}	5.30×10^{-3}	2.64×10^{-3}	1.01×10^{-1}	1.79×10^{-3}	3.27×10^{-1}
	10	3.64×10^{-1}	2.00×10^{-1}	1.26×10^{-1}	1.08×10^{0}	2.40×10^{-2}	7.42×10^{0}
	25	2.98×10^{1}	3.53×10^{1}	2.39×10^{2}	7.52×10^{1}	2.04×10^{2}	2.19×10^{2}
	30	2.01×10^{2}	1.69×10^{2}	1.30×10^{3}	3.06×10^{2}	5.44×10^{2}	6.05×10^{2}
10^{11}	3	9.04×10^{-39}	1.47×10^{-34}	4.13×10^{-36}	9.91×10^{-32}	3.44×10^{-40}	7.57×10^{-30}
	5	3.25×10^{-24}	6.41×10^{-21}	3.66×10^{-22}	5.78×10^{-19}	4.50×10^{-24}	1.25×10^{-17}
	10	1.22×10^{-12}	2.85×10^{-10}	3.97×10^{-11}	5.06×10^{-9}	1.12×10^{-11}	4.62×10^{-8}
	25	2.06×10^{-3}	5.81×10^{-2}	1.67×10^{-2}	1.35×10^{-1}	3.41×10^{-3}	4.02×10^{-2}
	30	5.92×10^{-2}	5.81×10^{-2}	3.85×10^{-1}	1.35×10^{-1}	7.84×10^{-2}	2.50×10^{-1}

Table 6. The sum of $\lambda^{\beta^-}+\lambda^{pc}$ for ^{113,114,116}Rh isotopes on various densities and temperatures.

ρY_e	T_9	^{113}Rh		^{114}Rh		^{116}Rh	
		pn-QRPA-FRDM	pn-QRPA-DDME2	pn-QRPA-FRDM	pn-QRPA-DDME2	pn-QRPA-FRDM	pn-QRPA-DDME2
10^7	3	1.28×10^{0}	1.45×10^{0}	2.14×10^{-1}	3.46×10^{0}	1.13×10^{1}	1.71×10^{1}
	5	1.46×10^{0}	1.66×10^{0}	2.83×10^{-1}	3.64×10^{0}	1.29×10^{1}	2.59×10^{1}
	10	4.22×10^{0}	3.73×10^{0}	8.09×10^{-1}	9.56×10^{0}	5.28×10^{1}	5.44×10^{1}
	25	2.56×10^{2}	1.89×10^{2}	3.06×10^{2}	2.19×10^{2}	2.49×10^{2}	3.42×10^{2}
	30	9.12×10^{2}	5.93×10^{2}	1.01×10^{3}	6.01×10^{2}	7.41×10^{2}	8.92×10^{2}
10^9	3	5.48×10^{-2}	2.28×10^{-2}	2.11×10^{-1}	1.57×10^{-1}	1.27×10^{0}	2.99×10^{0}
	5	1.09×10^{-1}	7.55×10^{-2}	3.64×10^{-1}	2.69×10^{-1}	1.29×10^{1}	5.75×10^{0}
	10	7.98×10^{-1}	7.97×10^{-1}	1.95×10^{0}	2.54×10^{0}	1.27×10^{1}	1.81×10^{1}
	25	8.64×10^{1}	6.75×10^{1}	1.09×10^{2}	9.34×10^{1}	2.49×10^{2}	1.46×10^{2}
	30	4.41×10^{2}	2.91×10^{2}	4.93×10^{2}	3.12×10^{2}	7.41×10^{2}	4.60×10^{2}
10^{11}	3	2.40×10^{-32}	2.63×10^{-32}	1.17×10^{-30}	5.87×10^{-30}	1.13×10^{-10}	1.08×10^{-8}
	5	5.64×10^{-20}	1.73×10^{-19}	6.12×10^{-19}	1.00×10^{-17}	6.12×10^{-9}	4.04×10^{-8}
	10	4.75×10^{-10}	2.01×10^{-9}	1.70×10^{-9}	4.04×10^{-8}	1.70×10^{-7}	2.77×10^{-8}
	25	7.69×10^{-3}	9.50×10^{-3}	1.15×10^{-2}	3.73×10^{-2}	1.15×10^{-2}	2.29×10^{-2}
	30	1.41×10^{-1}	1.12×10^{-1}	1.69×10^{-1}	2.36×10^{-1}	1.30×10^{-1}	2.02×10^{-1}

4. CONCLUSIONS

In this work, we performed the analysis for neutron-rich $^{104-116}$Rh isotopes using the RMF and pn-QRPA models. The nuclear shapes and their deformation are computed via the RMF framework, and the β-decay properties, including the GT strength, the decay half-lives, and the log ft values, are analyzed via the pn-QRPA framework. The half-lives and log ft values are obtained using the deformed pn-QRPA model, with β_2 taken from the FRDM and RMF DD-ME2 based interaction, are reasonably consistent with existing experimental data. Additionally, we have calculated the stellar β-decay rates based on the deformed pn-QRPA model. Our analysis demonstrates a strong dependence on both temperature and density. At lower temperatures, the ground-state transitions dominate the stellar weak rates because excited-state populations are lower, whereas excited-state populations increase significantly at higher temperatures, which impacts the stellar weak rates. Increasing the density generally suppresses β-decay rates due to phase-space constraints. Overall, stellar β-decay rates rise with temperature and fall with increasing density.

Declaration of competing interest: The authors declare that they have no known competing financial interests or personal relationships that could have appeared to influence the work reported in this paper.

ORCID

Abdul Kabir, https://orcid.org/0000-0002-9344-975X; **Jameel-Un Nabi**, https://orcid.org/0000-0002-8229-8757; **Rahat Badshah**, https://orcid.org/0009-0001-1900-6301; **Ayesha Anjum**, https://orcid.org/0009-0000-2290-7891

REFERENCES

[1] J.-Un Nabi, A. Kabir, and T. Bayram, Chin. J. Phys. **87**, 797 (2024) https://doi.org/10.1016/j.cjph.2023.12.036

[2] H. Kleis, M. Seidlitz, A. Blazhev, L. Kaya, P. Reiter, K. Arnswald, A. Dewald, *et al*. Phys. Rev. C, **104**, 034310 (2021). https://doi.org/10.1103/PhysRevC.104.034310

[3] J. P. Fernández-García, M. Cubero, L. Acosta, M. Alcorta, M. A. G. Alvarez, M. J. G. Borge, L. Buchmann, *et al*., Phys. Rev. C, **92**, 044608 (2015). https://doi.org/10.1103/PhysRevC.92.044608

[4] N. Paar, D. Vretenar, and P. Ring, Rept. Prog. Phys.**70**, 691 (2007). https://doi.org/10.48550/arXiv.nucl-th/0701081

[5] J. Engel, M. Bender, J. Dobaczewski, W. Nazarewicz, and R. Surman, *et al*., Phys. Rev. C, **60**, 014302 (1999). https://doi.org/10.1103/PhysRevC.60.014302

[6] Z. M. Niu, Y. F. Niu, H. Z. Liang, W. H. Long, and J. Meng, Phys. Rev. C, **95**, 044301 (2017). https://doi.org/10.1103/PhysRevC.95.044301

[7] A. Kabir, J.-Un Nabi, S.A. Rida, I. Anwaar, N.-Ul A. Raza, and H. Almujibah, Res. Astron. Astrophys. **25**, 015004 (2025). https://doi.org/10.1088/1674-4527/ad981d

[8] E. Bouchez, I. Matea, W. Korten, F. Becker, B. Blank3 C. Borcea, A. Buta, *et al*., Phys. Rev. Lett. **90**, 082502 (2003). https://doi.org/10.1103/PhysRevLett.90.082502

[9] M. Rajput, S. Singh, V. Rani, P. Verma, A. Bharti, G. H. Bhat, and J. A. Sheikh, Eur. Phys. J. A, **58**, 146 (2022). https://doi.org/10.1140/epja/s10050-022-00802-x

[10] U. Hager, V.-V. Elomaa, T. Eronen, J. Hakala, A. Jokinen, A. Kankainen, S. Rahaman, *et al*., Phys. Rev. C, **75**, 064302 (2007). https://doi.org/10.1103/PhysRevC.75.064302

[11] M. Hukkanen, W. Ryssens, P. Ascher, M. Bender, T. Eronen, S. Grévy, A. Kankainen, *et al*., Phys. Rev. C, **107**, 014306 (2024). https://doi.org/10.1103/PhysRevC.107.014306

[12] J. F. W. Lane, A. N. Andreyev, S. Antalic, D. Ackermann, J. Gerl, F. P. Heßberger, S. Hofmann, *et al*., Phys. Rev. C, **87**, 014318 (2013). https://doi.org/10.1103/PhysRevC.87.014318

[13] M. Versteegen, D. Denis-Petit, V. Méot, T. Bonnet, M. Comet, F. Gobet, F. Hannachi, *et al*., Phys. Rev. C, **94**, 044325 (2016). https://doi.org/10.1103/PhysRevC.94.044325

[14] J.-U. Nabi, H. V. Klapdor-Kleingrothaus, and H. Volker, At. Data Nucl. Data Tables **88**, 237 (2004). https://doi.org/10.1016/j.adt.2004.09.002

[15] A. Kabir, J.-U. Nabi, and M. Zubair, Eur. Phys. J. A, **141**, 249 (2026). https://doi.org/10.1140/epjp/s13360-026-07376-3

[16] J. D. Walecka, Ann. Phys. **83**, 491 (1974). https://doi.org/10.1016/0003-4916(74)90208-5

[17] P. Ring, Prog. Part. Nucl. Phys. **37**, 193 (1996). https://doi.org/10.1016/0146-6410(96)00054-3

[18] S. Typel, and H. H. Wolter, Nucl. Phys. A **656**, 331 (1999). https://doi.org/10.1016/S0375-9474(99)00310-3

[19] G. A. Lalazissis, T. Nikšić, D. Vretenar, and P. Ring, Phys. Rev. C **71**, 024312 (2005). https://doi.org/10.1103/PhysRevC.71.024312

[20] J. Meng, H. Toki, S.G. Zhou, S.Q. Zhang, W.H. Long, and L.S. Geng, Prog. Part. Nucl. Phys.**57**, 470 (2006). https://doi.org/10.1016/j.ppnp.2005.06.001

[21] T. Nikšić, D. Vretenar, and P. Ring, Phys. Rev. C, **78**, 034318 (2008). https://doi.org/10.1103/PhysRevC.78.034318

[22] J.-U. Nabi, W. Khalid, A. Kabir and S. A. Rida, Arab. J. Sci. Eng. **50**, 6865 (2025). https://doi.org/10.1007/s13369-024-09619-w

[23] T. Nikšić, N. Paar, D. Vretenar, and P. Ring, Comput. Phys. Commun. **185**, 1808 (2014). https://doi.org/10.1016/j.cpc.2014.02.027

[24] S. Karatzikos, A. V. Afanasjev, G. A. Lalazissis, and P. Ring, Phys. Lett. B, **689**, 72 (2010). https://doi.org/10.1016/j.physletb.2010.04.045

[25] B. Mottelson, The Nilsson Model and Sven Gösta Nilsson. Phys. Scr. **T125** (2006). https://doi.org/10.1088/0031-8949/2006/T125/E02

[26] K. Ikeda, S. Fujii, and J. I. Funjita, Phys Lett. **3**, 271 (1963). https://doi.org/10.1016/0031-9163(63)90255-5

[27] J. C. Hardy, and I. S. Towner, Phys. Rev. C, **79**, 055502 (2009). https://doi.org/10.1103/PhysRevC.79.055502

[28] M. Hirsch, A. Staudt, K. Muto, and H. V. Klapdor-Kleingrothaus, Nucl. Phys. A, **535,** 62 (1991). https://doi.org/10.1016/0375-9474(91)90515-8

[29] K. Muto, E. Bender, T. Oda, and H. V. Klapdor-Kleingrothaus, Phys. A - Hadron Nucl. **341**, 407 (1992). https://doi.org/10.1007/BF01301384

[30] N. B. Gove, and M. J. Martin, At. Data Nucl. Data Tables **10**, 205 (1971). https://doi.org/10.1016/S0092-640X(71)80026-8

[31] A. Kabir, J.-U. Nabi, N. U. A. Raza, and H. Almujibah, Nucl. Phys. A, **1057**, 123057 (2025). https://doi.org/10.1016/j.nuclphysa.2025.123057

[32] P. Möller, A.J. Sierk, T. Ichikawa, and H. Sagawa, At. Data Nucl. Data Tables, **109–110**, 1–204. (2016). https://doi.org/10.1016/j.adt.2015.10.002

[33] M. Wang, W. J. Huang, F. G. Kondev, G. Audi, and S. Naimi, Chin. Phys. C, **45**, 030003 (2021). https://doi.org/10.1088/1674-1137/abddaf

[34] National Nuclear Data Center, Brookhaven National Laboratory. "Nudat (nuclear structure and decay data)." (2008). https://www.nndc.bnl.gov/

[35] S. Usman, and A. Mushtaq Sci. Rep. **13** 15315 (2023). https://doi.org/10.1038/s41598-023-42397-3

СТОСОВНО ЯДЕРНОЇ СТРУКТУРИ ТА СЛАБКУ ШВИДКІСТЬ ЗОРЯНОГО РОЗПАДУ БАГАТОГО НА НЕЙТРОНИ ІЗОТОПУ $^{104-116}$Rh

Абдул Кабір[1], Джаміль-Ун Набі[2], Рахат Бадшах[1], Аєша Анджум[2]
[1]*Кафедра космічних наук, Інститут космічних технологій, Ісламабад, 44000, Пакистан*
[2]*Кафедра фізики, Університет Ваха, Ваканте, 47040, Пакистан*

Основний стан ядра та властивості бета-розпаду багатих на нейтрони непарних-непарних та непарних-A ізотопів родію $^{104-116}$Rh досліджуються за допомогою моделей релятивістського середнього поля (RMF) та наближення випадкової фази протон-нейтронних квазічастинок (pn-QRPA). Розподіл сили Гамова-Теллера (GT) та властивості β-розпаду отримані на основі параметрів деформації основного стану з розрахунків RMF та включені в структуру наближення квазічастинкової випадкової фази. Поверхні потенційної енергії та криві потенційної енергії досліджуються для дослідження ядерної стабільності та переходів форми. Розраховані періоди напіврозпаду та значення log *ft* добре узгоджуються з існуючими експериментальними даними, що підтверджує використання ядерних моделей. Крім того, швидкості слабкої взаємодії зі зорями розраховані як функція щільності та температури, що підкреслює їх вплив на нуклеосинтез в астрофізичних середовищах. Для нейтроно-багатих ізотопів Rh результати надають корисні дані про структуру ядра та надійні вхідні дані для моделювання r-процесу.
Ключові слова: *pn-QRPA; властивості основного стану ядра; ядерні деформації; поверхні потенційної енергії; log ft*

East European Journal of Physics. 3. 54–67 (2026)
DOI: 10.26565/2312-4334-2026-3-05 ISSN 2312-4334

COSMOLOGICAL MODEL WITH POLYTROPIC BULK VISCOSITY AND VARYING GRAVITATIONAL AND COSMOLOGICAL CONSTANTS

Archana Gajanan Ingle[1], Shailendra D. Deo[2], Praveen Kumar Dhankar[3*], Safiqul Islam[4], Kashika Srivastava[5], Bhagwat Thakran[6]
[1]*PGTD Mathematics, Gondwana University, Gadchiroli, Maharashtra, India*
[2]*Mahatma Gandhi College of Science, Gadchandur, Dist. Chandrapur. M. S.- 442908, India*
[3]*Symbiosis Institute of Technology, Nagpur Campus, Symbiosis International (Deemed University), Pune-440008, India*
[4]*Department of Mathematics and Statistics, College of Science, King Faisal University, P.O. Box 400, Al Ahsa 31982, Saudi Arabia*
[5]*Babu Banarasi Das University, Lucknow, Uttar Pradesh, India*
[6]*Department of Mathematics, G H Raisoni College of Engineering Nagpur, Maharashtra-440016, India*
[*]*Corresponding Author e-mail: pkumar6743@gmail.com*
Received April 4, 2026; revised June 28, 2026; accepted July 8, 2026

This paper investigates Einstein's field equations within a cosmological model that incorporates a polytropic bulk viscous fluid, with the gravitational and cosmological constants varying in a Bianchi type-I universe. It is observed that different time-dependent scenarios yield variations in physical parameters, which hold significant implications for cosmic evolution. Key physical parameters, including energy density, the gravitational constant, expansion scalar, the cosmological constant, the bulk viscosity coefficient and shear scalar are examined for their physical significance. The geometrical and observational interpretations of the cosmological model are also investigated.

Keywords: *Bianchi Type-I; Shear Scalar; Bulk Viscosity; Expansion Scalar*

1. INTRODUCTION

Cosmology investigates the origin and evolution of the universe, with a focus on its largest-scale structures and dynamics, including the motion of celestial bodies. Advances in the twentieth century established the Big Bang as the prevailing cosmological model, now widely accepted by the scientific community. These developments have also stimulated speculation regarding the very beginning of the universe. Bianchi type-I spacetimes represent simple generalizations of the flat Friedmann-Robertson-Walker (FRW) models. Observations, such as the late-time cosmic acceleration (Perlmutter et al. [1–3]; Riess et al. [4]; Allen et al. [5]; Peebles et al. [6]; Padmanabhan [7]; Lima [8]; Khadekar [9]; Dhankar [10–18]; Munyeshyaka [19–21]; Gadbail [22]; Panda [23]; Kumar [24]; Thakran [25]; Samanta [26]; Sanyal [27]), reveal that the universe is undergoing accelerated expansion.

The cosmological constant (Λ) is a subject of considerable interest, with recent observations suggesting a value of approximately $10^{-55}cm^{-2}$, which is dramatically smaller than the predictions from particle physics by about 120 orders of magnitude. Λ remains a cornerstone of modern cosmological theory. Bulk viscosity, arising from phase transitions in grand unified theories, may contribute to an inflationary phase in the early universe. There is substantial evidence supporting a non-zero cosmological constant Riess et al. [28]. For instance, Zhang et al. [29] investigated Friedmann cosmology on a codimension-2 brane with time-varying tension, demonstrating that Λ can remain independent of the brane tension. Tiwari and Sharma [30] studied Bianchi type-III models incorporating strings and bulk viscosity within general relativity, showing that such models can be shear-free. Wang [31–33], examined Bianchi type I–IX models in the presence of string clouds. Numerous studies have explored viscous fluid cosmologies in the early universe. Tiwari et al. [34] analyzed Bianchi type-I string cosmologies with bulk viscosity and a time-dependent Λ. Zeyauddin and Saha [35] studied Bianchi type-V models incorporating bulk viscosity and particle production. Beesham et al. [36] proposed a Bianchi type-I anisotropic model with a bulk viscous fluid, variable gravitational constant G, and Λ, where the bulk viscosity η is related to the energy density ρ via $\eta = \eta_0\rho^n$, with $\eta_0 \leq 0$. They derived the modified Friedmann equation $3H^2 = G\rho + \sigma^2 + \Lambda$, where σ denotes shear and H is the Hubble parameter.

Further investigations by Tiwari [37], Tiwari and jha [38], Tiwari and Dwivedi [39] (2008–2010) explored isotropic and anisotropic cosmologies, examining relationships among the cosmological constant Λ, the inverse power of the scale factor (R^{-m}), and the Hubble parameter H, with m as a constant. Tiwari and Sharma [40] analyzed LRS Bianchi type-II models featuring a decaying Λ, while Tiwari et al. [41] studied Bianchi type-I models with a perfect fluid in general relativity. Numerous other researchers [42–62] have also investigated the behavior and implications of the cosmological constant. Another intriguing topic is the possible variability of the gravitational constant G. While the conventional view, based on Newtonian gravity and Einstein's general relativity, treats G as constant, some theories allow for its variation over cosmic time. A time-varying G could revolutionize fundamental physics and have profound astrophysical consequences.

Cite as: A.G. Ingle, Sh.D. Deo, P.K. Dhankar, S. Islam, K. Srivastava, B. Thakran, East Eur. J. Phys. 3, 54 (2026), https://doi.org/10.26565/2312-4334-2026-3-05

Dirac [63] proposed that G decreases inversely with time when measured in atomic units, noting its approximate value as 10^{-40} at the present epoch.

Cosmological models that include bulk viscosity, together with time-dependent gravitational and cosmological constants, have received significant attention in contemporary theoretical physics [64, 65]. Bulk viscosity arises naturally in cosmic fluids due to particle interactions and phase transitions, and it can have a substantial impact on the dynamics of the early universe [66]. In anisotropic spacetimes, such as Bianchi type-I models, viscous effects provide a useful framework for exploring deviations from perfect fluid behavior while remaining compatible with observational constraints on cosmic expansion. Models with variable gravitational G and cosmological Λ constants offer an alternative to the standard ΛCDM framework, potentially addressing unresolved issues related to dark energy and late-time cosmic acceleration [67]. Polytropic equations of state have been applied to describe bulk viscous fluids, extending the barotropic case and capturing more intricate thermodynamic properties [68, 69]. These models often admit exact solutions to Einstein's field equations, allowing detailed investigations of the universe's expansion history and the dissipation of anisotropy [64]. Moreover, the combined influence of viscous effects and evolving G and Λ can produce scenarios consistent with current observations of cosmic acceleration without invoking exotic fields [70]. In this study, we focus on a Bianchi type-I cosmological model with polytropic bulk viscosity, permitting both G and Λ to vary over cosmic time, and we examine the evolution of key cosmological parameters.

The structure of this paper is as follows: Section 2 presents the Bianchi type-I bulk viscous polytropic cosmological model with variable G and Λ. In Section 3, we derive solutions to Einstein's field equations under specific equations of state and compute various physical quantities, including scale factors, the Hubble parameter, the expansion scalar, and the deceleration parameter. Section 4 summarizes our conclusions.

2. THE METRIC AND IT'S FIELD EQUATIONS

The spatially homogeneous and anisotropic Bianchi type-I spacetime is described by,

$$ds^2 = -dt^2 + X_1^2(t)dx^2 + X_2^2(t)dy^2 + X_3^2(t)dz^2, \tag{1}$$

where, $X_1(t)$, $X_2(t)$ and $X_3(t)$ are functions dependent solely on cosmic time t.

The energy–momentum tensor of a bulk viscous fluid is given by

$$T_\mu^\nu = (\rho + \bar{p})u_\mu u^\nu - \bar{p}\, g_\mu^\nu, \tag{2}$$

where the effective pressure is defined as

$$\bar{p} = p - 3\xi H. \tag{3}$$

Here, ρ and p denote the energy density and equilibrium pressure, respectively, ξ is the coefficient of bulk viscosity, H is the Hubble parameter, and the four-velocity u^μ satisfies the normalization condition $g_{\mu\nu}u^\mu u^\nu = -1$.

The Einstein field equations are expressed as

$$R_\mu^\nu - \frac{1}{2}Rg_\mu^\nu = -8\pi G T_\mu^\nu + \Lambda g_\mu^\nu, \tag{4}$$

where G and Λ are the time-dependent gravitational and cosmological constants, respectively.
The expressions for the shear scalar ρ and the expansion scalar Θ are provided as follows:

$$\Theta = u^\nu_{;\mu} = \frac{1}{3}\left(\frac{\dot{X}_1}{X_1} + \frac{\dot{X}_2}{X_2} + \frac{\dot{X}_3}{X_3}\right) = 3H,$$

$$\sigma^2 = \frac{1}{2}\sigma_{\mu\nu}\sigma^{\mu\nu}$$

$$= \frac{1}{3}\left(\frac{\dot{X}_1^2}{X_1^2} + \frac{\dot{X}_2^2}{X_2^2} + \frac{\dot{X}_3^2}{X_3^2} - \frac{\dot{X}_1\dot{X}_2}{X_1X_2} - \frac{\dot{X}_2\dot{X}_3}{X_2X_3} - \frac{\dot{X}_1\dot{X}_3}{X_1X_3}\right). \tag{5}$$

The Einstein's field equation (4) supporting the metric (1) now become

$$\frac{\ddot{X}_2}{X_2} + \frac{\ddot{X}_3}{X_3} + \frac{\dot{X}_2\dot{X}_3}{X_2X_3} = -8\pi G\bar{p} + \Lambda, \tag{6}$$

$$\frac{\ddot{X}_1}{X_1} + \frac{\ddot{X}_3}{X_3} + \frac{\dot{X}_1\dot{X}_3}{X_1X_3} = -8\pi G\bar{p} + \Lambda, \tag{7}$$

$$\frac{\ddot{X}_1}{X_1} + \frac{\ddot{X}_2}{X_2} + \frac{\dot{X}_1\dot{X}_2}{X_1X_2} = -8\pi G\bar{p} + \Lambda, \tag{8}$$

$$\frac{\dot{X}_1\dot{X}_2}{X_1X_2} + \frac{\dot{X}_2\dot{X}_3}{X_2X_3} + \frac{\dot{X}_1\dot{X}_3}{X_1X_3} = 8\pi G\rho + \Lambda, \tag{9}$$

The divergence of the Einstein tensor produces an additional equation for the time variations of Λ and G, namely:

$$\left(R^{\nu}_{\mu} - \frac{1}{2}Rg^{\nu}_{\mu}\right)_{;\nu} = 0$$

which leads to

$$\left(8\pi G T^{\nu}_{\mu} - \Lambda g^{\nu}_{\mu}\right)_{;\nu} = 0$$

yielding

$$8\pi\dot{G}\rho + \dot{\Lambda} + 8\pi G\left\{\dot{\rho} + \left(\frac{\dot{X}_1}{X_1} + \frac{\dot{X}_2}{X_2} + \frac{\dot{X}_3}{X_3}\right)(\rho + \bar{p})\right\} = 0. \tag{10}$$

The energy conservation Eq. (10) is divided into two equations after using Eq. (4), we get

$$\dot{\rho} + \left(\frac{\dot{X}_1}{X_1} + \frac{\dot{X}_2}{X_2} + \frac{\dot{X}_3}{X_3}\right)(\rho + \bar{p}) = 0, \tag{11}$$

$$\dot{\Lambda} + 8\pi\dot{G}\rho = 8\pi G\xi\left(\frac{\dot{X}_1}{X_1} + \frac{\dot{X}_2}{X_2} + \frac{\dot{X}_3}{X_3}\right)^2 = 0. \tag{12}$$

3. SOLUTIONS OF THE FIELD EQUATIONS

We consider the relation as

$$\xi = \xi_0\rho^{\beta} \tag{13}$$

where, $\xi_0 > 0$, and β is taken as a constant.
To derive the complete solution, we further consider the polytropic relation as follows:

$$\bar{p} = \alpha\rho^{\zeta} \tag{14}$$

where α and ζ are constants characterizing the polytropic fluid, and ρ denotes the energy density. For simplicity, we set the constant ζ to unity.

We assume that the solution to the system of equations takes the following form:

$$\frac{\dot{X}_1}{X_1} = \frac{\dot{X}_2}{X_2} = \frac{\alpha_1}{t^n}, \frac{\dot{X}_3}{X_3} = \frac{\alpha_2}{t^n} \tag{15}$$

where, α_1, α_2 both are constants [4].

Upon integrating equation (15), we obtain the solution as follows:

$$X_1 = X_2 = a.exp\left[\frac{\alpha_1 t^{1-n}}{(1-n)}\right], X_3 = b.exp\left[\frac{\alpha_2 t^{1-n}}{(1-n)}\right]. \tag{16}$$

where a and b are the constant of integration.
After using Eqns. (14) & (15) into Eq. (11), we have the values as given

$$\frac{\dot{\rho}}{\rho} = -\frac{(1+\alpha)(2\alpha_1 + \alpha_2)}{t^n} \tag{17}$$

After Integrating on both sides, we get

$$\rho = \alpha_3 exp\left[-(1+\alpha)(2\alpha_1 + \alpha_2)\frac{t^{1-n}}{(1-n)}\right], \tag{18}$$

Differentiating Eq. (18) on both sides, we have

$$\dot{\rho} = -\alpha_3\frac{(\alpha+1)(2\alpha_1+\alpha_2)}{t^n}exp\left[-\frac{(1+\alpha)(2\alpha_1+\alpha_2)}{(1-n)}t^{1-n}\right], \tag{19}$$

By using Eq. (9), (15), (16) and differentiating on both sides, we have

$$-\frac{2n(\alpha_1^2+2\alpha_1\alpha_2)}{t^{(1+2n)}}=8\pi G\dot{\rho}+8\pi G\xi\left[\frac{(2\alpha_1+\alpha_2)}{t^n}\right]^2, \tag{20}$$

Again, substituting Eqns. (13) & (19) into Eq. (20), we get the values as

$$G=-\frac{n(\alpha_1^2+2\alpha_1\alpha_2)}{4\pi\alpha_3 t^{2n+1}}.exp\left\{\frac{(\alpha+1)(2\alpha_1+\alpha_2)}{(1-n)}t^{1-n}\right\}\left[-\frac{(\alpha+1)(2\alpha_1+\alpha_2)}{t^n}+\xi_0\alpha_3^{\beta-1}.\right.$$

$$\left.exp\left\{-\frac{(\beta-1)(1+\alpha)(2\alpha_1+\alpha_2)}{(1-n)}t^{1-n}\right\}\right]^{-1} \tag{21}$$

$$\Lambda=\frac{(\alpha_1^2+2\alpha_1\alpha_2)}{t^{2n}}+2n\frac{(\alpha_1^2+2\alpha_1\alpha_2)}{t^{2n+1}}\left[-\frac{(\alpha+1)(2\alpha_1+\alpha_2)}{t^n}+\xi_0\alpha_3^{\beta-1}\right.$$

$$\left..exp\left\{-\frac{(\beta-1)(1+\alpha)(2\alpha_1+\alpha_2)}{(1-n)}t^{1-n}\right\}\right]^{-1} \tag{22}$$

It should be noted that the parameters α_1, α_2, and α_3 are dimensional constants with dimensions T^{n-1}, as dictated by the ansatz $\dot{X}_i/X_i=\alpha_i t^{-n}$, the dimension of t being T. Consequently, the expression for Λ remains dimensionally consistent with dimension L^{-2} (or T^{-2}) for arbitrary values of n. From the Eq. (13) and Eq. (18), we have

$$\xi=\xi_0\alpha_3^{\beta}.exp\left\{-\frac{\beta(1+\alpha)(2\alpha_1+\alpha_2)}{(1-n)}t^{1-n}\right\} \tag{23}$$

Here $n\neq 1$.
Hence the metric in Eq. (1) simplifies to the following:

$$ds^2=-dt^2+a^2.exp\left(\frac{2\alpha_1 t^{1-n}}{(1-n)}\right)(dx^2+dy^2)$$

$$+b^2.exp\left(\frac{2\alpha_2 t^{1-n}}{(1-n)}\right)dz^2. \tag{24}$$

For the model in Eq. (24), the energy density ρ, Hubble constant H_i, and coefficient of bulk viscosity ξ are given by:

$$\rho=\alpha_3.exp\left\{\frac{(1+\alpha)(2\alpha_1+\alpha_2)}{(n-1)t^{n-1}}\right\} \tag{25}$$

$$H_1=H_2=\frac{\alpha_1}{t^n}, H_3=\frac{\alpha_2}{t^n} \tag{26}$$

where $n>1$.

$$\xi=\xi_0\alpha_3^{\beta}.exp\left\{-\frac{\beta(1+\alpha)(2\alpha_1+\alpha_2)}{(1-n)}t^{1-n}\right\} \tag{27}$$

$$\bar{p}=\alpha.\alpha_3.exp\left\{\frac{(1+\alpha)(2\alpha_1+\alpha_2)}{(n-1)}t^{n-1}\right\} \tag{28}$$

4. GRAPHICAL REPRESENTATION OF PHYSICAL QUANTITIES

Figures 1 and 2 illustrate the temporal evolution of the energy density, ρ, which exhibits a mild increase at early times followed by a more pronounced growth at later cosmic epochs. This behavior is indicative of a cosmological model featuring dynamical phase transitions. The initial slow rise in ρ is consistent with radiation- or matter-dominated expansion, whereas the subsequent rapid enhancement signals a transition toward dark energy domination, driving the onset of late-time cosmic acceleration. In this context, the accelerated growth of ρ at late times reflects the increasing dynamical influence of dark energy on the expansion history of the universe.

Alternatively, the sharp spike observed in the inset may be interpreted as a brief inflationary phase in the primordial universe, characterized by a rapid amplification of the energy density over a short interval of cosmic time. The density profile shown in Fig. 3 further corroborates this interpretation, displaying a sequence of quasi-stationary plateaus punctuated by abrupt transitions. The presence of distinct vertical features indicates that the energy density remains approximately

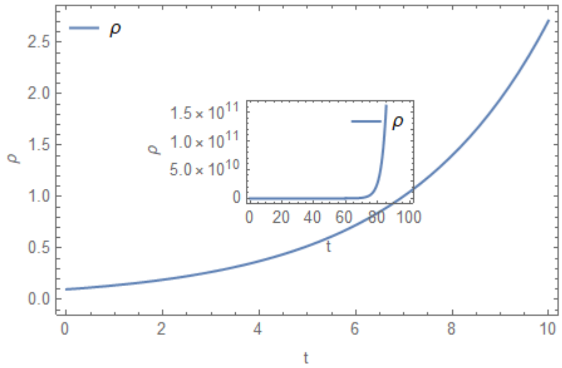

Figure 1. The relationship between energy density ρ and cosmic time t is defined with the parameters: $\alpha = 0.1$, $n = 2$, $\alpha_1 = 0.1$, $\alpha_2 = 0.1$ and $\alpha_3 = 0.1$.

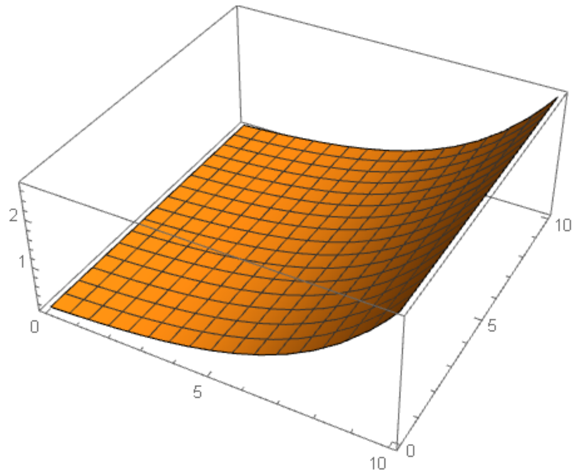

Figure 2. The relationship between energy density ρ and cosmic time t in three-Dimensional is defined with the parameters: $\alpha = 0.1$, $n = 2$, $\alpha_1 = 0.1$, $\alpha_2 = 0.1$ and $\alpha_3 = 0.1$.

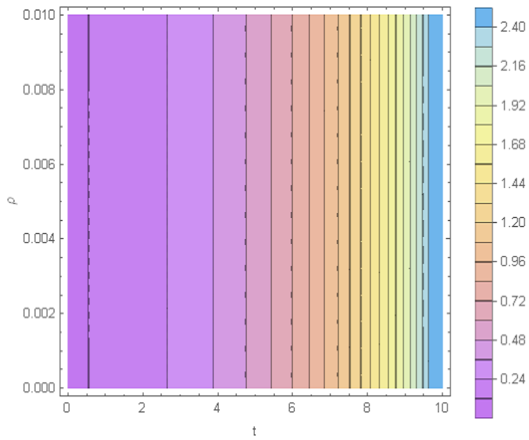

Figure 3. The relationship between energy density ρ and cosmic time t in Density plot view is defined with the parameters: $\alpha = 0.1$, $n = 2$, $\alpha_1 = 0.1$, $\alpha_2 = 0.1$ and $\alpha_3 = 0.1$.

constant over extended epochs before undergoing rapid changes at specific cosmic times, consistent with discrete phase transitions in the underlying cosmological dynamics.

Figures (4–6) illustrate the temporal evolution of the pressure, p, which grows approximately exponentially with cosmic time. During the early epochs ($t \ll t_0$), this growth is modest, while the pronounced steepening at later times signals a major dynamical transition, potentially corresponding to primordial inflation or a cosmological phase change, such as the onset of late-time acceleration driven by dark energy.

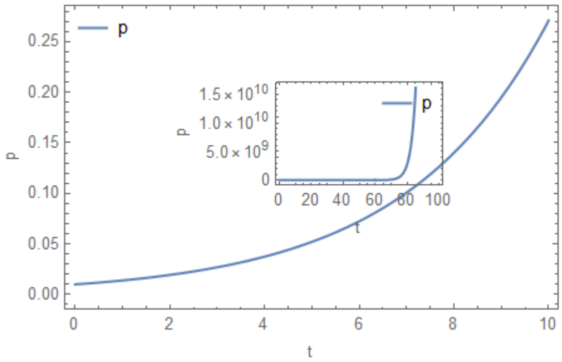

Figure 4. The relationship between pressure p and cosmic time t is defined with the parameters: $\alpha = 0.1$, $n = 2$, $\alpha_1 = 0.1$, $\alpha_2 = 0.1$ and $\alpha_3 = 0.1$.

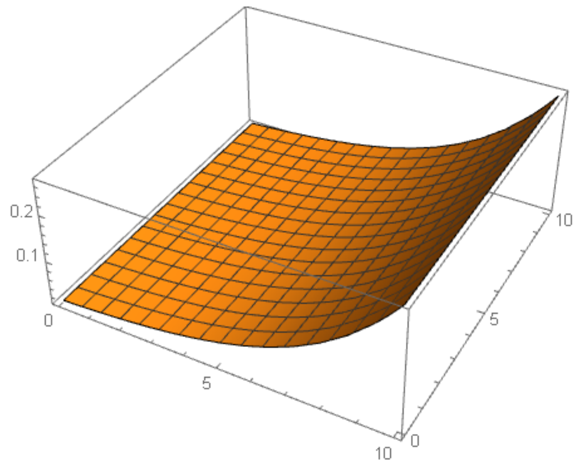

Figure 5. The relationship between pressure p and cosmic time t in three-Dimensional is defined with the parameters: $\alpha = 0.1$, $n = 2$, $\alpha_1 = 0.1$, $\alpha_2 = 0.1$ and $\alpha_3 = 0.1$.

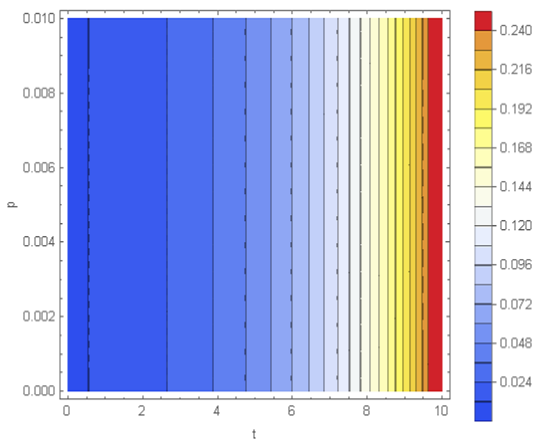

Figure 6. The relationship between pressure p and cosmic time t in Density plot view is defined with the parameters: $\alpha = 0.1$, $n = 2$, $\alpha_1 = 0.1$, $\alpha_2 = 0.1$ and $\alpha_3 = 0.1$.

Figures (7–9) show a monotonic decrease of the gravitational constant, G, over cosmic time, consistent with a broad spectrum of observational and experimental bounds, as detailed in the concluding section. This trend supports the plausibility of a slowly varying gravitational coupling within the current cosmological paradigm.

The evolution of the cosmological constant, Λ, depicted in Figs. (10–12), exhibits a three-phase pattern: rapid initial growth during the early universe, a peak in an intermediate epoch, and a subsequent decline toward near-zero values in the late universe. These dynamics align with theoretical expectations, with Λ increasing exponentially or as a power law

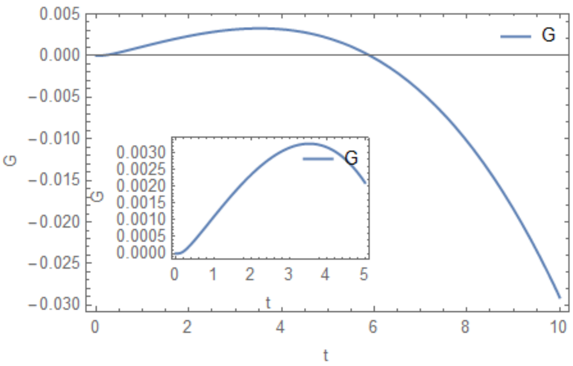

Figure 7. The relationship between Gravitational Constant G and cosmic time t is defined with the parameters: $\alpha = 0.1$, $n = 2$, $\alpha_1 = 0.1$, $\alpha_2 = 0.1$ and $\alpha_3 = 0.1$.

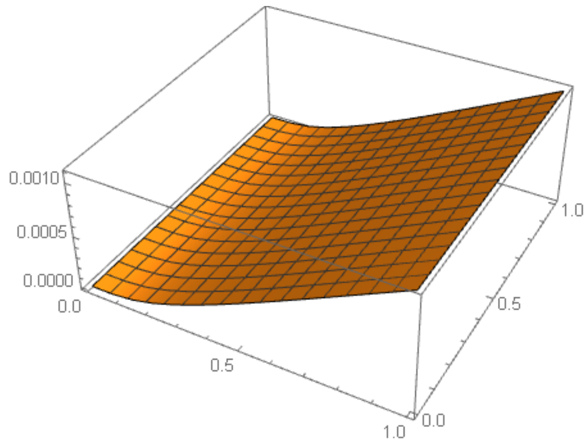

Figure 8. The relationship between Gravitational Constant G and cosmic time t in three-Dimensional is defined with the parameters: $\alpha = 0.1$, $n = 2$, $\alpha_1 = 0.1$, $\alpha_2 = 0.1$ and $\alpha_3 = 0.1$.

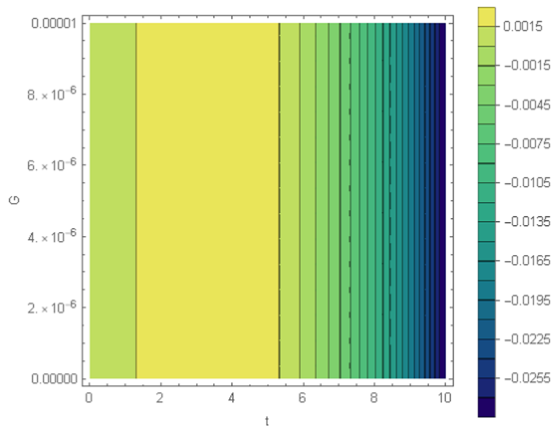

Figure 9. The relationship between Gravitational Constant G and cosmic time t in Density plot view is defined with the parameters: $\alpha = 0.1$, $n = 2$, $\alpha_1 = 0.1$, $\alpha_2 = 0.1$ and $\alpha_3 = 0.1$.

in the primordial phase, reaching a maximum in the intermediate era, and asymptotically approaching the small observed value at late times.

Finally, the behavior of the bulk viscosity coefficient, ξ, as a function of cosmic time is presented in Figs. (13–15) via density plots and three-dimensional visualizations. In the early universe, ξ rises rapidly, significantly impacting expansion dynamics; its growth continues at a slower rate during the intermediate epoch, and in the late universe, ξ stabilizes to an approximately constant value, reflecting the damping of dissipative effects as the universe expands.

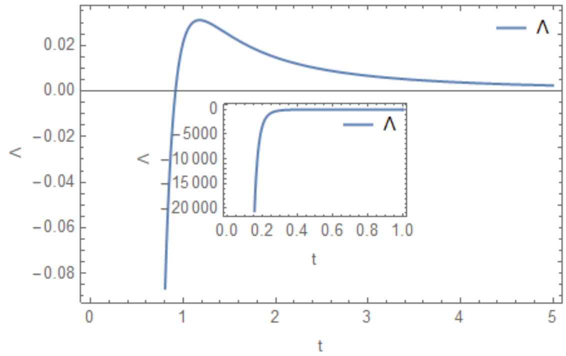

Figure 10. The relationship between Cosmological Constant Λ and cosmic time t is defined with the parameters: $\alpha = 0.1$, $n = 2$, $\alpha_1 = 0.1$, $\alpha_2 = 0.1$ and $\alpha_3 = 0.1$.

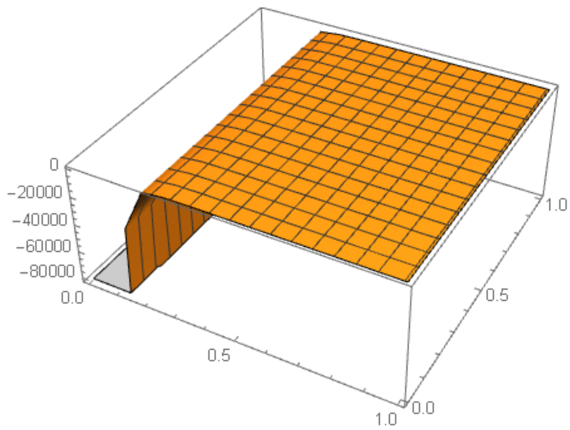

Figure 11. The relationship between Cosmological Constant Λ and cosmic time t in three-Dimensional is defined with the parameters: $\alpha = 0.1$, $n = 2$, $\alpha_1 = 0.1$, $\alpha_2 = 0.1$ and $\alpha_3 = 0.1$.

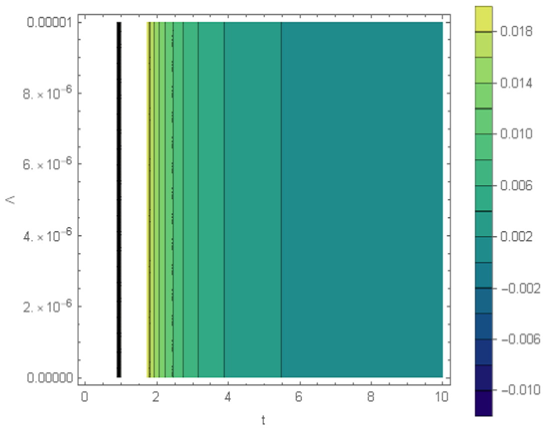

Figure 12. The relationship between Cosmological Constant Λ and cosmic time t in Density plot view is defined with the parameters: $\alpha = 0.1$, $n = 2$, $\alpha_1 = 0.1$, $\alpha_2 = 0.1$ and $\alpha_3 = 0.1$.

5. SPECIAL CASES:

When $\frac{\alpha_1}{2} = \alpha_2$ and $\beta = 1$, the Cosmological constant Λ, the shear scalar σ, Gravitational constant G, the expansion scalar θ and Hubble constant H_i for the Eq. (24) is expressed as,

$$G = -\frac{2n\alpha_2^2}{\pi\alpha_3 t^{2n+1}}.exp\left\{\frac{5\alpha_2(\alpha+1)}{1-n}t^{1-n}\right\}.\left\{\xi_0 - \frac{5\alpha_2(\alpha+1)}{t^n}\right\}^{-1}$$

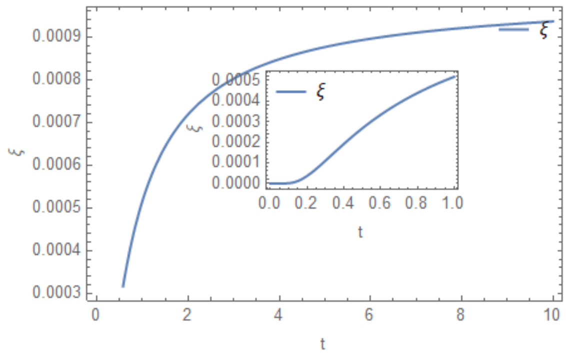

Figure 13. The relationship between coefficient of bulk viscosity ξ and cosmic time t is defined with the parameters: $\alpha = 0.1$, $n = 2$, $\alpha_1 = 0.1$, $\alpha_2 = 0.1$ and $\alpha_3 = 0.1$.

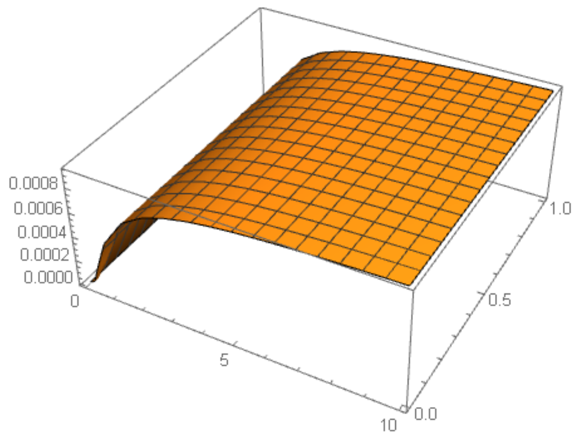

Figure 14. The relationship between coefficient of bulk viscosity ξ and cosmic time t in three-Dimensional is defined with the parameters: $\alpha = 0.1$, $n = 2$, $\alpha_1 = 0.1$, $\alpha_2 = 0.1$ and $\alpha_3 = 0.1$.

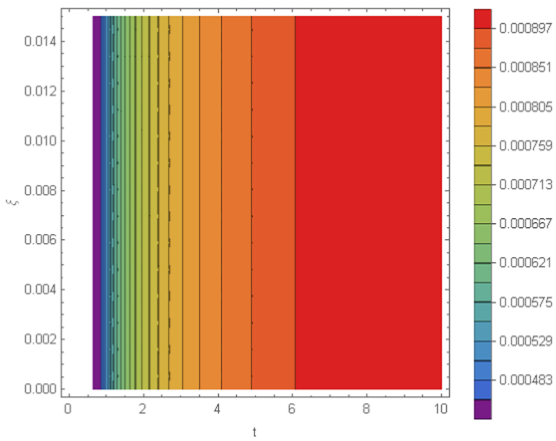

Figure 15. The relationship between coefficient of bulk viscosity ξ and cosmic time t in Density plot view is defined with the parameters: $\alpha = 0.1$, $n = 2$, $\alpha_1 = 0.1$, $\alpha_2 = 0.1$ and $\alpha_3 = 0.1$.

$$\Lambda = \frac{8\alpha_2^2}{t^{2n}} + \frac{16n\alpha_2^2}{t^{2n+1}}\left\{-\frac{5\alpha_2(\alpha+1)}{t^n} + \xi_0\right\}^{-1}$$

It should be noted that α_2 has the dimension T^{n-1}, as implied by the ansatz $\dot{X}_3/X_3 = \alpha_2 t^{-n}$, while ξ_0 has the dimension T^{-1}. Consequently, the above expression for Λ possesses the correct physical dimension T^{-2} (or L^{-2}) for arbitrary values of n, where the dimension of t is T. Further,

$$H_1 = H_2 = \frac{2\alpha_2}{t^n}, H_3 = \frac{\alpha_2}{t^n}$$

$$\Theta = \left(\frac{\dot{X}_1}{X_1} + \frac{\dot{X}_2}{X_2} + \frac{\dot{X}_3}{X_3}\right) = \frac{2\alpha_1 + \alpha_2}{t^n}$$

$$\frac{\dot{G}}{G} \propto H, \Lambda \propto \frac{1}{t^2}, H \propto \frac{1}{t}, G > 0, \rho > 0$$

.

When $n > 0$, the model in Eq. (24) initiates with a Big-Bang at $t = 0$, while the expansion scalar Θ decreases as time t increases. On the other hand, when $n < 0$, the expansion in the model increases over time. When $t \to 0$, both the Hubble parameter H and the shear scalar σ approach infinity; however, as $t \to \infty$, the Hubble parameter H and the shear scalar σ approach zero. Since, $\lim_{t\to\infty} \frac{\sigma}{\Theta} \neq 0$, the model however does not achieve isotropy for large values of t. As time t increases, the spatial volume V decreases, and the rate of expansion also slows down. Since, $\xi = \xi_0 \rho^\beta$ and $\beta > 1$, the model indicates the presence of inflationary phases.
When $n = 1$, Eq. (15) is expressed as,

$$\frac{\dot{X}_1}{X_1} = \frac{\dot{X}_2}{X_2} = \frac{\alpha_1}{t}, \frac{\dot{X}_3}{X_3} = \frac{\alpha_2}{t}$$

After integrating on both sides, we get

$$X_1 = X_2 = \alpha_4.t^{\alpha_1}, X_3 = \alpha_5.t^{\alpha_2}$$

Therefore, metric Eq. (1) reduces to

$$ds^2 = -dt^2 + \alpha_4^2.t^{2\alpha_1}(dx^2 + dy^2) + \alpha_5^2.t^{2\alpha_2}dz^2$$

Thus, the Gravitational constant G, the energy density ρ, Cosmological constant Λ, coefficient of bulk viscosity ξ, Hubble constant H_i, the shear scalar σ, spacial volume V and expansion scalar Θ are expressed as follows:

$$\rho = N.exp\left\{\frac{(1+\alpha)(2\alpha_1+\alpha_2)^2}{t}\right\}$$

$$\bar{p} = \alpha.N.exp\left\{\frac{(1+\alpha)(2\alpha_1+\alpha_2)^2}{t}\right\}$$

where N is the integration constant.

$$G = \frac{2\alpha_1(\alpha_1+2\alpha_2)t}{8\pi(1+\alpha)(2\alpha_1+\alpha_2)}\left[exp\left\{\frac{(1+\alpha)(2\alpha_1+\alpha_2)^2}{t}\right\}\right]^{-1}$$

$$\Lambda = \alpha_1(2\alpha_1+\alpha_2)t.\left\{\frac{1}{t^3} - \frac{2N}{(1+\alpha)(2\alpha_1+\alpha_2)}\right\}$$

$$\xi = \xi_0 N^\beta.exp\left\{\frac{\beta(1+\alpha)(2\alpha_1+\alpha_2)^2}{t}\right\}$$

$$H_1 = H_2 = \frac{\alpha_1}{t}, H_3 = \frac{\alpha_2}{t}$$

$$\sigma = \frac{1}{\sqrt{3}}\left(\frac{\alpha_1-\alpha_2}{t}\right) \tag{29}$$

$$\Theta = \frac{\dot{X}_1}{X_1} + \frac{\dot{X}_2}{X_2} + \frac{\dot{X}_3}{X_3} = \frac{2\alpha_1+\alpha_2}{t}$$

$$V = \alpha_4\alpha_5 t^{(2\alpha_1+\alpha_2)}$$

$$\frac{\dot{G}}{G} \propto H, \Lambda \propto \frac{1}{t^2}, H \propto \frac{1}{t}, G > 0, \rho > 0.$$

It may be noted that the above expression for Λ in eqn. (29) is dimensionally consistent provided the parameter N carries the dimension T^{-3} (or L^{-3} in geometrized units), thereby ensuring that Λ has the correct dimension T^{-2} (or L^{-2}), where T or L is the dimension of t. The expansion scalar Θ, shear scalar σ, Hubble parameter H, and cosmological constant Λ all exhibit a decreasing trend with time. As cosmic time t increases, σ, H, Θ, and Λ gradually decline, indicating that the universe experienced a rapid expansion in the past, which is slowing down over time. This behavior is consistent with observations reported by numerous astronomers (Riess et al. [4,28], Perlmutter et al. [1], etc.). In contrast, the gravitational constant G and the volume of the universe V show a positive correlation with time. Since the ratio $\frac{\sigma}{\Theta}$ remains constant, the model does not approach isotropy at late times. Moreover, if $\alpha_1 = \alpha_2$, it implies that the polytropic Bianchi type-I space-time is shear-free.

6. CONCLUSIONS

The decreasing trend of the gravitational constant, G, with cosmic time inferred from Figs. (7–9) is consistent with a broad range of independent constraints spanning cosmological, astrophysical, and laboratory scales. CMB observations from *Planck* (2018) limit fractional variations to $\Delta G/G < 0.1\%$ over ~ 13.8 Gyr, while BAO measurements from SDSS, BOSS, and DES constrain $\Delta G/G < 0.2\%$ over ~ 10 Gyr. Type Ia supernovae from the Union2.1 compilation impose $\Delta G/G < 0.3\%$ over ~ 9 Gyr. At shorter timescales, gravitational redshift tests of compact objects bound $\dot{G}/G < 10^{-13}\,\mathrm{yr}^{-1}$, binary pulsar timing yields $\dot{G}/G < 10^{-12}\,\mathrm{yr}^{-1}$, advanced LIGO O1–O2 observations constrain $\dot{G}/G < 10^{-15}\,\mathrm{yr}^{-1}$, and high-precision torsion balance and Cavendish-type experiments further tighten laboratory limits to $\dot{G}/G < 10^{-14}$–$10^{-15}\,\mathrm{yr}^{-1}$.

Astrophysical observations further support a mild temporal decrease of the gravitational constant, with analyses of the M67 star cluster indicating a $\sim 5\%$ reduction in G over ~ 4.5 Gyr, while galaxy rotation curve studies based on the SPARC dataset suggest a $\sim 3\%$ decrease over ~ 10 Gyr. Ongoing and forthcoming experimental and observational programs will continue to investigate the compelling possibility of a time–varying gravitational constant, G, with unprecedented accuracy. The Square Kilometre Array (SKA) is expected to place stringent constraints on deviations in G through high–precision measurements of baryon acoustic oscillations and cosmic shear, while the Laser Interferometer Space Antenna (LISA) will probe such variations using gravitational–wave observations of compact binary systems. In parallel, next–generation torsion balance experiments will further tighten laboratory bounds on both temporal and spatial variations of G, and the James Webb Space Telescope (JWST) will provide complementary astrophysical constraints by examining stellar evolution and age determinations across diverse cosmic environments.

In this paper, we derived solutions to Einstein's general relativity equations for a Bianchi type-I spacetime with a polytropic bulk viscous fluid. We observed that as time approaches $t \longrightarrow 0$, the spatial volume $V \longrightarrow \infty$, indicating that the universe begins with zero volume and expands infinitely in both the distant past and future. The influence of bulk viscosity on cosmic evolution, particularly in its early stages, appears to be significant. Additionally, when $t \longrightarrow 0$, the energy density ρ, cosmological constant Λ, expansion scalar Θ, shear scalar σ, coefficient of bulk viscosity ξ all tend to infinity. Conversely, as $t \longrightarrow \infty$, these quantities approach zero.

Since $\frac{\sigma}{\Theta}$ remains constant, the model does not approach isotropy for large values of t. The spatial volume V increases with time if $\alpha_2 > 0$, and since $\xi = \xi_0\rho^{\beta}, \beta > 0$, the model leads to an inflationary solution. The gravitational constant G increases with the universe's age, suggesting that gravity was weaker in the past and has been strengthening over time, consistent with previous results from Abdussattar and others (Vishwakarma [52], chow [45], Levitt [47]). The cosmological constant follows $\Lambda \propto \frac{1}{t^2}$, aligning with models from Kalligas et al. [46], Berman et al. [42], Berman et al. [42], Bertolami [43, 44] Singh [49], Tiwari [50, 51], is physically consistent with current observations indicating a small Λ in the present universe. Ultimately, the solutions developed in this work offer a coherent theoretical framework for analyzing the evolution of a Bianchi type-I universe with a polytropic bulk viscous fluid and time-varying G and Λ. They clarify the combined roles of bulk viscosity, anisotropy, and dynamical fundamental constants, while remaining consistent with observational constraints and providing meaningful insights into cosmic evolution. Further comprehensive analysis demonstrate that different time-dependent scenarios produce significant variations in key physical parameters, impacting the universe's dynamical evolution. The geometrical structure and observational implications of the model are further explored, offering insights into its consistency with cosmological data and theoretical predictions.

Acknowledgement

PKD expresses gratitude to COST Action CA18108 "Quantum gravity phenomenology in the multi-messenger approach" for the financial assistance to visit the University of Rijeka, Croatia, provided by the European Cooperation in Science & Technology (ECOST). Additionally, PKD acknowledges IUCAA, Pune, India, for granting him a visiting associateship position. We express our profound gratitude to the esteemed referee and the editor for their insightful recommendations, which have markedly enhanced the quality and presentation of our research.

ORCID

Archana Gajanan Ingle, https://orcid.org/0009-0003-2664-5739; **Shailendra D. Deo**, https://orcid.org/0009-0008-5413-9485; **Praveen Kumar Dhankar**, https://orcid.org/0000-0002-8201-6019; **Safiqul Islam**, https://orcid.org/0000-0003-1373-4137; **Kashika Srivastava**, https://orcid.org/0000-0002-9183-4080; **Bhagwat Thakran**, https://orcid.org/0009-0006-9471-9164

REFERENCES

[1] S. Perlmutter, S. Gabi, G. Goldhaber, A. Goobar, D. E. Groom, I. M. Hook, A. G. Kim, *et al.*, "Measurements of the cosmological parameters Ω and Λ from the first seven supernovae at $z \leq 0.35$," Astrophys. J. **483**(2), 565 (1997). https://doi.org/10.1086/304265

[2] S. Perlmutter, G. Aldering, G. Goldhaber, R. A. Knop, P. Nugent, P. G. Castro, S. Deustua, *et al.*, "Measurements of Ω and Λ from 42 high-redshift supernovae," Astrophys. J. **517**(2), 565 (1999). https://doi.org/10.1086/307221

[3] S. Perlmutter, G. Aldering, M. Della Valle, S. Deustua, R. S. Ellis, S. Fabbro, A. Fruchter, *et al.*, "Discovery of a supernova explosion at half the age of the Universe," Nature, **391**(6662), 51–54 (1998). https://doi.org/10.1038/34124

[4] A. G. Riess, A. V. Filippenko, P. Challis, A. Clocchiatti, A. Diercks, P. M. Garnavich, R. L. Gilliland, *et al.*, "Observational evidence from supernovae for an accelerating universe and a cosmological constant," Astron. J. **116**(3), 1009 (1998). https://doi.org/10.1086/300499

[5] S. W. Allen, R. W. Schmidt, H. Ebeling, A. C. Fabian, and L. Van Speybroeck, "Constraints on dark energy from Chandra observations of the largest relaxed galaxy clusters," Mon. Not. R. Astron. Soc. **353**(2), 457–467 (2004). https://doi.org/10.1111/j.1365-2966.2004.08080.x

[6] P. J. E. Peebles, and B. Ratra, "The cosmological constant and dark energy," Rev. Mod. Phys. **75**(2), 559 (2003). https://doi.org/10.1103/revmodphys.75.559

[7] T. Padmanabhan, "Cosmological constant—the weight of the vacuum," Phys. Rep. **380**(5–6), 235–320 (2003). https://doi.org/10.1016/s0370-1573(03)00120-0

[8] J. A. S. Lima, "Alternative dark energy models: An overview," Braz. J. Phys. **34**, 194–200 (2004). https://doi.org/10.1590/s0103-97332004000200009

[9] G. S. Khadekar, S. Ray, A. Sanyal, and P. K. Dhankar, "Holographic principle inspired dark energy description of unified early and late universe in viscous mimetic gravity," Phys. Dark Universe, 47, 101742 (2025). https://doi.org/10.1016/j.dark.2024.101742

[10] P. K. Dhankar, A. Sanyal, S. Islam, F. Rahaman, and B. Pourhassan, "Testing the generalized second law in (2+1)-dimensional cosmology: Holographic entropy bounds and observational constraints," arXiv:2508.13227 [gr-qc], (2025). https://doi.org/10.48550/arXiv.2508.13227

[11] P. K. Dhankar, S. Islam, S. Ray, A. Sanyal, and S. K. Maurya, "Observational constraints on holography in (2+1)-dimensional cosmology with a generalized equation of state," arXiv:2508.11701 [physics.gen-ph], (2025). https://doi.org/10.48550/arXiv.2508.11701

[12] P. K. Dhankar, A. Sanyal, A. Munyeshyaka, S. Ray, and B. Pourhassan, "Observational analysis of bulk viscous modified Chaplygin gas in (2+1)-dimensional Universe using MCMC," arXiv:2504.18612 [gr-qc], (2025). https://doi.org/10.48550/arXiv.2504.18612

[13] P. K. Dhankar, A. Munyeshyaka, S. Hussain, and T. Mutabazi, "Large-scale structure constraints and matter power spectrum in $f(Q, L_m)$ gravity," arXiv:2507.10631 [gr-qc], (2025). https://doi.org/10.48550/arXiv.2507.10631

[14] P. K. Dhankar, D. Mhamdi, A. Munyeshyaka, D. Kumar, J. Ntahompagaze, and T. Oualib, "Testing Gauss–Bonnet gravity with DESI BAO data," arXiv:2508.03602 [gr-qc], (2025). https://doi.org/10.48550/arXiv.2508.03602

[15] P. K. Dhankar, A. Munyeshyaka, A. Sanyal, S. Islam, and F. Rahaman, "Constraints on multi-fluid cosmology in modified Gauss–Bonnet gravity models with different observational data sets," arXiv:2507.22191 [gr-qc], (2025). https://doi.org/10.48550/arXiv.2507.22191

[16] M. Thakre, P. K. Dhankar, A. Munyeshyaka, and S. Islam, "Testing Logarithmic $f(G)$ Model with Observational Data Sets," Journal of Holography Applications in Physics, **6**(4), 185–216 (2026). https://doi.org/10.22128/jhap.2026.3248.1191

[17] R. Patel, P. K. Dhankar, S. Islam, A. Munyeshyaka, S. Mukhtar, and M. Ali, "Bayesian Analysis of Viscous FRW Cosmology with Inhomogeneous Equation of State," Mathematics, **14**(11), 1888 (2026). https://doi.org/10.3390/math14111888

[18] R. Patel, P. K. Dhankar, S. Islam, and M. Aamir, "Data analysis in (2+1)-D $\Lambda(z)$ gravity with BAO, Pantheon and Hubble dataset using MCMC method," Indian Journal of Physics, **100**, 2153–2163 (2026). https://doi.org/10.1007/s12648-026-03982-0

[19] A. Munyeshyaka, P. K. Dhankar, M. Thakre, S. Islam, F. Rahaman, and B. Pourhassan, "Background and Perturbation Constraints on Power-Law and Exponential $f(G)$ Gravity Models from Recent Cosmological Observations," Physics of the Dark Universe **45**, 102370 (2026). https://doi.org/10.1016/j.dark.2026.102370

[20] A. Munyeshyaka, P.K. Dhankar, and J. Ntahompagaze, Perturbations with bulk viscosity in modified Chaplygin gas cosmology, Int. J. Geom. Methods Mod. Phys. **22**(11), 2550073 (2025). https://doi.org/10.1142/S0219887825500732

[21] A. Munyeshyaka, P. K. Dhankar, and J. Ntahompagaze, "Matter power spectrum in a power-law $f(G)$ gravity," New Astron. **120**, 102423 (2025). https://doi.org/10.1016/j.newast.2025.102423

[22] G. N. Gadbail, S. Arora, P. Kumar, and P. K. Sahoo, "Interaction of divergence-free deceleration parameter in Weyl-type $f(Q,T)$ gravity," Chin. J. Phys. **79**, 246–255 (2022). https://doi.org/10.1016/j.cjph.2022.09.005

[23] A. Panda, G. Manna, S. Ray, M. Khlopov, and P. K. Dhankar, "Thermodynamics of a non-canonical $f(\bar{R},\bar{T})$ gravity," Phys. Dark Universe, **46**, 101697 (2024). https://doi.org/10.1016/j.dark.2024.101697

[24] D. Kumar, P.K. Dhankar, S. Ray, and F. Zhang, Joint analysis of constraints on $f(R)$ parametrization from recent cosmological observations, Phys. Dark Universe, **49**, 101989 (2025). https://doi.org/10.1016/j.dark.2025.101989

[25] B. Thakran, P.K. Dhankar, S. Raut, S. Ray, S.K. Maurya, and A. Sanyal, Cosmological constraints on interacting holographic dark energy and extended Chaplygin gas in higher dimensions using MCMC analysis, Int. J. Geom. Methods Mod. Phys. **23**, 2550254 (2025). https://doi.org/10.1142/S0219887825502548

[26] B. Samanta, F. Rahaman, B. Raychaudhuri, and P. K. Dhankar, "Tachyonic field coupled with global monopole in Brans–Dicke theory," Phys. Scr. **100**, 7 (2025). https://doi.org/10.1088/1402-4896/ade63c

[27] A. Sanyal, P. K. Dhankar, A. Munyeshyaka, S. Islam, and F. Rahaman, "Cosmic hysteresis in reconstructed $f(R)$ bounce models: A thermodynamic study," arXiv:2508.06590 [gr-qc], (2025). https://doi.org/10.48550/arXiv.2508.06590

[28] A. G. Riess, L.-G. Strolger, J. Tonry, S. Casertano, H. C. Ferguson, B. Mobasher, Peter Challis, *et al.*, "Type Ia supernova discoveries at $z > 1$ from the Hubble Space Telescope," Astrophys. J. **607**(2), 665 (2004). https://doi.org/10.1086/383612

[29] H. Zhang, Q. Guo, and R.-G. Cai, "Friedmann cosmology on codimension-2 brane with time-dependent tension," Mod. Phys. Lett. A, **21**(2), 159–167 (2006). https://doi.org/10.1142/s0217732306018706

[30] R. K. Tiwari, and S. Sharma, "Non-existence of shear in Bianchi type-III string cosmological models," Chin. Phys. Lett. **28**(2), 020401 (2011). https://doi.org/10.1088/0256-307x/28/2/020401

[31] X.-X. Wang, "Locally rotationally symmetric Bianchi type-I string cosmological model," Chin. Phys. Lett. **21**(7), 1205 (2004). https://doi.org/10.1088/0256-307x/21/7/006

[32] X.-X. Wang, "Bianchi type-III string cosmological model with bulk viscosity in general relativity," Chin. Phys. Lett. **22**(1), 29 (2005). https://doi.org/10.1088/0256-307x/22/1/009

[33] X.-X. Wang, "Bianchi type-III string cosmological model with bulk viscosity and magnetic field," Chin. Phys. Lett. **23**(7), 1702 (2006). https://doi.org/10.1088/0256-307x/23/7/013

[34] R. K. Tiwari, D. Tiwari, and P. Shukla, "LRS Bianchi type-II cosmological model with a decaying Λ term," Chin. Phys. Lett. **29**(1), 010403 (2012). https://doi.org/10.1088/0256-307x/29/1/010403

[35] M. Zeyauddin, and B. Saha, "Bianchi type-V bulk viscous cosmological models with particle creation in general relativity," Eur. Phys. J. Plus, **129**, 1–23 (2014). https://doi.org/10.1140/epjp/i2014-14177-0

[36] A. Beesham, S. G. Ghosh, and R. G. Lombard, "Anisotropic viscous cosmology with variable G and Λ," Gen. Relativ. Gravit. **32**, 471–477 (2000). https://doi.org/10.1023/A:1001924300321

[37] R. K. Tiwari, "Bianchi type-I cosmological models with time-dependent G and Λ," Astrophys. Space Sci. **318**, 243–247 (2008). https://doi.org/10.1007/s10509-008-9924-2

[38] R. K. Tiwari, and N. K. Jha, "Locally rotationally symmetric Bianchi type-I model with time-varying Λ term," Chin. Phys. Lett. 26(10), 100403 (2009). https://doi.org/10.1088/0256-307x/26/10/109804

[39] R. K. Tiwari, and U. Dwivedi, "Kantowski–Sachs cosmological models with time-varying G and Λ," Fizika B, **19**(1), 1–8 (2010).

[40] R. K. Tiwari, and S. Sharma, "Bianchi type-I string cosmological model with bulk viscosity and time-dependent Λ term," Chin. Phys. Lett. **28**(9), 090401 (2011). https://doi.org/10.1088/0256-307x/28/9/090401

[41] R. K. Tiwari, F. Rahaman, and S. Ray, "Five-dimensional cosmological models in general relativity," Int. J. Theor. Phys. **49**(10), 2348–2357 (2010). https://doi.org/10.1007/s10773-010-0421-3

[42] M. S. Berman, "Static universe in a modified Brans–Dicke cosmology," Int. J. Theor. Phys. **29**, 567–570 (1990). https://doi.org/10.1007/bf00672031

[43] O. Bertolami, A. A. Sen, S. Sen, and P. T. Silva, "Latest supernova data in the framework of the generalized Chaplygin gas model," Mon. Not. R. Astron. Soc. **353**(1), 329–337 (2004). https://doi.org/10.1111/j.1365-2966.2004.08079.x

[44] O. Bertolami, and P. J. Martins, "Nonminimal coupling and quintessence," Phys. Rev. D, **61**(6), 064007 (2000). https://doi.org/10.1103/physrevd.61.064007

[45] T. L. Chow, "Variability of the gravitational constant," Lett. Nuovo Cimento, **31**(4), (1981). https://doi.org/10.1007/bf02822409

[46] D. Kalligas, P. Wesson, and C. W. F. Everitt, "Flat FRW models with variable G and Λ," Gen. Relativ. Gravit. **24**, 351–357 (1992). https://doi.org/10.1007/bf00760411

[47] L. S. Levitt, "The gravitational constant at time zero," Lett. Nuovo Cimento, **29**, 23 (1980). https://doi.org/10.1007/bf02745337

[48] A. G. Ingle, P. K. Dhankar, K. Srivastava, and S. D. Deo, "Observational constraints of Bianchi type-I cosmological model with cosmological constant Λ," Stoch. Model. Comput. Sci. **3**(2), (2023).

[49] C. P. Singh and A. Beesham, "Particle creation in higher-dimensional space-time with variable G and Λ," Int. J. Theor. Phys. **51**, 3951–3962 (2012). https://doi.org/10.1007/s10773-012-1287-3

[50] R. K. Tiwari and R. Singh, "Flat universe with decaying cosmological constant," Eur. Phys. J. Plus, 129, 1–6 (2014). https://doi.org/10.1140/epjp/i2014-14253-5

[51] R. K. Tiwari, "Bianchi type-I cosmological models with perfect fluid in general relativity," Res. Astron. Astrophys. **10**(4), 291 (2010). https://doi.org/10.1088/1674-4527/10/4/001

[52] R. G. Vishwakarma, "A study of angular size–redshift relation for models in which Λ decays as the energy density," Classical Quantum Gravity, **17**(18), 3833 (2000). https://doi.org/10.1088/0264-9381/17/18/317

[53] G. S. Khadekar, P. Kumar, and S. Islam, "Modified Chaplygin gas with bulk viscous cosmology in FRW (2+1)-dimensional spacetime," J. Astrophys. Astron. **40**(5), 40 (2019). https://doi.org/10.1007/s12036-019-9606-1

[54] S. Islam, P. Kumar, G. S. Khadekar, and T. K. Das, "(2+1)-dimensional cosmological models in $f(R,T)$ gravity with $\Lambda(R,T)$," J. Phys.: Conf. Ser. **1258**(1), 012026 (2019). https://doi.org/10.1088/1742-6596/1258/1/012026

[55] S. G. Georgiev, G. S. Khadekar, and P. Kumar, "Two-dimensional integral inequalities on time scales," arXiv:2003.05309 [math.GM], (2020). https://doi.org/10.48550/arXiv.2003.05309

[56] P. Kumar, and G. S. Khadekar, "Holographic dark energy with modified Chaplygin gas and scalar field in (2+1)-dimensional spacetime," J. Tensor Soc. **15**(1), 17–44 (2021). https://doi.org/10.56424/jts.v15i01.10615

[57] S. Islam and P. Kumar, "Gravitational model of compact spherical Reissner–Nordström-type star under $f(R,T)$ gravity," J. Dyn. Syst. Geom. Theor. **19**(1), 135–154 (2021). https://doi.org/10.1080/1726037x.2021.1965705

[58] P. Kumar, G. S. Khadekar, and V. J. Dagwal, "Two-fluid cosmological model in (2+1)-dimensional Saez–Ballester scalar–tensor theory," J. Dyn. Syst. Geom. Theor. **20**(1), 91–114 (2022). https://doi.org/10.1080/1726037x.2022.2079267

[59] S. R. Kumbhare, P. Kumar, and S. Islam, "Strange quark matter attached to string cloud in general relativity under 5D space-time," J. Tensor Soc. **16**(1), 81–92 (2022).

[60] R. Talole, P. Kumar, and S. Islam, "Viscous modified ghost scalar field dark energy models with varying G," Rom. Astron. J. **33**, 81–109 (2023). https://doi.org/10.59277/RoAJ.2023.1-2.06

[61] N. A. Ramtekkar, P. Kumar, and G. S. Khadekar, "FRW viscous modified cosmic Chaplygin gas cosmology with variable cosmological constant Λ," J. Dyn. Syst. Geom. Theor. **21**(1), 29–44 (2023).

[62] S. Islam, P. K. Dhankar, B. Thakran, and S. R. Kumbhare, "String cloud with quark matter and viscous fluid admitting conformal motion," Rom. Astron. J. **34**(1-2), 15–32 (2024). https://doi.org/10.59277/roaj.2024.1-2.02

[63] P. A. M. Dirac, "The cosmological constants," Nature, **139**(3512), 323–323 (1937). https://doi.org/10.1038/139323a0

[64] R. K. Tiwari, M. Sharma, and S. Sharma, "Polytropic bulk viscous cosmological model with variable G and Λ," arXiv preprint arXiv:1403.2353. (2014). https://doi.org/10.48550/arXiv.1403.2353

[65] A. I. Arbab, "Cosmological models with variable G and Λ and bulk viscosity," arXiv:gr-qc/0105027, (2001). https://doi.org/10.48550/arXiv.gr-qc/0105027

[66] M. K. Mak, J. A. Belinchon, and T. Harko, "Causal bulk viscous dissipative cosmologies with variable gravitational and cosmological constants," arXiv:gr-qc/0110119, (2001). https://doi.org/10.48550/arXiv.gr-qc/0110119

[67] R. K. Tiwari, H. A. Alfedeel, D. Sofuoğlu, A. Abebe, E. I. Hassan, and B. K. Shukla, "A cosmological model with time-dependent Λ, G, and viscous fluid in general relativity," Front. Astron. Space Sci. **9**, (2022). https://doi.org/10.3389/fspas.2022.965652

[68] M. Dewri, "FRW cosmological models with bulk viscosity and polytropic equation of state parameter," in: *Innovative Research Trends in Science and Technology*, vol. 1, (Bhumi Publishing, 2025), pp. 100-105.

[69] P. Das, and K. P. Singh, "Thermodynamic behavior of the polytropic gas in cosmology," Ratio Math. **39**, 261-268 (2020).

[70] Thakran, et al., "Dynamics of Bianchi Type-III models with time-dependent gravitational and cosmological constants", J. Dynamical Systems and Geometric Theories, **23**(1&2), 81–98 (2025). https://doi.org/10.47974/JDSGT-2025-01001

КОСМОЛОГІЧНА МОДЕЛЬ З ПОЛІТРОПІЧНОЮ ОБ'ЄМНОЮ В'ЯЗКІСТЮ ТА ЗМІННИМИ ГРАВІТАЦІЙНИМИ ТА КОСМОЛОГІЧНИМИ СТАЛИМИ

Архана Гаджанан Інгл[1], Шайлендра Д. Део[2], Правін Кумар Дханкар[3], Сафікул Іслам[4], Кашіка Срівастава[5], Бхагват Такран[6]

[1]*PGTD Математика, Університет Гондвана, Гадчіролі, Махараштра, Індія*

[2]*Науковий коледж Махатми Ганді, Гадчандур, округ Чандрапур. М. С.- 442908, Індія*

[3]*Технологічний інститут Симбіозу, кампус Нагпур, Міжнародний симбіоз (Університет Демеда), Пуна-440008, Індія*

[4]*Кафедра математики та статистики, Коледж наук, Університет короля Фейсала, ПС 400, Аль-Ахса 31982, Саудівська Аравія*

[5]*Університет Бабу Банарасі Дас, Лакхнау, Уттар-Прадеш, Індія*

[6]*Кафедра математики, Інженерний коледж ім. Г. Х. Райсоні, Нагпур, Махараштра-440016, Індія*

У цій статті досліджуються рівняння поля Ейнштейна в рамках космологічної моделі, яка включає політропну об'ємну в'язку рідину, причому гравітаційні та космологічні константи змінюються у Всесвіті типу Біанкі I. Спостерігається, що різні сценарії, що залежать від часу, призводять до змін фізичних параметрів, що має значні наслідки для космічної еволюції. Ключові фізичні параметри, включаючи густину енергії, гравітаційну сталу, скаляр розширення, космологічну сталу, коефіцієнт об'ємної в'язкості та скаляр зсуву, досліджуються на предмет їхнього фізичного значення. Також досліджуються геометричні та спостережувальні інтерпретації космологічної моделі.

Ключові слова: *Б'янкі I типу; скаляр зсуву; об'ємна в'язкість; скаляр розширення*

East European Journal of Physics. 3. 68–77 (2026)
DOI: 10.26565/2312-4334-2026-3-06 ISSN 2312-4334

ANISOTROPIC COSMIC EVOLUTION AND STATEFINDER DIAGNOSTICS OF A BIANCHI TYPE VI_0 UNIVERSE WITH HYBRID SCALE FACTOR IN $f(R, L_m)$ GRAVITY

V. R. Patil[1], A. S. Panurkar[2*], P. A. Bolke[3]
[1]*Department of Mathematics, Arts, Science and Commerce College, Chikhaldara, Dist. Amravati (MS), India, 444807*
[2]*Department of Mathematics, Prof. Ram Meghe Institute of Technology and Research, Badnera, Dist. Amravati (MS), India, 444701*
[3]*Department of Mathematics, Prof. Ram Meghe College of Engineering and Management, Badnera, Dist. Amravati (MS), India*
[*]*Corresponding Author e-mail: asspan007@gmail.com*
Received April 23, 2026; revised August 4, 2026; accepted August 10, 2026

We investigate the dynamics of an anisotropic Bianchi type VI_0 cosmological model within the framework of $f(R, L_m)$ gravity by adopting a curvature–matter coupled form $f(R, L_m) = \frac{R}{2} + L_m^{\alpha}$. A hybrid expansion law $a(t) = e^{\beta t} t^{\gamma}$ is employed to describe the cosmic evolution, allowing a smooth transition from an early decelerated phase to a late-time accelerated expansion. The parameter $\alpha = 0.4$ is chosen to ensure stable and physically viable behavior of the model. The analysis shows that the scale factor and spatial volume increase monotonically with cosmic time, indicating a continuously expanding universe. The deceleration parameter exhibits a transition from positive to negative values and approaches the de Sitter limit at late times. The equation of state parameter evolves from a matter-dominated regime toward the quintessence region and asymptotically approaches $\omega = -1$. The energy density remains positive and decreases with time, while the pressure stays negative throughout the evolution, supporting accelerated expansion. Furthermore, the statefinder diagnostics in the $\{r, s\}$ and $\{r, q\}$ planes demonstrate that the model deviates from standard cosmology at intermediate epochs and converges to the ΛCDM fixed points at late times. These results indicate that the proposed model provides a consistent and viable description of dark energy-driven cosmic evolution.

Keywords: $f(R, L_m)$ *gravity; Bianchi type* VI_0 *universe; Hybrid expansion law; Anisotropic cosmology; Statefinder Diagnostics; Cosmic acceleration*

1. INTRODUCTION

Modern cosmology has undergone a significant transformation following compelling observational evidence indicating that the universe is currently undergoing a phase of late-time accelerated expansion. This phenomenon was first established through observations of Type Ia supernovae (SNe Ia) [1, 2], and was subsequently supported by measurements of the cosmic microwave background (CMB) radiation [3], large-scale structure (LSS) surveys [4], and high-precision observations from the Planck mission [5]. Within the framework of standard cosmology, the ΛCDM model provides the simplest explanation for this acceleration through the inclusion of the cosmological constant Λ. Despite its remarkable observational success, this model suffers from well-known theoretical issues, particularly the fine-tuning and cosmic coincidence problems [6–8]. These limitations have motivated the development of alternative theoretical approaches beyond general relativity. Among these, modified theories of gravity have emerged as promising alternatives. In particular, extensions such as $f(R)$ gravity and related frameworks have been extensively studied [9–11]. A further generalization is provided by the $f(R, L_m)$ theory of gravity, in which the gravitational action depends on both the Ricci scalar R and the matter Lagrangian density L_m [12]. This formulation introduces a non-minimal coupling between matter and geometry, leading to modified field equations and non-conservation of the energy-momentum tensor [13, 14]. Recent investigations have explored the cosmological implications of this theory in various contexts, including anisotropic models and hybrid expansion behavior [15–17]. Although the Friedmann–Lemaître–Robertson–Walker (FLRW) metric successfully describes a homogeneous and isotropic universe, it does not account for possible anisotropies that may have existed during the early stages of cosmic evolution. In this context, Bianchi-type cosmological models provide a natural generalization by allowing directional dependence in expansion rates. The pioneering works of Ellis and MacCallum [18], along with Collins [19], established the importance of anisotropic cosmologies. several studies have demonstrated that such models can effectively describe more realistic cosmic scenarios and their dynamical evolution [20, 21]. To describe a realistic cosmic history that includes both early-time deceleration and late-time acceleration, the hybrid expansion law (HEL), given by $a(t) = e^{\beta t} t^{\gamma}$, has been widely employed due to its ability to unify both phases of cosmic evolution [22]. In addition, the statefinder diagnostic pair $\{r, s\}$ introduced by Sahni et al. [23] provides an effective tool for distinguishing different dark energy models and for comparing them with the standard ΛCDM scenario. In particular, Bianchi type VI_0 cosmological models within modified gravity frameworks have been investigated in several studies, including those addressing anisotropic dynamics and exact solutions [24]. The formulation and field equations adopted in the present work are closely related to recent developments in this direction [25]. More recently, considerable attention has been devoted to examining the cosmological viability and broader implications of $f(R, L_m)$ gravity. Singh et al. [26] investigated a constrained cosmological scenario within this framework and demonstrated its potential for describing the observed accelerated expansion. The applicability of matter–geometry coupling to early-universe phenomena was further explored by Jaybhaye et al. [27] in the context of cosmological baryogenesis. Shukla et al. [28] analyzed FLRW dynamics by incorporating an equation-of-state parametrization, while Solanki et al. [29] extended the scope of $f(R, L_m)$ gravity to wormhole configurations. A more comprehensive examination of the cosmological background and perturbative evolution was presented by Sahlu et al. [30], providing useful constraints on the model parameters and its observational behavior. Beyond conventional late-time cosmology, bouncing scenarios

Cite as: V. R. Patil, A. S. Panurkar, P. A. Bolke, East Eur. J. Phys. 3, 68 (2026), https://doi.org/10.26565/2312-4334-2026-3-06

and their dynamical stability have also been investigated within this theory [31]. Recent studies have further applied matter–geometry coupling to string cosmological models [32], illustrating the versatility of the $f(R, L_m)$ framework in describing different matter sources and cosmic geometries. The growing emphasis on observational consistency is evident in recent analyses of late-time cosmic dynamics using contemporary datasets [33], as well as Bayesian investigations aimed at assessing the ability of $f(R, L_m)$ models to alleviate the Hubble tension [34]. Navarro-Coyd'an et al. [35] showed that matter–geometry coupling can support an accelerating late-time Universe and de Sitter-like evolution without adding a separate vacuum contribution. Goswami and Pradhan [36] assessed the consistency of this gravity framework with current cosmological observations and obtained bounds on the model parameters. Recent studies have further explored the cosmological relevance of $f(R, L_m)$ gravity by investigating its implications for anisotropic cosmological models, matter–geometry coupling, and the evolution of different matter sources under modified gravitational dynamics [37]. Collectively, these developments indicate that $f(R, L_m)$ gravity provides a flexible theoretical setting for studying early- and late-time cosmic evolution, non-standard matter configurations, anisotropic effects, and observational departures from the standard ΛCDM paradigm.

Motivated by these developments, the present work investigates a Bianchi type VI_0 cosmological model within the framework of $f(R, L_m)$ gravity by employing a hybrid expansion law. The physical behavior of the model is analyzed through key cosmological parameters, including the deceleration parameter, equation of state parameter, and statefinder diagnostics. The results are examined to assess the consistency of the model with current observational data and the standard cosmological paradigm.

1.1. $f(R, L_m)$ Field Equations

The gravitational dynamics in $f(R, L_m)$ gravity are described by a generalized action in which the Ricci scalar R and the matter Lagrangian density L_m are treated as independent variables. The action is given by

$$S = \int f(R, L_m)\sqrt{-g}\, d^4x. \tag{1}$$

where g denotes the determinant of the metric tensor.

In the present work, we consider the specific functional form

$$f(R, L_m) = \frac{R}{2} + L_m^{\alpha}, \tag{2}$$

where α is a constant parameter that characterizes the strength of the matter–geometry coupling. The corresponding partial derivatives of the function are

$$f_R = \frac{\partial f}{\partial R} = \frac{1}{2}, \quad f_{L_m} = \frac{\partial f}{\partial L_m} = \alpha L_m^{\alpha-1}. \tag{3}$$

By varying the action with respect to the metric tensor, the field equations in $f(R, L_m)$ gravity are obtained as [12, 14]

$$f_R R_{ij} - \frac{1}{2}(f - f_{L_m} L_m) g_{ij} + (g_{ij}\Box - \nabla_i\nabla_j) f_R = \frac{1}{2} f_{L_m} T_{ij}, \tag{4}$$

where $\Box = \nabla^k\nabla_k$ is the d'Alembert operator and ∇_i denotes the covariant derivative.

In $f(R, L_m)$ gravity, the choice of matter Lagrangian density for a perfect fluid is not unique. Common choices such as $L_m = -p$ and $L_m = \rho$ have been widely discussed in the literature [12–14]. In this work, we adopt the physically motivated choice $L_m = \rho$, which yields

$$f_{L_m} = \alpha\rho^{\alpha-1}. \tag{5}$$

Since $f_R = \frac{1}{2}$ is constant, the derivative term vanishes identically, i.e.,

$$(g_{ij}\Box - \nabla_i\nabla_j) f_R = 0.$$

Substituting the above results into the field equations, we obtain

$$\frac{1}{2}R_{ij} - \frac{1}{2}\left(\frac{R}{2} + (1-\alpha)\rho^{\alpha}\right) g_{ij} = \frac{1}{2}\alpha\rho^{\alpha-1} T_{ij}. \tag{6}$$

Multiplying throughout by 2 and simplifying, the modified field equations reduce to

$$R_{ij} - \frac{1}{2}R g_{ij} = \alpha\rho^{\alpha-1} T_{ij} - (\alpha - 1)\rho^{\alpha} g_{ij}. \tag{7}$$

This equation represents a modified form of Einstein's field equations in which the effective gravitational coupling becomes matter-dependent through the factor $\alpha\rho^{\alpha-1}$, and an additional term proportional to ρ^{α} emerges, which can be interpreted as an effective cosmological contribution arising from matter–geometry coupling.

2. GEOMETRICAL SETUP AND FIELD EQUATIONS

We consider a spatially homogeneous but anisotropic Bianchi type VI_0 space-time, represented by the metric

$$ds^2 = -dt^2 + A^2(t)\, dx^2 + B^2(t) e^{-2x}\, dy^2 + C^2(t) e^{2x}\, dz^2, \tag{8}$$

where $A(t)$, $B(t)$, and $C(t)$ denote the directional scale factors corresponding to the three spatial directions.

In order to analyze the geometrical structure of the model and derive the corresponding gravitational field equations, it is necessary to evaluate the curvature quantities associated with the metric. In particular, the Ricci tensor R_{ij}, which characterizes the curvature of space-time, is obtained through contraction of the Riemann curvature tensor. It can be expressed in terms of the Christoffel symbols Γ^k_{ij} as follows:

$$R_{ij} = \partial_j \Gamma^k_{ik} - \partial_k \Gamma^k_{ij} + \Gamma^k_{il}\Gamma^l_{jk} - \Gamma^k_{ij}\Gamma^l_{kl}. \tag{9}$$

The Ricci scalar, which provides a measure of the curvature of space-time, is defined as the contraction of the Ricci tensor with the metric tensor, and is given by

$$R = g^{ij} R_{ij}. \tag{10}$$

For the considered Bianchi type VI_0 metric, this expression reduces to

$$R = -2\left(\frac{\ddot{A}}{A} + \frac{\ddot{B}}{B} + \frac{\ddot{C}}{C}\right) - 2\left(\frac{\dot{A}\dot{B}}{AB} + \frac{\dot{B}\dot{C}}{BC} + \frac{\dot{A}\dot{C}}{AC}\right) + \frac{2}{A^2}. \tag{11}$$

We assume that the matter content of the universe is described by a perfect fluid in a space-time characterized by the metric signature $(-, +, +, +)$. The corresponding energy–momentum tensor is given by

$$T_{ij} = (\rho + p)u_i u_j + p g_{ij}, \tag{12}$$

where ρ and p denote the energy density and isotropic pressure of the fluid, respectively, and u^i represents the four-velocity vector. The four-velocity satisfies the normalization condition

$$u^i u_i = -1. \tag{13}$$

For a comoving observer, the fluid remains at rest in the chosen coordinate system, and hence the four-velocity is expressed as

$$u^i = (1, 0, 0, 0). \tag{14}$$

Using this form of the four-velocity along with the metric components, the non-zero components of the energy–momentum tensor are obtained as

$$T_{00} = \rho, \quad T_{11} = pA^2, \quad T_{22} = pB^2 e^{-2x}, \quad T_{33} = pC^2 e^{2x}. \tag{15}$$

3. FIELD EQUATIONS FOR BIANCHI TYPE VI_0 SPACE-TIME

By substituting the metric functions corresponding to the Bianchi type VI_0 space-time into the modified field equations of $f(R, L_m)$ gravity, we obtain a set of coupled non-linear differential equations that govern the dynamical evolution of the model. The independent field equations can be written as follows:

$$\frac{\ddot{B}}{B} + \frac{\ddot{C}}{C} + \frac{\dot{B}\dot{C}}{BC} + \frac{1}{A^2} = \alpha\rho^{\alpha-1}p - (\alpha - 1)\rho^{\alpha}, \tag{16}$$

$$\frac{\ddot{A}}{A} + \frac{\ddot{C}}{C} + \frac{\dot{A}\dot{C}}{AC} - \frac{1}{A^2} = \alpha\rho^{\alpha-1}p - (\alpha - 1)\rho^{\alpha}, \tag{17}$$

$$\frac{\ddot{A}}{A} + \frac{\ddot{B}}{B} + \frac{\dot{A}\dot{B}}{AB} - \frac{1}{A^2} = \alpha\rho^{\alpha-1}p - (\alpha - 1)\rho^{\alpha}, \tag{18}$$

$$\frac{\dot{A}\dot{B}}{AB} + \frac{\dot{B}\dot{C}}{BC} + \frac{\dot{A}\dot{C}}{AC} - \frac{1}{A^2} = (1 - 2\alpha)\rho^{\alpha}, \tag{19}$$

$$\frac{\dot{B}}{B} - \frac{\dot{C}}{C} = 0, \tag{20}$$

Equation (20) establishes a first-order differential relation between the metric functions B and C. This relation can be expressed in the form

$$\frac{d}{dt}(\ln B - \ln C) = 0, \tag{21}$$

which indicates that the difference $\ln B - \ln C$ remains invariant with respect to cosmic time.

Integrating Eq. (21), we obtain

$$\ln B - \ln C = \ln k, \tag{22}$$

where k is a constant of integration. This relation can be rewritten as

$$\frac{B}{C} = k. \tag{23}$$

Since the constant k can be absorbed through an appropriate rescaling of the spatial coordinates, it is convenient to choose $k = 1$ without affecting the generality of the solution. Consequently, Eq. (23) reduces to

$$B = C. \tag{24}$$

This result imposes a constraint on the metric potentials, effectively reducing the number of independent scale factors. As a consequence, the system of field equations becomes simpler and more manageable for further analysis. By applying the condition $B = C$ obtained in Eq. (24), the system of field equations (16)–(19) simplifies considerably. The resulting set of independent differential equations can be expressed as

$$2\frac{\ddot{B}}{B} + \left(\frac{\dot{B}}{B}\right)^2 + \frac{1}{A^2} = \alpha\rho^{\alpha-1}p - (\alpha-1)\rho^{\alpha}, \tag{25}$$

$$\frac{\ddot{A}}{A} + \frac{\ddot{B}}{B} + \frac{\dot{A}\dot{B}}{AB} - \frac{1}{A^2} = \alpha\rho^{\alpha-1}p - (\alpha-1)\rho^{\alpha}, \tag{26}$$

$$2\frac{\dot{A}\dot{B}}{AB} + \left(\frac{\dot{B}}{B}\right)^2 - \frac{1}{A^2} = (1-2\alpha)\rho^{\alpha}. \tag{27}$$

4. HYBRID SCALE FACTOR AND PHYSICAL PARAMETERS

To close the system of field equations, we assume that the ratio of the shear scalar σ to the expansion scalar θ remains constant, i.e.,

$$\frac{\sigma}{\theta} = \text{constant}. \tag{28}$$

This condition leads to a linear relation among the directional Hubble parameters and, upon integration, yields

$$A = B^m, \tag{29}$$

where m is a constant characterizing the anisotropy of the model. Using the relation $B = C$ (Eq. (24)), we obtain

$$A = B^m = C^m. \tag{30}$$

The average scale factor a is defined through the relation

$$a^3 = ABC, \tag{31}$$

which corresponds to the spatial volume. Substituting Eq. (30), we get

$$a^3 = B^{m+2}, \tag{32}$$

leading to

$$B = C = a^{\frac{3}{m+2}}, \quad A = a^{\frac{3m}{m+2}}. \tag{33}$$

To describe the cosmic evolution, we employ a hybrid expansion law characterized by the scale factor

$$a(t) = e^{\beta t}t^{\gamma}, \tag{34}$$

where β and γ are positive constants. This form allows a smooth transition from an early decelerating phase to a late-time accelerated expansion. Differentiating Eq. (34) with respect to cosmic time t, the first derivative of the scale factor is obtained as

$$\dot{a} = e^{\beta t}t^{\gamma}\left(\beta + \frac{\gamma}{t}\right), \tag{35}$$

The second derivative takes the form

$$\ddot{a} = e^{\beta t}t^{\gamma}\left[\left(\beta + \frac{\gamma}{t}\right)^2 - \frac{\gamma}{t^2}\right], \tag{36}$$

and the third derivative is given by

$$\dddot{a} = e^{\beta t}t^{\gamma}\left[\left(\beta + \frac{\gamma}{t}\right)^3 - \frac{3\gamma}{t^2}\left(\beta + \frac{\gamma}{t}\right) + \frac{2\gamma}{t^3}\right]. \tag{37}$$

The Hubble parameter, which characterizes the rate of expansion of the universe, is defined as

$$H = \frac{\dot{a}}{a}. \tag{38}$$

Substituting the expression for $\dot{a}$ from Eq. (35) into Eq. (38), we obtain

$$H = \beta + \frac{\gamma}{t}. \tag{39}$$

The spatial volume of the anisotropic universe is given by

$$V = a^3, \tag{40}$$

which represents the total volume expansion of the cosmological model. Using the hybrid scale factor defined in Eq. (34), the volume can be expressed as

$$V = e^{3\beta t}t^{3\gamma}. \tag{41}$$

The expansion scalar θ describes the rate of volume expansion of the universe and is related to the Hubble parameter by

$$\theta = 3H. \tag{42}$$

Substituting the expression for H from Eq. (39), we obtain

$$\theta = 3\left(\beta + \frac{\gamma}{t}\right). \tag{43}$$

The deceleration parameter q provides information about the acceleration or deceleration behavior of the universe and is defined as

$$q = -1 - \frac{\dot{H}}{H^2}. \tag{44}$$

Differentiating Eq. (39) with respect to cosmic time t, we obtain

$$\dot{H} = -\frac{\gamma}{t^2}. \tag{45}$$

Substituting Eqs. (39) and (45) into Eq. (44), the deceleration parameter is expressed as

$$q = -1 + \frac{\gamma}{(\beta t + \gamma)^2}. \tag{46}$$

From Eq. (46), it follows that at early cosmic times (small t), the second term dominates, leading to $q > 0$, which corresponds to a decelerating phase. In contrast, for sufficiently large values of t, the parameter approaches $q \to -1$, indicating a transition to an accelerated expansion phase consistent with late-time cosmological observations. By utilizing the reduced field equations (25)–(27) together with the hybrid scale factor defined in Eq. (34), the expression for the energy density of the cosmic fluid is obtained as

$$\rho(t) = \frac{1}{1-2\alpha}\left[\frac{9(2m+1)}{(m+2)^2}\left(\beta + \frac{\gamma}{t}\right)^2 - \frac{1}{\left(e^{\beta t}t^{\gamma}\right)^{\frac{6m}{m+2}}}\right]^{\frac{1}{\alpha}} \tag{47}$$

with the restriction $\alpha \neq \frac{1}{2}$ to avoid singular behavior.

Substituting the above expression for the energy density into the modified field equations, we obtain the corresponding pressure of the cosmic fluid as

$$p = \frac{1}{\alpha\rho^{\alpha-1}}\left[\frac{(15-6m)}{(m+2)^2}\left(\beta + \frac{\gamma}{t}\right)^2 + \frac{6}{m+2}\left(\frac{\gamma(\gamma-1)}{t^2} + \frac{2\beta\gamma}{t} + \beta^2\right) + \frac{1}{\left(e^{\beta t}t^{\gamma}\right)^{\frac{6m}{m+2}}} - (1-\alpha)\rho^{\alpha}\right]. \tag{48}$$

5. STATEFINDER DIAGNOSTIC

To analyze the evolutionary behavior of the proposed cosmological model, we make use of the statefinder diagnostic, which provides a geometrical characterization of dark energy models through higher-order derivatives of the scale factor. The statefinder parameters are defined as

$$r = \frac{\dddot{a}}{aH^3}, \tag{49}$$

$$s = \frac{r-1}{3\left(q - \frac{1}{2}\right)}, \tag{50}$$

where q denotes the deceleration parameter.

Using the expression of the deceleration parameter derived earlier, we write

$$q = -1 + \frac{\gamma}{t^2\left(\beta + \frac{\gamma}{t}\right)^2}. \tag{51}$$

Substituting the expressions for a, $\dot{a}$, $\ddot{a}$, and $\dddot{a}$ from Eqs. (34), (35), and (37), along with the Hubble parameter given in Eq. (39), into Eq. (49), we obtain the statefinder parameter r in the form

$$r = 1 - \frac{3\gamma}{t^2\left(\beta + \frac{\gamma}{t}\right)^2} + \frac{2\gamma}{t^3\left(\beta + \frac{\gamma}{t}\right)^3}. \tag{52}$$

Further, substituting Eqs. (51) and (52) into Eq. (50), the parameter s can be expressed as

$$s = \frac{-3\gamma}{3t^2\left(\beta + \frac{\gamma}{t}\right)^2\left(q - \frac{1}{2}\right)} + \frac{2\gamma}{3t^3\left(\beta + \frac{\gamma}{t}\right)^3\left(q - \frac{1}{2}\right)}. \tag{53}$$

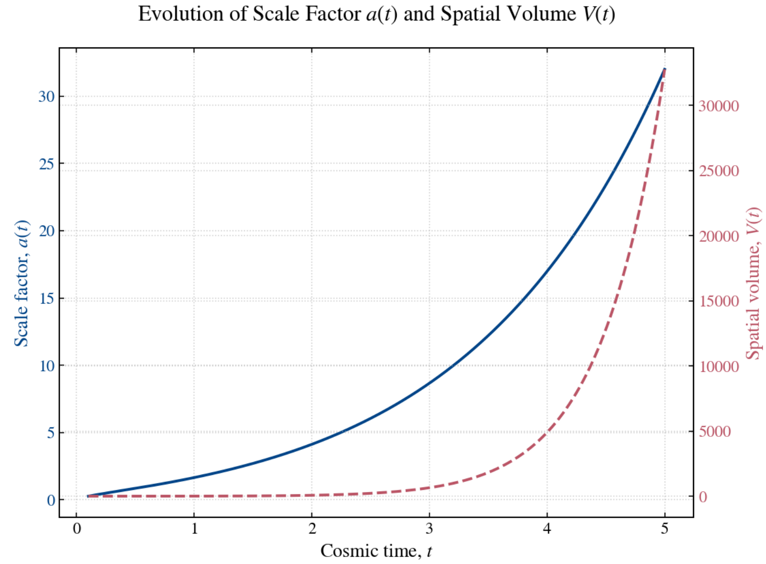

Figure 1. Evolution of the scale factor $a(t)$ and spatial volume $V(t)$ with cosmic time t for $\beta = 0.5$ and $\gamma = 0.6$.

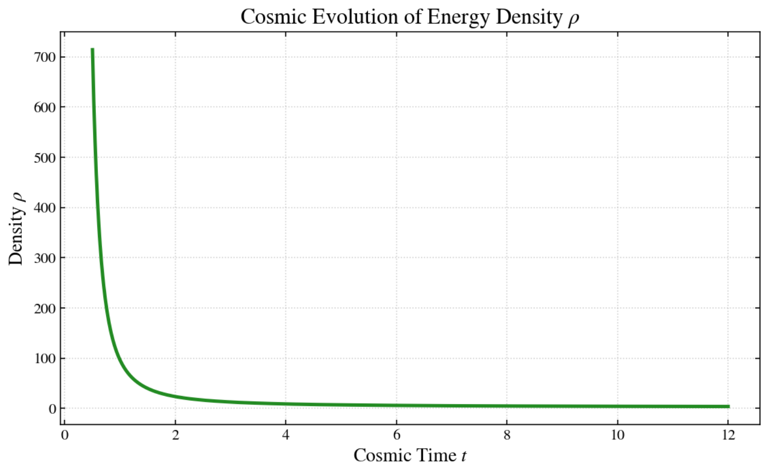

Figure 2. Energy density $\rho(t)$ versus cosmic time t for $\beta = 0.5$, $\gamma = 0.6$, and $\alpha = 0.4$.

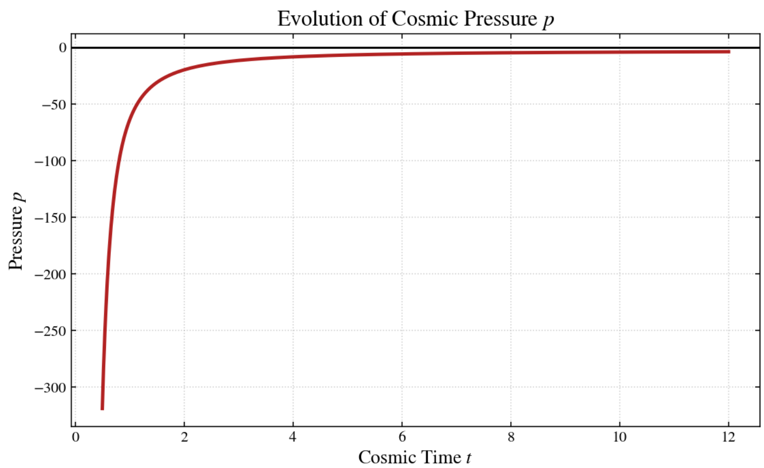

Figure 3. Thermodynamic pressure $p(t)$ as a function of cosmic time t for $\beta = 0.5$ and $\gamma = 0.6$.

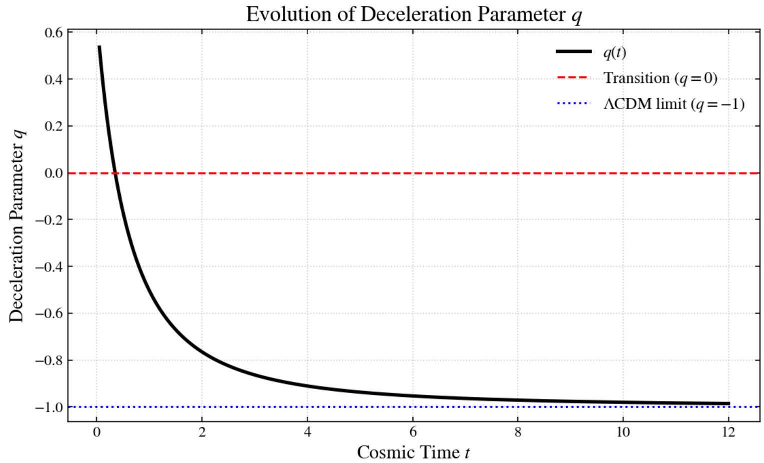

Figure 4. Deceleration parameter $q(t)$ versus cosmic time t for $\beta = 0.5$ and $\gamma = 0.6$.

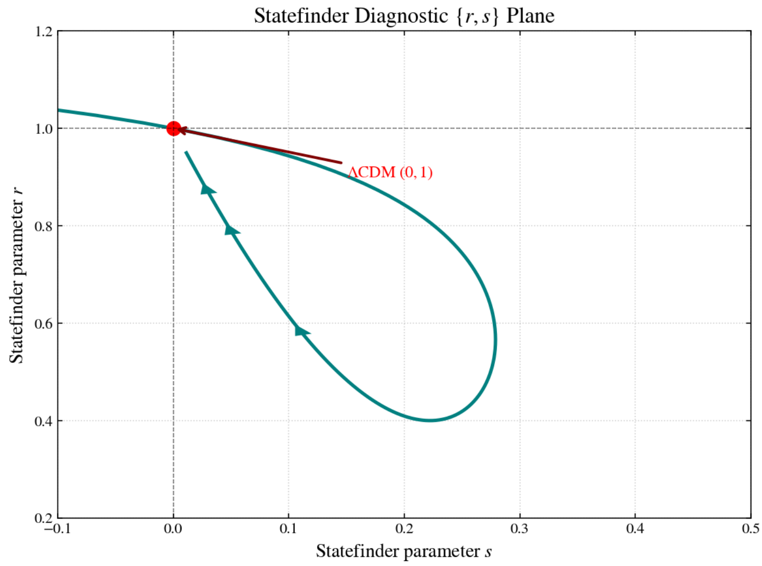

Figure 5. Statefinder trajectory in the (s, r) plane for $\beta = 0.5$ and $\gamma = 0.6$.

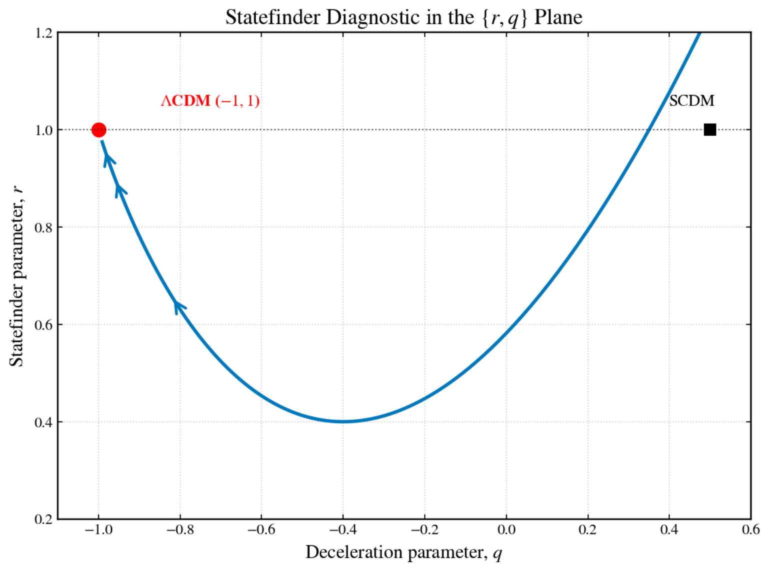

Figure 6. Statefinder trajectory in the (q, r) plane for $\beta = 0.5$ and $\gamma = 0.6$.

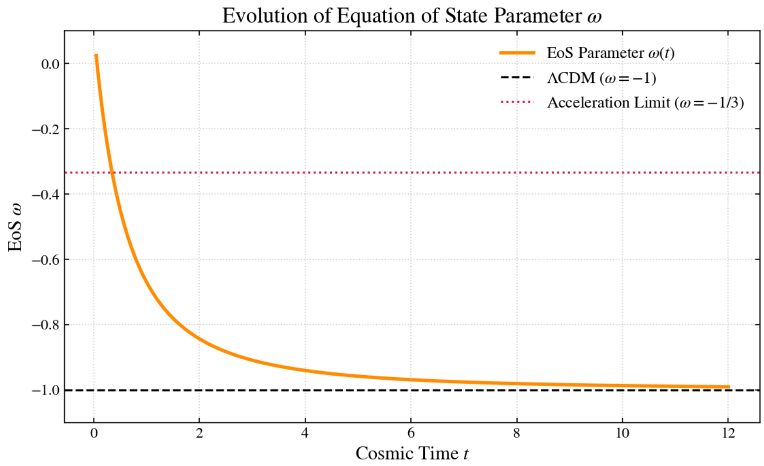

Figure 7. Equation of state parameter $\omega(t)$ versus cosmic time t for $\beta = 0.5$ and $\gamma = 0.6$.

6. DISCUSSION AND CONCLUDING REMARKS

The present study investigates a dynamical dark energy model governed by a hybrid expansion law within the framework of $f(R, L_m)$ gravity. Based on the analytical expressions and graphical analysis of the cosmological parameters, the following conclusions are drawn:

- The evolution of the scale factor $a(t)$ and spatial volume $V(t)$, shown in Fig. 1, demonstrates a continuous and monotonic increase with cosmic time. This confirms a persistently expanding universe without any indication of recollapse. The rapid growth of the spatial volume at later times reflects the accelerated expansion governed by the hybrid expansion law.

- The energy density $\rho(t)$, depicted in Fig. 2, remains strictly positive throughout the evolution and decreases monotonically with time. The initially large value of ρ at early times followed by gradual dilution is consistent with an expanding universe and satisfies the Weak Energy Condition.

- The thermodynamic pressure $p(t)$, shown in Fig. 3, remains negative for all cosmic time. The large negative pressure at early epochs gradually approaches a small negative value at late times, providing the repulsive effect responsible for the observed accelerated expansion.

- The deceleration parameter $q(t)$, illustrated in Fig. 4, exhibits a smooth transition from a decelerated phase ($q > 0$) to an accelerated phase ($q < 0$). The transition occurs at early cosmic time, and at late times q asymptotically approaches -1, indicating convergence toward a de Sitter phase.

- The statefinder diagnostics in the $\{r, s\}$ and $\{r, q\}$ planes, shown in Fig. 5 and Fig. 6, respectively, reveal that the model deviates from the ΛCDM behavior during intermediate stages and eventually converges to the fixed points $(0, 1)$ and $(-1, 1)$ respectively.

- The equation of state parameter $\omega(t)$, illustrated in Fig. 7, evolves from values close to zero at early times into the quintessence region ($-1 < \omega < -1/3$), and asymptotically approaches $\omega \to -1$. The condition $\omega < -1/3$ is consistent with the negative values of the deceleration parameter shown in Fig. 4, confirming accelerated expansion.

Overall, the proposed model successfully describes a transition from an early decelerated phase to a late-time accelerated universe. The consistent behavior of q, ω, ρ, and p, along with the convergence of statefinder parameters toward the ΛCDM limits, confirms the physical viability of the model as a realistic description of dark energy-dominated cosmic evolution.

6.1. Statefinder Diagnostic Analysis

The $\{r, s\}$ statefinder diagnostic, introduced by Sahni et al. [23], is employed to characterize the evolutionary trajectory of the proposed dark energy model and to distinguish it from standard cosmological scenarios. As shown in Fig. 5, the trajectory originates in the vicinity of the ΛCDM fixed point $(s, r) = (0, 1)$ and then evolves into the region $s > 0$ with $r < 1$, which is typically associated with quintessence-like behavior.

A notable feature of the evolution is the non-monotonic, hook-like trajectory observed in the s–r plane. The model departs from the ΛCDM point during the intermediate stages of cosmic evolution, reaching a minimum value of the statefinder parameter r before turning back toward the fixed point. This behavior reflects the dynamical nature of the dark energy component.

The directional arrows in the figure indicate the progression of cosmic time, showing that the trajectory gradually returns and asymptotically approaches the de Sitter attractor at $(s, r) = (0, 1)$. This convergence suggests that the model becomes effectively indistinguishable from the ΛCDM scenario at late times.

Overall, the characteristic loop-like evolution in the $\{r, s\}$ plane highlights the transient deviation from the cosmological constant behavior and provides a useful diagnostic feature for comparing the present model with other dark energy scenarios.

6.2. Geometrical Diagnostic in the $\{r, q\}$ Plane

To further investigate the expansion dynamics, we analyze the trajectory in the $\{r, q\}$ statefinder–deceleration plane, as shown in Fig. 6. This diagnostic provides a geometrical interpretation of cosmic evolution by relating the deceleration parameter q and the statefinder parameter r [23].

The trajectory begins in the decelerated regime ($q > 0$) with $r \approx 1$, and then evolves toward lower values of r as the universe transitions into the accelerated phase ($q < 0$). A distinct minimum in r is observed during the intermediate stage of evolution, indicating a departure from the standard ΛCDM behavior.

As cosmic time progresses, the trajectory turns upward and asymptotically approaches the de Sitter fixed point $(q, r) = (-1, 1)$. This convergence confirms that the model ultimately evolves toward a late-time accelerated phase consistent with the ΛCDM scenario.

The smooth and continuous nature of the trajectory across the $q = 0$ transition demonstrates a stable evolution from deceleration to acceleration, without any abrupt changes in the expansion dynamics. The characteristic curved path in the $\{r, q\}$ plane reflects the dynamical nature of the model and distinguishes it from the constant behavior of the standard cosmological constant model.

ORCID

V. R. Patil, https://orcid.org/0000-0002-0442-3962; **A. S. Panurkar**, https://orcid.org/0009-0009-0445-912X; **P. A. Bolke**, https://orcid.org/0000-0002-1212-5260

REFERENCES

[1] A. G. Riess, A. V. Filippenko, P. Challis, *et al*. "Observational evidence from supernovae for an accelerating universe and a cosmological constant," Astron. J. **116**, (1009) (1998). https://doi.org/10.1086/300499

[2] S. Perlmutter, G. Aldering, G. Goldhaber, *et al*. "Measurements of Ω and Λ from 42 high-redshift supernovae," Astrophys. J. **517**, (565) (1999). https://doi.org/10.1086/307221

[3] D. N. Spergel, L. Verde, H. V. Peiris, *et al*. "First-year Wilkinson Microwave Anisotropy Probe observations: Determination of cosmological parameters," Astrophys. J. Suppl. Ser. **148**, (175) (2003). https://doi.org/10.1086/377226

[4] M. Tegmark, M. A. Strauss, M. R. Blanton, *et al*. "Cosmological parameters from SDSS and WMAP," Phys. Rev. D, **69**, (103501) (2004). https://doi.org/10.1103/PhysRevD.69.103501

[5] N. Aghanim, Y. Akrami, M. Ashdown, *et al*. "Planck 2018 results. VI. Cosmological parameters," Astron. Astrophys. **641**, (A6) (2020). https://doi.org/10.1051/0004-6361/201833910

[6] S. Weinberg, "The cosmological constant problem," Rev. Mod. Phys. **61**, 1 (1989). https://doi.org/10.1103/RevModPhys.61.1

[7] T. Padmanabhan, "Cosmological constant—The weight of the vacuum," Phys. Rep. **380**, 235-320 (2003). https://doi.org/10.1016/S0370-1573(03)00120-0

[8] E. J. Copeland, M. Sami, and S. Tsujikawa, "Dynamics of dark energy," Int. J. Mod. Phys. D, **15**, 1753-1935 (2006). https://doi.org/10.1142/S021827180600942X

[9] S. Nojiri, and S. D. Odintsov, "Unified cosmic history in modified gravity: From $F(R)$ theory to Lorentz non-invariant models," Phys. Rep. **505**, 59-144 (2011). https://doi.org/10.1016/j.physrep.2011.04.001

[10] A. De Felice, and S. Tsujikawa, "$f(R)$ theories," Living Rev. Relativ. **13**, 3 (2010). https://doi.org/10.12942/lrr-2010-3

[11] S. Capozziello, M. De Laurentis, "Extended theories of gravity," Phys. Rep. **509**, 167-321 (2011). https://doi.org/10.1016/j.physrep.2011.09.003

[12] O. Bertolami, C. G. Böhmer, T. Harko, and F. S. N. Lobo, "Extra force in $f(R)$ modified theories of gravity," Phys. Rev. D, **75**, 104016 (2007). https://doi.org/10.1103/PhysRevD.75.104016

[13] T. Harko, and F. S. N. Lobo, "$f(R, L_m)$ gravity," Eur. Phys. J. C, **70**, 373-379 (2010). https://doi.org/10.1140/epjc/s10052-010-1467-3

[14] T. Harko, F. S. N. Lobo, S. Nojiri, and S. D. Odintsov, "$f(R, T)$ gravity," Phys. Rev. D, **84**, 024020 (2011). https://doi.org/10.1103/PhysRevD.84.024020

[15] L. V. Jaybhaye, R. Solanki, S. Mandal, P. K. Sahoo, "Cosmology in $f(R, L_m)$ gravity," Phys. Lett. B, **831**, 137148 (2022). https://doi.org/10.1016/j.physletb.2022.137148

[16] J. Pawde, R. Mapari, V. Patil, and D. Pawar, "Anisotropic behavior of universe in $f(R, L_m)$ gravity with varying deceleration parameter," Eur. Phys. J. C, **84**, 320 (2024). https://doi.org/10.1140/epjc/s10052-024-12646-4

[17] V. Patil, J. Pawde, R. Mapari, and S. Waghmare, "FLRW cosmology with hybrid scale factor in $f(R, L_m)$ gravity," East Eur. J. Phys. (4), 8-17 (2023). https://doi.org/10.26565/2312-4334-2023-4-01

[18] G. F. R. Ellis, and M. A. H. MacCallum, "A class of homogeneous cosmological models," Commun. Math. Phys. **12**, 108-141 (1969). https://doi.org/10.1007/BF01645908

[19] C. B. Collins, "More qualitative cosmology," Commun. Math. Phys. **23**, 137–158 (1971). https://doi.org/10.1007/BF01877756

[20] T. Vinutha, and K. S. Kavya, "Bianchi type cosmological models in $f(R, T)$ theory with quadratic functional form," *Eur. Phys. J. Plus*, **135**, 306 (2020). https://doi.org/10.1140/epjp/s13360-020-00309-8

[21] H. Amirhashchi, A. Pradhan, and B. Saha, "Variable equation of state for Bianchi type-VI_0 dark energy models," Astrophys. Space Sci., **333**, 295-303 (2011). https://doi.org/10.1007/s10509-010-0577-6

[22] Ö. Akarsu, S. Kumar, R. Myrzakulov, M. Sami, and L. Xu, "Cosmology with hybrid expansion law: Scalar field reconstruction of cosmic history and observational constraints," J. Cosmol. Astropart. Phys. **2014**(01), 022 (2014). https://doi.org/10.1088/1475-7516/2014/01/022

[23] V. Sahni, T. D. Saini, A. A. Starobinsky, AND U. Alam, "Statefinder: A new geometrical diagnostic of dark energy," JETP Lett. **77**, 201-206 (2003). https://doi.org/10.1134/1.1574831

[24] K. Pawar, and A. K. Dabre, "Perfect fluid coupled string universe in $f(R,T)$ gravity," J. Sci. Res. **15**, 695-704 (2023). https://doi.org/10.3329/jsr.v15i3.64173

[25] S. P. Hatkar, D. P. Tadas, and S. D. Katore, "Domain wall Bianchi type VI_0 universe in $f(R,T)$ gravity," Astrophysics **67**, 537–555 (2024). https://doi.org/10.1007/s10511-025-09850-9

[26] J. K. Singh, Shaily, R. Myrzakulov, and H. Balhara, "A constrained cosmological model in $f(R, L_m)$ gravity," New Astron. **104**, 102070 (2023). https://doi.org/10.1016/j.newast.2023.102070

[27] L. V. Jaybhaye, S. Bhattacharjee, and P. K. Sahoo, "Baryogenesis in $f(R, L_m)$ gravity," Phys. Dark Universe, **40**, 101223 (2023). https://doi.org/10.1016/j.dark.2023.101223

[28] B. K. Shukla, R. K. Tiwari, D. Sofuoğlu, and A. Beesham, "FLRW universe in $f(R, L_m)$ gravity with equation of state parameter," East Eur. J. Phys. (4), 376-389 (2023). https://doi.org/10.26565/2312-4334-2023-4-48

[29] R. Solanki, Z. Hassan, and P. K. Sahoo, "Wormhole solutions in $f(R, L_m)$ gravity," Chin. J. Phys. **85**, 74-88 (2023). https://doi.org/10.1016/j.cjph.2023.06.005

[30] S. Sahlu, A. H. A. Alfedeel, and A. Abebe, "The cosmology of $f(R, L_m)$ gravity: constraining the background and perturbed dynamics," Eur. Phys. J. C, **84**, 982 (2024). https://doi.org/10.1140/epjc/s10052-024-13307-2

[31] Shaily, J. K. Singh, D. Sethi, R. Rani, and K. Bamba, "Bouncing cosmology and the dynamical stability analysis in $f(R, L_m)$-gravity," Nucl. Phys. B, **1013,** 116854 (2025). https://doi.org/10.1016/j.nuclphysb.2025.116854

[32] S. D. Katore, P. R. Agrawal, H. G. Paralikar, and A. P. Nile, "Dynamics of string cosmological model in $f(R, L_m)$ theory of gravity," East Eur. J. Phys. (1), 70-78 (2025). https://doi.org/10.26565/2312-4334-2025-1-06

[33] A. Samaddar, and S. Surendra Singh, "Late-time cosmic dynamics in $f(R, L_m)$ gravity with recent observations," J. High Energy Astrophys. **51**, 100558 (2026). https://doi.org/10.1016/j.jheap.2026.100558

[34] A. Dixit, S. Verma, A. Pradhan, and M. S. Barak, "Easing the Hubble tension in $f(R, L_m)$ gravity: A Bayesian MCMC analysis with CC and Pantheon Plus & SH0ES datasets," Universe, **12**, 66 (2026). https://doi.org/10.3390/universe12030066

[35] L. Navarro-Coydán, J. A. Vázquez, I. Quiros, R. García-Salcedo, "Late-time acceleration without a vacuum term in $f(R, L_m)$ gravity: scaling de Sitter dynamics and parameter constraints," arXiv:2601.10699 (2026). https://doi.org/10.48550/arXiv.2601.10699

[36] G. K. Goswami, and A. Pradhan, "Constraining a $f(R, L_m)$ gravity cosmological model with observational data," arXiv:2505.18226 (2025). https://doi.org/10.48550/arXiv.2505.18226

[37] K. P. Singh, S. Sabanam, A. K. Yadav, A. J. Meitei, "Modeling through the cubic parametrization of the deceleration parameter in $f(R, L_m)$ gravity with observational constraints," Nucl. Phys. B, **1018**, 117061 (2025). https://doi.org/10.1016/j.nuclphysb.2025.117061

АНІЗОТРОПНА КОСМІЧНА ЕВОЛЮЦІЯ ТА ДІАГНОСТИКА СТАНУ ВСЕСВІТУ ТИПУ Б'ЯНКІ VI_0 З ГІБРИДНИМ МАСШТАБНИМ ФАКТОРОМ У $f(R, L_m)$ ГРАВІТАЦІЇ

В. Р. Патіл[1], А. С. Пануркар[2], П. А. Болке[3]
[1]*Кафедра математики, мистецтв, науки та комерції, Коледж, Чікхалдара, округ Амраваті (MS), Індія, 444807*
[2]*Кафедра математики, проф. Інститут технологій та досліджень ім. Рама Меге, Баднера, округ Амраваті (MS), Індія, 444701*
[3]*Кафедра математики, проф. Коледж інженерії та менеджменту ім. Рама Меге, Баднера, округ Амраваті (MS), Індія*

Ми досліджуємо динаміку анізотропної космологічної моделі типу Б'янкі VI_0 в рамках гравітації $f(R, L_m)$, приймаючи форму зв'язку кривизни та матерії $f(R, L_m) = \frac{R}{2} + L_m^{\alpha}$. Для опису космічної еволюції використовується гібридний закон розширення $a(t) = e^{\beta t} t^{\gamma}$, що дозволяє плавний перехід від ранньої уповільненої фази до прискореного розширення наприкінці часу. Параметр $\alpha = 0.4$ вибрано для забезпечення стабільної та фізично життєздатної поведінки моделі. Аналіз показує, що масштабний коефіцієнт та просторовий об'єм монотонно зростають з космічним часом, що вказує на безперервно розширюваний Всесвіт. Параметр уповільнення демонструє перехід від позитивних до негативних значень та наближається до межі де Сіттера на пізніх етапах часу. Параметр рівняння стану еволюціонує від режиму домінування матерії до області квінтесенції та асимптотично наближається до $\omega = -1$. Густина енергії залишається позитивною та зменшується з часом, тоді як тиск залишається негативним протягом усієї еволюції, що підтверджує прискорене розширення. Крім того, діагностика стану в площинах $\{r, s\}$ та $\{r, q\}$ демонструє, що модель відхиляється від стандартної космології в проміжні епохи та сходиться до фіксованих точок ΛCDM на пізніх етапах часу. Ці результати вказують на те, що запропонована модель забезпечує послідовний та життєздатний опис космічної еволюції, керованої темною енергією.

Keywords: $f(R, L_m)$ *гравітація; Всесвіт типу Б'янкі* VI_0*; гібридний закон розширення; анізотропна космологія; діагностика statefinder; космічне прискорення*

EAST EUROPEAN JOURNAL OF PHYSICS. 3. 78-89 (2026)
DOI:10.26565/2312-4334-2026-3-07 ISSN 2312-4334

COSMIC ACCELERATION AND STABILITY OF KALUZA-KLEIN UNIVERSE IN $f(Q,T)$ GRAVITY

M.T. Sarode[1*], V.G. Mete[2#], A.S. Nimkar[3†]
[1]*Department of Mathematics, Shri Shivaji College of Arts, Commerce & Science, Akola (M.S.), India*
[2]*Department of Mathematics, R. D. I. K. & K. D. College, Badnera – Amravati (M.S.), India*
[3]*Department of Mathematics, Shri Dr. R. G. Rathod Arts & Science College, Murtizapur Dist. Akola (M.S.), India*
[*]*Corresponding Author E-mail: mtsarode17@gmail.com, [#]E-mail: vmete5622@gmail.com; [†]E-mail: anilnimkar@gmail.com*
Received May 17, 2026; revised August 11, 2026; accepted August 14, 2026

The $f(Q,T)$ gravity has been used in this research to study the Kaluza-Klein universe in the presence of matter distribution. In this theory of gravity, the action contains an arbitrary function $f(Q,T)$ where Q and T respectively denote the non-metricity and the trace of energy momentum tensor. The linear and additive form of $f(Q,T)$ gravity, $f(Q,T) = \alpha Q + \beta T$ where α and β are arbitrary constants, is taken into account in this work. To achieve a physically viable solution of the field equations, we have considered power law and exponential expansion law. We investigate the evolving character of the universe with physical and geometrical properties within this theoretical framework. To enhance clarity, statefinder diagnostic and EoS parameter are examined, to characterize different phases of the universe. The energy conditions of the models are also analyzed and found to be consistent with recent cosmological observations. Besides, one of our models inherently allows a phantom region for dark energy. Further the models examined in this work are confirmed through stability analysis.
Keywords: *$f(Q,T)$ gravity; Kaluza-Klein space-time; Equation of state; Energy conditions*

1. INTRODUCTION

The study of universe's accelerating expansion confirmed by numerous observations over the last two decades, is a major cosmological enigma among researchers. This concept of accelerated expansion of the universe is strongly backed by astronomical observations of type Ia Supernovae [1-3] and measurements of cosmic microwave background (CMB) from the Wilkinson Microwave Anisotropy Probe (WAMP) [4-5]. Over the past few years, many researchers have explored dark energy models and are probing the dynamic relationship between dark energy (DE) and cosmic evolution. Modifying the geometric part of the Einstein-Hilbert action is a promising approach for understanding DE. Researchers have proposed modified gravity theories to explain the universe's acceleration, offering alternative frameworks to understand this phenomenon. Several modified theories have emerged such as $f(G)$ gravity [6], $f(R)$ gravity [7], $f(R,T)$ gravity [8], $f(T)$ gravity [9], $f(G,T)$ gravity [10], $f(R,T,R_{\mu\nu}T^{\mu\nu})$ gravity [11], $f(Q)$ gravity [12] and the recently proposed $f(Q,T)$ gravity [13-14] to explore the dark energy and other cosmological challenges.

Among the several modified theories of gravitation, $f(Q,T)$ theory of gravity proposed by Xu et al. [13] has received a lot of interest in recent years. It has been suggested that cosmic acceleration can be achieved by replacing the Einstein - Hilbert action of general relativity with a function $f(Q,T)$ where Q and T denotes the non-metricity and the trace of energy momentum tensor respectively. The $f(Q,T)$ gravity is an extension of symmetric teleparallel gravity, which is built on the non-minimal coupling between the non-metricity Q and the trace T of matter energy momentum tensor. This coupling yields results in the non-conservation of the energy-momentum tensor possibly offering mechanisms for matter generation or decay in the early or late universe and potentially explaining cosmic acceleration. Inspired by this, we employ the $f(Q,T)$ gravity theory to explore plausible explanations for various cosmological phenomena occurring in the universe. Subsequently, $f(Q,T)$ gravity has been widely explored across cosmological and astrophysical contexts, including studies of investigations of cosmic acceleration [15-18], energy conditions [19], cosmological inflation [20-21], wormhole solution [22-24], viability of $f(Q,T)$ gravity [25-26], Baryogenesis [27], bounce cosmology [28-30], Rip cosmology [31].

In the present era, research on higher-dimensional space-time is a highly active area of investigation. Today's conventional four-dimensional space-time could have been preceded by a multi-dimensional phase. Higher dimensional cosmology may provide solutions to basic inquiries concerning the universe, encompassing its origin, structure and evolution. It also seeks to merge the two essential natural forces, gravity and electro-magnetism. The idea of an additional dimension was initially presented by Theodor Kaluza [32] and subsequently developed by Oskar Klein [33]. Kaluza added a fifth dimension to ordinary four-dimensional space-time and suggested that the geometry of higher dimensional space-time could account for both gravity and electromagnetism in single framework. Kaluza-Klein theory provides solutions to the flatness, horizon and cosmological constant issues found in the conventional cosmological model. This is achieved by introducing extra spatial dimensions, in which fundamental constants such as the gravitational constant and gauge couplings are treated as dynamical fields. These fields evolve during the

Cite as: M.T. Sarode, V.G. Mete, A.S. Nimkar, East Eur. J. Phys. 3, 78 (2026), https://doi.org/10.26565/2312-4334-2026-3-07

compactification process in the early universe. Nowadays, higher dimensional cosmology has attracted the interest of numerous researchers. The five-dimensional Kaluza-Klein theory now captures the attention of many scholars [34-35]. Recently, Ray and Baruah [36] have delved into five-dimensional Kaluza-Klein cosmological model featuring two fluid sources. Pawar et al. [37], Katore et al. [38] have investigated the behavior of strange quark matter for Kaluza-Klein cosmological model in Lyra Geometry and $f(R,T)$ gravity respectively. Wankhade and Nimkar [39] studied the dynamic behavior of Kaluza-Klein universe in scalar tensor theory of gravitation. Authors of [40-41] have explored different aspects of Kaluza-Klein cosmological model in modified theories of gravity. Recently Ugale et al. [42] have investigated cosmological model with matter distribution in Brans-Dicke Theory of Gravitation. Wath and Nimkar [43], Nimkar and Hadole [44] have studied stability of cosmological model with matter distribution in Ruban's background and self-creation theory respectively.

In this paper, we propose to investigate five-dimensional Kaluza-Klein metric in presence of matter distribution within the framework of $f(Q,T)$ gravity by considering two different kinds of volumetric expansion namely power law and exponential expansion law. The paper is structured as follows: Section 1 contains a concise introduction and the motivation behind the current work. The framework of $f(Q,T)$ gravity is given in Section 2. In Section 3, we have derived the metric and field equations. In Section 4, we derived the solution of field equations. The physical and kinematical characteristics of power and exponential expansion law models are explored in Sections 5 and 6. Statefinder diagnostic, energy conditions and stability analysis are examined in Section 7. Conclusion is presented in Section 8.

2. THE FRAMEWORK OF $f(Q,T)$ GRAVITY

The field equations of modified $f(Q,T)$ gravity are derived from Hilbert Einstein variational action principle [13]

$$S = \int \left(\frac{1}{16\pi} f(Q,T) + L_m\right)\sqrt{-g}\, d^4x \tag{1}$$

where $f(Q,T)$ is a function of the non-metricity scalar Q and the trace of the matter-energy-momentum tensor T , also L_m is Lagrangian of the matter and $g = \det(g_{\mu\nu})$. The non-metricity scalar Q is defined as

$$Q = -g^{\mu\nu}\left(L^{\alpha}{}_{\beta\mu}L^{\beta}{}_{\nu\alpha} - L^{\alpha}{}_{\beta\alpha}L^{\beta}{}_{\mu\nu}\right) \tag{2}$$

where $L^{\alpha}{}_{\beta\gamma}$ represents the disformation tensor which is given by,

$$L^{\alpha}{}_{\beta\gamma} = -\frac{1}{2}g^{\alpha\delta}\left(\nabla_{\gamma}g_{\beta\delta} + \nabla_{\beta}g_{\delta\gamma} - \nabla_{\delta}g_{\beta\gamma}\right) \tag{3}$$

The non-metricity tensor is defined as

$$Q_{\gamma\mu\nu} = \nabla_{\gamma}g_{\mu\nu} \tag{4}$$

The trace of the non-metricity tensor is derived as follows

$$Q_{\alpha} = g^{\mu\nu}Q_{\alpha\mu\nu}\,, \tilde{Q}_{\alpha} = g^{\mu\nu}Q_{\mu\alpha\nu} \tag{5}$$

The superpotential or the non-metricity conjugate of the model is given by

$$P^{\alpha}{}_{\mu\nu} = -\frac{1}{2}L^{\alpha}{}_{\mu\nu} + \frac{1}{4}\left(Q^{\alpha} - \tilde{Q}^{\alpha}\right)g_{\mu\nu} - \frac{1}{4}\delta^{\alpha}{}_{(\mu}Q_{\nu)} \tag{6}$$

The energy-momentum tensor is defined as

$$T_{\mu\nu} = -\frac{2}{\sqrt{-g}}\frac{\delta(\sqrt{-g}L_m)}{\delta g^{\mu\nu}} \quad \text{and} \quad \theta_{\mu\nu} = g^{\alpha\beta}\frac{\delta T_{\alpha\beta}}{\delta g^{\mu\nu}} \tag{7}$$

The field equation of $f(Q,T)$ gravity is obtained by varying the action (1) with respect to the metric tensor $g_{\mu\nu}$ as [13]

$$-\frac{2}{\sqrt{-g}}\nabla_{\alpha}\left(f_Q\sqrt{-g}P^{\alpha}{}_{\mu\nu}\right) - \frac{1}{2}f g_{\mu\nu} + f_T\left(T_{\mu\nu} + \theta_{\mu\nu}\right) - f_Q\left(P_{\mu\alpha\beta}Q_{\nu}{}^{\alpha\beta} - 2Q^{\alpha\beta}{}_{\mu}P_{\alpha\beta\nu}\right) = 8\pi T_{\mu\nu} \tag{8}$$

where $f_Q = \frac{\partial f}{\partial Q}$, $f_T = \frac{\partial f}{\partial T}$ and the non-metricity tensors $Q_{\nu}{}^{\alpha\beta} = -\nabla_{\nu}g^{\alpha\beta}$, $Q^{\alpha\beta}{}_{\mu} = g^{\alpha\gamma}g^{\beta\rho}\nabla_{\gamma}g_{\rho\mu}$

3. THE METRIC AND FIELD EQUATIONS

We have considered the five-dimensional Kaluza-Klein space-time as

$$ds^2 = dt^2 - A^2[dx^2 + dy^2 + dz^2] - B^2 d\psi^2 \tag{9}$$

where the metric potentials A, B are functions of cosmic time t only and the fifth coordinate ψ is taken to be space-like. The energy momentum tensor of matter (Landau and Lifshitz [45]) is given by

$$T_{ij} = (\varepsilon + p)u_i u_j - p g_{ij} \tag{10}$$

where p and ε are pressure and energy density respectively and $u_i = (1, 0, 0, 0, 0)$ is the velocity vector in comoving coordinates which satisfies the condition $u^i u_i = 1$.
From Eq. (10), we get

$$T_1^1 = T_2^2 = T_3^3 = T_4^4 = -p \ , \ T_0^0 = \varepsilon \, , \ T = \varepsilon - 4p \tag{11}$$

θ_j^i is derived as

$$\theta_j^i = \delta_j^i p - 2T_j^i = \text{diag}\,(p - 2\varepsilon, 3p, 3p, 3p, 3p) \tag{12}$$

For given cosmological model, the non-metricity scalar Q is found to be

$$Q = -6\left(\frac{\dot{A}^2}{A^2} + \frac{\dot{A}\dot{B}}{AB}\right) \tag{13}$$

The field Eq. (8) for the line element (9) with energy momentum tensor (11), also using Eqs. (12) and (13) can be written as

$$\frac{1}{2}f + 6f_Q\left(\frac{\dot{A}^2}{A^2} + \frac{\dot{A}\dot{B}}{AB}\right) = 8\pi\tilde{G}p - 8\pi\big(1 + \tilde{G}\big)\varepsilon \tag{14}$$

$$\frac{1}{2}f + f_Q\left(2\frac{\ddot{A}}{A} + \frac{\ddot{B}}{B} + 4\frac{\dot{A}^2}{A^2} + 5\frac{\dot{A}\dot{B}}{AB}\right) + \dot{f}_Q\left(2\frac{\dot{A}}{A} + \frac{\dot{B}}{B}\right) = 8\pi\big(1 + 2\tilde{G}\big)p \tag{15}$$

$$\frac{1}{2}f + 3f_Q\left(\frac{\ddot{A}}{A} + 2\frac{\dot{A}^2}{A^2} + \frac{\dot{A}\dot{B}}{AB}\right) + 3\dot{f}_Q\frac{\dot{A}}{A} = 8\pi(1 + 2\tilde{G})p \tag{16}$$

where $f_T = 8\pi\tilde{G}$ and an overhead dot refers to derivative with respect to time t.
For the given cosmological model, the physical parameters are defined as follows. The spatial volume V is given by

$$V = a^4 = A^3 B \tag{17}$$

where a is the average scale factor.
The generalized mean Hubble's parameter H is expressed as

$$H = \frac{1}{4}\big(H_x + H_y + H_z + H_\psi\big) = \frac{1}{4}\big(3H_x + H_\psi\big) \tag{18}$$

where $H_x = \frac{\dot{A}}{A} = H_y = H_z$ and $H_\psi = \frac{\dot{B}}{B}$ are the directional Hubble parameters in the direction of x, y, z and ψ respectively.
The expansion scalar θ, mean anisotropy parameter A_m, the shear scalar σ^2 are expressed as

$$\theta = 4H \tag{19}$$

$$A_m = \frac{1}{4}\sum_{i=1}^{4}\left(\frac{H_i - H}{H}\right)^2 \tag{20}$$

$$\sigma^2 = \frac{3}{2}H^2 A_m \tag{21}$$

4. SOLUTIONS OF THE FIELD EQUATIONS

There are various forms of the function $f(Q,T)$ which is commonly used in the literature [13]. Here we shall focus on the linear and additive form of $f(Q,T)$ function [14] as $f(Q,T) = \alpha Q + \beta T$, where α and β are arbitrary constants. Here $f_Q = \alpha,\ f_T = \beta = 8\pi\tilde{G}\ ,\tilde{G} = \frac{\beta}{8\pi}$.
Thus, the field Eqs. (14) - (16) can be reduced to

$$3\alpha\left(\frac{\dot{A}^2}{A^2} + \frac{\dot{A}\dot{B}}{AB}\right) = 3\beta p - \left(8\pi + \frac{3\beta}{2}\right)\varepsilon \tag{22}$$

$$\alpha\left(2\frac{d}{dt}\left(\frac{\dot{A}}{A}\right) + \frac{d}{dt}\left(\frac{\dot{B}}{B}\right) + 3\frac{\dot{A}^2}{A^2} + \frac{\dot{B}^2}{B^2} + 2\frac{\dot{A}\dot{B}}{AB}\right) = (8\pi + 4\beta)p - \frac{\beta}{2}\varepsilon \tag{23}$$

$$3\alpha\left(\frac{d}{dt}\left(\frac{\dot{A}}{A}\right) + 2\frac{\dot{A}^2}{A^2}\right) = (8\pi + 4\beta)p - \frac{\beta}{2}\varepsilon \tag{24}$$

Subtracting Eq. (24) from (23), we get

$$\frac{d}{dt}\left(\frac{\dot{B}}{B} - \frac{\dot{A}}{A}\right) + \left(\frac{\dot{B}}{B} - \frac{\dot{A}}{A}\right)\frac{\dot{V}}{V} = 0 \tag{25}$$

which on integration yields

$$\frac{B}{A} = c_2 exp\left[c_1 \int \frac{dt}{V}\right] \tag{26}$$

where c_1 and c_2 are constants of integration.
Using Eq. (17), the scale factors A and B can be written explicitly as

$$A = c_2^{-\frac{1}{4}}\, V^{\frac{1}{4}}\, exp\left[-\frac{c_1}{4}\int \frac{dt}{V}\right] \tag{27}$$

$$B = c_2^{\frac{3}{4}}\, V^{\frac{1}{4}}\, exp\left[\frac{3c_1}{4}\int \frac{dt}{V}\right] \tag{28}$$

In terms of the directional Hubble parameters, we can express the fields Eqs. (22) – (24) as

$$3\alpha\left(H_x^2 + H_x H_\psi\right) = 3\beta p - \left(8\pi + \frac{3\beta}{2}\right)\varepsilon \tag{29}$$

$$\alpha\left(2\dot{H}_x + \dot{H}_\psi + 3H_x^2 + H_\psi^2 + 2H_x H_\psi\right) = (8\pi + 4\beta)p - \frac{\beta}{2}\varepsilon \tag{30}$$

$$3\alpha\left(2H_x^2 + \dot{H}_x\right) = (8\pi + 4\beta)p - \frac{\beta}{2}\varepsilon \tag{31}$$

Equations (29), (30) provide us the general formulations for the physical parameters of the $f(Q,T)$ model. Pressure and energy density for the model can be explicitly expressed in terms of the directional Hubble parameters as

$$p = \frac{\delta}{(8\pi+4\beta)}\left\{2(3\beta^2 + 32\pi^2 + 22\pi\beta)\dot{H}_x + (10\beta^2 + 128\pi^2 + 84\pi\beta)H_x^2 - \frac{\beta}{2}(8\pi + 4\beta)H_x H_\psi\right\} \tag{32}$$

$$\varepsilon = \delta\left\{3\beta\dot{H}_x - 2(4\pi - \beta)H_x^2 - (8\pi + 4\beta)H_x H_\psi\right\} \tag{33}$$

where

$$\delta = \frac{3\alpha}{\frac{9}{2}\beta^2 + 64\pi^2 + 44\pi\beta}$$

Equation of state is considered to be an important quantity for the description of dynamics of the universe. The equation of state parameter as a whole determines a relation between energy density and pressure. Using the expressions of p and ε , the equation of state parameter can be calculated as

$$\omega = \frac{2\left(3\beta^2+32\pi^2+22\pi\beta\right)\dot{H}_x+\left(10\beta^2+128\pi^2+84\pi\beta\right)H_x^2-\frac{\beta}{2}(8\pi+4\beta)H_x H_\psi}{(8\pi+4\beta)\left\{3\beta\dot{H}_x-2(4\pi-\beta)H_x^2-(8\pi+4\beta)H_x H_\psi\right\}} \tag{34}$$

Further, we have three independent equations (14) to (16) in four unknowns A, B, ε, p. To obtain viable cosmological model with determinate solutions, we require some additional condition. After thoroughly reviewing References [38] and [46], two different volumetric expansions are considered such as power law expansion and exponential law expansion.

5. POWER LAW EXPANSION MODEL

Here, we consider a power law volumetric expansion

$$V = t^{4m} \tag{35}$$

where m is a positive constant. The positivity of the exponent m aligns with empirical observations suggesting an expanding universe. Spatial volume of the universe starts with big-bang initially and with the increase of time, it expands. This demonstrates that universe begins its evolution with zero volume and expands with time t.

The power law expansion of the cosmos predicts a deceleration parameter $q = -1 + \frac{d}{dt}\left(\frac{1}{H}\right) = -1 + \frac{1}{m}$. Maintaining an outlook on the recent observational evidence favouring an accelerating cosmos, we choose to go in support of a negative deceleration parameter. For the current framework, this implies that the value of m should be greater than 1.

The metric potentials A and B can be obtained by using Eq. (35) in Eqs. (27) and (28) as

$$A = c_2^{-\frac{1}{4}}\, t^m\, exp\left[-\frac{c_1 t^{1-4m}}{4(1-4m)}\right] \tag{36}$$

$$B = c_2^{\frac{3}{4}}\, t^m\, exp\left[\frac{3c_1 t^{1-4m}}{4(1-4m)}\right] \tag{37}$$

It is seen that initially the scale factors A and B vanishes possessing initial singularity and at $t \to \infty$, both A and B diverge to infinity which aligns perfectly with the Big-Bang model of the universe.

Accordingly, the directional Hubble parameters in respective directions are

$$H_x = H_y = H_z = H - \frac{c_1}{4} t^{-4m} \tag{38}$$

$$H_\psi = H + \frac{3c_1}{4} t^{-4m} \tag{39}$$

The various cosmological parameters such as Hubble parameter H, expansion scalar θ, the shear scalar σ^2 and the mean anisotropic parameter A_m are obtained as

$$H = \frac{m}{t} \tag{40}$$

$$\theta = \frac{4m}{t} \tag{41}$$

$$\sigma^2 = \frac{9}{32} c_1^2 t^{-8m} \tag{42}$$

$$A_m = \frac{3c_1^2 t^{2(1-4m)}}{16m^2} \tag{43}$$

From the expression (40), (41) and (42), it is observed that Hubble parameter H, expansion scalar θ and shear scalar σ^2 are decreasing function of time. They diverge to infinity as $t \to 0$ and becomes zero as $t \to \infty$. The shear scalar diminishes but doesn't entirely disappear, implying that the universe's anisotropic nature gradually weakens, but never attains a perfectly isotropic state. The mean anisotropy parameter A_m is extremely high at $t = 0$ and approaches zero as $t \to \infty$. This rapid decline indicates that the universe is initially anisotropic but evolves towards isotropy at later times.

Pressure p, energy density ε for the model (9) can be obtained from Eqs. (32)-(33) and Eqs. (38)-(39) as

$$p = \frac{\delta}{(8\pi+4\beta)}\left\{\left[\frac{1}{2}(4m-3)\beta^2 + 16(2m-1)\pi^2 + (20m-11)\pi\beta\right]\frac{4m}{t^2} + (\beta^2 + 8\pi^2 + 6\pi\beta)c_1^2 t^{-8m}\right\} \tag{44}$$

$$\varepsilon = \frac{\delta}{8}\left\{(8\pi + 7\beta)c_1^2 t^{-8m} - \left[\beta\left(\frac{3}{2m} + 1\right) + 8\pi\right]\frac{16m^2}{t^2}\right\} \tag{45}$$

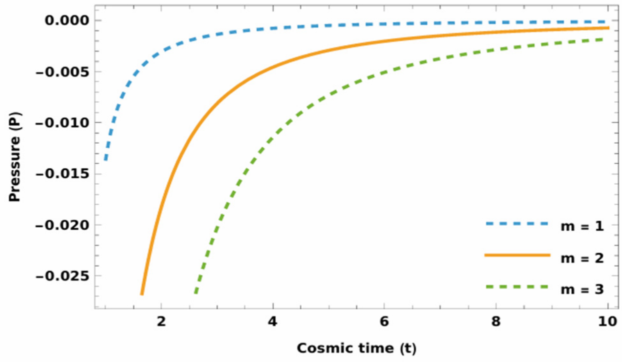

Figure 1. Plot of Pressure vs cosmic time $\boldsymbol{t}$ with $\boldsymbol{\alpha = \beta = -0.1, c_1 = 1}$

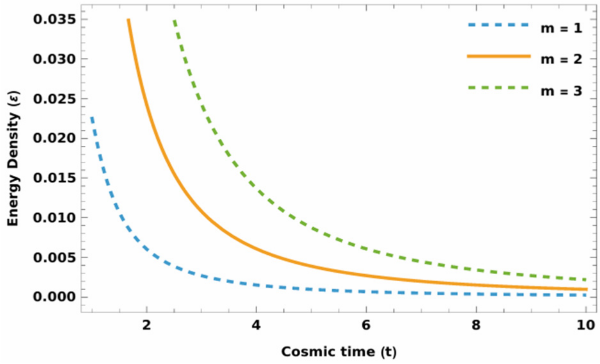

Figure 2. Plot of Energy density vs cosmic time $\boldsymbol{t}$ with $\boldsymbol{\alpha = \beta = -0.1, c_1 = 1}$

Figure 1 depicts the behavior of pressure over cosmic time reflects the dynamic character of dark energy within the universe. Pressure remains negative throughout cosmic evolution, gradually increasing from a highly negative value and vanishes at infinite time. Again, supporting additional evidence for the universe's accelerated expansion. This trend is typical of certain dark energy models, where dark energy's impact diminishes over time, resulting in a more stable universe. A negative pressure is thought to be necessary for generating an anti-gravity effect that drives this acceleration. Figure 2 depicts the energy density for the power law model. Energy density is positive throughout the time evolution and decreases over time. The initial density is extremely large and drops swiftly to a constant value, as parameter m becomes larger. For small values of m, density settles close to zero, signifying lasting steady condition where the effect on the universe's expansion remains constant.

The equation of state parameter for this model is

$$\omega = \left(\frac{2}{2\pi+\beta}\right)\left\{\frac{\left[\frac{1}{2}(4m-3)\beta^2+16(2m-1)\pi^2+(20m-11)\pi\beta\right]\frac{4m}{t^2}+(\beta^2+8\pi^2+6\pi\beta)c_1^2t^{-8m}}{(8\pi+7\beta)c_1^2t^{-8m}-\left[\beta\left(\frac{3}{2m}+1\right)+8\pi\right]\frac{16m^2}{t^2}}\right\} \tag{46}$$

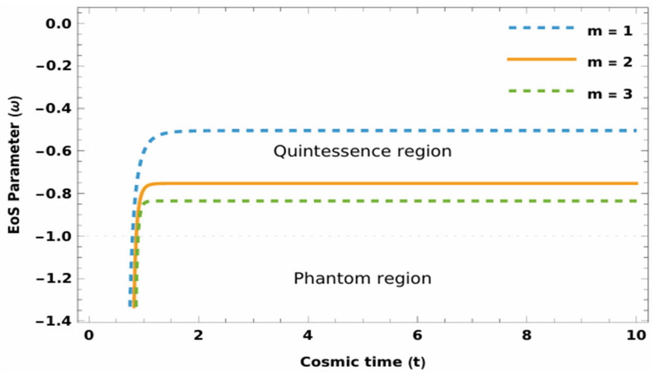

Figure 3. Plot of EoS parameter vs cosmic time $\boldsymbol{t}$ with $\boldsymbol{\alpha = \beta = -0.1, c_1 = 1}$

Figure 3 represents the graphical representation of EoS parameter (ω) and cosmic time. Initially, the universe evolves in the phantom region $(\omega < -1)$, crossing the divide line $\omega = -1$, suddenly enters into quintessence region $-1 < \omega < -{}^{1}/_{3}$ and ω remains fixed with advancing time. A similar behavior of EoS parameter has been observed by some researcher [38].

6. EXPONENTIAL EXPANSION MODEL

The exponential expansion of volume factor

$$V = e^{4nt} \tag{47}$$

typically results in a de Sitter kind of universe. Here n is constant. The Hubble parameter is a constant quantity throughout the universe's expansion. For this choice, the directional Hubble parameters will be

$$H_x = H_y = H_z = n - \frac{c_1}{4}e^{-4nt} \tag{48}$$

$$H_\psi = n + \frac{3c_1}{4} e^{-4nt} \tag{49}$$

It's noteworthy that although the mean Hubble parameter is a constant quantity, the directional Hubble values exhibit time dependence. The expansion rate along the conventional axes increases from $n - \frac{c_1}{4}$ in the initial stage to the constant value n at the later stage. Whereas, the expansion rate along the extra dimension diminishes from $n + \frac{3c_1}{4}$ in the initial stage to the constant value n at the later stage. The deceleration parameter for this model is $q = -1$. The obtained model matches the current scenario of accelerating expansion of the universe, as the sign of deceleration parameter is negative.

For this model, the metric potentials A and B using the Eq. (47) are obtained as

$$A = c_2^{-\frac{1}{4}} exp\left[nt + \frac{c_1}{16n} e^{-4nt}\right] \tag{50}$$

$$B = c_2^{\frac{3}{4}} exp\left[nt - \frac{3c_1}{16n} e^{-4nt}\right] \tag{51}$$

Initially the model has no singularity as the metric potentials A and B are constant at $t = 0$.

The various cosmological parameters such as Hubble parameter H, expansion scalar θ, the shear scalar σ^2 and the mean anisotropic parameter A_m are found to be

$$H = n \tag{52}$$

$$\theta = 4n \tag{53}$$

$$\sigma^2 = \frac{9}{32} c_1^2 e^{-8nt} \tag{54}$$

$$A_m = \frac{3c_1^2 e^{-8nt}}{16n^2} \tag{55}$$

From the Eqs. (52) and (53), it is observed that Hubble parameter H, expansion scalar θ are constant throughout the evolution. Shear scalar σ^2 is decreasing function of time t. It can be observed that the shear scalar $\sigma^2 \to 0$ as $t \to \infty$. The ratio of shear scalar to expansion scalar was non-zero initially, but decreased to zero as time progressed, indicating the universe was initially anisotropic and at a later time it approaches isotropy. The mean anisotropic parameter A_m remains fixed in an initial phase i.e. the universe was anisotropic in the early stage and evolves isotropically in later times.

Pressure p, energy density ε for the model (9) can be obtained from Eqs. (32)-(33) and Eqs. (48)-(49) as

$$p = \frac{\delta}{(8\pi + 4\beta)}\{8(\beta^2 + 16\pi^2 + 10\pi\beta)n^2 + (\beta^2 + 8\pi^2 + 6\pi\beta)c_1^2 e^{-8nt}\} \tag{56}$$

$$\varepsilon = \delta\left\{-2(8\pi + \beta)n^2 + \frac{1}{8}(8\pi + 7\beta)c_1^2 e^{-8nt}\right\} \tag{57}$$

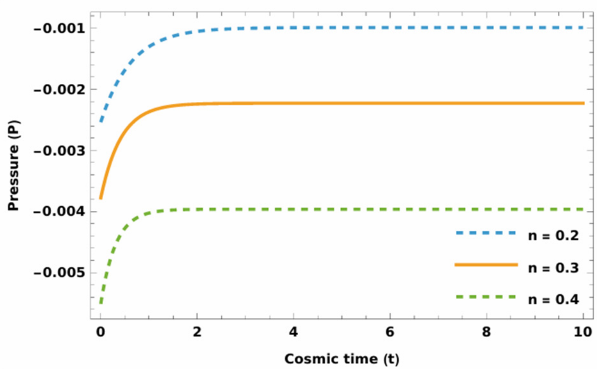

Figure 4. Plot of Pressure vs cosmic time $\boldsymbol{t}$ with $\boldsymbol{\alpha = \beta = -0.1, c_1 = 1}$

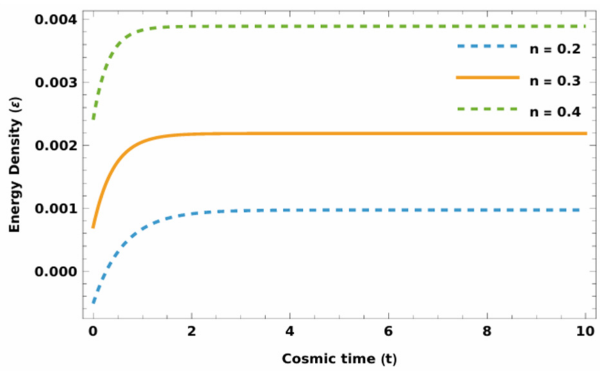

Figure 5. Plot of Energy density vs cosmic time $\boldsymbol{t}$ with $\boldsymbol{\alpha = \beta = -0.1, c_1 = 1}$

Figures 4 and 5 depicted the graphical behavior of pressure and energy density. The pressure is negative throughout the time of evolution which indicates that the matter behaves like dark energy. Pressure and energy density are increasing function of cosmic time. Pressure increases from a large negative value at the initial epoch and approaches to a constant value. Energy density was constant near $t = 0$, then increased slightly to its maximum value and remains constant over time. So, in this model, a steady state for pressure and energy density is rapidly achieved.
The equation of state parameter for this model is found to be

$$\omega = \left(\frac{1}{8\pi+4\beta}\right)\left\{\frac{8(\beta^2+16\pi^2+10\pi\beta)n^2+(\beta^2+8\pi^2+6\pi\beta)c_1^2e^{-8nt}}{-2(8\pi+\beta)n^2+\frac{1}{8}(8\pi+7\beta)c_1^2e^{-8nt}}\right\} \tag{58}$$

The evolution trajectory of EoS parameter (ω) depicted in Fig. 6. It is clear that, ω lies in the phantom region. As time grows, it increases from a high negative value, approaches to -1.02 at late times.

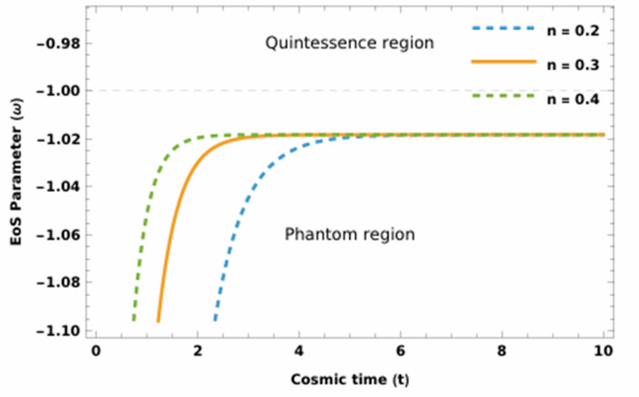

Figure 6. Plot of EoS parameter vs cosmic time $\boldsymbol{t}$ with $\boldsymbol{\alpha = \beta = -0.1, c_1 = 1}$

7. STATEFINDER DIAGNOSTIC, ENERGY CONDITIONS AND STABILITY ANALYSIS

7.1. Statefinder Diagnostic

Statefinder analysis is a cosmological method used to study the dynamics of the universe. It is a key approach to understand various dark energy models. A statefinder pair (r, s) consists of two dimensionless parameters employed in cosmology to distinguish between various cosmological models by investigating the evolution of the cosmic scale factor a and its temporal derivatives. Sahni et al. [47] were the first to introduce these parameters as an extension of the EoS parameter (ω) to analyze the dark energy and the expansion history of the universe. The statefinder parameters are defined as follows:

$$r = \frac{\dddot{a}}{aH^3} = 2q^2 + q - \frac{\dot{q}}{H} \quad \text{and} \quad s = \frac{(r-1)}{3(q-1/2)} \tag{59}$$

The statefinder parameter r measures how much cosmic expansion deviates from a pure-law behavior, while parameter s describes its acceleration. It is a model-dependent approach to distinguish between different dark energy scenarios such as the ΛCDM (Lambda Cold Dark Matter), SCDM (Standard Cold Dark Matter), HDE (Holographic Dark Energy), CG (Chaplygin Gas) and quintessence. For corresponding values of r and s parameters, here are some DE scenarios:

- $(r, s) = (1, 0)$ represents ΛCDM scenario.
- $(r, s) = (1, 1)$ represents SCDM scenario.
- $(r, s) = (1, 2/3)$ represents HDE scenario.
- $r > 1, s < 0$ represents CG scenario.
- $r < 1, s > 0$ represents Quintessence scenario.

In power law model, the relationship between the two statefinder parameter is

$$r = \frac{9s^2-9s+2}{2} \tag{60}$$

The graphical plot of the statefinder parameter r versus s is presented in Fig. 7. Its evolution moves through the dark energy zone of Chaplygin gas and quintessence in the r-s plane and tends to approach the ΛCDM model in the upcoming epoch, which is consistence with the findings discussed by Shaikh [40,48].

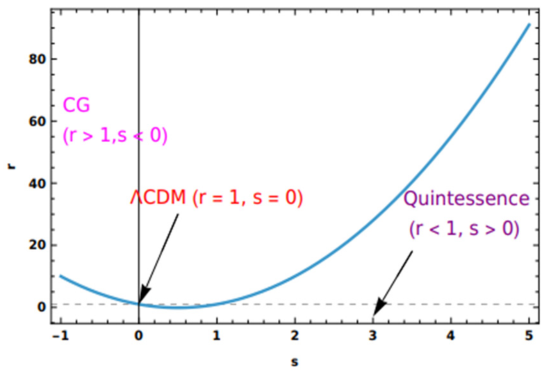

Figure 7. Plot of $\boldsymbol{r}$ versus $\boldsymbol{s}$ in power law model

In exponential model, the statefinder parameters are found as $r = 1$ and $s = 0$. Hence the model behaves like ∧CDM model currently and in the future cosmic evolution which is consistent with the investigations of Katore et al. [38] and Shaikh [40].

7.2. Energy Conditions

The energy conditions are the expressions that describe how energy density and pressure relate linearly. It plays a crucial role in understanding the singularity theorem, describing the nature of geodesics and studying black holes properties. The energy conditions are also intrinsic for comprehending the geodesics of the universe from the cosmological point of view. The energy conditions are constraints on the energy-momentum tensor which are obtained by linking Raychaudhuri equation [49] and the Einstein field equation. There are four widely used fundamental energy conditions. These energy conditions are described in $f(Q,T)$ gravity, specifically in terms of energy density ε and pressure p as follows:

- SEC (Strong Energy condition): $\varepsilon + 3p \geq 0$
- NEC (Null Energy condition): $\varepsilon + p \geq 0$
- WEC (Weak Energy condition): $\varepsilon \geq 0$, $\varepsilon + p \geq 0$
- DEC (Dominant Energy condition): $\varepsilon \geq |p|$, $\varepsilon \geq 0$

Figures 8 and 9 illustrates graphical representation of SEC, NEC and DEC versus cosmic time for power law and exponential law respectively. In power law model, we have observed a consistent fulfillment of WEC($\varepsilon \geq 0$), NEC($\varepsilon + p \geq 0$), DEC($\varepsilon - p \geq 0$) throughtout the cosmic evolution. However SEC is found to be violated in this model. Further, the violation of SEC results in accelerating expansion of the universe. It should be noted that our investigation agrees with the investigation of Koussour et al. [50]. In exponential law model, we observed that NEC and SEC are violated while DEC is satisfied as shown in Fig. 9, which is consistent with the investigations of Koussour [51]. As a result, violation of SEC and NEC causes the universe to accelerate and behave like a phantom model.

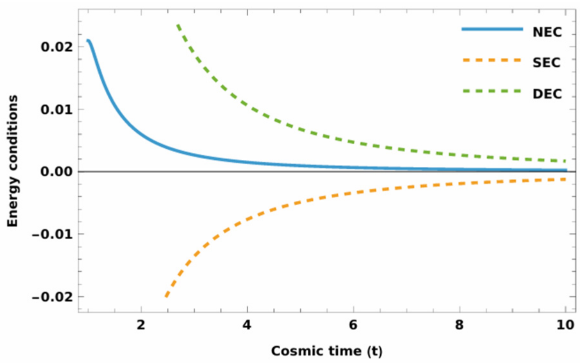

Figure 8. Plot of Energy conditions vs cosmic time $\boldsymbol{t}$ in power law model

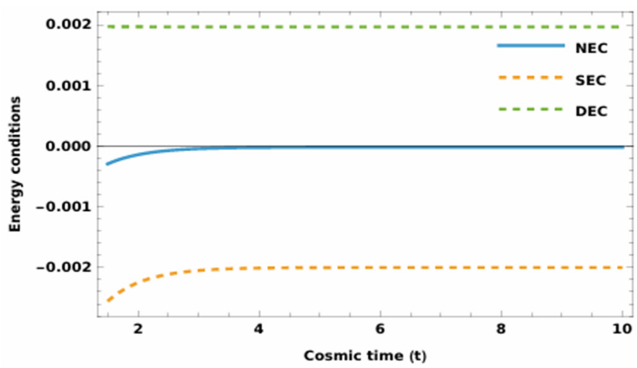

Figure 9. Plot of Energy conditions vs cosmic time $\boldsymbol{t}$ in exponential law model

7.3. Stability Analysis

Depending on the sign of the squared sound speed υ_s^2, it becomes simpler to check the compatibility of dark energy models. The model's stability is examined by the positive sign of υ_s^2, while instability is determined by a

negative υ_s^2. Also, to ensure mechanical stability, υ_s^2 should not exceed 1. Therefore, the region bounded by $0 < \upsilon_s^2 < 1$ gives stable solutions.
The stability parameter of the model is defined as

$$\upsilon_s^2 = \frac{dp}{d\varepsilon} \tag{61}$$

For power expansion law model, the stability parameter υ_s^2 is found to be

$$\upsilon_s^2 = \left(\frac{2}{2\pi+\beta}\right)\left\{\frac{\left[\frac{1}{2}(4m-3)\beta^2+16(2m-1)\pi^2+(20m-11)\pi\beta\right]\frac{1}{t^3}+(\beta^2+8\pi^2+6\pi\beta)c_1^2 t^{-8m-1}}{(8\pi+7\beta)c_1^2 t^{-8m-1}-\left[\beta\left(\frac{3}{2m}+1\right)+8\pi\right]\frac{4m}{t^3}}\right\} \tag{62}$$

Figure 10 plots the squared sound speed versus cosmic time in power law model. It is observed that in power law model, $\upsilon_s^2 < 0$ for $m \geq 0.5$, hence the model is unstable in the present and late-time phases of cosmic evolution. For $m < 0.5$, the squared sound speed υ_s^2 is negative at the early stages of the cosmic evolution and tends to positive at late-time. Thus for $m < 0.5$, the model exhibits instability in early cosmic evolution and become stable as the universe evolves.

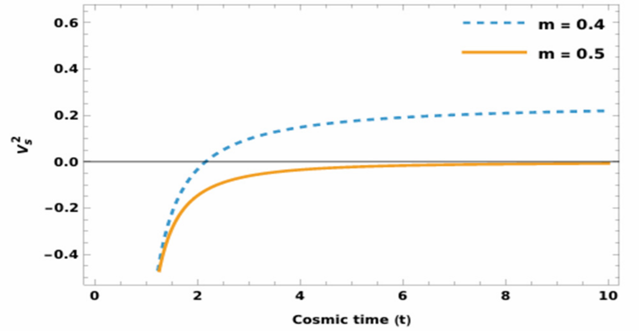

Figure 10. Plot of Squared speed sound vs cosmic time t in power law model

For Exponential expansion law model, the stability parameter υ_s^2 is found to be

$$\upsilon_s^2 = \frac{8(\beta^2+8\pi^2+6\pi\beta)}{(8\pi+4\beta)(8\pi+7\beta)} \tag{63}$$

Thus, the model is stable as $\upsilon_s^2 > 0$.

8. CONCLUSION

In this work, the dynamics of a five-dimensional Kaluza-Klein metric in presence of matter distribution is studied in the framework of $f(Q,T)$ gravity by considering two different kinds of volumetric expansion namely power law and exponential volumetric expansion.
In power law model:

- The metric potentials vanish initially and eventually diverge to infinity as $t \longrightarrow \infty$. Thus, the model consistent with a big-bang model and has an initial singularity.
- Hubble parameter and expansion scalar diverges initially but approaches zero monotonically as time tends to infinity.
- Mean anisotropy parameter decreases with time and approaches to zero as $t \longrightarrow \infty$. This rapid decline indicates that the universe is initially anisotropic but evolves towards isotropy at later times.
- For the value of parameter $m > 1$, the deceleration parameter is negative which shows that universe undergoes accelerated expansion.
- The initial density is extremely large and drops swiftly to a constant value signifying steady condition.
- The dynamics of the universe is studied using equation of state parameter. In this model, initially the universe evolves in the phantom region, crossing the phantom divide line, suddenly enters into quintessence region and ω remains fixed with advancing time.
- From the statefinder diagnosis, we observed that r-s trajectory moves through the dark energy zone of Chaplygin gas and quintessence and tends to approach the $\wedge$CDM model in the upcoming epoch as shown in Fig. 7.

- The model satisfies NEC and DEC but SEC is violated as shown in Fig. 8. The violation of SEC results in accelerating expansion of the universe.
- The model is unstable for $m \geq 0.5$ as shown in Fig. 10. However, for $m < 0.5,$ the model is unstable at the early phases of cosmic evolution and is stable at late-time.

In Exponential volumetric expansion law:

- The metric potentials accept constant value at initial time and after which they eventually diverge to infinity. Thus, it is free from any type of singularity.
- Hubble parameter and expansion scalar exhibits constant value throughout the evolution indicating uniform exponential expansion i.e. as time t increases, the universe expands homogeneously from initial epoch to infinity.
- Mean anisotropy parameter shows a constant value at initial epoch, indicating that universe approaches isotropy.
- The deceleration parameter is $q = -1$ which indicates that universe accelerating expansion matches current observations.
- Energy density was constant near $t = 0$ and then increased slightly and remains constant as time increases achieving steady state.
- EoS parameter ω lies in the phantom region. As time progresses, it increases from a high negative value and approaches to value -1.2 at late times.
- From the statefinder diagnosis, we observed that the exponential law model behaves more like a ΛCDM model having statefinder pair $(r, s) = (1,0)$.
- NEC and SEC are violated while DEC is satisfied as shown in Fig. 9.
- The model is stable.

It is important to note that for both models, the pressure is negative throughout the time of evolution gradually increasing from a highly negative value and vanishes at infinite time which indicates that the matter behave like dark energy.

Overall, the proposed model effectively describes cosmic evolution and offers a flexible framework for understanding the late-time acceleration of the universe.

Acknowledgments

We would like to express sincere gratitude to the anonymous reviewers for their valuable comments and constructive suggestions, which significantly improved the quality and clarity of this manuscript.

ORCID

M.T. Sarode, https://orcid.org/0009-0001-8467-4744; **V.G. Mete,** https://orcid.org/0000-0002-0526-6372

REFERENCES

[1] A. G. Riess, *et al.*, Astron. J. **116**, 1009 (1998). https://doi.org/10.1086/300499
[2] A. G. Riess, *et al.*, Astrophys. J. **560**, 49 (2001). https://doi.org/10.1086/322348
[3] S. Perlmutter, *et al.,* Astrophys. J. **517**, 565 (1999). https://doi.org/10.1086/307221
[4] C. L. Bennett, *et al.*, Astrophys. J. **583**, 1 (2003). https://doi.org/10.1086/345346
[5] D. N. Spergel, *et al.,* Astrophys. J. Suppl. Ser. **148**, 175 (2003). https://doi.org/10.1086/377226
[6] S. I. Nojiri, S. D. Odintsov and P. V. Tretyakov, Phys. Lett. B **651**, 224 (2007). https://doi.org/10.1016/j.physletb.2007.06.029
[7] H. A. Buchdahl, Mon. Not. R. Astron. Soc. **150**, 1 (1970). https://doi.org/10.1093/mnras/150.1.1
[8] T. Harko, F. S. Lobo, S. I. Nojiri and S. D. Odintsov, Phys. Rev. D **84**, 024020 (2011). https://doi.org/10.1103/PhysRevD.84.024020
[9] Y. F. Cai, S. Capozziello, M. De. Laurentis and E. N. Saridakis, Rep. Prog. Phys. **79**, 106901 (2016). https://doi.org/10.1088/0034-4885/79/10/106901
[10] M. Sharif and A. Ikram, Eur. Phys. J. C **76**, 640 (2016). http://doi.org/10.1140/epjc/s10052-016-4502-1
[11] I. Ayuso, J. Beltrán Jiménez and Á. de la Cruz-Dombriz, Phys. Rev. D **91**, 104003 (2015). https://doi.org/10.1103/PhysRevD.91.104003
[12] J. M. Nester and H. J. Yo, arXiv preprint gr-qc/9809049 (1998). https://doi.org/10.48550/arXiv.gr-qc/9809049
[13] Y. Xu, G. Li, T. Harko and S. D. Liang, Eur. Phys. J. *C* **79**, 708 (2019). https://doi.org/10.1140/epjc/s10052-019-7207-4
[14] Y. Xu, T. Harko, S. Shahidi and S. D. Liang, Eur. Phys. J. C **80**, 449 (2020). https://doi.org/10.1140/epjc/s10052-020-8023-6
[15] V. G. Mete, M. T. Sarode, J. S. Wath, Sch J Phys Math Stat **13***,* 49 (2026). https://doi.org/10.36347/sjpms.2026.v13i01.006
[16] N. Godani and G. C. Samanta, Int. J. Geom. Methods Mod. Phys. **18**, 2150134 (2021). https://doi.org/10.1142/S0219887821501346
[17] R. Zia, D. C. Maurya and A. K. Shukla, Int. J. Geom. Methods Mod. Phys. **18**, 2150051 (2021). https://doi.org/10.1142/S0219887821500511
[18] M. Narzary and M. Dewri, J. Sci. Res. **18**, 53 (2026). https://dx.doi.org/10.3329/jsr.v18i1.81063

[19] S. Arora and P. K. Sahoo, Phys. Scr. **95**, 095003 (2020). https://doi.org/10.1088/1402-4896/abaddc
[20] M. Shiravand, S. Fakhry and M. Farhoudi, Phy. Dark Univ. **37**, 101106 (2022). https://doi.org/10.1016/j.dark.2022.101106
[21] K. El Bourakadi, M. Koussour, G. Otalora, M. Bennai and T. Ouali, Phy. Dark Univ. **41**, 101246 (2023). https://doi.org/10.1016/j.dark.2023.101246
[22] M. Tayde, Z. Hassan and P. K. Sahoo, Nucl. Phys. B **1000**, 116478 (2024). https://doi.org/10.1016/j.nuclphysb.2024.116478
[23] M. Tayde, J. R. Santos, J. N. Araujo and P. K. Sahoo, Eur. Phys. J. Plus **138**, 539 (2023). https://doi.org/10.1140/epjp/s13360-023-04172-1
[24] M. Tayde, S. Ghosh and P. K. Sahoo, Chin. Phys. C **47**, 075102 (2023). https://doi.org/10.1088/1674-1137/acd2b7
[25] R. Bhagat, S. V. Lohakare and B. Mishra, Phy. Dark Univ. **49**, 102048 (2025). https://doi.org/10.1016/j.dark.2025.102048
[26] A. Nájera and A. Fajardo, Phy. Dark Univ. **34**, 100889 (2021). https://doi.org/10.1016/j.dark.2021.100889
[27] S. Bhattacharjee and P. K. Sahoo, Eur. Phys. J. C **80**, 289 (2020). https://doi.org/10.1140/epjc/s10052-020-7844-7
[28] A. S. Agrawal, L. Pati, S. K. Tripathy and B. Mishra, Phy. Dark Univ. **33**, 100863 (2021). https://doi.org/10.1016/j.dark.2021.100863
[29] A. Zhadyranova, M. Koussour and S. Bekkhozhayev, Chin. J. Phys. **89**, 1483 (2024). https://doi.org/10.1016/j.cjph.2024.04.023
[30] M. Narzary and M. Dewri, Edelweiss Appl. Sci. Technol. **9**, 2623 (2025). https://doi.org/10.55214/25768484.v9i5.7526
[31] L. Pati, S. A. Kadam, S. K. Tripathy and B. Mishra, Phy. Dark Univ. **35**, 100925 (2022). https://doi.org/10.1016/j.dark.2021.100925
[32] T. Kaluza, Sitzungsber. Preuss. Akad. Wiss. Berlin (Math. Phys.) **1921**, 966 (1921). https://doi.org/10.1142/S0218271818700017
[33] O. Klein, Zeitschrift für Physik **37**, 895 (1926). https://doi.org/10.1007/BF01397481
[34] V. G. Mete, V. S. Deshmukh and D. V. Kapse, J. Sci. Res. **16**, 479 (2024). https://doi.org/10.3329/jsr.v16i2.68364
[35] N. I. Jain, Int. J. Math. Phys. **14**, 95 (2023). https://doi.org/10.26577/ijmph.2023.v14.i1.011
[36] P. K. Ray, R. Roy Baruah, East Eur. J. Phys. **2**, 452 (2025). https://doi.org/10.26565/2312-4334-2025-2-56
[37] D. D. Pawar, B. L. Jakore and V. J. Dagwal, Int. J. Geom. Methods Mod. Phys. **20**, 2350079 (2023). https://doi.org/10.1142/S0219887823500792
[38] S. D. Katore, S. P. Hatkar and D. P. Tadas, Astrophys. **66**, 98 (2023). https://doi.org/10.1007/s10511-023-09773-3
[39] S. C. Wankhade, A.S. Nimkar, Eur. Phys. J. C **85**, 769 (2025). https://doi.org/10.1140/epjc/s10052-025-14464-8
[40] A. Y. Shaikh, Bulg. J. Phys. **49**, 190 (2022). https://doi.org/10.55318/bgjp.2022.49.2.190
[41] P. K. Sahoo, B. Mishra and S. K. Tripathy, Indian J. Phys. **90**, 485 (2016). https://doi.org/10.1007/s12648-015-0759-8
[42] M. R. Ugale, H. A. Nimkar, A. O. Dhore, Sch J Phys Math Stat **12**, 357 (2025). https://doi.org/10.36347/sjpms.2025.v12i08.003
[43] J. S. Wath and A. S. Nimkar, Jnanabha **54**, 1 (2024). https://doi.org/10.58250/jnanabha.2024.54101
[44] A. S. Nimkar and S. R. Hadole, J. Sci. Res. **15**, 55 (2023). https://doi.org/10.3329/jsr.v15i1.59676
[45] L. D. Landau and E. M. Lifshitz, *The Classical Theory of Fields*, Fourth Revised English Edition (Pergamon Press ,1994).
[46] S. Thakre, R. Mapari and V. Thakare, East Eur. J. Phys. **2**, 21 (2024). https://doi.org/10.26565/2312-4334-2024-2-02
[47] V. Sahni, T. D. Saini, A. A. Starobinsky and U. Alam, JETP Letters **77**, 201 (2003). https://doi.org/10.1134/1.1574831
[48] A. Shaikh, A. Jenekar and S. Shingne, East Eur. J. Phys. **3**, 4 (2025). https://doi.org/10.26565/2312-4334-2025-3-01
[49] A. Raychaudhuri, Phys. Rev. **98**, 1123 (1955). https://doi.org/10.1103/PhysRev.98.1123
[50] M. Koussour, N. Myrzakulov, J. Rayimbaev, A. Errehymy and O. Donmez, Chin. J. Phys. **90**, 108 (2024). https://doi.org/10.1016/j.cjph.2024.04.024
[51] M. Koussour, Chin. J. Phys. **83**, 454 (2023). https://doi.org/10.1016/j.cjph.2023.04.003

КОСМІЧНЕ ПРИСКОРЕННЯ ТА СТАБІЛЬНІСТЬ ВСЕСВІТУ КАЛУЦИ-КЛЕЙНА В f(Q,T) ГРАВІТАЦІЇ

М.Т. Сароде[1], В.Г. Мете[2], А.С. Німкар[3]
[1]*Факультет математики, коледж мистецтв, торгівлі та науки Шрі Шіваджі, Акола (М.С.), Індія*
[2]*Кафедра математики, коледж R. D. I. K. & K. D., Баднера – Амраваті (MS), Індія*
[3]*Кафедра математики, коледж мистецтв і науки Шрі доктора Р. Г. Ратода, округ Муртізапур. Акола (MS), Індія*

Гравітація f(Q,T) була використана в цьому дослідженні для вивчення Всесвіту Калуци-Клейна за наявності розподілу матерії. У цій теорії гравітації дія містить довільну функцію f(Q,T), де Q та T відповідно позначають неметричність та слід тензора імпульсу енергії. У цій роботі враховується лінійна та адитивна форма гравітації f(Q,T), $f(Q,T)=\alpha Q+\beta T$, де α та β - довільні константи. Щоб досягти фізично життєздатного розв'язку рівнянь поля, ми розглянули степеневий закон та закон експоненціального розширення. Ми досліджуємо еволюціонуючий характер Всесвіту з фізичними та геометричними властивостями в рамках цієї теоретичної бази. Для кращої ясності досліджуються діагностика пошуку стану та параметр EoS, щоб охарактеризувати різні фази Всесвіту. Енергетичні умови моделей також аналізуються та виявляються такими, що узгоджуються з останніми космологічними спостереженнями. Крім того, одна з наших моделей за своєю суттю допускає фантомну область для темної енергії. Далі моделі, розглянуті в цій роботі, підтверджені за допомогою аналізу стійкості.

Ключові слова: *гравітація f(Q,T); простір-час Калуци-Клейна; рівняння стану; енергетичні умови*

East European Journal of Physics. **3**. 90–102 (2026)
DOI: 10.26565/2312-4334-2026-3-08 ISSN 2312-4334

COSMOLOGICAL EVOLUTION OF AN ANISOTROPIC BIANCHI TYPE-VI$_0$ UNIVERSE WITH RÉNYI HOLOGRAPHIC DARK ENERGY

Chandra Rekha Mahanta, **Rajashree Mahanta***
Department of Mathematics, Gauhati University, Guwahati - 781014 (INDIA)
**Corresponding Author e-mail: rajashree.mahanta@gauhati.ac.in*
Received April 6, 2025; revised July 26, 2025; in final form August 16, 2026; accepted August 16, 2026

In this work, we investigate a spatially homogeneous and anisotropic Bianchi type-VI$_0$ cosmological model within the framework of General Relativity by considering a non-interacting mixture of pressureless dark matter and Rényi holographic dark energy (RHDE), with the Hubble horizon serving as the infrared cutoff. Exact solutions of the Einstein field equations are obtained by adopting the hyperbolic scale factor $a(t) = (\sinh(\beta t))^{1/n}$. The model parameters are constrained through a Markov Chain Monte Carlo (MCMC) analysis using 77 Observational Hubble Data (OHD) measurements of the Hubble parameter, yielding the best-fit values $H_0 = 67.9$ km s^{-1} Mpc^{-1} and $n = 1.3$. A comparison with the standard ΛCDM model reveals a slightly lower minimum χ^2 value together with negative values of ΔAIC and ΔBIC, indicating a modest statistical preference for the proposed model. The reconstructed cosmic evolution exhibits a smooth transition from a matter-dominated decelerating phase to the present accelerated epoch, with the transition redshift lying within the observationally favored range $0.5 \lesssim z_t \lesssim 0.7$. Furthermore, the evolution of the matter and RHDE energy densities, dark energy pressure, equation-of-state parameter, anisotropy parameter and skewness parameter demonstrates that the model successfully reproduces the observed late-time accelerated expansion while undergoing a gradual isotropization. Overall, the proposed RHDE model provides a physically consistent and observationally viable framework for describing the late-time evolution of the Universe.

Keywords: *Cold dark matter; Bianchi type-VI_0 spacetime; Cosmic acceleration; Rényi holographic dark energy; Deceleration parameter; Equation of state parameter*

1. INTRODUCTION

Hubble's 1929 work [1] represented a major milestone in cosmology, providing strong evidence for one of the twentieth century's most significant discoveries - the expansion of the universe. In the late twentieth century, observations from two independent teams - the High-redshift Supernova Search Team led by A. G. Riess [2] and the Supernova Cosmology Project led by S. Perlmutter [3] demonstrated that the universe is presently undergoing an accelerated expansion. Since that period, multiple astrophysical and cosmological observations, such as CMB temperature anisotropies [4–6], large-scale structures including galaxy clustering [7–9], and Baryon Acoustic Oscillations (BAO) [10] have consistently supported the evidence for the universe's accelerated expansion. But the origin of the observed late-time cosmic acceleration remains unclear and continues to be a significant open problem in modern cosmology, even after more than two decades since its discovery. Dark matter is another exotic component of the universe that does not interact with electromagnetic radiation, and hence cannot be directly observed, but its existence is inferred from its gravitational effects on visible matter [11]. Observational evidence indicates that the dark components together make up about 95% of the total energy density of the universe, with dark matter (DM), a non-relativistic component that interacts very weakly with baryonic matter, contributing nearly 27%, and dark energy (DE) accounting for approximately 68%, while only about 5% consists of ordinary baryonic matter. To understand the nature of dark energy and the current accelerated expansion of the universe, several dark energy candidates have been proposed in the literature. The cosmological constant Λ, introduced by Einstein in his field equations, is the simplest and most natural candidate for dark energy. It can be interpreted as vacuum energy density with an equation of state parameter $\omega_{de} = \frac{p_{de}}{\rho_{de}} = -1$. Although it is in good agreement with observational data, it suffers from certain cosmological issues, including the fine-tuning and cosmic coincidence problems [12–14]. Therefore, a variety of dark energy models have been widely studied, including scalar field models such as quintessence [15, 16], k-essence [17], phantom [18], tachyon [19, 20], quintom [21], as well as exotic fluid models like the Chaplygin gas [22] etc.

In recent years, the holographic dark energy (HDE) model has gained significant interest as an alternative approach to describe the evolution of the universe. It is based on the holographic principle from quantum gravity, connecting dark energy with fundamental aspects of quantum physics. The development of this model is strongly influenced by Bekenstein's work on black hole thermodynamics [23]. Again, Hawking [24] demonstrated that the surface area of a black hole cannot decrease over time. According to this result, in a system of multiple black holes, the area of each black hole remains non-decreasing, and when two black holes combine, the final area is at least equal to the total area of the original ones [25]. This property closely resembles the behavior of entropy in thermodynamics. Bekenstein proposed that the entropy of a black hole is proportional to the area of its event horizon and can be expressed as $S_{BH} = \frac{A}{4\pi}$, where A denotes the area of the horizon [23]. Later, G.t'Hooft [26] introduced the holographic principle within the context of black hole physics, based on the relationship between entropy and the surface area of the black hole. Fischler and Susskind [27] subsequently

Cite as: C. R. Mahanta, R. Mahanta, East Eur. J. Phys. 3, 90 (2026), https://doi.org/10.26565/2312-4334-2026-3-08

generalized this idea to a cosmological context. The principle suggests that the entropy of a system is governed by its surface area rather than its volume. In this framework, the ultraviolet (UV) cutoff at short distances is linked to the infrared (IR) cutoff at large distances through limits set by black hole formation. Additionally, if the total energy within a region exceeds the mass of a black hole of the same size, gravitational collapse may occur. Extending this idea to the entire universe, one can interpret it as a system whose vacuum energy has a holographic origin, thereby giving rise to a dynamical model of holographic dark energy. Based on the holographic principle, Cohen *et al.* [28] established a connection between the system entropy S, the infrared (IR) cutoff L, and the ultraviolet (UV) cutoff Λ, given by $L^3\Lambda^4 \leq LM_p^2$, where $M_p = (8\pi G)^{-1/2}$ is the reduced Planck mass. By considering the largest possible IR cutoff L and using the relation $\rho_{\rm de} \approx \Lambda^4$, the holographic dark energy density can be written as $\rho_{\rm de} = 3c^2M_p^2L^{-2}$, where c is a dimensionless constant [29]. Several other suitable choices for the IR cutoff have also been proposed in the literature, including the Hubble horizon H^{-1}, event horizon, particle horizon, the universe's conformal age, the Ricci scalar radius, and the Granda-Oliveros cutoff. However, each of these choices can lead to new cosmological challenges. Li [29] proposed a holographic dark energy model in 2004, observing that cosmic acceleration could not be explained using either the particle horizon or the Hubble horizon. The future event horizon, however, can provide a viable explanation but a significant drawback of this model is its dependence on the universe's future evolution, making it challenging to precisely determine the universe's age [30]. To address this limitation, alternative infrared (IR) cutoffs have been proposed to describe the universe's current and future evolution. Granda and Oliveros [31, 32] introduced a new IR cutoff that depends on both the square of the Hubble parameter and its time derivative. This approach leads to the New Holographic Dark Energy (NHDE) model, with the energy density given by $\rho_{\rm de} = 3c^2M_p^2\left(\alpha H^2 + \beta\dot{H}\right)$,where α and β are constants. Gao *et al.* [33] developed an alternative holographic dark energy model, known as the Holographic Ricci Dark Energy (HRDE) model, in which the future event horizon is replaced by the inverse of the Ricci scalar, $L \approx R^{-1/2}$. Consequently, the energy density becomes proportional to the Ricci scalar R.

In recent years, different entropy frameworks have been proposed and applied to study various cosmological scenarios. In 2018, the Tsallis holographic dark energy (THDE) model was introduced [34], employing the Tsallis generalized entropy $S_\delta = \gamma A^\delta$ where δ is a non-additive parameter, A denotes the area of the event horizon, and γ is a constant [35]. Barrow [36] proposed a new approach to black hole entropy that incorporates quantum gravity effects, and Saridakis [37] constructed the Barrow Holographic Dark Energy (BHDE) model by using Barrow entropy in place of the standard Bekenstein-Hawking entropy. Recent studies indicate that the Bekenstein entropy $S = \frac{A}{4}$ can be interpreted as a special case of Tsallis entropy [38–44], which leads to a convenient expression for Rényi entropy [45] given by $S = \frac{1}{\delta}\ln\left(\frac{\delta}{4}A + 1\right)$. By applying this relation together with the assumption $\rho_{\rm de}dV \propto TdS$ [46], the energy density of Rényi holographic dark energy (RHDE) is obtained as $\rho_{\rm de} = \frac{3c^2H^2}{8\pi\left(1+\frac{\pi\delta}{H^2}\right)}$, where c^2 is a numerical constant. Jahromi *et al.* [47] proposed a new holographic dark energy model, known as Sharma–Mittal HDE, by incorporating Sharma–Mittal entropy [48] within the framework of the holographic principle, where the Hubble horizon is taken as the IR cutoff. Their analysis shows that the model exhibits behavior in good agreement with observational results. Kaniadakis introduced another form of entropy, which represents a one-parameter generalization of the classical entropy, expressed as $S_K = \frac{1}{K}\sinh(KS_{BH})$, where K is a dimensionless parameter [49]. The usual Bekenstein-Hawking entropy is recovered in the limit $K \to 0$. Using this entropy framework along with the holographic dark energy concept, a new model called Kaniadakis Holographic Dark Energy (KHDE) has been proposed in the literature [50, 51].

The RHDE model has been investigated using different choices of infrared (IR) cutoffs [52, 53]. Prasanthi and Aditya [53] constructed anisotropic and spatially homogeneous Bianchi type-VI_0 Rényi holographic dark energy (RHDE) models by taking both the Hubble horizon and the Granda-Oliveros horizon as infrared (IR) cutoffs. Their analysis shows that the squared speed of sound indicates stability for the RHDE model with the Hubble horizon, whereas it exhibits instability when the Granda-Oliveros horizon is used. Younas *et al.* [54] examined the cosmological implications, such as stability and the equation of state (EoS) parameter, of Rényi entropy-based holographic dark energy models within the framework of Chern–Simons gravity. Maity and Debnath [55] studied Rényi holographic dark energy in a D-dimensional fractal universe by exploring its cosmological implications. T. Chinnappalanaidu *et al.* [56] studied the dynamical behavior of a homogeneous and anisotropic Kantowski-Sachs universe filled with Rényi holographic dark energy, using a generalized scalar-tensor theory as the gravitational framework. Iqbal and Jawad [57] studied the cosmological parameters of the RHDE model by considering the Hubble horizon as the infrared (IR) cutoff within the DGP brane-world framework, and found that the model exhibits unstable behavior. Jawad *et al.* [58] examined the RHDE model in the framework of loop quantum cosmology by considering the Hubble horizon as the infrared (IR) cutoff. The RHDE model has been examined by several researchers in different frameworks to study the universe's present expansion and its associated characteristics.

Almost all these studies in the literature focus on anisotropic and homogeneous universe models because although the present universe appears to be homogeneous and isotropic on large scales and is well described by the Friedmann-Lemaître-Robertson-Walker framework, there is no definitive observational evidence that completely excludes the possibility of anisotropy. It is possible that anisotropies were present in the early universe, as suggested by the observations of anisotropies in the Cosmic Microwave Background (CMB). Spatially homogeneous and anisotropic Bianchi models are widely studied to improve our understanding of the dynamics of the evolving universe. These models provide some of the simplest descriptions of anisotropic backgrounds and play an important role in explaining the large-scale behavior of the universe. The FLRW cosmological model, which is homogeneous and isotropic, can be considered as a particular case of the Bianchi type I universe. As a result, spatially homogeneous and anisotropic Bianchi cosmological models have been widely studied in various contexts. Motivated by the above discussion, our aim is to examine a Rényi holographic dark energy model in a Bianchi type VI_0 universe within the framework of General Relativity.

The structure of the paper is as follows: In Section 2, we consider a spatially homogeneous and anisotropic Bianchi type VI_0 universe consisting of pressureless cold dark matter and non-interacting Rényi holographic dark energy. In this section, the Hubble horizon $L = H^{-1}$ is chosen as the infrared (IR) cutoff, and the corresponding Einstein field equations are derived. Section 3 presents exact solutions of the field equations obtained by considering a hyperbolic form of the scale factor. Section 4 focuses on the physical and kinematical aspects of the model through the study of the evolution of key cosmological parameters. Section 5 summarizes the main conclusions of this work.

2. METRIC AND GOVERNING EQUATIONS

We consider the Bianchi type-VI_0 spacetime in the following form:

$$ds^2 = -dt^2 + A^2dx^2 + B^2e^{2\alpha x}dy^2 + C^2e^{-2\alpha x}dz^2 \tag{1}$$

The scale factors $A(t)$, $B(t)$ and $C(t)$ vary only with cosmic time t and $\alpha \neq 0$ is taken as a constant. The metric reduces to the Bianchi type-I case when $\alpha = 0$,

It is assumed that the universe contains cold dark matter along with a proposed anisotropic fluid, which serves as the components of holographic dark energy.

The energy-momentum tensor T^i_j for cold dark matter is

$$T^i_j = diag[-1, 0, 0, 0]\rho_m \tag{2}$$

where ρ_m represents the energy density of cold dark matter.

The energy-momentum tensor for Rényi holographic dark energy $\bar{T}^i_j$, takes the following form

$$\bar{T}^i_j = diag[-\rho_{de}, p^{de}_x, p^{de}_y, p^{de}_z] \tag{3}$$

where, ρ_{de} denotes the energy density of Rényi holographic dark energy [46], while p^{de}_x, p^{de}_y, and p^{de}_z signify the pressures of Rényi holographic dark energy in the x, y and z directions, respectively.

Density of Rényi holographic dark energy ρ_{de}, is defined by

$$\rho_{de} = \frac{3D^2H^2}{8\pi\left(1 + \frac{\delta\pi}{H^2}\right)} \tag{4}$$

where D^2 is treated as a numerical constant and H is the Hubble parameter.

By permitting anisotropy in the pressure of Rényi holographic dark energy, p_{de} and in its equation of state parameter, $\omega_{de} = \frac{p_{de}}{\rho_{de}}$, we obtain.

$$\begin{aligned}\bar{T}^i_j &= diag[-1, \omega^{de}_x, \omega^{de}_y, \omega^{de}_z]\rho_{de}\\ &= diag[-1, \omega_{de}, (\omega_{de} + \eta), (\omega_{de} + \eta)]\rho_{de}\end{aligned} \tag{5}$$

where $\omega^{de}_x = \omega_{de}$, $\omega^{de}_y = (\omega_{de} + \eta)$, and $\omega^{de}_z = (\omega_{de} + \eta)$ are the directional equation of state parameters for the Rényi holographic dark energy along the x, y and z axes, respectively. The skewness parameter η indicates the deviations from ω_{de} along the directions of y and z. The 4-velocity vector $u^i = (1, 0, 0, 0)$ is taken to satisfy the condition $u^iu_i = -1$.

In Relativitistic units, Einstein's field equation is defined as

$$R_{ij} - \frac{1}{2}g_{ij}R = T_{ij} + \bar{T}_{ij} \tag{6}$$

In this equation, R_{ij} denotes the Ricci tensor, g_{ij} refers to the metric tensor, and $R = g^{ij}R_{ij}$ represents the Ricci scalar curvature.

In a comoving coordinate system, Einstein's field equation (6), along with equations (2) and (5) for the metric (1), results in the following set of field equations.

$$\frac{\dot{A}}{A}\frac{\dot{B}}{B} + \frac{\dot{B}}{B}\frac{\dot{C}}{C} + \frac{\dot{C}}{C}\frac{\dot{A}}{A} - \left(\frac{\alpha}{A}\right)^2 = \rho_m + \rho_{de} \tag{7}$$

$$\frac{\ddot{B}}{B} + \frac{\ddot{C}}{C} + \frac{\dot{B}}{B}\frac{\dot{C}}{C} + \left(\frac{\alpha}{A}\right)^2 = -\omega_{de}\rho_{de} \tag{8}$$

$$\frac{\ddot{A}}{A}+\frac{\ddot{B}}{B}+\frac{\dot{A}}{A}\frac{\dot{B}}{B}-\left(\frac{\alpha}{A}\right)^2=-\left(\omega_{de}+\eta\right)\rho_{de} \tag{9}$$

$$\frac{\ddot{A}}{A}+\frac{\ddot{C}}{C}+\frac{\dot{A}}{A}\frac{\dot{C}}{C}-\left(\frac{\alpha}{A}\right)^2=-\left(\omega_{de}+\eta\right)\rho_{de} \tag{10}$$

$$\frac{\dot{C}}{C}-\frac{\dot{B}}{B}=0 \tag{11}$$

where the overdot symbol indicates the derivative with respect to the cosmic time t.

From equations (7)–(11), we derive the continuity equation as:

$$\dot{\rho}_m+3H\rho_m+\dot{\rho}_{de}+3H\left(1+\omega_{de}\right)\rho_{de}+\eta\left(\frac{\dot{B}}{B}+\frac{\dot{C}}{C}\right)\rho_{de}=0 \tag{12}$$

We assume that the two components of the universe evolve independently without interaction. Hence, continuity equation (12) leads to separate conservation equations for matter and dark energy as

$$\dot{\rho}_m+3H\rho_m=0 \tag{13}$$

$$\dot{\rho}_{de}+3H\left(1+\omega_{de}\right)\rho_{de}+\eta\left(\frac{\dot{B}}{B}+\frac{\dot{C}}{C}\right)\rho_{de}=0 \tag{14}$$

3. THE SOLUTIONS OF THE FIELD EQUATIONS

The Hubble parameters corresponding to the directions of x, y, and z for the Bianchi type-VI$_0$ metric are

$$H_x=\frac{\dot{A}}{A}, \qquad H_y=\frac{\dot{B}}{B}, \qquad H_z=\frac{\dot{C}}{C} \tag{15}$$

The average scale factor a and the volume V are defined as follows

$$a=(ABC)^{\frac{1}{3}} \qquad V=a^3=ABC \tag{16}$$

The average value of Hubble parameter H is defined as

$$H=\frac{1}{3}\frac{\dot{V}}{V}=\frac{1}{3}\left(\frac{\dot{A}}{A}+\frac{\dot{B}}{B}+\frac{\dot{C}}{C}\right)=\frac{1}{3}\left(H_x+H_y+H_z\right) \tag{17}$$

The mathematical form of the average anisotropy parameter A_m is

$$A_m=\frac{1}{3}\sum_{i=1}^{3}\left(\frac{\Delta H_i}{H}\right)^2 \tag{18}$$

Here, $\Delta H=H_i-H$, where H_i (for $i=x,y,z$) denotes the directional Hubble parameters along the x, y and z directions. The anisotropy parameter measures how much the expansion deviates from isotropy. Evaluating this parameter is essential for determining whether the cosmological model tends toward isotropy over time.

From Eq. (11), we obtain

$$B=mC \tag{19}$$

where $m>0$ is an integration constant.

Using equations (15) , (17) and (19), the expression for the anisotropy parameter in (18) can be written as:

$$A_m=\frac{2}{9H^2}\left(H_x-H_z\right)^2 \tag{20}$$

Substituting Eq. (19) into the field equations (7)- (11), we obtain

$$\left(\frac{\dot{C}}{C}\right)^2+2\frac{\dot{C}}{C}\frac{\dot{A}}{A}-\left(\frac{\alpha}{A}\right)^2=\rho_m+\rho_{de} \tag{21}$$

$$\left(\frac{\dot{C}}{C}\right)^2 + 2\frac{\ddot{C}}{C} + \left(\frac{\alpha}{A}\right)^2 = -\omega_{de}\rho_{de} \tag{22}$$

$$\frac{\ddot{A}}{A} + \frac{\ddot{C}}{C} + \frac{\dot{A}}{A}\frac{\dot{C}}{C} - \left(\frac{\alpha}{A}\right)^2 = -\left(\omega_{de} + \eta\right)\rho_{de} \tag{23}$$

By subtracting equation (22) from equation (23), we obtain:

$$\frac{\dot{A}}{A} - \frac{\dot{C}}{C} = H_x - H_z = \frac{\lambda}{V} + \frac{1}{V}\int\left(\frac{2\alpha^2}{A^2} - \eta\rho_{de}\right)V dt \tag{24}$$

Here, λ is an integration constant, and the term η appears due to the possible intrinsic anisotropy of the fluid,

Finally, substituting equation (24) into equation (20), we obtain the anisotropy parameter of the expansion as follows:

$$A_m = \frac{2}{9}\frac{1}{H^2}\left[\lambda + \int\left(\frac{2\alpha^2}{A^2} - \eta\rho_{de}\right)V dt\right]^2 V^{-2} \tag{25}$$

Following [59], we take

$$\eta = \frac{2\alpha^2}{\rho_{de}A^2} \tag{26}$$

Substituting equation (26) into equation (25), we obtain the reduced anisotropy parameter of the expansion as

$$A_m = \frac{2}{9}\frac{\lambda^2}{H^2}V^{-2} \tag{27}$$

Equations (21)-(23) of the Einstein field equations, along with (26), lead to:

$$\left(\frac{\dot{C}}{C}\right)^2 + 2\frac{\dot{C}}{C}\frac{\dot{A}}{A} = \rho_m + \left(1 + \frac{\eta}{2}\right)\rho_{de} \tag{28}$$

$$\left(\frac{\dot{C}}{C}\right)^2 + 2\frac{\ddot{C}}{C} = -\left(\omega_{de} + \frac{\eta}{2}\right)\rho_{de} \tag{29}$$

$$\frac{\ddot{A}}{A} + \frac{\ddot{C}}{C} + \frac{\dot{A}}{A}\frac{\dot{C}}{C} - \left(\frac{\alpha}{A}\right)^2 = -\left(\omega_{de} + \frac{\eta}{2}\right)\rho_{de} \tag{30}$$

The relative rate of expansion (or contraction) of the universe is described by the expansion scalar θ, while the shear scalar σ measures the deformation caused by density fluctuations. The scalar expansion θ and shear scalar σ are defined as

$$\theta = 3H = H_x + 2H_z \tag{31}$$

$$\sigma^2 = \frac{1}{2}[H_x^2 + 2H_z^2] - \frac{\theta^2}{6} = \frac{1}{3}\left(H_x - H_z\right)^2 \tag{32}$$

The three equations, (28)–(30) involve six unknowns, namely $A, C, \rho_m, \rho_{de}, \omega_{de}$ and η, together with (4) indicate that the system remains unsolved without additional constraints .

Thus, in order to obtain a determinate solution, two additional conditions are required. We consider the following physically relevant constraints:

(i) We assume that the shear scalar is proportional to the scalar expansion which gives

$$A = C^k \tag{33}$$

where, k is a nonzero integration constant.

(ii) Next, we assume the average scale factor $a(t)$ as

$$a(t) = \left(\sinh\left(\beta t\right)\right)^{\frac{1}{n}} \tag{34}$$

where, β is an arbitrary constant and n represents a positive constant.

Equation (34), is a generalization of the scale factor obtained by Amirhashchi *et al.* [60] and Pradhan *et al.* [61] for dark energy models in FRW and Bianchi type-VI_0 space-times, respectively.

Substituting the average scale factor from Equation (34) into Equations (16), (19) and (33), we derive the directional scale factors.

$$A = \left(\frac{\sinh^{\frac{3}{n}}(\beta t)}{m}\right)^{\frac{k}{(k+2)}} \tag{35}$$

$$B = m\left(\frac{\sinh^{\frac{3}{n}}(\beta t)}{m}\right)^{\frac{1}{(k+2)}} \tag{36}$$

$$C = \left(\frac{\sinh^{\frac{3}{n}}(\beta t)}{m}\right)^{\frac{1}{(k+2)}} \tag{37}$$

Thus, the metric (1) takes the form:

$$ds^2 = -dt^2 + \left(\frac{\sinh^{\frac{3}{n}}(\beta t)}{m}\right)^{\frac{2k}{(k+2)}} dx^2 + m\left(\frac{\sinh^{\frac{3}{n}}(\beta t)}{m}\right)^{\frac{2}{(k+2)}} e^{2\alpha x}dy^2 + \left(\frac{\sinh^{\frac{3}{n}}(\beta t)}{m}\right)^{\frac{2}{(k+2)}} e^{-2\alpha x}dz^2 \tag{38}$$

4. RELEVANT PHYSICAL PROPERTIES

The average Hubble parameter, H, is a fundamental cosmological quantity that characterizes the expansion rate of the universe. By employing the scale factor $a(t) = [\sinh(\beta t)]^{1/n}$, from which the Hubble parameter can be expressed in terms of the cosmic time t as:

$$H = \frac{\dot{a}}{a} = \frac{\beta}{n}\coth(\beta t) \tag{39}$$

To describe the cosmic expansion in terms of the observable redshift, z, we employ the standard relation between the scale factor and redshift $a(t) = \frac{1}{1+z}$, where the present value of the scale factor is normalized to unity, i.e., $a_0 = 1$. Therefore, the Hubble parameter in terms of the redshift is obtained as

$$H(z) = \frac{\beta}{n}\sqrt{1 + (1+z)^{2n}} \tag{40}$$

Imposing the normalization condition at the present epoch, $H_0 \equiv H(z=0)$, yields $H_0 = \frac{\beta}{n}\sqrt{2}$ from which it follows that $\frac{\beta}{n} = \frac{H_0}{\sqrt{2}}$. Consequently, the normalized Hubble parameter assumes the form

$$H(z) = H_0\sqrt{\frac{1 + (1+z)^{2n}}{2}} \tag{41}$$

which will be employed throughout the subsequent analysis.

The deceleration parameter is evaluated using the kinematic relation

$$q(z) = -1 + \frac{(1+z)}{H(z)}\frac{dH(z)}{dz}$$

Substituting the normalized Hubble parameter (41) and performing the differentiation with respect to the redshift yields

$$q(z) = -1 + \frac{n(1+z)^{2n}}{1 + (1+z)^{2n}} \tag{42}$$

which provides the evolution of the cosmic expansion directly in terms of the observable redshift. For the proposed cosmological model to be physically viable, the model parameter n must satisfy the following conditions:

1. In the high-redshift limit ($z \gg 1$), the deceleration parameter approaches $q(z) \to n - 1$.. To ensure a decelerating early Universe, which is essential for the formation of large-scale structures, the condition $q(z) > 0$ must be satisfied, implying $n > 1$.
2. At the present epoch ($z = 0$), the deceleration parameter is given by $q_0 \equiv q(0) = \frac{n-2}{2}$. The observed late-time accelerated expansion requires $q_0 < 0$, which leads to the constraint $n < 2$.

Accordingly, the physically admissible range of the model parameter is $1 < n < 2$. Within this interval, the transition from decelerated to accelerated expansion occurs at the transition redshift z_t, defined by the condition $q(z_t) = 0$. Solving this condition yields

$$z_t = \left(\frac{1}{n-1}\right)^{\frac{1}{2n}} - 1 \tag{43}$$

For all $n \in (1, 2)$, the transition redshift is real, positive, and uniquely determined, thereby ensuring a physically consistent cosmic evolution from an early decelerating phase to the present accelerated epoch.
To investigate the evolution of the cosmological quantities, namely the dark energy density $\rho_{de}(z)$, matter density $\rho_m(z)$, dark energy pressure $p_{de}(z)$, equation-of-state parameter $\omega_{de}(z)$, and deceleration parameter $q(z)$, the model parameters H_0 and n are first constrained using the observational Hubble data (OHD) set. The resulting best-fit values are subsequently employed in the analysis of the model.

4.1. Observational constraints

To constrain the free parameters, $\{H_0, n\}$, of the proposed HDE model, a statistical analysis is performed using the normalized Hubble parameter given in Eq. (41). The resulting best-fit values are subsequently employed in the cosmological analysis. A total of 77 observational Hubble parameter $[H(z)]$ data points are employed to constrain the model parameters, H_0 and n. The dataset spans the redshift range $0 \leq z \leq 2.36$ and is adopted from Ref. [62]. The corresponding chi-square (χ^2) statistic is defined as

$$\chi^2_{OHD} = \sum_{i=1}^{77} \left[\frac{H_{\rm obs}(z_i) - H_{\rm th}(z_i; H_0, n)}{\sigma_{H,i}}\right]^2 \tag{44}$$

where $H_{\rm obs}(z_i)$ and $H_{\rm th}(z_i; H_0, n)$ denote the observed and theoretical values of the Hubble parameter at redshift z_i, respectively, while $\sigma_{H,i}$ represents the corresponding observational uncertainty. The model parameters are constrained using the Markov Chain Monte Carlo (MCMC) technique through the minimization of the chi-square statistic, χ^2. Under the assumption of Gaussian-distributed observational uncertainties, the likelihood function is defined as $\mathcal{L}(\boldsymbol{\theta}) \propto \exp\left(-\frac{\chi^2(\boldsymbol{\theta})}{2}\right)$, where $\boldsymbol{\theta} = \{H_0, n\}$ denotes the set of free model parameters. The corresponding marginalized 1σ and 2σ confidence regions are displayed through the likelihood contour plots. The parameter constraints obtained from the OHD dataset are presented in Fig. 1. To assess the viability of the proposed HDE model, its performance is compared with that of the spatially flat ΛCDM model, whose Hubble parameter is given by $H(z) = H_0\sqrt{\Omega_m(1+z)^3 + \Omega_\Lambda}$, where Ω_m and Ω_Λ denote the present-day matter density parameter and cosmological constant density parameter, respectively. The relative performance of the competing models is further evaluated using the Akaike Information Criterion (AIC) [63] and the Bayesian Information Criterion (BIC) [64], defined as $\text{AIC} = \chi^2_{\rm min} + 2\kappa$, and $\text{BIC} = \chi^2_{\rm min} + \kappa \ln N$, respectively. Here, κ represents the number of free model parameters, while N denotes the total number of observational data points. In general, models with lower AIC and BIC values are statistically preferred, as they provide a better balance between the goodness of fit and model complexity. Table 1 presents the best-fit values of the model parameters together with their corresponding 1σ confidence intervals for both the proposed HDE model and the standard ΛCDM cosmology. For the OHD dataset, the proposed model yields a marginally lower minimum chi-square value, $\chi^2_{\rm min}$, than the ΛCDM model, indicating a slightly better agreement with the observational data. To further assess the relative performance of the two models, the differences in the Akaike Information Criterion (AIC) and the Bayesian Information Criterion (BIC) are evaluated. For the OHD dataset, these are obtained as $\Delta\text{AIC} = \text{AIC}_{\rm HDE} - \text{AIC}_{\Lambda\rm CDM} = -2.484$, and $\Delta\text{BIC} = \text{BIC}_{\rm HDE} - \text{BIC}_{\Lambda\rm CDM} = -2.484$. The negative values of both ΔAIC and ΔBIC indicate that the proposed HDE model is statistically preferred over the standard ΛCDM model. Consequently, the analysis based on the OHD dataset provides statistical support for the proposed model. The best-fit value of the Hubble constant obtained in this work, $H_0 = 67.90 \pm 0.88$ km s^{-1} Mpc^{-1}, is consistent with the Planck 2018 CMB measurement, $H_0 = 67.4 \pm 0.5$ km s^{-1} Mpc^{-1} [65], and the recent DESI Data Release 1 BAO determination, $H_0 = 67.97 \pm 0.38$ km s^{-1} Mpc^{-1} [66].

Table 1. Comparison of the best-fit parameter values obtained from OHD datasets for both our model and the ΛCDM model.

Model	H_0	Ω_m	n	$\chi^2_{\rm min}$	AIC	BIC
Our model	$67.90^{+0.88}_{-0.88}$	–	$1.30^{+0.019}_{-0.019}$	70.566	74.566	79.254
ΛCDM	$67.41^{+1.14}_{-1.16}$	$0.299^{+0.016}_{-0.015}$	–	73.050	77.050	81.738

Now, employing the relation between the scale factor and the redshift, $a(t) = (1+z)^{-1}$, and substituting the obtained expression $a(t) = [\sinh(\beta t)]^{1/n}$, yields $\sinh(\beta t) = (1+z)^{-n}$. Consequently, using the normalization relation $\beta = \frac{nH_0}{\sqrt{2}}$, the cosmic time as a function of the redshift is obtained as

$$t(z) = \frac{\sqrt{2}}{nH_0} \sinh^{-1}[(1+z)^{-n}] \tag{45}$$

4.2. Evolution of the deceleration parameter q(z) and phase transition

Figure 2 depicts the redshift evolution of the deceleration parameter obtained using the best-fit values of the model parameters. As expected, the model exhibits a transition from an early decelerating Universe to the current phase of accelerated expansion. The inferred transition redshift,$z_t = 0.589 \pm 0.052$, is fully consistent with the 1σ range derived from model-independent CC observations [67] and the combined DESI BAO and Pantheon+ Type Ia Supernova (SNe Ia) analyses, which constrain the transition redshift to the range $z_t \in [0.55, 0.70]$ [68]. Furthermore, the present value of the deceleration parameter is obtained as $q_0 = -0.350 \pm 0.0095$. Having constrained the model parameters through observational data and the subsequent analysis focuses on the evolution of the remaining cosmological parameters.

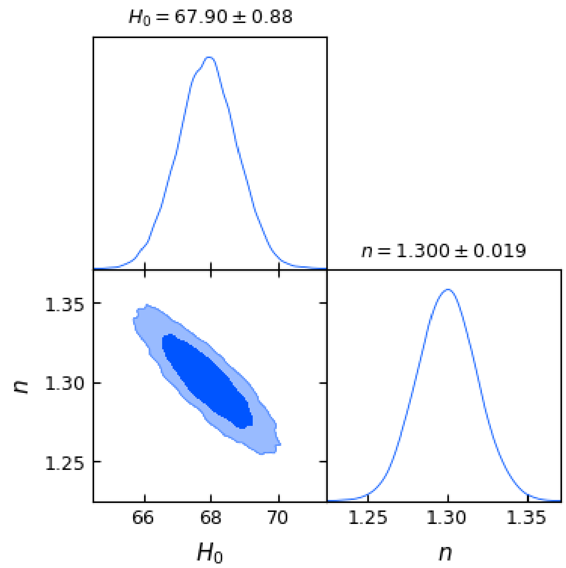

Figure 1. One-dimensional marginalized posterior distributions together with the corresponding two-dimensional marginalized confidence contours at the 1σ and 2σ confidence levels for the proposed cosmological model, constrained using the OHD dataset.

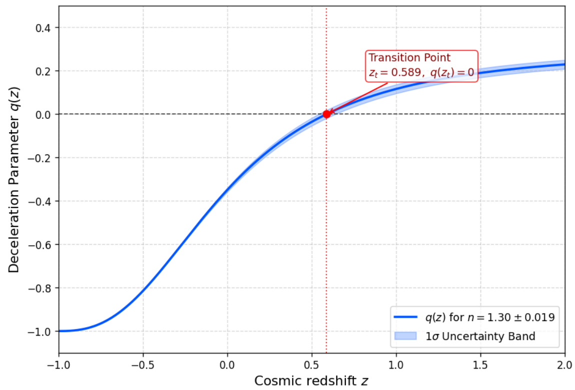

Figure 2. Behaviour of the deceleration parameter

4.3. Evolution of the matter and dark energy density

Using Eq.(13), together with the scale factor $a(t) = [\sinh(\beta t)]^{1/n}$, and the standard scale factor-redshift relation, $a = (1+z)^{-1}$ the matter energy density is obtained as

$$\rho_m(z) = \rho_{m0}(1+z)^3 \tag{46}$$

where ρ_{m0} denotes the present-day matter energy density. The present matter energy density can be expressed in terms of the model parameters H_0 and n by relating it to the present critical density, $\rho_{c0} = 3H_0^2$ through the matter density parameter, $\Omega_{m0} = \frac{\rho_{m0}}{\rho_{c0}}$. At the present epoch ($z = 0$), the field equations for the Bianchi VI$_0$ spacetime satisfy the closure relation $\Omega_{m0} + \Omega_{\text{de}0} = 1$, where the present-day matter and Rényi holographic dark energy density parameters are given by $\Omega_{m0} = \frac{2-n}{2}$ and $\Omega_{\text{de}0} = \frac{n}{2}$ Hence, the present matter energy density is determined as $\rho_{m0} = \Omega_{m0}\rho_{c0} = \left(\frac{2-n}{2}\right)(3H_0^2) = \frac{3}{2}H_0^2(2-n)$. Substituting this expression into the above relation gives the matter energy density as a function of redshift,

$$\rho_m(z) = \frac{3}{2}H_0^2(2-n)(1+z)^3 \tag{47}$$

Substituting the normalized Hubble parameter given by Eq.(41) into Eq.(4), the Rényi holographic dark energy density is obtained as

$$\rho_{de}(z) = \frac{3D^2H_0^4\left[1+(1+z)^{2n}\right]^2}{2H_0^2\left[1+(1+z)^{2n}\right] + 4\delta\pi} \tag{48}$$

At the present epoch ($z = 0$), the above expression reduces to $\rho_{de}(0) = \frac{3D^2H_0^4}{H_0^2+\delta\pi}$. Expressing the present-day dark energy density in terms of the critical density, $\rho_{c0} = 3H_0^2$, and using the relation $\Omega_{de}(0) = \frac{\rho_{de}(0)}{\rho_{c0}} = \frac{n}{2}$, one obtains the following algebraic constraint on D:

$$D^2 = \frac{n}{2}\left(1 + \frac{\delta\pi}{H_0^2}\right) \tag{49}$$

Consequently, D^2 can be expressed uniquely in terms of the primary model parameters.

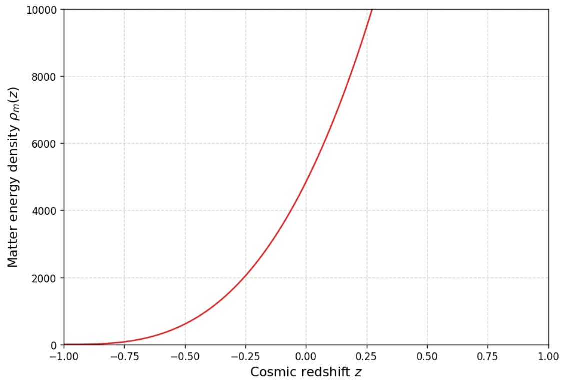

Figure 3. Behaviour of the matter energy density

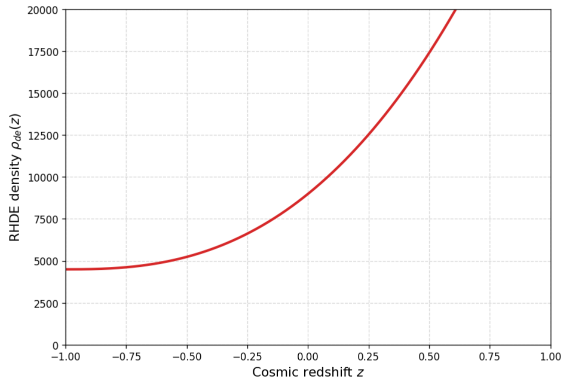

Figure 4. Behaviour of the RHDE density for $\delta = 1.4$

Figures 3 and 4 present the evolution of the matter energy density, $\rho_m(z)$, and the Rényi holographic dark energy (RHDE) density, $\rho_{de}(z)$, as functions of the redshift for the best-fit parameter values $n = 1.3$, $H_0 = 67.9$ km s^{-1} Mpc^{-1}, and $\delta = 1.4$. Figure 3 demonstrates that the matter energy density exhibits the standard cosmological evolution, $\rho_m(z) \propto (1+z)^3$ decreasing continuously with cosmic expansion. It attains large values during the early Universe and progressively diminishes toward zero as the redshift approaches $z = -1$, reflecting the expected dilution of non-relativistic matter. The evolution of the RHDE density is displayed in Fig.4. It is evident that $\rho_{de}(z)$ remains positive throughout the entire redshift range considered. In the high-redshift regime, the matter component dominates over the RHDE density, thereby providing favorable conditions for the formation of cosmic structures. As the Universe evolves toward lower redshifts, the RHDE density gradually overtakes the matter component and eventually approaches a finite positive value in the far future ($z \to -1$). This asymptotic behavior is consistent with a sustained phase of accelerated cosmic expansion. Furthermore, the present-day relation,$\rho_{de}(0) > \rho_m(0)$, indicates that the proposed cosmological model has entered a dark-energy-dominated epoch following the transition from an earlier matter-dominated decelerating phase. The convergence of $\rho_{de}(z)$ to a finite positive constant at late times further suggests that the RHDE component effectively mimics a cosmological constant, ensuring a stable future evolution and excluding the occurrence of Big Rip.

4.4. Evolution of the anisotropy parameter and skewness parameter

Using Eqs.(27) and (40), the anisotropy parameter can be expressed explicitly as a function of the redshift in the form

$$A_m(z) = \frac{4\lambda^2}{9H_0^2}\frac{(1+z)^6}{1+(1+z)^{2n}} \tag{50}$$

By combining Eqs. (40), (48), and (26), the redshift-dependent skewness parameter is obtained as

$$\eta(z) = \frac{2\alpha^2 m^{\frac{2k}{k+2}}(1+z)^{\frac{6k}{k+2}}\left[2H_0^2\left(1+(1+z)^{2n}\right)+4\delta\pi\right]}{3D^2H_0^4\left[1+(1+z)^{2n}\right]^2} \tag{51}$$

where D^2 is determined by $D^2 = \frac{n}{2}\left(1 + \frac{\delta\pi}{H_0^2}\right)$

The evolution of the anisotropy parameter is presented in Fig.5. It is evident that the anisotropy parameter decreases monotonically from relatively large values in the early Universe ($z > 0$) to $A_m(0) \approx 0.044$ at the present epoch, and ultimately approaches zero in the asymptotic future ($z \to -1$). This behavior indicates that the spatial anisotropy is progressively suppressed during the cosmic evolution, leading the proposed cosmological model toward an isotropic limit at late times. Such an evolution is consistent with the high degree of isotropy inferred from observations of the Cosmic Microwave Background (CMB). Figure 6 illustrates the redshift evolution of the skewness parameter, $\eta(z)$, which quantifies

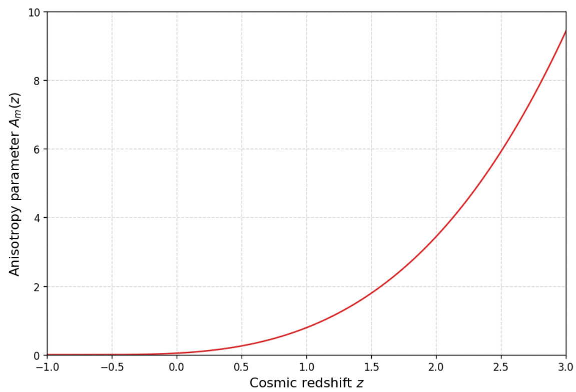

Figure 5. Behaviour of the anisotropy parameter for $\lambda = 30$

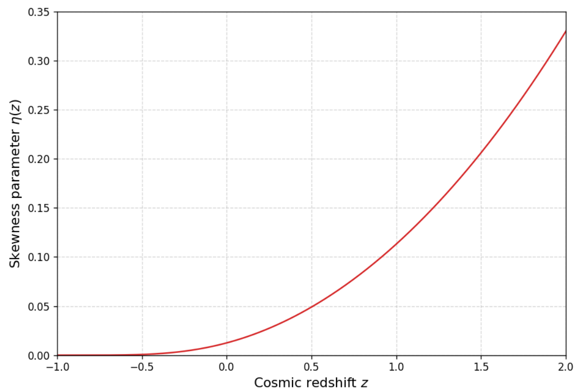

Figure 6. Behaviour of the skewness parameter for $\alpha = 3$, $m = 3$, $k = 10$ and $\delta = 1.4$

the directional anisotropy in the pressure distribution of the cosmic fluid. The parameter decreases continuously from $\eta \approx 0.33$ at $z = 2$ to $\eta(0) \approx 0.013$ at the present epoch and asymptotically vanishes as $z \to -1$. The decay of $\eta(z)$ signifies the gradual disappearance of directional pressure anisotropies, indicating that the dark energy fluid evolves toward an effectively isotropic configuration capable of sustaining the observed late-time accelerated expansion. The simultaneous suppression of both the anisotropy parameter, $A_m(z)$, and the skewness parameter, $\eta(z)$, demonstrates that the proposed cosmological model undergoes a natural isotropization throughout its evolution. Their asymptotic convergence to zero at late times implies that the model approaches an effectively isotropic, in agreement with the stringent isotropy constraints provided by contemporary CMB observations.

4.5. Evolution of the equation of state parameter and the pressure for Rényi holographic dark energy

We now discuss the cosmic role of the equation of state parameter (EoS), which is defined as

$$\omega_{de} = \frac{p_{de}}{\rho_{de}} \tag{52}$$

Here, ρ_{de} and p_{de} represent the energy density and pressure of Rényi holographic dark energy, respectively. The equation of state (EoS) parameter ω_{de} is a key factor in determining the universe's dynamical evolution. Depending on its value, the universe can be classified into different cosmological phases: when $\omega_{de} = 0$, the universe behaves like non-relativistic matter; for $-1 < \omega_{de} < -\frac{1}{3}$, it corresponds to a quintessence phase; a value of $\omega_{de} = -1$ represents a cosmological constant-dominated universe; and when $\omega_{de} < -1$, the universe is in a phantom phase.
From Eqs. (14), (48) and (51), we obtain the equation-of-state parameter as

$$\omega_{\rm de}(z) = -1 - \frac{1}{3H(z)}\left[\frac{\sqrt{2}nH_0H(z)^2(1+z)^{4n}}{H(z)^2+\delta\pi} - \frac{2\sqrt{2}nH_0(1+z)^{2n}}{\sqrt{1+(1+z)^{2n}}} + \frac{4\alpha^2 m^{\frac{2k}{k+2}}(1+z)^{\frac{6k}{k+2}}\left(H(z)^2+\delta\pi\right)}{D^2(k+2)H(z)^3}\right] \tag{53}$$

From Eqs. (48), (52) and (53), the pressure equation for R enyi holographic dark energy is obtained as

$$p_{\rm de}(z) = -\frac{3D^2H(z)^4}{H(z)^2+\delta\pi} - \frac{3D^2H(z)^4}{H(z)^2+\delta\pi}\left[\frac{nH_0^2(1+z)^{2n}}{3\left(H(z)^2+\delta\pi\right)} - \frac{4n(1+z)^{2n}}{3\left[1+(1+z)^{2n}\right]}\right] - \frac{4\alpha\, m^{\frac{2k}{k+2}}(1+z)^{\frac{6k}{k+2}}}{k+2} \tag{54}$$

where $H(z) = \frac{H_0}{\sqrt{2}}\sqrt{1+(1+z)^{2n}}$ and $D^2 = \frac{n}{2}\left(1+\frac{\delta\pi}{H_0^2}\right)$

Figures 7 and 8 present the redshift evolution of the dark energy pressure, $p_{de}(z)$, and the dark energy equation-of-state (EoS) parameter, $\omega_{de}(z)$, respectively. As illustrated in Fig.7, the dark energy pressure remains negative throughout the entire cosmic evolution. Its magnitude evolves smoothly from relatively large negative values at high redshifts to a finite negative constant in the asymptotic future ($z \to -1$). The persistence of negative pressure throughout the cosmic history provides the repulsive effect required to account for the observed late-time accelerated expansion of the Universe. Figure 8 depicts the evolution of the EoS parameter, $\omega_{de}(z)$. The results indicate that the EoS remains in the phantom regime ($\omega_{de} < -1$) over a finite period of cosmic evolution before gradually approaching the cosmological-constant limit, $\omega_{de} = -1$, as $z \to -1$. Such behavior is characteristic of a transient phantom phase, in which the phantom nature of dark energy is only temporary and the cosmological dynamics eventually converge toward a de Sitter phase. At the present epoch, the model yields $\omega_{\rm de}(0) \approx -0.73$, implying that the current accelerated expansion is driven by a quintessence-like dark energy component. In contrast to the standard ΛCDM model, where the dark energy equation-of-state remains

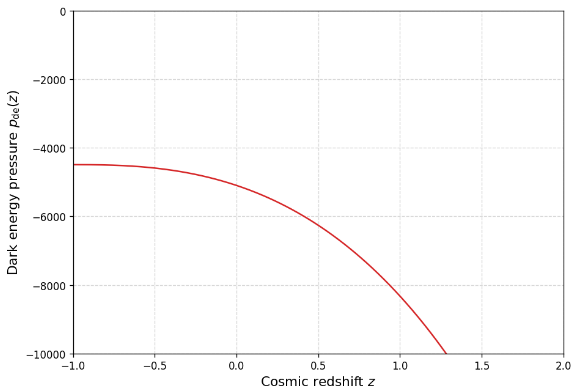

Figure 7. Behaviour of the dark energy pressure for $\alpha = 3$, $m = 3$, $k = 10$ and $\delta = 1.4$

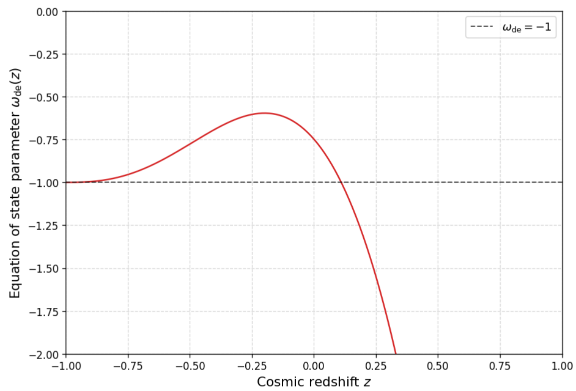

Figure 8. Behaviour of the EoS parameter for $\alpha = 3$, $m = 3$, $k = 10$ and $\delta = 1.4$

fixed at $\omega_{de} = -1$, the Rényi holographic dark energy model predicts a dynamical evolution of $\omega_{de}(z)$ from a transient phantom phase to a present quintessence phase, before asymptotically approaching the de Sitter limit in the far future. This late-time convergence to the cosmological-constant boundary suggests a stable future evolution and is consistent with dynamical dark energy scenarios that avoid future singularities, including the Big Rip, through suitable cosmological evolution mechanisms [69, 70].

5. DISCUSSION AND CONCLUSION

In the present work, we have investigated a spatially homogeneous and anisotropic Bianchi type-VI$_0$ cosmological model within the framework of General Relativity by considering Rényi holographic dark energy (RHDE), with the Hubble horizon serving as the infrared cutoff. The cosmic matter content is assumed to comprise pressureless dark matter and RHDE, with no interaction between the two components. Exact solutions of the Einstein field equations have been obtained by adopting the average scale factor $a(t) = (\sinh(\beta t))^{1/n}$. The free model parameters have been constrained through a Markov Chain Monte Carlo (MCMC) analysis using a compilation of 77 Observational Hubble Data (OHD) measurements of the Hubble parameter, $H(z)$. The analysis yields the best-fit values $H_0 = 67.9\ \mathrm{km\,s^{-1}\,Mpc^{-1}}$ and $n = 1.3$. Based on these observationally constrained parameters, the physical and kinematical properties of the model have been investigated through the evolution of the relevant cosmological observables. The main findings of the present analysis are summarized as follows:

- The matter energy density evolves according to the standard relation $\rho_m(z) \propto (1+z)^3$, decreasing continuously as the Universe expands and tending to zero in the asymptotic future ($z \to -1$). By contrast, the Rényi holographic dark energy density remains finite and positive throughout the cosmic evolution, asymptotically approaching a constant value at late times. This behavior naturally supports a sustained phase of cosmic acceleration.

- The anisotropy parameter, $A_m(z)$, together with the skewness parameter, $\eta(z)$, decreases continuously during the cosmic evolution and approaches zero in the asymptotic future ($z \to -1$). The vanishing of these quantities signifies the gradual disappearance of both spatial and fluid anisotropies, indicating that the proposed cosmological model evolves toward an isotropic state at late times. This behavior is in agreement with the high degree of isotropy revealed by contemporary Cosmic Microwave Background (CMB) observations.

- The dark energy pressure, $p_{\mathrm{de}}(z)$, remains negative throughout the cosmic evolution, while the equation-of-state (EoS) parameter, $\omega_{\mathrm{de}}(z)$, undergoes a transient phantom phase ($\omega_{\mathrm{de}} < -1$), passes through a quintessence phase at the present epoch, before asymptotically approaching the cosmological constant boundary, $\omega_{\mathrm{de}} \to -1$, as $z \to -1$. The convergence of the EoS parameter to the de Sitter limit ensures a stable late-time evolution and prevents the occurrence of future singularities, including the Big Rip.

ORCID

Chandra Rekha Mahanta, https://orcid.org/0000-0002-8019-8824; **Rajashree Mahanta**, https://orcid.org/0009-0009-2656-115X

REFERENCES

[1] E.Hubble, Proceedings of the national academy of sciences, **15**(3), pp.168-173 (1929), https://doi.org/10.1073/pnas.15.3.168

[2] A.G. Riess, *et al.*, The Astronomical Journal, **116**, 1009-1038 (1998). https://doi.org/10.1086/300499

[3] S. Perlmutter, *et al.*, The Astrophysical Journal, **517**, 565-586 (1999). https://doi.org/10.1086/307221

[4] D.N. Spergel, *et al.*, The Astrophysical Journal Supplement Series. **148**, 175–194 (2003). https://doi.org/10.1086/377226

[5] D.N. Spergel, *et al.*, The Astrophysical Journal Supplement Series, **170**, 377 (2007). https://doi.org/10.1086/513700

[6] E. Komatsu, *et al.*,The Astrophysical Journal Supplement Series. **180**, 330 (2009). https://doi.org/10.1088/0067-0049/180/2/330

[7] M.Tegmark, *et al.*, Physical review D, **69**, 103501 (2004). https://doi.org/10.1103/PhysRevD.69.103501

[8] U. Seljak, *et al.*, Physical Review D, **71**, 103515 (2005). https://doi.org/10.1103/PhysRevD.71.103515

[9] M. Tegmark, *et al.*, Physical Review D, **74**, 123507 (2006). https://doi.org/10.1103/PhysRevD.74.123507

[10] D.J. Eisenstein, *et al.*, The Astronomical Journal, **633**, 560-574 (2005). https://doi.org/10.1086/466512

[11] F. Zwicky, Helv. Phys. Acta, **6**, 110–127 (1933). https://arxiv.org/abs/1612.00805

[12] S. Weinberg, Reviews of modern physics **61**(1), (1989). https://doi.org/10.1103/RevModPhys.61.1

[13] S.M. Carroll, Living reviews in relativity **4**(1), 1–56 (2001). https://doi.org/10.12942/lrr-2001-1

[14] E.J. Copeland, *et al.*, International Journal of Modern Physics D, **15**(11), 1753–1935 (2006). https://doi.org/10.1142/S021827180600942X

[15] T. Barreiro, *et al.*, Physical Review D, **61**(12), 127301 (2000). https://doi.org/10.1103/PhysRevD.61.127301.

[16] V. Sahni, and L. Wang, Physical Review D, **62**(10), 103517 (2000). https://doi.org/10.1103/PhysRevD.62.103517

[17] C. Armendariz-Picon, *et al.*, Physical Review D,**63**(10), 103510 (2001). https://doi.org/10.1103/PhysRevD.63.103510

[18] R.R. Caldwell, Physics Letters B, **545**(1–2), 23–29 (2002). https://doi.org/10.1016/S0370-2693(02)02589-3

[19] G. Feinberg, Physical Review, **159**(5), 1089 (1967). https://doi.org/10.1103/PhysRev.159.1089

[20] T. Padmanabhan, Physical Review D, **66**(2), 021301 (2002). https://doi.org/10.1103/PhysRevD.66.021301

[21] B. Feng *et al.*, Physics Letters B, **607**(1–2), 35–41 (2005). https://doi.org/10.1016/j.physletb.2004.12.071

[22] A. Kamenshchik, *et al.*, Physics Letters B, **511**(2–4), 265–268 (2001).https://doi.org/10.1016/S0370-2693(01)00571-8

[23] J.D. Bekenstein, Physical Review D, **7**(8), 2333 (1973). https://doi.org/10.1103/PhysRevD.7.2333

[24] SW Hawking, Communications in mathematical physics, **43**, 199–220 (1975). https://doi.org/10.1007/BF02345020

[25] S.W. Hawking, Communications in Mathematical Physics, **25**, 152–166 (1972). https://doi.org/10.1007/BF01877517

[26] G. t'Hooft, (1993). ArXiv preprint, https://doi.org/10.48550/arXiv.gr-qc/9310026

[27] W. Fischler, and L. Susskind, (1998), ArXiv preprint, https://doi.org/10.48550/arXiv.hep-th/9806039

[28] A.G. Cohen, *et al.*, Physical Review Letters, **82**(25), 4971 (1999). https://doi.org/10.1103/PhysRevLett.82.4971

[29] M. Li, Physics Letters B, **603**(1–2), 1–5 (2004). https://doi.org/10.1016/j.physletb.2004.10.014

[30] H. Wei, and S.N. Zhang, Physical Review D—Particles, Fields, Gravitation, and Cosmology, **76**(6), 063003 (2007). https://doi.org/10.1103/PhysRevD.76.063003

[31] L. Granda, and A. Oliveros, Physics Letters B, **669**(5), 275–277 (2008). https://doi.org/10.1016/j.physletb.2008.10.017

[32] L. Granda and A. Oliveros, Physics Letters B, **671**(2), 199–202 (2009). https://doi.org/10.1016/j.physletb.2008.12.025

[33] C. Gao, *et al.*, Physical Review D—Particles, Fields, Gravitation, and Cosmology, **79**(4), 043511 (2009). https://doi.org/10.1103/PhysRevD.79.043511

[34] M. Tavayef, *et al.*,Physics Letters B, **781**, 195–200 (2018).https://doi.org/10.1016/j.physletb.2018.04.001

[35] C. Tsallis, and L.J.L. Cirto, The European Physical Journal C, **73**, 2487 (2013). https://doi.org/10.1140/epjc/s10052-013-2487-6

[36] J.D. Barrow, Physics Letters B, **808**, 135643 (2020). https://doi.org/10.1016/j.physletb.2020.135643

[37] E.N. Saridakis, Physical Review D, **102**(12), 123525 (2020). https://doi.org/10.1103/PhysRevD.102.123525

[38] H. Moradpour *et al*., Physics Letters B, **783**, 82 (2018). https://doi.org/10.1016/j.physletb.2018.06.040

[39] S. Abe, Physical Review E, **63**, 061105 (2001). https://doi.org/10.1103/PhysRevE.63.061105

[40] A. Majhi, Physics Letters B, **775**, 32-36 (2017). https://doi.org/10.1016/j.physletb.2017.10.043

[41] T.S. Biro, and V.G. Czinner, Physics Letters B, **726**, 861-865 (2013). https://doi.org/10.1016/j.physletb.2013.09.032

[42] V.G. Czinner, and H. Iguchi, Physics Letters B, **752**, 306-310 (2016). https://doi.org/10.1016/j.physletb.2015.11.061

[43] N. Komatsu, The European Physical Journal C, **77**, 229 (2017). https://doi.org/10.1140/epjc/s10052-017-4800-2

[44] H. Moradpour *et al.*, Physical Review D, **96**, 123504 (2017). https://doi.org/10.1103/PhysRevD.96.123504

[45] A. Renyi, in: *Proceedings of the fourth Berkeley symposium on mathematical statistics and probability, vol. 1: Contributions to the theory of statistics*, vol. 4, (University of California Press, 1961), pp. 547-561.

[46] H. Moradpour, *et al.*, The European Physical Journal C, **78**, 829 (2018). https://doi.org/10.1140/epjc/s10052-018-6309-8

[47] A.S. Jahromi, *et al.*, Physics Letters B, **780**, 21–24 (2018). https://doi.org/10.1016/j.physletb.2018.02.052

[48] B.D. Sharma, and D.P. Mittal, Journal of Combinatorics Information & System Sciences, **2**(4), 122–132 (1977)

[49] G. Kaniadakis, Physical review E, **66**(5), 056125 (2002). https://doi.org/10.1103/PhysRevE.66.056125

[50] H. Moradpour, *et al.*, The European Physical Journal C, **80**, 732 (2020). https://doi.org/10.1140/epjc/s10052-020-8307-x

[51] N. Drepanou, *et al.*, The European Physical Journal C, **82**(5), 449 (2022). https://doi.org/10.1140/epjc/s10052-022-10415-9

[52] S. Chunlen, and P. Rangdee, (2020). https://arxiv.org/abs/2008.13730

[53] U.Y.D. Prasanthi, and Y. Aditya, Results in Physics, **17**, 103101 (2020). https://doi.org/10.1016/j.rinp.2020.103101

[54] M. Younas, et al., Advances in High Energy Physics, **2019**, 1287932 (2019). 10.1155/2019/1287932

[55] S. Maity, and U. Debnath, European Physical Journal Plus, **134**(10), 514 (2019). 10.1140/epjp/i2019-12884-6

[56] T. Chinnappalanaidu, *et al.*, East European Journal of Physics. (2), 159–172 (2025). https://doi.org/10.26565/2312-4334-2025-2-16

[57] A. Iqbal, and A. Jawad, Physics of the Dark Universe, **26**, 100349 (2019). https://doi.org/10.1016/j.dark.2019.100349

[58] A. Jawad, *et al.*, Symmetry, **10**(11), 635 (2018). https://doi.org/10.3390/sym10110635

[59] K.S. Adhav, *et al.*, Astrophysics and Space Science, **332**, 497–502 (2011). https://doi.org/10.1007/s10509-010-0519-3

[60] H. Amirhashchi, *et al.*, International Journal of Theoretical Physics, **50**, 3529–3543 (2011), https://doi.org/10.1007/s10773-011-0861-4

[61] A. Pradhan, *et al.*, Astrophysics and Space Science, **337**, 401-413 (2012). https://doi.org/10.1007/s10509-011-0835-2

[62] R. Sharma, and R. K. Mishra, Modern Physics Letters A, **41**07, 2650017 (2026). https://doi.org/10.1142/S0217732326500173

[63] H. Akaike, IEEE transactions on automatic control, **19**(6), 716-723 (1974). https://doi.org/10.1109/TAC.1974.1100705

[64] G. Schwarz, The Annals of Statistics, **6**(2), 461-464 (1978). https://www.jstor.org/stable/2958889

[65] N. Aghanim, *et al.*, Astron. Astrophys, **641**, A6 (2020). https://doi.org/10.1051/0004-6361/201833910

[66] A. G. Adame, *et al*., Journal of Cosmology and Astroparticle Physics, 2025(02), p. 021. https://doi.org/10.1088/1475-7516/2025/02/021

[67] M. Moresco, *et al.*, Journal of Cosmology and Astroparticle Physics, **2016**(05), 014-014 (2016). https://doi.org/10.1088/1475-7516/2016/05/014

[68] D. Brout, *et al.*, The Astrophysical Journal, **938**(2), 110 (2022). https://doi.org/10.3847/1538-4357/ac8e04

[69] B. Feng, *et al.*, Physics Letters B, **607**, 35–41 (2005). https://doi.org/10.1016/j.physletb.2004.12.071

[70] M. Cruz, and S. Lepe, Physics of the Dark Universe, **42**, 101367 (2023). https://doi.org/10.1016/j.dark.2023.101367

КОСМОЛОГІЧНА ЕВОЛЮЦІЯ АНІЗОТРОПНОГО ВСЕСВІТУ ТИПУ Б'ЯНКІ VI_0 З ГОЛОГРАФІЧНОЮ ТЕМНОЮ ЕНЕРГІЄЮ РЕНЬЇ

Чандра Рекха Маханта, **Раджашрі Маханта**
Кафедра математики, Університет Гаухаті, Гувахаті - 781014 (ІНДІЯ)

У цій роботі ми досліджуємо просторово однорідну та анізотропну космологічну модель типу Б'янкі VI_0 в рамках загальної теорії відносності, розглядаючи невзаємодіючу суміш темної матерії без тиску та голографічної темної енергії Рен'ї (ГТЕ), де горизонт Хаббла служить інфрачервоним обрізом. Точні розв'язки рівнянь поля Ейнштейна отримані шляхом прийняття гіперболічного масштабного коефіцієнта $a(t) = (\sinh(\beta t))^{1/n}$. Параметри моделі обмежені за допомогою аналізу методом Монте-Карло з використанням ланцюгів Маркова (MCMC) з використанням 77 вимірювань параметра Хаббла, отриманих за допомогою спостережних даних Хаббла (OHD), що дає значення найкращого наближення $H_0 = 67.9\ \mathrm{km\,s^{-1}\,Mpc^{-1}}$ та $n = 1.3$. Порівняння зі стандартною моделлю ΛCDM показує дещо нижче мінімальне значення χ^2 разом із негативними значеннями ΔAIC та ΔBIC, що вказує на помірну статистичну перевагу запропонованої моделі. Реконструйована космічна еволюція демонструє плавний перехід від фази уповільнення з домінуванням матерії до сучасної прискореної епохи, при цьому червоне зміщення переходу знаходиться в межах діапазону $0.5 \lesssim z_t \lesssim 0.7$, що є сприятливим для спостережень. Крім того, еволюція матерії та густини енергії, тиску темної енергії, параметра рівняння стану, параметра анізотропії та параметра асиметрії демонструють, що модель успішно відтворює спостережуване прискорене розширення наприкінці часу, одночасно зазнаючи поступової ізотропізації. Загалом, запропонована модель РДДЕ забезпечує фізично узгоджену та спостережливо життєздатну основу для опису еволюції Всесвіту наприкінці часу.

Ключові слова: *холодна темна матерія; простір-час типу Б'янкі* VI_0*; космічне прискорення; голографічна темна енергія Реньї; параметр уповільнення; параметр рівняння стану*

East European Journal of Physics. 3. 103-113 (2026)
DOI:10.26565/2312-4334-2026-3-09 ISSN 2312-4334

VISCOUS STRING COSMOLOGICAL MODEL WITH ELECTROMAGNETIC FIELD IN SAEZ-BALLESTER THEORY

Mohini R. Ugale[1]*, Sagar A. Bhakte[2†]
[1]*Department of Science and Humanities, Sipna College of Engineering and Technology, Amravati, 444 701 Maharastra, India*
[2]*Department of Mathematics, Prof Ram Meghe college of Engineering and Management,*
Badnera, Dist. Amravati 444 701 Maharastra , India
[†]*Corresponding Author: sagarbhakte25@gmail.com,* [*]*E-mail: mrugale@sipnaengg.ac.in*
Received May 15, 2026; revised August 11; accepted August 18, 2026

The framework of Saez-Ballester formalism is employed to study Bianchi Type III metrics, which is homogeneous and anisotropic, wherein the energy-momentum tensor is derived from a bulk viscous fluid containing one-dimensional strings embedded within an electromagnetic field. To obtain exact solutions, we utilized the proportionality relation between the expansion and shear scalars, as well as the average scale factor of a special form. In addition to the energy conditions, several dynamical and physical parameters were calculated, and their physical implications on cosmology were examined.
Keywords: *Bianchi type III Metric; Bulk Viscous Fluid; Cosmic Strings; Electromagnetic Field; Saez-Ballester theory*

1. INTRODUCTION

There has been increasing evidence over the past few decades that the universe is in accelerating expansion. This accelerating expansion has been confirmed by recent findings [1], [2], [3]. This accelerated expansion is believed to be driven by a substance known as 'Dark Energy. In modern cosmology, the mystery of its origin remains unresolved; nevertheless, it is indirectly viewed as a consequence of 'negative pressure' within the universe. Caldwell and Kamionkowski [4] provided the physics of cosmic acceleration. Silvestri and Trodden [5] presented an approach to understanding cosmic acceleration. Astier and Pain [6] gave observational evidence of the accelerated expansion of the universe. Perivolaropoulos [7] provided accelerating Universe's observational status. However, to be more precise, two different approaches have been proposed to resolve this problem: one involves developing viable 'dark energy' models, and the other involves modifying Einstein's theory of gravity. In this context, Turner and Huterer [8] investigated cosmic acceleration, dark energy and fundamental physics. Dolgov and Kawasaki [9] discussed whether modified gravity explains accelerated cosmic expansion. Nojiri and Odintsov [10] studied modified gravity and its reconstruction from the universe expansion history. Again, Nojiri and Odintsov [11] consider modifying GR theory - termed as the modified gravity approach. Again, Nojiri et al. [12], [13], [14] discussed some recent developments in modified gravity and unified cosmic history in addition to covering a number of common challenges.

The scalar tensor theories put forth by Lyra [15], Sen [16], Brans and Dicke [17], Sen and Dunn [18], Barber [19], Lau and Prokhovnik [20], Saez and Ballester [21] etc., have garnered a lot of attention in the past few decades. In the theory of Saez and Ballester [21], the metric is coupled to a dimensionless scalar field in a remarkably simple manner. This coupling provides a satisfactory description of weak fields; in such fields, despite the dimensionless nature of the scalar field's behaviour, a distinct regime of 'anti-gravity' is observed. This theory proposes a potential solution to the problem of 'missing matter' in non-FRW models. In this context, higher-dimensional Bianchi type-III string cosmological models with dark energy in Saez–Ballester theory is investigated by Dabgar and Bhabor [22]. Chetia et al. [23] studied particle creation and bulk viscosity in Bianchi-I universe in Saez–Ballester theory with different deceleration parameters. Kumawat et al. [24] studied an anisotropic Bianchi type VI_0 Spacetime with Barotropic Fluid in Sáez - Ballester Theory of Gravitation. Ram et al. [25] examined Bianchi type-V cosmological models with perfect fluid and heat flow in Saez-Ballester theory. Rao et al. [26] discussed Bianchi type-I and -III modified holographic Ricci Dark energy models in Saez-Ballester theory.

Bulk viscosity is important in cosmology and describes the universe's fast expansion, often known as the Big Bang epoch. Using a bulk-viscous fluid as the energy-momentum tensor (EMT), several cosmologists have investigated the theoretical evolution of the universe as well as the impact of bulk viscosity on cosmic history. Behera et al. [27] studied bulk viscous Bianchi-III models with time-dependent G and Λ. Bali and Pradhan [28] discussed Bianchi type III string cosmological models with time-dependent bulk viscosity. Constraining a bulk viscous Bianchi type I dark energy dominated universe with recent observational data observed by Yadav et al. [29]. Goswami et al. [30] studied modeling of an accelerating universe with bulk viscous fluid in Bianchi V spacetime. Bulk viscous cosmological model with varying deceleration parameter in modified gravity examined by Tiwari et al. [31]. Pawar and Dabre discussed [32] a bulk viscous string cosmological model with power law volumetric expansion in teleparallel gravity. Shukla et al. [33] studied viscous fluid dynamics in Bianchi type-I universe with decaying cosmological term.

Cite as: M.R. Ugale, S.A. Bhakte, East Eur. J. Phys. 3, 103 (2026), https://doi.org/10.26565/2312-4334-2026-3-09

Cosmic strings are one-dimensional topological defects that might have evolved during symmetry-breaking phase transitions in the early Universe. They should be separated from the basic strings found in string theory, since the two ideas have distinct physical origins and meanings. In this paper, the word "string" refers only to cosmology cosmic strings represented by a string-cloud energy-momentum tensor, not the basic strings of string theory. Cosmic strings may have a major role in the dynamics of the early Universe [34], contributing to density perturbations and the development of large-scale structures [35, 36]. Their stress-energy may also affect the anisotropic development of spacetime. Vilenkin and Shellard [37] provide a full study of cosmic strings and associated topological flaws. In this framework, Singh [38] examined a string LRS Bianchi type-I universe with a functional relationship for the Hubble parameter. Rao et al. [39] investigated a Bianchi type-III magnetised string model with a constant deceleration parameter in general relativity. Pawar et al. [40] investigated a plane-symmetric string cosmology model with a zero-mass scalar field in modified gravity theory, while Mete et al. [41] investigated the dynamics of cosmic strings and domain barriers using a specific version of the deceleration parameter.

Cosmic magnetic fields, which are parts of the electromagnetic field, may have a substantial impact on the distribution of energy and the anisotropic development of the Universe because of the existence of ionised matter. Magnetic fields may be amplified by adiabatic compression within astrophysical objects, and the stress-energy of large-scale electromagnetic fields may contribute to spacetime anisotropy. Thus, the electromagnetic energy-momentum tensor is used to reliably integrate the magnetic contribution in the current task. Wang [42] investigated the Bianchi type-III string cosmological model with bulk viscosity and magnetic field. Tripathy et al. [43] studied string cloud cosmologies for Bianchi type-III models with electromagnetic field. Brahma and Dewri [44] discussed the role of $f(R, T)$ gravity in Bianchi Type-V dark energy model with electromagnetic field based on Lyra geometry. Rehman et al. [45] studied electromagnetic field effects on anisotropic cylindrically symmetric compact objects within the framework of $f(R, L_m, T)$ gravity. Five-dimensional Bianchi type-I anisotropic cloud string cosmological model with electromagnetic field in Sáez-Ballester theory, examined by Daimary and Baruah [46]. Ramprasad [47] investigated a study on cosmological model of anisotropic universe with electromagnetic field and cloud strings in the framework of general relativity.

A variety of topics related to anisotropic cosmology, cosmic strings, bulk viscosity, electromagnetic fields, and Saez-Ballester gravity are covered in the works discussed above. However, further research is need to fully understand the simultaneous impact of these components in a Bianchi type-III cosmological scenario. For instance, Dabgar and Bhabor [22] examines a higher-dimensional Bianchi type-III string cosmology with dark energy in Saez–Ballester theory, whereas Chetia et al [23] studies bulk viscosity and particle formation in a Bianchi type-I universe. In contrast, a five-dimensional Bianchi type-I anisotropic cloud-string cosmological model with an electromagnetic field in Saez–Ballester theory is studied by Daimary and Baruah [45]. Motivated by these findings, the current study examines a four-dimensional Bianchi type-III spacetime including a bulk-viscous fluid and one-dimensional cosmic strings contained in an electromagnetic field inside the Saez-Ballester gravitational framework. The goal is to acquire accurate solutions and look into the combined effects of anisotropy, bulk viscosity, string tension, the electromagnetic field, and the Saez-Ballester scalar field on cosmic development. We next examine the kinematical parameters, matter variables, effective pressure, and energy conditions to evaluate the model's physical behaviour.

2. METRIC & FIELD EQUATIONS

We consider a homogeneous and anisotropic space-time described by a Bianchi type-III metric as

$$ds^2 = dt^2 - A^2 dx^2 - B^2 e^{-2mx} dy^2 - C^2 dz^2, \tag{1}$$

where *A, B* and *C* are the metric potentials considered as functions of cosmic time *t* only.
The field equations given by Saez and Ballester [21] for the combined scalar ω and tensor fields are

$$G_i^j - \omega\varphi^n \left(\varphi_{,i}\varphi^{,j} - \frac{1}{2}\delta_i^j \varphi_{,k}\varphi^{,k} \right) = -T_i^j, \tag{2}$$

The scalar field φ satisfies the equation

$$2\varphi^n \varphi^i_{;i} + n\varphi^{n-1}\varphi_{,k}\varphi^{k} = 0, \tag{3}$$

Where $G_j^i = R_j^i - \frac{1}{2}\delta_j^i R$ is Einstein's equation and *n* are constants, T_i^j is the stress energy-momentum tensor, comma and semicolon represent partial and covariant differentiation, respectively.
A bulk viscous fluid with one-dimensional strings immersed in an electromagnetic field, as an EMT, is calculated as

$$T_\mu^\nu = (\rho + \bar{p}) u_\mu u^\nu - \bar{p} g_\mu^\nu - \lambda x_\mu x^\nu + E_\mu^\nu, \tag{4}$$

And

$$\bar{p} = p - 3\xi H, \tag{5}$$

where $\rho = \rho_p + \lambda$ is the proper string energy density with particles attached to them, and ρ_p is the particle energy density, λ is the string's tension density, $3\xi H$ is bulk viscous pressure, $\xi(t)$ is the coefficient of bulk viscosity, H is Hubble's parameter, x^ν denotes a unit space-like vector for the cloud string and u^ν denotes a four-velocity vector satisfying the conditions, $u^\nu u_\nu = 1 = -x^\nu x_\nu$ and $u_\nu x^\nu = 0$.
In a co-moving coordinate system, we have

$$u^\nu = (0,0,0,1), \;\; x^\nu = (0,0,C^{-1},0). \tag{6}$$

Also, $E_{\mu\nu}$ is a part of EMT given as

$$E_{\mu\nu} = \frac{1}{4\pi}\left[F_{\mu\alpha}F_{\nu\beta}g^{\alpha\beta} - \frac{1}{4}g_{\mu\nu}F^{\alpha\beta}F_{\alpha\beta}\right], \tag{7}$$

where $F_{\mu\nu}$ is electromagnetic field tensor that satisfies Maxwell equations,

$$F_{[\mu\nu,k]} = 0. \tag{8}$$

In a comoving coordinate system, the incident magnetic field is taken along z-axes with the help of Maxwell equation (8), the components of $F_{\mu\nu}$ except F_{12} vanish, i.e. F_{12} is the only non-vanishing component along z-axes.

$$F_{12} = \text{Constant} = M \;\; (\text{Say})$$

From equation (7), we have

$$E_1^1 = E_2^2 = \frac{M^2}{8\pi A^4} \;\text{ and }\; E_3^3 = E_4^4 = -\frac{M^2}{8\pi A^4}. \tag{9}$$

Now, the field equations (2) & (3) from metric (1) using (4), we get,

$$\frac{\ddot{B}}{B} + \frac{\ddot{C}}{C} + \frac{\dot{B}}{B}\frac{\dot{C}}{C} - \frac{\omega}{2}\varphi^n\dot{\varphi}^2 = -(p - 3\xi H) + \frac{M^2}{8\pi A^4}, \tag{10}$$

$$\frac{\ddot{A}}{A} + \frac{\ddot{C}}{C} + \frac{\dot{A}}{A}\frac{\dot{C}}{C} - \frac{\omega}{2}\varphi^n\dot{\varphi}^2 = -(p - 3\xi H) + \frac{M^2}{8\pi A^4}, \tag{11}$$

$$\frac{\ddot{A}}{A} + \frac{\ddot{B}}{B} + \frac{\dot{A}}{A}\frac{\dot{B}}{B} - \frac{m^2}{A^2} - \frac{\omega}{2}\varphi^n\dot{\varphi}^2 = -(p - 3\xi H) + \lambda - \frac{M^2}{8\pi A^4}, \tag{12}$$

$$\frac{\dot{A}}{A}\frac{\dot{B}}{B} + \frac{\dot{B}}{B}\frac{\dot{C}}{C} + \frac{\dot{A}}{A}\frac{\dot{C}}{C} - \frac{m^2}{A^2} + \frac{\omega}{2}\varphi^n\dot{\varphi}^2 = \rho - \frac{M^2}{8\pi A^4}, \tag{13}$$

$$\frac{\dot{A}}{A} - \frac{\dot{B}}{B} = 0, \tag{14}$$

$$\ddot{\varphi} + \left(\frac{\dot{A}}{A} + \frac{\dot{B}}{B} + \frac{\dot{C}}{C}\right)\dot{\varphi} + \frac{n}{2}\frac{\dot{\varphi}^2}{\varphi} = 0, \tag{15}$$

where the overhead dot $(\cdot)$ denotes the derivative with respect to cosmic time *t*. By solving (14), one can get $A = kB$, where k is an integrating constant. Without loss of generality, we take $k = 1$. Then (10) - (13) reduces to

$$\frac{\ddot{B}}{B} + \frac{\ddot{C}}{C} + \frac{\dot{B}}{B}\frac{\dot{C}}{C} - \frac{\omega}{2}\varphi^n\dot{\varphi}^2 = -(p - 3\xi H) + \frac{M^2}{8\pi B^4}, \tag{16}$$

$$2\frac{\ddot{B}}{B} + \frac{\dot{B}^2}{B^2} - \frac{m^2}{A^2} - \frac{\omega}{2}\varphi^n\dot{\varphi}^2 = -(p - 3\xi H) + \lambda - \frac{M^2}{8\pi B^4}, \tag{17}$$

$$\frac{\dot{B}^2}{B^2} + 2\frac{\dot{B}}{B}\frac{\dot{C}}{C} - \frac{m^2}{A^2} + \frac{\omega}{2}\varphi^n\dot{\varphi}^2 = \rho - \frac{M^2}{8\pi B^4}, \tag{18}$$

Here we have three non-linear differential field equations with seven unknowns, namely B, C, p, ξ, λ, ρ and φ. The solution of these unknowns is discussed in the next section.

Now, we find some kinematical space-time quantities of physical interest in cosmology, as follows:

The average scale factor a and the spatial volume V are respectively defined as

$$a = \sqrt[3]{B^2 C}, \text{ and } V = a^3. \tag{19}$$

The volumetric expansion rate of the universe is described by the generalised mean Hubble's parameter H & given by

$$H = \frac{1}{3}\sum_{i=1}^{3} H_i = \frac{1}{3}\left(H_1 + H_2 + H_3\right), \tag{20}$$

in which $H_1 = H_2 = \frac{\dot{B}}{B}$, and $H_3 = \frac{\dot{C}}{C}$ denotes the directional Hubble's parameters.

Using (19) and (20), we have obtained the expansion scalar θ, mean anisotropy parameter Δ, shear scalar σ, and deceleration parameter q, respectively, as

$$\theta = 3H, \tag{21}$$

$$\Delta = \frac{1}{3}\sum_{i=1}^{3}\left(\frac{H_i - H}{H}\right)^2, \tag{22}$$

$$\sigma^2 = \frac{1}{2}\left(\sum_{i=1}^{3} H_i^2 - \theta^2\right), \tag{23}$$

$$q = -\frac{a\ddot{a}}{\dot{a}^2} = -1 + \frac{d}{dt}\left(\frac{1}{H}\right). \tag{24}$$

3. SOLUTION OF FIELD EQUATIONS

The three nonlinear differential field equations (16) - (18) and seven unknowns are solved by taking into account the following physically possible possibilities.

Initially, we took the mean scale factor's spatial form as

$$a = \left(ct + d\right)^{\frac{1}{m}}, \tag{25}$$

where, c, d and m are non-negative constants.

Next, we argued that the shear scalar is proportional to the expansion scalar, providing the analytical relation.

$$B = C^{\zeta}, \tag{26}$$

Using (19), (25), & (26), we obtained

$$A = B = \left(ct + d\right)^{\frac{3\zeta}{m(1+2\zeta)}} \text{ and } C = \left(ct + d\right)^{\frac{3}{m(1+2\zeta)}}. \tag{27}$$

From (27) in (1), we have

$$ds^2 = dt^2 - \left(ct + d\right)^{\frac{6\zeta}{m(1+2\zeta)}} dx^2 - \left(ct + d\right)^{\frac{6\zeta}{m(1+2\zeta)}} e^{-2mx} dy^2 - \left(ct + d\right)^{\frac{6}{m(1+2\zeta)}} dz^2. \tag{28}$$

The model generated in expression (27) is devoid of any form of singularity until infinite cosmic time.

The Volume

$$V = a^3 = \left(ct + d\right)^{\frac{3}{m}}. \tag{29}$$

It is evident from expression (29) that this formulation is in power law form, which establishes that volume grows with time.

The Hubble parameter & expansion scalar

$$H = \frac{1}{3}\sum_{i=1}^{3} H_i = \frac{c}{m\left(ct + d\right)}, \tag{30}$$

$$\theta = 3H = \frac{3c}{m(ct+d)}. \tag{31}$$

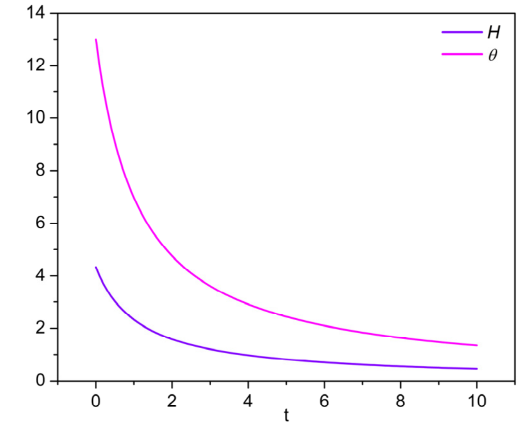

Figure 1. Plot of the expansion scalar & Hubble parameter vs. time for $c = 1.3,\ d = 1.5,\ m = 0.2$.

Figure 1 shows a diminishing graphical representation of the Hubble parameter and expansion scalar over time, implying that the universe's expansion rate is slowing.

The mean anisotropy parameter & shear scalar is

$$\Delta = \frac{1}{3}\sum_{i=1}^{3}\left(\frac{H_i - H}{H}\right)^2 = \frac{2(\zeta-1)^2}{(1+2\zeta)^2}. \tag{32}$$

$$\sigma^2 = \frac{1}{2}\left(\sum_{i=1}^{3} H_i^2 - \theta^2\right) = \frac{3(\zeta-1)^2 c^2}{(1+2\zeta)^2 m^2 (ct+d)^2}. \tag{33}$$

Expressions (32) and (33) show that, with the exception of $\varsigma = 1$, the universe never approaches isotropy and maintains shear.

The deceleration parameter (DP)

$$q = -1 + \frac{d}{dt}\left(\frac{1}{H}\right) = m - 1. \tag{34}$$

The model's acceleration is indicated by the sign of q. A decelerating phase of the universe is indicated by a positive sign of DP q for $m > 1$, an acceleration phase is indicated by $-1 \le q < 0$, and a stable rate of evolution is indicated by $q = 0$. The accelerated phase of the cosmos is supported by recent observations [48], [49], [50]. Additionally, for the selected choice of constants, i.e. $m = 0.2$, the value of DP is $q = -0.8$, showing accelerated expansion.

From (15), the scalar field can be obtained as

$$\varphi = \left(\frac{m(2+n)(ct+d)(ct+d)^{-\frac{3}{m}} + 2c(m-3)c_1}{2c(m-3)}\right)^{\frac{2}{2+n}}. \tag{35}$$

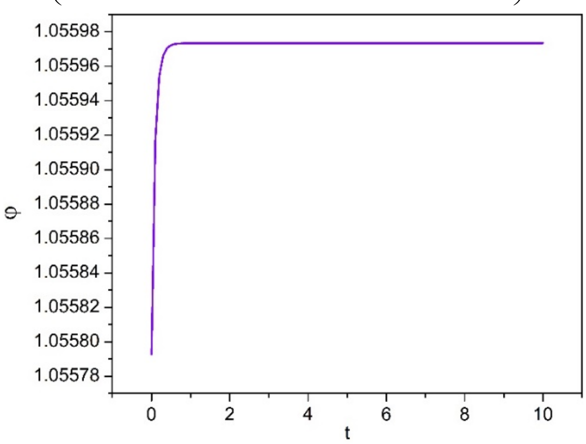

Figure 2. Plot of the scalar field vs. time for $c = 1.3,\ d = 1.5,\ m = 0.2,\ n = 1.5,\ c_1 = 1.1$.

As seen in Figure 2, the scalar field graph first climbs rapidly throughout the range of $t = 0$ to 0.4 up to $\varphi = 1.055973$, and it remains at this constant value for the rest of the evolution.
From (18), the energy density is

$$\rho = \frac{M^2(ct+d)^{-\frac{12\zeta}{m(1+2\zeta)}} m^2(1+2\zeta)^2(ct+d)^2 - 4\pi\left[\begin{array}{l} 2m^4(ct+d)^{-\frac{6\zeta}{m(1+2\zeta)}}(1+2\zeta)^2(ct+d)^2 \\ -\omega(ct+d)^{-\frac{6}{m}} m^2(1+2\zeta)^2(ct+d)^2 - 18\zeta c^2(\zeta+2) \end{array}\right]}{8(1+2\zeta)^2(ct+d)^2 m^2\pi}. \tag{36}$$

Solving (16) & (17), the tension density is

$$\lambda = \frac{(1+2\zeta)M^2(ct+d)^{-\frac{12\zeta}{m(1+2\zeta)}} m^2(ct+d)^2 - 4\pi\left[m^4(1+2\zeta)(ct+d)^2(ct+d)^{-\frac{6\zeta}{m(1+2\zeta)}} + 3c^2(\zeta-1)(m-3)\right]}{4m^2\pi(1+2\zeta)(ct+d)^2}. \tag{37}$$

The particle density is

$$\rho_p = \frac{\begin{array}{l} 4\pi\left\{m^2\omega(1+2\zeta)^2(ct+d)^{\frac{2m-6}{m}} + 6c^2\left[\left(2\zeta^2-\zeta-1\right)m - 3\left(\zeta^2+3\zeta+1\right)\right]\right\} \\ -m^2(1+2\zeta)^2 M^2(ct+d)^{\frac{(2+4\zeta)m-12\zeta}{m(1+2\zeta)}} \end{array}}{8m^2\pi(1+2\zeta)^2(ct+d)^2}. \tag{38}$$

Letelier [51] examined the prospect that strings would vanish during the universe's history, leaving only particles, and noted that the string tension density could be either positive or negative. The physical behaviour of particles, tension, and energy density is viewed in the context of cosmic time, which is illustrated in Figure 3; this figure demonstrates that as cosmic time progresses, both of these densities decrease. In our model, the condition $\lambda > 0$ during the evolution of the universe signifies the existence of strings; however, particles ultimately dominate the universe, as the contribution of strings is negligible compared to that of particles.

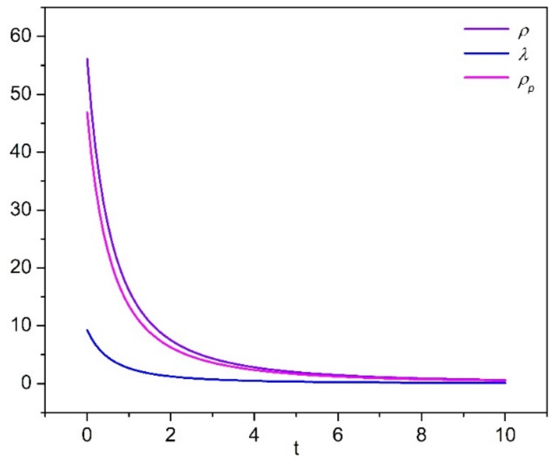

Figure 3. Plot of the energy, tension & particle density vs. time for $M = 2,\ \zeta = 1.2,\ c = 1.3,\ d = 1.5,\ m = 0.2,\ \omega = 0.1$.

We assume that the coefficient of viscosity should vary with the expansion scalar in such a way that

$$\xi\theta = \xi_0 = \text{Constant}. \tag{39}$$

Therefore, we obtain

$$\xi = \frac{m\xi_0(ct+d)}{3c}. \tag{40}$$

The bulk viscosity coefficient is a strictly rising function of cosmic time, as seen in Figure 4.

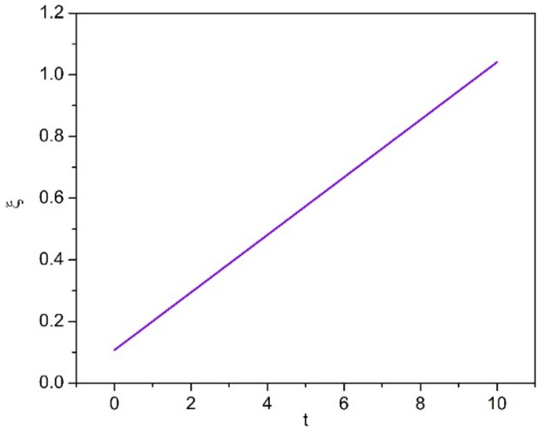

Figure 4. Plot of the viscosity coefficient vs. time for $c=1.3,\ d=1.5,\ m=0.2,\ \xi_0=1.4$.

From (16), the pressure is

$$p=\frac{M^2\left(ct+d\right)^{-\frac{12\zeta}{m(1+2\zeta)}}m^2\left(1+2\zeta\right)^2\left(ct+d\right)^2+4\pi\left[\begin{array}{l}\omega\left(ct+d\right)^{-\frac{6}{m}}m^2\left(1+2\zeta\right)^2\left(ct+d\right)^2\\+2\left(1+2\zeta\right)^2\left(ct+d\right)^2\xi_0 m^2\\+6\left(1+2\zeta\right)\left(\zeta+1\right)c^2m-18c^2\left(\zeta^2+\zeta+1\right)\end{array}\right]}{8m^2\pi\left(1+2\zeta\right)^2\left(ct+d\right)^2}. \tag{41}$$

From (5), the effective pressure is

$$\bar{p}=\frac{m^2\left(1+2\zeta\right)^2M^2\left(ct+d\right)^{\frac{(2+4\zeta)m-12\zeta}{m(1+2\zeta)}}+4\pi\left\{m^2\omega\left(1+2\zeta\right)^2\left(ct+d\right)^{\frac{2m-6}{m}}+6c^2\left[\left(2\zeta^2+3\zeta+1\right)m-3\left(\zeta^2-\zeta-1\right)\right]\right\}}{8m^2\pi\left(1+2\zeta\right)^2\left(ct+d\right)^2}. \tag{42}$$

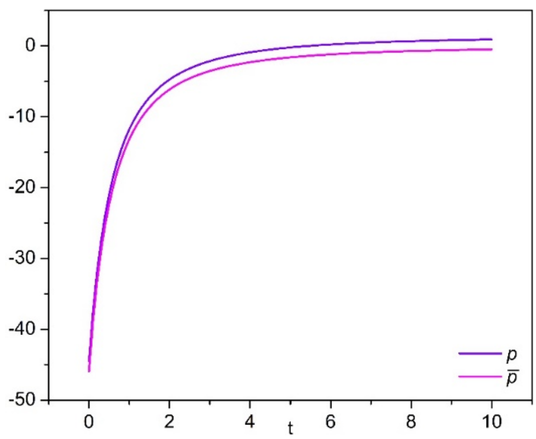

Figure 5. Plot of the pressure & effective pressure vs. time for $M=2,\ \zeta=1.2,\ c=1.3,\ d=1.5,\ m=0.2,\ \omega=0.1,\ \xi_0=1.4$.

A graph illustrating pressure and effective pressure is presented in Figure 5. It is evident from Figure 5 that both these parameters commence with negative values and increase over the course of cosmic time; however, in subsequent epochs, the cosmic pressure becomes slightly positive, whereas the effective pressure remains negative. It is a well-established fact that negative cosmic pressure serves as an indicator of cosmic acceleration.

The Energy Conditions

The energy conditions are respectively defined as [52]

i. Null Energy Condition (NEC) : $\rho+p\geq 0$
ii. Weak Energy Condition (WEC) : $\rho\geq 0,\ \rho+p\geq 0$
iii. Strong Energy Condition (SEC) : $\rho+3p\geq 0$
iv. Dominant Energy Condition (DEC) : $\rho\geq 0,\ \rho\pm p\geq 0$

From (32) and (37), we can express the conditions as

$$\rho+p=\frac{m^2(1+2\zeta)^2M^2(ct+d)^{\frac{(2+4\zeta)m-12\zeta}{m(1+2\zeta)}}+4\pi\begin{bmatrix}m^2\omega(1+2\zeta)^2(ct+d)^{\frac{2m-6}{m}}-(ct+d)^{\frac{(2+4\zeta)m-6\zeta}{m(1+2\zeta)}}(1+2\zeta)^2m^4\\+(1+2\zeta)^2(ct+d)^2\xi_0m^2+3(1+2\zeta)(\zeta+1)c^2m+9c^2(\zeta-1)\end{bmatrix}}{4m^2\pi(1+2\zeta)^2(ct+d)^2}, \tag{43}$$

$$\rho+3p=\frac{4m^2(1+2\zeta)^2M^2(ct+d)^{\frac{(2+4\zeta)m-12\zeta}{m(1+2\zeta)}}-8\pi\left\{\begin{matrix}(1+2\zeta)^2\begin{bmatrix}(ct+d)^{\frac{(2+4\zeta)m-6\zeta}{m(1+2\zeta)}}m^4\\-2m^2\omega(ct+d)^{\frac{2m-6}{m}}-3(ct+d)^2\xi_0m^2\end{bmatrix}\\-9c^2\left[2(m-1)\zeta^2+(3m-1)\zeta+m-3\right]\end{matrix}\right\}}{8m^2\pi(1+2\zeta)^2(ct+d)^2}, \tag{44}$$

$$\rho-p=-\left\{\frac{(1+2\zeta)\left[(ct+d)^{\frac{(2+4\zeta)m-6\zeta}{m(1+2\zeta)}}m^4+(ct+d)^2\xi_0m^2\right]+3c^2(\zeta+1)[m-3]}{(1+2\zeta)m^2(ct+d)^2}\right\}. \tag{45}$$

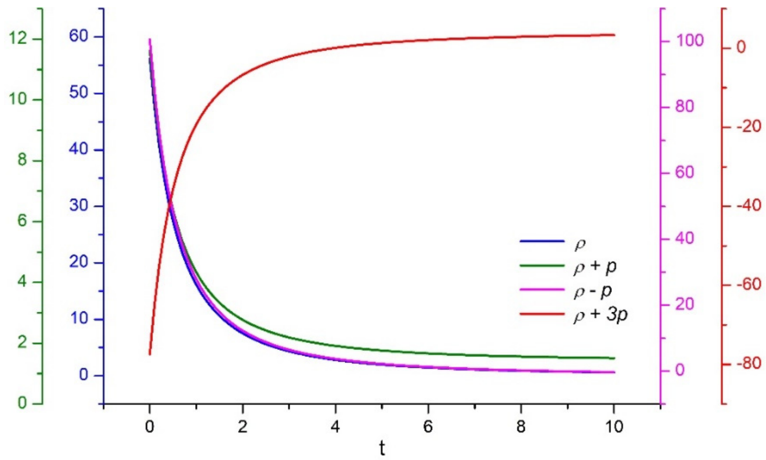

Figure 6. Plot of the energy conditions vs. time for $M=2,\ \zeta=1.2,\ c=1.3,\ d=1.5,\ m=0.2,\ \omega=0.1,\ \xi_0=1.4$.

A graph of the energy conditions is presented in Figure 6. The figure reveals that, during the evolution of the universe, since only $\rho+3p<0$, all energy conditions with the exception of the SEC are satisfied. The SEC has significant implications for cosmology. Negative pressure is sufficient to violate the SEC; that is, a violation of the SEC accelerates cosmic expansion, and therefore, it supports the inflation and dark energy models. Furthermore, a violation of the SEC implies that this model can avoid a singularity. These findings are fully consistent with [53], [54].

4. CONCLUSIONS

Within the framework of Saez-Ballester theory, in this research, the authors have investigated a homogeneous and anisotropic Bianchi Type III metric, wherein the EMT consists of a viscous fluid coupled with a string of clouds embedded in an electromagnetic field. To obtain exact solutions to the field equations, a specific form of the average scale factor and a shear-expansion scalar relationship are utilized. Some kinematic and physical parameters were calculated in addition to energy conditions, and their physical implications in cosmology were examined.

The created model behaves like a conventional cosmological model that is free of singularities until infinite duration, is accelerating, expanding with a decreasing rate of expansion over time, and anisotropic with holding shear. The scalar field of the model increases rapidly from $t=0$ to 0.4, reaching a value of $\varphi=1.055973$, and remains constant for the remainder of its evolution. Both the energy, tension, and particle density are positive and exhibit a decreasing trend. In our model, we have detected the presence of strings; however, particles ultimately dominate the universe, as the contribution of strings is negligible compared to that of particles. The bulk viscosity coefficient is a strictly increasing function of cosmic time. The values for both pressure and effective pressure are negative and increase with cosmic time; however, in subsequent epochs, only the cosmic pressure becomes slightly positive. Furthermore, except for the SEC, all energy conditions are satisfied. The SEC has significant implications in cosmology. Negative pressure is sufficient to violate the SEC; that is, a violation of the SEC accelerates cosmic expansion and, consequently, lends support to inflationary and dark energy models. Moreover, a violation of the SEC suggests that this model may be able to avoid a singularity. The findings obtained in this research are fully consistent with recent observational data.

Compared to the previous research presented in the Introduction, the current analysis contains Bianchi type-III anisotropy, a bulk-viscous cosmic-string fluid, an electromagnetic field, and the Saez-Ballester scalar degree of freedom. The resultant model shows rapid expansion for the chosen model parameters, whereas the Hubble parameter and expansion scalar decrease with cosmic time. The matter, string-tension, and particle densities decline throughout evolution, whereas the effective pressure stays negative throughout the relevant era. The model remains anisotropic except for the exceptional isotropic limit. These characteristics define the cosmic behaviour of the matter-gravity system under consideration. The Saez-Ballester theory introduces a dimensionless scalar field that is connected to the gravitational sector. In this study, it is viewed as an effective gravitational field and is not associated with the Higgs field or any empirically discovered basic scalar particle. Thus, its function in the model is phenomenological under the Saez-Ballester gravitational framework.

Future research might expand on the current work by investigating the model's dynamical stability, cosmic disturbances, other forms of the bulk-viscosity coefficient, and the impact of various electromagnetic-field configurations. It would also be interesting to restrict the free model parameters using empirical datasets and look into the approach to the isotropic limit at late cosmic periods.

ORCID

Mohini R. Ugale, https://orcid.org/0000-0001-5819-6139; **Sagar A. Bhakte,** https://orcid.org/0009-0003-8828-5003

REFERENCES

[1] B.P. Schmidt, et al., "The High-Z Supernova Search: Measuring Cosmic Deceleration and Global Curvature of the Universe Using Type Ia Supernovae", Astrophys. J. **507**(1), 46–63 (1998). https://doi.org/10.1086/306308
[2] S. Perlmutter et al., "Measurements of Ω and Λ from 42 High-Redshift Supernovae," Astrophys. J. **517**(2), 565–586 (1999). https://doi.org/10.1086/307221
[3] A.G. Riess, et al., "Observational Evidence from Supernovae for an Accelerating Universe and a Cosmological Constant," Astron. J. **116**(3), 1009–1038 (19980. https://doi.org/10.1086/300499
[4] R.R. Caldwell, and M. Kamionkowski, "The Physics of Cosmic Acceleration," Annual Review of Nuclear and Particle Science, **59**(1), 397–429 (2009). https://doi.org/10.1146/annurev-nucl-010709-151330
[5] A. Silvestri, and M. Trodden, "Approaches to understanding cosmic acceleration," Reports on Progress in Physics, **72**(9), 096901 (2009). https://doi.org/10.1088/0034-4885/72/9/096901
[6] P. Astier, and R. Pain, "Observational evidence of the accelerated expansion of the universe," C. R. Phys. **13**(6–7), 521–538 (2012). https://doi.org/10.1016/j.crhy.2012.04.009
[7] L. Perivolaropoulos, "Accelerating Universe : Observational Status," **290**, 257–258 (2007). https://doi.org/10.1007/978-3-540-71013-4
[8] M.S. Turner, and D. Huterer, "Cosmic Acceleration, Dark Energy and Fundamental Physics," **76**, 111015 (2007). https://doi.org/10.1143/JPSJ.76.111015
[9] A.D.D. Dolgov, and M. Kawasaki, "Can modified gravity explain accelerated cosmic expansion?" Physics Letters B, **573**(1-4), 1–4 (2003). https://doi.org/10.1016/j.physletb.2003.08.039
[10] S. Nojiri, and S. D. Odintsov, 'Modified gravity and its reconstruction from the universe expansion history', J. Phys. Conf. Ser. **66**(1), (2007). https://doi.org/10.1088/1742-6596/66/1/012005
[11] S.S. Nojiri, and S. D. Odintsov, "Unified cosmic history in modified gravity: From F(R) theory to Lorentz non-invariant models," Phys. Rep. **505**(2–4), 59–144 (2011). https://doi.org/10.1016/j.physrep.2011.04.001
[12] S. Nojiri, S. D. Odintsov, and V. K. Oikonomou, "Modified gravity theories on a nutshell: Inflation, bounce and late-time evolution," Phys. Rep. **692**(1–104), (2017). https://doi.org/10.1016/j.physrep.2017.06.001
[13] S. Nojiri, and S. D. Odintsov, "Unified cosmic history in modified gravity: from F (R) theory to Lorentz non-invariant models," Physics Reports, **505**(2-4), 59-144 (2011). https://doi.org/10.1016/j.physrep.2011.04.001
[14] S. Nojiri, and S.D. Odintsov, "Introduction to modified gravity and gravitational alternative for dark energy," International Journal of Geometric Methods in Modern Physics, **4**(01), 115-145 (2007). https://doi.org/10.1142/S0219887807001928
[15] G. Lyra, "Über eine Modifikation der Riemannschen Geometrie," Mathematische Zeitschrift, **54**(1), (1951). https://doi.org/10.1007/BF01175135
[16] D.K. Sen, "A static cosmological model," Zeitschrift für Physik, **149**(3), 311–323 (1957). https://doi.org/10.1007/BF01333146/METRICS
[17] C. Brans, and R. H. Dicke, "Mach's Principle and a Relativistic Theory of Gravitation," Physical Review, **124**(3), 925 (1961). https://doi.org/10.1103/PhysRev.124.925
[18] D.K. Sen, and K. A. Dunn, "A Scalar-Tensor Theory of Gravitation in a Modified Riemannian Manifold," J. Math. Phys. **12**(4), 578–586 (1971). https://doi.org/10.1063/1.1665623
[19] G.A. Barber, "On two "self-creation" cosmologies," Gen. Relativ. Gravit. **14**(2), 117–136 (1982). https://doi.org/10.1007/BF00756918
[20] Y. Lau, and S. Prokhovnik, "The Large Numbers Hypothesis and a Relativistic Theory of Gravitation," Australian Journal of Physics, **39**(3), 339–346 (1986). https://doi.org/10.1071/ph860339
[21] D. Sáez, and V. J. Ballester, "A simple coupling with cosmological implications," Phys. Lett. A, **113**(9), 467–470 (1986). https://doi.org/10.1016/0375-9601(86)90121-0

[22] R.K. Dabgar, and A. K. Bhabor, "Higher dimensional Bianchi type-III string cosmological models with dark energy in Saez–Ballester scalar-tensor theory of gravitation," Journal of Astrophysics and Astronomy, **44**(2), 78 (2023). https://doi.org/10.1007/s12036-023-09971-7
[23] C. Chetia, M. M. Gohain, and K. Bhuyan, "Particle creation and bulk viscosity in Bianchi-I universe in Saez–Ballester theory with different deceleration parameters," Gen. Relativ. Gravit. **55**(10), 107 (2023). https://doi.org/10.1007/s10714-023-03155-y
[24] P. Kumawat, R. Goyal, and S. Choudhary, "Anisotropic Bianchi type VI0 Space-Time with Barotropic Fluid in Sáez – Ballester Theory of Gravitation," Journal of Scientific Research, **16**(3), 695–703 (2024). https://doi.org/10.3329/jsr.v16i3.70809
[25] S. Ram, M. Zeyauddin, and C. P. Singh, 'Bianchi type-V cosmological models with perfect fluid and heat flow in Saez-Ballester theory', Pramana, **72**(2), 415–427 (2009). https://doi.org/10.1007/s12043-009-0037-4
[26] V.U. M. Rao, and U. Y. Divya Prasanthi, "Bianchi type-I and -III modified holographic Ricci Dark energy models in Saez-Ballester theory," The European Physical Journal Plus, **132**(2), 64 (2017). https://doi.org/10.1140/epjp/i2017-11328-9
[27] D. Behera, S. K. Tripathy, and T. R. Routray, "Bulk Viscous Bianchi-III Models with Time Dependent G and Λ," International Journal of Theoretical Physics, **49**(10), 2569–2581 (2010). https://doi.org/10.1007/s10773-010-0448-5
[28] R. Bali and A. Pradhan, "Bianchi Type-III String Cosmological Models with Time Dependent Bulk Viscosity," Chinese Physics Letters, **24**(2), 585 (2007). https://doi.org/10.1088/0256-307X/24/2/079
[29] A.K. Yadav, A. K. Yadav, M. Singh, R. Prasad, N. Ahmad, and K. P. Singh, "Constraining a bulk viscous Bianchi type I dark energy dominated universe with recent observational data," Physical Review D, **104**(6), 064044 (2021). https://doi.org/10.1103/PhysRevD.104.064044
[30] G.K. Goswami, A. K. Yadav, B. Mishra, and S. K. Tripathy, "Modeling of Accelerating Universe with Bulk Viscous Fluid in Bianchi V Space-Time," Fortschritte der Physik, **69**(6), 2100007 (2021). https://doi.org/10.1002/prop.202100007
[31] R. K. Tiwari, A. Beesham, and A. K. Jaiswal, "Bulk viscous cosmological model with varying deceleration parameter in modified gravity," International Journal of Geometric Methods in Modern Physics, **23**(18), 2650087 (2026). https://doi.org/10.1142/S0219887826500878
[32] K. Pawar, and A. K. Dabre, "Bulk Viscous String Cosmological Model with Power Law Volumetric Expansion in Teleparallel Gravity," Astrophysics, **66**(1), 114–126 (2023). https://doi.org/10.1007/s10511-023-09774-2
[33] B.K. Shukla, A. Beesham, D. Sofuoğlu, R. K. Dubey, and P. Mishra, "Viscous fluid dynamics in Bianchi type-I universe with decaying cosmological term," International Journal of Geometric Methods in Modern Physics, **23**(08), 2550226 (2026). https://doi.org/10.1142/S0219887825502263
[34] T.W.B. Kibble, "Topology of cosmic domains and strings," J. Phys. A Math. Gen. **9**(8), 1387 (1976). https://doi.org/10.1088/0305-4470/9/8/029
[35] Y. B. Zel'dovich, I. Y. Kobzarev, and L. B. Okun, "Cosmological consequences of spontaneous violation of discrete symmetry," Zh. Eksp. Teor. Fiz. **40**, 3–11 (1974). Accessed: Mar. 23, 2026. [Online]. Available: https://cds.cern.ch/record/411756
[36] A.E. Everett, "Cosmic strings in unified gauge theories," Physical Review D, **24**(4), 858 (1981). https://doi.org/10.1103/PhysRevD.24.858
[37] A. Vilenkin, and E. P. S. Shellard, *Cosmic Strings and Other Topological Defects*, (Cambridge University Press, Cambridge, 1994).
[38] Singh, "String LRS Bianchi type I universe with functional relation on Hubble parameter," Indian Journal of Physics, **99**(7), 2717–2723 (2024). https://doi.org/10.1007/s12648-024-03431-w
[39] M.P.V.V. B. Rao, T. Ramprasad, M. Kiran, and S. Bora, "Bianchi type-III magnetized string model with constant decelerating parameter in general theory of relativity," **12758**, 35–42 (2023). https://doi.org/10.1117/12.2684024
[40] K. Pawar, A. K. Dabre, and P. Makode, "Plane Symmetric String Cosmological Model with Zero Mass Scalar Field in f (R) Gravity," Astrophysics, **66**(3), 353–365 (2023). https://doi.org/10.1007/S10511-023-09796-w
[41] V.G. Mete, S. N. Bayaskar, A. A. Dhanagare, and A. A. Jalamkar, "Dynamics of Cosmic String and Domain Wall Cosmological Model with a Special Form of Deceleration Parameter," Journal of Scientific Research, **18**(1), 107–122 (2026). https://doi.org/10.3329/jsr.v18i1.82279
[42] X.X. Wang, "Bianchi Type-III String Cosmological Model With Bulk Viscosity and Magnetic Field," Chinese Physics Letters, **23**(7), 1702 (2006). https://doi.org/10.1088/0256-307X/23/7/013
[43] S.K. Tripathy, S. K. Sahu, and T. R. Routray, "String cloud cosmologies for Bianchi type-III models with electromagnetic field," Astrophysics and Space Science, **315**(1), 105–110 (2008). https://doi.org/10.1007/s10509-008-9805-8
[44] B.P. Brahma and M. Dewri, "Role of f(R,T) Gravity in Bianchi Type-V Dark Energy Model with Electromagnetic Field based on Lyra Geometry," Journal of Scientific Research, **14**(3), 721–733 (2022). https://doi.org/10.3329/jsr.v14i3.56416
[45] A. Rehman, M. Yousaf, J. Rayimbaev, and M. Zakarya, "Electromagnetic field effects on anisotropic cylindrically symmetric compact objects within the framework of $f(R,L_m,T)$ gravity," General Relativity and Gravitation, **58**(2), 15 (2026). https://doi.org/10.1007/s10714-025-03510-1
[46] J. Daimary and R. Roy Baruah, "Five Dimensional Bianchi Type-I Anisotropic Cloud String Cosmological Model with Electromagnetic Field in Saez-Ballester Theory," Frontiers in Astronomy and Space Sciences, **9**, 878653 (2022). https://doi.org/10.3389/fspas.2022.878653
[47] T. Ramprasad, "A Study on Cosmological Model of Anisotropic Universe with Electromagnetic Field and Cloud Strings in the Frame Work of General Relativity," Mapana Journal of Sciences, **22**(4), 85 (2023). https://doi.org/10.12723/mjs.67.6
[48] A.G. Riess et al., "Observational Evidence from Supernovae for an Accelerating Universe and a Cosmological Constant," Astron. J. **116**(3), 1009–1038 (1998). https://doi.org/10.1086/300499
[49] S. Perlmutter, et al., "Measurements of Ω and Λ from 42 High-Redshift Supernovae," Astrophys. J. **517**(2), 565–586 (1999). https://doi.org/10.1086/307221
[50] R.A. Knop, et al., "New Constraints on Ω_M, Ω_Λ, and w from an Independent Set of 11 High-Redshift Supernovae Observed with the Hubble Space Telescope," Astrophys. J. **598**(1), 102–137 (2003). https://doi.org/10.1086/378560
[51] P.S. Letelier, "String cosmologies," Physical Review D, **28**(10), 2414–2419 (1983). https://doi.org/10.1103/PhysRevD.28.2414

[52] A. Dabre, and P. Makode, "Viscous Plane Symmetric String Cosmological Model in f (R) Gravity," Astrophysics, **67**(2), 161-177 (2024). https://doi.org/10.1007/S10511-024-09826-1/METRICS
[53] H.E. Kandrup, "Violations of the strong energy condition for interacting systems of particles," Physical Review D, **46**(12), 5360 (1992). https://doi.org/10.1103/PhysRevD.46.5360
[54] L. Parker, and Y. Wang, "Avoidance of singularities in relativity through two-body interactions," Physical Review D, **42**(6), 1877 (1990). https://doi.org/10.1103/PhysRevD.42.1877

КОСМОЛОГІЧНА МОДЕЛЬ В'ЯЗКИХ СТРУН З ЕЛЕКТРОМАГНІТНИМ ПОЛЕМ У ТЕОРІЇ САЕЗА-БАЛЛЕСТЕРА

Мохіні Р. Угале, Сагар А. Бхакте
1Кафедра природничих наук та гуманітарних наук, Інженерно-технологічний коледж Сіпна, Амраваті, 444 701 Махараштра, Індія
2Кафедра математики, Інженерно-технологічний коледж професора Рама Мегхе, Баднера, округ Амраваті 444 701 Махараштра, Індія

Для вивчення метрик Б'янкі III типу, які є однорідними та анізотропними, де тензор енергії-імпульсу виводиться з об'ємної в'язкої рідини, що містить одновимірні струни, вбудовані в електромагнітне поле. Для отримання точних розв'язків ми використовували співвідношення пропорційності між скалярами розширення та зсуву, а також середній масштабний коефіцієнт спеціальної форми. Окрім енергетичних умов, було розраховано кілька динамічних та фізичних параметрів, а також досліджено їхній фізичний вплив на космологію.

Ключові слова: *метрика Біанкі III типу; об'ємна в'язка рідина; космічні струни; електромагнітне поле; Теорія Саеза-Баллестера*

DOI: 10.26565/2312-4334-2026-3-10 ISSN 2312-4334

EXPLORING BIANCHI TYPE-VI$_o$ VISCOUS HOLOGRAPHIC RICCI DARK ENERGY COSMOLOGICAL MODEL IN BRANS-DICKE THEORY OF GRAVITATION

K.P.S. Suryanarayana*, **K.V.S. Sireesha**, **R. Sathibabu**
Department of Mathematics and Statistics, GSS, GITAM Deemed to be University, Visakhapatnam, India
**Corresponding Author e-mail: skuppili2@gitam.edu*
Received May 24, 2026; revised August 13, 2026; accepted August 20, 2026

- A viscous holographic Ricci dark energy (VHRDE) model is investigated within the framework of Brans–Dicke (BD) gravity.
- Bulk viscosity generates effective negative pressure, while the BD scalar field dynamically regulates the gravitational coupling.
- A natural transition from an early matter-dominated decelerated phase to a late-time dark-energy-dominated accelerated expansion is obtained.
- The model extends beyond ΛCDM, exhibiting a dynamically evolving equation of state that can approach or cross the phantom divide $\omega < -1$
- Anisotropy and shear decay with cosmic time, leading to late-time isotropization consistent with observational (CMB) constraints.

We investigate a viscous holographic Ricci dark energy (VHRDE) model in Bianchi type (BT) - VI$_o$ spacetime within Brans–Dicke (BD) gravity, incorporating a pressure-less matter component. Assuming a relationship between metric potentials and a parameterised bulk viscosity coefficient, exact solutions of the BD field equations are found. The combined effects of anisotropy, Ricci holographic cutoff, and bulk viscosity yield a dynamical framework that can describe multiple phases of cosmic evolution. We examine the progression of significant measurements, including the scalar field, energy densities, bulk viscosity, viscous pressure, equation of state (EoS), expansion variables, and the deceleration parameter, revealing a transition from a decelerated, matter-dominated epoch to an accelerated, dark-energy-dominated phase. Bulk viscosity generates effective negative pressure driving acceleration, while the BD scalar field modulates gravitational coupling. Comparison with previous studies confirms that this model provides a viable mechanism for cosmic acceleration without requiring a cosmological constant.

Keywords: *Bianchi type- VI$_o$ metric; Holographic Ricci dark energy (HRDE); Bulk Viscosity; Brans-Dicke theory*

1. INTRODUCTION

The accelerated expansion of the Universe, revealed through observations of SN Ia, CMB anisotropies, and large-scale structure surveys, stands as one of the most profound and unresolved challenges in modern cosmology. This phenomenon is generally attributed to an unknown component characterised by a negative pressure, known as dark energy (DE), which currently predominates the cosmic energy amount. Our current understanding suggests that dark energy constitutes approximately 73% of the universe, with dark matter comprising 23% and baryonic matter making up 4%, while radiation contributes negligibly at the present epoch [1–5].Two essential methodologies have been established to better understand this late-time acceleration. The first introduces new dynamical energy components, such as quintessence, phantom fields, k-essence, tachyon models, and Chaplygin gas. The second modification extends Einstein's general relativity, leading to alternative gravitational frameworks, such as scalar–tensor (ST) theories and $f(R)$ or $f(R,T)$ gravities [6–12]. Among the many DE candidates, the holographic dark energy (HDE) model [13] is particularly compelling, as it emerges naturally from the holographic principle, which relates the degrees of freedom of a physical system to the area of its boundary surface [14, 15]. The holographic framework was initially developed by Cohen *et al.*, who related the vacuum energy density (ED) to the Hubble scale ($L \simeq H^{-1}$), while Li proposed the HDE density as $\rho_d = 3C^2 M_{\rm pl}^2 L^{-2}$. Gao *et al.*, modified this formulation by adopting the Ricci scalar cutoff ($L \simeq R^{-\frac{1}{2}}$), leading to the RDE model, while Granda and Oliveros [14–19] introduced a generalized form involving both H^2 and $\dot{H}$. Chen and Jing [20] further extended it to the modified HRDE model, expressed as

$$\rho_d = \frac{3}{8\pi G}\left(\varepsilon_0 H^2 + \eta\,\dot{H} + \zeta\,\frac{\ddot{H}}{H}\right) \tag{1}$$

These models, and their extensions, have been widely studied and shown to describe key features of cosmic acceleration [21–24]. Parallel to these developments, bulk viscosity has been proposed as a natural mechanism for generating effective negative pressure. In the early Universe, neutrino interactions led matter to behave like a viscous fluid, decreasing viscosity as expansion progressed. Bulk viscosity arises when a system departs from local thermodynamic equilibrium and has been shown to drive both early inflation and late-time acceleration without a cosmological constant [25–28]. Recent works have applied viscosity to holographic models in anisotropic spacetimes, highlighting its role as a viable candidate for DE [29].

Cite as: K.P.S. Suryanarayana, K.V.S. Sireesha, R. Sathibabu, East Eur. J. Phys. 3, 114 (2026), https://doi.org/10.26565/2312-4334-2026-3-10

Scalar–tensor theories, particularly BD gravity, provide a natural framework for extending general relativity. In BD theory, the gravitational constant is replaced by a dynamical scalar field ϕ, which couples to geometry through the dimensionless parameter ω. The BD field equations can be written as

$$G_{\mu\vartheta} = -\frac{8\pi}{\phi} T_{\mu\vartheta} - \frac{\omega}{\phi^2}\left(\phi_{,\mu}\phi_{,\vartheta} - \frac{1}{2} g_{\mu\vartheta}\phi_{,k}\phi^{,k}\right) - \frac{1}{\phi}\left(\phi_{;\mu\vartheta} - g_{\mu\vartheta}\Box\phi\right) \tag{2}$$

and

$$\Box\phi = \frac{8\pi}{3+2\omega} T \tag{3}$$

together with the conservation law

$$T^{\mu\vartheta}_{;\vartheta} = 0 \tag{4}$$

This framework has been successfully applied to both isotropic and anisotropic cosmologies, offering flexibility in explaining dynamical features of cosmic evolution [30–35]. Motivated by these considerations, the present work investigates a VHRDE model in a BT–VI$_o$ anisotropic spacetime within BD gravity, incorporating a pressureless matter component. The combined effects of anisotropy, Ricci holographic cutoff, and bulk viscosity generate a rich dynamical system capable of reproducing different cosmic phases. Exact solutions of the BD field equations are obtained by assuming a relation among metric potentials and a parameterized bulk viscosity coefficient. The time evolution of key cosmological parameters is analyzed to examine the roles of viscous effects and anisotropies in shaping cosmic dynamics. The structure of the paper is as follows: Section 2 formulates the governing field equations, Section 3 develops the exact analytical solutions, Section 4 provides a detailed analysis of the physical characteristics of the model, and Section 5 synthesizes the principal findings and implications.

2. METRIC AND FIELD EQUATIONS

We consider a spatially homogeneous BT - VI$_o$ metric form.

$$ds^2 = dt^2 - A_1^2\, dx^2 - A_2^2 e^{-2x}\, dy^2 - A_3^2 e^{2x}\, dz^2 \tag{5}$$

Where A_1, A_2, and A_3 are functions of 't' only. The HRDE energy-momentum tensor with bulk viscosity is

$$T_{\mu\vartheta} = T^m_{\mu\vartheta} + T^d_{\mu\vartheta}$$

Where $T^m_{\mu\vartheta}$ and $T^d_{\mu\vartheta}$ are the energy-momentum tensor for matter and the HRDE, respectively. They are

$$T^d_{\mu\vartheta} = (\rho_d + \bar{p}_d)\, u_\mu u_\vartheta - \bar{p}_d\, g_{\mu\vartheta} \tag{6}$$

and

$$T^m_{\mu\vartheta} = \rho_m\, u_\mu u_\vartheta \tag{7}$$

Where ρ_m and ρ_d are the matter and the holographic Ricci dark energy densities, respectively, and $\bar{p}$ means the viscous HDE pressure.
In the co-moving frame of reference, we will get

$$T^1_1 = T^2_2 = T^3_3 = -\bar{p}_d, \qquad T^4_4 = \rho_m + \rho_d \tag{8}$$

Where ρ_m, ρ_d and $\bar{p}_d$ are all functions of time 't' only.
The pressure of VHRDE is governed by the corresponding relation. $\bar{p}_d = p_d - 3\epsilon H$. In the late-time evolution of the Universe, the inclusion of bulk viscosity in the DE sector facilitates a rapid phantom-like expansion. Throughout this analysis, dark matter is treated as a pressureless component, while the effective pressure of VHRDE is consistently modelled as the combined contribution of the HRDE pressure and the bulk viscous term.
The BD field equations (2), using metric (5) and supported by equations (6)-(8) are given by:

$$\frac{\ddot{A}_2}{A_2} + \frac{\ddot{A}_3}{A_3} + \frac{\dot{A}_2\dot{A}_3}{A_2A_3} + \frac{\omega}{2}\frac{\dot{\phi}^2}{\phi^2} + \frac{\ddot{\phi}}{\phi} + \frac{\dot{A}_2\dot{\phi}}{A_2\phi} + \frac{\dot{A}_3\dot{\phi}}{A_3\phi} + \frac{1}{A_1^2} = -8\pi\phi^{-1}\bar{p}_d \tag{9}$$

$$\frac{\ddot{A}_1}{A_1} + \frac{\ddot{A}_3}{A_3} + \frac{\dot{A}_1\dot{A}_3}{A_1A_3} + \frac{\omega}{2}\frac{\dot{\phi}^2}{\phi^2} + \frac{\ddot{\phi}}{\phi} + \frac{\dot{A}_1\dot{\phi}}{A_1\phi} + \frac{\dot{A}_3\dot{\phi}}{A_3\phi} - \frac{1}{A_1^2} = -8\pi\phi^{-1}\bar{p}_d \tag{10}$$

$$\frac{\ddot{A}_1}{A_1} + \frac{\ddot{A}_2}{A_2} + \frac{\dot{A}_1\dot{A}_2}{A_1A_2} + \frac{\omega}{2}\frac{\dot{\phi}^2}{\phi^2} + \frac{\ddot{\phi}}{\phi} + \frac{\dot{A}_1\dot{\phi}}{A_1\phi} + \frac{\dot{A}_2\dot{\phi}}{A_2\phi} - \frac{1}{A_1^2} = -8\pi\phi^{-1}\bar{p}_d \tag{11}$$

$$\frac{\dot{A}_1\dot{A}_2}{A_1A_2}+\frac{\dot{A}_2\dot{A}_3}{A_2A_3}+\frac{\dot{A}_1\dot{A}_3}{A_1A_3}-\frac{\omega}{2}\frac{\dot{\phi}^2}{\phi^2}+\frac{\dot{\phi}}{\phi}\left(\frac{\dot{A}_1}{A_1}+\frac{\dot{A}_2}{A_2}+\frac{\dot{A}_3}{A_3}\right)-\frac{1}{A_1^2}=-8\pi\phi^{-1}(\rho_m+\rho_d) \tag{12}$$

$$\frac{1}{A_1^2}\left(\frac{\dot{A}_2}{A_2}-\frac{\dot{A}_3}{A_3}\right)=0 \tag{13}$$

$$\ddot{\phi}+\dot{\phi}\left(\frac{\dot{A}_1}{A_1}+\frac{\dot{A}_2}{A_2}+\frac{\dot{A}_3}{A_3}\right)=\frac{8\pi}{3+2\omega}\left(\rho_m+\rho_d-3\bar{p}_d\right) \tag{14}$$

$$\frac{\ddot{A}_1}{A_1}-\frac{\ddot{A}_2}{A_2}+\frac{\dot{A}_2}{A_2}\left(\frac{\dot{A}_1}{A_1}-\frac{\dot{A}_2}{A_2}\right)+\frac{\dot{\phi}}{\phi}\left(\frac{\dot{A}_1}{A_1}-\frac{\dot{A}_2}{A_2}\right)-\frac{2}{A_1^2}=0 \tag{15}$$

3. VHRDE COSMOLOGICAL MODELS

From equation (13), we get $A_2 = c_1A_3$,by taking $c_1 = 1$ without loss of generality, we have

$$A_2 = A_3 \tag{16}$$

The field equations (9)–(15) constitute a set of independent, nonlinear relations involving seven unknown functions of cosmic time t: $A_1, A_2, A_3, \rho_m, \rho_d, \bar{p}_d,$ & ϕ.The following physically motivated conditions are imposed to ensure a well-determined solution.

1. The relation between the scalar field and the average scale factor a(t) is established as given by Johri and Kalyani [36]

$$\phi = a^m = (A_1A_2A_3)^{\left(\frac{m}{3}\right)}, \quad \text{where } m \text{ is a constant} \tag{17}$$

2. Since $\sigma \propto \theta$ leads to the metric potentials relation (Collins et al. [37])

$$A_1 = A_2^n, \quad \text{where } n \text{ is an arbitrary constant.} \tag{18}$$

We adopt the parameterized form of bulk viscosity as proposed by Ren and Meng [38]

$$\epsilon = \epsilon_1 + \epsilon_2\frac{\dot{a}}{a} + \epsilon_3\frac{\ddot{a}}{\dot{a}} \tag{19}$$

Where $\epsilon_1, \epsilon_2, \&\epsilon_3$ are constants. From equations (9)-(11), (17), and (18), we get

$$\frac{\ddot{A}_2}{A_2}+(n+1)\frac{\dot{A}_2^2}{A_2^2}+\frac{\dot{A}_2\dot{\phi}}{A_2\phi}-\frac{2}{(n-1)\,A_2^{2n}}=0 \tag{20}$$

Using equations (17) & (18), from equation (20), we get

$$A_2 = A_3 = \left(\frac{k}{l}\right)^{-\frac{1}{n}}\left[\tanh^2(nkt)-1\right]^{-\frac{1}{2n}} \tag{21}$$

$$A_1 = \left(\frac{l}{k}\right)\left[\tanh^2(nkt)-1\right]^{-\frac{1}{2}} \tag{22}$$

From equations (17), (21), and (22), we get

$$\phi = \left(\frac{k}{l}\right)^{\frac{n+2}{n}}\left[\tanh^2(nkt)-1\right]^{\frac{n+2}{2n}} \tag{23}$$

Where $l^2 = \frac{2}{n(1-n)}$ & k is an integrating constant.

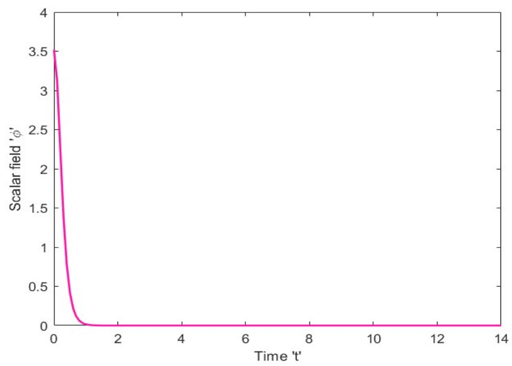

Figure 1. Variation of the BD scalar field $\phi(t)$ vs. time 't' for k=1.5 & n=2.45

For the specified parameters, Figure 1 shows how the BD scalar field $\phi(t)$ changes over time in the VHRDE model. Initially, $\phi(t)$ starts at a high value ($\phi \approx 3.6$) and decreases rapidly due to the combined influence of viscous effects and holographic corrections, reflecting a strong dynamical contribution in the early universe. Around $t \gtrsim 2$, the decay slows, and the field stabilizes near zero, remaining effectively constant at late times. This behaviour indicates a transition from an early scalar-dominated regime to a dark energy dominated phase, consistent with the dissipative nature of VHRDE and supporting a stable, slowly evolving dark energy component in the present epoch. Unlike Lambda CDM, where the gravitational coupling is constant and the scalar field plays no dynamical role, the VHRDE framework allows $\phi(t)$ to evolve, reflecting richer dynamics influenced by viscosity and holographic effects.

The Hubble parameter H is

$$H = \frac{k(n+2)}{3}\tanh(nkt) \tag{24}$$

Now, metric (5) can be written as

$$ds^2 = dt^2 - \frac{1}{k^2}\left[\tanh^2(nkt) - 1\right]^{-1} dx^2 - \left(\frac{k}{l}\right)^{-\frac{2}{n}}\left[\tanh^2(nkt) - 1\right]^{-\frac{1}{n}}\left(e^{-2x}dy^2 + e^{2x}dz^2\right) \tag{25}$$

The HRDE energy density can be evaluated from equations (1) and (24) as follows

$$\rho_d = \frac{3\phi k^2}{8\pi}\left[\epsilon_0\left(\frac{n+2}{3}\tanh(nkt)\right)^2 + \eta\frac{n(n+2)}{3}\,\mathrm{sech}^2(nkt) - 2\zeta n^2\,\mathrm{sech}^2(nkt)\right] \tag{26}$$

Where $\phi = \left(\frac{k}{l}\right)^{\frac{n+2}{n}}\left[\tanh^2(nkt) - 1\right]^{\frac{n+2}{2n}}$

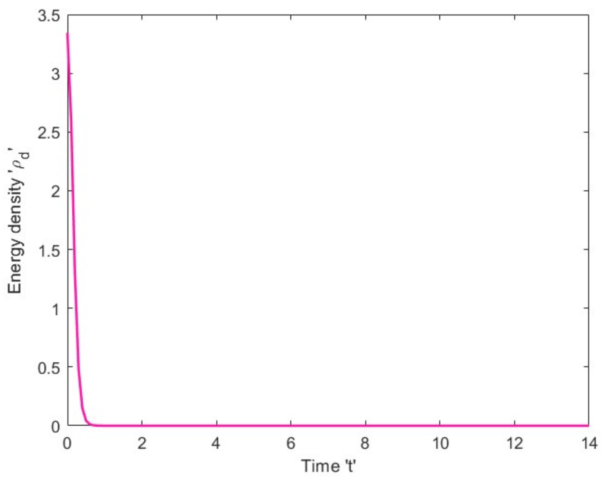

Figure 2. Variation of HRDE density ρ_d with time t for $k = 1.5$, $n = 2.45$, $\epsilon_0 = 0.025$, $\eta = 1.155$, $\zeta = 0.055$.

In the VHRDE model, Figure 2 shows how the ED ρ_d has evolved across cosmic time. Initially, ρ_d starts at a relatively high value ($\rho_d \approx 3.4$), reflecting a dominant DE component influenced by strong holographic and viscous effects. As time progresses, the ED undergoes a steep decline, approaching near-zero values around $t \approx 4$, after which it asymptotically flattens and remains nearly constant. This behaviour indicates rapid energy dissipation due to viscous interactions during the early universe, followed by a quasi-static regime corresponding to a stabilized DE-dominated era. The late-time plateau suggests a de Sitter–like accelerated expansion, which is consistent with observations and the expected behaviour of HRDE models with bulk viscosity. At late times, it shows that the VHRDE effectively mimics a cosmological constant. Additionally, ρ_d gradually decreases over time, ensuring the physical condition $\rho_d \geqslant 0$. Unlike Lambda CDM, where the DE density remains constant, the VHRDE framework exhibits dynamic decay before stabilizing, reflecting richer dissipative physics. A minimal interaction is assumed between pressure-less matter and the viscous HRDE component, allowing them to evolve independently, in line with the approach of Sarkar [39]. As a result, the conservation equation yields:

$$\dot{\rho}_m + \left(\frac{\dot{A}_1}{A_1} + \frac{\dot{A}_2}{A_2} + \frac{\dot{A}_3}{A_3}\right)\rho_m = 0 \tag{27}$$

$$\dot{\rho}_d + \left(\frac{\dot{A}_1}{A_1} + \frac{\dot{A}_2}{A_2} + \frac{\dot{A}_3}{A_3}\right)(\rho_d + \bar{p}_d) = 0 \tag{28}$$

From eqs. (21), (22), and (27), we get

$$\rho_m = k_1 \left(\frac{k}{l}\right)^{\frac{n+2}{n}} \left[\tanh^2(nkt) - 1\right]^{\frac{n+2}{2n}} \tag{29}$$

Where k_1 is an integrating constant.

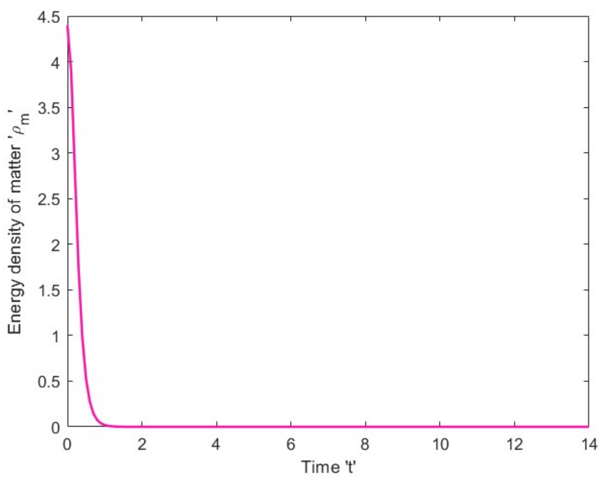

Figure 3. Variation of the ED of matter ρ_m vs. time ‘t’ for $k = 1.5, n = 2.45$ & $k_1 = 1.25$

In the VHRDE cosmological framework, Figure 3 displays the variation of the matter ED ρ_m across time. Initially, ρ_m is high ($\rho_m \approx 4.3$), reflecting a matter-dominated epoch in the early universe. The curve declines sharply as time progresses, indicating rapid dilution of matter density due to cosmic expansion. Around $t \approx 3$, ρ_m approaches zero and stabilizes at an almost negligible value, marking the transition from matter domination to DE domination. The asymptotic behaviour demonstrates that matter becomes dynamically irrelevant in the late-time universe, consistent with the current DE-dominated phase. The steep decay further highlights the combined influence of bulk viscosity and holographic constraints in accelerating the dissipation of matter’s contribution in VHRDE cosmologies. In Lambda CDM, matter dilutes as a^{-3} without viscous corrections, while in VHRDE, the decay is sharper, reflecting more substantial dissipative effects.

The bulk viscosity coefficient is expressed by

$$\epsilon = \epsilon_1 + \epsilon_2 \left[\frac{k(n+2)}{3}\tanh(nkt)\right] + \epsilon_3(nk)\left[\frac{\operatorname{sech}^2(nkt)}{\tanh(nkt)} + 2\tanh(nkt) \quad + 2\frac{7n+2}{6n}\frac{\tanh(nkt)}{\operatorname{sech}^2(nkt)}\right] \tag{30}$$

Figure 4 illustrates the evolution of the coefficient $\epsilon(t)$ of bulk viscosity in the VHRDE model. During the early and intermediate epochs($t \lesssim 12$), bulk viscosity remains extremely small and nearly constant, indicating negligible viscous effects in the initial stages of cosmic evolution. However, as the universe approaches the far-future regime, $\epsilon(t)$ exhibits a dramatic rise, diverging sharply and reaching values of the order 10^{45} near $t \approx 14$. This rapid growth suggests that dissipative processes become increasingly dominant at late times. The divergence of ϵ may signal the onset of a non-equilibrium state or a possible future phase transition driven by strong viscous effects. Physically, such behaviour could correspond to a highly accelerated expansion or a phantom-like scenario, where bulk viscosity mimics or amplifies dark energy. These results emphasize the crucial role of viscosity in shaping the future dynamics of the universe, particularly within holographic and scalar–tensor cosmologies. In contrast, Lambda CDM assumes no viscous terms, making bulk viscosity identically zero. The sharp divergence in VHRDE highlights a key departure from the Lambda CDM paradigm.

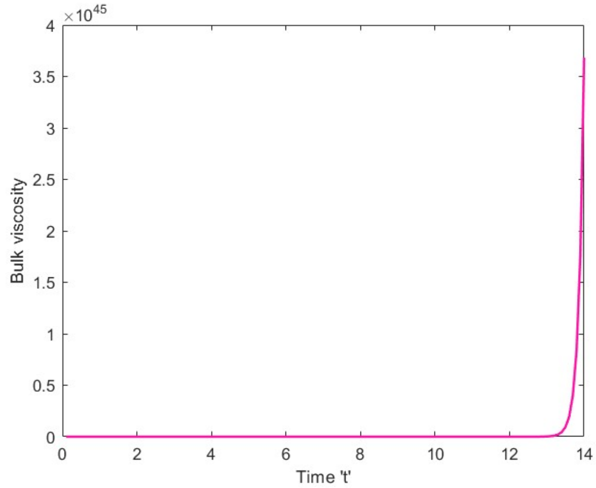

Figure 4. Variation of the bulk viscosity ϵ vs. time 't' for $k = 1.5, n = 2.45, \epsilon_1 = 2.035, \epsilon_2 = 1.025 \,\&\epsilon_3 = 3.15$

By solving equations (21) through (23), we may determine the HRDE's viscous pressure as

$$\bar{p}_d = \frac{\phi k^2}{16\pi}\left\{(n+1)\left[(n-1)\ \operatorname{sech}^2(nkt)+1\right]+\left[(3n+1)-(\omega+2)(n+2)^2\right]\tanh^2(nkt)\right\} \tag{31}$$

where $\phi = \left(\frac{k}{l}\right)^{\frac{n+2}{n}}\left[\tanh^2(nkt)-1\right]^{\frac{n+2}{2n}}$

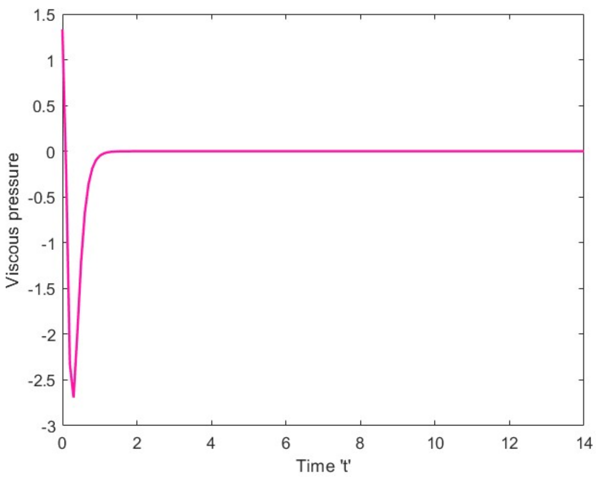

Figure 5. Variation of the viscous pressure $\bar{p}_d$ vs. time 't' for $k = 1.5, n = 2.45, \epsilon_0 = 0.025, \eta = 1.155, \omega = 2.25 \,\&\, \zeta = 0.055$

In the VHRDE model, Figure 5 depicts how the viscous pressure $\bar{p}_d$ alters across cosmic time. Initially, $\bar{p}_d$ is strongly positive, exceeding unity, but it rapidly falls into the negative region, reaching a minimum of about $\bar{p}_d \approx -2.8$ at early times ($t \lesssim 1$). This sharp decline indicates that viscous effects acted as an effective negative pressure in the early universe, potentially driving an acceleration of the inflation-like phase. Thereafter, $\bar{p}_d$ gradually increases and approaches zero from below, stabilizing for $t > 4$. This asymptotic flattening implies that viscous contributions become negligible late, consistent with a quasi-equilibrium, DE-dominated phase. The overall trend highlights the dissipative nature of the cosmic fluid and its significant role in shaping both early and intermediate expansion dynamics. In Lambda CDM, the effective pressure is constant, whereas VHRDE introduces time-dependent viscous contributions that enrich the early and mid-time dynamics.

The HRDE's pressure as

$$\begin{aligned} p_d = \frac{\phi k^2}{16\pi}\left\{(n+1)\left[(n-1)\,\mathrm{sech}^2(nkt)+1\right]+\left[(3n+1)-(\omega+2)(n+2)^2\right]\tanh^2(nkt)\right\} \\ +\left[k(n+2)\tanh(nkt)\right]\left\{\varepsilon_1+\varepsilon_2\left[\frac{k(n+2)}{3}\tanh(nkt)\right]\right. \\ \left.+\varepsilon_3(nk)\left[\frac{\mathrm{sech}^2(nkt)}{\tanh(nkt)}+2\tanh(nkt)+\frac{2(7n+2)}{6n}\,\frac{\tanh(nkt)}{\mathrm{sech}^2(nkt)}\right]\right\} \end{aligned} \tag{32}$$

where $\phi = \left(\frac{k}{l}\right)^{\frac{n+2}{n}}\left[(\tanh(nkt))^2-1\right]^{\frac{n+2}{2n}}$

From equations (26) and (32), we obtain The HRDE's EoS parameter as

$$\omega_d = \frac{p_d}{\rho_d} \tag{33}$$

Where

$$\begin{aligned} p_d = \frac{\phi k^2}{16\pi}\left\{(n+1)\left[(n-1)\,\mathrm{sech}^2(nkt)+1\right]+\left[(3n+1)-(\omega+2)(n+2)^2\right]\tanh^2(nkt)\right\} \\ +\left[k(n+2)\tanh(nkt)\right]\left\{\varepsilon_1+\varepsilon_2\left[\frac{k(n+2)}{3}\tanh(nkt)\right]\right. \\ \left.+\varepsilon_3(nk)\left[\frac{\mathrm{sech}^2(nkt)}{\tanh(nkt)}+2\tanh(nkt)+\frac{2(7n+2)}{6n}\,\frac{\tanh(nkt)}{\mathrm{sech}^2(nkt)}\right]\right\} \end{aligned}$$

and $\rho_d = \frac{3\phi k^2}{8\pi}\left[\epsilon_0\left(\frac{n+2}{3}\tanh(nkt)\right)^2+\eta\frac{n(n+2)}{3}\,\mathrm{sech}^2(nkt)-2\zeta n^2\,\mathrm{sech}^2(nkt)\right]$

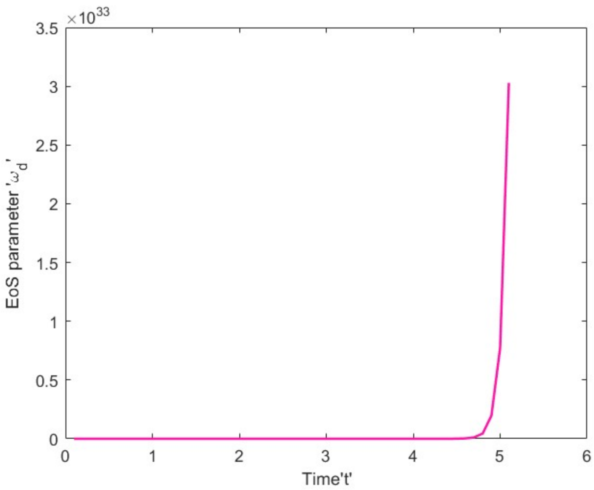

Figure 6. Variation of the EoS parameter ω_d vs. time 't' for$k = 1.5, n = 2.45, \epsilon_0 = 0.025, \eta = 1.155, \omega = 2.25$ & $\zeta = 0.055$

The EoS parameter is defined as $\omega_d = \frac{p}{\rho}$. Different values of ω_d correspond to distinct evolutionary phases of the Universe. During the decelerated expansion, $\omega_d = 1$ denotes stiff fluid, $\omega_d = \frac{1}{3}$ represents radiation, and $\omega_d = 0$ corresponds to a dust-dominated epoch. In contrast, the accelerated expansion phase includes quintessence $-1 < \omega_d < \frac{1}{3}$, the cosmological constant ($\omega_d = -1$), and phantom energy ($-1 < \omega_d$). Figure 6 shows how the VHRDE model's EoS parameter has changed over time. At early times, $\omega > -1$, placing the universe in a quintessence-like regime with relatively weaker negative pressure. As cosmic time increases, viscous and holographic effects dominate, driving ω_d toward more negative values. Depending on the parameter set, ω_d either asymptotically approaches the cosmological constant boundary ($\omega_d = -1$) or crosses into the phantom regime ($\omega_d < -1$). In the latter case, the model indicates a possible big-rip–like future driven by rapidly increasing negative pressure. The substantial time dependence of ω_d reflects the combined influence of bulk viscosity, scalar field dynamics, and the Ricci cutoff. In contrast, the standard Lambda CDM model assumes a strictly constant $\omega_d = -1$, corresponding to a true cosmological constant. The deviation of ω_d , the fixed value in the VHRDE framework highlights its dynamical character, offering a richer phenomenology that can capture transitions between quintessence, Λ-like, and phantom regimes. Such flexibility may help reconcile theoretical predictions with Planck and other observational constraints that mildly favour evolving DE over a pure cosmological constant.

The coincidence parameter is

$$r = \frac{\rho_d}{\rho_m} = \frac{\frac{3\phi k^2}{8\pi}\left[\ \xi_0\left(\frac{n+2}{3}\tanh(nkt)\right)^2 + \eta\,\frac{n(n+2)}{3}\,\mathrm{sech}^2(nkt) - 2\zeta n^2\,\mathrm{sech}^2(nkt)\ \right]}{k_1\left(\frac{k}{l}\right)^{\frac{n+2}{n}}\left[\tanh^2(nkt)-1\right]^{\frac{n+2}{2n}}} \tag{34}$$

4. SOME ESSENTIAL PROPERTIES OF THE MODEL

The spatial volume is

$$V = \left(\frac{k}{l}\right)^{-\frac{n+2}{n}}\left(\tanh^2(nkt)-1\right)^{-\frac{n+2}{2n}} \tag{35}$$

The average scale factor is

$$a(t) = V(t)^{1/3} = \left(\frac{k}{l}\right)^{-\frac{n+2}{3n}}\left(\tanh^2(nkt)-1\right)^{-\frac{n+2}{6n}} \tag{36}$$

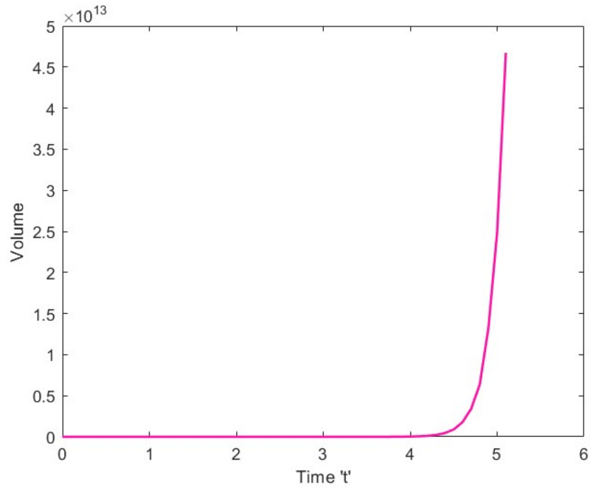

Figure 7. Variation of the Volume V vs. time 't' for k=1.5 & n=2.45

Figure 7 presents the time progression of the volume scale factor $V(t)$ in the VHRDE model. During the early epoch ($t \lesssim 4$), the volume remains extremely small and nearly constant, reflecting a slowly expanding or quasi-static universe. A sharp transition occurs around $t \approx 4.5$, where $V(t)$ grows rapidly by several orders of magnitude. This exponential-like rise signals late-time accelerated expansion, driven by the combined influence of HDE and bulk viscosity. The asymptotic behaviour of $V(t)$ at later times indicates a dark energy–dominated regime that may evolve toward a de Sitter–like or phantom scenario. In contrast, the standard Lambda CDM model predicts smooth exponential expansion with a constant DE density and no viscosity effects. The VHRDE framework, by incorporating dissipative processes, provides a richer dynamical picture that can capture both the observed acceleration and possible deviations from Lambda CDM in the universe's long-term evolution.

For the flow vector u^μ, the corresponding expressions for the expansion and shear scalars are obtained as follows.

$$\theta = 3H = k(n+2)\tanh(nkt) \tag{37}$$

$$\sigma^2 = \frac{7}{18}\,\theta^2 = \frac{7}{18}\,[k(n+2)\tanh(nkt)]^2 \tag{38}$$

Figure 8 shows the evolution of the Hubble parameter $H(t)$ (solid line) and the expansion scalar $\theta(t)$ (dashed line) in the

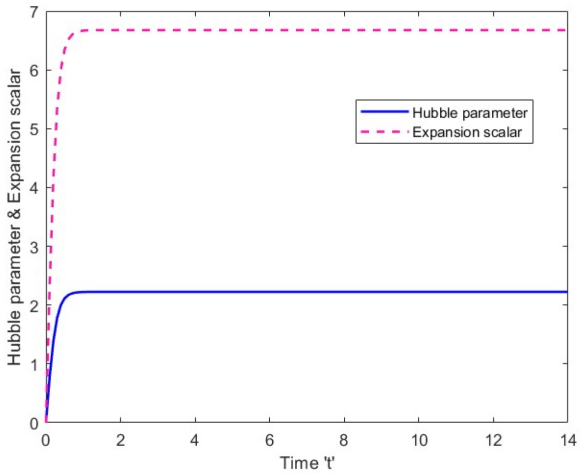

Figure 8. Variation of the Hubble parameter & Expansion scalar vs. time't' for k=1.5 & n=2.45

VHRDE model. Initially, both quantities rise rapidly, reflecting an early phase of significant expansion. As time increases, the Hubble parameter stabilizes near a constant value $H \approx 2.3$, while θ, proportional to $3H$, asymptotically approaches $\theta \approx 6.9$, consistent with theoretical expectations. This convergence signals the transition from a dynamic early epoch to a quasi–de Sitter regime in the late universe. The constancy of H and θ at late times indicates a steady accelerated expansion, driven by the interplay of the Ricci holographic cutoff and bulk viscous effects, which together guide the universe toward an asymptotic inflation-like state without a future singularity. In contrast, due to a true cosmological constant, the Lambda CDM model predicts a constant H only at asymptotic times. The VHRDE scenario generalizes this behaviour by allowing viscosity-driven dynamics, yielding a richer description of cosmic acceleration.
The average anisotropy parameter is defined by

$$A_m = \frac{1}{3}\sum_{i=1}^{3}\left(\frac{H_i - H}{H}\right)^2 = \frac{2\,(n-1)^2}{(2n+1)^2} \tag{39}$$

The deceleration parameter given by

$$q = -\frac{3\dot{\theta}}{\theta^2} - 1 = -\frac{3n}{(n+2)}\;\mathrm{csch}^2(nkt) - 1 \tag{40}$$

Figure 9 illustrates the evolution of the deceleration parameter $q(t)$ in the VHRDE model. Initially, $q(t)$ takes a very large negative value ($q \approx -13$), indicating a phase of rapid super-acceleration driven by strong viscous and holographic effects in the early universe. As time progresses, $q(t)$ increases toward an asymptotic value around $q \approx -1$, signalling a transition to steady accelerated expansion resembling a de Sitter phase. The model exhibits super-acceleration ($q < -1$) at early times and normal accelerated expansion ($-1 \leq q < 0$) at late times. At $t_0 = 13.8$ Gyr, q is consistent with current observational estimates of a nearly de Sitter–like universe. In contrast, the Lambda CDM model predicts $q \approx -0.55$ at the present epoch and approaches $q = -1$ only asymptotically due to a constant cosmological constant. The VHRDE framework, with viscosity and holographic corrections, captures stronger early acceleration and a richer time-dependent behaviour, distinguishing it from standard Lambda CDM predictions.

5. COMPARISON OF OUR RESULTS

Recent VHRDE investigations have been carried out in both isotropic and anisotropic cosmologies under different gravity theories. In spatially flat FRW models, linear bulk viscosity has been shown to generate viable late-time acceleration and to regulate the transition from decelerated to accelerated expansion [40,41]. Extensions to anisotropic settings, such as axially symmetric, Ruban, and BT–III spacetimes, indicate that bulk viscosity coupled with scalar–tensor dynamics plays

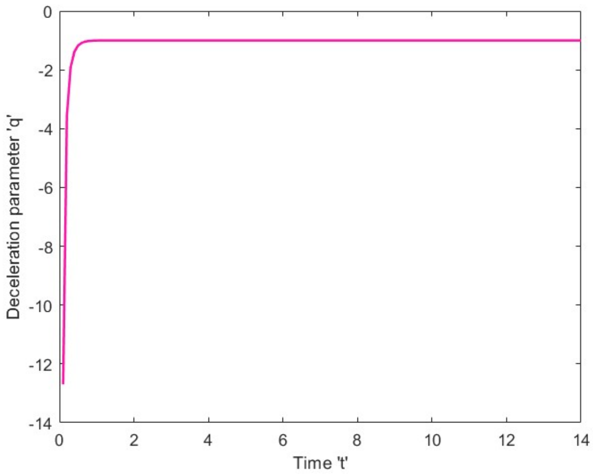

Figure 9. Variation of the deceleration parameter q vs.time ‘t’ for k=1.5 & n=2.45

a crucial role in suppressing anisotropy and initiating accelerated expansion [29, 42, 43]. Furthermore, studies in modified gravity frameworks, including $f(R,T)$ theory, demonstrate that viscosity ensures thermodynamic consistency, supports the generalized second law, and accounts for transitions between cosmic phases [44]. Our BT–VI$_o$ model under BD gravity is consistent with these earlier results yet extends them in several important respects. First, the BT - VI$_o$ geometry introduces a richer anisotropic structure, allowing us to track the detailed decay of shear and anisotropy parameters. Second, the BD scalar field provides a dynamical gravitational coupling that modulates the influence of viscosity, offering new insight into how anisotropy and scalar–tensor effects jointly shape cosmic evolution. Third, we obtain explicit solutions showing that (i) anisotropy and shear decay monotonically, (ii) the deceleration parameter undergoes a sign flip, indicating a transition from decelerated to accelerated expansion, and (iii) A late-time de Sitter phase is indicated by the fact that the EoS value is getting close to -1. These behaviours mirror the general trends observed in FRW and anisotropic VHRDE models, but are derived in a more general anisotropic background with explicit scalar–tensor coupling. Unlike Lambda CDM, where dark energy is constant and acceleration emerges gradually, the VHRDE–BD model exhibits a dynamical evolution in which viscosity and scalar–tensor effects drive early super-acceleration, while the EoS parameter approaches -1 at late times, yielding a de Sitter–like phase that aligns with our findings. Table 1 compares the key cosmological parameters of the Lambda CDM and VHRDE models in BD gravity, showing the effect of viscosity and HRDE on cosmic evolution.

Table 1. Comparison of Key Cosmological Parameters between Lambda CDM and the Present VHRDE Model

Parameter	**Lambda CDM Model**	**VHRDE Model**
Gravitational coupling / scalar field	Constant gravitational coupling (no scalar field; G = const.).	Dynamical Brans–Dicke scalar field $\phi(t)$; positive, initially large (≈ 3.6) and decreases to a nearly constant value at late times.
Dark energy density ρ_d	Constant (cosmological constant).	Time-dependent; begins large (≈ 3.4), decays rapidly, and stabilizes at a small constant value at late times.
Matter density ρ_m	Varies as a^{-3}; dominates early epoch.	Decays faster than a^{-3}; initially ≈ 4.3 and becomes negligible around $t \approx 3$ due to viscous dissipation.
Bulk viscosity coefficient $\varepsilon(t)$	Zero (no viscosity term).	Positive and time-dependent; nearly constant early, rises sharply and diverges ($\sim 10^{45}$) at late times.
Viscous pressure $\bar{p}_d(t)$	Absent.	Initially positive, then becomes negative (≈ -2.8 early), approaching zero from below.
Equation of state $w_d = p_d/\rho_d$	Constant, $w_d = -1$.	Dynamic; evolves from quintessence ($-1 < w_d < -1/3$) toward $w_d \to -1$ or crosses the phantom divide ($w_d < -1$).
Deceleration parameter $q(t)$	Present value $q_0 \approx -0.55$; tends to -1 at late times.	Strongly time-dependent; early super-acceleration ($q \approx -13$), converging to $q \approx -1$ at late times.
Hubble parameter $H(t)$	Decreases and approaches constant value at late times.	Evolves dynamically; stabilizes near $H \approx 2.3$ (model units).
Anisotropy / shear	Zero (isotropic FRW).	Non-zero initially (Bianchi VI$_o$) but decays monotonically.
Spatial volume / scale factor	Smooth exponential-like expansion at late times.	Slow initial growth followed by sharp exponential increase near $t \approx 4$.
Coincidence parameter $r = \rho_d/\rho_m$	Decreases slowly; ≈ 1 at present epoch.	Falls rapidly; matter becomes dynamically negligible earlier than in ΛCDM.
Thermodynamic consistency	Trivial (no viscous contribution).	Maintained by $\varepsilon(t) > 0$.
Observational concordance	Consistent with SNe Ia, CMB, and BAO data.	Qualitatively consistent at late times ($w \to -1$, $q \to -1$); quantitative fitting required.

Table 1 clearly demonstrates that the VHRDE model provides an extended framework beyond Lambda CDM by incorporating bulk viscosity, anisotropy, and scalar–tensor dynamics. The model reproduces late-time acceleration without invoking a cosmological constant and aligns well with observed cosmological behaviour.

6. CONCLUSIONS

This paper investigates a VHRDE model in a BT–VI$_o$ anisotropic spacetime under BD gravity with a pressure-less matter component. Precise solutions of the BD field equations are obtained by assuming a relation among the metric potentials and a parameterized bulk viscosity coefficient. The combined role of anisotropy, Ricci infrared cutoff, and viscosity is analysed to explain different phases of cosmic evolution. The Brans–Dicke scalar field ϕ remains positive for all cosmic times (Fig. 1). It decreases monotonically with the expansion, which indicates a gradual strengthening of the effective gravitational coupling in the late epoch. The scalar field's evolution significantly affects the HRDE and expansion dynamics. The VHRDE density ρ_d is positive throughout the evolution (Fig. 2). It starts with large values in the early anisotropic phase and decreases steadily to a small constant value at late times, supporting accelerated expansion. The matter ED ρ_m is also positive and decreases monotonically (Fig. 3). This behaviour corresponds to the expected dilution of pressure-less matter due to cosmic expansion. The bulk viscosity coefficient ϵ remains positive, ensuring thermodynamic consistency. It increases with time, which shows that viscous effects become more important in the DE–dominated era. This enhancement contributes to the negative pressure required for acceleration. The effective viscous pressure is negative for the entire evolution (Fig. 5). Its magnitude is large in the early epoch, providing a strong acceleration-driving mechanism. It decreases gradually with time, leading to a more stable expansion phase. The EoS parameter ω_d starts with positive values, decreases as time evolves, and approaches zero in the late epoch. This indicates a smooth transition from a matter-like regime to a dust-like regime driven by the combined effects of HRDE and viscosity. The expanding nature of the Universe is confirmed by the spatial volume increasing monotonically from zero at $t = 0$. Both the mean Hubble parameter $H(t)$ and the expansion scalar $\theta(t)$ are always positive. In the early Universe, both were large and in later eras, they tend to be constant, corresponding to a steady accelerated expansion similar to de Sitter behaviour. The deceleration parameter $q(t)$ remains negative throughout the evolution, indicating continuous accelerated expansion of the universe. At early times, $q(t) < -1$ corresponds to a super-accelerated phase, while at late times it approaches $q = -1$, indicating a de Sitter-like expansion. Finally, the VHRDE model in BD theory demonstrates how anisotropy, bulk viscosity, and HRDE can drive cosmic evolution shifted from matter domination to DE acceleration. The scalar field regulates the effective gravitational coupling, while viscosity provides the mechanism for sustained acceleration. The results show that a cosmological constant is unnecessary to explain late-time acceleration in anisotropic backgrounds.

Author contributions
K.P.S. Suryanarayana:conceptualisation, theoretical formulation, and supervision of the research work.
K.V.S. Sireesha(Corresponding Author): Methodology, validation, manuscript review and editing, project administration, and correspondence with the journal.
R. Sathibabu: Analytical calculations,data analysis, preparation of figures, and drafting of initial sections of the manuscript.
Funding information No funding was received for conducting this study.
Data availability No new data were created or analysed during this study. Data sharing is not applicable to this article.
Declarations
Ethical statement There is no ethical issue, presently, the manuscript is submitted in this journal.
Competing interests The authors declare no competing interests.

Acknowledgement

The authors are grateful to the Editor and the anonymous Reviewer for their valuable comments and constructive suggestions, which have significantly improved the quality and presentation of the manuscript.

ORCID

K.P.S. Suryanarayana, https://orcid.org/0000-0002-8793-3588; **K.V.S. Sireesha**, https://orcid.org/0000-0002-9751-2787; **R. Sathibabu**, https://orcid.org/0009-0007-4043-4750

REFERENCES

[1] S. Perlmutter, G. Aldering, G. Goldhaber, R. A. Knop, P. Nugent, P. G. Castro, S. Deustua, *et al.*, "Measurements of Omega and Lambda from 42 high redshift supernovae," Astrophysical Journal, 517(2), 565–586 (1999). https://doi.org/10.1086/307221

[2] A. G. Riess, L.-G. Strolger, S. Casertano, H. C. Ferguson, B. Mobasher, B. Gold, P. J. Challis, *et al.*, "New Hubble Space Telescope discoveries of type Ia supernovae at $z \geq 1$: narrowing constraints on the early behaviour of dark energy," Astrophysical Journal, **659**(1), 98–121 (2007). https://doi.org/10.1086/510378

[3] R. von Marttens, L. Lombriser, M. Kunz, V. Marra, L. Casarini, and J. Alcaniz, "Dark degeneracy I: Dynamical or interacting dark energy ?" Physics of the Dark Universe, **28**, 100490 (2020). https://doi.org/10.1016/j.dark.2020.100490

[4] S. M. Carroll, "The cosmological constant," Living Reviews in Relativity, **4**(1), 1–56 (2001). arXiv:astro-ph/0004075. https://doi.org/10.12942/lrr-2001-1

[5] T. Padmanabhan, "Cosmological constant—the weight of the vacuum," Physics Reports, **380**(5–6), 235–320 (2003). https://doi.org/10.1016/S0370-1573(03)00120-0

[6] T. Padmanabhan, "Accelerated expansion of the universe driven by tachyonic matter," Physical Review D, **66**(2), 021301 (2002). https://doi.org/10.1103/PhysRevD.66.021301

[7] T. Padmanabhan, "Dark energy and gravity," General Relativity and Gravitation, **40**(2), 529–564 (2008). https://doi.org/10.1007/s10714-007-0555-7

[8] M. C. Bento, O. Bertolami, and A. A. Sen, "Generalized Chaplygin gas, accelerated expansion, and dark-energy-matter unification," Physical Review D, **66**(4), 043507 (2002). https://doi.org/10.1103/PhysRevD.66.043507

[9] R. R. Caldwell, "A phantom menace? Cosmological consequences of a dark energy component with super-negative equation of state," Physics Letters B, **545**(1–2), 23–29 (2002). https://doi.org/10.1016/S0370-2693(02)02589-3

[10] S. I. Nojiri, and S. D. Odintsov, "Cosmological bound from the Neutron Star Merger GW170817 in scalar–tensor and F(R) gravity theories," Physics Letters B, **779**, 425–429 (2018). https://doi.org/10.1016/j.physletb.2018.01.078

[11] B. Feng, X. Wang, and X. Zhang, "Dark energy constraints from the cosmic age and supernova," Physics Letters B, **607**(1-2), 35–41 (2005). https://doi.org/10.1016/j.physletb.2004.12.071

[12] A. Kamenshchik, U. Moschella, and V. Pasquier, "An alternative to quintessence," Physics Letters B, **511**(2–4), 265–268 (2001). https://doi.org/10.1016/S0370-2693(01)00571-8

[13] V. Sahni, and Y. Shtanov, "Braneworld models of dark energy," Journal of Cosmology and Astroparticle Physics, (11), 014 (2003). https://doi.org/10.1088/1475-7516/2003/11/014

[14] G. 't Hooft, "Dimensional reduction in quantum gravity," arXiv preprint gr-qc/9310026, (1993). https://doi.org/10.48550/arXiv.gr-qc/9310026

[15] A. G. Cohen, D. B. Kaplan, and A. E. Nelson, "Effective field theory, black holes, and the cosmological constant," Physical Review Letters, **82**(25), 4971–4974 (1999). https://doi.org/10.1103/PhysRevLett.82.4971

[16] R. G. Landim, and E. Abdalla, "Metastable dark energy," Physics Letters B, **764**, 271–276 (2017). https://doi.org/10.1016/j.physletb.2016.11.044

[17] C. Gao, F. Wu, X. Chen, and Y. G. Shen, "Holographic dark energy model from Ricci scalar curvature," Physical Review D, **79**(4), 043511 (2009). https://doi.org/10.1103/PhysRevD.79.043511

[18] L. N. Granda and A. Oliveros, "Infrared cut-off proposal for the holographic density," Physics Letters B, **669**(5), 275–277 (2008). https://doi.org/10.1016/j.physletb.2008.10.017

[19] M. Krishna, S. Kappala, and R. Santhikumar, "Cylindrically symmetric generalized ghost pilgrim dark energy cosmological universe," Journal of Siberian Federal University. Mathematics & Physics, **17**(2), 257–265 (2024).

[20] S. Chen and J. Jing, "Dark energy model with higher derivative of Hubble parameter," Physics Letters B, **679**(2), 144–150 (2009). https://doi.org/10.1016/j.physletb.2009.07.018

[21] C. J. Feng, "Statefinder diagnosis for Ricci dark energy," Physics Letters B, **670**(3), 231–234 (2008). https://doi.org/10.1016/j.physletb.2008.11.005

[22] M. Bouhmadi-López and Y. Tavakoli, "Why is the running vacuum energy more benign than the holographic Ricci dark energy?," Physical Review D, **87**(2), 023515 (2013). https://doi.org/10.1103/PhysRevD.87.023515

[23] M. Suwa, K. Kobayashi, and H. Oshima, "The interacting generalized Ricci dark energy model in a non-flat universe," arXiv preprint arXiv:1412.5241, 2014. https://doi.org/10.48550/arXiv.1412.5241

[24] S. Ghaffari, A. Sheykhi, and M. H. Dehghani, "Statefinder diagnosis for holographic dark energy in the DGP braneworld," Physical Review D, **91**(2), 023007 (2015). https://doi.org/10.1103/PhysRevD.91.023007

[25] C. W. Misner, "Transport processes in the primordial fireball," Nature, **214**(5083), 40–41 (1967). https://doi.org/10.1038/214040a0

[26] C. W. Misner, "The isotropy of the universe," Astrophysical Journal, **151**, 431–457 (1968). https://doi.org/10.1086/149448

[27] V. U. M. Rao, M. Vijaya Santhi, K. V. S. Sireesha, and N. Sandhya Rani, "Bulk viscous string cosmological models in Saez–Ballester theory of gravitation," Iranian Journal of Physics Research, **18**(3), 497–504 (2019). https://doi.org/10.29252/ijpr.18.3.497

[28] G. Chakraborty and S. Chattopadhyay, "Cosmology of a generalised version of holographic dark energy in the presence of bulk viscosity and its inflationary dynamics through slow roll parameters," International Journal of Modern Physics D, **29**(03), 2050024 (2020). https://doi.org/10.1142/S0218271820500248

[29] P. E. Satyanarayana and K. V. S. Sireesha, "Bianchi Type-III viscous holographic Ricci dark energy cosmological model in Brans-Dicke theory of gravitation," East European Journal of Physics, (1), 127–135 (2024). https://doi.org/10.26565/2312-4334-2024-1-10

[30] R. V. Wagoner, "Scalar-tensor theory and gravitational waves," Physical Review D, **1**(12), 3209–3216 (1970). https://doi.org/10.1103/PhysRevD.1.3209

[31] V. U. M. Rao and K. V. S. Sireesha, "A higher-dimensional string cosmological model in a scalar-tensor theory of gravitation," European Physical Journal Plus, **127**(33), 1-6 (2012). https://doi.org/10.1140/epjp/i2012-12033-y

[32] V. U. M. Rao, M. V. Santhi, K. V. S. Sireesha, and N. S. Rani, "Five-dimensional FRW string cosmological models with bulk viscosity in Brans–Dicke theory of gravitation," Prespacetime Journal, **7**(3), 520-536 (2016). https://mail.prespacetime.com/index.php/pst/article/view/946/0?utm_source=chatgpt.com

[33] R. Santhi Kumar and B. Satyanarayana, "Accelerating anisotropic cosmological model in F(R, T) theory of gravity," Indian Journal of Physics, **91**(10), 1293–1296 (2017). https://doi.org/10.1007/s12648-017-1017-z

[34] N. S. Rani, K. V. S. Sireesha, and V. U. M. Rao, "Bianchi type-III, V and VI0 generalized ghost dark energy models with polytropic gas in Brans–Dicke theory of gravitation," Journal of Physics: Conference Series, **1344**(1), 012045 (2019). https://doi.org/10.1088/1742-6596/1344/1/012045

[35] K. V. S. Sireesha and V. U. M. Rao, "Bianchi type-II, VIII & IX holographic dark energy cosmological models in Brans–Dicke theory of gravitation," African Review of Physics, **14**(0010), 79-86 (2019). https://www.researchgate.net/publication/349813258

[36] V. B. Johri and K. Desikan, "Cosmological models with constant deceleration parameter in Brans–Dicke theory," General Relativity and Gravitation, **26**(12), 1217–1232 (1994). https://doi.org/10.1007/BF02106714

[37] C. B. Collins, E. N. Glass, and D. A. Wilkinson, "Exact spatially homogeneous cosmologies," General Relativity and Gravitation, **12**(10), 805–823 (1980). https://doi.org/10.1007/BF00763057

[38] J. Ren and X. H. Meng, "Dark viscous fluid described by a unified equation of state in cosmology," International Journal of Modern Physics D, **16**(08), 1341–1348 (2007). https://doi.org/10.1142/S0218271807010821

[39] S. Sarkar, "Holographic dark energy model with linearly varying deceleration parameter and generalised Chaplygin gas dark energy model in Bianchi type-I universe," Astrophysics and Space Science, **349**(2), 985–993 (2014). https://doi.org/10.1007/s10509-013-1684-y

[40] E. H. Baffou, M. J. S. Houndjo, I. G. Salako, F. K. Ahloui, and A. D. Kanfon, "Observational constraints on viscous Ricci dark energy model coupled with F(R, T) gravity," Chinese Journal of Physics, **84**, 248–257 (2023). https://doi.org/10.1016/j.cjph.2022.11.014

[41] C. P. Singh and A. Kumar, "Holographic Ricci dark energy with constant bulk viscosity in F(R, T) gravity," Gravitation and Cosmology, **25**(1), 58–68 (2019). https://doi.org/10.1134/S0202289319010109

[42] M. Vijaya Santhi, Y. Sobhanbabu, "Study of axially symmetric viscous Ricci dark energy model in Brans–Dicke theory," New Astronomy, **95**, 101823 (2022). https://doi.org/10.1016/j.newast.2022.101823

[43] M. Vijaya Santhi, T. Chinnappalanaidu, and S. Srivani Madhu, "Viscous Ricci dark energy cosmological models in Brans–Dicke theory," Astrophysics, **66**(4), 559–589 (2023). https://doi.org/10.1007/s10511-024-09810-9

[44] S. Kaur, M. Srivastava, and B. Mangku, "Bulk viscosity analysis with new holographic dark energy in f (R, T) theory," Canadian Journal of Physics, **103**(5), 455–460 (2024). https://doi.org/10.1139/cjp-2024-0109

ДОСЛІДЖЕННЯ КОСМОЛОГІЧНОЇ МОДЕЛІ В'ЯЗКОЇ ГОЛОГРАФІЧНОЇ КОСМОЛОГІЧНОЇ МОДЕЛІ ТЕМНОЇ ЕНЕРГІЇ РІЧЧІ ТИПУ БІАНКІ В ТЕОРІЇ ГРАВІТАЦІЇ БРАНСА-ДІКЕ

К.П.С. Сур'янараяна, К.В.С. Сіріша, Р. Сатібабу
Кафедра математики та статистики, GSS, GITAM, вважається Університетом, Вішакхапатнам, Індія

- Досліджено в'язку голографічну модель темної енергії Річчі (VHRDE) в рамках гравітації Бранса-Діке (BD).
- Об'ємна в'язкість генерує ефективний негативний тиск, тоді як скалярне поле BD динамічно регулює гравітаційний зв'язок.
- Отримано природний перехід від ранньої уповільненої фази з домінуванням матерії до пізньої прискореної фази розширення з домінуванням темної енергії.
- Модель виходить за межі ΛCDM, демонструючи динамічно еволюціонуюче рівняння стану, яке може наближатися або перетинати фантомну межу $\omega < -1$
- Анізотропія та зсувний спад з космічним часом, що призводить до ізотропізації наприкінці часу, що узгоджується з обмеженнями спостережень (CMB).

Ми досліджуємо в'язку голографічну модель темної енергії Річчі (VHRDE) у просторі-часі типу Б'янкі (BT) - VI_o в межах гравітації Бранса-Дікке (BD), включаючи компонент матерії без тиску. Припускаючи зв'язок між метричними потенціалами та параметризованим коефіцієнтом об'ємної в'язкості, знайдено точні розв'язки рівнянь поля BD. Комбінований вплив анізотропії, голографічного обрізання Річчі та об'ємної в'язкості дають динамічний каркас, який може описувати кілька фаз космічної еволюції. Ми досліджуємо прогресію важливих вимірювань, включаючи скалярне поле, густину енергії, об'ємну в'язкість, в'язкий тиск, рівняння стану (EoS), змінні розширення та параметр уповільнення, виявляючи перехід від уповільненої епохи, де домінує матерія, до прискореної фази, де домінує темна енергія. Об'ємна в'язкість генерує ефективний негативний тиск, що зумовлює прискорення, тоді як скалярне поле BD модулює гравітаційний зв'язок. Порівняння з попередніми дослідженнями підтверджує, що ця модель забезпечує життєздатний механізм космічного прискорення без необхідності космологічної константи.

Keywords: *метрика типу Б'янкі - VI_o; голографічна темна енергія Річчі (HRDE); об'ємна в'язкість; теорія Бранса-Дікке*

East European Journal of Physics. **3**. 127–137 (2026)
DOI: 10.26565/2312-4334-2026-3-11 ISSN 2312-4334

TRAVERSABLE WORMHOLE SOLUTIONS THROUGH DECOUPLING APPROACH IN RASTALL THEORY

Muhammad Sharif[1,2*], **Malick Sallah**[1], **Tayyab Naseer**[1*]
[1]*Department of Mathematics and Statistics, The University of Lahore, 1-KM Defence Road Lahore-54000, Pakistan*
[2]*Jadara Research Center, Jadara University, Irbid 21110, Jordan*
[*]*Corresponding Author e-mail: msharif.math@pu.edu.pk; tayyabnaseer48@yahoo.com*
Received May 17, 2026; revised August 11, 2026; accepted August 17, 2026

This paper explores the construction of traversable wormhole solutions in the context of Rastall's gravity using the extended gravitational decoupling method. Based on the modified field equations of this new theory, we apply the present scheme to incorporate an extra gravitational source, which leads to a fully transformed version of the Schwarzschild solution. By means of an appropriate coordinate transformation, this modified geometry is reinterpreted as a wormhole spacetime. The analysis proceeds by investigating the resulting configuration's fundamental physical and geometric features, specifically, null energy conditions' violation, gravitational mass behavior, volume integral quantifier evaluation, and embedding diagram. A key finding is that the wormhole neck arises obviously from the distorted geometry while also satisfying the traversability-required flare-out criterion. Plotting the energy conditions for various Rastall parameter values reveal localized null energy condition violations near the throat, which is consistent with the presence of exotic matter. However, the total exotic matter content is shown to be minimal and highly sensitive to the choice of model parameters. These results underscore the potential of Rastall gravity, in conjunction with gravitational decoupling, to support physically plausible wormhole geometries with reduced exotic matter requirements.

Keywords: *Rastall theory; Gravitational decoupling; Wormholes; Exotic fluid*

1. INTRODUCTION

In recent years, modified gravity frameworks have garnered considerable attention as viable alternatives to general relativity (GR), especially in addressing challenges related to dark energy, cosmic expansion, and spacetime singularities. Among the most prominent approaches are $f(\mathcal{R})$ gravity and scalar-tensor formulations, both of which have been extensively studied for their potential to offer deeper insights into gravitational dynamics [1, 2]. Within this broader investigative landscape, the Rastall theory [3] stands out by deviating from the standard conservation of the energy-momentum tensor (EMT) in curved geometries. By introducing a coupling between the EMT divergence and the gradient of the Ricci scalar, Rastall's model proposes a non-minimal interaction between matter and geometry, suggesting novel implications for both cosmology and astrophysics.

Although Rastall gravity introduces an unconventional mechanism, it has not escaped scrutiny. Visser [4] questioned its physical distinctiveness, suggesting it could be merely a reformulation of GR, while Golovnev [5] criticized the absence of a well-defined variational principle and cast doubt on its phenomenological utility. Despite such reservations, subsequent investigations have mounted compelling defenses of the theory. Darabi et al. [6], for instance, demonstrated its empirical adequacy in specific cosmological models, while others have constructed physically meaningful solutions that are not replicable within standard GR [7, 8]. This theory has also been affirmed in compact star modeling: Shahzad and Abbas employed the $\mathbb{MIT}$ bag model to examine strange stars [9], and later extended their work to include hybrid [10] and quintessence [11] stars. Naseer investigated the influence of the Rastall parameter on novel spherical solutions [12], and further explored the effects of gravitational decoupling in relation to isotropization and structural complexity [13]. His collaborative work with Sharif [14] involved the Krori-Barua and Tolman IV metrics within the context of decoupling and Rastall parameters. Other contributions include isotropic models derived using the Durgapal-Lake ansatz by Waseem and Naeem [15], and investigations by ourselves that generalized regular Hayward and Bardeen black holes [16]. Several promising results have emerged from various investigations into self-gravitating compact stars conducted within the context of this non-conserved gravity [17]-[24].

Gravitational decoupling, a method grounded in the application of geometric deformations - either in their minimal (MGD) or extended (EGD) form - has proven to be a robust framework for constructing novel solutions to the gravitational field equations. Within both GR and several modified gravity theories, this technique permits systematic generalizations through the separation of a known (commonly isotropic) solution from an auxiliary source term that produces direction-dependent behavior. The MGD and EGD schemes were both formulated by Ovalle [25, 26], where the minimal version involves deforming only g_{rr}, while the extended version modifies both g_{rr} and g_{tt}. These decoupling schemes have been instrumental in generalizing well-known solutions, such as the Tolman IV and Krori-Barua metrics, within GR and in the context of Brans-Dicke theory, to yield anisotropic models. Additionally, Ovalle and collaborators [27] employed this framework to derive hairy black hole solutions by extending the Schwarzschild vacuum geometry. The influence of the

Cite as: M. Sharif, M. Sallah, T. Naseer, East Eur. J. Phys. 3, 127 (2026), https://doi.org/10.26565/2312-4334-2026-3-11

2-step GD method has also been explored in the context of structural complexity [28]. In a recent investigation, Maurya et al. [29] applied the EGD scheme to extend the Tolman IV solution to a more complex domain and obtained a physical acceptable model.

In this study, we apply the EGD framework to deform the Schwarzschild black hole solution, subsequently linking it to a wormhole geometry. For detailed discussions on black hole deformations within this context, readers are referred to our earlier works [16, 29]. The theoretical origins of wormholes exist in the fundamental work of Misner and Wheeler [30, 31], who analyzed the creation of charge quantity from the continuity of field lines across discontinuities in spacetime. Wheeler [32, 33] was the first to propose “geons” and the concept of spacetime foam, thereby suggesting that the structure of spacetime becomes fundamentally intricate when examined at quantum-level resolutions. Even earlier, Einstein and Rosen had developed a geometric construct (now famously known as the Einstein-Rosen bridge [34]) which envisioned a throat-like structure connecting two asymptotically flat regions of spacetime. Although redolent of potential inter-universal passages, the viability of this configuration was subsequently contested by Fuller and Wheeler [35], who proved that the bridge is inherently unstable and undergoes collapse too rapidly to facilitate the traversal of either particles or light.

The resurgence of interest in wormhole physics can be traced largely to the seminal work of Morris and Thorne [36], who, through specific choices of redshift and shape functions, presented static, spherically symmetric, traversable wormhole solutions within the GR framework. A fundamental issue with these models, however, lies in their reliance on exotic matter - substances that violate the null energy conditions (NECs), thereby introduces deep theoretical complications. This challenge has sparked a shift towards exploring wormholes in the realm of modified gravity theories, where the violation of energy conditions can emerge from geometric modifications rather than physically implausible forms of matter. In such theories, effective EMTs can absorb the NECs violations through curvature-related contributions. As a result, wormhole solutions have been extensively studied in alternative frameworks like $f(\mathcal{R})$ gravity [37], Gauss-Bonnet gravity [38], and, significantly, in Rastall theory [39], where the usual conservation of the EMT is relaxed. This modification enables richer matter-geometry couplings that support wormhole structures without invoking exotic matter in the conventional sense. These developments not only offer plausible wormhole geometries but also deepen our understanding of how non-trivial topological configurations may naturally arise in extended theories of gravity.

The structure of the paper is given as follows. Section **2** is devoted to the formulation of the gravitational field equations within the Rastall gravity paradigm, thereby furnishing the theoretical groundwork to be used in the later analysis. In section **3**, the EGD formalism is used to split the field equations into decoupled sectors, making tractable solutions possible. Section **4** focuses on deriving a transformed static, spherically symmetric black hole solution and establishing its geometric link to a traversable wormhole configuration. This section also sets forth an extensive investigation of the wormhole derived, involving an inspection of NECs' violation, a calculation of active mass, an estimation of the volume integral quantifier ($\mathcal{VIQ}$), and a geometric illustration through an embedding schematic. Lastly, section **5** offers concluding remarks, highlighting the broader implications of our results for wormhole construction in the setting of modified gravity theories.

2. FIELD EQUATIONS

Within the context of the Rastall gravity, the equations dictating the dynamics adopt the following expression

$$G_{\mu\nu} = \kappa(T_{\mu\nu} - \xi\mathcal{R}g_{\mu\nu}). \tag{1}$$

Here, $G_{\mu\nu}$ is the Einstein tensor, $g_{\mu\nu}$ the metric tensor, $\mathcal{R}$ the Ricci scalar, κ the coupling constant, $T_{\mu\nu}$ the EMT, and the Rastall's coupling parameter $\lambda = \kappa\xi$. Within this approach, the EMT obeys the relationship given by

$$\nabla_\nu T^{\mu\nu} = \lambda g^{\mu\nu}\nabla_\nu\mathcal{R}, \tag{2}$$

which implies the usual covariant conservation law is violated. However, in the case where the λ parameter disappears, the ordinary conservation law of GR is once again obtained. From the relation in Eq.(1), it follows that

$$\mathcal{R}(4\lambda - 1) = \kappa T, \tag{3}$$

where T signifies the trace of the EMT $T_{\mu\nu}$. Finally, the governing equations of the spacetime geometry (1) may be written alternatively as

$$G_{\mu\nu} + \lambda\mathcal{R}g_{\mu\nu} = \frac{8\pi(1-4\lambda)}{1-6\lambda}T_{\mu\nu}. \tag{4}$$

Let us assume that $T_{\mu\nu}$ takes the form of an anisotropic fluid within the $(+,-,-,-)$ metric convention, written explicitly as

$$T_{\mu\nu} = (\rho + P_t)\mathcal{Y}_\mu\mathcal{Y}_\nu + (P_r - P_t)\mathcal{Z}_\mu\mathcal{Z}_\nu - P_t g_{\mu\nu}, \tag{5}$$

where

- $\mathcal{Y}_\mu = \delta^0_\mu\sqrt{g_{00}}$: 4-vector and $\mathcal{Z}_\mu = -\delta^0_\mu\sqrt{-g_{11}}$: four-velocity,
- ρ: density,

- P_r: radial pressure and P_t: transverse pressure.

Moreover, $\mathcal{Y}^\mu\mathcal{Y}_\mu = 1$, $\mathcal{Y}^\mu\mathcal{Z}_\mu = 0$ and $\mathcal{Z}^\mu\mathcal{Z}_\mu = -1$. To perform the gravitational decoupling technique, we alter the governing equations of the spacetime geometry (4) by employing a multi-sourced EMT, expressed in the following way as

$$G_{\mu\nu} + \lambda\mathcal{R}g_{\mu\nu} = \frac{8\pi(1-4\lambda)}{1-6\lambda}T^{(tot)}_{\mu\nu}, \tag{6}$$

where

$$T^{(tot)}_{\mu\nu} = T_{\mu\nu} + \delta\Psi_{\mu\nu}. \tag{7}$$

The incorporation of a supplementary source, denoted $\Psi_{\mu\nu}$, is achieved through the decoupling parameter δ, where δ dictates the magnitude of the coupling linking the sources. By introducing this term, anisotropic behavior emerges within the once-isotropic seed solution, which in turn expands its range of applicability to diverse contexts.

For the interior region, the geometric arrangement is provided by the following metric

$$ds^2 = -(d\theta^2 + \sin^2\theta d\phi^2)r^2 - e^{\mathcal{B}(r)}dr^2 + e^{\mathcal{A}(r)}dt^2. \tag{8}$$

After substitution, the field equations (6) are given by

$$\begin{aligned}8\pi\left(\frac{4\lambda-1}{6\lambda-1}\right)\left(\rho+\delta\Psi^0_0\right) &= \lambda\left[e^{-\mathcal{B}}\left(\mathcal{A}''+\frac{\mathcal{A}'}{2}(\mathcal{A}'-\mathcal{B}')+\frac{2}{r}(\mathcal{A}'-\mathcal{B}')+\frac{2}{r^2}\right)-\frac{2}{r^2}\right]\\ &+e^{-\mathcal{B}}\left(\frac{\mathcal{B}'}{r}-\frac{1}{r^2}\right)+\frac{1}{r^2},\end{aligned} \tag{9}$$

$$\begin{aligned}8\pi\left(\frac{4\lambda-1}{6\lambda-1}\right)\left(P_r-\delta\Psi^1_1\right) &= -\lambda\left[e^{-\mathcal{B}}\left(\mathcal{A}''+\frac{\mathcal{A}'}{2}(\mathcal{A}'-\mathcal{B}')+\frac{2}{r}(\mathcal{A}'-\mathcal{B}')+\frac{2}{r^2}\right)-\frac{2}{r^2}\right]\\ &+e^{-\mathcal{B}}\left(\frac{\mathcal{A}'}{r}+\frac{1}{r^2}\right)-\frac{1}{r^2},\end{aligned} \tag{10}$$

$$\begin{aligned}8\pi\left(\frac{4\lambda-1}{6\lambda-1}\right)\left(P_t-\delta\Psi^2_2\right) &= -\lambda\left[e^{-\mathcal{B}}\left(\mathcal{A}''+\frac{\mathcal{A}'}{2}(\mathcal{A}'-\mathcal{B}')+\frac{2}{r}(\mathcal{A}'-\mathcal{B}')+\frac{2}{r^2}\right)-\frac{2}{r^2}\right]\\ &+e^{-\mathcal{B}}\left[\frac{\mathcal{A}''}{2}+\frac{\mathcal{A}'^2}{4}-\frac{\mathcal{A}'\mathcal{B}'}{4}+\frac{\mathcal{A}'-\mathcal{B}'}{2r}\right].\end{aligned} \tag{11}$$

There are three nonlinear ordinary differential equations in the above system, expressed in terms of $\mathcal{A}, \mathcal{B}, \rho, P_r, P_t, \Psi^0_0, \Psi^1_1, \Psi^2_2$, where the prime notation means $' = \frac{d}{dr}$. With the help of this system, we formulate the effective variables in the following manner

$$\tilde{\rho} = \rho + \delta\Psi^0_0, \quad \tilde{P}_r = P_r - \delta\Psi^1_1, \quad \tilde{P}_t = P_t - \delta\Psi^2_2, \tag{12}$$

and anisotropic parameter

$$\tilde{\Delta} = \tilde{P}_t - \tilde{P}_r = \delta(\Psi^1_1 - \Psi^2_2). \tag{13}$$

The condition $\Psi^1_1 = \Psi^2_2$ implies the absence of anisotropy in the additional source, indicating that the anisotropic factor vanishes. In the subsequent section, we apply the EGD method to address the field equations (9)-(11). This technique facilitates the decomposition of the full system into two distinct subsystems: one associated with the original (seed) EMT $T_{\mu\nu}$, and the other corresponding to the supplementary source $\Psi_{\mu\nu}$. Owing to the reduced coupling, each sector can be treated and solved independently. The full solution to the field equations is then constructed through a linear superposition of these individual solutions, as prescribed in Eq.(12).

3. AN EGD APPROACH

To address the system of equations (9)-(11), we adopt the EGD approach, which introduces linear deformations to both g_{rr} and g_{tt}. Through these deformations, the original system is effectively decoupled into two distinct sectors. The first corresponds to a perfect fluid configuration (achieved by setting $\delta = 0$), while the second incorporates the effects of the additional source $\Psi_{\mu\nu}$, expressed in terms of the deformation functions. As a starting point, we consider a well-established ideal fluid solution to the field equations, characterized by the following metric

$$ds^2 = -(d\theta^2 + \sin^2\theta d\phi^2)r^2 - \frac{dr^2}{\mathcal{D}(r)} + e^{\mathcal{C}(r)}dt^2, \tag{14}$$

with
$$\mathcal{D}(r) = 1 - \frac{2m(r)}{r}, \tag{15}$$
where m represents the Misner-Sharp mass. The linear transformations that characterize the geometric deformation are given by
$$C(r) \mapsto \mathcal{A}(r) = C(r) + \delta f(r), \quad \mathcal{D}(r) \mapsto e^{-\mathcal{B}(r)} = \mathcal{D}(r) + \delta g(r), \tag{16}$$
where $f(r)$ and $g(r)$ denote the deformations applied to the g_{tt} and g_{rr}, respectively. Substituting Eq.(16) into the field equations produces the first set given below
$$8\pi\left(\frac{1-4\lambda}{1-6\lambda}\right)\rho = \mathcal{D}\left(\lambda C'' + \frac{\lambda C'^2}{2} + \frac{2\lambda C'}{r} + \frac{2\lambda}{r^2} - \frac{1}{r^2}\right) - \frac{2\lambda}{r^2} + \frac{1}{r^2} + \mathcal{D}'\left(\frac{\lambda C'}{2} + \frac{2\lambda}{r} - \frac{1}{r}\right), \tag{17}$$
$$8\pi\left(\frac{1-4\lambda}{1-6\lambda}\right)P_r = \mathcal{D}\left(\frac{C'}{r} + \frac{1}{r^2} - \frac{2\lambda}{r^2} - \frac{2\lambda C'}{r} - \frac{\lambda C'^2}{2} - \lambda C''\right) + \frac{2\lambda}{r^2} - \frac{1}{r^2} - \mathcal{D}'\left(\frac{\lambda C'}{2} + \frac{2\lambda}{r}\right), \tag{18}$$
$$8\pi\left(\frac{1-4\lambda}{1-6\lambda}\right)P_t = \mathcal{D}\left(\frac{C''}{2} - \lambda C'' - \frac{\lambda C'^2}{2} - \frac{2\lambda C'}{r} - \frac{2\lambda}{r^2} + \frac{C'^2}{4} + \frac{C'}{2r}\right) + \frac{2\lambda}{r^2} + \mathcal{D}'\left(\frac{C'}{4} + \frac{1}{2r} - \frac{\lambda C'}{2} - \frac{2\lambda}{r}\right). \tag{19}$$
Since the system consists of three linearly independent equations involving five unknowns: $C, \mathcal{D}, \rho, P_r$, and P_t, two additional constraints are required to render it solvable. In the following section, we impose these constraints by invoking the vacuum Schwarzschild solution as the guiding framework.

The second set of equations, which separates the contribution from the supplemental source and the deformation function, may be expressed as
$$8\pi\left(\frac{1-4\lambda}{1-6\lambda}\right)\Psi_0^0 = \lambda\left[g\left(C'' + \frac{(C')^2}{2} + \frac{2C'}{r}\right) + g'\left(\frac{C'}{2} + \frac{2}{r}\right) + \mathcal{D}f'' + \mathcal{D}C'f' + \frac{\mathcal{D}\delta(f')^2}{2} + \frac{\mathcal{D}'f'}{2} + \frac{2\mathcal{D}f'}{r}\right] - \frac{g'}{r} - \frac{g}{r^2}, \tag{20}$$
$$8\pi\left(\frac{1-4\lambda}{1-6\lambda}\right)\Psi_1^1 = \lambda\left[g\left(C'' + \frac{(C')^2}{2} + \frac{2C'}{r}\right) + g'\left(\frac{C'}{2} + \frac{2}{r}\right) + \mathcal{D}f'' + \mathcal{D}C'f' + \frac{\mathcal{D}\delta(f')^2}{2} + \frac{\mathcal{D}'f'}{2} + \frac{2\mathcal{D}f'}{r}\right] - g\left(\frac{C'}{r} + \frac{1}{r^2}\right) - \frac{\mathcal{D}f'}{r}, \tag{21}$$
$$8\pi\left(\frac{1-4\lambda}{1-6\lambda}\right)\Psi_2^2 = \lambda\left[g\left(C'' + \frac{(C')^2}{2} + \frac{2C'}{r}\right) + g'\left(\frac{C'}{2} + \frac{2}{r}\right) + \mathcal{D}f'' + \mathcal{D}C'f' + \frac{\mathcal{D}\delta(f')^2}{2} + \frac{\mathcal{D}'f'}{2} + \frac{2\mathcal{D}f'}{r}\right] - g\left(\frac{C''}{2} + \frac{(C')^2}{4} + \frac{C'}{2r}\right) - \frac{\mathcal{D}'f'}{4} - g'\left(\frac{C'}{4} + \frac{1}{2r}\right) - \mathcal{D}\left(\frac{f''}{2} + \frac{\delta(f')^2}{4} + \frac{\mathcal{D}'f'}{2} + \frac{f'}{2r}\right). \tag{22}$$
To solve the system of equations (20)-(22), we impose two supplementary constraints, given that it contains five unknowns but only three independent equations. To be more precise, we adopt both a linear $\mathbb{E}\text{o}\mathbb{S}$ and a mimic constraint expressed in terms of the total pressure. The equation sets (17)-(19) and (20)-(22) provide a decoupled representation of the primary field equations (9)-(11), and the full solution to the original system can be recovered by linearly adding the solutions obtained from each.

4. FROM BLACK HOLE TO WORMHOLE MODELS

This portion of the work explores the development of a wormhole model connected to a totally distorted black hole of the non-Schwarzschild sort. Considering the Schwarzschild spacetime

$$ds^2 = \left(1 - \frac{2M}{r}\right) dt^2 - \frac{dr^2}{\left(1 - \frac{2M}{r}\right)} - r^2 d\Omega^2, \tag{23}$$

the EGD scheme described in the previous section deforms this metric to

$$ds^2 = \left(1 - \frac{2M}{r}\right) e^{\delta f(r)} dt^2 - \frac{dr^2}{\left(1 - \frac{2M}{r} + \delta g(r)\right)} - r^2 d\Omega^2. \tag{24}$$

Clearly, the deformed spacetime depicted the above configuration differs from Schwarzschild geometry in that $|g_{tt}(r)| \neq |g_{rr}^{-1}(r)|$. It thus represents a non-Schwarzschild black hole. Our objective is to generate a wormhole geometry in association with the present spacetime. To do this however, we must first of all determine the deformation functions $f(r)$ and $g(r)$ in order to completely represent the deformed spacetime above. We obtain these deformation functions by employing two constraints in the system of equations (20)-(22). For the first of these constraints, we employ a linear $\mathbb{E}\mathrm{o}\mathbb{S}$ on $\Psi_{\mu\nu}$ given as

$$\Psi_0^0 - \zeta_1 \Psi_1^1 - \zeta_2 \Psi_2^2 = 0, \tag{25}$$

where ζ_1 and ζ_2 are real constants. By setting $\zeta_1 = 1$ and $\zeta_2 = 0$, we obtain the simplified form given by

$$\Psi_0^0 = \Psi_1^1. \tag{26}$$

Using Eqs.(20) and (21), this equation turns out to

$$f'(r) = \frac{g'(r) - g(r)C'(r)}{\mathcal{D}(r)}. \tag{27}$$

For the second constraint, we adopt the total pressure mimic-constraint given by

$$\frac{1}{3}\left(P_r + 2P_t\right) = \frac{1}{3}\left(\Psi_1^1(r) + 2\Psi_2^2(r)\right). \tag{28}$$

However, since $P_r = P_t = 0$ due to the vacuum seed solution, this equation reduces to

$$\Psi_1^1(r) + 2\Psi_2^2(r) = 0. \tag{29}$$

Using Eq.(27) in this constraint, we deduce numerical solutions for the deformations which are plotted in **Figure 1**. It is important to emphasize that our objective here is not to analyze the physical characteristics of the black hole spacetime itself, but rather to construct a wormhole geometry that is geometrically connected to it. For a detailed treatment of the extended gravitational decoupling of the Schwarzschild black hole, we refer readers to our earlier work [29]. In the discussion that follows, we focus on identifying the conditions under which the spacetime described by Eq.(24) can be interpreted as a viable wormhole solution.

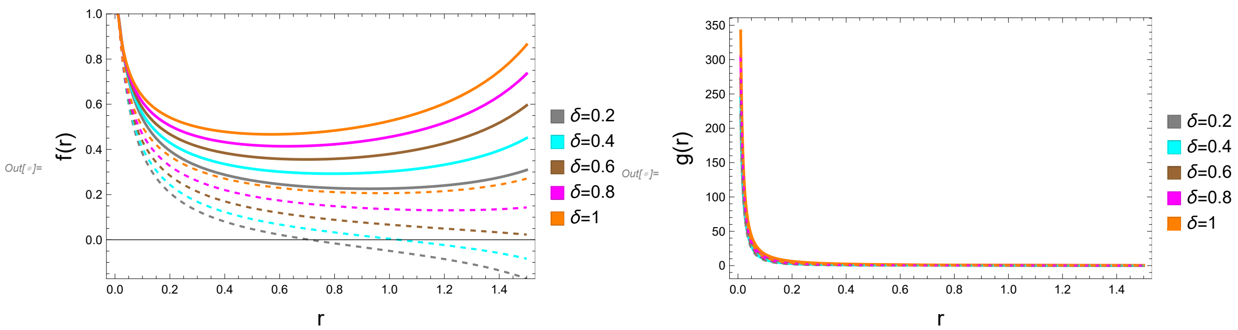

Figure 1. Deformation functions $f(r)$ and $g(r)$.

4.1. A Wormhole Solution

The Morris-Thorne metric, representing the most general spacetime, is adopted for the description of the wormhole geometry [36]

$$ds^2 = e^{2\eta(r)}dt^2 - \frac{dr^2}{1-\frac{\chi(r)}{r}} - r^2 d\Omega^2. \tag{30}$$

Here, the wormhole structure is described by the shape function $\chi(r)$, and $\eta(r)$ plays the role of the redshift function. Relating this spacetime interval to the one from Eq.(24) gives the direct consequence that

$$\eta(r) = \frac{1}{2}\left(\delta f(r) + \ln\left|1 - \frac{2M}{r}\right|\right), \tag{31}$$

and

$$\chi(r) = 2M - \delta r g(r). \tag{32}$$

The wormhole throat (r_0) is obtained from the relation $\chi(r_0) = r$. However, an explicit form of the wormhole throat cannot be given as the deformation function $g(t)$ is numerically approximated. To reinforce the validity of the proposed wormhole model, we examine several essential geometric conditions, illustrated in **Figure 2**. Among these, the flare-out condition plays a central role. Mathematically, it is expressed as

$$\frac{\chi(r) - r\chi'(r)}{2\chi^2(r)} > 0, \tag{33}$$

such a condition ensures the throat takes the shape of a minimal surface that expands outward, a key prerequisite for keeping the throat stable and ensuring it can be crossed. This condition provides an essential bridge between wormhole geometry and the requirement for exotic matter, marking it as a foundational concept in wormhole physics. Moreover, we demonstrate how the shape function $\chi(r)$ behaves under the condition $\chi(r) < r$, applicable for every r. We also confirm asymptotic flatness by plotting $\chi(r)/r$ and demonstrating its vanishing behavior at large radial distances. In each of the pertinent plots, we use representative choices of the Rastall parameter as $\lambda = 0.175$ (solid) and $\lambda = 0.225$ (dashed). The decoupling parameter δ takes specific values for each figure, and these are indicated alongside wherever applicable.

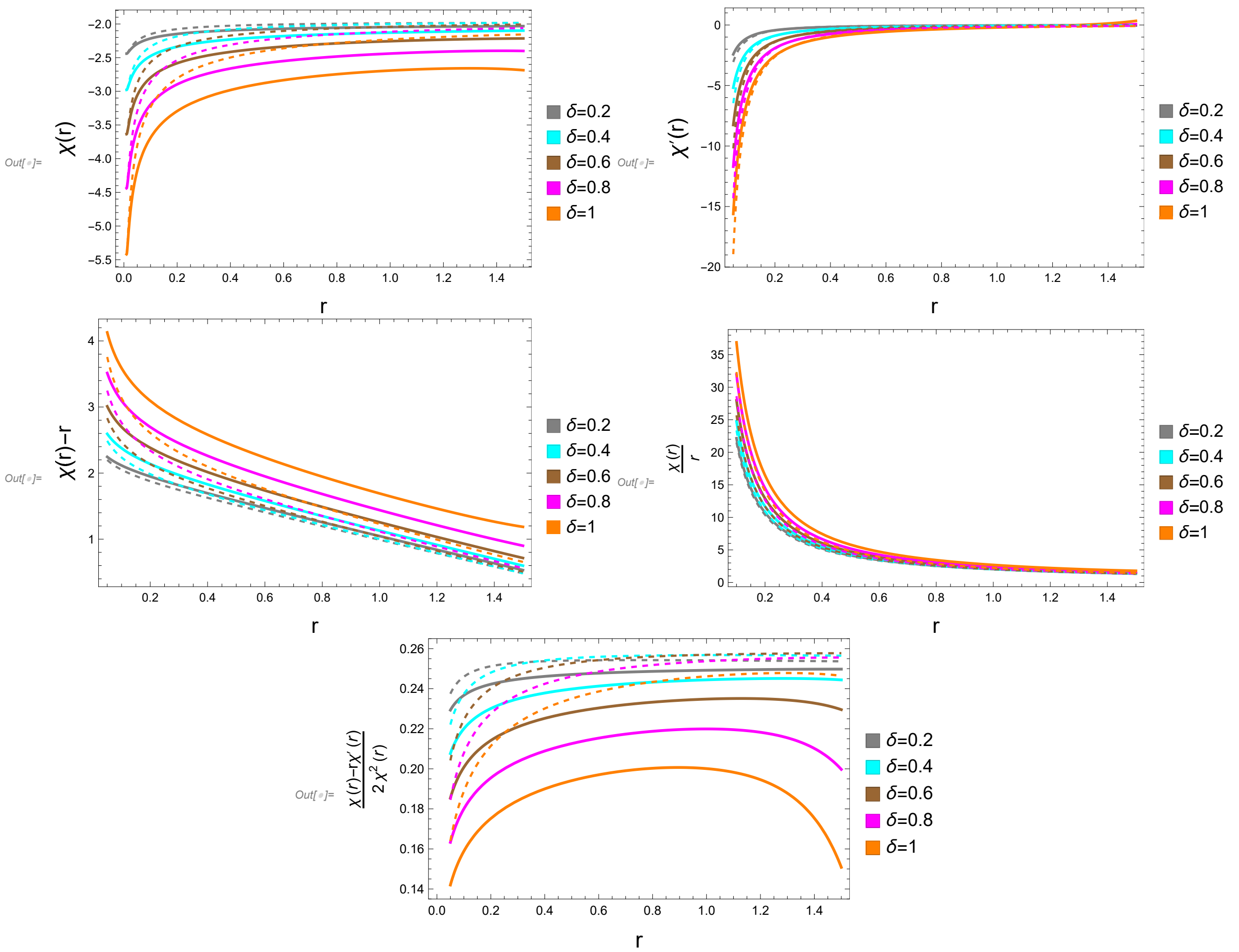

Figure 2. Some geometric properties with $\lambda = 0.175$ (solid) and 0.225 (dashed).

4.2. Energy Conditions

Energy conditions represent foundational constraints in theoretical physics, governing the permissible distributions of energy and momentum throughout spacetime. A complete appreciation of these conditions is indispensable for exploring the sophisticated interactions occurring between geometry and matter. The universe consists of numerous energy forms, including baryonic matter, dark matter, exotic matter, and dark energy, all of which respond in context-dependent ways to the physical conditions around them. Identifying suitable geometric frameworks capable of accommodating such varied forms of energy remains a central and ongoing challenge in modern gravitational theory.

The analysis of traversable wormholes becomes significantly more complicated, given that their production involves transgressing the usual energy condition framework. These requirements are customarily separated into four basic categories, which are the null, weak, dominant, and strong conditions. The occurrence of non-standard matter is generally accompanied by the violation of these conditions. Among them, the NECs are particularly critical, as their violation often entails the breakdown of the remaining three. For this reason, our investigation into the viability and physical properties of the wormhole solution focuses primarily on the behavior of the NECs, expressed as

$$\tilde{\rho} + \tilde{P}_r \geq 0, \quad \tilde{\rho} + \tilde{P}_t \geq 0.$$

These inequalities are evaluated and illustrated in **Figure 3**, where the plots clearly indicate that the NECs are violated, thus confirming the presence of exotic matter required to sustain the wormhole geometry.

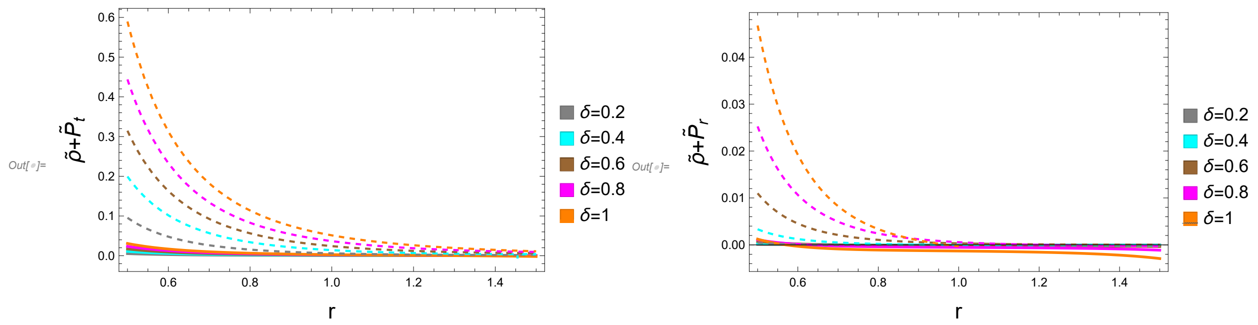

Figure 3. NECs with $\lambda = 0.175$ (solid) and 0.225 (dashed).

4.3. Embedding Diagram

An embedding diagram offers a visual representation of the spatial curvature around a wormhole by depicting a lower-dimensional spatial slice embedded in a higher-dimensional Euclidean space. Although wormholes exist in four-dimensional spacetime, these diagrams simplify the geometry-typically by focusing on an equatorial, constant-time surface-to illustrate key features such as the flaring at the throat, which geometrically manifests the throat expansion condition.

The construction of this diagram takes as its point of departure the Morris-Thorne metric given by Eq.(30). To examine the geometric properties of space, we adopt a static equatorial slice defined by t = constant and $\theta = \frac{\pi}{2}$; this procedure results in the following two-dimensional spatial line element

$$ds^2 = \frac{dr^2}{1 - \frac{\eta(r)}{r}} + r^2 d\phi^2. \tag{34}$$

We target the embedding of this two-dimensional surface visualized within flat three-dimensional Euclidean geometry parameterized by cylindrical coordinates (r, ϕ, z), for which the metric can be expressed as

$$ds^2 = \left[1 + \left(\frac{dZ}{dr}\right)^2\right] dr^2 + r^2 d\phi^2. \tag{35}$$

Comparing Eq.(34) with (35) above, we obtain

$$\frac{dZ}{dr} = \pm\sqrt{\frac{\chi(r)}{r - \chi(r)}}. \tag{36}$$

Setting Eq.(34) equal to (35) allows us to obtain the differential equation governing the embedding surface $Z(r)$ as

$$\frac{dZ}{dr} = \pm\sqrt{\frac{\chi(r)}{r - \chi(r)}}. \tag{37}$$

This relation defines how the spatial geometry of the wormhole can be embedded in a higher-dimensional Euclidean space. **Figure 4** demonstrates the resulting embedding diagram, where the horizontal axis corresponds to the radial coordinate. The graph shows how each $Z(r)$ curve distinguishes between the higher ($Z(r) > 0$) and lower ($Z(r) < 0$) portions of space, creating a clear geometric representation of the wormhole's anatomy. Consistent with the flaring-out condition for traversability, the figure shows the throat as the narrowest point and the surrounding geometry expanding outward with larger r. Consistent with the flaring-out condition for traversability, the figure shows the throat serving as the constriction point and the surrounding geometry expanding outward with larger r.

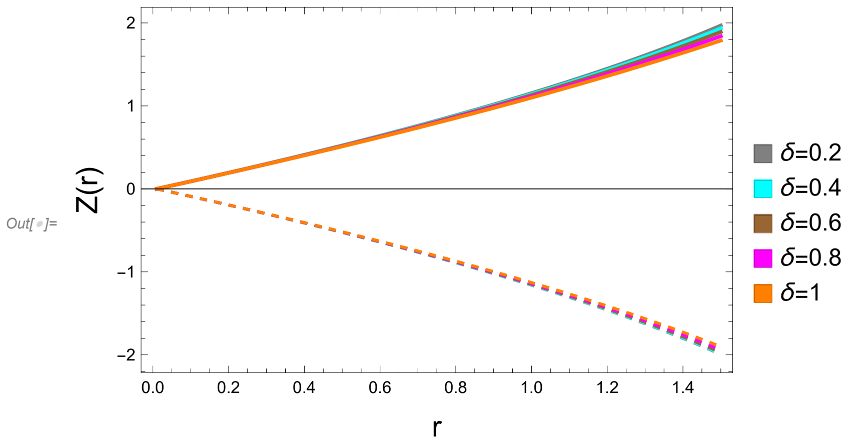

Figure 4. Embedding diagram with $\lambda = 0.175$ (solid) and 0.225 (dashed).

4.4. Gravitational Mass

This section is devoted to analyzing the effective gravitational mass associated with the wormhole configuration, particularly in the context of dark matter-supported geometries. We compute the mass across the wormhole's spatial region, which runs from the neck radius r_0 to an unspecified radial coordinate r, using the integral expression provided by [40]

$$M_G = 4\pi \int_{r_0}^{r} \tilde{\rho}\, r^2\, dr, \tag{38}$$

that we assess through numerical evaluation. The results indicate that the mass accumulates more rapidly in the vicinity of the throat, underscoring the throat's dominant influence on the wormhole gravitational characteristics. This quantity of effective mass is essential for calculating the gravitational environment that nearby material objects encounter. Our investigation prioritizes the active gravitational mass obtained from the wormhole geometry, which is presented in **Figure 5**. A discernible trend emerges from the figure: the active mass commences at a relatively elevated value and steadily falls off with increasing radial coordinate. Interestingly, it becomes negative near the wormhole mouth, signaling the presence of exotic matter in that region. Such a negative mass behavior is a strong indication of energy condition violations, further supporting the physical plausibility of Passable wormholes within the present theoretical framework.

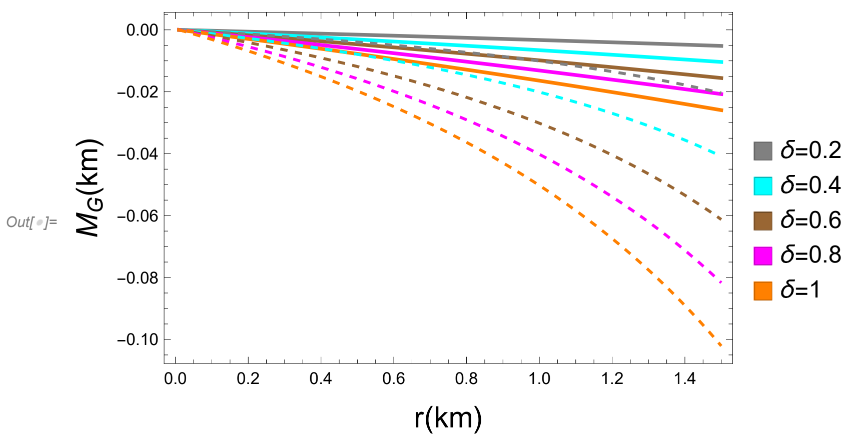

Figure 5. Gravitational mass for $\lambda = 0.175$ (solid) and 0.225 (dashed).

4.5. Volume Integral Quantifier

The $\mathcal{VIQ}$ functions as a helpful diagnostic in wormhole theory, specifically designed to calculate the aggregate exotic matter necessary for maintaining a traversable wormhole. This method, originally presented by Visser and colleagues [41], evaluates the potential to minimize any violation of the NECs. Specifically, the $\mathcal{VIQ}$ assesses the total integrated presence of matter violating the null energy condition by carrying out a spatial volume integral across the relevant parts of the EMT, given as

$$\mathcal{VIQ} = \int (\tilde{\rho} + \tilde{P}r)dV = 8\pi \int_{r_0}^{\infty} (\tilde{\rho} + \tilde{P}_r)r^2 dr. \tag{39}$$

This integral is assessed through numerical technique, and its values are presented in **Figure 6**. A negative value for $\mathcal{VIQ}$ substantiates the existence of exotic matter inside the wormhole's interior. Notably, the magnitude of this exotic matter decreases sharply near the throat, indicating that only a small quantity is necessary in that region to maintain the wormhole's structure. This result suggests that, with an appropriately chosen geometric profile, the total requirement for exotic matter can be significantly reduced.

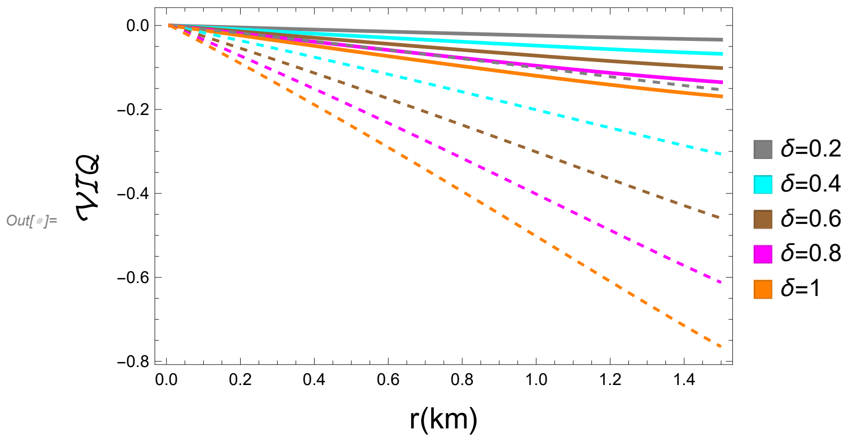

Figure 6. $\mathcal{VIQ}$ for $\lambda = 0.175$ (solid) and 0.225 (dashed).

5. CONCLUSIONS

This investigation reports a traversable wormhole solution constructed in Rastall gravity through the application of the EGD approach to the Schwarzschild black hole. We began our study using the updated Rastall field equations and, using the EGD technique, inserted a supplemental gravitational source that keeps all metric components altered. This led to a black hole solution that is minimally deformed, which was then smoothly converted into a wormhole spacetime by appropriately matching it to the Morris-Thorne expression. Our wormhole metric maintained asymptotic flatness while displaying a well-defined throat, its position and behavior were derived from the collective contribution of the mass function, the δ parameter, and the λ parameter. The redshift function stayed limited and singularity-free, verifying the lack of event horizons and confirming that the solution allows traversal. A detailed geometric study revealed that the flare-out requirement is perfectly satisfied at the throat, demonstrating that the wormhole structure is physically feasible.

To substantiate the viability of the model, we have conducted a comprehensive investigation of several physical and geometric indicators. We investigated the NECs using the effective EMT and discovered that they were violated close to the neck across all parameter configurations, indicating the manifestation of exotic material. Nonetheless, the violation is localized in space and becomes progressively smaller at larger values of r. We clearly visualized the wormhole structure and its two asymptotically flat regions through the geometric representation provided by the embedding diagram. We have furthermore investigated the gravitational mass, which demonstrates a diminishing trend and attains negativity in the throat region, an additional fingerprint of exotic matter. Additionally, we have evaluated the $\mathcal{VIQ}$ to estimate the total amount of NECs-violating matter. Our numerical outcomes suggest that the exotic matter necessarily can be kept quite small when the Rastall and decoupling parameters are chosen appropriately. Overall, our analysis demonstrates that Rastall gravity, when supplemented via the EGD technique, gives an appealing avenue for generating physically plausible wormholes, thereby decreasing the theoretical obstacles that have hampered their acceptance. Future investigations may explore extensions to dynamical or rotating wormhole geometries, as well as stability analysis under linear or nonlinear perturbations.

Data Availability Statement: No data was used for the work described in this research.

ORCID

Muhammad Sharif, https://orcid.org/0000-0001-6845-3506; **Malick Sallah**, https://orcid.org/0009-0007-9677-6653; **Tayyab Naseer**, https://orcid.org/0000-0002-9436-810X

REFERENCES

[1] S. Capozzielo, E. De-Filippis, and V. Salzano, Mon. Not. R. Astron. Soc. **394**, 947 (2009). https://doi.org/10.1111/j.1365-2966.2008.14382.x

[2] A.V. Astashenok, S. Capoziello, M.D. Laurentis, and S.D. Odinstov, J. Cosmol. Astropart. Phys. **01**, 001 (2015). https://doi.org/10.1088/1475-7516/2015/01/001

[3] P. Rastall, Phys. Rev. D, **6**, 3357 (1972). https://doi.org/10.1103/physrevd.6.3357

[4] M. Visser, Phys. Lett. B, **782**, 83 (2018). https://doi.org/10.1016/j.physletb.2018.05.028

[5] A. Golovnev, Ann. Phys. **461**, 169580 (2024). https://doi.org/10.1016/j.aop.2023.169580

[6] F. Darabi, H. Moradpour, I. Licata, Y. Heydarzade, and C. Corda, Eur. Phys. J. C, **78**, 25 (2018). https://doi.org/10.1140/epjc/s10052-017-5502-5

[7] F. Darabi, K. Atazadeh, and Y. Heydarzade, Eur. Phys. J. Plus, **133**, 249 (2018). https://doi.org/10.1140/epjp/i2018-12083-1

[8] S. Hansraj, A. Banerjee, and P. Channuie, Ann. Phys. **400**, 320 (2019). https://doi.org/10.1016/j.aop.2018.12.003

[9] M.R. Shahzad, and G. Abbas, Int. J. Geom. Methods Mod. Phys. **16**, 1950132 (2019). https://doi.org/10.1142/s0219887819501329

[10] M.R. Shahzad, and G. Abbas, Astrophys. Space Sci. **365**, 147 (2020). https://doi.org/10.1007/s10509-020-03861-y

[11] M.R. Shahzad, and G. Abbas, Eur. Phys. J. Plus, **135**, 1 (2020). https://doi.org/10.1140/epjp/s13360-020-00508-3

[12] T. Naseer, Phys. Dark Universe, **46**, 101663 (2024). https://doi.org/10.1016/j.dark.2024.101663

[13] T. Naseer, Eur. Phys. J. C, **84**, 1256 (2024). https://doi.org/10.1140/epjc/s10052-024-13634-4

[14] T. Naseer, and M. Sharif, Class. Quantum Grav. **41**, 245006 (2024). https://doi.org/10.1088/1361-6382/ad8d9d

[15] A. Waseem, and S. Naeem, Phys. Scr. **99**, 125023 (2024). https://doi.org/10.1088/1402-4896/ad8e92

[16] M. Sharif, and M. Sallah, Chin. J. Phys. **92**, 794 (2024). https://doi.org/10.1016/j.cjph.2024.09.027

[17] C.E. Mota, L.C.N. Santos, G. Grams, F.M. da Silva, and D.P. Menezes, Phys. Rev. D, **100**, 024043 (2019). https://doi.org/10.1103/PhysRevD.100.024043

[18] P. Bhar, F. Tello-Ortiz, Á. Rincón, and Y. Gomez-Leyton, Astrophys. Space Sci. **365**, 145 (2020). https://doi.org/10.1007/s10509-020-03859-6

[19] G. Mustafa, and T.C. Xia, Int. J. Mod. Phys. A, **35**, 2050109 (2020). https://doi.org/10.1142/s0217751x20501092

[20] M. Zubair, S. Waheed, M.F. Jamal, and G. Mustafa, Results Phys. **29**, 104787 (2021). https://doi.org/10.1016/j.rinp.2021.104787

[21] C.E. Mota, L.C.N. Santos, F.M. da Silva, G. Grams, I. P. Lobo, and D.P. Menezes: Int. J. Mod. Phys. D, **31**(4), 2250023 (2022). https://doi.org/10.1142/S0218271822500237

[22] G.G.L. Nashed, Universe, **8**, 510 (2022). https://doi.org/10.3390/universe8100510

[23] A. Ashraf, M.R. Shahzad, Z. Zhang, E. Güdekli, and M.F. Jamal, Phys. Scr. **98**, 035027 (2023). https://doi.org/10.1088/1402-4896/acb6bd

[24] W. El Hanafy, and A. Awad, Astrophys. J., **951**, 144 (2023). https://doi.org/10.3847/1538-4357/acd93c

[25] J. Ovalle, Phys. Rev. D, **95**, 104019 (2017). https://doi.org/10.1103/physrevd.95.104019

[26] J. Ovalle, Phys. Lett. B, **788**, 213 (2019). https://doi.org/10.1016/j.physletb.2018.11.029

[27] J. Ovalle, R. Casadio, E. Contreras, and A. Sotomayor, Phys. Dark Universe, **31**, 100744 (2021). https://doi.org/10.1016/j.dark.2020.100744

[28] C.L. Heras, and P. Leon, Gen. Relativ. Gravit. **54**, 138 (2022). https://doi.org/10.1007/s10714-022-03031-1

[29] S.K. Maurya, K.N. Singh, and B. Dayanandan, Eur. Phys. J. C, **80**, 448 (2020). https://doi.org/10.1140/epjc/s10052-020-8005-8

[30] C.W. Misner, and J.A. Wheeler, Ann. Phys. **2**, 525 (1957). https://doi.org/10.1016/0003-4916(57)90049-0

[31] C.W. Misner, Phys. Rev. **118**, 1110 (1960). https://doi.org/10.1103/physrev.118.1110

[32] J.A. Wheeler, Ann. Phys. **2**, 604 (1957). https://doi.org/10.1016/0003-4916(57)90050-7

[33] J.A. Wheeler, Int. J. Mod. Phys. A, **3**, 2207 (1988). https://doi.org/10.1142/s0217751x88000941

[34] A. Einstein, and N. Rosen, Phys. Rev. **48**, 73 (1935). https://doi.org/10.1103/physrev.48.73

[35] R.W. Fuller, and J.A. Wheeler, Phys. Rev. **128**, 919 (1962). https://doi.org/10.1103/physrev.128.919

[36] M.S. Morris, and K.S. Thorne, Am. J. Phys. **56**, 395 (1988). https://doi.org/10.1119/1.15620

[37] F.S.N. Lobo, and M.A. Oliveira, Phys. Rev. D, **80**, 104012 (2009). https://doi.org/10.1103/physreva.80.012112

[38] M. R. Mehdizadeh, M. K. Zangeneh, and F. S. N. Lobo, Phys. Rev. D, **91**, 084004 (2015). https://doi.org/10.1103/physrevd.91.084004

[39] H. Moradpour, N. Sadeghnezhad, and S.H. Hendi, Can. J. Phys. **95**, 1257 (2017). https://doi.org/10.1139/cjp-2017-0040

[40] C.W. Misner, and D.H. Sharp, Phys. Rev. **136**, B571 (1964). https://doi.org/10.1103/physrev.136.b571

[41] M. Visser, S. Kar, and N. Dadhich, Phys. Rev. Lett. **90**, 201102 (2003). https://doi.org/10.1103/physrevlett.90.201102

РІШЕННЯ ДЛЯ ПРОХОДНИХ ЧЕРВОТОЧКОВИХ РІШЕНЬ ЗА ДОПОМОГОЮ ПІДХОДУ РОЗДІЛУ В ТЕОРІЇ РАСТАЛЛА

Мухаммад Шаріф[1,2], **Малік Саллах**[1], **Тайяб Насір**[1]
[1]*Кафедра математики та статистики, Лахорський університет, 1-KM Defence Road Lahore-54000, Пакистан*
[2]*Дослідницький центр Джадара, Університет Джадара, Ірбід 21110, Йорданія*

У цій статті досліджується побудова рішень прохідних червоточин у контексті гравітації Расталла з використанням розширеного методу гравітаційного розв'язання. На основі модифікованих польових рівнянь цієї нової теорії ми застосовуємо цю схему для включення додаткового гравітаційного джерела, що призводить до повністю перетвореної версії рішення Шварцшильда. За допомогою відповідного перетворення координат ця модифікована геометрія переосмислюється як простір-час червоточини. Аналіз продовжується дослідженням фундаментальних фізичних та геометричних характеристик результуючої конфігурації, зокрема, порушення умов нульової енергії, поведінки гравітаційної маси, оцінки квантора об'ємного інтеграла та діаграми вбудовування. Ключовим висновком є те, що шийка червоточини очевидно виникає внаслідок спотвореної геометрії, водночас задовольняючи критерій розширення, необхідний для прохідності. Побудова графіків енергетичних умов для різних значень параметрів Расталла виявляє локалізовані порушення умов нульової енергії поблизу шийки, що узгоджується з наявністю екзотичної матерії. Однак, показано, що загальний вміст екзотичної матерії є мінімальним та дуже чутливим до вибору параметрів моделі. Ці результати підкреслюють потенціал гравітації Расталла, у поєднанні з гравітаційним роз'єднанням, для підтримки фізично правдоподібних геометрій червоточин зі зменшеними вимогами до екзотичної матерії.

Ключові слова: *теорія Расталла; гравітаційне роз'єднання; червоточини; екзотична рідина*

DOI: 10.26565/2312-4334-2026-3-12 ISSN 2312-4334

FINITE-SIZE SCALING OF THERMAL SUSCEPTIBILITY AND SPECIFIC HEAT DENSITY NEAR THE QCD DECONFINEMENT PHASE TRANSITION

B. Moussaoui[1,2], A. Ait El Djoudi[1*], H. Mouloudj[1,3], M. A. Lakehal[1,4]
[1]*Particle and Statistical Physics Laboratory, Ecole Normale Supérieure-Kouba, Vieux-Kouba, B.P.92, 16050 Algiers, Algeria*
[2]*Theoretical Physics Laboratory, Faculty of Physics, USTHB Bab-Ezzouar, El Alia, BP 32, 16111 Algiers, Algeria*
[3]*Hassiba Benbouali University, Chlef, Algeria*
[4]*M'hamed Bougara University, Boumerdes, Algeria*
[*]*Corresponding Author e-mail: amal.aiteldjoudi@g.ens-kouba.dz*
Received June 25, 2026; accepted August 17, 2026

The properties of the thermally driven deconfinement phase transition (DPT) from a hadronic gas (HG) to a color-singlet quark-gluon plasma (QGP) containing gluons and massless up and down quarks, at a nonzero quark chemical potential μ, are investigated by considering the volumetric coexistence of the hadronic gas and the QGP in a finite-size system. Finite-size effects are analyzed for the thermally driven DPT at different μ values. The critical exponents are determined using a numerical finite-size scaling (FSS) analysis, by fitting the results as a function of the system size. The effective transition temperature (T_c) exhibits a shift toward higher values as the system size decreases, indicating a critical behavior in the region of the thermally driven DPT from a HG to the QGP. Crucially, all three scaling critical exponents are found to be independent of the quark chemical potential μ, establishing the universality of the finite-size scaling structure with respect to μ.

Keywords: *Thermally driven deconfinement phase transition (DPT); Color-singlet; Quark chemical potential; Finite-size scaling (FSS) analysis; Transition temperature*

1. INTRODUCTION

Understanding the phase transition between hadronic gas (HG) phase and the quark-gluon plasma (QGP) phase represents one of the most fundamental phenomena in contemporary high-energy and nuclear physics, and continues to be the subject of intense theoretical and experimental investigation [1, 2]. Quarks and gluons, the fundamental components of hadrons, interact via the strong interaction governed by Quantum Chromodynamics (QCD), the theory of the strong force. Their behavior is studied in heavy-ion collisions at the Relativistic Heavy Ion Collider (RHIC) and the Large Hadron Collider (LHC) [1]. The Deconfinement phase transition (DPT) describes the transition from the HG phase to the QGP near effective transition temperature of 150-175MeV for three quark flavors [3], a result that finds consistent support from recent high-precision lattice QCD simulations conducted at both vanishing and finite chemical potential [4, 5].

While most QCD studies assume infinite systems, the QGP formed in experiments is finite, with volumes ranging from 50 fm^3 to 250 fm^3 [6, 7]. This fundamental discrepancy between infinite volume theoretical frameworks and the genuinely finite nature of the physical system motivates a rigorous and systematic investigation of finite-size effects on the DPT. Recent model-based studies have confirmed that a reduction in system volume leads to significant modifications of key thermodynamic response functions, including the pressure, energy density, specific heat, speed of sound, and conserved-charge susceptibilities, and that the QCD crossover transition is generally observed to become progressively smoother as the system size decreases [8]. Finite-size effects strongly influence the position of the effective transition point and other thermodynamic quantities in the phase coexistence model (PCM) [9–11]. Recent lattice QCD analyses have further demonstrated that the volume and quark chemical potential dependence of the deconfinement crossover differs completely from that of the chiral transition [12], underscoring the necessity of a careful and dedicated finite-size analysis for the deconfinement sector specifically. Furthermore, the recent application of finite-size scaling (FSS) methodology to experimental net-proton cumulant data from RHIC has yielded the first experimental evidence for a QCD critical point within a range consistent with theoretical predictions [13], imparting further importance to comprehensive FSS investigations.

The present paper extends the FSS analysis of the thermally driven DPT in finite volume (V), first conducted at vanishing chemical potential in Ref. [10], to the case of nonzero quark chemical potential within the color-singlet partition function framework. While Ref. [10] established the FSS exponents at $\mu = 0$, the explicit dependence of the FSS structure on μ, in particular whether the critical exponents remain universal as μ is varied, has not previously been demonstrated for the thermally driven transition. This constitutes the principal new contribution of the present work. We systematically demonstrate, for the first time, that the FSS critical exponents governing the transition width, and the temperature shift are all independent of μ, thereby establishing the universality of the finite-size scaling laws with respect to the quark chemical potential.

Cite as: B. Moussaoui, A. Ait El Djoudi , H. Mouloudj, M. A. Lakehal, East Eur. J. Phys. 3, 138 (2026), https://doi.org/10.26565/2312-4334-2026-3-12

This paper is organized as follows. In Sec. 2, we describe the mixed HG-QGP in finite volume system within the MIT bag model, using the PCM, and we derive the exact total color-singlet partition function (CS-PF) at nonzero quark chemical potential μ using the group theoretical projection method [14, 15]. In Sec. 3, we introduce the key thermodynamic response functions: the order parameter, the thermal susceptibility, and the specific heat density. We also present a detailed discussion of the numerical results characterizing the finite-size behavior of these quantities at $\mu = 0$ and $\mu = 100$ MeV. Section 4 is devoted to the numerical FSS analysis and the determination of the critical exponents. Section 5 summarizes the principal conclusions of our study.

2. THE MIXED HG-QGP EQUATION OF STATE AT NON-VANISHING CHEMICAL POTENTIAL

To describe the QCD-DPT in a finite system, we use the PCM [11]. This model assumes a mixed system consisting of HG and QGP phases coexisting within a total volume V. The HG phase occupies a fractional volume $V_{HG} = hV$ and the QGP phase occupies the complementary volume $V_{QGP} = (1 - h)V$, where the fraction $h \in [0, 1]$ parametrizes the partitioning of the volume between the two phases. The PCM is employed here within the MIT bag model, using massless up and down quarks and treating the two phases as non-interacting. There is evidence suggesting that the effects of quark masses on the transition point in the $T - \mu$ plane at lower densities are indeed small [16], and the model is well-established for qualitative finite-size analyses and captures the essential thermodynamics of the DPT. Using the PCM, the mean value of a physical quantity $<A(T, \mu, V)>$ of the mixed system can be written as [11]:

$$\langle A(T,\mu,V)\rangle = \frac{\int_0^1 A(h,T,\mu,V)\, Z(h,T,\mu,V)\, dh}{\int_0^1 Z(h,T,\mu,V)\, dh} \tag{1}$$

where $A(h, T, \mu, V)$ is the total thermodynamic quantity in the state h, and $Z(h, T, \mu, V)$ is the total partition function of the system with the requirement of color-singletness accounted for using the group theoretical projection method [14, 15]. Under the assumption of a non-zero quark chemical potential and considering non-interacting phases, $Z(h, T, \mu, V)$, calculated in our previous work [16] for a HG of massless pions and a QGP containing massless up and down quarks, can be written as:

$$Z(h,T,\mu,V) = \frac{4}{9\pi^2} \exp\left(\frac{\pi^2}{30} V T^3\right) \int_{-\pi}^{\pi}\int_{-\pi}^{\pi} d\phi\, d\psi\; M(\phi,\psi) \exp\left[(1-h) R(T,\mu,V;\phi,\psi)\right], \tag{2}$$

where $M(\phi, \psi)$ represents the Haar measure for the $SU(3)$ group integration:

$$M(\phi,\psi) = \left[\sin\left(\frac{1}{2}\left(\psi + \frac{\phi}{2}\right)\right) \sin\left(\frac{\phi}{2}\right) \sin\left(\frac{1}{2}\left(\psi - \frac{\phi}{2}\right)\right)\right]^2, \tag{3}$$

and

$$R(T,\mu,V;\phi,\psi) = VT^3 \left(g(\phi,\psi,\mu/T) - \frac{\pi^2}{30} - \frac{B}{T^4}\right), \tag{4}$$

where $g(\phi, \psi, \mu/T) = g_0(\phi, \psi) + g_1(\phi, \psi, \mu/T)$, with $g_0(\phi, \psi)$ given by:

$$\begin{aligned} g_0(\phi,\psi) = {} & \frac{\pi^2}{12}\left(\frac{21}{30} d_Q + \frac{16}{15} d_G\right) + \frac{\pi^2}{12}\frac{d_Q}{2} \sum_{q=r,b,g} \left\{\left[\left(\frac{\theta_q}{\pi}\right)^2 - 1\right]^2 - 1\right\} \\ & - \frac{\pi^2}{12}\frac{d_G}{2} \sum_{G=1}^{4} \left[\left(\frac{\theta_G - \pi}{\pi}\right)^2 - 1\right]^2, \end{aligned} \tag{5}$$

where d_Q and d_G are the degeneracy factors of quarks and gluons respectively. The angles θ_q (for $q = r, g, b$) are given by:

$$\theta_r = \frac{\phi}{2} + \frac{\psi}{3}, \qquad \theta_g = -\frac{\phi}{2} + \frac{\psi}{3}, \qquad \theta_b = \frac{-2\psi}{3}, \tag{6}$$

and θ_G (for $G = 1, \ldots, 4$) are expressed as follows:

$$\theta_1 = \theta_r - \theta_g, \qquad \theta_2 = \theta_g - \theta_b, \qquad \theta_3 = \theta_b - \theta_r, \qquad \theta_4 = 0, \tag{7}$$

and the function $g_1(\phi, \psi, \mu/T)$ is given by:

$$g_1(\phi,\psi,\mu/T) = \left(1 - \frac{\phi^2}{2\pi^2} - \frac{2\psi^2}{3\pi^2}\right)\left(\frac{\mu}{T}\right)^2 + \frac{1}{2\pi^2}\left(\frac{\mu}{T}\right)^4. \tag{8}$$

3. FINITE-SIZE EFFECTS ON THE THERMALLY DRIVEN DPT: THERMAL SUSCEPTIBILITY AND SPECIFIC HEAT DENSITY

The main quantities of interest in this study are the thermal susceptibility and the specific heat density. First, we derive the order parameter $<h(T,\mu,V)>$, represented by the mean value of the HG volume fraction, which may be written as:

$$\langle h(T,\mu,V)\rangle = \frac{\int_0^1 h(T,\mu,V)\,Z(h,T,\mu,V)\,dh}{\int_0^1 Z(h,T,\mu,V)\,dh} \tag{9}$$

The thermal susceptibility is defined as the first derivative of the order parameter $<h(T,\mu,V)>$, with respect to temperature:

$$\chi_T(T,\mu,V) = \left.\frac{\partial\langle h(T,\mu,V)\rangle}{\partial T}\right|_{\mu,V} \tag{10}$$

The specific heat density $c_T(T,\mu,V)$ is calculated from the derivative of the energy density $<\epsilon(T,\mu,V)>$ with respect to temperature as:

$$c_T(T,\mu,V) = \left.\frac{\partial\langle \varepsilon(T,\mu,V)\rangle}{\partial T}\right|_{\mu,V} \tag{11}$$

$$\langle\varepsilon(T,\mu,V)\rangle = \frac{T^2}{V}\left\langle\left(\frac{\partial \ln Z(h,T,\mu,V)}{\partial T}\right)_{\mu,V}\right\rangle + \frac{\mu T}{V}\left\langle\left(\frac{\partial \ln Z(h,T,\mu,V)}{\partial \mu}\right)_{T,V}\right\rangle \tag{12}$$

Figures 1 and 2 show the behavior of the order parameter $<h>$ (left panel) and the thermal susceptibility χ_T (right panel) as functions of temperature, calculated at $\mu = 0$ and $\mu = 100MeV$, respectively for several system volumes with $B^{1/4} = 200MeV$. In both cases, the DPT exhibits characteristic finite-size rounding: at small volumes, thermal fluctuations strongly smear the transition, resulting in smooth, rounded changes in ⟨h⟩, while for large volumes the order parameter develops a nearly sharp step-like discontinuity at the transition temperature characteristic of a first-order transition, known to occur at the thermodynamic limit [17].

The magnitude of the thermal susceptibility peaks, $|\chi_T^{max}(V)|$, increases systematically with system size, and the position of each peak defines the volume-dependent effective transition temperature $T_c^{\text{Fixed}\,\mu}(V)$. As the system size decreases, the thermal width $\delta T_c(V)$ of the transition region broadens and shifts to higher temperatures, reflecting the reduction of QGP degrees of freedom imposed by color-singletness [11, 14, 15]. The shifting of $T_c^{\text{Fixed}\,\mu}(V)$ to higher values at smaller volumes is a direct consequence of the fact that in finite systems the QGP color-singlet state requires additional thermal energy to be formed compared to the infinite-volume case.

In the thermodynamic limit, the true transition temperatures are found to be $T_c^{(\mu=0)}(\infty) = 143.928MeV$ and $T_c^{(\mu=100MeV)}(\infty) = 139.229MeV$, consistent with theoretical estimates obtained from recent lattice QCD simulations [18, 19]. A nonzero chemical potential shifts the entire transition region to lower temperatures without altering the qualitative finite-size structure.

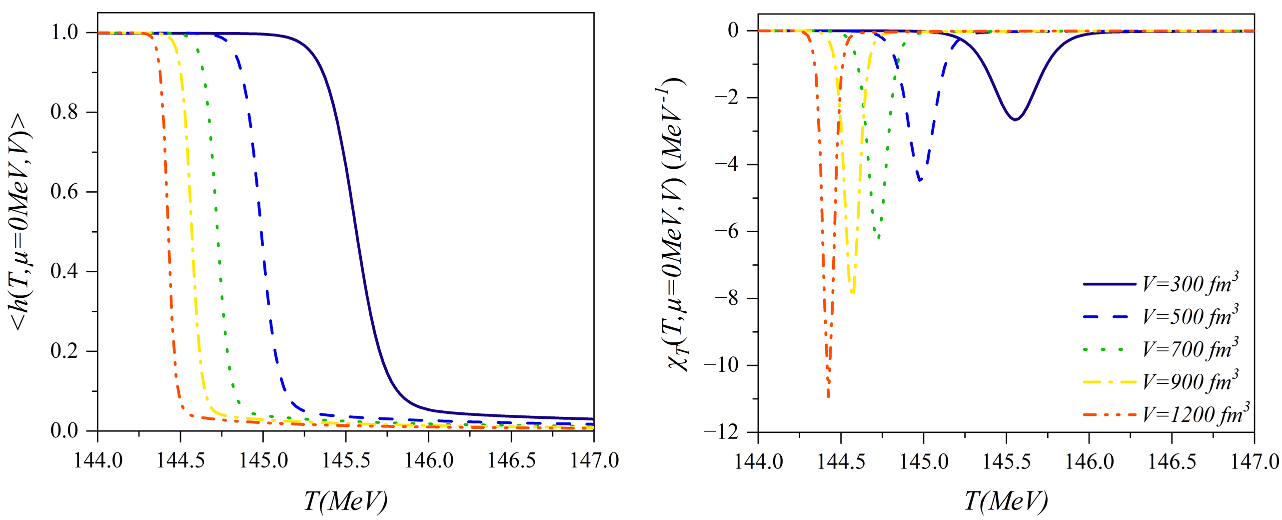

Figure 1. Variations of the order parameter $\langle h\rangle$ (left panel) and the thermal susceptibility χ_T (right panel) as a function of the temperature at $\mu = 0MeV$, for various volume selections with $B^{1/4} = 200MeV$.

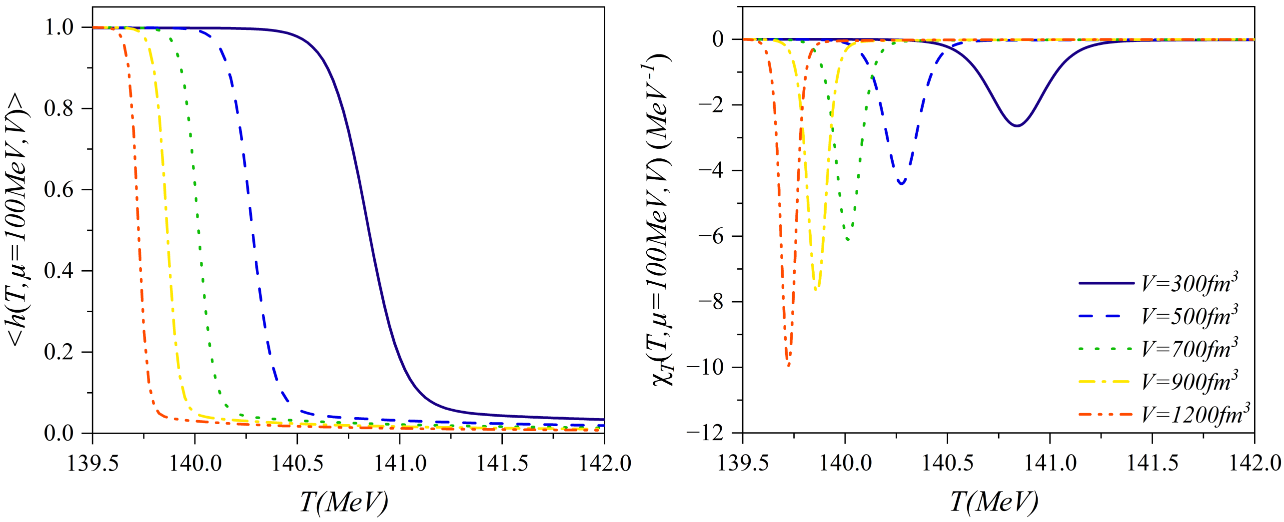

Figure 2. Variations of the order parameter $\langle h\rangle$ (left panel) and the thermal susceptibility χ_T (right panel) as a function of the temperature at $\mu = 100MeV$, for various volume selections with $B^{1/4} = 200MeV$.

Figure 3 shows the specific heat density c_T as a function of temperature at $\mu = 0$ (left panel) and $\mu = 100$ MeV (right panel), for several volume selections. The specific heat density exhibits well-defined peaks whose maxima $c_T^{\max}$ increase sharply with increasing volume, while their widths $\delta T_c(V)$ decrease, in agreement with the expectation that the transition sharpens in larger systems [20]. The localization of the maximum $c_T^{\max}$ at temperature $T_c(V)$ provides an independent determination of the effective transition temperature, consistent with the location of the thermal susceptibility peak. A similar volume dependence of the specific heat density has been reported in Refs. [8,21]. Importantly, the quark chemical potential μ does not alter the qualitative behavior of either χ_T or c_T as functions of volume: it merely shifts the entire temperature transition $\delta T_c(V)$ to a lower temperature, while leaving the finite-size scaling structure unchanged. This observation motivates the systematic FSS analysis presented in the next section.

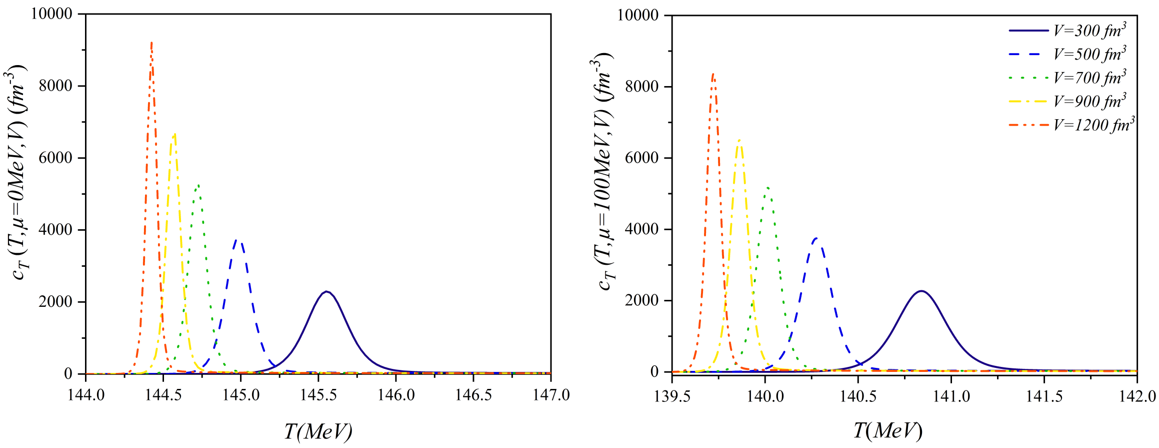

Figure 3. Plots of the specific heat density c_T as a function of temperature, (left panel) at $\mu = 0$, and (right panel) $\mu = 100MeV$, for several volume selections with $B^{1/4} = 200MeV$.

4. FINITE-SIZE SCALING ANALYSIS: CRITICAL EXPONENTS FOR THE THERMAL DPT

In the thermodynamic limit, several thermodynamic quantities associated with the thermally driven DPT diverge or become discontinuous at the critical temperature. In a finite system of volume V, these singularities are rounded over a finite temperature transition region $\delta T_c(V)$, around an effective transition temperature $T_c(V)$, which is shifted relative to the true transition temperature $T_c(\infty)$. The resulting shift is: $\tau_T(V) = T_c(V) - T_c(\infty)$. The FSS theory for a first-order phase transition [22–25] predicts characteristic power-law dependences on the system volume. The critical exponents characterizing their power-law evolution with the volume are [10]:

$$\begin{cases} c_T^{\max}(\text{Fixed }\mu, V) \sim V^{\alpha_T}, \\ \delta T_c(\text{Fixed }\mu, V) = T_2(V) - T_1(V) \sim V^{-\theta_T}, \\ \tau_T(\text{Fixed }\mu, V) = T_c(V) - T_c(\infty) \sim V^{-\lambda_T}. \end{cases} \tag{13}$$

For a first-order phase transition at fixed quark chemical potential, the scaling critical exponents are expected to be equal to unity: $\alpha_T = \theta_T = \lambda_T = 1$.

Figure 4 shows the peak maxima c_T^{max} of the specific heat density as functions of the volume, at $\mu = 0$ (left panel) and $\mu = 100MeV$ (right panel), with $B^{1/4} = 200MeV$. A power-law fit of the form $c_T^{\max}(\text{Fixed }\mu, V) \sim V^{\alpha_T}$ yields: $\alpha_T = 1.012 \pm 0.004$ ($\mu = 0$), $\alpha_T = 1.017 \pm 0.006$ ($\mu = 100MeV$).

The scaling of the specific heat density peak maximum with volume (exponent $\alpha_T \approx 1$) is the hallmark signature of a first-order phase transition [10]. The slight deviation from unity is within the systematic numerical uncertainty of the fitting procedure. It is noteworthy that the exponent values at $\mu = 0$ and $\mu = 100MeV$ are statistically indistinguishable within the quoted uncertainties, providing the first evidence that the FSS of the specific heat density maximum is insensitive to the quark chemical potential.

Figure 5 displays the width of the transition temperature region $\delta T_c(\text{Fixed }\mu, V)$, as a function of the inverse volume $1/V$, at $\mu = 0$ (left panel) and $\mu = 100MeV$ (right panel). This allows the determination of the value of the critical exponent θ_T defined in the scaling: $\delta T_c(\text{Fixed }\mu, V) \sim V^{-\theta_T}$, and we find the numerical result: $\theta_T = 1.010 \pm 0.001$ ($\mu = 0$), $\theta_T = 1.007 \pm 0.001$ ($\mu = 100MeV$). These values confirm, with high numerical precision, the expected linear scaling of the transition width with $1/V$ for a first-order phase transition. Again, the critical exponents at $\mu = 0$ and $\mu = 100MeV$ are statistically consistent, reinforcing the independence of the FSS structure from the quark chemical potential.

Figure 6 shows the shift of the effective transition temperature $\tau_T(\text{Fixed }\mu, V)$, extracted from the position of the thermal susceptibility peak, as a function of $1/V$. A power-law fit to the form $\tau_T(\text{Fixed }\mu, V) = V^{-\lambda_T}$, gives the numerical result of the shift scaling exponent: $\lambda_T = 0.859 \pm 0.003$ ($\mu = 0$), $\lambda_T = 0.860 \pm 0.003$ ($\mu = 100MeV$). According to [10], such a value $\lambda_T \neq 1$ suggests the contribution of additional terms with higher powers of V^{-1}, such that the parametrization should be with the laws: $A_1 V^{-\lambda} + A_2 V^{-2}$ or $A_1 V^{-\lambda} + A_2 V^{-2} + A_3 V^{-3}$, where A_1, A_2, A_3, expected to be independent of the quark chemical potential.

Taken together, the results of the FSS analysis show that the scaling exponents α_T and θ_T are equal to unity within numerical precision, while λ_T deviates slightly from unity due to subleading corrections. All three exponents are independent of the quark chemical potential μ, and are collectively consistent with a first-order phase transition. We conclude that the thermally driven DPT, in the presence of a nonzero quark chemical potential, obeys the same FSS scaling laws as those obtained at $\mu = 0$ [10], and that the critical exponents are universal with respect to μ. This conclusion parallels the analogous finding for the density driven DPT reported in Ref. [16], where the scaling exponents were found to be independent of the fixed temperature at which the density-driven transition is studied.

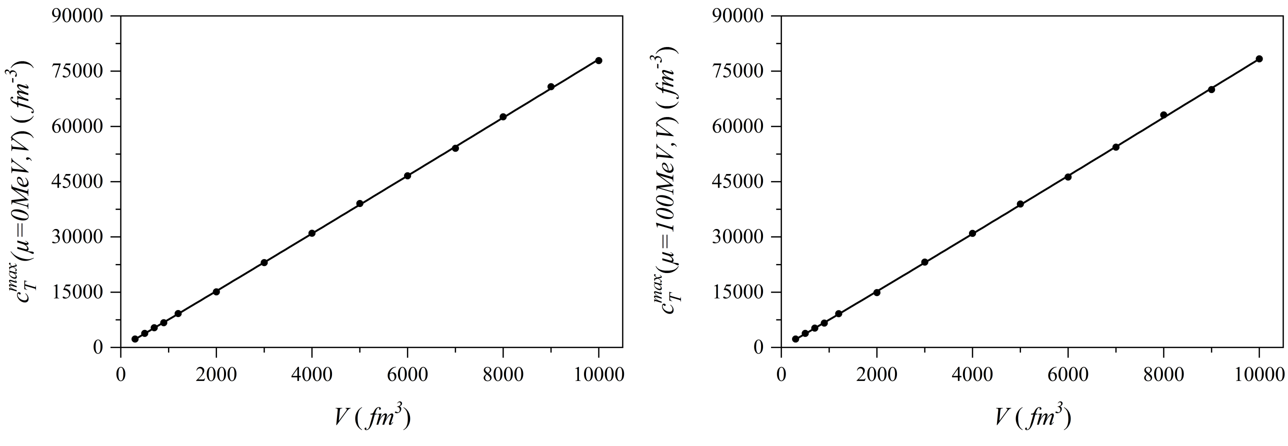

Figure 4. Plot of the peak maxima of the specific heat density $c_T^{\max}$ with volume, as a function of volume, at $\mu = 0$ (left panel) and $\mu = 100MeV$ (right panel), with $B^{1/4} = 200MeV$.

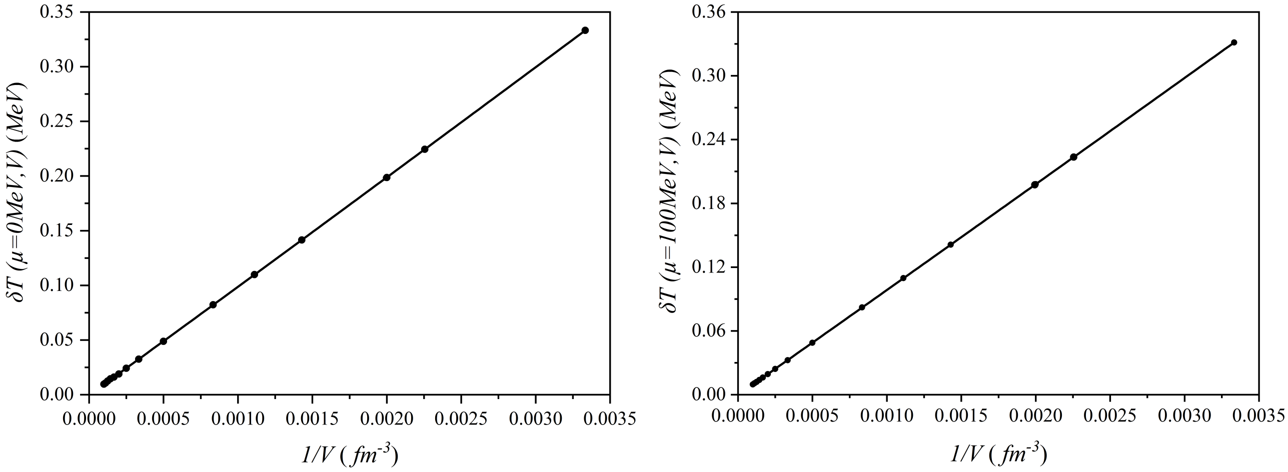

Figure 5. Plot of the width of the temperature transition region $\delta T(V)$, as a function of inverse volume, at $\mu = 0$ (left panel) and $\mu = 100MeV$ (right panel), with $B^{1/4} = 200MeV$.

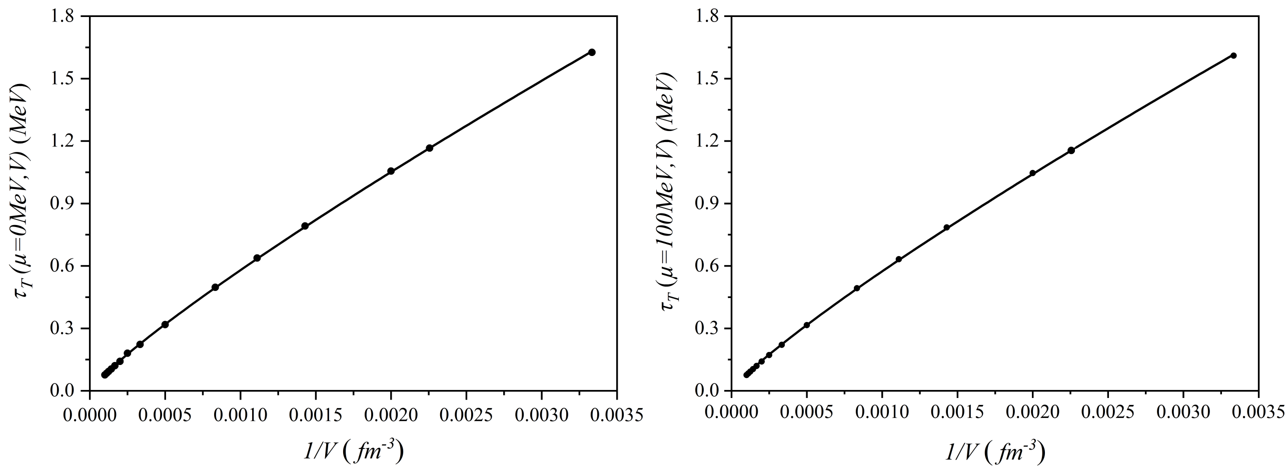

Figure 6. Plot of the shift of the effective transition temperature $\tau_T(V)$ from the thermal susceptibility, as a function of inverse volume, at $\mu = 0$ (left panel) and $\mu = 100MeV$ (right panel), with $B^{1/4} = 200MeV$.

5. CONCLUSIONS

In the present work, we have investigated the finite-size effects on the thermally driven deconfinement phase transition (DPT) from a hadronic gas (HG) consisting of massless pions to a color-singlet quark-gluon plasma (QGP) containing gluons and massless up and down quarks. Using the exact color-singlet partition function (CS-PF) within the phase coexistence model (PCM), we have computed the key thermodynamic response functions such as the order parameter $\langle \mathrm{h} \rangle$, the susceptibility χ_T, and the specific heat density c_T as functions of temperature, at fixed quark chemical potential μ, and varying volume V.

In small volumes, a smooth crossover is observed due to strong thermodynamic fluctuations, while in the thermodynamic limit a sharp discontinuity in the order parameter $\langle h \rangle$ appears at the true transition temperature $T_c(\text{Fixed}\,\mu, \infty)$, signaling a first-order DPT. A systematic variation of the effective transition temperature $T_c(V)$ with system size is observed, which diminishes for larger volumes and converges to $T_c(\text{Fixed}\,\mu, \infty)$ in the thermodynamic limit. The quark chemical potential does not affect the width $\delta T_c(\text{Fixed}\,\mu, V)$ of the transition region; it only shifts the true transition temperature $T_c(\text{Fixed}\,\mu, \infty)$ to lower values. A similar volume dependence has been reported in Refs. [8, 21].

A numerical FSS analysis of the behavior of the maxima of the rounded peaks of the specific heat density $c_T^{\max}$, the width of the temperature transition region $\delta T_c(V)$, and the shift of the effective transition temperature $\tau_T(V)$, yields the scaling critical exponents α_T, θ_T, λ_T. All three exponents converge to unity when subleading corrections are properly accounted for, confirming that the thermally driven DPT is of first order.

The principal new finding of this work is that all three FSS critical exponents are independent of the quark chemical potential μ. Based on our results and those of Refs. [10, 16], we conclude that the thermally driven DPT obeys a universal finite-size scaling law governed by the system volume, with critical exponents characteristic of a first-order transition and independent of μ, identical to those found for the density-driven DPT [16]. This universality of the FSS structure with respect to the thermodynamic control parameters (μ and T) represents a robust property of the color singlet QCD deconfinement transition in the PCM framework.

Acknowledgments

This research work is supported by the Algerian Ministry of Higher Education and Scientific Research.

Funding

No funding was received for conducting this study.

Conflict of interest

The authors declare that there are no conflicts of interest.

ORCID

B. Moussaoui, https://orcid.org/0000-0001-8580-9412; **A. Ait El Djoudi**, https://orcid.org/0009-0005-7773-0401; **H. Mouloudj**, https://orcid.org/0009-0006-0376-9642; **M. A. Lakehal**, https://orcid.org/0009-0007-8930-0454

REFERENCES

[1] K. Adcox, et al., "Formation of dense partonic matter in relativistic nucleus-nucleus collisions at RHIC: Experimental evaluation by the PHENIX Collaboration," Nucl. Phys. A, **757**, 184 (2005). https://doi.org/10.1016/j.nuclphysa.2005.03.086

[2] X. An, et al., "The BEST framework for the search for the QCD critical point and the chiral magnetic effect," Nucl. Phys. A, **1017**, 122343 (2022). https://doi.org/10.1016/j.nuclphysa.2021.122343

[3] F. Karsch, et al., "Quark mass and flavour dependence of the QCD phase transition," Nucl. Phys. B, **605**, 579 (2001). https://doi.org/10.1016/S0550-3213(01)00200-0

[4] S. Borsanyi, R. Kara, Z. Fodor, D. A. Godzieba, P. Parotto, and D. Sexty, "Precision study of the continuum SU(3) Yang-Mills theory: How to use parallel tempering to improve on supercritical slowing down for first-order phase transitions,)" Phys. Rev. D, **105**(7), 074513 (2022). https://doi.org/10.1103/PhysRevD.105.074513

[5] S. Borsanyi, Z.Fodor, J.N. Guenther, P. Parotto, A. Pasztor, L. Pirelli, K.K. Szabó, and C.H. Wong, "QCD deconfinement transition line up to μ_B = 400 MeV from finite volume lattice simulations," Phys. Rev. D, **110**(11), 114507 (2024). https://doi.org/10.1103/PhysRevD.110.114507

[6] L.F. Palhares, E.S. Fraga, and T. Kodama, "Chiral transition in a finite system and possible use of finite size scaling in relativistic heavy-ion collisions," J. Phys. G, **38**(8), 085101 (2011). https://doi.org/10.1088/0954-3899/38/8/085101

[7] S.A. Basset, et al., "Reaction dynamics in Pb + Pb at the CERN/SPS: From partonic degrees of freedom to freeze-out," Prog. Part. Nucl. Phys. **42**, 313 (1999). https://doi.org/10.1016/S0146-6410(99)00086-1

[8] S. Pal, A. Motornenko, V. Vovchenko, A. Bhattacharyya, J. Steinheimer, and H. Stoecker, "Effect of finite volume on thermodynamics of quark-hadron matter," Phys. Rev. D, **109**(1), 014009 (2024). https://doi.org/10.1103/PhysRevD.109.014009

[9] M.E. Fisher, and M.N. Barber, "Scaling theory for finite-size effects in the critical region," Phys. Rev. Lett. **28**(23), 1516 (1972). https://doi.org/10.1103/PhysRevLett.28.1516

[10] M. Ladrem, and A. Ait-El-Djoudi, "Finite-size effects and scaling for the thermal QCD deconfinement phase transition within the exact color-singlet partition function," Eur. Phys. J. C, **44**(2), 257-265 (2005). https://doi.org/10.1140/epjc/s2005-02357-y

[11] C. Spieles, H. Stöcker, and C. Greiner, "Phase transition of a finite quark-gluon plasma," Phys. Rev. C, **57**(2), 908 (1998). https://doi.org/10.1103/PhysRevC.57.908

[12] S. Borsanyi, Z. Fodor, J.N. Guenther, R. Kara, P. Parotto, A. Pasztor, L. Pirelli, and C.H. Wong, "Chiral versus deconfinement properties of the QCD crossover: Differences in the volume and chemical potential dependence from the lattice," Phys. Rev. D, **111**(1), 014506 (2025). https://doi.org/10.1103/PhysRevD.111.014506

[13] A. Sorensen, and P. Sorensen, "Locating the critical point for the hadron to quark-gluon plasma phase transition from finite-size scaling of proton cumulants in heavyion collisions," arXiv:2405.10278 [nucl-th] (2024). https://doi.org/10.48550/arXiv.2405.10278

[14] H.-T. Elze, U. Heinz, and T. Kodama, "On the color-singlet quark-glue plasma," Phys. Lett. B, **124**(6), 515 (1983). https://doi.org/10.1016/0370-2693(83)91564-2

[15] H.-T. Elze, U. Heinz, and T. Kodama, "Finite size effects for quark-gluon plasma droplets," Phys. Lett. B, **179**(4), 385 (1986). https://doi.org/10.1016/0370-2693(86)90498-3

[16] B. Moussaoui, A. Ait El Djoudi, and A. Tawfik, "Finite-Size Effects Near QCD Critical Point: Quark Number Susceptibility," Int. J. Theor. Phys. **61**(6), N181 (2022). https://doi.org/10.1007/s10773-022-05159-x

[17] T.D. Lee and C.N. Yang, "Statistical theory of equations of state and phase transitions. II. Lattice gas and Ising model," Phys. Rev. **87**, 410 (1952). https://doi.org/10.1103/PhysRev.87.410

[18] E.S. Fraga, "QCD under extreme conditions: An informal discussion," (2013). https://doi.org/10.48550/arXiv.1310.6656

[19] O. Philipsen, "The QCD equation of state from the lattice," Prog. Part. Nucl. Phys. **70**, 55 (2013). https://doi.org/10.1016/j.ppnp.2012.09.003

[20] S. Basu, S. Chatterjee, R. Chatterjee, T.K. Nayak, and B.K. Nandi, "Specific heat of matter formed in relativistic nuclear collisions," Phys. Rev. C, **94** (4), 044901 (2016). https://doi.org/10.1103/PhysRevC.94.044901

[21] N. Magdy, M. Csanad, and R.A. Lacey, "Influence of finite volume and magnetic field effects on the QCD phase diagram," J. Phys. G, **44** (2), 025101 (2017). https://doi.org/10.1088/1361-6471/44/2/025101

[22] M.E. Fisher and A.N. Berker, "Scaling for first-order phase transitions in thermodynamic and finite systems," Phys. Rev. B, **26** (5), 2507 (1982). https://doi.org/10.1103/PhysRevB.26.2507

[23] V. Privman and M.E. Fisher, "Finite-size effects at first-order transitions," J. Stat. Phys. **33** (2), 385 (1983). https://doi.org/10.1007/BF01009803

[24] K. Binder, and D.W. Heermann, "Monte Carlo Simulations in Statistical Physics," 2nd ed. (Springer-Verlag, New York, 2002).

[25] H. Meyer-Ortmanns, "Phase transitions in quantum chromodynamics," Rev. Mod. Phys. **68**(2), 473 (1996). https://doi.org/10.1103/RevModPhys.68.473

СКІНЧЕННО-РОЗМІРНЕ МАСШТАБУВАННЯ ТЕПЛОВОЇ СПРИЙНЯТЛИВОСТІ ТА ПИТОМОЇ ТЕПЛОЄМНОСТІ ПОБЛИЗУ КХД ФАЗОВОГО ПЕРЕХОДУ З ДЕКОНФАЙНМЕНТОМ

Б. Мусауї[1,2], А. Айт Ель Джуді[1], Н. Мулудж[1,3], М. А. Лейкхал[1,4]

[1]*Лабораторія фізики елементарних частинок та статистичної фізики, Вища нормальна школа-Куба, В'є-Куба, B.P.92, 16050 Алжир, Алжир*

[2]*Лабораторія теоретичної фізики, Фізичний факультет, USTHB Bab-Ezzouar, Ель-Алія, BP 32, 16111 Алжир, Алжир*

[3]*Університет Хассіби Бенбуалі, Шлеф, Алжир*

[4]*Університет Мхамеда Бугари, Бумердес, Алжир*

Властивості термічно керованого фазового переходу деконфайнменту (DPT) від адронного газу (HG) до кольорової синглетної кварк-глюонної плазми (QGP), що містить глюони та безмасові верхні та нижні кварки, при ненульовому хімічному потенціалі кварка μ, досліджуються з урахуванням об'ємного співіснування адронного газу та QGP у системі скінченних розмірів. Ефекти скінченних розмірів аналізуються для термічно керованого DPT при різних значеннях μ. Критичні показники визначаються за допомогою числового аналізу масштабування скінченних розмірів (FSS) шляхом апроксимації результатів як функції розміру системи. Ефективна температура переходу (T_c) демонструє зсув до вищих значень зі зменшенням розміру системи, що вказує на критичну поведінку в області термічно керованого DPT від високорозмірної форми до QGP. Важливо, що всі три критичні показники масштабування виявляються незалежними від хімічного потенціалу кварків μ, що встановлює універсальність структури масштабування скінченних розмірів відносно μ.

Ключові слова: *термічно керований фазовий перехід деконфайнменту (DPT); кольоровий синглет; хімічний потенціал кварків; аналіз масштабування скінченних розмірів (FSS); температура переходу*

East European Journal of Physics. 3. 146–159 (2026)

DOI: 10.26565/2312-4334-2026-3-13 ISSN 2312-4334

FINITE-SIZE SCALING ANALYSIS FOR THE QCD DECONFINING PHASE TRANSITION TO A COLOR-SINGLET QUARK-GLUON PLASMA WITH THE THREE u, d AND s QUARK FLAVORS

Hayet Sahi[1,2], Amal Ait El Djoudi[*2], Abdelkader Cheddad[2]

[1]M'hammed Bougara University of Boumerdes, Algeria

[2]Particle and Statistical Physics Laboratory, Higher Normal School of Kouba, B.P. 92, 16050, Vieux-Kouba, Algiers, Algeria

[*]Corresponding Author e-mail: amal.aiteldjoudi@g.ens-kouba.dz

Received June 2, 2026; revised August 18, 2026; accepted August 20, 2026

In this work, we calculate the partition function of the Quark-Gluon plasma (QGP) projected on the SU(3) color-singlet representation, using the projection method, within a density of states for quarks and gluons given by the Multiple Reflexion Expansion (MRE) approximation. We examine the impact of incorporating the area and curvature terms, in addition to the volume term in the density of states, on the behavior of several physical quantities characterizing the deconfining phase transition from a hadronic gas phase of massive pions, to a Quark-Gluon plasma (QGP) phase made up of gluons, massless up and down quarks, and massive strange quarks along with their antiquarks, within the Bag model and a phenomenological phase coexistence model.By means of a finite-size scaling analysis, we investigate the behavior of some scaling exponents relevant to the occurring deconfining phase transition in a finite volume, especially that of the scaling exponent relative to the shift of the effective transition temperature, by considering contributions of the curvature term only, the area term only in the density of states additionally to the volume term, then the contribution of all three terms, by analyzing the value of the shift critical exponent λ compared to that obtained previously using the volume term only in the quarks and gluons density of states.

Keywords: *Deconfining phase transition; Quark-Gluon Plasma; Color-singletness; Projection method; Finite-size scaling analysis*

1. INTRODUCTION

Under ordinary conditions of temperature and/or density, quarks and gluons, which make up protons, neutrons and all hadrons [1, 2], are bound together by the strong interaction, which is described by Quantum Chromodynamics (QCD) (For a recent review see for example [3, 4]). This means that quarks and gluons are confined within hadrons. However, at high temperatures and/or densities, the strong interactions become negligible, and hadronic matter undergoes a transition to a deconfined phase, where quarks and gluons are no longer confined and move freely in a hot and dense state [5, 6]. This new state of nuclear matter is called the Quark-Gluon Plasma (QGP) [7, 8]. The color confinement suggests that this QGP phase may exist in a color-singlet state [9–11]. It is thought that the QGP exists in the cores of neutron stars, also known as dense stars [12, 13], where the density is so high. It also dominated the universe in the first 10^{-5} seconds after the Big Bang when the temperature was extremely high [14, 15]. However, as the temperature rapidly decreased, these particles began to combine and form hadrons. To study the QGP phase, a "little bang" is recreated in laboratories by conducting ultra-relativistic heavy-ion collisions at high energy in accelerators [16, 17]. This was first proposed in 1983 by J. D. Bjorken, who gave an initial description of the evolution of the QGP [18].

This work is a continuation of the previous studies of one of us [19–21], where we examined the thermally driven deconfinement phase transition (DPT) in a finite size, at zero chemical potential ($\mu = 0$), and of [22] where we examined the density driven deconfinement phase transition (DPT) at fixed temperature, from a hadronic gas (HG) phase to the QGP phase projected on the color-singlet SU(3) representation using the projection method [23, 24]. Therein, only the contribution of the volume term was considered in the quarks and gluons density of states, and the behavior of several physical quantities has been studied near the transition. Then, by means of a finite-size scaling analysis [25–27], we investigated the universal quantities called critical exponents, considered as indicators of the order of the occurring phase transition [28–30]. Our goal is to improve the value of the shift scaling exponent, which was found in our previous work [19] considerably deviating from the expected value 1, known to characterize a first-order phase transition, and which was obtained for the three other scaling exponents characterizing the width of the transition region as well as the heights of the peaks of both thermal susceptibility and specific heat density. This will be achieved by considering more realistic conditions in the studied system, treating the pions in the hadronic phase as massive particles and including the massive strange quarks in addition to the massless up and down quarks and the gluons in the QGP phase. Also, we consider the area and curvature contributions, in addition to the volume contribution, in the quarks and gluons density of states determined by the Multiple Reflection Expansion (MRE) approximation [31, 32], commonly called the asymptotic expansion of the density of states, used in the projection method for the calculation of the color-singlet QGP partition function.

We describe the thermally driven QCD deconfinement phase transition at zero chemical potential using the MIT bag model [7, 33], which states that at low density and/or temperature the real vacuum exerts an external pressure, called the

Cite as: H. Sahi, A.A. El Djoudi, A. Cheddad, East Eur. J. Phys. 3, 146 (2026), https://doi.org/10.26565/2312-4334-2026-3-13

bag constant B, on the QCD perturbative vacuum of the hadron bag, keeping the quarks and gluons confined inside the bag, for further details see [34, 35]. We also assume the coexistence of the HG and QGP phases in a finite volume, using a phenomenological model proposed in [36]. Initially, we investigate the behavior of several thermodynamic quantities, such as the order parameter and its first and second derivatives with respect to temperature, for different volumes at zero chemical potential ($\mu = 0$). We aim to study how the area and curvature terms affect the temperature at which the phase transition occurs, and also the scaling critical exponent that describes the variations of the shift of this transition temperature with the system volume. We compare the obtained results with those of our previous works [19, 20], where only the volume term was included in the density of states, and with those obtained in [21] with the contribution of the volume and curvature terms in the quarks and gluons density of states.

2. PARTITION FUNCTIONS OF THE HADRONIC GAS AND THE COLOR-SINGLET QGP PHASES

Let us recall that as in our previous works [19–21], we consider a mixed system of HG and QGP phases in a finite total volume: $V = V_{\mathrm{HG}} + V_{\mathrm{QGP}}$. In this system, the hadronic phase occupies a volume V_{HG} with a fraction h of the total system volume, such that $V_{\mathrm{HG}} = hV$. The parameter h represents the quantitative characterization of the macroscopic state of the system, and the QGP phase occupies a volume V_{QGP}, such that $V_{\mathrm{QGP}} = (1-h)V$, where $h = 1$ corresponds to the system being entirely in the hadronic phase, and $h = 0$ corresponds to the system being entirely in the QGP phase. In such a phenomenological model used in [36], the probability density to find the system in the state h is given by:

$$p(h,T,\mu,V) = \frac{Z(h,T,\mu,V)}{\int_0^1 Z(h,T,\mu,V)\,dh} \tag{1}$$

and the mean value of any thermodynamic quantity $A(T,\mu,V)$ of the system can then be written in the following form:

$$\langle A(T,\mu,V)\rangle = \int_0^1 A(h,T,\mu,V)\,p(h,T,\mu,V)\,dh \tag{2}$$

where $A(h,T,\mu,V)$ is the thermodynamic quantity in the state h, given in the case of an intensive quantity by:

$$A(h,T,\mu,V) = hA_{\mathrm{HG}}(T,\mu,hV) + (1-h)A_{\mathrm{QGP}}(T,\mu,(1-h)V) \tag{3}$$

with A_{HG} and A_{QGP} the thermodynamic quantities relative to the individual HG and QGP phases respectively; $Z(h,T,\mu,V)$ is the total partition function of the mixed HG-QGP system:

$$Z(h,T,\mu,V) = Z_{\mathrm{QGP}}(h,T,\mu,V)\,Z_{\mathrm{HG}}(h,T,\mu,V)\,Z_{\mathrm{vac}}(h,T,\mu,V) \tag{4}$$

where $Z_{\mathrm{QGP}}(h,T,\mu,V)$ and $Z_{\mathrm{HG}}(h,T,\mu,V)$ are the partition functions of the QGP and HG phases respectively, and $Z_{\mathrm{vac}}(h,T,\mu,V)$ reads for the real vacuum pressure B as mentioned above:

$$Z_{\mathrm{vac}} = \exp\left(-\frac{BV_{\mathrm{QGP}}}{T}\right) \tag{5}$$

For the calculation of $Z_{\mathrm{HG}}(h,T,\mu,V)$, we consider a hadronic gas consisting of massive pions ($m_\pi = 138\,\mathrm{MeV}$), and we obtain:

$$Z_{\mathrm{HG}} = \exp\left(\frac{d_\pi V_{\mathrm{HG}}}{2\pi^2 T}\int_0^\infty \frac{k^4\,dk}{\sqrt{k^2+m_\pi^2}\left(e^{\beta\sqrt{k^2+m_\pi^2}}-1\right)}\right) \tag{6}$$

where k is the momentum, d_π the pion degeneracy factor, and $\beta = 1/T$.

To calculate $Z_{\mathrm{QGP}}(h,T,\mu,V)$ projected on the color-singlet SU(3) representation, we implement the color-singletness constraint into the quantum statistical description of the QGP phase, using the group theoretical projection method formulated by Redlich and Turko [22, 23], and for this we consider a QGP phase consisting of gluons, massless up and down quarks and massive strange quarks with their antiquarks, and we assume non-interaction between these particles. Such a partition function of a color-singlet QGP, in a volume V, at temperature T and chemical potential μ, can be written as in [37, 38]:

$$Z_{\mathrm{QGP}}(T,V,\mu) = \frac{4}{9\pi^2}\int_{-\pi}^{+\pi}\int_{-\pi}^{+\pi} d\phi\,d\psi\,M(\phi,\psi)\,\tilde{Z}_{\mathrm{QGP}}(T,V,\mu,\phi,\psi) \tag{7}$$

where $M(\phi,\psi)$ is the weight function or the Haar measure, given by:

$$M(\phi,\psi) = \left(\sin\left(\frac{1}{2}\left(\psi+\frac{\phi}{2}\right)\right)\sin\left(\frac{\phi}{2}\right)\sin\left(\frac{1}{2}\left(\psi-\frac{\phi}{2}\right)\right)\right)^2 \tag{8}$$

and $\tilde{Z}_{\text{QGP}}$ the generating function, given for a system of quarks, antiquarks and gluons, at a temperature T and chemical potential μ in a volume V by:

$$\tilde{Z}_{\text{QGP}}(T,V,\mu,\phi,\psi) = \tilde{Z}_{\text{quark}}(T,V,\mu,\phi,\psi)\,\tilde{Z}_{\text{gluon}}(T,V,\mu,\phi,\psi) \tag{9}$$

where $\tilde{Z}_{\text{quark}}$ and $\tilde{Z}_{\text{gluon}}$ are the generating functions corresponding to the quarks-antiquarks and gluons respectively, expressed as:

$$\ln\tilde{Z}_{\text{quark}} = \sum_{q=r,b,g}\sum_{\alpha}\left\{\ln\left[1+e^{-\beta(\sqrt{k^2+m_q^2}-\mu)+i\theta_q}\right]+\ln\left[1+e^{-\beta(\sqrt{k^2+m_q^2}+\mu)-i\theta_q}\right]\right\} \tag{10}$$

$$\ln\tilde{Z}_{\text{gluon}} = \sum_{G=1}^{4}\sum_{\alpha}\left\{\ln\left[1+e^{-\beta k+i\theta_G}\right]^{-1}+\ln\left[1+e^{-\beta k-i\theta_G}\right]^{-1}\right\} \tag{11}$$

m_q being the quark mass. From [37], the explicit expressions of the angles θ_q $(q=r,b,g)$ and θ_G $(G=1,\ldots,4)$ in SU(3) are respectively:

$$\theta_r = \frac{\phi}{2}+\frac{\psi}{3},\quad \theta_g = -\frac{\phi}{2}+\frac{\psi}{3},\quad \theta_b = -\frac{2\psi}{3} \tag{12}$$

$$\theta_1 = \theta_r-\theta_g,\quad \theta_2=\theta_g-\theta_b,\quad \theta_3=\theta_b-\theta_r,\quad \theta_4=0 \tag{13}$$

In the continuum approximation for single-particle energy levels, the summation $\sum_\alpha$ can be replaced by an integral using a density of states, expressed for quarks-antiquarks and gluons respectively as:

$$\ln\tilde{Z}_{\text{quark}} = \sum_{q=r,b,g} d_Q\int_0^\infty\left\{\ln\left[1+e^{-\beta(\sqrt{k^2+m_q^2}-\mu)+i\theta_q}\right]+\ln\left[1+e^{-\beta(\sqrt{k^2+m_q^2}+\mu)-i\theta_q}\right]\right\}\rho_Q(k,V)\,dk \tag{14}$$

$$\ln\tilde{Z}_{\text{gluon}} = \sum_{G=1}^{4} d_G\int_0^\infty\left\{\ln\left[1+e^{-\beta k+i\theta_G}\right]^{-1}+\ln\left[1+e^{-\beta k-i\theta_G}\right]^{-1}\right\}\rho_G(k,V)\,dk \tag{15}$$

d_Q and d_G are the spin-isospin degeneracy factors for quarks-antiquarks and gluons respectively; $\rho_Q(k,V)$, $\rho_G(k,V)$ are the density of states for quarks and gluons respectively, with a spherical volume $V_{\text{QGP}}=\frac{4}{3}\pi R^3$ described by the bag model [32, 38], R being the radius of the bag [14]. In the following, we shall use the density of states ρ_i $(i=Q,G)$ given by the Multiple Reflection Expansion (MRE) approximation proposed by Balian and Bloch [27], and used for example in [39], expressed by the sum of a volume term, an area term and a curvature term on the form:

$$\rho_i(k,V) = \frac{V_{\text{QGP}}k^2}{2\pi^2}+f_{A,i}4\pi R^2k+f_{C,i}8\pi R+\cdots,\quad i=Q,G \tag{16}$$

where $f_{A,i}$ and $f_{C,i}$ are the area and curvature coefficients respectively [41–44], given by:

$$f_{A,Q} = -\frac{1}{8\pi}\left(1-\frac{1}{2\pi}\arctan\frac{k}{m}\right)\to f_{A,Q}=0 \text{ when } m=0 \tag{17}$$

$$f_{C,Q} = \frac{1}{12\pi^2}\left[1-\frac{3k}{2m}\left(\frac{\pi}{2}-\arctan\frac{k}{m}\right)\right]\to f_{C,Q}=-\frac{1}{24\pi^2} \text{ when } m=0 \tag{18}$$

$$f_{A,G}=0,\qquad f_{C,G}=-\frac{1}{6\pi^2} \tag{19}$$

After proper calculations and simplifications, we find:

$$Z_{\text{QGP}}(T,V,\mu=0) = \frac{4}{9\pi^2}\int_{-\pi}^{+\pi}\int_{-\pi}^{+\pi}d\phi\,d\psi\,M(\phi,\psi)\,e^{g_1+g_2+g_3} \tag{20}$$

where g_1, g_2, g_3 result respectively from the contributions of the volume, area and curvature terms in the quarks and gluons density of states, and they are given by:

$$\begin{aligned} g_1 = d_QV_{\text{QGP}}\sum_{q=r,b,g}&\left\{\frac{\pi^2}{6}T^3\left[\frac{7}{30}-\left(\frac{\theta_q}{\pi}\right)^2+\frac{1}{2}\left(\frac{\theta_q}{\pi}\right)^4\right]\right.\\ &\left.+\frac{(m_ST)^{3/2}}{\sqrt{2}\,\pi^{3/2}}\left(1-\frac{\theta_q^2}{2!}+\frac{\theta_q^4}{4!}\right)e^{-m_S/T}\right\}\\ &+d_GV_{\text{QGP}}T^3\sum_{G=1}^{4}\frac{\pi^2}{12}\left[-\frac{7}{30}+\left(\frac{\theta_G-\pi}{\pi}\right)^2-\frac{1}{2}\left(\frac{\theta_G-\pi}{\pi}\right)^4\right] \end{aligned} \tag{21}$$

$$g_2 = d_Q\left(\frac{3V_{\text{QGP}}}{4\pi}\right)^{2/3}\left(\sqrt{\frac{2m_S}{\pi}}T^{3/2} - m_S T\right)\sum_{q=r,b,g}\left(1 - \frac{\theta_q^2}{2!} + \frac{\theta_q^4}{4!}\right)e^{-m_S/T} \tag{22}$$

$$\begin{aligned} g_3 = {} & d_Q\left(\frac{3V_{\text{QGP}}}{4\pi}\right)^{1/3}\sum_{q=r,b,g}\left\{\frac{\pi}{3}T\left(-\frac{1}{3} + \left(\frac{\theta_q}{\pi}\right)^2\right)\right. \\ & \left. + \left(\frac{2}{3}\sqrt{\frac{2T}{\pi m_S}} - T + \sqrt{\frac{2}{\pi m_S}}T^{3/2}\right)\left(1 - \frac{\theta_q^2}{2!} + \frac{\theta_q^4}{4!}\right)e^{-m_S/T}\right\} \\ & + d_G\left(\frac{3V_{\text{QGP}}}{4\pi}\right)^{1/3}\sum_{G=1}^{4}\frac{2\pi}{3}T\left[\frac{1}{3} - \left(\frac{\theta_G - \pi}{\pi}\right)^2\right] \end{aligned} \tag{23}$$

Let us note that we have used some approximations in the calculation of the PF of the massive strange quarks [39].

3. BEHAVIOR OF THE ORDER PARAMETER AND ITS FIRST AND SECOND DERIVATIVES WITHIN DIFFERENT CONTRIBUTIONS IN THE DENSITY OF STATES

In a first step, we will study the variations of the mean value of the order parameter with temperature T for different system sizes V, as in the previous work of one of us [19], but now by adding the area and curvature terms in the quarks and gluons density of states, then studying the effect of these terms on the variations of the order parameter, which is nothing but the mean value of the hadronic volume fraction $\langle h(T,V)\rangle$, then on the transition temperature at finite volume $T_c(V)$ deduced from $\langle h(T,V)\rangle$. We find the following expression of the order parameter:

$$\langle h(T,V)\rangle = \frac{\int_0^1 h\,dh\int_{-\pi}^{+\pi}\int_{-\pi}^{+\pi} d\phi\,d\psi\,M(\phi,\psi)\,e^{X_1}}{\int_0^1 dh\int_{-\pi}^{+\pi}\int_{-\pi}^{+\pi} d\phi\,d\psi\,M(\phi,\psi)\,e^{X_1}} \tag{24}$$

where

$$X_1 = -\frac{(1-h)VB}{T} + g_1 + g_2 + g_3 + \frac{hVd_\pi}{2\pi^2 T}I_1 \tag{25}$$

and

$$I_1 = \int_0^\infty \frac{k^4\,dk}{\sqrt{k^2+m_\pi^2}\left(e^{\beta\sqrt{k^2+m_\pi^2}} - 1\right)} \tag{26}$$

The order parameter is calculated using a suitable numerical integration method, and the integrals are evaluated at different values of the system volume V, over a temperature interval around the transition temperature. The variations of the order parameter as a function of temperature for different volumes are shown in Figure 1, with a bag constant value $B^{1/4} = 225\,\text{MeV}$, at zero chemical potential ($\mu = 0$), considering different contributions to the quarks and gluons density of states: the volume term only, volume and area terms, volume and curvature terms, and volume, area and curvature terms.

From the various curves on Figure 1, it can clearly be observed that for large system volumes, there is a sharp jump of $\langle h(T,V)\rangle$ from the value 1 in the HG phase to zero in the QGP phase, at a temperature approaching the true transition temperature, noted $T_c(\infty)$, and found to have the value $T_c(\infty) = 158.522\,\text{MeV}$, for $B^{1/4} = 225\,\text{MeV}$. This jump, mathematically described by the Heaviside function, reflects the existence of a latent heat during the transition, signifying that the transition is of first order. For small system volumes, this discontinuity becomes smoothed and rounded off, around an effective transition temperature, noted $T_c(V)$, which can be defined as the temperature at which the order parameter reaches the value $\langle h\rangle = 0.5$ [36], indicating that the HG and QGP phases contribute equally to the system. This effective transition temperature in a finite volume is shifted to temperatures higher than $T_c(\infty)$. This shift is due to the color-singletness condition, which reduces the effective number of internal degrees of freedom as the volume decreases, causing the system to reach the necessary pressure for the phase transition at higher temperatures in smaller volumes [37].

It can also be noted from Figure 1 that the general shape of the order parameter $\langle h(T,V)\rangle$ is similar in all four cases, with a difference in the effective transition temperature at which the transition occurs, since it is well expected that the transition temperature at a fixed volume varies with the contributions to the quarks and gluons density of states. The obtained results show that it takes its highest value when all three terms are included (volume, area, and curvature) and its lowest value when only the volume term is included, with:

$$T_c^{(\text{Vol})}(V) < T_c^{(\text{Vol+Area})}(V) < T_c^{(\text{Vol+Curv})}(V) < T_c^{(\text{Vol+Area+Curv})}(V). \tag{27}$$

Table 1 illustrates the effective transition temperature $T_c(V)$ for different volumes, for all considered contributions to the density of states.

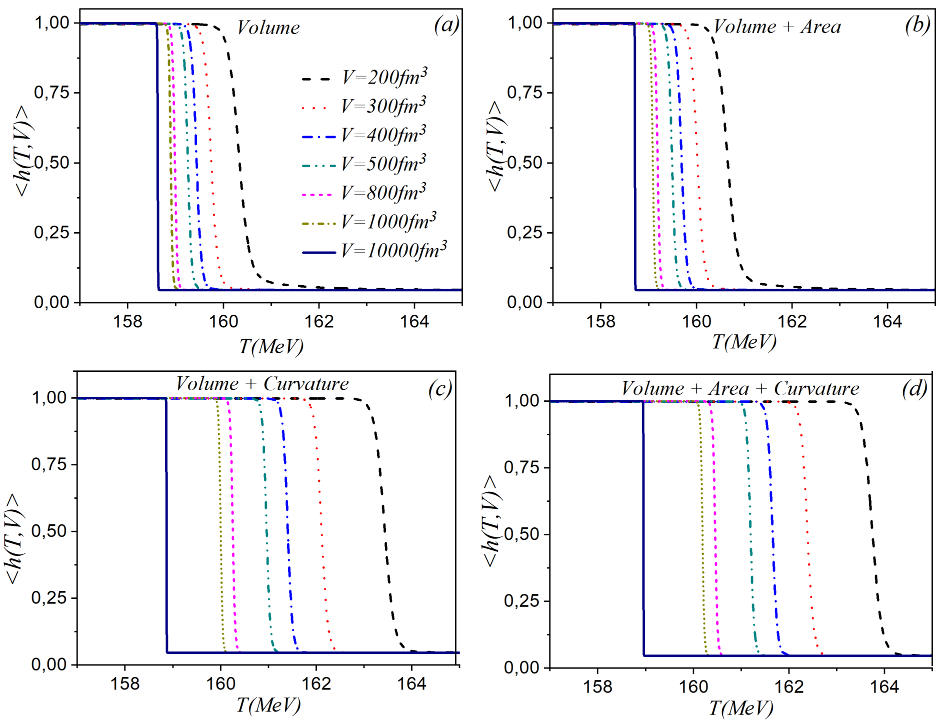

Figure 1. Variations of the order parameter $\langle h(T,V)\rangle$ as a function of temperature T, for different volumes, at $\mu = 0$ and $B^{1/4} = 225$ MeV, with the four contributions in the density of states.

Table 1. Values of the effective transition temperature $T_c(V)$ for various volumes, with different terms contributing to the density of states.

System Volume (fm^3)	$T_c^{(\mathrm{Vol})}(V)$ (MeV)	$T_c^{(\mathrm{Vol+Area})}(V)$ (MeV)	$T_c^{(\mathrm{Vol+Curv})}(V)$ (MeV)	$T_c^{(\mathrm{Vol+Area+Curv})}(V)$ (MeV)
200	160.338	160.654	163.434	163.747
300	159.746	160.021	162.111	162.387
500	159.255	159.489	160.961	161.196
800	158.984	159.186	160.253	160.455
1000	158.897	159.085	159.999	160.188
2000	158.737	158.888	159.442	159.593
3000	158.690	158.821	159.228	159.360
4000	158.666	158.785	159.111	159.230
5000	158.652	158.763	159.035	159.146
6000	158.642	158.747	158.982	159.087
8000	158.631	158.725	158.911	159.006
10000	158.624	158.712	158.865	158.954

From the above analysis, it follows that the first thermal derivative of the order parameter, known as the thermal susceptibility $\chi(T,V)$, reaches its minimum value at the effective transition temperature $T_c(V)$, corresponding to the value $\langle h\rangle = 0.5$ of the order parameter, and subsequently to a vanishing second derivative $\langle h(T,V)\rangle''$ of the order parameter with respect to temperature.

Consequently, one can also investigate the influence of various contributions by analyzing the first and second derivatives of the order parameter with respect to temperature T, defined as follows:

$$\chi(T,V) = \frac{\partial\langle h(T,V)\rangle}{\partial T} \tag{28}$$

$$\langle h(T,V)\rangle'' = \frac{\partial^2 \langle h(T,V)\rangle}{\partial T^2} = \frac{\partial \chi(T,V)}{\partial T} \tag{29}$$

Our results for the variations of the thermal susceptibility are illustrated in Figure 2. It is noted that the behavior of the susceptibility $\chi(T,V)$ as a function of temperature T at a fixed system volume V, is similar for the four cases of the quarks and gluons density of states: with the contributions of the volume term only, volume and area terms, volume and curvature terms, and all three terms. The key difference is the shift of the curves to higher temperatures when the area term is included, and the temperature further increases when the curvature term is added, reaching the highest values when all terms are included. For example, at $V = 200\,\mathrm{fm}^3$, the transition temperature is $T_c^{(\mathrm{Vol})} = 160.865\,\mathrm{MeV}$ with the volume term only, and it increases to $T_c^{(\mathrm{Vol+Area})} = 161.215\,\mathrm{MeV}$, while with the volume and curvature terms it attains $T_c^{(\mathrm{Vol+Curv})} = 164.652\,\mathrm{MeV}$, and it reaches its highest value $T_c^{(\mathrm{Vol+Area+Curv})} = 164.997\,\mathrm{MeV}$ with the volume, area and curvature terms contribution.

From Figure 2, we observe that in all four cases, the singularity of the Dirac delta function in $\chi(T,V)$, which occurs at the thermodynamic limit, spreads out into a finite peak acquiring a finite width $\delta T(V)$ in small volumes. This spreading corresponds to the rounding of the order parameter and is due to the finite probability of presence for the QGP phase below the transition temperature $T_c(V)$ and of the HG phase above $T_c(V)$, induced by significant thermodynamic fluctuations. This result is expected since the finite discontinuity of the order parameter, described by the Heaviside function, becomes a delta function δ at the level of the first derivative, i.e., in the susceptibility [19].

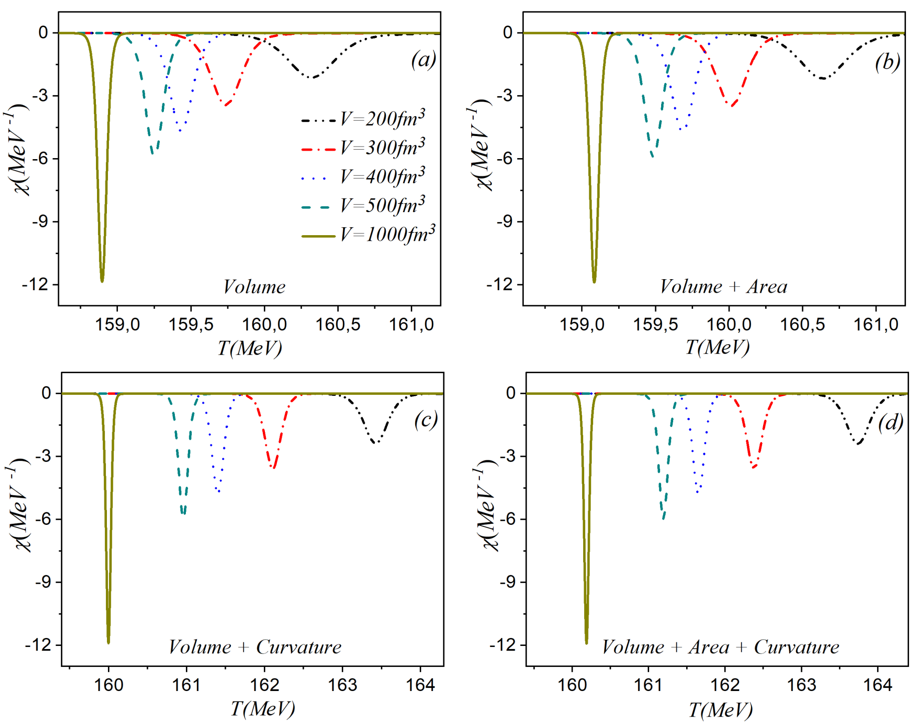

Figure 2. Variations of the susceptibility $\chi(T,V)$ versus temperature, for different system volumes, at $\mu = 0$ and $B^{1/4} = 225\,\mathrm{MeV}$, with the four contributions in the density of states.

To better understand the width $\delta T(V)$ of the region over which the transition is rounded off, we plot the second derivative of the order parameter $\langle h(T,V)\rangle''$ as a function of temperature T for different system sizes in Figure 3, across all contributions. The second derivative is zero at the transition temperature $T_c(V)$. The width of the transition region $\delta T(V)$ is defined as the difference between the temperatures $T_1(V)$ and $T_2(V)$ at which the second derivative reaches its minimum and maximum respectively [19], i.e., $\delta T(V) = T_2(V) - T_1(V)$.

For further clarity, Figure 4 illustrates the order parameter $\langle h(T,V)\rangle$ (black solid line), its first thermal derivative $\chi(T,V)$ (red dashed line), and its second thermal derivative $\langle h(T,V)\rangle''$ (blue dotted line) versus temperature for $V = 200\,\mathrm{fm}^3$, considering the volume term only in the quarks and gluons density of states. According to Figures 2, 3 and 4, the shift of the transition temperature $\tau_T(V)$ defined as $\tau_T(V) = T_c(V) - T_c(\infty)$ decreases with increasing volume V, as noted in previous works [19–21]. The same behavior holds for the width of the transition region $\delta T(V)$, while the height of the susceptibility peak $|\chi_T|^{\max}(V)$ increases with increasing volume V. This is because the fluctuations driving the transition are weaker in larger systems.

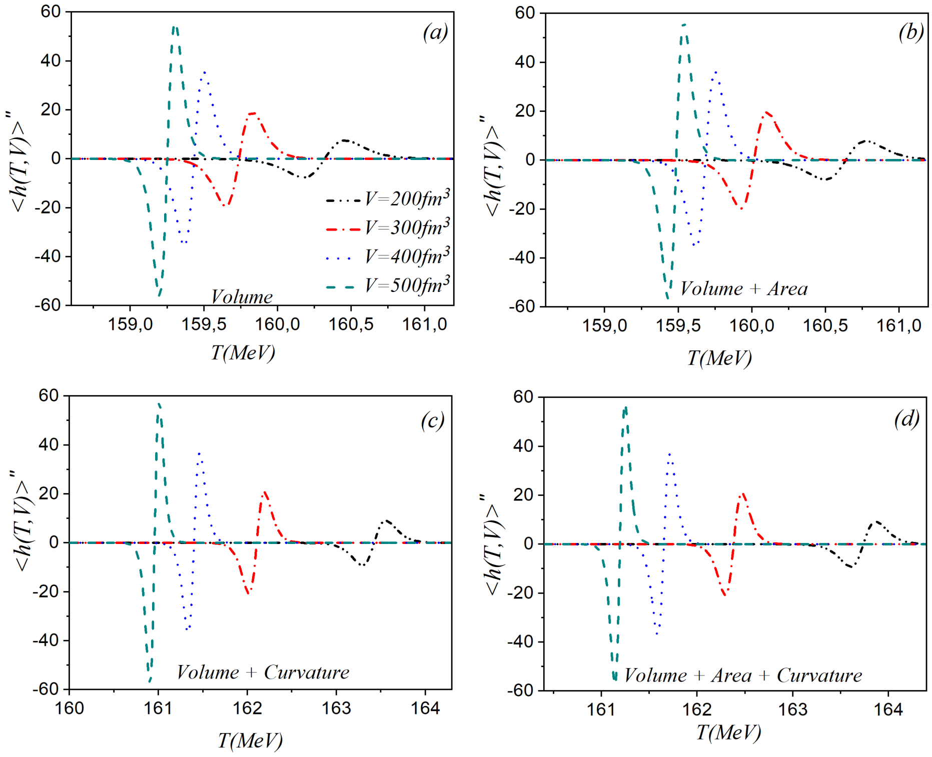

Figure 3. Variations of the second derivative of the order parameter $\langle h(T,V)\rangle''$ versus temperature, for different system sizes, at $\mu = 0$ and $B^{1/4} = 225\,\mathrm{MeV}$, with the four contributions in the density of states.

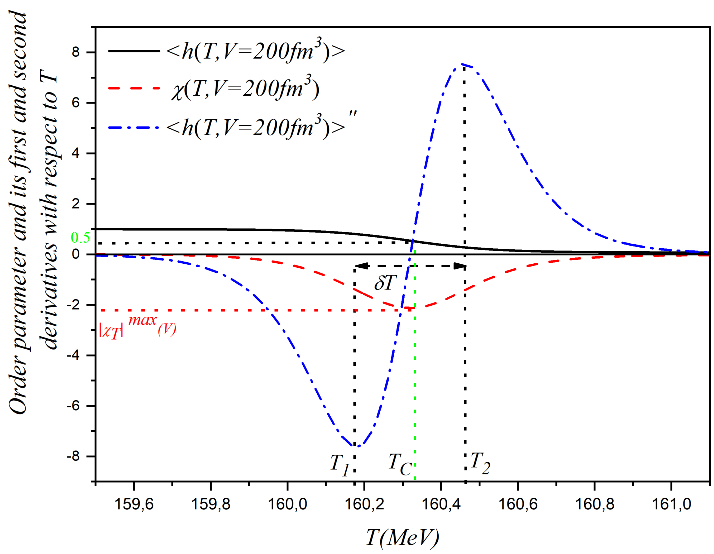

Figure 4. Plot of the order parameter $\langle h(T,V)\rangle$ (black solid line), its first thermal derivative $\chi(T,V)$ (red dashed line), and its second thermal derivative $\langle h(T,V)\rangle''$ (blue dotted line) versus temperature for a volume $V = 200\,\mathrm{fm}^3$, with the contribution of the volume term only in the density of states.

4. EFFECT OF THE CURVATURE AND THE AREA TERMS ON THE CRITICAL EXPONENTS FOR THE THERMAL DECONFINEMENT PHASE TRANSITION

It is well known in the theory of phase transitions that characteristic quantities such as the shift of the effective transition temperature $T_c(V)$ relative to the true transition temperature $T_c(\infty)$, the width of the transition region $\delta T(V)$ and the susceptibility maxima $|\chi_T|^{\max}(V)$ follow scaling behaviors, expressed as power laws of the volume V, characterized by critical scaling exponents. The power laws for a first-order phase transition are given by:

$$\begin{cases} \tau_T(V) = T_c(V) - T_c(\infty) \sim V^{-\lambda}, \\ \delta T(V) \sim V^{-\theta}, \\ |\chi_T|^{\max}(V) \sim V^{\gamma}. \end{cases} \tag{30}$$

where λ, θ and γ are the scaling exponents, which are expected to be equal to unity for a first-order phase transition, as shown in finite-size scaling (FSS) theory [45–47].

In this part of the work, we study the behavior of these three quantities with varying volume V, by incorporating the contribution of curvature and area terms in the density of states, additionally to the volume term, which has been previously considered alone in [19]. A finite-size scaling analysis, using a numerical parametrization of the data with the power-law forms defined in Eq. (30), yields very interesting results, which we illustrate in the following and compare with previous findings from [19].

4.1. The shift scaling exponent

In the aim of exploring the impact of the terms contributing to the density of states on the shift scaling exponent λ, associated with the shift of the transition temperature, we first determine the effective transition temperature $T_c(V)$ in a finite volume, and calculate its deviation from $T_c(\infty)$, to obtain the shift: $\tau_T(V) = T_c(V) - T_c(\infty)$. Table 2 shows the values of the shift of the transition temperature at various volumes, for the four cases of contributions in the quarks and gluons density of states.

Table 2. Values of the shift of the transition temperature for different terms contributing to the density of states.

System Volume (fm^3)	$\tau_T^{(\mathrm{Vol})}(V)$ (MeV)	$\tau_T^{(\mathrm{Vol+Area})}(V)$ (MeV)	$\tau_T^{(\mathrm{Vol+Curv})}(V)$ (MeV)	$\tau_T^{(\mathrm{Vol+Area+Curv})}(V)$ (MeV)
200	1.816	2.132	4.912	5.225
300	1.223	1.500	3.589	3.865
500	0.732	0.966	2.439	2.673
1000	0.375	0.562	1.477	1.666
3000	0.167	0.307	0.706	0.837
5000	0.129	0.240	0.513	0.624
6000	0.120	0.224	0.460	0.564
8000	0.108	0.203	0.389	0.484
9000	0.104	0.196	0.364	0.455
10000	0.102	0.189	0.343	0.431

As mentioned earlier, the shift of the effective transition temperature $\tau_T(V)$, relative to the true transition temperature $T_c(\infty)$, is expected to behave as a power of the system volume, according to Eq. (30), where the shift scaling exponent λ is expected to be equal to one. The obtained data for the shift $\tau_T(V)$ are plotted in Figure 5, and the values of the shift scaling exponent λ for the four contributions are summarized in Table 3.

Table 3. Values of the shift scaling exponent for the four cases of contributing terms to the density of states.

Shift scaling exponent	λ_1	λ_2	λ_3	λ_4
Contributions	Vol	Vol+Area	Vol+Curv	Vol+Area+Curv
Values	0.960 ± 0.018	0.788 ± 0.022	0.734 ± 0.007	0.692 ± 0.008

At first glance, we notice that for the volume term contribution only in the density of states, we obtain a shift scaling exponent: $\lambda_1(\mathrm{Vol}) = 0.960 \pm 0.018$, which is approximately equal to 1. When comparing this value to that of our previous work [19], in which: $\lambda = 0.876 \pm 0.041$ with the volume contribution only, our findings turn out to be an improvement. It can also be noted that with the addition of the area and curvature terms, the value of the shift exponent decreases consistently to $\lambda_4(\mathrm{Vol} + \mathrm{Area} + \mathrm{Curv}) = 0.692 \pm 0.008$. Initially, we assumed that adding the area and curvature terms would refine the result for the shift scaling exponent λ, making it more accurate or insightful. However, after completing the calculations, we found oppositely that incorporating these terms actually decreased the λ value.

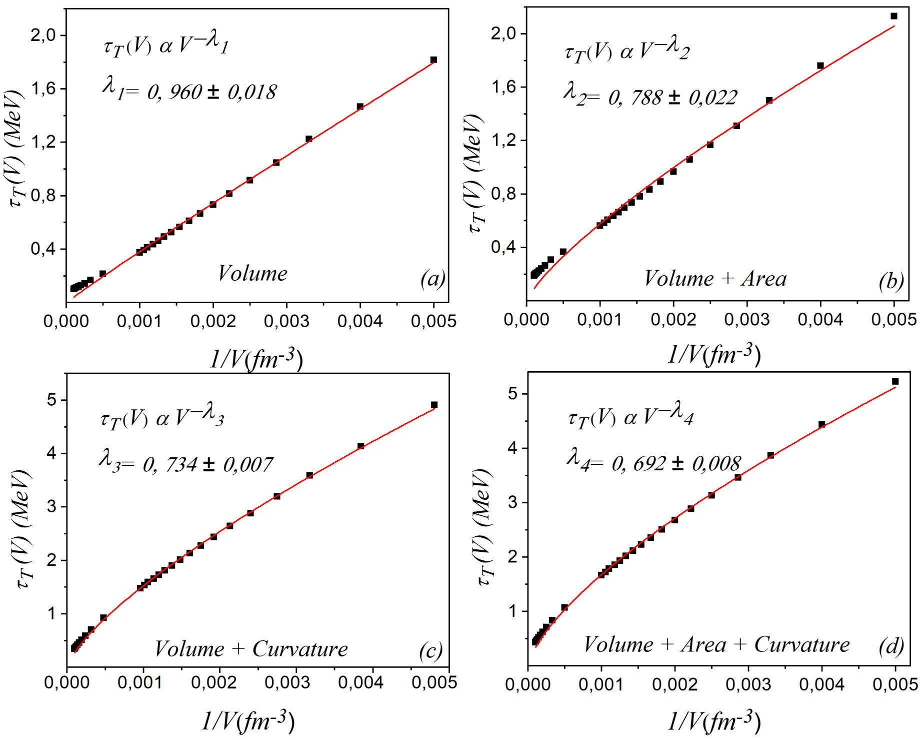

Figure 5. Variations of the shift of the transition temperature $\tau_T(V)$ with inversed volume, for the four contributions in the density of states.

This outcome could be attributed to several factors, such as the increasing complexity of the calculation or inherent limitations of the model. This discrepancy is partly due to the mass of the particles involved. Let us recall that our previous work [19] considered only massless up and down quarks in the QGP phase, and massless pions in the hadronic gas phase, while in the present work, we introduced a third massive quark (the strange quark) in the QGP phase and accounted for the mass of the pions in the HG phase.

We also observed that the shift scaling exponent has different values when the fit of the data of the shift of the transition temperature is carried out in the interval of small volumes or that of large ones. This is illustrated in Figure 6, which shows the shift of the transition temperature as a function of inverse volume, both for (a) small and (b) large volumes, when considering the volume term only in the density of states. The obtained result of the shift exponent $\lambda_1(\mathrm{Vol}) = 0.997 \pm 0.005$, with a fit in the small-volumes interval, suggests that our model matches better in small volumes, where the color-singletness condition applies, and where there are fewer numerical difficulties. When the fit is carried out in the interval of large volumes, the obtained value of the shift exponent $\lambda'_1(\mathrm{Vol}) = 0.620 \pm 0.030$, is rather far from the value 1 expected for a first-order phase transition. To fully understand the influence of the area and curvature terms on the overall behavior of the critical exponents, we investigate the width of the transition region $\delta T(V)$ and the height of the susceptibility peak $|\chi_T|^{\max}(V)$ within the contribution of these terms in the density of states and we illustrate our findings in the following.

4.2. The smearing scaling exponent

Figure 7 shows the width of the transition region $\delta T(V)$ as a function of inverse volume, for the four cases of contributing terms in the quarks and gluons density of states.

A numerical parametrization with the power-law form $\delta T(V) \sim V^{-\theta}$, gives the values of the smearing critical exponent shown in Table 4.

Table 4. Values of the smearing scaling exponent for the four cases of contributing terms to the density of states.

Smearing scaling exponent	θ_1	θ_2	θ_3	θ_4
Contributions	Vol	Vol+Area	Vol+Curv	Vol+Area+Curv
Values	1.038 ± 0.006	1.033 ± 0.005	0.993 ± 0.004	0.992 ± 0.002

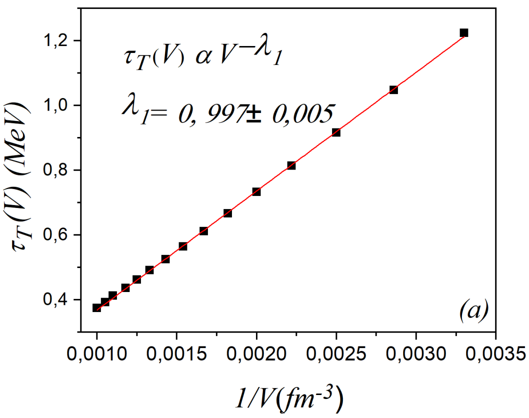

Figure 6. Variations of the shift of the transition temperature $\tau_T(V)$ with inversed volume, for (a) small and (b) large volumes, with the contribution of the volume term only in the density of states.

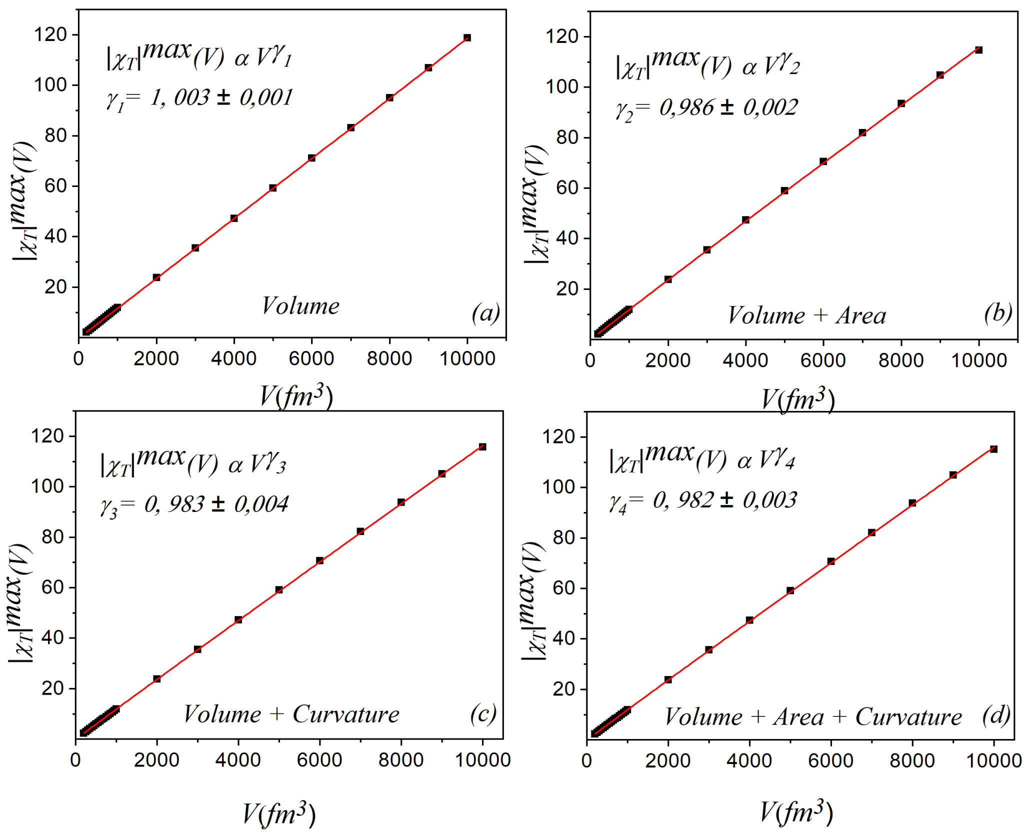

Figure 7. Variations of the width $\delta T(V)$ of the temperature region over which the transition is smeared out, with inversed volume, for the four contributions in the density of states.

4.3. The susceptibility scaling exponent

Figure 8 shows the variations of the height of the susceptibility peak $|\chi_T|^{\max}(V)$, with varying volume V, for the four cases of contributing terms in the quarks and gluons density of states.

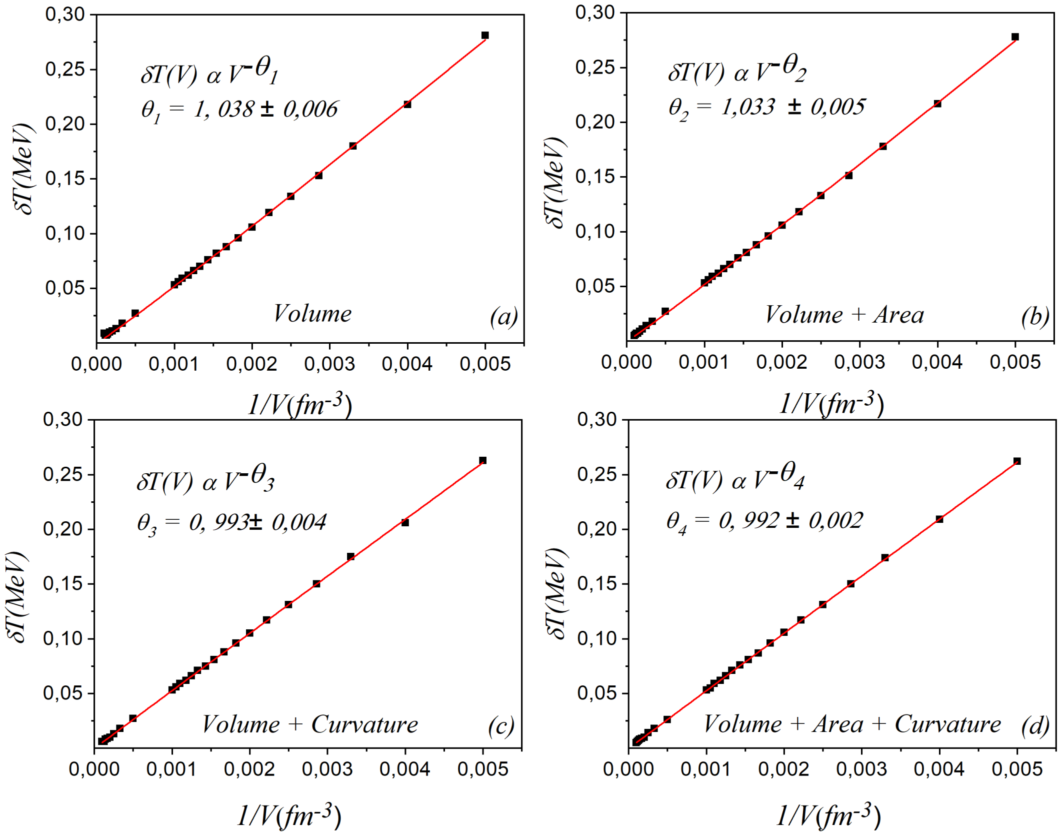

Figure 8. Variations of the susceptibility maxima $|\chi_T|^{\max}(V)$ versus volume, for the four contributions in the density of states.

A numerical parametrization with the power-law form $|\chi_T|^{\max}(V) \sim V^{\gamma}$, gives the values of the susceptibility critical exponent shown in Table 5.

Table 5. Values of the susceptibility scaling exponent for the four cases of contributing terms to the density of states.

Susceptibility scaling exponent	γ_1	γ_2	γ_3	γ_4
Contributions	Vol	Vol+Area	Vol+Curv	Vol+Area+Curv
Values	1.003 ± 0.001	0.986 ± 0.002	0.983 ± 0.004	0.982 ± 0.003

We notice from Table 4 and Table 5 that the values of the smearing scaling exponent θ and the susceptibility scaling exponent γ are equal to 1 when considering only the volume term contribution: $\theta_1(\text{Vol}) = 1.038 \pm 0.006$ and $\gamma_1(\text{Vol}) = 1.003 \pm 0.001$. However, with the addition of area and curvature terms, both values decrease slightly to $\theta_4(\text{Vol} + \text{Area} + \text{Curv}) = 0.992 \pm 0.002$, and $\gamma_4(\text{Vol} + \text{Area} + \text{Curv}) = 0.982 \pm 0.003$. This confirms that adding the area and curvature terms reduces the values of all critical exponents, including θ and γ, as well as λ.

5. CONCLUSIONS

In the present work, we studied the thermal DPT in a finite volume, at zero chemical potential $\mu = 0$ and with $B^{1/4} = 225$ MeV for the bag constant, based on the equations of state of a hadronic gas phase consisting of massive pions and of a color-singlet QGP phase containing gluons, massless up and down quarks and massive strange quarks along with their antiquarks. The primary aim was to investigate the influence of the area and curvature contributions to the density of states used in the calculation of the QGP equation of state on physical quantities characterizing the DPT occurring in a finite volume, and specifically the scaling exponent relative to the shift of the transition temperature, and then compare these findings with previous results from [19], obtained therein with the volume term contribution only in the density of states and reporting $\lambda = 0.876 \pm 0.041$.

Initially, we hypothesized that adding the area and curvature terms would improve the accuracy or significance of the shift scaling exponent λ deviating from the value 1, expected for a first-order phase transition. However, after completing our analysis, the obtained results revealed that including these terms actually led to a decrease in the value of the shift critical exponent λ. This could be attributed to various factors, such as the increasing complexity of the calculation or limitations in the model. To verify this, we determined the width of the transition region $\delta T(V)$ and the maximum of the susceptibility peak $|\chi_T|^{\max}(V)$ from the calculations incorporating the curvature and area terms into the quarks and gluons density of states. We found that the smearing scaling exponent θ and the susceptibility scaling exponent γ both equal unity, with the contribution of the volume term only to the density of states, but their values decreased when the area and curvature terms were added to the quarks and gluons density of states.

Our current result for the shift scaling exponent, $\lambda_1 = 0.960 \pm 0.018$, is an improvement over the previous result, $\lambda = 0.876 \pm 0.041$ [19], for the volume term contribution only in the density of states. This improvement in our results can be partially explained by the mass of the particles involved, since previous studies assumed that the QGP phase contained only massless up and down quarks, while the hadronic gas phase contained massless pions. In contrast, this work introduced a third quark to the QGP phase, namely the massive strange quark, and accounted for the pion mass in the HG phase. Finally, we observed that the value of the shift critical exponent changes when the parametrization $\tau_T(V) \sim V^{-\lambda}$ is performed on an interval of small volumes or large volumes. For small volumes, we recovered the expected value and found $\lambda_1(\mathrm{Vol}) = 0.997 \pm 0.005$, whereas for large volumes, the obtained value is $\lambda'_1(\mathrm{Vol}) = 0.620 \pm 0.030$. This suggests that our model matches better for small volumes, where there are fewer numerical difficulties and where the "color-singletness" condition applies, since it is well known that the finite-size corrections between a color-unprojected QGP and a color-projected one disappear as the size and/or temperature of the system increase, because the color projection no longer plays any role in this limit [9]. This obtained result for the shift scaling exponent agrees very well with those of finite-size scaling (FSS) theory, which expects the characteristic scaling exponents to be equal to unity for a first-order phase transition [45–47].

Acknowledgments: This research work is supported by the Algerian Ministry of Higher Education and Scientific Research.

Funding: No funding was received for conducting this work.

Conflict of interest: The authors declare that there are no conflicts of interest.

ORCID

Hayet Sahi, https://orcid.org/0009-0006-1847-9680; **Amal Ait El Djoudi**, https://orcid.org/0009-0005-7773-0401; **Abdelkader Cheddad**, https://orcid.org/0009-0008-8868-3139

REFERENCES

[1] M. Gell-Mann, Phys. Lett. **8**, 214-215 (1964). https://doi.org/10.1016/S0031-9163(64)92001-3

[2] G. Zweig, CERN. Th. preprint. **412** (1964). https://doi.org/10.17181/CERN-TH-401

[3] F. Gross, E. Klempt, S. J. Brodsky, A. J. Buras, V. D. Burkert, G. Heinrich, K. Jakobs, *et al.* Eur. Phys. J. C, **83**, 1125 (2023). https://doi.org/10.1140/epjc/s10052-023-11949-2

[4] Q. Y. Shou, Y. G. Ma, S. Zhang, J. H. Zhu, Y. X. Mao, H. Pei, Z. B. Yin, *et al.* Nucl. Sci. Tech. **35**(12), 219 (2024). https://doi.org/10.1007/s41365-024-01583-2

[5] J. C. Collins, and M. J. Perry, Phys. Rev. Lett. **34**, 1353 (1975). https://doi.org/10.1103/PhysRevLett.34.1353

[6] M. Huang, and P. Zhuang, Symmetry **15**(2), 541 (2023) https://doi.org/10.3390/sym15020541

[7] J. Cleymans, R. V. Gavai, and E. Suhonen, Phys. Rept. **130**, 217 (1986). https://doi.org/10.1016/0370-1573(86)90169-9

[8] M. Frasca, A. Ghoshal, and S. Groote, Phys. Lett. B, **846**, 138209 (2023) https://doi.org/10.1016/j.physletb.2023.138209

[9] M. I. Gorenstein, S. I. Lipskikh, V. K. Petrov, and G. M. Zinovev, Phys. Lett. B **123**, 437 (1983). https://doi.org/10.1016/0370-2693(83)90988-7

[10] M. G. Mustafa, Phys. Lett. B, **318**, 517 (1993). https://doi.org/10.1016/0370-2693(93)91549-3

[11] M. G. Mustafa, D. K. Srivastava, and B. Sinha, Eur. Phys. J. C, **5**, 711 (1998). https://doi.org/10.1007/s100520050314

[12] N. Itoh, Prog. Theor. Phys. **44**, 291 (1970). https://doi.org/10.1143/PTP.44.291

[13] F. Iachello, W. D. Langer, and A. Lande, Nucl. Phys. A, **219**, 612 (1974). https://doi.org/10.1016/0375-9474(74)90122-5

[14] K. Johnson, Acta Phys. Polon. B, **6**, 865 (1975). MIT-CTP-494.

[15] J. W. Harris and B. Müller, Eur. Phys. J. C, **84**(3), 247 (2024). https://doi.org/10.1140/epjc/s10052-024-12533-y

[16] E. Shuryak, Prog. Part. Nucl. Phys. **62**, 48 (2009); G. Baym, Nucl. Phys. A, **956**, 1 (2016). https://doi:10.1016/j.nuclphysa.2016.03.007

[17] M. I. Abdulhamid, B. E. Aboona, J. Adam, J. R. Adams, G. Agakishiev, I. Aggarwal, M. M. Aggarwal, *et al.*, [STAR Collaboration], Phys. Rev. X, **14**(1), 011028 (2024). https://doi.org/10.1103/PhysRevX.14.011028

[18] J. D. Bjorken, Phys. Rev. D, **27**, 140 (1983). https://doi.org/10.1103/PhysRevD.27.140

[19] M. Ladrem and A. Ait-El-Djoudi, Eur. Phys. J. C, **44**, 257 (2005). https://doi.org/10.1140/epjc/s2005-02357-y

[20] A. A. El Djoudi, Can. J. Phys. **91**, 793 (2013). https://doi.org/10.1139/cjp-2012-0578

[21] A. A. El Djoudi, R. Djida, K. Mezouar, and N. Abbad, J. Phys. Conf. Ser. **1766**(1), 012017 (2021) https://doi.org/10.1088/1742-6596/1766/1/012017

[22] B. Moussaoui, A. Ait El Djoudi, and A. Tawfik, Int. J. Theor. Phys. **61**(6), 181 (2022) https://doi.org/10.1007/s10773-022-05159-x

[23] K. Redlich and L. Turko, Z. Phys. C, **5**, 201 (1980). https://doi.org/10.1007/BF01421776

[24] L. Turko, Phys. Lett. B, **104**, 153 (1981). https://doi.org/10.1016/0370-2693(81)90579-7

[25] V. Privman, and M. E. Fisher, J. Stat. Phys. **33**, 385 (1983). https://doi.org/10.1007/BF01009803

[26] K. Binder, and D. P. Landau, Phys. Rev. B, **30**(3), 1477 (1984). https://doi.org/10.1103/PhysRevB.30.1477

[27] K. Binder, Rep. Prog. Phys. **50**, 783 (1987). https://doi.org/10.1088/0034-4885/50/7/001

[28] M. Fukugita, H. Mino, M. Okawa, and A. Ukawa, Nucl. Phys. B Proc. Suppl. **17**, 180 (1990). https://doi.org/10.1016/0920-5632(90)90233-K

[29] M. Henkel, *Conformal Invariance and Critical Phenomena*, Springer, Berlin, Heidelberg (1999). https://doi.org/10.1007/978-3-662-03937-3

[30] J. G. Brankov, D. M. Danchev, and N. S. Tonchev, *Theory of Critical Phenomena in Finite-Size Systems: Scaling and Quantum Effects*, Series in Condensed Matter Physics, Vol. 9, (World Scientific, Singapore, 2000).

[31] R. Balian, and C. Bloch, Annals Phys. **60**, 401 (1970). https://doi.org/10.1016/0003-4916(70)90497-5

[32] D. Agassi, and Y. Avishai, Phys. Lett. B, **74**, 18 (1978). https://doi.org/10.1016/0370-2693(78)90048-5

[33] A. Chodos, R. L. Jaffe, K. Johnson, C. B. Thorn, and V. F. Weisskopf, Phys. Rev. D, **9**, 3471 (1974), https://doi.org/10.1103/PhysRevD.9.3471

[34] Z. Han, B. Chen, and Y. Liu, Chin. Phys. Lett. **37**, 112501 (2020), https://doi.org/10.1088/0256-307X/37/11/112501.

[35] K. Mameda, and K. Takizawa, Phys. Lett. B **847**, 138317 (2023), https://doi.org/10.1016/j.physletb.2023.138317

[36] C. Spieles, H. Stoecker, and C. Greiner, Phys. Rev. C **57**, 908 (1998). https://doi.org/10.1103/PhysRevC.57.908

[37] H. T. Elze, W. Greiner, and J. Rafelski, Phys. Lett. B **124**, 515 (1983), https://doi.org/10.1016/0370-2693(83)91564-2; Z. Phys. C **24**, 361 (1984). https://doi.org/10.1007/BF01410375

[38] H. T. Elze and W. Greiner, Phys. Lett. B, **179**, 385 (1986). https://doi.org/10.1016/0370-2693(86)90498-3

[39] E. N. Rodionov, *The MIT bag model in nuclear and particle physics*, PhD Thesis, University of Adelaide, Adelaide, Australia (1997).

[40] X. Li, S. Shu, and J.-R. Li, Phys. Rev. C, **105**, 045203 (2022), https://doi.org/10.1103/PhysRevC.105.045203

[41] M. S. Berger, and R. L. Jaffe, "Radioactivity in strange quark matter," Phys. Rev. C, **35**, 213 (1987), ibid. **44**, 566 (1991). https://doi.org/10.1103/PhysRevC.35.213

[42] J. Madsen, Phys. Rev. D, **50**, 3328 (1994). https://doi.org/10.1103/PhysRevD.50.3328

[43] E. Farhi, and R. L. Jaffe, Phys. Rev. D, **30**, 2379 (1984). https://doi.org/10.1103/PhysRevD.30.2379

[44] S. A. Fulling, and G. Kennedy, "On the Casimir effect and the heat kernel expansion," Trans. Amer. Math. Soc. **310**, 313 (1988). https://doi.org/10.1090/S0002-9947-1988-0965756-7

[45] K. Binder, and D. W. Heermann, *Monte Carlo Simulation in Statistical Physics: An Introduction*, 6th ed., Graduate Texts in Physics, (Springer, Cham, 2019). https://doi.org/10.1007/978-3-030-10758-1

[46] H. Meyer-Ortmanns, Rev. Mod. Phys. **68**, 473 (1996). https://doi.org/10.1103/RevModPhys.68.473

[47] M. S. Challa, D. P. Landau, and K. Binder, Phys. Rev. B, **34**, 1841 (1986). https://doi.org/10.1103/PhysRevB.34.1841

АНАЛІЗ СКІНЧЕННО-РОЗМІРНОГО МАШТАБУВАННЯ ДЛЯ ФАЗОВОГО ПЕРЕХОДУ КХД З ДЕКОНФАЙНМЕНТОМ ДО КОЛЬОРОВО-СИНГЛЕТНОЇ КВАРК-ГЛЮОННОЇ ПЛАЗМИ З ТРЬОМА КВАРКОВИМИ АРОМАТАМИ u, d, s

Хаєт Сахі[1,2], Амаль Айт Ель Джуді[2], Абделькадер Чеддад[2]
[1] *Університет Бумердеса імені М'хаммеда Бугари, Алжир*
[2] *Лабораторія фізики частинок та статистичної фізики, Вища нормальна школа Куби, Б.П. 92, 16050, В'є-Куба, Алжир, Алжир*

У цій роботі ми обчислюємо функцію розподілу кварк-глюонної плазми (QGP), спроектованої на кольорове синглетне представлення SU(3), використовуючи метод проекції, в межах густини станів для кварків та глюонів, заданої наближенням множинного відбиття (MRE). Ми досліджуємо вплив включення членів площі та кривизни, на додаток до члена об'єму в густину станів, на поведінку кількох фізичних величин, що характеризують деконфінуючий фазовий перехід від адронної газової фази масивних піонів до фази кварк-глюонної плазми (КГП), що складається з глюонів, безмасових верхніх та нижніх кварків, масивних дивних кварків разом з їхніми антикварками, в рамках моделі Бега та феноменологічної моделі співіснування фаз. За допомогою аналізу масштабування скінченних розмірів ми досліджуємо поведінку деяких показників масштабування, що стосуються деконфінуючого фазового переходу, що відбувається в скінченному об'ємі, особливо показника масштабування відносно зсуву ефективної температури переходу, розглядаючи внески лише члена кривизни, лише члена площі в густину станів, крім члена об'єму, а потім внесок усіх трьох членів, аналізуючи значення критичного показника зсуву λ порівняно з тим, що було отримано раніше з використанням лише члена об'єму в густині станів кварків та глюонів.
Ключові слова: *деконфінуючий фазовий перехід; кварк-глюонна плазма; синглетність кольору; проекційний метод; аналіз масштабування скінченних розмірів*

EAST EUROPEAN JOURNAL OF PHYSICS. 3. 160–178 (2026)
DOI: 10.26565/2312-4334-2026-3-14 ISSN 2312-4334

OPTICAL SOLITONS FOR THE CONCATENATION MODEL WITH DIFFERENTIAL GROUP DELAY BY LIE SYMMETRY AND KUMAR-MALIK APPROACH

Rajveer Singhay[1], Sachin Kumar[1], Mohamed E. M. Alngar[2], Reham M. A. Shohib[3], Lina S. Calucag[4], Anjan Biswas[5,6,7,8,9*]

[1]*Department of Mathematics and Statistics, Central University of Punjab, Bathinda, 151401, Punjab, India*
[2]*Mathematics Education Program, Faculty of Education and Arts, Sohar University, Sohar 311, Oman*
[3]*Basic Science Department, Faculty of Economics and Business Administration, Innovation University, Sharqia, Egypt*
[4]*Department of Mathematics and Science, University of Technology Bahrain, Kingdom of Bahrain*
[5]*Department of Mathematics and Physics, Grambling State University, Grambling, LA–71245, USA*
[6]*Department of Mathematics, Faculty of Science, Karadeniz Technical University, Trabzon—61080, Türkiye*
[7]*Department of Physics and Electronics, Khazar University, Baku, AZ—1096, Azerbaijan*
[8]*Department of Mathematics and Applied Mathematics, Sefako Makgatho Health Sciences University, Medunsa—0204, Pretoria, South Africa*
[9]*Applied Science Research Center, Applied Science Private University, Amman—11937, Jordan*
[*]*Corresponding Author e-mail: biswas.anjan@gmail.com*

Received March 27, 2026; revised August 15, 2026; accepted August 23, 2026

This work examines a generalized concatenation model for birefringent optical fibers and obtains new exact soliton solutions. Using Lie symmetry analysis, the coupled evolution equations are transformed through suitable similarity variables into a manageable system of ordinary differential equations. The resulting reduced system is then treated with the Kumar–Malik method to derive multiple classes of explicit solutions written in Jacobi elliptic, bright soliton, dark soliton, and trigonometric solutions. With appropriate parameter restrictions, these classes simplify to the familiar bright, dark, and periodic soliton waves. To illustrate the physical behavior of the derived structures, representative plots are presented that highlight their propagation features and qualitative stability. Overall, combining symmetry reduction with the Kumar–Malik scheme expands the catalogue of analytical solutions for the concatenation model and deepens understanding of nonlinear pulse dynamics in birefringent media.

Keywords: *Concatenation framework; Lie group symmetry analysis; Kumar–Malik technique; Optical soliton waves; Birefringent fiber media; Jacobi elliptic function solutions*

1. INTRODUCTION

Nonlinear pulse propagation in optical fibers remains a cornerstone of modern nonlinear optics and mathematical physics, particularly in parameter regimes where dispersion, birefringence, and nonlinearity cooperate to generate persistent coherent structures such as solitons, breathers, and rogue waves. With the advent of ultrashort-pulse sources and broadband transmission, higher-order dispersive and nonlinear effects become non-negligible, which naturally motivates the analysis of generalized Schrödinger-type evolution equations and their solution families.

At the modeling level, the nonlinear Schrödinger equation (NLSE) provides a canonical framework for describing envelope dynamics in weakly nonlinear dispersive media, and continues to be refined and applied in diverse optical settings [3, 4]. Beyond the standard NLSE, integrable higher-order extensions have been intensively studied because they preserve analytical tractability while capturing additional physical mechanisms. In this direction, Ankiewicz and Akhmediev presented a higher-order integrable evolution equation together with its soliton solutions, illustrating how higher-order corrections alter waveform characteristics without destroying integrability [1]. Closely related extended NLSE models that include higher-order odd and even terms were further shown to admit extreme localized events, including rogue-wave solutions [2]. Moreover, the integrable quintic nonlinear Schrödinger hierarchy enriches the nonlinear landscape through quintic contributions: soliton solutions were constructed in [9], while breather-to-soliton conversions and breather interactions were investigated in [10, 11]. Collectively, these developments emphasize that higher-order and quintic terms are

Cite as: R. Singhay, S. Kumar, M.E.M. Alngar, R.M.A. Shohib, L.S. Calucag, A. Biswas, East Eur. J. Phys. 3, 160 (2026), https://doi.org/10.26565/2312-4334-2026-3-14

not merely small perturbations; rather, they can substantially broaden the admissible classes of localized structures and transition scenarios.

Another important strand of research concerns unified descriptions that connect several prominent Schrödinger-type equations within a single formalism. In particular, concatenation-type models provide a coupled framework that can incorporate higher-order dispersion and nonlinear corrections systematically, while linking to celebrated integrable equations such as the NLSE [3, 4], the Lakshmanan–Porsezian–Daniel (LPD) equation [5, 6], and the Sasa–Satsuma equation (SSE) [7, 8]. Recent studies have also highlighted the relevance of concatenation settings for realistic birefringent configurations by incorporating differential group delay and constructing corresponding optical soliton solutions [12, 13]. Despite the growing literature, explicit closed-form solutions remain of continuing value: they provide benchmarks for numerical algorithms, enable parametric studies of waveform switching (e.g., bright versus dark profiles), and clarify how higher-order coefficients shape pulse evolution.

Motivated by these considerations, the present work investigates the coupled concatenation system (Eqs. (1)–(2)) for the complex envelopes $q(x,t)$ and $r(x,t)$, which represent two orthogonally polarized field components. By exploiting Lie symmetries, we determine appropriate invariants that transform the governing PDE system into an equivalent ODE system. The reduced equations are then solved exactly using the Kumar–Malik technique. The resulting waveforms are expressed in Jacobi elliptic, hyperbolic, and trigonometric forms and, under suitable parameter constraints, yield bright-, dark-, and periodic-soliton profiles. Finally, representative plots are provided to illustrate characteristic propagation features and to demonstrate the influence of key physical and model parameters.

1.1. Governing Model

In this study, we consider the following coupled concatenation model [12, 13]:

$$
\begin{aligned}
&iq_t + a_1 q_{xx} + \left(b_1|q|^2 + c_1|r|^2\right)q + c_{11}\Big[\sigma_{11}q_{xxxx} + \{\alpha_1(q_x)^2 + \mathfrak{w}_1(r_x)^2\}q^* \\
&\quad + (\gamma_1|q_x|^2 + \lambda_1|r_x|^2)q + (\delta_1|q|^2 + \zeta_1|r|^2)q_{xx} + (\mu_1 q^2 + \rho_1 r^2)q^*_{xx} \\
&\quad + (f_1|q|^4 + g_1|q|^2|r|^2 + h_1|r|^4)q\Big] + ic_{21}\Big[\sigma_{71}q_{xxx} + (\eta_1|q|^2 + \theta_1|r|^2)q_x \\
&\quad + (\varepsilon_1 q^2 + \tau_1 r^2)q^*_x\Big] = 0,
\end{aligned}
\tag{1}
$$

$$
\begin{aligned}
&ir_t + a_2 r_{xx} + \left(b_2|r|^2 + c_2|q|^2\right)r + c_{12}\Big[\sigma_{12}r_{xxxx} + \{\alpha_2(r_x)^2 + \mathfrak{w}_2(q_x)^2\}r^* \\
&\quad + (\gamma_2|r_x|^2 + \lambda_2|q_x|^2)r + (\delta_2|r|^2 + \zeta_2|q|^2)r_{xx} + (\mu_2 r^2 + \rho_2 q^2)r^*_{xx} \\
&\quad + (f_2|r|^4 + g_2|r|^2|q|^2 + h_2|q|^4)r\Big] + ic_{22}\Big[\sigma_{72}r_{xxx} + (\eta_2|r|^2 + \theta_2|q|^2)r_x \\
&\quad + (\varepsilon_2 r^2 + \tau_2 q^2)r^*_x\Big] = 0.
\end{aligned}
\tag{2}
$$

In this system, $q(x,t)$ and $r(x,t)$ represent the complex slowly varying envelopes associated with two mutually orthogonal polarization modes. The coefficients a_1 and a_2 characterize the group-velocity dispersion, while b_j and c_j $(j = 1, 2)$ measure self-phase modulation and cross-phase modulation, respectively. The set of parameters σ, α, $\mathfrak{w}$, γ, λ, δ, ζ, μ, ρ, f, g, and h models higher-order mechanisms such as nonlinear dispersion, self-frequency shifting, and fourth-order corrections. Hence, the coupled system captures the dynamics of birefringent optical pulses influenced by cubic–quartic nonlinearities together with third- and fourth-order dispersion.

In this study, we employ Lie symmetry analysis for the concatenation model (1)–(2). The admitted symmetries provide suitable similarity transformations that reduce the coupled PDE system to a tractable set of ordinary differential equations. The reduced system is then treated analytically via the Kumar–Malik method, leading to several new classes of exact solutions in Jacobi elliptic, hyperbolic, and trigonometric forms. For appropriate choices of the governing parameters, these solution families recover the familiar bright-, dark-, and periodic-soliton profiles reported in the literature.

Graphical illustrations are presented to highlight the propagation features of the derived solutions and to explore the impact of the physical parameters on soliton amplitude, width, and robustness. These findings broaden the available catalogue of analytical solutions for the concatenation model and offer further insight into nonlinear pulse evolution in birefringent optical fibers.

The remainder of this paper is organized as follows. In Section 2, we perform the Lie symmetry analysis of the model and determine the associated infinitesimal generators. Section 3 is devoted to the similarity reductions that convert the governing PDE system into a reduced set of ODEs. In Section 4, the Kumar–Malik method is implemented to obtain exact analytical soliton solutions. Section 5 presents representative plots and discusses their physical implications. Finally, Section 6 summarizes the main findings and outlines possible directions for future work.

2. LIE SYMMETRY ANALYSIS

The Lie symmetry approach [14] provides a systematic framework for reducing nonlinear partial differential equations to ordinary differential equations by exploiting their admitted continuous symmetry groups. After determining the infinitesimal symmetry generators, one constructs the associated invariants (similarity variables), which transform the original PDE into a reduced equation of lower dimensionality. In the present work, this methodology is applied to the concatenation model (1) to derive its symmetry algebra and to obtain the corresponding similarity reductions.

Next, we introduce the real-valued decompositions

$$q(t,x) = u_1(t,x) + i\, v_1(t,x), \qquad r(t,x) = u_2(t,x) + i\, v_2(t,x),$$

and substitute them into Eq. (1). Separating the resulting expression into its real and imaginary components leads to the following system of partial differential equations:

$$\begin{aligned}
&c_{1l}\,\sigma_{1l}\,(v_l)_{xxxx} + c_{2l}\,\sigma_{7l}\,(u_l)_{xxx} + \Big(c_{1l}(\mu_l+\delta_l)\,v_l^2 - c_{1l}(\mu_l-\delta_l)\,u_l^2 - c_{1l}(\rho_l-\zeta_l)\,u_m^2\\
&\quad + c_{1l}(\rho_l+\zeta_l)\,v_m^2 + a_l\Big)(v_l)_{xx} + 2c_{1l}\big(\mu_l u_l v_l + \rho_l u_m v_m\big)(u_l)_{xx} - v_l c_{1l}(\alpha_l-\gamma_l)(u_{l,x})^2\\
&\quad + \Big(2c_{1l}\alpha_l(v_{l,x})u_l + c_{2l}\big((\eta_l-\varepsilon_l)v_l^2 + (\eta_l+\varepsilon_l)u_l^2 + (\tau_l+\theta_l)u_m^2 - v_m^2(\tau_l-\theta_l)\big)\Big)(u_{l,x})\\
&\quad + v_l c_{1l}(\alpha_l+\gamma_l)(v_{l,x})^2 + 2c_{2l}\big(\tau_l u_m v_m + \varepsilon_l u_l v_l\big)(v_{l,x}) - v_l c_{1l}(\mathfrak{w}_l-\lambda_l)(u_{m,x})^2\\
&\quad + 2c_{1l}\mathfrak{w}_l(u_{m,x})(v_{m,x})u_l + v_l c_{1l}(\mathfrak{w}_l+\lambda_l)(v_{m,x})^2 + u_{l,t}\\
&\quad + c_{1l} f_l v_l^5 + \big(2f_l c_{1l} u_l^2 + g_l c_{1l} u_m^2 + g_l c_{1l} v_m^2 + b_l\big)v_l^3\\
&\quad + \Big(f_l c_{1l} u_l^4 + (g_l c_{1l} u_m^2 + g_l c_{1l} v_m^2 + b_l)u_l^2 + h_l c_{1l} u_m^4 + (2h_l c_{1l} v_m^2 + c_l)u_m^2 + h_l c_{1l} v_m^4 + c_l v_m^2\Big)v_l = 0,\\
&c_{1l}\,\sigma_{1l}\,(u_l)_{xxxx} - c_{2l}\,\sigma_{7l}\,(v_l)_{xxx} + \Big(c_{1l}(\mu_l+\delta_l)\,u_l^2 - c_{1l}(\mu_l-\delta_l)\,v_l^2 + c_{1l}(\rho_l+\zeta_l)\,u_m^2\\
&\quad - c_{1l}(\rho_l-\zeta_l)\,v_m^2 + a_l\Big)(u_l)_{xx} + 2c_{1l}\big(\mu_l u_l v_l + \rho_l u_m v_m\big)(v_l)_{xx} - u_l c_{1l}(\alpha_l-\gamma_l)(v_{l,x})^2\\
&\quad + \Big(2c_{1l}\alpha_l(u_{l,x})v_l - c_{2l}\big((\eta_l-\varepsilon_l)u_l^2 + (\eta_l+\varepsilon_l)v_l^2 + (-\tau_l+\theta_l)u_m^2 + v_m^2(\tau_l+\theta_l)\big)\Big)(v_{l,x})\\
&\quad + u_l c_{1l}(\alpha_l+\gamma_l)(u_{l,x})^2 - 2c_{2l}\big(\tau_l u_m v_m + \varepsilon_l u_l v_l\big)(u_{l,x})\\
&\quad + u_l c_{1l}(\mathfrak{w}_l+\lambda_l)(u_{m,x})^2 + 2c_{1l}\mathfrak{w}_l(u_{m,x})(v_{m,x})v_l - u_l c_{1l}(\mathfrak{w}_l-\lambda_l)(v_{m,x})^2 - v_{l,t}\\
&\quad + c_{1l} f_l u_l^5 + \big(g_l c_{1l} u_m^2 + 2f_l c_{1l} v_l^2 + g_l c_{1l} v_m^2 + b_l\big)u_l^3\\
&\quad + \Big(f_l c_{1l} v_l^4 + (g_l c_{1l} u_m^2 + g_l c_{1l} v_m^2 + b_l)v_l^2 + h_l c_{1l} u_m^4 + (2h_l c_{1l} v_m^2 + c_l)u_m^2 + h_l c_{1l} v_m^4 + c_l v_m^2\Big)u_l = 0,
\end{aligned} \tag{3}$$

where $l \in \{1,2\}$ and $m = 3 - l$ denotes the complementary index.

Next, we introduce a one-parameter Lie group of infinitesimal transformations defined by:

$$\begin{aligned}
x^* &= x + \epsilon\chi(x,t,u_1,v_1,u_2,v_2) + O(\epsilon^2),\\
t^* &= t + \epsilon\Theta(x,t,u_1,v_1,u_2,v_2) + O(\epsilon^2),\\
{u_1}^* &= u_1 + \epsilon\Psi_1(x,t,u_1,v_1,u_2,v_2) + O(\epsilon^2),\\
{v_1}^* &= v_1 + \epsilon\Phi_1(x,t,u_1,v_1,u_2,v_2) + O(\epsilon^2), \qquad (4)\\
{u_2}^* &= u_2 + \epsilon\Psi_2(x,t,u_1,v_1,u_2,v_2) + O(\epsilon^2),\\
{v_2}^* &= v_2 + \epsilon\Phi_2(x,t,u_1,v_1,u_2,v_2) + O(\epsilon^2), \qquad (5)
\end{aligned}$$

Here, χ, Θ, Ψ_1, Φ_1, Ψ_2, and Φ_2 denote the infinitesimal generator components associated with the variables x, t, u_1, v_1, u_2, and v_2, respectively, and $\epsilon \in \mathbb{R}$ is the group parameter. These transformations are required to leave Eq. (3) invariant under the induced Lie-group action.

The corresponding infinitesimal vector field is given by:

$$X = \chi\frac{\partial}{\partial x} + \Theta\frac{\partial}{\partial t} + \sum_{l=1}^{2}\left(\Psi_l\frac{\partial}{\partial u_l} + \Phi_l\frac{\partial}{\partial v_l}\right). \tag{6}$$

To compute the admitted symmetries, we impose the standard invariance condition:

$$\mathrm{pr}^{(4)}(X)(\Delta)\big|_{\Delta=0} = 0, \tag{7}$$

where $\mathrm{pr}^{(4)}X$ denotes the fourth-order prolongation of the vector field X, defined by:

$$\begin{aligned}\mathrm{pr}^{(4)}X =& X + \sum_{l=1}^{2}\left(\Psi_l^t\frac{\partial}{\partial u_{l,t}} + \Psi_l^x\frac{\partial}{\partial u_{l,x}} + \Psi_l^{xx}\frac{\partial}{\partial u_{l,xx}} + \Psi_l^{xxx}\frac{\partial}{\partial u_{l,xxx}} + \Psi_l^{xxxx}\frac{\partial}{\partial u_{l,xxxx}}\right)\\ &+ \sum_{l=1}^{2}\left(\Phi_l^t\frac{\partial}{\partial v_{l,t}} + \Phi_l^x\frac{\partial}{\partial v_{l,x}} + \Phi_l^{xx}\frac{\partial}{\partial v_{l,xx}} + \Phi_l^{xxx}\frac{\partial}{\partial v_{l,xxx}} + \Phi_l^{xxxx}\frac{\partial}{\partial v_{l,xxxx}}\right).\end{aligned}$$

The coefficients of the prolonged vector field are evaluated using the total derivative operators:

$$\begin{aligned}\Psi_l^t &= D_t(\Psi_l) - D_t(\chi)\,u_{l,x} - D_t(\Theta)\,u_{l,t},\\ \Phi_l^t &= D_t(\Phi_l) - D_t(\chi)\,v_{l,x} - D_t(\Theta)\,v_{l,t},\\ \Psi_l^x &= D_x(\Psi_l) - D_x(\chi)\,u_{l,x} - D_x(\Theta)\,u_{l,t},\\ \Phi_l^x &= D_x(\Phi_l) - D_x(\chi)\,v_{l,x} - D_x(\Theta)\,v_{l,t},\\ \Psi_l^{xx} &= D_x(\Psi_l^x) - D_x(\chi)\,u_{l,xx} - D_x(\Theta)\,u_{l,xt},\\ \Phi_l^{xx} &= D_x(\Phi_l^x) - D_x(\chi)\,v_{l,xx} - D_x(\Theta)\,v_{l,xt},\\ \Psi_l^{xxx} &= D_x(\Psi_l^{xx}) - D_x(\chi)\,u_{l,xxx} - D_x(\Theta)\,u_{l,xxt},\\ \Phi_l^{xxx} &= D_x(\Phi_l^{xx}) - D_x(\chi)\,v_{l,xxx} - D_x(\Theta)\,v_{l,xxt},\\ \Psi_l^{xxxx} &= D_x(\Psi_l^{xxx}) - D_x(\chi)\,u_{l,xxxx} - D_x(\Theta)\,u_{l,xxxt},\\ \Phi_l^{xxxx} &= D_x(\Phi_l^{xxx}) - D_x(\chi)\,v_{l,xxxx} - D_x(\Theta)\,v_{l,xxxt},\end{aligned}$$

Here, D_x and D_t are the total-derivative operators with respect to x and t, respectively, as described in [15]. Applying the invariance condition (7) to Eq. (3) yields:

$$
\begin{aligned}
&\Big(\big((\mu_l+\delta_l)\,v_l^2+(-\mu_l+\delta_l)\,u_l^2+(-\rho_l+\zeta_l)\,u_m^2+(\rho_l+\zeta_l)\,v_m^2\big)\,c_{1l}+a_l\Big)\,\Phi_l^{\{xx\}}+2\,\Psi_l^{\{xx\}}\,c_{1l}\,(\mu_l u_l v_l+\rho_l u_m v_m)\\
&+\Phi_l^{\{xxxx\}}\,c_{1l}\,\sigma_{1l}+\Psi_l^{\{xxx\}}\,c_{2l}\,\sigma_{7l}+\Big(\big(-2\,u_{l,x}(\alpha_l-\gamma_l)\,v_l+2\,v_{l,x}\alpha_l\,u_l\big)\,c_{1l}+c_{2l}\big((\eta_l-\varepsilon_l)v_l^2+(\eta_l+\varepsilon_l)u_l^2\\
&+(\tau_l+\theta_l)u_m^2-(\tau_l-\theta_l)v_m^2\big)\Big)\,\Psi_l^x+\Big(\big(2\,v_{l,x}(\alpha_l+\gamma_l)\,v_l+2\,u_{l,x}\alpha_l\,u_l\big)\,c_{1l}+2\,c_{2l}(\tau_l u_m v_m+\varepsilon_l u_l v_l)\Big)\,\Phi_l^x\\
&+2\big(v_{m,x}(\mathfrak{w}_l+\lambda_l)\,v_l+u_{m,x}\mathfrak{w}_l\,u_l\big)\,c_{1l}\,\Phi_m^x-2\big(u_{m,x}(\mathfrak{w}_l-\lambda_l)\,v_l-v_{m,x}\mathfrak{w}_l\,u_l\big)\,c_{1l}\,\Psi_m^x+\Psi_l^t\\
&+\Big(5\,\Phi_l\,f_l\,v_l^4+\big(2\Phi_m\,g_l\,v_m+4\Psi_l\,f_l\,u_l+2\Psi_m\,g_l\,u_m\big)\,v_l^3+\big(6f_l\,u_l^2+3g_l\,u_m^2+3g_l\,v_m^2\big)\,\Phi_l\,v_l^2\\
&+\Big((2\mu_l+2\delta_l)\,v_{l,xx}\,\Phi_l+4\Psi_l\,f_l\,u_l^3+(2\Phi_m\,g_l\,v_m+2\Psi_m\,g_l\,u_m)\,u_l^2+(2\Psi_l\,g_l\,u_m^2+2\Psi_l\,g_l\,v_m^2)\,u_l\\
&+4\Psi_m\,h_l\,u_m^3+4\Phi_m\,h_l\,u_m^2 v_m+4\Psi_m\,h_l\,u_m v_m^2+4\Phi_m\,h_l\,v_m^3+2\Psi_l\,\mu_l\,u_{l,xx}\Big)\,v_l+\Big(f_l\,u_l^4+(g_l\,u_m^2+g_l\,v_m^2)\,u_l^2\\
&+2\mu_l u_l\,u_{l,xx}+h_l\,u_m^4+2h_l u_m^2 v_m^2+h_l v_m^4+(-\alpha_l+\gamma_l)\,u_{l,x}^2+(\alpha_l+\gamma_l)\,v_{l,x}^2+(-u_{m,x}^2+v_{m,x}^2)\mathfrak{w}_l+u_{m,x}^2\lambda_l\\
&+v_{m,x}^2\lambda_l\Big)\,\Phi_l+(-2\mu_l+2\delta_l)\,v_{l,xx}\,\Psi_l\,u_l+\big(2\rho_l\,u_{l,xx}\,\Phi_m+(-2\rho_l+2\zeta_l)\,v_{l,xx}\,\Psi_m\big)\,u_m\\
&+\big((2\rho_l+2\zeta_l)\,v_{l,xx}\,\Phi_m+2\Psi_m\,\rho_l\,u_{l,xx}\big)\,v_m+2\Psi_l\,\alpha_l\,u_{l,x}v_{l,x}+2\Psi_l\,\mathfrak{w}_l\,u_{m,x}v_{m,x}\Big)\,c_{1l}+3\Phi_l\,b_l\,v_l^2\\
&+\Big((2\eta_l-2\varepsilon_l)\,u_{l,x}\,c_{2l}\,\Phi_l+2c_{2l}\Psi_l\,v_{l,x}\,\varepsilon_l+2\Psi_m\,c_l\,u_m+2\Phi_m\,c_l\,v_m+2\Psi_l\,b_l\,u_l\Big)\,v_l\\
&+\big(2c_{2l}u_l\varepsilon_l v_{l,x}+b_l\,u_l^2+c_l\,u_m^2+c_l\,v_m^2\big)\,\Phi_l+(2\eta_l+2\varepsilon_l)\,\Psi_l\,u_{l,x}\,c_{2l}\,u_l\\
&+\big((2\tau_l+2\theta_l)\Psi_m\,u_{l,x}+2\Phi_m\,\tau_l\,v_{l,x}\big)\,c_{2l}\,u_m+\big((-2\tau_l+2\theta_l)\Phi_m\,u_{l,x}+2\Psi_m\,\tau_l\,v_{l,x}\big)\,c_{2l}\,v_m\;=\;0,\\
&\Big(\big((\mu_l+\delta_l)\,u_l^2+(-\mu_l+\delta_l)\,v_l^2+(\rho_l+\zeta_l)\,u_m^2-(\rho_l-\zeta_l)\,v_m^2\big)\,c_{1l}+a_l\Big)\,\Psi_l^{\{xx\}}+2\,\Phi_l^{\{xx\}}\,c_{1l}\,(\mu_l u_l v_l+\rho_l u_m v_m)\\
&+\Psi_l^{\{xxxx\}}\,c_{1l}\,\sigma_{1l}-\Phi_l^{\{xxx\}}\,c_{2l}\,\sigma_{7l}+\Big(\big(-2\,v_{l,x}(\alpha_l-\gamma_l)\,u_l+2\,v_l\,u_{l,x}\alpha_l\big)\,c_{1l}+c_{2l}\big((-\eta_l+\varepsilon_l)u_l^2\\
&+(-\eta_l-\varepsilon_l)v_l^2+(\tau_l-\theta_l)u_m^2-(\tau_l+\theta_l)v_m^2\big)\Big)\,\Phi_l^x+\Big(\big(2\,u_{l,x}(\alpha_l+\gamma_l)\,u_l+2\,v_l\,v_{l,x}\alpha_l\big)\,c_{1l}\\
&-2\,c_{2l}(\tau_l u_m v_m+\varepsilon_l u_l v_l)\Big)\,\Psi_l^x+2\big(-v_{m,x}(\mathfrak{w}_l-\lambda_l)\,u_l+v_l\,u_{m,x}\mathfrak{w}_l\big)\,c_{1l}\,\Phi_m^x+2\,c_{1l}\big(u_{m,x}(\mathfrak{w}_l+\lambda_l)\,u_l\\
&+v_l\,v_{m,x}\mathfrak{w}_l\big)\,\Psi_m^x-\Phi_l^t+\Big(5\,\Psi_l\,f_l\,u_l^4+\big(4\Phi_l\,f_l\,v_l+2\Phi_m\,g_l\,v_m+2\Psi_m\,g_l\,u_m\big)\,u_l^3\\
&+\big(6f_l\,v_l^2+3g_l\,u_m^2+3g_l\,v_m^2\big)\,\Psi_l\,u_l^2+\Big((2\mu_l+2\delta_l)\,u_{l,xx}\,\Psi_l+4\Phi_l\,f_l\,v_l^3+(2\Phi_m\,g_l\,v_m+2\Psi_m\,g_l\,u_m)\,v_l^2\\
&+(2\Phi_l\,g_l\,u_m^2+2\Phi_l\,g_l\,v_m^2)\,v_l+4\Psi_m\,h_l\,u_m^3+4\Phi_m\,h_l\,u_m^2 v_m+4\Psi_m\,h_l\,u_m v_m^2+4\Phi_m\,h_l\,v_m^3+2\Phi_l\,\mu_l\,v_{l,xx}\Big)\,u_l\\
&+\Big(f_l\,v_l^4+(g_l\,u_m^2+g_l\,v_m^2)\,v_l^2+2\mu_l v_l\,v_{l,xx}+h_l\,u_m^4+2h_l u_m^2 v_m^2+h_l v_m^4+(-\alpha_l+\gamma_l)\,v_{l,x}^2\\
&+(\alpha_l+\gamma_l)\,u_{l,x}^2+(u_{m,x}^2-v_{m,x}^2)\mathfrak{w}_l+u_{m,x}^2\lambda_l+v_{m,x}^2\lambda_l\Big)\,\Psi_l+(-2\mu_l+2\delta_l)\,u_{l,xx}\,\Phi_l\,v_l\\
&+\big(2\rho_l\,v_{l,xx}\,\Phi_m+(2\rho_l+2\zeta_l)\,u_{l,xx}\,\Psi_m\big)\,u_m+\big((-2\rho_l+2\zeta_l)\,u_{l,xx}\,\Phi_m+2\Psi_m\,\rho_l\,v_{l,xx}\big)\,v_m\\
&+2\Phi_l\,\alpha_l\,u_{l,x}v_{l,x}+2\Phi_l\,\mathfrak{w}_l\,u_{m,x}v_{m,x}\Big)\,c_{1l}+3\Psi_l\,b_l\,u_l^2+\Big((-2\eta_l+2\varepsilon_l)\,v_{l,x}\,c_{2l}\,\Psi_l-2c_{2l}\Phi_l\,u_{l,x}\,\varepsilon_l\\
&+2\Psi_m\,c_l\,u_m+2\Phi_l\,b_l\,v_l+2\Phi_m\,c_l\,v_m\Big)\,u_l+\big(-2c_{2l}v_l\varepsilon_l u_{l,x}+b_l\,v_l^2+c_l\,u_m^2+c_l\,v_m^2\big)\,\Psi_l\\
&+(-2\eta_l-2\varepsilon_l)\,\Phi_l\,v_{l,x}\,c_{2l}\,v_l+\big((2\tau_l-2\theta_l)\Psi_m\,v_{l,x}-2\Phi_m\,\tau_l\,u_{l,x}\big)\,c_{2l}\,u_m+\big((-2\tau_l-2\theta_l)\Phi_m\,v_{l,x}\\
&-2\Psi_m\,\tau_l\,u_{l,x}\big)\,c_{2l}\,v_m\;=\;0
\end{aligned}
\tag{8}
$$

where $l=1,2$ and $m=3-l$.

Substituting the expressions for $(\Psi_l^x,\Phi_l^x,\Psi_l^{\{xx\}},\Phi_l^{\{xx\}},\Psi_l^t,\Phi_l^t,\dots)$ into Eq. (8), we obtain the following determining system:

$$
\begin{aligned}
&\Psi_{1t} = 0, \quad \Psi_{1u_1} = 0, \quad \Psi_{1u_2} = 0, \quad \Psi_{1v_1} = \frac{\Psi_1}{v_1}, \quad \Psi_{1v_2} = 0, \quad \Psi_{1x} = 0,\\
&\Theta_t = 0, \quad \Theta_{u_1} = 0, \quad \Theta_{u_2} = 0, \quad \Theta_{v_1} = 0, \quad \Theta_{v_2} = 0, \quad \Theta_x = 0,\\
&\chi_t = 0, \quad \chi_{u_1} = 0, \quad \chi_{u_2} = 0, \quad \chi_{v_1} = 0, \quad \chi_{v_2} = 0, \quad \chi_x = 0,\\
&\Psi_2 = \Psi_1 \frac{v_2}{v_1}, \quad \Phi_1 = -\Psi_1 \frac{u_1}{v_1}, \quad \Phi_2 = -\Psi_1 \frac{u_2}{v_1}.
\end{aligned}
\tag{9}
$$

Throughout, subscripts such as t, x, u_1, u_2, v_1, and v_2 indicate partial differentiation with respect to the corresponding variables; for instance,

$$\Psi_{1t} = \frac{\partial \Psi_1}{\partial t}.$$

Solving the determining system (9) yields the following infinitesimal symmetries:

$$
\begin{aligned}
&\Psi_l(x, t, u_1, v_1, u_2, v_2) = C_3\, v_l, \qquad \Phi_l(x, t, u_1, v_1, u_2, v_2) = -C_3\, u_l,\\
&\Theta(x, t, u_1, v_1, u_2, v_2) = C_1, \qquad \chi(x, t, u_1, v_1, u_2, v_2) = C_2,
\end{aligned}
\qquad \text{where } l = 1, 2.
\tag{10}
$$

Substituting the obtained expressions for χ, Θ, Ψ_l, and Φ_l into the infinitesimal generator produces three basis vector fields that span the symmetry algebra of system (3):

$$
\begin{aligned}
X_1 &= \partial_t,\\
X_2 &= \partial_x,\\
X_3 &= \sum_{l=1}^{2} \left(v_l \partial_{u_l} - u_l \partial_{v_l} \right).
\end{aligned}
\tag{11}
$$

3. SYMMETRY REDUCTION

We now perform the symmetry reduction of Eq. (1) associated with the vector field $\varrho_1 X_1 + \varrho_2 X_2 + X_3$, where ϱ_1 and ϱ_2 are arbitrary constants, is obtained from Lagrange's auxiliary equations:

$$\frac{dt}{\varrho_1} = \frac{dx}{\varrho_2} = \frac{du_1}{v_1} = \frac{dv_1}{-u_1} = \frac{du_2}{v_2} = \frac{dv_2}{-u_2}. \tag{12}$$

Solving Eq. (12) gives the similarity variables

$$\xi = \varrho_1 x - \varrho_2 t, \quad u_l(x, t) = P_l(\xi) \cos Q, \qquad v_l(x, t) = P_l(\xi) \sin Q, \tag{13}$$

where $Q = -\kappa x + \omega t + \theta_0$ and $l = 1, 2$.

From Eq. (13), we obtain

$$
\begin{aligned}
q(x, t) &= P_1(\xi) e^{iQ},\\
r(x, t) &= P_2(\xi) e^{iQ}.
\end{aligned}
\tag{14}
$$

Substituting the similarity form (14) into Eq. (1) and splitting the result into its real and imaginary components leads to the following reduced system of ordinary differential equations:

for $l = 1, 2,\ m = 3 - l$:

$$\begin{aligned}
&\big(-4\,c_{1l}\,\kappa\,\sigma_{1l} + c_{2l}\,\sigma_{7l}\big)\,\varrho_1^3\,\frac{d^3P_l}{d\xi^3} + \frac{dP_l}{d\xi}\Bigg\{\varrho_1\Big[\,4\,c_{1l}\,\sigma_{1l}\,\kappa^3 - 3\,c_{2l}\,\sigma_{7l}\,\kappa^2 - 2\,\kappa\,a_l\,\Big] - \varrho_2\\
&\quad + \varrho_1\Big[\,\big(2\kappa\,c_{1l}(\mu_l - \alpha_l - \delta_l) + c_{2l}(\eta_l + \varepsilon_l)\big)\,P_l(\xi)^2\Big] + \varrho_1\Big[\,\big(2\kappa\,c_{1l}(\rho_l - \zeta_l) + c_{2l}(\tau_l + \theta_l)\big)\,P_m(\xi)^2\Big]\Bigg\}\\
&\quad - 2\,\mathfrak{w}_l\,c_{1l}\,\kappa\,\varrho_1\,P_l(\xi)\,P_m(\xi)\,\frac{dP_m}{d\xi} \;=\; 0,\\
&c_{1l}\,\varrho_1^4\,\sigma_{1l}\,\frac{d^4P_l}{d\xi^4} + \Big(-6\,c_{1l}\,\kappa^2\,\sigma_{1l} + 3\,\kappa\,c_{2l}\,\sigma_{7l} + c_{1l}(\mu_l + \delta_l)\,P_l(\xi)^2 + c_{1l}(\rho_l + \zeta_l)\,P_m(\xi)^2 + a_l\Big)\,\varrho_1^2\,\frac{d^2P_l}{d\xi^2}\\
&+ P_l(\xi)\Big[c_{1l}\,\kappa^4\,\sigma_{1l} - c_{2l}\,\kappa^3\,\sigma_{7l} - \kappa^2\Big(c_{1l}(\mu_l + \alpha_l + \delta_l - \gamma_l)\,P_l(\xi)^2 + c_{1l}(\rho_l + \zeta_l + \mathfrak{w}_l - \lambda_l)\,P_m(\xi)^2 + a_l\Big)\\
&+ \kappa\,c_{2l}\Big((\eta_l - \varepsilon_l)\,P_l(\xi)^2 - (\tau_l - \theta_l)\,P_m(\xi)^2\Big) + \big(h_l\,c_{1l}\,P_m(\xi)^4 + c_l\,P_m(\xi)^2\big)\Big] + P_l(\xi)\,c_{1l}(\alpha_l + \gamma_l)\left(\frac{dP_l}{d\xi}\right)^2\varrho_1^2\\
&+\ c_{1l}\varrho_1^2(\mathfrak{w}_l + \lambda_l)P_l(\xi)\left(\frac{dP_m}{d\xi}\right)^2 - \omega\,P_l(\xi) + c_{1l}\,f_l\,P_l(\xi)^5 + \big(g_l\,c_{1l}\,P_m(\xi)^2 + b_l\big)\,P_l(\xi)^3 = 0.
\end{aligned} \tag{15}$$

Taking the soliton speed ϱ_2 as

$$\varrho_2 = 4\,c_{1l}\,\kappa^3\,\sigma_{1l}\,\varrho_1 - 3\,c_{2l}\,\kappa^2\,\sigma_{7l}\,\varrho_1 - 2\,a_l\,\kappa\,\varrho_1, \qquad l = 1, 2. \tag{16}$$

Under the following parametric restrictions

$$\begin{aligned}
&2\,c_{1l}\,(\rho_l - \zeta_l)\,\varrho_1\,\kappa + c_{2l}\,(\tau_l + \theta_l)\,\varrho_1 = 0,\\
&2\,(\mu_l - \alpha_l - \delta_l)\,c_{1l}\,\varrho_1\,\kappa + c_{2l}\,(\eta_l + \varepsilon_l)\,\varrho_1 = 0,\\
&-4\,c_{1l}\,\kappa\,\sigma_{1l} + c_{2l}\,\sigma_{7l} = 0,\\
&\mathfrak{w}_l = 0, \qquad l = 1, 2.
\end{aligned} \tag{17}$$

Moreover, equating the two expressions for the wave speed and using the above parameter constraints yields

$$\begin{aligned}
&a_1 = a_2 = a, \qquad c_{21} = c_{22} = c_7, \qquad \sigma_{71} = \sigma_{72} = \sigma_7,\\
&\zeta_l = 2\,\sigma_{1l}\,\frac{(\tau_l + \theta_l)}{\sigma_7} + \rho_l, \qquad l = 1, 2,\\
&\eta_l = \frac{(-\mu_l + \alpha_l + \delta_l)\,\sigma_7}{2\,\sigma_{1l}} - \varepsilon_l, \qquad l = 1, 2,\\
&c_{11} = c_{12}\,\frac{\sigma_{12}}{\sigma_{11}}, \qquad c_7 = \frac{4\,c_{12}\,\kappa\,\sigma_{12}}{\sigma_7}.
\end{aligned} \tag{18}$$

Consequently, the wave speed can be expressed in the equivalent form

$$\varrho_2 = -2\,\kappa\,\varrho_1\,\big(c_7\,\kappa\,\sigma_7 + a\big). \tag{19}$$

Under these conditions, the system (15) reduces to:

$$\begin{aligned}
&\varphi_1^{(l)}P_l^5 + \varphi_4^{(l)}P_l^3 + \varphi_5^{(l)}\left(\frac{d^2P_l}{d\xi^2}\right)P_l^2 + \varphi_2^{(l)}P_l^3P_m^2\\
&+ \varphi_3^{(l)}P_lP_m^4 + \varphi_{11}^{(l)}P_lP_m^2 + \varphi_6^{(l)}\left(\frac{dP_l}{d\xi}\right)^2P_l + \varphi_7^{(l)}\left(\frac{dP_m}{d\xi}\right)^2P_l\\
&+ \varphi_8^{(l)}P_l + \varphi_9^{(l)}\left(\frac{d^2P_l}{d\xi^2}\right) + \varphi_{10}^{(l)}\left(\frac{d^4P_l}{d\xi^4}\right) = 0.
\end{aligned} \tag{20}$$

Here, $l = 1, 2$ and $m = 3 - l$. The functions P_l and P_m depend on the similarity variable ξ, whereas $\varphi_i^{(l)}$ $(i = 1, 2, 3, \ldots, 10)$ are arbitrary constants whose explicit expressions are listed in APPENDIX 1.

4. EXACT SOLUTIONS

In this section, we obtain exact solutions of system (1) by solving the reduced system (20) via the Kumar–Malik method. The main steps of the procedure are summarized as follows.

4.1. Kumar-Malik Method

The Kumar–Malik method offers a structured framework for deriving exact analytical solutions of nonlinear differential systems. In brief, the procedure consists of the following steps:

Step 1. Consider a general nonlinear system of ordinary differential equations of the form

$$\mathcal{F}(U, U', U'', U''', \ldots) = 0, \tag{21}$$

where $U = (U_1(\xi), U_2(\xi))$ denotes the unknown vector function and the prime ($'$) indicates differentiation with respect to ξ.

Step 2. Assume that each component $U_l(\xi)$ can be represented as a finite polynomial in an auxiliary function $G(\xi)$, namely,

$$U_l(\xi) = B_0^{\{l\}} + B_1^{\{l\}} G(\xi) + B_2^{\{l\}} G^2(\xi) + \cdots + B_{N_l}^{\{l\}} G^{N_l}(\xi), \tag{22}$$

where $B_j^{\{l\}}$ $(j = 0, 1, 2, \ldots, N_l)$ are constants to be determined. The function $G(\xi)$ satisfies the following auxiliary equation:

$$\left(G'(\xi)\right)^2 = \beta_4 G^4(\xi) + \beta_3 G^3(\xi) + \beta_2 G^2(\xi) + \beta_1 G(\xi) + \beta_0, \tag{23}$$

where β_j $(j = 0, 1, 2, 3, 4)$ are arbitrary parameters.

Step 3. The positive integers N_l are determined by applying the homogeneous balance principle, matching the highest-order derivative terms with the dominant nonlinear terms in Eq. (21).

Step 4. Substituting the polynomial ansatz (22) into Eq. (21) and using the auxiliary relation (23) to remove higher-order derivatives of $G(\xi)$ reduces Eq. (21) to a polynomial in $G(\xi)$. By setting the coefficients of identical powers of $G(\xi)$ equal to zero, one obtains an algebraic system for the unknown parameters $B_j^{\{l\}}$. Solving this algebraic system yields explicit expressions for the coefficients.

Finally, inserting the computed constants $B_j^{\{l\}}$ into (22) provides the closed-form expression of $U_l(\xi)$, and hence an exact solution of the original nonlinear system (21).

4.1.1. Family of Solutions to the Auxiliar Equation (23) In this subsection, we derive explicit solutions of the auxiliary nonlinear ordinary differential equation

$$(G'(\xi))^2 = \beta_4 G^4(\xi) + \beta_3 G^3(\xi) + \beta_2 G^2(\xi) + \beta_1 G(\xi) + \beta_0, \tag{24}$$

in Jacobi elliptic, hyperbolic, and trigonometric forms. The resulting families are classified according to the parameter regimes of β_j $(j = 0, 1, 2, 3, 4)$.
Throughout this work, the quantities Δ_1, Δ_2, Δ_3, and Δ_4 are chosen as:

$$\Delta_1 = 4\beta_2\beta_4 - \beta_3^2, \quad \Delta_2 = 16\beta_2\beta_4 - 5\beta_3^2, \quad \Delta_3 = 8\beta_2\beta_4 - 3\beta_3^2, \quad \Delta_4 = -\frac{\beta_3}{4\beta_4}.$$

Case 1: Assume that $\beta_0 = 0$ and $\beta_1 = \dfrac{\beta_3\Delta_1}{8\beta_4^2}$. Under these assumptions, the auxiliary ODE admits the following Jacobi elliptic function solutions for different parameter conditions:
Sub-case 1.1: If $\beta_4 < 0$ and $\Delta_1 > 0$,

$$G_1(\xi) = \Delta_4 \pm \frac{\beta_3}{4\beta_4}\mathrm{cn}\left(\frac{\sqrt{-\beta_4\Delta_1}\,\xi}{2\beta_4}, \frac{\beta_3}{2\sqrt{\Delta_1}}\right), \tag{25}$$

$$G_2(\xi) = \Delta_4 \pm \frac{\beta_3}{4\beta_4}\mathrm{dn}\left(\frac{\beta_3\xi}{4\sqrt{-\beta_4}}, \frac{2\sqrt{\Delta_1}}{\beta_3}\right). \tag{26}$$

Sub-case 1.2: If $\beta_4 < 0$, $\Delta_1 < 0$, and $\Delta_2 < 0$,

$$G_3(\xi) = \Delta_4 \pm \frac{\sqrt{-\Delta_2}}{4\beta_4}\mathrm{cn}\left(-\frac{\sqrt{\beta_4\Delta_1}\,\xi}{2\beta_4}, \frac{\sqrt{\Delta_1\Delta_2}}{2\Delta_1}\right), \tag{27}$$

$$G_4(\xi) = \Delta_4 \pm \frac{\sqrt{-\Delta_2}}{4\beta_4}\mathrm{dn}\left(-\frac{\sqrt{\beta_4\Delta_2}\,\xi}{4\beta_4}, \frac{2\sqrt{\Delta_1\Delta_2}}{\Delta_2}\right). \tag{28}$$

Sub-case 1.3: If $\beta_4 < 0$, $\Delta_1 > 0$, and $\Delta_2 < 0$,

$$G_5(\xi) = \Delta_4 \pm \frac{\sqrt{-\Delta_2}}{4\beta_4}\mathrm{nc}\left(\frac{\sqrt{-\beta_4\Delta_1}\,\xi}{2\beta_4}, \frac{\beta_3}{2\sqrt{\Delta_1}}\right), \tag{29}$$

$$G_6(\xi) = \Delta_4 \pm \frac{\sqrt{-\Delta_2}}{4\beta_4}\mathrm{nd}\left(-\frac{\beta_3\xi}{4\sqrt{-\beta_4}}, \frac{2\sqrt{\Delta_1}}{\beta_3}\right). \tag{30}$$

Sub-case 1.4: If $\beta_4\Delta_1 > 0$ and $\Delta_1\Delta_2 > 0$,

$$G_7(\xi) = \Delta_4 \pm \frac{\beta_3}{4\beta_4}\mathrm{nc}\left(\frac{\sqrt{\beta_4\Delta_1}\,\xi}{2\beta_4}, \frac{\sqrt{\Delta_1\Delta_2}}{2\Delta_1}\right), \tag{31}$$

$$G_8(\xi) = \Delta_4 \pm \frac{\beta_3}{4\beta_4}\mathrm{nd}\left(\frac{\sqrt{\beta_4\Delta_2}\,\xi}{4\beta_4}, \frac{2\sqrt{\Delta_1\Delta_2}}{\Delta_2}\right). \tag{32}$$

Sub-case 1.5: If $\beta_4 > 0$ and $\Delta_2 < 0$,

$$G_9(\xi) = \Delta_4 \pm \frac{\beta_3}{4\beta_4}\mathrm{ns}\left(-\frac{\beta_3\xi}{4\sqrt{\beta_4}}, \frac{\sqrt{-\Delta_2}}{\beta_3}\right), \tag{33}$$

$$G_{10}(\xi) = \Delta_4 \pm \frac{\sqrt{-\Delta_2}}{4\beta_4}\mathrm{ns}\left(-\frac{\sqrt{-\beta_4\Delta_2}\,\xi}{4\beta_4}, \frac{\beta_3}{\sqrt{-\Delta_2}}\right), \tag{34}$$

$$G_{11}(\xi) = \Delta_4 \pm \frac{\beta_3}{4\beta_4}\mathrm{sn}\left(-\frac{\beta_3\xi}{4\sqrt{\beta_4}}, \frac{\sqrt{-\Delta_2}}{\beta_3}\right), \tag{35}$$

$$G_{12}(\xi) = \Delta_4 \pm \frac{\sqrt{-\Delta_2}}{4\beta_4}\mathrm{sn}\left(-\frac{\sqrt{-\beta_4\Delta_2}\,\xi}{4\beta_4}, \frac{\beta_3}{\sqrt{-\Delta_2}}\right). \tag{36}$$

Case 2: $\beta_0 = \frac{\Delta_1^2}{64\beta_4^3}$, $\beta_1 = \frac{\beta_3\Delta_1}{8\beta_4^2}$. Then the auxiliary ODE admits the following hyperbolic, and trigonometric function solutions under different conditions:

Sub-case 2.1: $\beta_4 > 0$, $\Delta_3 < 0$

$$G_{13}(\xi) = \Delta_4 \pm \frac{\sqrt{-\Delta_3}}{4\beta_4}\tanh\left(\frac{\sqrt{-\beta_4\Delta_3}\,\xi}{4\beta_4}\right), \tag{37}$$

$$G_{14}(\xi) = \Delta_4 \pm \frac{\sqrt{-\Delta_3}}{4\beta_4}\coth\left(\frac{\sqrt{-\beta_4\Delta_3}\,\xi}{4\beta_4}\right). \tag{38}$$

Sub-case 2.2: $\beta_4 > 0$, $\Delta_3 > 0$

In this case, the resulting solutions are periodic and fall outside the scope of the present study; hence, they are omitted.

Case 3: $\beta_0 = \frac{\beta_3^2\Delta_2}{256\beta_4^3}$, $\beta_1 = \frac{\beta_3\Delta_1}{8\beta_4^2}$. Under these conditions, the auxiliary ODE admits the following hyperbolic and trigonometric function solutions for various parameter regimes:

Sub-case 3.1: $\beta_4 < 0$, $\Delta_3 < 0$

$$G_{17}(\xi) = \Delta_4 \pm \frac{\sqrt{-2\Delta_3}}{4\beta_4}\mathrm{sech}\left(\frac{\sqrt{2\beta_4\Delta_3}\,\xi}{4\beta_4}\right). \tag{39}$$

Sub-case 3.2: $\beta_4 > 0, \Delta_3 > 0$

$$G_{18}(\xi) = \Delta_4 \pm \frac{\sqrt{2\Delta_3}}{4\beta_4}\mathrm{csch}\left(\frac{\sqrt{2\beta_4\Delta_3}\,\xi}{4\beta_4}\right). \tag{40}$$

Sub-case 3.3: $\beta_4 > 0, \Delta_3 < 0$

In this case, the corresponding solutions are beyond the scope of the present work and are therefore not presented.

Case 4: $\beta_0 = 0, \beta_1 = 0, \beta_3 = 0$

$$G_{21}(\xi) = \frac{4\rho\beta_2}{4\rho^2 \mathrm{e}^{\sqrt{\beta_2}\xi} - \beta_4\beta_2\mathrm{e}^{-\sqrt{\beta_2}\xi}}. \tag{41}$$

4.2. Application of Kumar-Malik Method

Assume that the solution of Eq. (20) is sought in the form:

$$P_l(\xi) = A_0^{(l)} + A_1^{(l)}R(\xi) + A_2^{(l)}R^2(\xi) + A_3^{(l)}R^3(\xi) + \ldots + A_{N_l}^{(l)}R^{N_l}(\xi), \tag{42}$$

where $l = 1, 2$. Substituting the ansatz (42) with $N_l = 1$ into the reduced system (20), and following the procedure outlined in Section 4.1, we obtain two polynomial expressions in $R(\xi)$. Equating to zero the coefficients of each power of $R(\xi)$ (together with the constant terms) produces an algebraic system for the unknown parameters. Solving this system yields the following values:

$$A_0^{(1)} = -\frac{\beta_3\sqrt{30}\,\vartheta_1}{4\beta_4\,\vartheta_2}, \quad A_1^{(1)} = \frac{4A_0^{(1)}}{\beta_3},$$

$$A_0^{(2)} = -\frac{\beta_3\sqrt{30}\sqrt{\beta_4\vartheta_3\,\sigma_7\sigma_{12}\left((\alpha_1+\gamma_1)\sigma_{12}+\lambda_2\sigma_{11}\right)}\,\varrho_1}{4\beta_4\,\vartheta_3}, \quad A_1^{(2)} = \frac{4A_0^{(2)}}{\beta_3}\,\vartheta_3,$$

$$b_1 = \frac{-160F_1\beta c_{12}\sigma_{12}^3\varrho_1^2 + 80F_4 a\beta_4\sigma_{11}^2\sigma_7 + F_2\sigma_{12}^2 + F_3\sigma_{11}\sigma_{12}}{240\,\beta_4\,\sigma_7\,\sigma_{12}\,\sigma_{11}\left(\sigma_{11}(\alpha_2+\gamma_2) - \lambda_1\sigma_{12}\right)},$$

$$b_2 = \frac{-160F_{11}\beta c_{12}\sigma_{12}^3\varrho_1^2 - 80F_{44}a\beta_4\sigma_{11}\sigma_7 + F_{22}\sigma_{12}^2 + F_{33}\sigma_{12}}{240\,\beta_4\,\sigma_7\,\sigma_{12}\left(\sigma_{12}(\alpha_1+\gamma_1) - \lambda_2\sigma_{11}\right)},$$

$$\delta_1 = \frac{\sigma_{11}^2\left(E_1\,\sigma_{12} + 2E_2\,\sigma_7\right) - \sigma_{11}\sigma_{12}\left(E_3\,\sigma_{12} + E_4\,\sigma_7\right) + \sigma_{12}^2\sigma_7 E_5}{\sigma_7\,\sigma_{12}\left[-\lambda_1\sigma_{12} + \sigma_{11}(\alpha_2+\gamma_2)\right]},$$

$$f_1 = \frac{X_7\,\sigma_{12}^4 + X_8\,\sigma_{12}^3 + X_9\,\sigma_{12}^2 + \left(16\,X_1\,\sigma_{11}^3\,\sigma_7\,(\alpha_2+\gamma_2)(\tau_2+\theta_2) + 6\,X_1X_2\,\sigma_{11}^2\,\sigma_7^2\right)\sigma_{12} + 8\,X_1^2\,\sigma_{11}^3\,\sigma_7^2}{50\,\sigma_7^2\,\sigma_{12}^2\left(\sigma_{11}(\alpha_2+\gamma_2) - \lambda_1\sigma_{12}\right)^2},$$

$$f_2 = \frac{8\,\lambda_1^2\,\sigma_{12}^4\,(\tau_2+\theta_2)^2 + 50\,X_{10}\,\lambda_1\,\sigma_{12}^3 + X_{11}\,\sigma_{12}^2 + 50\,X_{12}\,\sigma_{11}\,\sigma_7\,\sigma_{12} + 8\,X_1^2\,\sigma_{11}^2\,\sigma_7^2}{50\,\sigma_7^2\,\sigma_{12}\left(\lambda_2\sigma_{11} - (\alpha_1+\gamma_1)\sigma_{12}\right)^2},$$

$$\kappa = \sqrt{\frac{2\left[\left(\frac{3\beta_3^2}{8} - \beta_2\beta_4\right)c_{12}\varrho_1^2\sigma_{12} - a\beta_4\right]}{c_{12}\sigma_{12}\beta_4}}$$

$$\omega = \frac{18432\,\lambda_1\varrho_1^4c_{12}^2\sigma_{12}^4(\tau_2+\theta_2)Z_1 + 4608\,\varrho_1^4c_{12}^2\sigma_{12}^3Z_5 - \sigma_{12}^2Z_6 - 128\,a^2\beta_4^2\sigma_{12}Z_7 - 128\,\sigma_7a^2\sigma_{11}\beta_4^2Z_2}{1536\,\sigma_{12}\beta_4^2c_{12}\left(\lambda_1\sigma_{12}^2(\tau_2+\theta_2) - \sigma_{12}Z_7 - \sigma_7\sigma_{11}Z_2\right)}.$$

See **??** for further details. Substituting the above parameter values into the similarity form (14), the solution of Eq. (1) can be written as:

$$\begin{aligned} q(t,x) &= P_1(t,x)e^{i(-\kappa x+\omega t+\theta_0)}, \\ r(t,x) &= P_2(t,x)e^{i(-\kappa x+\omega t+\theta_0)}, \end{aligned} \tag{43}$$

where the functions $P_l(t,x)$ $(l=1,2)$ are specified in the cases listed below.
Throughout this paper, the constants $C_{0,l}$ and $C_{1,l}$ are defined by:

$$C_{0,l}=\begin{cases}A_0^{(1)}, & l=1,\\ A_0^{(2)}, & l=2,\end{cases}\qquad C_{1,l}=\begin{cases}A_1^{(1)}, & l=1,\\ A_1^{(2)}, & l=2.\end{cases}$$

Case 1: Assume that $\beta_0=0$ and

$$\beta_1=\frac{\beta_3\left(4\beta_2\beta_4-\beta_3^2\right)}{8\beta_4^2}.$$

Under these assumptions, $P_l(t,x)$ admits the following Jacobi elliptic function solutions:
Sub-case 1.1: If $\beta_4<0$ and $\Delta_1>0$, then

$$P_l^{(1)}(t,x)=C_{0,l}+C_{1,l}\left(\Delta_4\pm\frac{\beta_3}{4\beta_4}\,\mathrm{cn}\left(\frac{\sqrt{-\beta_4\Delta_1}\,(\varrho_1x-\varrho_2t)}{2\beta_4},\frac{\beta_3}{2\sqrt{\Delta_1}}\right)\right),\tag{44}$$

$$P_l^{(2)}(t,x)=C_{0,l}+C_{1,l}\left(\Delta_4\pm\frac{\beta_3}{4\beta_4}\,\mathrm{dn}\left(\frac{\beta_3(\varrho_1x-\varrho_2t)}{4\sqrt{-\beta_4}},\frac{2\sqrt{\Delta_1}}{\beta_3}\right)\right).\tag{45}$$

Sub-case 1.2: If $\beta_4<0$, $\Delta_1<0$, and $\Delta_2<0$,

$$P_l^{(3)}(t,x)=C_{0,l}+C_{1,l}\left(\Delta_4\pm\frac{\sqrt{-\Delta_2}}{4\beta_4}\mathrm{cn}\left(-\frac{\sqrt{\beta_4\Delta_1}\,(\varrho_1x-\varrho_2t)}{2\beta_4},\frac{\sqrt{\Delta_1\Delta_2}}{2\Delta_1}\right)\right),\tag{46}$$

$$P_l^{(4)}(t,x)=C_{0,l}+C_{1,l}\left(\Delta_4\pm\frac{\sqrt{-\Delta_2}}{4\beta_4}\mathrm{dn}\left(-\frac{\sqrt{\beta_4\Delta_2}\,(\varrho_1x-\varrho_2t)}{4\beta_4},\frac{2\sqrt{\Delta_1\Delta_2}}{\Delta_2}\right)\right).\tag{47}$$

Sub-case 1.3: If $\beta_4<0$, $\Delta_1>0$, and $\Delta_2<0$,

$$P_l^{(5)}(t,x)=C_{0,l}+C_{1,l}\left(\Delta_4\pm\frac{\sqrt{-\Delta_2}}{4\beta_4}\mathrm{nc}\left(\frac{\sqrt{-\beta_4\Delta_1}\,(\varrho_1x-\varrho_2t)}{2\beta_4},\frac{\beta_3}{2\sqrt{\Delta_1}}\right)\right),\tag{48}$$

$$P_l^{(6)}(t,x)=C_{0,l}+C_{1,l}\left(\Delta_4\pm\frac{\sqrt{-\Delta_2}}{4\beta_4}\mathrm{nd}\left(-\frac{\beta_3(\varrho_1x-\varrho_2t)}{4\sqrt{-\beta_4}},\frac{2\sqrt{\Delta_1}}{\beta_3}\right)\right).\tag{49}$$

Sub-case 1.4: If $\beta_4\Delta_1>0$ and $\Delta_1\Delta_2>0$,

$$P_l^{(7)}(t,x)=C_{0,l}+C_{1,l}\left(\Delta_4\pm\frac{\beta_3}{4\beta_4}\mathrm{nc}\left(\frac{\sqrt{\beta_4\Delta_1}\,(\varrho_1x-\varrho_2t)}{2\beta_4},\frac{\sqrt{\Delta_1\Delta_2}}{2\Delta_1}\right)\right),\tag{50}$$

$$P_l^{(8)}(t,x)=C_{0,l}+C_{1,l}\left(\Delta_4\pm\frac{\beta_3}{4\beta_4}\mathrm{nd}\left(\frac{\sqrt{\beta_4\Delta_2}\,(\varrho_1x-\varrho_2t)}{4\beta_4},\frac{2\sqrt{\Delta_1\Delta_2}}{\Delta_2}\right)\right).\tag{51}$$

Sub-case 1.5: If $\beta_4>0$ and $\Delta_2<0$,

$$P_l^{(9)}(t,x)=C_{0,l}+C_{1,l}\left(\Delta_4\pm\frac{\beta_3}{4\beta_4}\mathrm{ns}\left(-\frac{\beta_3(\varrho_1x-\varrho_2t)}{4\sqrt{\beta_4}},\frac{\sqrt{-\Delta_2}}{\beta_3}\right)\right),\tag{52}$$

$$P_l^{(10)}(t,x)=C_{0,l}+C_{1,l}\left(\Delta_4\pm\frac{\sqrt{-\Delta_2}}{4\beta_4}\mathrm{ns}\left(-\frac{\sqrt{-\beta_4\Delta_2}\,(\varrho_1x-\varrho_2t)}{4\beta_4},\frac{\beta_3}{\sqrt{-\Delta_2}}\right)\right),\tag{53}$$

$$P_l^{(11)}(t,x)=C_{0,l}+C_{1,l}\left(\Delta_4\pm\frac{\beta_3}{4\beta_4}\mathrm{sn}\left(-\frac{\beta_3(\varrho_1x-\varrho_2t)}{4\sqrt{\beta_4}},\frac{\sqrt{-\Delta_2}}{\beta_3}\right)\right),\tag{54}$$

$$P_l^{(12)}(t,x)=C_{0,l}+C_{1,l}\left(\Delta_4\pm\frac{\sqrt{-\Delta_2}}{4\beta_4}\mathrm{sn}\left(-\frac{\sqrt{-\beta_4\Delta_2}\,(\varrho_1x-\varrho_2t)}{4\beta_4},\frac{\beta_3}{\sqrt{-\Delta_2}}\right)\right).\tag{55}$$

Case 2: $\beta_0=\frac{\Delta_1^2}{64\beta_4^3}$, $\beta_1=\frac{\beta_3\Delta_1}{8\beta_4^2}$. Under these conditions, $P_l(t,x)$ admits the following hyperbolic and trigonometric function solutions for the corresponding parameter regimes: *Sub-case 2.1:* $\beta_4>0$, $\Delta_3<0$

$$P_l^{(13)}(t,x)=C_{0,l}+C_{1,l}\left(\Delta_4\pm\frac{\sqrt{-\Delta_3}}{4\beta_4}\tanh\left(\frac{\sqrt{-\beta_4\Delta_3}\,(\varrho_1x-\varrho_2t)}{4\beta_4}\right)\right),\tag{56}$$

$$P_l^{(14)}(t,x) = C_{0,l} + C_{1,l}\left(\Delta_4 \pm \frac{\sqrt{-\Delta_3}}{4\beta_4}\coth\left(\frac{\sqrt{-\beta_4\Delta_3}\,(\varrho_1 x - \varrho_2 t)}{4\beta_4}\right)\right). \tag{57}$$

Sub-case 2.2: $\beta_4 > 0, \Delta_3 > 0$

In this case, the solutions are periodic; since they are not central to the objectives of this study, they are not pursued further.

Case 3: $\beta_0 = \frac{\beta_3^2\Delta_2}{256\beta_4^3}, \beta_1 = \frac{\beta_3\Delta_1}{8\beta_4^2}$. Accordingly, $P_l(t,x)$ admits the following hyperbolic and trigonometric solutions under the associated parameter conditions:

Sub-case 3.1: $\beta_4 < 0, \Delta_3 < 0$

$$P_l^{(17)}(t,x) = C_{0,l} + C_{1,l}\left(\Delta_4 \pm \frac{\sqrt{-2\Delta_3}}{4\beta_4}\operatorname{sech}\left(\frac{\sqrt{2\beta_4\Delta_3}\,(\varrho_1 x - \varrho_2 t)}{4\beta_4}\right)\right). \tag{58}$$

Sub-case 3.2: $\beta_4 > 0, \Delta_3 > 0$

$$P_l^{(18)}(t,x) = C_{0,l} + C_{1,l}\left(\Delta_4 \pm \frac{\sqrt{2\Delta_3}}{4\beta_4}\operatorname{csch}\left(\frac{\sqrt{2\beta_4\Delta_3}\,(\varrho_1 x - \varrho_2 t)}{4\beta_4}\right)\right). \tag{59}$$

Sub-case 3.3: $\beta_4 > 0, \Delta_3 < 0$

Although this case yields periodic waveforms, they are not relevant to the aims of the present analysis and are therefore omitted.

Case 4: $\beta_0 = 0, \beta_1 = 0, \beta_3 = 0, \beta_2 > 0$

$$P_l^{(21)}(t,x) = C_{0,l} + C_{1,l}\left(\frac{4\rho\beta_2}{4\rho^2 e^{\sqrt{\beta_2}(\varrho_1 x - \varrho_2 t)} - \beta_4\beta_2 e^{-\sqrt{\beta_2}(\varrho_1 x - \varrho_2 t)}}\right). \tag{60}$$

5. GRAPHICAL REPRESENTATION AND PHYSICAL INTERPRETATION

In this section, we examine the spatiotemporal evolution of the coupled complex fields $q(x,t)$ and $r(x,t)$ arising from the general traveling–wave representation (43), using two distinct closed-form choices for the amplitude functions. Specifically, we consider the dark-soliton profiles given in (56) and the bright-soliton profiles given in (58). For visualization, we display the corresponding intensities $|q(x,t)|^2$ and $|r(x,t)|^2$ using 3D surface plots, contour maps, and 2D cross-sections at several fixed time levels.

5.1. Dark Soliton Dynamics

Figure 1 displays the intensity distributions obtained by inserting (56) into the traveling–wave form (43). The resulting dark-soliton profile is characterized by an intensity dip superimposed on a nonzero continuous background. This localized notch travels along the trajectory specified by the wave variable $\xi = \varrho_1 x - \varrho_2 t$, which appears in the contour plots as an oblique band marking the transition region. Such behavior is typical of dark solitons: the field approaches a finite pedestal as $|\xi| \to \infty$, while the dispersion–nonlinearity balance sustains a stable localized depression that retains its shape during propagation. From a physical viewpoint, dark solitons are commonly associated with defocusing nonlinear regimes (or an effective defocusing response in coupled settings), where the nonlinear interaction supports a robust dip on a finite background rather than a localized peak.

5.2. Bright Soliton Dynamics

Figure 2 depicts the spatiotemporal behavior obtained by substituting (58) into the traveling–wave expression (43). Unlike the dark-soliton case, the bright-soliton profile exhibits a *localized intensity peak* that attains its maximum near the soliton core and decays rapidly as $|\xi|$ increases. In the contour maps, this structure appears as a thin ridge propagating along the characteristic direction prescribed by $\xi = \varrho_1 x - \varrho_2 t$, indicating a coherent pulse traveling with the corresponding wave speed. This is the defining signature of a bright soliton, namely a self-confined wave packet sustained by the balance between dispersion (or diffraction) and nonlinear self-focusing. Physically, bright solitons are typically supported in focusing nonlinear regimes (or in coupled systems with an effective focusing response), where the nonlinear interaction counteracts dispersive spreading and maintains a stable localized hump.

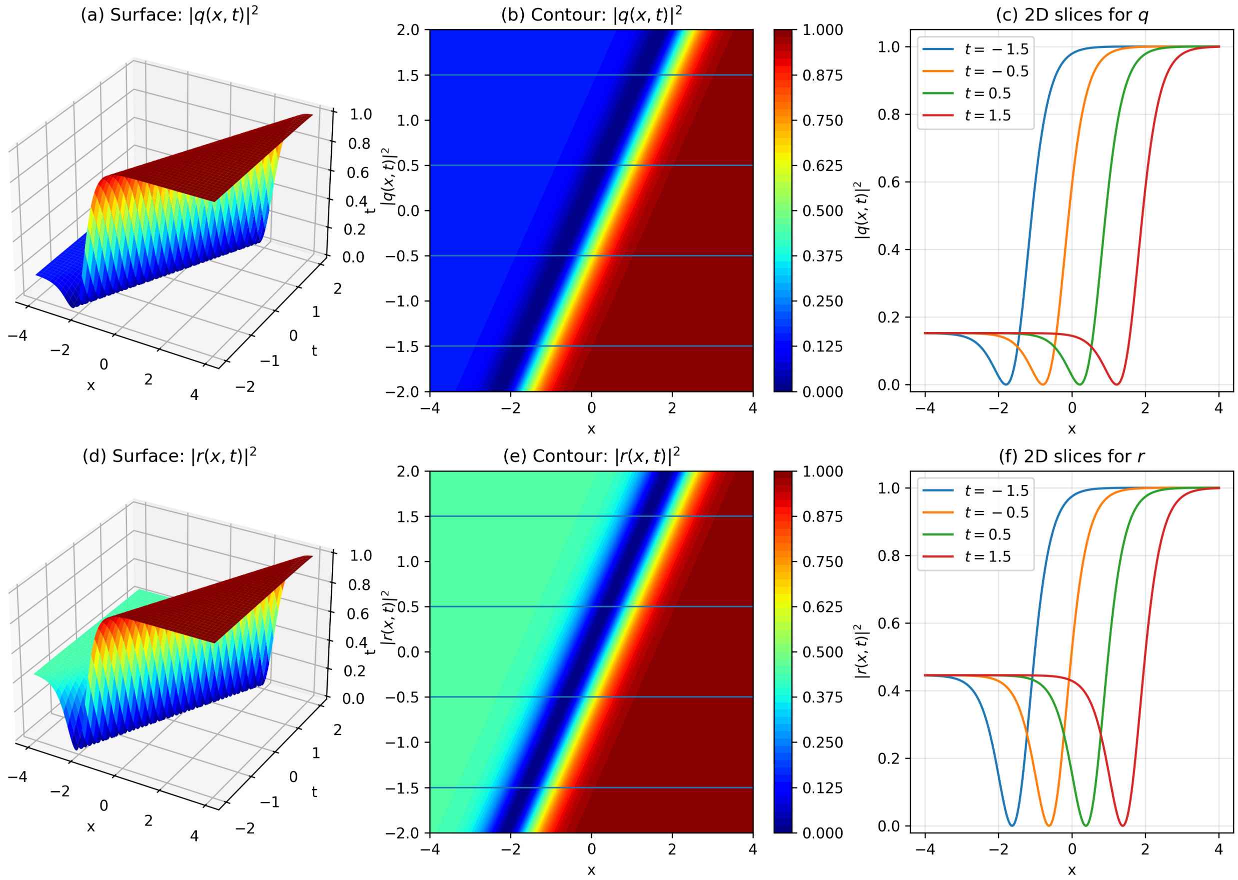

Figure 1. Surface (left), contour (middle), and 2D profiles (right) of the coupled fields $q(x,t)$ and $r(x,t)$ corresponding to the analytical solution (43) constructed from the dark soliton solution (56). The first row depicts $|q(x,t)|^2$, while the second row depicts $|r(x,t)|^2$. The 2D panels show $|q(x,t)|^2$ and $|r(x,t)|^2$ as functions of x at several fixed time instants (as indicated in the legends), and the same time levels are marked on the contour plots for reference.

5.3. Comparison and Physical Meaning

A comparison of Figures 1 and 2 reveals the qualitative distinctions between the two solution classes:

- **Background behavior:** The dark-soliton pattern propagates as an intensity *depression* on a finite continuous background, whereas the bright-soliton pattern manifests as a localized intensity *hump* that decays rapidly away from its center.

- **Type of localization:** The bright soliton is localized through spatial confinement of a peak, while the dark soliton is localized via a notch embedded in a nonzero pedestal.

- **Propagation characteristics:** In both cases, the waveforms translate along the traveling variable $\xi = \varrho_1 x - \varrho_2 t$ without distortion, with an effective speed determined by ϱ_2/ϱ_1.

- **Coupled-field features:** The two intensities $|q|^2$ and $|r|^2$ exhibit the same traveling structure, but their amplitudes and offsets can differ according to the free parameters in (43), indicating how the coupling redistributes energy between the polarization modes.

Hence, the two functional profiles describe distinct nonlinear propagation regimes within the same coupled framework: a dark-soliton regime characterized by intensity depletion on a continuous-wave background, and a bright-soliton regime characterized by a self-confined pulse supported by effective focusing. The numerical visualizations corroborate the solitonic character of the derived closed-form solutions and demonstrate that the selected amplitude profile governs the qualitative propagation physics in the modeled birefringent medium.

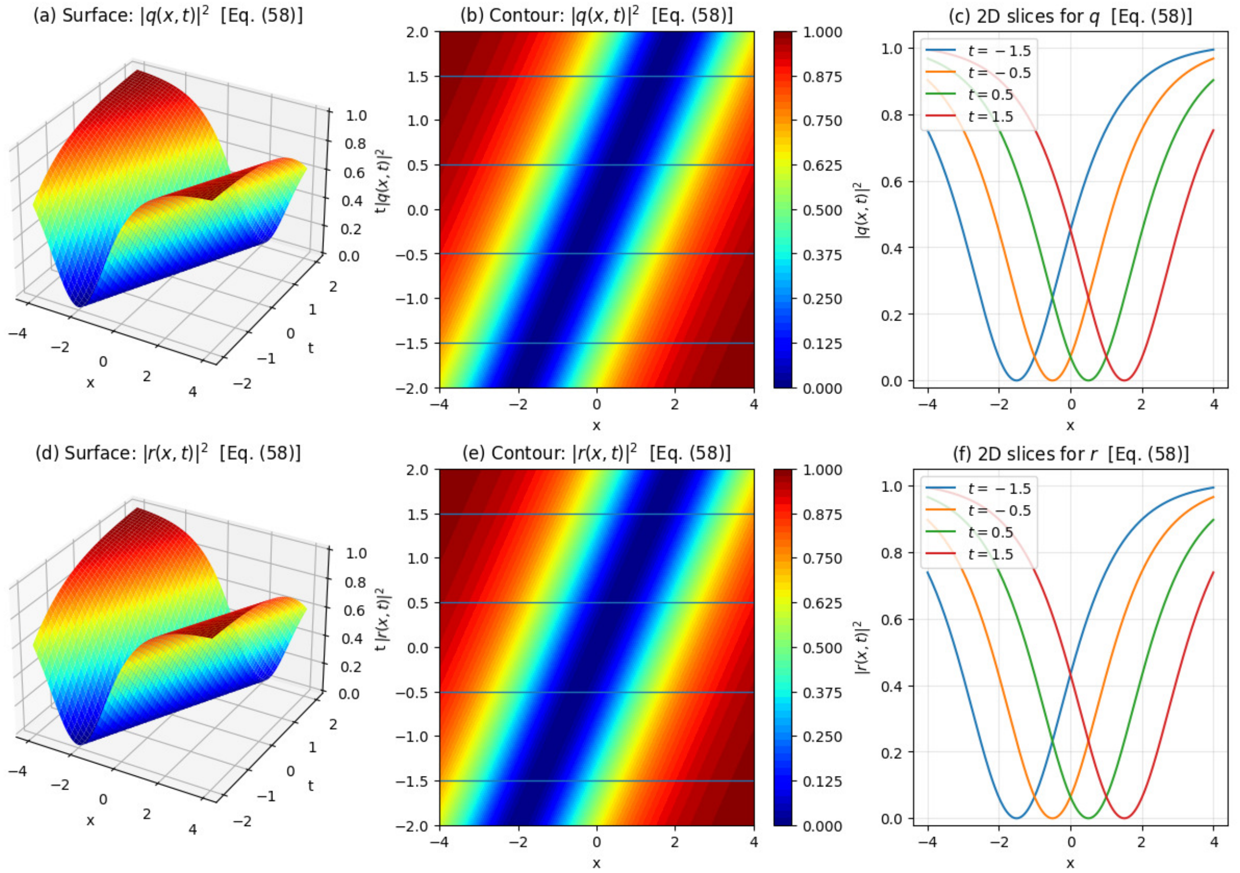

Figure 2. Surface (left), contour (middle), and 2D profiles (right) of the coupled fields $q(x,t)$ and $r(x,t)$ corresponding to the analytical solution (43) constructed from the bright soliton solution (58). The first row depicts $|q(x,t)|^2$, while the second row depicts $|r(x,t)|^2$. The 2D panels show $|q(x,t)|^2$ and $|r(x,t)|^2$ as functions of x at several fixed time instants (as indicated in the legends), and the same time levels are marked on the contour plots for reference.

6. CONCLUSIONS

In this work, we investigated a generalized concatenation model for birefringent optical fibers and derived new exact soliton solutions. By means of Lie symmetry analysis, the coupled nonlinear evolution equations were reduced, through appropriate similarity variables, to a tractable system of ordinary differential equations. The reduced system was then solved analytically using the Kumar–Malik method, which produced several families of closed-form solutions expressed in Jacobi elliptic, hyperbolic, and trigonometric functions. For suitable parameter constraints, these solution families degenerate to the standard bright-, dark-, and periodic-soliton regimes, thereby demonstrating that the model supports qualitatively distinct waveform classes within a unified higher-order coupled framework. Representative graphical illustrations further confirmed the physical relevance of the obtained structures and highlighted the influence of parameters on the propagation characteristics.

Overall, the combination of symmetry reduction and the Kumar–Malik technique provides an efficient analytical route for exploring higher-order coupled optical systems. The explicit solutions reported here can serve as benchmark test cases for numerical simulations and may facilitate further theoretical studies. Possible extensions include the investigation of perturbed or fractional forms of the concatenation model, the derivation of conservation laws, and a detailed analysis of modulation instability, as well as interaction dynamics among solitons, breathers, and other localized waveforms in birefringent media.

Funding: This research received no external funding.

Acknowledgments: The author, Rajveer Singh, is very much thankful to UGC for providing financial support in the form of SRF fellowship via letter UGC ID: 211610023103. The author, Sachin Kumar, wants to acknowledge the financial

support provided under the scheme "Fund for Improvement of S&T Infrastructure (FIST)" of the Department of Science & Technology (DST), Government of India via letter no. SR/FST/MS-I/2021/104 to the Department of Mathematics and Statistics, Central University of Punjab.
This work was funded from the budget of Grambling State University for the Endowed Chair of Mathematics. No additional grants have been received to conduct or direct this particular study.

Conflicts of interest: The authors declare no conflicts of interest.

APPENDIX 1

$$\varphi_1^{(l)} = \begin{cases} c_{12}\,\sigma_{12}\,\sigma_7\,f_1, & l = 1 \\ c_{12}\,\sigma_7\,f_2, & l = 2 \end{cases}$$

$$\varphi_2^{(l)} = \begin{cases} c_{12}\,\sigma_{12}\,\sigma_7\,g_1, & l = 1 \\ c_{12}\,\sigma_7\,g_2, & l = 2 \end{cases}$$

$$\varphi_3^{(l)} = \begin{cases} c_{12}\,\sigma_{12}\,\sigma_7\,h_1, & l = 1 \\ c_{12}\,\sigma_7\,h_2, & l = 2 \end{cases}$$

$$\varphi_4^{(l)} = \begin{cases} c_{12}\,\kappa^2\,\sigma_{12}(\alpha_1 + \delta_1 + \gamma_1 - 3\mu_1) + b_1\sigma_{11}\sigma_7 - 8c_{12}\kappa^2\sigma_{11}\sigma_{12}\varepsilon_1, & l = 1 \\ c_{12}\,\kappa^2(\alpha_2 + \delta_2 + \gamma_2 - 3\mu_2) + b_2\sigma_7 - 8c_{12}\kappa^2\sigma_{12}\varepsilon_2, & l = 2 \end{cases}$$

$$\varphi_5^{(l)} = \begin{cases} c_{12}\,\sigma_{12}\,\sigma_7\,\varrho_1^2(\delta_1 + \mu_1), & l = 1 \\ c_{12}\,\sigma_7\,\varrho_1^2(\delta_2 + \mu_2), & l = 2 \end{cases}$$

$$\varphi_6^{(l)} = \begin{cases} c_{12}\,\sigma_{12}\,\sigma_7(\alpha_1 + \gamma_1)\varrho_1^2, & l = 1 \\ c_{12}\,\sigma_7(\alpha_2 + \gamma_2)\varrho_1^2, & l = 2 \end{cases}$$

$$\varphi_7^{(l)} = \begin{cases} \lambda_1\,\sigma_{12}\,\varrho_1^2\,c_{12}\,\sigma_7, & l = 1 \\ \lambda_2\,\varrho_1^2\,c_{12}\,\sigma_7, & l = 2 \end{cases}$$

$$\varphi_8^{(l)} = \begin{cases} -3c_{12}\kappa^4\sigma_{11}\sigma_{12}\sigma_7 - a\kappa^2\sigma_{11}\sigma_7 - \omega\sigma_{11}\sigma_7, & l = 1 \\ -3c_{12}\kappa^4\sigma_{12}\sigma_7 - a\kappa^2\sigma_7 - \omega\sigma_7, & l = 2 \end{cases}$$

$$\varphi_9^{(l)} = \begin{cases} 6c_{12}\kappa^2\sigma_{11}\sigma_{12}\varrho_1^2 + a\sigma_{11}\sigma_7\varrho_1^2, & l = 1 \\ 6c_{12}\kappa^2\sigma_{12}\sigma_7\varrho_1^2 + a\sigma_7\varrho_1^2, & l = 2 \end{cases}$$

$$\varphi_{10}^{(l)} = \begin{cases} \sigma_{11}\sigma_{12}\varrho_1^4 c_{12}\sigma_7, & l = 1 \\ \sigma_{12}\varrho_1^4 c_{12}\sigma_7, & l = 2 \end{cases}$$

$$\varphi_{11}^{(l)} = \begin{cases} c_{12}\kappa^2\sigma_{12}\sigma_7\lambda_1 - 2c_{12}\kappa^2\sigma_{12}\sigma_7\rho_1 - 6c_{12}\kappa^2\sigma_{11}\sigma_{12}\tau_1 + 2c_{12}\kappa^2\sigma_{11}\sigma_{12}\theta_1 + c_1\sigma_{11}\sigma_7, & l = 1 \\ c_{12}\kappa^2\sigma_7\lambda_2 - 2c_{12}\kappa^2\sigma_7\rho_2 - 6c_{12}\kappa^2\sigma_{12}\tau_2 + 2c_{12}\kappa^2\sigma_{12}\theta_2 + c_2\sigma_7. & l = 2 \end{cases}$$

APPENDIX 2
APPLICATION OF KUMAR-MALIK METHOD

Let the solution of Eq. (20) takes the form:

$$P_l(\xi) = A_0^{(l)} + A_1^{(l)}R(\xi) + A_2^{(l)}R^2(\xi) + A_3^{(l)}R^3(\xi) + \ldots + A_{N_l}^{(l)}R^{N_l}(\xi), \tag{61}$$

where $l = 1, 2$. Substituting Eq. (61) with $N_l = 1$ into system (20), and using procedure mentioned in Section 4.1, we arrive at two polynomial equations in $R(\xi)$. Setting the coefficients of powers of $R(\xi)$, combined with the constant terms, to zero yields the system of equations, after solving that system gives the values of $A_0^{(1)}, A_1^{(1)}, A_0^{(2)}, A_1^{(2)}, b_1, b_2, \delta_1, f_1, f_2$ and ω as follows:

- $A_0^{(1)} = -\dfrac{\beta_3\sqrt{30}\,\vartheta_1}{4\beta_4\,\vartheta_2},\quad A_1^{(1)} = \dfrac{4A_0^{(1)}}{\beta_3},$

  $A_0^{(2)} = -\dfrac{\beta_3\sqrt{30}\,\sqrt{\beta_4\vartheta_3\,\sigma_7\sigma_{12}\left((\alpha_1+\gamma_1)\sigma_{12}+\lambda_2\sigma_{11}\right)}\,\varrho_1}{4\beta_4\,\vartheta_3},\quad A_1^{(2)} = \dfrac{4A_0^{(2)}\,\vartheta_3}{\beta_3}$

  where

$$
\begin{aligned}
\vartheta_1 &= \sqrt{\beta_4\,\varrho_1^2\,\sigma_7\sigma_{12}\left(\sigma_{11}(\alpha_2+\gamma_2)-\lambda_1\sigma_{12}\right)},\\
\vartheta_2 &= \left((\tau_2+\theta_2)\sigma_{11}+(\alpha_1+\gamma_1)\sigma_7\right)\sigma_{12}+\rho_2\sigma_{11}\sigma_7,\\
\vartheta_3 &= 2\lambda_1(\tau_2+\theta_2)\sigma_{12}^2+\Big[\big((-2\alpha_1-2\gamma_1)\alpha_2+(-2\alpha_1-2\gamma_1)\gamma_2+(2\lambda_2+2\rho_2)\lambda_1-(\alpha_1+\gamma_1)(\mu_2+\delta_2)\big)\sigma_7\\
&\quad-2\sigma_{11}(\alpha_2+\gamma_2)(\tau_2+\theta_2)\Big]\sigma_{12}+\sigma_{11}(-2\rho_2\alpha_2-2\rho_2\gamma_2+\lambda_2(\mu_2+\delta_2))\sigma_7.
\end{aligned}
\tag{62}
$$

- $b_1 = \dfrac{-160F_1\beta c_{12}\sigma_{12}^3\varrho_1^2+80F_4 a\beta_4\sigma_{11}^2\sigma_7+F_2\sigma_{12}^2+F_3\sigma_{11}\sigma_{12}}{240\,\beta_4\,\sigma_7\,\sigma_{12}\,\sigma_{11}\left(\sigma_{11}(\alpha_2+\gamma_2)-\lambda_1\sigma_{12}\right)},$

  $b_2 = \dfrac{-160F_{11}\beta c_{12}\sigma_{12}^3\varrho_1^2-80F_{44}a\beta_4\sigma_{11}\sigma_7+F_{22}\sigma_{12}^2+F_{33}\sigma_{12}}{240\,\beta_4\,\sigma_7\,\sigma_{12}\left(\sigma_{12}(\alpha_1+\gamma_1)-\lambda_2\sigma_{11}\right)}$

where

$$
\begin{aligned}
F_1 &= \Big[\big(-\tfrac{7\theta_2}{10}-2\varepsilon_1-\tfrac{7\tau_2}{10}\big)\lambda_1+2\tau_1(\alpha_1+\gamma_1)\Big]\sigma_{11}+\sigma_7\big[-\mu_1\lambda_1+\rho_1(\alpha_1+\gamma_1)\big],\\
F_{11} &= 2\varepsilon_2(\alpha_1+\gamma_1)-\tfrac{7}{10}(\theta_2+\tfrac{27\tau_2}{7})\lambda_1,\\
F_2 &= -112\,c_{12}\,\beta\,\varrho_1^2\,\sigma_{11}^2\Big[(\tau_2+\theta_2+\tfrac{20\varepsilon_1}{7})(\alpha_2+\gamma_2)-\tfrac{20\tau_1\lambda_2}{7}\Big]\\
&\quad+88\,c_{12}\,\beta_2\,\sigma_7\,\varrho_1^2\Big[(\alpha_1+\gamma_1-\tfrac{20\mu_1}{11})(\alpha_2+\gamma_2)+(-\lambda_2+\tfrac{14\rho_2}{11})\lambda_1+(-\tfrac{7\delta_2}{11}-\tfrac{7\mu_2}{11})(\alpha_1+\gamma_1)+\tfrac{20\rho_1\lambda_2}{11}\Big]\\
&\quad-240\,c_1\,\sigma_7\,(\alpha_1+\gamma_1)-320\,a\,\beta_4\Big[\big(\tfrac{\theta_2}{4}-\varepsilon_1+\tfrac{\tau_2}{4}\big)\lambda_1+\tau_1(\alpha_1+\gamma_1)\Big]\\
&\quad-33\,c_{12}\,\beta_3^2\,\sigma_7\,\varrho_1^2\Big[(\alpha_1+\gamma_1-\tfrac{20\mu_1}{11})(\alpha_2+\gamma_2)+(-\lambda_2+\tfrac{14\rho_2}{11})\lambda_1+(-\tfrac{7\delta_2}{11}-\tfrac{7\mu_2}{11})(\alpha_1+\gamma_1)+\tfrac{20\rho_1\lambda_2}{11}\Big]\sigma_{11}\\
&\quad-160\,a\,\beta_4\,\sigma_7\big[-\mu_1\lambda_1+\rho_1(\alpha_1+\gamma_1)\big],\\
F_{22} &= 88\,c_{12}\,\beta_2\,\varrho_1^2\,\sigma_7\Big[(\gamma_2-\tfrac{27\mu_2}{11}+\alpha_2-\tfrac{7\delta_2}{11})\alpha_1+\alpha_2\gamma_1+(\gamma_2-\tfrac{27\mu_2}{11}-\tfrac{7\delta_2}{11})\gamma_1-\lambda_1(\lambda_2-\tfrac{34\rho_2}{11})\Big]\\
&\quad-\tfrac{14}{11}\,c_{12}\,\beta_2\,\sigma_{11}\,\varrho_1^2\Big[(\theta_2+\tfrac{27\tau_2}{7})(\alpha_2+\gamma_2)-\tfrac{20\lambda_2\varepsilon_2}{7}\Big]\\
&\quad+240\,c_2\,\sigma_7\,\lambda_1\,\beta_4-320\,a\,\beta_4\Big[\varepsilon_2(\alpha_1+\gamma_1)+\lambda_1\tfrac{(\theta_2-3\tau_2)}{4}\Big]\\
&\quad-33\,c_{12}\,\beta_3^2\,\varrho_1^2\Big[(\gamma_2-\tfrac{27\mu_2}{11}+\alpha_2-\tfrac{7\delta_2}{11})\alpha_1+\alpha_2\gamma_1+(\gamma_2-\tfrac{27\mu_2}{11}-\tfrac{7\delta_2}{11})\gamma_1\\
&\quad-\lambda_1(\lambda_2-\tfrac{34\rho_2}{11})-\tfrac{14\sigma_{11}}{11}\Big[(\theta_2+\tfrac{27\tau_2}{7})(\alpha_2+\gamma_2)-\tfrac{20\lambda_2\varepsilon_2}{7}\Big]\Big],\\
F_3 &= -\tfrac{14}{5}\,c_{12}\,\beta_2\,\beta_4\,\sigma_7\,\varrho_1^2\big[\rho_2(\alpha_2+\gamma_2)-\tfrac{\lambda_2(\mu_2+\delta_2)}{2}\big]+6\,c_1\,\sigma_7\,\lambda_2\,\beta_4\\
&\quad+2\,a\,\beta_4\Big[(\tau_2+\theta_2-4\varepsilon_1)(\alpha_2+\gamma_2)+4\tau_1\lambda_2\Big]+\tfrac{21}{20}\,c_{12}\,\beta_3^2\,\sigma_{11}\,\sigma_7\,\varrho_1^2\big[\rho_2(\alpha_2+\gamma_2)-\tfrac{\lambda_2(\mu_2+\delta_2)}{2}\big]\\
&\quad+a\,\beta_4\,\sigma_7\Big[(\alpha_1+\gamma_1-4\mu_1)(\alpha_2+\gamma_2)+(-\lambda_2-2\rho_2)\lambda_1+(\mu_2+\delta_2)(\alpha_1+\gamma_1)+4\rho_1\lambda_2\Big],\\
F_{33} &= 40\Big\{\beta_4\Big[-272\,c_{12}\,\beta_2\,\sigma_{11}\,\sigma_7\,\varrho_1^2\Big(\rho_2(\alpha_2+\gamma_2)-\tfrac{27\lambda_2(\mu_2+\frac{7\delta_2}{27})}{34}\Big)-240\,c_2\,\sigma_{11}\,\sigma_7\,(\alpha_2+\gamma_2)\Big]
\end{aligned}
$$

$$+ 40\, a\, \beta_4\, \sigma_7 \Big[(\gamma_2 - 3\mu_2 + \alpha_2 + \delta_2)\alpha_1 + \alpha_2\gamma_1 + (\gamma_2 - 3\mu_2 + \delta_2)\gamma_1 - \lambda_1(\lambda_2 - 2\rho_2) \Big]$$
$$+ 80\, a\, \beta_4\, \sigma_{11} \Big[(\theta_2 - 3\tau_2)(\alpha_2 + \gamma_2) + 4\lambda_2\varepsilon_2 \Big] + 102\, c_{12}\, \beta_3^2\, \sigma_{11}\, \sigma_7\, \varrho_1^2 \Big[\rho_2(\alpha_2 + \gamma_2) - \tfrac{27\lambda_2(\mu_2 + \frac{7\delta_2}{27})}{34} \Big] \Big\},$$

$$F_4 = \rho_2(\alpha_2 + \gamma_2) - \tfrac{\lambda_2(\mu_2 + \delta_2)}{2},$$

$$F_{44} = \rho_2(\alpha_2 + \gamma_2) - \tfrac{3\lambda_2(\mu_2 - \frac{\delta_2}{3})}{2},$$

$$\beta = \beta_2\beta_4 - \tfrac{3\beta_3^2}{8}.$$

- $$\delta_1 = \frac{\sigma_{11}^2 \big(E_1\, \sigma_{12} + 2E_2\, \sigma_7\big) - \sigma_{11}\sigma_{12}\big(E_3\, \sigma_{12} + E_4\, \sigma_7\big) + \sigma_{12}^2\sigma_7 E_5}{\sigma_7\, \sigma_{12}\, \big[-\lambda_1\sigma_{12} + \sigma_{11}(\alpha_2 + \gamma_2) \big]}.$$

where

$$E_1 = 2(\theta_1 + \tau_1)\lambda_2 + 2(\tau_2 + \theta_2)(\alpha_2 + \gamma_2),$$
$$E_2 = \rho_2(\alpha_2 + \gamma_2) - \tfrac{1}{2}(\mu_2 + \delta_2)\lambda_2,$$
$$E_3 = 2\lambda_1(\tau_2 + \theta_2) + 2(\theta_1 + \tau_1)(\alpha_1 + \gamma_1),$$
$$E_4 = 2(\lambda_1\rho_2 - \rho_1\lambda_2) - (\alpha_1 + \gamma_1)(\mu_2 + \delta_2) + (\alpha_2 + \gamma_2)\mu_1,$$
$$E_5 = \lambda_1\mu_1 - 2\rho_1(\alpha_1 + \gamma_1).$$

- $$f_1 = \frac{X_7\, \sigma_{12}^4 + X_8\, \sigma_{12}^3 + X_9\, \sigma_{12}^2 + \Big(16\, X_1\, \sigma_{11}^3\, \sigma_7\, (\alpha_2 + \gamma_2)(\tau_2 + \theta_2) + 6\, X_1 X_2\, \sigma_{11}^2\, \sigma_7^2\Big)\sigma_{12} + 8\, X_1^2\, \sigma_{11}^3\, \sigma_7^2}{50\, \sigma_7^2\, \sigma_{12}^2\, \big(\sigma_{11}(\alpha_2 + \gamma_2) - \lambda_1\sigma_{12}\big)^2},$$

$$f_2 = \frac{8\, \lambda_1^2\, \sigma_{12}^4\, (\tau_2 + \theta_2)^2 + 50\, X_{10}\, \lambda_1\, \sigma_{12}^3 + X_{11}\, \sigma_{12}^2 + 50\, X_{12}\, \sigma_{11}\, \sigma_7\, \sigma_{12} + 8\, X_1^2\, \sigma_{11}^2\, \sigma_7^2}{50\, \sigma_7^2\, \sigma_{12}\, \big(\lambda_2\sigma_{11} - (\alpha_1 + \gamma_1)\sigma_{12}\big)^2}.$$

where

$$X_1 = \rho_2(\alpha_2 + \gamma_2) - \tfrac{\lambda_2}{2}(\mu_2 + \delta_2),$$

$$X_2 = (\alpha_1 + \gamma_1)(\alpha_2 + \gamma_2) - \lambda_1\Big(\lambda_2 + \tfrac{8\rho_2}{3}\Big) + \tfrac{4}{3}(\alpha_1 + \gamma_1)(\mu_2 + \delta_2),$$

$$X_3 = \tfrac{4}{3}(\alpha_1 + \gamma_1)(\mu_2 + \delta_2) - \lambda_1\Big(\lambda_2 + \tfrac{16\rho_2}{3}\Big),$$

$$X_4 = 2(\alpha_1 + \gamma_1)\gamma_2 + X_3,$$

$$X_5 = (\alpha_1 + \gamma_1)(\alpha_2^2 + \gamma_2^2) + \alpha_2 X_4 - \lambda_1\gamma_2\Big(\lambda_2 + \tfrac{16\rho_2}{3}\Big) + \tfrac{4}{3}\lambda_1\lambda_2(\mu_2 + \delta_2),$$

$$\begin{aligned} X_6 = \sigma_{11} &\Big[\lambda_1(100h_2\alpha_2 + 100h_2\gamma_2 - 50g_2\lambda_2) - 50g_2(\alpha_1 + \gamma_1)(\alpha_2 + \gamma_2) \Big] \\ &- 2\Big[(\alpha_1 + \gamma_1)(\alpha_2 + \gamma_2) + \lambda_1(-\lambda_2 + 4\rho_2) - 2(\alpha_1 + \gamma_1)(\mu_2 + \delta_2) \Big] \\ &\times \Big[(\alpha_1 + \gamma_1)(\alpha_2 + \gamma_2) + \lambda_1(-\lambda_2 - \rho_2) + \tfrac{1}{2}(\alpha_1 + \gamma_1)(\mu_2 + \delta_2) \Big], \end{aligned}$$

$$X_7 = 8\sigma_{11}\lambda_1^2(\tau_2 + \theta_2)^2 + 50\sigma_7^2(\alpha_1 + \gamma_1)(g_1\lambda_1 - h_1(\alpha_1 + \gamma_1)),$$

$$\begin{aligned} X_8 = &-16\, \lambda_1(\tau_2 + \theta_2)^2(\alpha_2 + \gamma_2)\, \sigma_{11}^2 \\ &- 50\, \sigma_7^2\sigma_{11} \Big[g_1(\alpha_1 + \gamma_1)(\alpha_2 + \gamma_2) + \lambda_2\big(g_1\lambda_1 - 2h_1(\alpha_1 + \gamma_1)\big) \Big] \\ &- 6\, (\tau_2 + \theta_2)\, \lambda_1\, X_2\, \sigma_7\, \sigma_{11}, \end{aligned}$$

$$X_9 = 8(\tau_2 + \theta_2)^2(\alpha_2 + \gamma_2)^2\sigma_{11}^3 + 50\sigma_7\sigma_{11}^2 \Big[\lambda_2\sigma_7(g_1(\alpha_2 + \gamma_2) - h_1\lambda_2) + \tfrac{3}{25}(\tau_2 + \theta_2)X_5 \Big]$$

$$
\begin{aligned}
&-2\sigma_7^2\Big[(\alpha_1+\gamma_1)(\alpha_2+\gamma_2)+\lambda_1(-\lambda_2+4\rho_2)-2(\alpha_1+\gamma_1)(\mu_2+\delta_2)\Big]\\
&\times\Big[(\alpha_1+\gamma_1)(\alpha_2+\gamma_2)+\lambda_1(-\lambda_2-\rho_2)+\tfrac{1}{2}(\alpha_1+\gamma_1)(\mu_2+\delta_2)\Big],
\end{aligned}
$$

$$
X_{10}=\sigma_7^2\big[g_2(\alpha_1+\gamma_1)-\lambda_1 h_2\big]-\tfrac{3}{25}(\tau_2+\theta_2)X_2\sigma_7-\tfrac{8}{25}(\tau_2+\theta_2)^2(\alpha_2+\gamma_2)\sigma_{11},
$$

$$
X_{11}=\sigma_7^2X_6+6\sigma_{11}\sigma_7X_5(\tau_2+\theta_2)+8\sigma_{11}^2(\tau_2+\theta_2)^2(\alpha_2+\gamma_2)^2,
$$

$$
X_{12}=\sigma_7\Big[\sigma_{11}(\alpha_2+\gamma_2)(g_2\lambda_2-h_2(\alpha_2+\gamma_2))+\tfrac{3}{25}X_1X_2\Big]+\tfrac{8}{25}(\tau_2+\theta_2)(\alpha_2+\gamma_2)\sigma_{11}X_1.
$$

- $\kappa=\sqrt{\dfrac{2\left[\left(\frac{3\beta_3^2}{8}-\beta_2\beta_4\right)c_{12}\varrho_1^2\sigma_{12}-a\beta_4\right]}{c_{12}\sigma_{12}\beta_4}}.$
- $\omega=\dfrac{18432\,\lambda_1\varrho_1^4c_{12}^2\sigma_{12}^4(\tau_2+\theta_2)Z_1+4608\,\varrho_1^4c_{12}^2\sigma_{12}^3Z_5-\sigma_{12}^2Z_6-128\,a^2\beta_4^2\sigma_{12}Z_7-128\,\sigma_7a^2\sigma_{11}\beta_4^2Z_2}{1536\,\sigma_{12}\beta_4^2c_{12}\left(\lambda_1\sigma_{12}^2(\tau_2+\theta_2)-\sigma_{12}Z_7-\sigma_7\sigma_{11}Z_2\right)}.$

where

$$
\begin{aligned}
Z_1&=\beta_0\beta_4^3-\left(\frac{\beta_1\beta_3}{4}+\frac{\beta_2^2}{144}\right)\beta_4^2+\frac{13}{192}\beta_2\beta_3^2\beta_4-\frac{13}{1024}\beta_3^4,\\
Z_2&=\rho_2(\alpha_2+\gamma_2)-\frac{\lambda_2}{2}(\mu_2+\delta_2),\\
Z_3&=\sigma_7\Big[(\alpha_1+\gamma_1)\big(\alpha_2+\gamma_2-\tfrac{13}{4}(\mu_2+\delta_2)\big)-\lambda_1\lambda_2+\tfrac{13}{2}\lambda_1\rho_2\Big]\\
&\quad-\tfrac{13}{2}\sigma_{11}(\alpha_2+\gamma_2)(\tau_2+\theta_2),\\
Z_4&=(\alpha_1+\gamma_1)\big(\alpha_2+\gamma_2-2(\mu_2+\delta_2)\big)-\lambda_1\lambda_2+4\lambda_1\rho_2,\\
Z_5&=\beta_4^2\Bigg\{\beta_0\beta_4\Big[Z_4\,\sigma_7-4\,\sigma_{11}(\alpha_2+\gamma_2)(\tau_2+\theta_2)\Big]\\
&\qquad+\sigma_7\Big[\frac{\beta_2^2}{36}\Big((\alpha_1+\gamma_1)(\alpha_2+\gamma_2+\tfrac{1}{2}(\mu_2+\delta_2))-(\lambda_2+\rho_2)\lambda_1\Big)-\frac{\beta_1\beta_3}{4}Z_4\Big]\\
&\qquad+\sigma_{11}(\alpha_2+\gamma_2)(\tau_2+\theta_2)\Big(\beta_1\beta_3+\frac{\beta_2^2}{36}\Big)\Bigg\}+Z_3\left(\frac{\beta_3^2\beta_2}{24}\beta_4-\frac{\beta_3^4}{128}\right),\\
Z_6&=\sigma_7Z_2\varrho_1^4c_{12}^2\sigma_{11}\Big[18432\,\beta_0\beta_4^3-4608\,\beta_4^2\Big(\beta_1\beta_3+\frac{\beta_2^2}{36}\Big)+1248\,\beta_2\beta_3^2\beta_4-234\,\beta_3^4\Big]-128\,\beta_4^2a^2\lambda_1(\tau_2+\theta_2),\\
Z_7&=\sigma_7\Big[(\alpha_1+\gamma_1)\Big(\alpha_2+\gamma_2+\tfrac{1}{2}(\mu_2+\delta_2)\Big)-\lambda_1(\lambda_2+\rho_2)\Big]+\sigma_{11}(\alpha_2+\gamma_2)(\tau_2+\theta_2).
\end{aligned}
$$

ORCID

Rajveer Singhay, https://orcid.org/0009-0009-9938-2064; **Sachin Kumar**, https://orcid.org/0000-0001-6883-7788; **Mohamed E. M. Alngar**, https://orcid.org/0000-0002-5436-7268; **Reham M. A. Shohib**, https://orcid.org/0000-0001-8352-5491; **Lina S. Calucag**, https://orcid.org/0000-0002-9090-3283; **Anjan Biswas**, https://orcid.org/0000-0002-8131-6044

REFERENCES

[1] A. Ankiewicz, and N. Akhmediev, "Higher-order integrable evolution equation and its soliton solutions," Phys. Lett. A, **378**, 358–361 (2014). https://doi.org/10.1016/j.physleta.2013.11.031

[2] A. Ankiewicz, Y. Wang, S. Wabnitz, and N. Akhmediev, "Extended nonlinear Schrödinger equation with higher-order odd and even terms and its rogue wave solutions," Phys. Rev. E, **89**, 012907 (2014). https://doi.org/10.1103/physreve.89.012907

[3] N. Karjanto, "Modeling wave packet dynamics and exploring applications: a comprehensive guide to the nonlinear Schrödinger equation," Mathematics, **12**(5), 744 (2024). https://doi.org/10.3390/math12050744

[4] A. R. Seadawy, and B. Alsaedi, "Contraction of variational principle and optical soliton solutions for two models of nonlinear Schrödinger equation with polynomial law nonlinearity," AIMS Mathematics, **9**(3), 6336–6367 (2024). https://doi.org/10.3934/math.2024309

[5] C. Peng, Z. Li, and H. Zhao, "New exact solutions to the Lakshmanan–Porsezian–Daniel equation with Kerr law of nonlinearity," Mathematical Problems in Engineering, **2022**(1), 7340373 (2022). https://doi.org/10.1155/2022/7340373

[6] H. H. Hussein, H. M. Ahmed, and W. Alexan, "Analytical soliton solutions for cubic–quartic perturbations of the Lakshmanan–Porsezian–Daniel equation using the modified extended tanh function method," Ain Shams Engineering Journal, **15**(3), 102513 (2024). https://doi.org/10.1016/j.asej.2023.102513

[7] N. A. Kudryashov, "Painlevé analysis of the Sasa–Satsuma equation," Phys. Lett. A, **525**, 129900 (2024). https://doi.org/10.1016/j.physleta.2024.129900

[8] P. Li, S. Shi, C. Xu, and M. U. Rahman, "Bifurcations, chaotic behavior, sensitivity analysis and new optical solitons solutions of Sasa–Satsuma equation," Nonlinear Dynamics, **112**(9), 7405–7415 (2024). https://doi.org/10.1007/s11071-024-09438-6

[9] A. Chowdury, D. J. Kedziora, A. Ankiewicz, and N. Akhmediev, "Soliton solutions of an integrable nonlinear Schrödinger equation with quintic terms," Phys. Rev. E, **91**, 032922 (2015). https://doi.org/10.1103/physreve.90.032922

[10] A. Chowdury, D. J. Kedziora, A. Ankiewicz, and N. Akhmediev, "Breather-to-soliton conversions described by the quintic equation of the nonlinear Schrödinger hierarchy," Phys. Rev. E, **91**, 032928 (2015). https://doi.org/10.1103/physreve.91.032928

[11] A. Chowdury, D. J. Kedziora, A. Ankiewicz, and N. Akhmediev, "Breather solutions of the integrable quintic nonlinear Schrödinger equation and their interactions," Phys. Rev. E, **91**, 022919 (2015). https://doi.org/10.1103/physreve.91.022919

[12] A. Biswas, J. Vega-Guzman, Y. Yıldırım, L. Moraru, C. Iticescu, and A. A. Alghamdi, "Optical solitons for the concatenation model with differential group delay: undetermined coefficients," Mathematics, **11**(9), 2012 (2023). https://doi.org/10.3390/math11092012

[13] A. H. Arnous, A. Biswas, Y. Yildirim, and A. S. Alshomrani, "Optical solitons for the dispersive concatenation model with differential group delay," Nonlinear Optics, Quantum Optics: Concepts in Modern Optics, **61** (2025).

[14] R. Singh, and S. Kumar, "Lie symmetry analysis, closed-form solutions and dynamics for the kinetics of phase separation in iron (Fe–Cr–X (X = Mo, Cu)) based on ternary alloys," Nonlinear Dynamics, **112**, 20255–20267 (2024). https://doi.org/10.1007/s11071-024-10112-0

[15] P. J. Olver, *Applications of Lie Groups to Differential Equations*, 2nd edn., Graduate Texts in Mathematics, vol. 107, (Springer, New York, NY, 1993).

ОПТИЧНІ СОЛІТОНИ ДЛЯ МОДЕЛІ КОНКАТЕНАЦІЇ З ДИФЕРЕНЦІАЛЬНОЮ ГРУПОВОЮ ЗАТРИМКОЮ, ПОБУДОВАНІ НА ОСНОВІ СИМЕТРІЇ ЛІ ТА ПІДХОДУ КУМАРА-МАЛІКА

Раджвір Сінгхай[1], Сачін Кумар[1], Мохамед Е. М. Алнгар[2], Рехам М. А. Шохіб[3], Ліна С. Калукаг[4], Анджан Бісвас[5,6,7,8,9*]

[1]*Кафедра математики та статистики, Центральний університет Пенджабу, Батінда, 151401, Пенджаб, Індія*

[2]*Програма математичної освіти, Факультет освіти та мистецтв, Університет Сохар, Сохар 311, Оман*

[3]*Кафедра фундаментальних наук, Факультет економіки та бізнес-адміністрування, Інноваційний університет, Шаркія, Єгипет*

[4]*Кафедра математики та природничих наук, Технологічний університет Бахрейну, Королівство Бахрейн*

[5]*Кафедра математики та фізики, Державний університет Грамблінга, Грамблінг, Луїзіана–71245, США*

[6]*Кафедра математики, Факультет природничих наук, Технічний університет Караденіз, Трабзон—61080, Туреччина*

[7]*Кафедра фізики та електроніки, Університет Хазар, Баку, Аризона—1096, Азербайджан*

[8]*Кафедра математики та прикладної математики, Університет медичних наук Сефако Макгатхо, Медунса—0204, Преторія, Південна Африка*

[9]*Науково-дослідний центр прикладних наук, Приватний університет прикладних наук, Амман—11937, Йорданія*

У цій роботі розглядається узагальнена модель конкатенації для двопроменевих оптичних волокон та отримані нові точні солітонні розв'язки. Використовуючи аналіз симетрії Лі, зв'язані еволюційні рівняння перетворюються через відповідні змінні подібності в керовану систему звичайних диференціальних рівнянь. Отримана редукована система потім обробляється методом Кумара-Маліка для отримання кількох класів явних розв'язків, записаних еліптичними, яскравими солітонними, темними солітонними та тригонометричними розв'язками Якобі. З відповідними обмеженнями параметрів ці класи спрощуються до знайомих яскравих, темних та періодичних солітонних хвиль. Для ілюстрації фізичної поведінки отриманих структур представлені репрезентативні графіки, які підкреслюють їхні особливості поширення та якісну стабільність. Загалом, поєднання редукції симетрії зі схемою Кумара-Маліка розширює каталог аналітичних розв'язків для моделі конкатенації та поглиблює розуміння нелінійної динаміки імпульсів у двопроменевих середовищах.

Ключові слова: *структура конкатенації; аналіз симетрії групи Лі; метод Кумара-Маліка; оптичні солітонні хвилі; двопроменеві волоконні середовища; розв'язки еліптичної функції Якобі*